

**Design and application of a novel Laser-Doppler Velocimeter for turbulence structural measurements in turbulent boundary layers**

Kevin Todd Lowe

Dissertation submitted to the faculty of the Virginia Polytechnic Institute and State University in partial fulfillment of the requirements for the degree of

Doctor of Philosophy  
In  
Aerospace Engineering

Roger L. Simpson, Committee Chair  
William J. Devenport  
James F. Marchman  
Saad Ragab  
Alfred L. Wicks

September 18, 2006  
Blacksburg, Virginia

Keywords: flow measurement techniques, non-intrusive flow measurement, laser flow diagnostics, laser-Doppler velocimetry, laser-Doppler anemometry, acceleration measurement, Reynolds stress transport, turbulence, boundary layers, transient signal processing, chirp signal processing

# **Design and application of a novel Laser-Doppler Velocimeter for turbulence structural measurements in turbulent boundary layers**

Kevin Todd Lowe

## **ABSTRACT**

An advanced laser-Doppler velocimeter (LDV), deemed the ‘comprehensive LDV’ (CompLDV), is designed to acquire fully-resolved turbulence structural measurements in high Reynolds number two- and three-dimensional turbulent boundary layers. The new instrument combines, for the first time, new techniques allowing for the direct measurement of particle acceleration and sub-measurement-volume-scale position resolution so that second-order 3D particle trajectories may be measured at high repetitions. Using these measurements, several terms in the Reynolds stress transport equations may be directly estimated, giving new data for modeling and understanding the processes leading to the transport of turbulence in boundary layer flows.

Due to the unique performance of the probe, many aspects of LDV instrumentation development were addressed. The LDV configuration was optimized for lowest uncertainties by considering the demanding applications of particle position and acceleration measurements. Low noise light detection and signal conditioning was specified for the three electronic channels. A high-throughput data acquisition system allows for exceptional burst rate acquisition. Signal detection and processing algorithms have been implemented which draw from previous techniques but also address distinctive problems with the current system. In short, the instrument was designed to advance the state-of-the-art in LDV systems.

Measurements presented include turbulence dissipation rate and fluctuating velocity-pressure gradient correlations that have been measured in 2D and 3D turbulent boundary layers using the unique capabilities of the CompLDV—many of these measurements are the first of their kind ever acquired in high Reynolds number turbulent flows. The flat-plate turbulent boundary layer is studied at several Reynolds numbers up to  $Re_\theta \approx 7500$  to examine Reynolds numbers effects on terms such as the velocity-pressure gradient correlation and the dissipation rate in the Reynolds transport equations. Measurements are also presented in a pressure-driven three-dimensional turbulent boundary layer created upstream from a wing-body junction. The current results complement the extensive data from previous studies and provide even richer depth of knowledge on the most-completely-documented 3D boundary layer flow in existence. Further measurements include the wakes of three circular-cylinder protuberances submerged in a constant pressure turbulent boundary layer.

## **Acknowledgements**

The sincerest thanks go to my wife, Natasha, and my family for their ever-present support and patience throughout my education. The role of the loving encouragement that they continue to provide cannot be understated.

It has been an honor to study under my advisor, Dr. Roger L. Simpson. In addition to the immense role that he has played in my education, he has been an inspiration due the example he sets with his leadership—both professionally and in the community. Dr. Simpson has shaped my graduate education and professional maturation through many avenues, and the freedom that he granted to me to explore my research will always be appreciated.

The members of my advisory committee, Drs. William Devenport, Jim Marchman, Saad Ragab, and Alfred Wicks, have been a source of encouragement and advice; and their interest in my project and success has been sincere and appreciated by the author. Each of these esteemed professionals has contributed much to my education—in the classroom and beyond. I sincerely appreciate the time and commitment that they have given to serve.

It would be impossible to conduct this research without the kind assistance that many donate. Numerous problems were solved and hardware was developed with the help of the professional staff of AOE. Steve Edwards, James Lambert, Luke Scharf, Bruce Stanger, and Mike Vaught have all contributed much time and energy to my project—in building new parts, fixing ones that I messed-up, solving software problems, debugging equipment, and contributing their perspective in conversations that led to new solutions. The student researchers with whom I have worked have also given their time selflessly and kindly—Jeremy Bennington, Gwibo Byun, Joshua DeMoss, John Fussell, Jacob George, Kenneth Granlund, Andrew Hopkins, Deirdre Hunter, David Kuhl, Edgar Orsi, Devin Stewart, Qing Tian, Genglin Tang, and Nathaniel Varano. I also wish to thank those professionals at NASA Langley Research Center who gave time and resources to contribute to this project, including Dan Neuhart for the on-site particle sizing measurements and Ronald Gouge for hardware fabrication work. Thanks go out to the kind individuals in the Department of AOE who have helped so much with the logistics of conducting this project and obtaining my graduate education—Gail Coe, Wanda Foushee, Jane Johnston, Sue Teel, and Betty Williams.

Without the gracious sponsorship that has been provided from outside sources, none of this work would exist. Several organizations including the National Science Foundation, Air Force Office of Scientific Research, and NASA have seen it fit to foster the development of our advanced instrumentation and in doing so fund my graduate education—this is sincerely appreciated.

Finally, I wish to thank the entire faculty of the Department of AOE through whom my zeal for knowledge in the aerospace sciences has been sustained and is now greater than ever. It has been an honor and pleasure to study in this department and to know the distinguished faculty that makes it one of the best.

# TABLE OF CONTENTS

1	Introduction.....	1
1.1	Motivation for advanced turbulence measurements .....	2
1.2	Review of advanced measurement techniques .....	5
1.2.1	Velocity gradient measurement .....	5
1.2.2	Lagrangian acceleration measurement.....	6
1.3	Structure of the dissertation .....	8
1.4	References.....	8
2	Instrumentation and apparatus .....	12
2.1	Advanced turbulent flow instrumentation development.....	12
2.2	Recent work .....	12
2.2.1	Laser-Doppler acceleration measurement.....	12
2.2.2	Enhanced-spatial-resolution laser-Doppler velocimetry.....	13
2.2.3	Velocity gradient laser-Doppler measurements.....	14
2.2.4	Laser-Doppler signal processing.....	14
2.3	Comprehensive laser-Doppler velocimetry .....	14
2.3.1	General Uncertainty Estimation.....	15
2.3.2	Preliminary specifications for the CompLDV .....	17
2.3.3	The CompLDV design process.....	17
2.4	Facilities and apparatus.....	107
2.4.1	Measurement facilities.....	107
2.4.2	Flow Seeding .....	107
2.5	References.....	112
3	Signal processing .....	117
3.1	Laser-Doppler Burst Processing .....	117
3.1.1	Signal description.....	117
3.1.2	Burst Recognition and Envelope Estimation .....	121
3.1.3	Validation of the complete burst processor .....	148
3.2	Spectral Analysis for Non-equidistantly Sampled Data .....	149
3.2.1	Methods for estimating time-delay and frequency-domain information from LDV data.....	150
3.2.2	Slot correlation validation.....	152
3.3	References.....	159
4	Results.....	162
4.1	2D flat-plate turbulent boundary layers .....	162
4.1.1	CompLDV Measurements .....	165
4.1.2	Volume-averaged velocity statistics .....	171
4.1.3	Spectral analysis.....	176
4.1.4	Turbulence transport.....	186
4.2	Isolated Protuberances .....	206
4.2.1	Volume-averaged statistics .....	207
4.2.2	Spectral analysis.....	213
4.3	3D Turbulent Boundary Layers .....	223
4.3.1	Setup and oil-flow.....	223
4.3.2	CompLDV3 data.....	224

4.3.3	Turbulence transport .....	240
4.4	References .....	244
5	Concluding remarks .....	248
Appendix A.1	The real-time PC-based 3D LDV signal acquisition and processing system: a User's Manual .....	251
Appendix A.2	A multiple channel coincidence-testing trigger for laser-Doppler signal detection .....	264

## List of Figures

Figure 2.1.	Schematic of the optical arrangement for measuring the gradients of the 'U' and 'V' velocities; the components for measuring 'W' gradients are not shown since they do not lie in the same plane, although the arrangement is identical to that of the 'U' s .....	24
Figure 2.2.	Schematic illustrating the components of the $\Delta v$ prototype system. Each component is labeled as follows: PCX: plano-convex lens, M: mirror, PH: pinhole array and alignment apparatus, PMT: photomultiplier tube, CYL-PCX: cylindrical plano-convex lens, PR .....	25
Figure 2.3.	Orientation and dimensions of the pinhole array used to spatially filter the image of the measurement volume. ....	25
Figure 2.4.	Photograph of the Prototype ROSVOR system.....	26
Figure 2.5.	Schematic of the complete ROSVOR LDV. Note the gross features of the design: base-plate mounted onto the heavy-duty three-axis traverse, two identical transmitting system three receiving systems mounted to base-plate, truss structure mounted to the base plate with two sets of receiving lens and mirror systems for $\Delta u$ and $\Delta w$ . ....	26
Figure 2.6.	Plot of the calibration of the prototype ROSVOR LDV. ....	27
Figure 2.7.	Schematic of the intersection of two coherent laser beams forming an interference fringe pattern.....	29
Figure 2.8.	Schematic of overlapping fringe sets with varying fringe spacings along the measurement volume beam-bisector.....	29
Figure 2.9.	Schematic of the off-waist intersection of two coherent laser beams forming interference fringes with $\frac{\partial d}{\partial x'} > 0$ .....	30
Figure 2.10.	Schematic of the comprehensive LDV generation 1 probe.....	31
Figure 2.11.	Photograph of the comprehensive LDV laser beams in a test flow. ....	32
Figure 2.12.	Example of fringe calibration function from the published data of Czarske et al. (2002). ....	34
Figure 2.13.	Schematic of the optical table configuration used for the first CompLDV optical system. Schematic is credited to Devin Stewart. ....	39
Figure 2.14.	Schematic of the optical table configuration used for the three-color CompLDV optical systems. ....	39
Figure 2.15.	Diagram of the light separation and detection optics and photonics. F, multimode fiber optic transmitting received light; L, 19mm focal length lens; D, dichroic filter; I, interference narrow bandpass filter; PMT, photomultiplier tube; A, anode signal out; HV, high voltage in. ....	42
Figure 2.16.	Predicted fringe variation from Gaussian beam propagation due to off-waist crossing of beams with parameters for the CompLDV1. ....	47

Figure 2.17. Relative truncation error of equation (2.27) compared to the exact equation (2.19) where $d_0 \equiv \frac{\lambda}{2 \sin \theta}$ .....	47
Figure 2.18. 20:1 uncertainties in the mean velocities throughout a 2D flat plate turbulent boundary layer profile non-dimensionalized on the wall friction velocity.....	48
Figure 2.19. 20:1 uncertainties in the Reynolds normal stresses throughout a 2D flat plate turbulent boundary layer profile non-dimensionalized on the wall friction velocity. ....	49
Figure 2.20. 20:1 uncertainties in the Reynolds shear stresses throughout a 2D flat plate turbulent boundary layer profile non-dimensionalized on the wall friction velocity. ....	49
Figure 2.21. 20:1 uncertainties in velocity triple-products throughout a 2D flat plate turbulent boundary layer profile non-dimensionalized on the wall friction velocity. ....	50
Figure 2.22. 20:1 uncertainties in velocity triple-products throughout a 2D flat plate turbulent boundary layer profile non-dimensionalized on the wall friction velocity. ....	50
Figure 2.23. 20:1 uncertainties in velocity triple-products throughout a 2D flat plate turbulent boundary layer profile non-dimensionalized on the wall friction velocity. ....	51
Figure 2.24. Geometry of the beam and measurement vectors for a pair of interfering beams forming a measurement volume. ....	52
Figure 2.25. Example of the results from the wire/wheel calibration.....	55
Figure 2.26. Schematic depicting the 4 $\mu m$ diameter tungsten wire affixed to the optical chopper wheel. ....	56
Figure 2.27. Photograph of the calibration rig.....	56
Figure 2.28. Scatter plot of instantaneous Doppler frequency measurements versus the ratio between these Doppler frequencies for (a) inner and (b) outer overlapping measurement volumes sharing a single bisector direction.....	58
Figure 2.29. Plot of mean fringe space measurements versus the ratio between these Doppler frequencies for (a) inner and (b) outer overlapping measurement volumes sharing a single bisector direction for two different runs. Exhibits the repeatability of the technique. Note the range of scales on the ordinates. ....	59
Figure 2.30. Photograph of a highly-magnified fringe pattern in the cross-section of a dual-beam LDV measurement volume. ....	61
Figure 2.31. Photograph of the fringe image obtained for the design waist condition. ....	62
Figure 2.32. Schematic of the plate and cone viscometer arrangement.....	63
Figure 2.33. Oil flow visualization photograph for cone angular rate of 1600 RPM. ....	65
Figure 2.34. Mean velocity as a function of position along the measurement volume for a) 40 MHz volumes @ 2200 RPM, b) 60 MHz volumes @ 3400 RPM, and c) 80 MHz volumes @ 1500 RPM.....	68
Figure 2.35. RMS velocities as a function of position along the measurement volume for a) 40 MHz volumes @ 2200 RPM, b) 60 MHz volumes @ 3400 RPM, and c) 80 MHz volumes @ 1500 RPM.....	69
Figure 2.36. Volume-averaged statistics for the plate and cone flow measured by the modified CompLDV1. ....	71

Figure 2.37. Scatter plots of the instantaneous measurements of (a) tangential, (b) normal-to-plate, and (c) radial velocities for the plate and cone flow measured with the modified CompLDV1. ....	73
Figure 2.38. Statistics of velocity/position data from the plate and cone flow measured with the modified CompLDV1. ....	73
Figure 2.39. Schematic of the head-on view of the blue and green/purple transmitting heads. Pairs of beams with the same label interfere to form fringes. Converging fringe sets in measurement volume: 1, 3, 5; Diverging fringe sets in measurement volume: 2, 4. ....	77
Figure 2.40. Schematic of the probe geometry. ....	78
Figure 2.41. Photograph of CompLDV generation 3 configuration. ....	78
Figure 2.42. Photograph of laser beam configuration for the CompLDV3. ....	79
Figure 2.43. 20:1 uncertainties in the mean velocities throughout a 2D flat plate turbulent boundary layer profile non-dimensionalized on the wall friction velocity. ....	82
Figure 2.44. 20:1 uncertainties in the Reynolds normal stresses throughout a 2D flat plate turbulent boundary layer profile non-dimensionalized on the wall friction velocity. ....	82
Figure 2.45. 20:1 uncertainties in the Reynolds shear stresses throughout a 2D flat plate turbulent boundary layer profile non-dimensionalized on the wall friction velocity. ....	83
Figure 2.46. 20:1 uncertainties in velocity triple-products throughout a 2D flat plate turbulent boundary layer profile non-dimensionalized on the wall friction velocity. ....	83
Figure 2.47. 20:1 uncertainties in velocity triple-products throughout a 2D flat plate turbulent boundary layer profile non-dimensionalized on the wall friction velocity. ....	84
Figure 2.48. 20:1 uncertainties in velocity triple-products throughout a 2D flat plate turbulent boundary layer profile non-dimensionalized on the wall friction velocity. ....	84
Figure 2.49. Schematic of an instance for the CompLDV3 extrapolated measurement volume containing several particles with estimated velocities and positions. $\vec{r}_i$ is the position vector of the $i^{th}$ particle, $\vec{U}_i$ is the velocity vector of the $i^{th}$ particle, $\vec{r}_c$ is the position vector of the centroid of the $N$ particles considered for velocity gradient tensor estimation, and $\vec{U}_c$ is the centroid velocity vector for the $N$ particles. ....	86
Figure 2.50. Normalized histogram illustrating the similarity of histograms for each of the three gradients considered. ....	94
Figure 2.51. Normalized histogram for each of the three gradients considered when a Gaussian distribution of velocity gradients are simulated with variances given by Honkan and Andreopoulos (1997). ....	94
Figure 2.52. Sub-measurement volume resolution measurements in a 2D flat plate turbulent boundary layer with assumed fringe gradients. ....	101
Figure 2.53. Sub-measurement volume resolution measurements in a 2D flat plate turbulent boundary layer with calibrated fringe gradients. ....	101
Figure 2.54. Volume-averaged mean azimuthal velocities in the plate and cone flow as measured with the CompLDV3. ....	104

Figure 2.55. Volume-averaged mean velocities normalized by the local cone velocity and measured gap-height for the plate and cone flow with the CompLDV3. ....	104
Figure 2.56. Volume-averaged Reynolds stresses normalized by the local cone velocity and measured gap-height for the plate and cone flow with the CompLDV3. ....	105
Figure 2.57. Sub-measurement-volume resolved mean azimuthal velocity measurements in the plate and cone flow using the CompLDV3.....	105
Figure 2.58. Sub-measurement-volume resolved mean radial velocity measurements in the plate and cone flow using the CompLDV3.....	106
Figure 2.59. Sub-measurement-volume resolved mean flow-angle measurements in the plate and cone flow using the CompLDV3.....	106
Figure 2.60. The VAP/CON monodisperse aerosol generator (figure due to Devin Stewart).....	110
Figure 2.61. Normalized concentration histogram of the DOP particle diameter distribution for a Laskin nozzle supply air pressure of 16 psi and a VAP/CON outer surface temperature of 768°F.....	111
Figure 2.62. Normalized concentration histogram of the DOP particle diameter distribution for a Laskin nozzle supply air pressure of 15 psi without VAP/CON unit. ....	111
Figure 3.1. Model burst with noise. ....	119
Figure 3.2. Comparison of the SNR for signals with constant noise levels versus noise levels that vary in time as a Gaussian. ....	119
Figure 3.3. (a) Time series and (b) spectrogram of an LDV burst containing two Doppler signals. Note that the noise is not constant amplitude throughout the signal but varies with time. ....	120
Figure 3.4. Burst amplitude (black) and 2x the RMS power (blue circles) for a typical LDV signal snippet. ....	123
Figure 3.5. Final burst detection metric versus sample index.....	125
Figure 3.6. Semi-logarithmic amplitude of burst time-series for a dual burst, along with the RMS power metric. ....	126
Figure 3.7. First burst in the dual burst pair example. ....	127
Figure 3.8. Second burst in the dual burst pair example.....	127
Figure 3.9. The Cramer-Rao Lower Bound for the standard deviation in frequency for the signal described by equation (3.14). ....	131
Figure 3.10. The Cramer-Rao Lower Bound for the standard deviation in chirp for the signal described by equation (3.14). ....	131
Figure 3.11. Spectrum of a signal with and without zero-padding. $f_s$ is the sampling frequency of the signal.....	134
Figure 3.12. Illustration of a chirped burst and two nominal processing zones. ....	135
Figure 3.13. RMS error in midpoint frequency calculations for signal simulations of a chirped burst with noise. Gaussian, Gaussian frequency interpolation; Centroid, Centroid frequency interpolation; whole, entire burst used for computing single DFT; average, burst broken into two parts to form two power spectral densities and frequency result determined by average; ZP, N zeros padded.....	137
Figure 3.14. Bias of the frequency measurement for the parameters of signal 1. Gaussian, Gaussian frequency interpolation; Centroid, Centroid frequency interpolation; whole, entire burst used for computing single DFT; average, burst broken into two	

parts to form two power spectral densities and frequency result determined by average; ZP, N zeros padded. ....	138
Figure 3.15. RMS chirp rate error from signal simulations of a chirped burst with noise for . Gaussian, Gaussian frequency interpolation; Centroid, Centroid frequency interpolation; ZP, N zeros padded. ....	138
Figure 3.16. Bias in the chirp rate. Gaussian, Gaussian frequency interpolation; Centroid, Centroid frequency interpolation; ZP, N zeros padded. ....	139
Figure 3.17. Simulation results for the DFT with Gaussian interpolation to determine the frequency of a Gaussian windowed LDV burst over a cycle of one frequency spectral line and several chirp lines. (a) Contours of frequency bias errors normalized by the spectral line width. (b) Contours of RMS errors for the estimated frequency normalized by the Cramer-Rao Lower Bound. ....	142
Figure 3.18. Uncertainty of estimated Doppler frequency chirp ( $\gamma$ ) as a function of normalized signal-to-noise ratio, $SNR_I$ for finite difference methods (FD) and discrete chirp Fourier transform methods (DCFT). CRLB: Cramer-Rao lower bound, ZP: 2-times zero-padding, Parabolic: Parabolic interpolation of chirp power distribution, Centroid: centroid interpolation of chirp power distribution. ....	144
Figure 3.19. Relative frequency estimator RMS error over a frequency sweep with $SNR_I=24$ dB. Gaussian, Gaussian interpolation of spectral lines in frequency domain; Gaussian + ZP, Gaussian interpolation of spectral lines in frequency domain with $N$ zeros padded; CRLB, Cramer-Rao Lower Bound. ....	144
Figure 3.20. Relative frequency estimator bias error over a frequency sweep with $SNR_I=24$ dB. Gaussian, Gaussian interpolation of spectral lines in frequency domain; Gaussian + ZP, Gaussian interpolation of spectral lines in frequency domain with $N$ zeros padded. ....	145
Figure 3.21. Relative chirp rate estimator RMS error over a frequency sweep with $SNR_I=24$ dB. Parabolic, Parabolic interpolation of chirp lines; Parabolic + ZP, Parabolic interpolation of chirp lines with $N$ zeros padded. Centroid, Centroid interpolation of chirp lines; Centroid + ZP, Parabolic interpolation of chirp lines with $N$ zeros padded; CRLB, Cramer-Rao Lower Bound. ....	145
Figure 3.22. Relative chirp rate estimator bias error over a frequency sweep with $SNR_I=24$ dB. Parabolic, Parabolic interpolation of chirp lines; Parabolic + ZP, Parabolic interpolation of chirp lines with $N$ zeros padded. Centroid, Centroid interpolation of chirp lines; Centroid + ZP, Parabolic interpolation of chirp lines with $N$ zeros padded; CRLB, Cramer-Rao Lower Bound. ....	146
Figure 3.23. Simulation results for the DFT/DCFT combination technique with Gaussian interpolation to determine the frequency of a Gaussian windowed LDV burst over a cycle of one frequency spectral line and several chirp lines. (a) Contours of frequency bias errors normalized by the spectral line width. (b) Contours of RMS errors for the estimated frequency normalized by the Cramer-Rao Lower Bound. ....	147
Figure 3.24. Comparison of the simulated U signal with the one processed using the CompLDV processing algorithms. ....	149
Figure 3.25. Graphical depiction of the Poisson arrival time statistics for particle-laden flows. ....	150
Figure 3.26. Cross-correlation of sine-cosine pair. ....	154
Figure 3.27. Cross-correlation of sine-cosine pair near zero delay. ....	155

Figure 3.28. Autocorrelation of sine.....	155
Figure 3.29. Autocorrelation of sine near zero delay.....	156
Figure 3.30. Autocorrelation of Gaussian noise as computed with the slot correlation with linear interpolation.....	156
Figure 3.31. Autocorrelation of linearly interpolated Gaussian noise near zero delay as computed with the slot correlation.....	157
Figure 3.32. Autocorrelation of regularly sampled data obtained from linearly interpolated Gaussian noise.....	157
Figure 3.33. Autocorrelation of Gaussian noise with no interpolation as computed with the slot correlation.....	158
Figure 3.34. Autocorrelation of Gaussian noise with no interpolation near zero delay as computed with the slot correlation.....	158
Figure 3.35. Cross-correlation of two Gaussian noise signals with no interpolation as computed with the slot correlation.....	159
Figure 4.1. Resolved measurements of the stream-wise mean velocity in the 2DFPTBL at $Re_\theta = 4113$ .....	167
Figure 4.2. Resolved measurements of the stream-wise mean velocity in the 2DFPTBL at $Re_\theta = 5929$ .....	167
Figure 4.3. Resolved measurements of the stream-wise mean velocity in the 2DFPTBL at $Re_\theta = 7497$ .....	168
Figure 4.4. Resolved measurements of the Reynolds normal stresses in the 2DFPTBL at $Re_\theta = 4113$ .....	168
Figure 4.5. Resolved measurements of the Reynolds normal stresses in the 2DFPTBL at $Re_\theta = 5929$ .....	169
Figure 4.6. Resolved measurements of the Reynolds normal stresses in the 2DFPTBL at $Re_\theta = 7497$ .....	169
Figure 4.7. Resolved measurements of the Reynolds normal stresses in the 2DFPTBL at $Re_\theta = 4113$ .....	170
Figure 4.8. Resolved measurements of the Reynolds normal stresses in the 2DFPTBL at $Re_\theta = 5929$ .....	170
Figure 4.9. Resolved measurements of the Reynolds normal stresses in the 2DFPTBL at $Re_\theta = 7497$ .....	171
Figure 4.10. Stream-wise mean velocities in the 2DFPTBL at four Reynolds numbers. C1: Measurements acquired with the CompLDV1; C3: Measurements acquired with the CompLDV3.....	172
Figure 4.11. Comparison of the stream-wise mean velocities in the 2DFPTBL compared to the results of DeGraaff and Eaton (2000). C1: Measurements acquired with the CompLDV1; C3: Measurements acquired with the CompLDV3; D&E: measurements reported by DeGraaff and Eaton (2000). .....	173
Figure 4.12. Comparison of the stream-wise Reynolds stress in the 2DFPTBL compared to the results of DeGraaff and Eaton (2000). C1: Measurements acquired with the CompLDV1; C3: Measurements acquired with the CompLDV3; D&E: measurements reported by DeGraaff and Eaton (2000). .....	173

Figure 4.13. Comparison of the normal-to-wall Reynolds stress in the 2DFPTBL compared to the results of DeGraaff and Eaton (2000). C1: Measurements acquired with the CompLDV1; C3: Measurements acquired with the CompLDV3; D&E: measurements reported by DeGraaff and Eaton (2000). .....	174
Figure 4.14. Span-wise Reynolds stress in the 2DFPTBL at four Reynolds numbers. C1: Measurements acquired with the CompLDV1; C3: Measurements acquired with the CompLDV3.....	174
Figure 4.15. Comparison of the Reynolds shear stress in the 2DFPTBL compared to the results of DeGraaff and Eaton (2000). C1: Measurements acquired with the CompLDV1; C3: Measurements acquired with the CompLDV3; D&E: measurements reported by DeGraaff and Eaton (2000). .....	175
Figure 4.16. Comparison of the stream-wise Reynolds normal stress in the 2DFPTBL compared to the results of DeGraaff and Eaton (2000) with mixed scaling to account for Reynolds number effects. C1: Measurements acquired with the CompLDV1; C3: Measurements acquired with the CompLDV3; D&E: measurements reported by DeGraaff and Eaton (2000). .....	175
Figure 4.17. Span-wise Reynolds normal stress in the 2DFPTBL with mixed scaling to account for Reynolds number effects. C1: Measurements acquired with the CompLDV1; C3: Measurements acquired with the CompLDV3; D&E: measurements reported by DeGraaff and Eaton (2000). .....	176
Figure 4.18. Energy spectra on viscous wall scaling for the stream-wise Reynolds normal stress in the 2DFPTBL at $Re_\theta = 4113$ . The legend gives vertical locations in $y^+$ . The lines in the plot are at slopes $\sim f^1$ and $\sim f^{5/3}$ .....	178
Figure 4.19. Energy spectra on viscous wall scaling for the stream-wise Reynolds normal stress in the 2DFPTBL at $Re_\theta = 5929$ . The legend gives vertical locations in $y^+$ . The lines in the plot are at slopes $\sim f^1$ and $\sim f^{5/3}$ .....	179
Figure 4.20. Energy spectra on viscous wall scaling for the stream-wise Reynolds normal stress in the 2DFPTBL at $Re_\theta = 7497$ . The legend gives vertical locations in $y^+$ . The lines in the plot are at slopes $\sim f^1$ and $\sim f^{5/3}$ .....	179
Figure 4.21. Energy spectra on viscous wall scaling for the normal-to-wall Reynolds normal stress in the 2DFPTBL at $Re_\theta = 4113$ . The legend gives vertical locations in $y^+$ . The lines in the plot are at slopes $\sim f^1$ and $\sim f^{5/3}$ .....	180
Figure 4.22. Energy spectra on viscous wall scaling for the normal-to-wall Reynolds normal stress in the 2DFPTBL at $Re_\theta = 5929$ . The legend gives vertical locations in $y^+$ . The lines in the plot are at slopes $\sim f^1$ and $\sim f^{5/3}$ .....	180
Figure 4.23. Energy spectra on viscous wall scaling for the normal-to-wall Reynolds normal stress in the 2DFPTBL at $Re_\theta = 7497$ . The legend gives vertical locations in $y^+$ . The lines in the plot are at slopes $\sim f^1$ and $\sim f^{5/3}$ .....	181
Figure 4.24. Energy spectra on viscous wall scaling for the span-wise Reynolds normal stress in the 2DFPTBL at $Re_\theta = 4113$ . The legend gives vertical locations in $y^+$ . The lines in the plot are at slopes $\sim f^1$ and $\sim f^{5/3}$ .....	181
Figure 4.25. Energy spectra on viscous wall scaling for the span-wise Reynolds normal stress in the 2DFPTBL at $Re_\theta = 5929$ . The legend gives vertical locations in $y^+$ . The lines in the plot are at slopes $\sim f^1$ and $\sim f^{5/3}$ .....	182

Figure 4.26. Energy spectra on viscous wall scaling for the span-wise Reynolds normal stress in the 2DFPTBL at $Re_\theta = 7497$ . The legend gives vertical locations in $y^+$ . The lines in the plot are at slopes $\sim f^1$ and $\sim f^{5/3}$ .	182
Figure 4.27. Energy spectra on viscous wall scaling for the Reynolds shear stress in the 2DFPTBL at $Re_\theta = 4113$ . The legend gives vertical locations in $y^+$ . The line in the plot is at a slope of $\sim f^{7/3}$ .	183
Figure 4.28. Energy spectra on viscous wall scaling for the Reynolds shear stress in the 2DFPTBL at $Re_\theta = 5929$ . The legend gives vertical locations in $y^+$ . The line in the plot is at a slope of $\sim f^{7/3}$ .	183
Figure 4.29. Energy spectra on viscous wall scaling for the Reynolds shear stress in the 2DFPTBL at $Re_\theta = 7497$ . The legend gives vertical locations in $y^+$ . The line in the plot is at a slope of $\sim f^{7/3}$ .	184
Figure 4.30. Coherency measurements for the Reynolds shear stress for the 2DFPTBL at $Re_\theta = 4113$ . The legend gives vertical locations in $y^+$ .	185
Figure 4.31. Coherency measurements for the Reynolds shear stress for the 2DFPTBL at $Re_\theta = 5929$ . The legend gives vertical locations in $y^+$ .	185
Figure 4.32. Coherency measurements for the Reynolds shear stress for the 2DFPTBL at $Re_\theta = 7497$ . The legend gives vertical locations in $y^+$ .	186
Figure 4.33. Stream-wise velocity acceleration correlation for the 2D FPTBL at $Re_\theta = 6350$ compared to the data of a) Spalart (1988) and b) Abe et al. (2001). Adapted from Lowe and Simpson (2006).	188
Figure 4.34. Velocity quadrant analysis of the streamwise velocity–acceleration correlation for the 2D FPTBL at $Re_\theta = 6350$ . Adapted from Lowe and Simpson (2006).	189
Figure 4.35. Skewness of the streamwise velocity fluctuation. (*) Current data, (a) data of DeGraaff and Eaton (2000). The dashed line indicates the value for a Gaussian distribution. Adapted from Lowe and Simpson (2006).	189
Figure 4.36. Transport budget for the turbulent kinetic energy in the 2D FPTBL at $Re_\theta = 6350$ . Adapted from Lowe and Simpson (2006).	191
Figure 4.37. The balance of the stream-wise velocity-acceleration equation using isotropic dissipation estimates and measurements of the viscous diffusion and velocity–acceleration correlation in the 2D FPTBL at $Re_\theta = 6350$ . Adapted from Lowe and Simpson (2006).	191
Figure 4.38. Fit to Pope’s model for the stream-wise velocity auto-spectrum of the ComplDV3 from the 2DFPTBL at $Re_\theta = 7497$ at $y^+=600$ where $\eta = 61\mu m$ and	
$L = \left( \frac{3}{2} \overline{u^2} \right)^{3/2} / \varepsilon$	194
Figure 4.39. Same as Figure 4.38, but with $L \equiv k^{3/2} / \varepsilon$ .	194
Figure 4.40. Comparison of the dissipation estimate for the directly-estimated stream-wise velocity gradient in the stream-wise direction to the spectral dissipation rate estimates and the production for the 2DFPTBL at $Re_\theta = 5929$ . VG, Directly-estimated dissipation rate from velocity gradients; S, Spectral-estimates of	

dissipation rate; Diamonds are TKE production computed from Reynolds-averaged statistics.....	196
Figure 4.41. Raw mean-square velocity gradient information for the 2DFPTBL at $Re_\theta = 5929$ .....	197
Figure 4.42. Corrected mean-square velocity gradient information for the 2DFPTBL at $Re_\theta = 5929$ .....	198
Figure 4.43. Dissipation rate measurements for the 2DFPTBL at $Re_\theta = 5929$ . VG, Direct estimation of velocity gradients; S, Spectral estimation with Taylor's Hypothesis; DNS, Low Reynolds number simulation data of Spalart (1988). .....	199
Figure 4.44. Dissipation rate measurements for the 2DFPTBL at $Re_\theta = 7497$ . VG, Direct estimation of velocity gradients; S, Spectral estimation with Taylor's Hypothesis; DNS, Low Reynolds number simulation data of Spalart (1988). .....	199
Figure 4.45. Non-isotropic Reynolds stress dissipation rates measured in the 2DFPTBL at $Re_\theta = 5929$ . C3, CompLDV3; DNS, Simulation data of Spalart (1988). .....	200
Figure 4.46. Non-isotropic Reynolds stress dissipation rate measured in the 2DFPTBL at $Re_\theta = 7497$ . C3, CompLDV3; DNS, Simulation data of Spalart (1988). .....	200
Figure 4.47. Reynolds stress transport balances using the non-isotropic dissipation rates for the 2DFPTBL at $Re_\theta = 5929$ . (a) $\overline{u^2}^+$ , (b) $\overline{v^2}^+$ , (c) $\overline{w^2}^+$ , (d) $\overline{uv}^+$ , (e) $\frac{1}{2}(\overline{u^2}^+ + \overline{v^2}^+ + \overline{w^2}^+)$ . $\mathcal{P}_{ij}$ =Production; $\mathcal{C}_{ij}$ =Convection; $\mathcal{D}_{vij}$ =Viscous diffusion; $\mathcal{D}_{Tij}$ =Turbulent diffusion; $\epsilon_{ij}$ =Dissipation rate; $\Pi_{ij}$ =Velocity/pressure gradient correlation. ....	203
Figure 4.48. Same as Figure 4.47 for $Re_\theta = 7497$ .....	206
Figure 4.49 Stream-wise mean velocity profile for the small isolated cylinder at the location $x/d=2.75, z/d=0$ . C3, CompLDV3 measurements; G2005, George (2005) measurements; 2DC3, 2DFPTBL measured with the CompLDV3.....	207
Figure 4.50. Reynolds normal stress profiles for the small isolated cylinder at the location $x/d=2.75, z/d=0$ . C3, CompLDV3 measurements; G2005, George (2005) measurements; 2DC3, 2DFPTBL measured with the CompLDV3.....	208
Figure 4.51. Reynolds shear stress profiles for the small isolated cylinder at the location $x/d=2.75, z/d=0$ . C3, CompLDV3 measurements; G2005, George (2005) measurements; 2DC3, 2DFPTBL measured with the CompLDV3.....	208
Figure 4.52. Stream-wise mean velocity profile for the medium-height isolated cylinder at the location $x/d=2.75, z/d=0$ . C3, CompLDV3 measurements; G2005, George (2005) measurements; 2DC3, 2DFPTBL measured with the CompLDV3. ....	209
Figure 4.53. Stream-wise Reynolds normal stress profiles for the medium-height isolated cylinder at the location $x/d=2.75, z/d=0$ . C3, CompLDV3 measurements; G2005, George (2005) measurements; 2DC3, 2DFPTBL measured with the CompLDV3. ....	209
Figure 4.54. Span-wise and normal-to-wall Reynolds normal stress profiles for the medium-height isolated cylinder at the location $x/d=2.75, z/d=0$ . C3, CompLDV3 measurements; G2005, George (2005) measurements; 2DC3, 2DFPTBL measured with the CompLDV3.....	210

Figure 4.55. Reynolds shear stress profiles for the medium-height isolated cylinder at the location $x/d=2.75, z/d=0$ . C3, CompLDV3 measurements; G2005, George (2005) measurements; 2DC3, 2DFPTBL measured with the CompLDV3.....	210
Figure 4.56. Stream-wise mean velocity profile for the large isolated cylinder at the location $x/d=2.75, z/d=0$ . C3, CompLDV3 measurements; G2005, George (2005) measurements; 2DC3, 2DFPTBL measured with the CompLDV3.....	211
Figure 4.57. Normal-to-wall and span-wise mean velocity profiles for the large isolated cylinder at the location $x/d=2.75, z/d=0$ . C3, CompLDV3 measurements; G2005, George (2005) measurements; 2DC3, 2DFPTBL measured with the CompLDV3. .....	211
Figure 4.58. Stream-wise Reynolds normal stress profiles for the large isolated cylinder at the location $x/d=2.75, z/d=0$ . C3, CompLDV3 measurements; G2005, George (2005) measurements; 2DC3, 2DFPTBL measured with the CompLDV3. ....	212
Figure 4.59. Normal-to-wall and span-wise Reynolds normal stress profiles for the large isolated cylinder at the location $x/d=2.75, z/d=0$ . C3, CompLDV3 measurements; G2005, George (2005) measurements; 2DC3, 2DFPTBL measured with the CompLDV3.....	212
Figure 4.60. Reynolds shear stress profiles for the medium-height isolated cylinder at the location $x/d=2.75, z/d=0$ . C3, CompLDV3 measurements; G2005, George (2005) measurements; 2DC3, 2DFPTBL measured with the CompLDV3.....	213
Figure 4.61. Auto-spectra of the stream-wise velocity fluctuations behind the small cylinder at the location $x/d=2.75, z/d=0$ . The legend gives the measurement height in $y^+$ .....	214
Figure 4.62. Auto-spectra of the normal-to-wall velocity fluctuations behind the small cylinder at the location $x/d=2.75, z/d=0$ . The legend gives the measurement height in $y^+$ .....	215
Figure 4.63. Auto-spectra of the span-wise velocity fluctuations behind the small cylinder at the location $x/d=2.75, z/d=0$ . The legend gives the measurement height in $y^+$ ..	215
Figure 4.64. Cross-spectra of the Reynolds shear stress components, $u'$ and $v'$ , behind the small cylinder at the location $x/d=2.75, z/d=0$ . The legend gives the measurement height in $y^+$ .....	216
Figure 4.65. Spectral coherency between the Reynolds shear stress components, $u'$ and $v'$ , behind the small cylinder at the location $x/d=2.75, z/d=0$ . The legend gives the measurement height in $y^+$ .....	216
Figure 4.66. Auto-spectra of the stream-wise velocity fluctuations behind the medium-height cylinder at the location $x/d=2.75, z/d=0$ . The legend gives the measurement height in $y^+$ .....	217
Figure 4.67. Auto-spectra of the normal-to-wall velocity fluctuations behind the medium-height cylinder at the location $x/d=2.75, z/d=0$ . The legend gives the measurement height in $y^+$ .....	218
Figure 4.68. Auto-spectra of the span-wise velocity fluctuations behind the medium-height cylinder at the location $x/d=2.75, z/d=0$ . The legend gives the measurement height in $y^+$ .....	218
Figure 4.69. Cross-spectra of the Reynolds shear stress components, $u'$ and $v'$ , behind the medium-height cylinder at the location $x/d=2.75, z/d=0$ . The legend gives the measurement height in $y^+$ .....	219

Figure 4.70. Spectral coherency between the Reynolds shear stress components, $u'$ and $v'$ , behind the medium-height cylinder at the location $x/d=2.75, z/d=0$ . The legend gives the measurement height in $y^+$ .	219
Figure 4.71. Auto-spectra of the stream-wise velocity fluctuations behind the large cylinder at the location $x/d=2.75, z/d=0$ . The legend gives the measurement height in $y^+$ .	221
Figure 4.72. Auto-spectra of the normal-to-wall velocity fluctuations behind the large cylinder at the location $x/d=2.75, z/d=0$ . The legend gives the measurement height in $y^+$ .	221
Figure 4.73. Auto-spectra of the span-wise velocity fluctuations behind the large cylinder at the location $x/d=2.75, z/d=0$ . The legend gives the measurement height in $y^+$ .	222
Figure 4.74. Cross-spectra of the Reynolds shear stress components, $u'$ and $v'$ , behind the medium-height cylinder at the location $x/d=2.75, z/d=0$ . The legend gives the measurement height in $y^+$ .	222
Figure 4.75. Spectral coherency between the Reynolds shear stress components, $u'$ and $v'$ , behind the medium-height cylinder at the location $x/d=2.75, z/d=0$ . The legend gives the measurement height in $y^+$ .	223
Figure 4.76. Oil-flow visualization for the wind-tunnel floor in the vicinity of the wing junction. The lines on the plot were drawn using mechanical drawing software and are equal length from the chord-line of the wing. Credit goes to Joshua DeMoss for this figure.	224
Figure 4.77. Plot of the 3D boundary layer measurements in the vicinity of the wind-tunnel floor near a wing junction. The filled arrow heads indicate the direction of the wall shear while the open arrows indicate the free-stream velocity direction. The box surrounding station 5 represents the CompLDV3 probe orientation with the length aligned with the projection of the beam bisectors of the two heads. This figure adapted from figure 1 in Ölçmen et al. (2001a) with kind permission of Springer Science and Business Media.	225
Figure 4.78. Sub-measurement volume resolution mean velocities for the wing/body junction flow at station 3.	226
Figure 4.79. Sub-measurement volume resolution Reynolds normal stresses for the wing/body junction flow at station 3.	227
Figure 4.80. Sub-measurement volume resolution Reynolds shear stresses for the wing/body junction flow at station 3.	227
Figure 4.81. Sub-measurement volume resolution mean velocities for the wing/body junction flow at station 5.	228
Figure 4.82. Sub-measurement volume resolution mean flow angle for the wing/body junction flow at station 5.	228
Figure 4.83. Sub-measurement volume resolution Reynolds normal stresses for the wing/body junction flow at station 5.	229
Figure 4.84. Sub-measurement volume resolution Reynolds shear stresses for the wing/body junction flow at station 5.	229
Figure 4.85. Mean velocities for the wing/body junction flow at station 3. C3: CompLDV3; Ö&S: Ölçmen and Simpson (1995).	230
Figure 4.86. Mean flow angle for the wing/body junction flow at station 3. C3: CompLDV3; Ö&S: Ölçmen and Simpson (1995).	231

Figure 4.87. Reynolds normal stresses for the wing/body junction flow at station 3. C3: CompLDV3; Ö&S: Ölçmen and Simpson (1995).	231
Figure 4.88. Reynolds shear stresses for the wing/body junction flow at station 3. C3: CompLDV3; Ö&S: Ölçmen and Simpson (1995).	232
Figure 4.89. Mean velocities for the wing/body junction flow at station 5. C3: CompLDV3; Ö&S: Ölçmen and Simpson (1995).	232
Figure 4.90. Mean flow angle for the wing/body junction flow at station 5. C3: CompLDV3; Ö&S: Ölçmen and Simpson (1995).	233
Figure 4.91. Reynolds normal stresses for the wing/body junction flow at station 5. C3: CompLDV3; Ö&S: Ölçmen and Simpson (1995).	233
Figure 4.92. Reynolds shear stresses for the wing/body junction flow at station 5. C3: CompLDV3; Ö&S: Ölçmen and Simpson (1995).	234
Figure 4.93. Auto-spectra of the stream-wise velocity fluctuations at station 3 in the WBJ flow with viscous wall scaling. The legend gives measurement positions in $y^+$ . The lines in the plot are at slopes $\sim f^1$ and $\sim f^{5/3}$ .	235
Figure 4.94. Auto-spectra of the normal-to-wall velocity fluctuations at station 3 in the WBJ flow with viscous wall scaling. The legend gives measurement positions in $y^+$ . The lines in the plot are at slopes $\sim f^1$ and $\sim f^{5/3}$ .	235
Figure 4.95. Auto-spectra of the span-wise velocity fluctuations at station 3 in the WBJ flow with viscous wall scaling. The legend gives measurement positions in $y^+$ . The lines in the plot are at slopes $\sim f^1$ and $\sim f^{5/3}$ .	236
Figure 4.96. Cross-spectra of the Reynolds shear stress components, $u'$ and $v'$ , at station 3 in the WBJ flow with viscous wall scaling. The legend gives measurement positions in $y^+$ . The line in the plot is at a slope of $\sim f^{7/3}$ .	236
Figure 4.97. Coherency measurements for the Reynolds shear stress, $\overline{uv}$ , at station 3. The legend gives vertical locations in $y^+$ .	237
Figure 4.98. Auto-spectra of the stream-wise velocity fluctuations at station 5 in the WBJ flow with viscous wall scaling. The legend gives measurement positions in $y^+$ . The lines in the plot are at slopes $\sim f^1$ and $\sim f^{5/3}$ .	237
Figure 4.99. Auto-spectra of the normal-to-wall velocity fluctuations at station 5 in the WBJ flow with viscous wall scaling. The legend gives measurement positions in $y^+$ . The lines in the plot are at slopes $\sim f^1$ and $\sim f^{5/3}$ .	238
Figure 4.100. Auto-spectra of the span-wise velocity fluctuations at station 5 in the WBJ flow with viscous wall scaling. The legend gives measurement positions in $y^+$ . The lines in the plot are at slopes $\sim f^1$ and $\sim f^{5/3}$ .	238
Figure 4.101. Cross-spectra of the Reynolds shear stress components, $u'$ and $v'$ , at station 5 in the WBJ flow with viscous wall scaling. The legend gives measurement positions in $y^+$ . The line in the plot is at a slope of $\sim f^{7/3}$ .	239
Figure 4.102. Coherency measurements for the Reynolds shear stress, $\overline{uv}$ , at station 5. The legend gives vertical locations in $y^+$ .	239
Figure 4.103. TKE dissipation rate and production for station 5 in the wing/body junction flow. VG, direct estimation of the dissipation rate using the velocity gradient tensor; S, estimation of the dissipation rate using spectral fits; 2DFPDNS, 2D flat plate data of Spalart.	241

Figure 4.104. Non-isotropic dissipation rate measurements at station 5 in the wing/body junction flow. C3, CompLDV3 measurement; 2DFPDNS, 2D flat plate data of Spalart. ....	241
Figure 4.105. Reynolds stress transport balances using the non-isotropic dissipation rates for the wing/body junction flow at station 5. (a) $\overline{u^{2+}}$ , (b) $\overline{v^{2+}}$ , (c) $\overline{w^{2+}}$ , (d) $\overline{uv^+}$ , (e) $\frac{1}{2}(\overline{u^{2+}} + \overline{v^{2+}} + \overline{w^{2+}})$ . $\mathcal{P}_{ij}$ =Production; $C_{ij}$ =Convection; $\mathcal{D}_{vij}$ =Viscous diffusion; $\mathcal{D}_{Tij}$ =Turbulent diffusion; $\varepsilon_{ij}$ =Dissipation rate; $\Pi_{ij}$ =Velocity/pressure gradient correlation. ....	244

## List of Tables

Table 2.1 CompLDV measurement quantities.....	15
Table 2.2. Optical specifications for the first CompLDV.....	35
Table 2.3. Specifications of the measurement volume for the first CompLDV. ....	36
Table 2.4. 20:1 Uncertainties in instantaneous measurement quantities for a single measurement head in the CompLDV1.....	46
Table 2.5. 20:1 uncertainties for instantaneously-measured velocities and positions as determined by the sensitivities from equations (2.47) for these quantities.....	81
Table 2.6. Parameters for the velocity gradient uncertainty simulations at $Re_\theta = 7500$ and $y^+ = 100$ . ....	91
Table 2.7. Velocity gradient uncertainty simulation cases and results. ....	91
Table 2.8. Velocity gradient uncertainty simulation results in viscous wall scaling.....	92
Table 2.9. Velocity gradient simulation with statistical variations given by the expected results in the 2D flat-plate TBL at $Re_\theta = 7500$ and $y^+ = 100$ . ....	92
Table 2.10. Comparison of velocity gradient measurements at $y^+ = 100$ for three bodies of work in the 2D flat plate turbulent boundary layer.....	93
Table 2.11. Uncertainty simulations for the least-squares velocity gradient estimation method.....	97
Table 2.12. Parameters for the CompLDV3 measurements in the plate and cone flow. ....	103
Table 3.1. Signal parameters for the reported Cramer-Rao Lower Bound.....	130
Table 3.2. The Cramer-Rao Lower Bound for the signal parameters in Table 3.1. ....	130
Table 3.3. Signal parameters for the chirped burst simulation. ....	136
Table 3.4. Processing cases for the chirped burst simulation study. Note: “Whole burst” means that the mid-point frequency was estimated from power spectrum of entire burst; “Average” means mid-point frequency was estimated by averaging the frequency determined from the two portions of the burst.....	137
Table 4.1. Flow parameters for the 2DFPTBLs measured for the current study.....	165
Table 5.1 List of first-ever-reported measurements obtained in the CompLDV technologies .....	250

# 1 Introduction

Most practical mechanical systems which are measurably affected by fluid flow encounter or produce turbulent flow fields. These flow fields are characterized by a chaotic and time-dependent fluid motion that has a wide range of characteristic space- and time-scales (Simpson 2003). The existence of many scales of chaotic motion makes turbulent flow phenomena very complex and difficult to predict, even for the most basic situations. Fundamental turbulence research continues to be necessary in order to advance our understanding of turbulence and how it affects important phenomena such as wall skin friction, flow separation, and acoustic noise.

Fundamental turbulence research may be generally classified into two approaches. Theoretical and computational research seeks to reveal aspects of turbulence by mathematically dissecting the Navier-Stokes (N-S) equations which govern all flow of a sufficiently continuous medium. Studies either attempt to simplify the equations to obtain analytical approximations to ideal problems such as in asymptotic analyses or to numerically solve some form of the N-S equations such as done with direct numerical simulation (DNS). Experimental turbulence research involves obtaining measurements in real turbulent flows in hopes of characterizing the interactions of the flow parameters. The two approaches are certainly not totally separate endeavors. Only through well-conducted experiments can theoretical assertions be verified. Likewise, experimental studies expose important behaviors which may later be explained by theoretical analysis.

The complex, broad-scale nature of turbulence makes solutions to general problems impossible, particularly at practical Reynolds numbers (Pope 2000). Therefore, useful computational techniques must somehow simplify the complexity of the phenomena so that solutions are obtained within reasonable times. The two methods commonly used to do this involve obtaining solutions of the Reynolds-averaged N-S (RANS) equations or by large-eddy simulation (LES). The RANS equations are obtained by substituting the decomposed velocity,  $U = \bar{U} + u$ , where  $U$  is the instantaneous velocity,  $\bar{U}$  is the mean velocity, and  $u$  is the instantaneous velocity fluctuation from the mean velocity, into the N-S equations and time-averaging the result so that the dependent variables in the equations are the expected values of statistical quantities. The resulting RANS equations for incompressible, constant temperature flow are

$$\frac{D\bar{U}_j}{Dt} = -\frac{1}{\rho} \frac{\partial \bar{P}}{\partial x_j} + \nu \nabla^2 \bar{U}_j - \frac{\partial \overline{u_i u_j}}{\partial x_i} \quad (1.1)$$

$$\frac{\partial \bar{U}_i}{\partial x_i} = 0 \quad (1.2)$$

where the usual subscript summing conventions are employed,  $\rho$  is the fluid density,  $\nu$  is the fluid viscosity and  $\bar{P}$  is the mean static pressure. The fundamental problem with this set of equations is that there are more unknowns than equations thanks to the introduction of the Reynolds stress tensor,  $\overline{u_i u_j}$ . In comparison to RANS, in LES the N-S equations are spatially filtered so that only scales larger than some chosen size are

directly solved (see Sagaut 2001 for a more detailed discussion of LES filtering). This results in a loss of information from the unresolved small scales which must be taken into account for a proper solution. In order to solve the RANS equations or to obtain meaningful results from LES, some mathematical models for the information lost due to time-averaging (contained in the Reynolds stress tensor for RANS and the sub-grid stresses in LES) must be used to obtain the additional relationships needed for the Reynolds stresses (RANS) or the effects of the subgrid scales (LES). These models must be devised based upon experimental results, theoretical developments, or DNS from flows of practical applicability to the problem at hand.

Of particular interest in the current research is the mechanics of turbulence within the thin boundary layer region adjacent to solid surfaces. Attached boundary layer flows are characterized by very large gradients in the normal-to-wall direction accompanied with small velocity magnitudes in the same direction. This leads to a simplification of the equations (1.1) and (1.2) since only gradients normal to the wall are significant (Schetz 1993). Unfortunately, many flows are not fully-attached, but have some degree of boundary layer separation where the usual assumptions fail. Furthermore, three-dimensionality introduced by span-wise pressure gradients results in the generation of streamwise vorticity which also causes deviations from the boundary layer assumptions. In this research we wish to characterize the flow physics by obtaining and analyzing new kinematics data on the velocity fields within two- and three-dimensional turbulent boundary layers.

## 1.1 Motivation for advanced turbulence measurements

In the past, measurement techniques such as hot-wire anemometry (HWA) and laser-Doppler velocimetry (LDV) have proved useful for obtaining statistics directly related to the velocity field. These measurements generate statistical information about the velocity at discrete regions in the flow. From the measurements, the values of mean velocities, Reynolds stresses and higher-order statistics may be determined along with some time- and space-correlations such as velocity-fluctuation frequency spectra or two-point velocity correlations. While these measurements have certainly advanced the understanding of turbulent flow phenomena tremendously, more information in the form of novel measurements, such as flow gradient statistics and acceleration statistics, is needed to accurately model the processes involved in unsteady, vortical flows.

To begin to examine the need for more-advanced measurements, in particular the instantaneous velocity gradient and acceleration measurements, the Reynolds-stress transport (RST) equations are given below in tensor notation:

$$\frac{Du_i u_j}{Dt} = P_{ij} + \Pi_{ij} + \nu \nabla^2 \overline{u_i u_j} - \varepsilon_{ij} - \frac{\partial u_i u_j u_k}{\partial x_k} \quad (1.3)$$

where the production rate of the Reynolds stress tensor  $\overline{u_i u_j}$  is  $P_{ij} = -\overline{u_i u_k} \frac{\partial \overline{U_j}}{\partial x_k} - \overline{u_j u_k} \frac{\partial \overline{U_i}}{\partial x_k}$ , the velocity-pressure-gradient tensor is

$$\Pi_{ij} = -\frac{1}{\rho} \overline{u_i \frac{\partial p}{\partial x_j}} + \overline{u_j \frac{\partial p}{\partial x_i}}$$

with  $p$  being the fluctuating static pressure, and the dissipation-

rate tensor is  $\varepsilon_{ij} = 2\nu \overline{\frac{\partial u_i}{\partial x_k} \frac{\partial u_j}{\partial x_k}}$ . These equations are developed directly from the N-S

momentum equations with the motivation of distilling the individual processes that result in the transport of the Reynolds stresses models. When RST modeling is employed during RANS solutions, the system of equations (1.3) is used for closure of the system of equations (1.1) by providing additional equations for each Reynolds stress gradient,

$\frac{\partial \overline{u_i u_j}}{\partial x_j}$ . This technique is attractive since the Reynolds-stress terms are determined by

solving physically-significant differential equations, which unlike simpler eddy-viscosity models, can account for the Reynolds stress anisotropy which exists in all real turbulent flows (Durbin and Petterson Reif 2001).

To solve the system in (1.3), it is necessary to model several of the terms using either experimental findings or theoretical and computational results. Velocity field measurements, as done with HWA or traditional LDV, allow for direct estimation of each of the terms in equations (1.3) except for the dissipation rate,  $\varepsilon_{ij}$ , and the velocity-fluctuation pressure gradient-fluctuation correlation,  $\Pi_{ij}$ . The dissipation rate is determined when the instantaneous velocity gradients are measured, as the current system design allows. The velocity-fluctuation pressure gradient-fluctuation correlation can be determined by considering the *linear* form of the instantaneous N-S equations in the Lagrangian reference frame:

$$A_i = -\frac{1}{\rho} \frac{\partial P}{\partial x_i} + \nu \nabla^2 U_i \quad (1.4)$$

where  $A_i$  is the Lagrangian fluid particle acceleration. Since this equation is linear, the fluctuating form is analogous. By multiplying the fluctuating form of equation (1.4) by the fluctuating velocity  $u_j$  and Reynolds-averaging one obtains

$$\overline{a_i u_j} = -\frac{1}{\rho} \overline{u_j \frac{\partial P}{\partial x_i}} + \overline{\nu u_j \nabla^2 u_i} \quad (1.5)$$

By switching the indices in equation (1.5) and adding the result back with the original equation, the follow form results:

$$\overline{a_i u_j} + \overline{a_j u_i} = -\frac{1}{\rho} \overline{u_j \frac{\partial P}{\partial x_i}} + \overline{u_i \frac{\partial P}{\partial x_j}} + \overline{\nu u_j \nabla^2 u_i + u_i \nabla^2 u_j} \quad (1.6)$$

In equation (1.6) we note that the original form of the velocity-fluctuation pressure gradient-fluctuation correlation is regained. In order to find this term, coincident velocity-acceleration measurements allow for direct measurement of the left hand side while the

dissipative/diffusive Laplacian terms may be decomposed into the following measured quantities, as shown by Pope (2001):

$$\overline{v u_j \nabla^2 u_i + u_i \nabla^2 u_j} = -2\nu \overline{\frac{\partial u_i}{\partial x_k} \frac{\partial u_j}{\partial x_k}} + \nu \nabla^2 \overline{u_i u_j} \quad (1.7)$$

where we note that the right-hand-side of equation (1.7) is given by the difference between the Reynolds stress diffusion rate and the Reynolds stress dissipation rate. Therefore, the velocity-fluctuation pressure gradient-fluctuation correlation which appears directly in the RST equations may be decomposed of measurable kinematics quantities,

$$\frac{1}{\rho} \overline{u_j \frac{\partial P}{\partial x_i} + u_i \frac{\partial P}{\partial x_j}} = -(\overline{a_i u_j} + \overline{a_j u_i}) - 2\nu \overline{\frac{\partial u_i}{\partial x_k} \frac{\partial u_j}{\partial x_k}} + \nu \nabla^2 \overline{u_i u_j} \quad (1.8)$$

In addition to improvements to RST models, velocity gradient measurements allow for the study of vorticity, a fundamental quantity in turbulent flows. The vorticity equations offer an advantage over the basic N-S equations in that the pressure terms vanish. The vorticity is defined as the curl of the velocity:  $\vec{\Omega} \equiv \nabla \times \vec{U}$ . By taking the curl of equation (1.1), we may obtain the instantaneous vorticity equations which then may be Reynolds-averaged to obtain

$$\frac{D\overline{\Omega}_i}{Dt} = \overline{\Omega}_j \frac{\partial U_i}{\partial x_j} + \nu \nabla^2 \overline{\Omega}_i - \overline{\frac{\partial u_j \omega_i}{\partial x_i}} - \overline{\frac{\partial u_i \omega_j}{\partial x_j}} \quad (1.9)$$

$$\frac{\partial \overline{\Omega}_i}{\partial x_i} = 0 \quad (1.10)$$

where  $\overline{\Omega}$  is the mean vorticity and  $\omega$  is the fluctuating vorticity. In an analogous manner as the RANS equations, the fluctuating velocity-fluctuating vorticity tensor,  $\overline{u_j \omega_i}$ , must be modeled in order to close the Reynolds averaged vorticity equations in (1.9) and (1.10).

For purposes of analysis, one half of the  $L^2$ -norm of the vorticity, known as the enstrophy, is often studied (Tennekes and Lumley 1972). By multiplying equation (1.9) by  $\overline{\Omega}$ , the result becomes a single transport equation for the mean enstrophy,  $\frac{1}{2} \overline{\Omega_i \Omega_i}$ ,

$$\frac{D\left(\frac{1}{2} \overline{\Omega_i \Omega_i}\right)}{Dt} = \overline{\Omega_i \omega_i s_{ij}} + \nu \frac{\partial^2 \left(\frac{1}{2} \overline{\Omega_i \Omega_i}\right)}{\partial x_j \partial x_j} - \nu \frac{\partial \overline{\Omega}_i}{\partial x_j} \frac{\partial \overline{\Omega}_i}{\partial x_j} - \frac{\partial \left(\overline{\Omega_i \omega_i u_j}\right)}{\partial x_j} \quad (1.11)$$

where the fluctuating rate-of-strain tensor is given by  $s_{ij} \equiv \frac{1}{2} \left( \frac{\partial u_i}{\partial x_j} + \frac{\partial u_j}{\partial x_i} \right)$ . An analogous equation to the TKE equation (i.e., one half times equation (1.3) with  $i=j$ ) is formed by considering the fluctuating enstrophy,  $\frac{1}{2} \overline{\omega_i \omega_i}$ ,

$$\frac{D\left(\frac{1}{2}\overline{\omega_i\omega_i}\right)}{Dt} = \overline{\omega_i\omega_j s_{ij}} + \overline{\omega_i\omega_j S_{ij}} + \overline{\Omega_j\omega_i s_{ij}} + \nu \frac{\partial^2\left(\frac{1}{2}\overline{\omega_i\omega_i}\right)}{\partial x_j\partial x_j} - \nu \frac{\partial\overline{\omega_i}}{\partial x_j} \frac{\partial\overline{\omega_i}}{\partial x_j} - \overline{u_j\omega_i} \frac{\partial\overline{\Omega_i}}{\partial x_j} - \frac{1}{2} \frac{\partial(\overline{u_j\omega_i\omega_i})}{\partial x_j} \quad (1.12)$$

where the mean rate-of-strain tensor is  $\overline{S_{ij}} \equiv \frac{1}{2} \left( \frac{\partial\overline{U_i}}{\partial x_j} + \frac{\partial\overline{U_j}}{\partial x_i} \right)$ .

A measurement technique which can resolve instantaneous velocity gradients, and thus vorticity, offers the possibility of measuring all the processes involved in the Reynolds-averaged vorticity equations and the mean-square vorticity fluctuation transport equations with the exception of the dissipation of mean-square vorticity fluctuations which may be determined by subtraction. A more thorough coverage of vorticity dynamics may be found in the works by Tennekes and Lumley (1972) and Morton (1984).

## 1.2 Review of advanced measurement techniques

### 1.2.1 Velocity gradient measurement

Much interest in experimental fluid mechanics has been placed in advancing the state-of-the-art of instantaneous velocity gradient measurements in turbulent flows. Several researchers have utilized HWA in multiple-wire configurations to achieve velocity gradient measurements (Balint et al. 1991, Wallace and Foss 1995, Honkan and Andreopoulos 1997, Wang and Sen 1999, Honkan and Andreopoulos 2001, and Kholmyansky et al. 2001). Although able to measure three components of vorticity, these techniques are intrusive, thus preventing near-wall measurements, and spatially unresolved, with probe sizes no smaller than twice the size of the smallest scales of turbulence in their flows.

Stereo-, holographic-, and micro-Particle Imaging Velocimetry (PIV) offer the possibility for high-spatial-resolution velocity-gradient measurements (Zhang et al. 1997, Santiago et al. 1998, Meneveau and Katz 2000, Tao et al. 2000, Hu et al. 2001, Hu et al. 2002, van der Bos et al. 2002, and Mullin and Dahm 2004, 2006). Of these techniques, micro-PIV offers the greatest spatial resolution, with  $O(1\mu m)$  interrogation volumes possible. Even in two-dimensions, this technique often suffers from having very short working distances and is mostly limited to micro-fluidic studies (Santiago 1998), although some work on so-called 'long-distance' micro-PIV has shown limited success (Kähler et al. 2006). To the author's knowledge, micro-PIV has yet to be implemented in dual-plane or holographic forms, so measurement of the complete velocity gradient tensor has not been realized. The holographic techniques afford measurements of three components of velocity and position, but suffer from significant resolution penalties due to depth-of-focus issues in the volume (Mullin and Dahm 2004), and thus fully-resolved velocity gradients have not been reported. Only recently have fully-resolved velocity gradient measurements in three-dimensions been realized; Mullin and Dahm (2004) utilized a stereo-PIV arrangement to achieve fully-resolved gradient measurements in a self-similar

axisymmetric co-flowing jet. The technique utilizing stereo-PIV is very complicated since the streamwise gradients require two complete stereo-PIV systems (i.e., dual-plane stereo-PIV). Though no fewer than three groups have implemented such systems (Mullin and Dahm 2004, Kähler et al. 2002, and Hu et al. 2001), only Mullin and Dahm (2004) have reported velocity gradient field measurements, apparently due to the complexities of obtaining low-uncertainty/unbiased gradient measurements. These systems also suffer from the well-known increased out-of-plane velocity uncertainty, which Mullin and Dahm (2004, 2006) quantify as twice that of the in-plane components, which are still somewhat greater than the uncertainties expected for point-wise techniques. Further difficulties arise when trying to obtain near-wall measurements due to the large dynamic range of velocities, flare from the wall, and the relatively low number of particles compared to the outer layer (Somandepalli and Mungal 2004).

There have also been recent efforts to utilize LDV for gradient measurements. A dual-parallel beam LDV method for measuring the velocity difference of two particles has been developed and verified by multiple groups (Tarau et al. 2002, Yao et al. 2001). This technique has been successfully employed for one component of vorticity measurement with spatial resolution as small as  $420\ \mu\text{m}$ . Perhaps the biggest drawback in this technique is that the velocity is not measured along with the difference, making velocity/velocity gradient correlations impossible and the necessity for an additional technique to document the velocity statistics of the flow. Another drawback is the difficulty in achieving a system with high signal-to-noise ratio (SNR). The Doppler equation describing this technique contains a dependence of the Doppler frequency on the light receiving direction, requiring a small angle for received light (Durst et al. 1981). This reduces the SNR of the signal and increases uncertainty, particularly when trying to extend the method to multiple dimensions. Agui and Andreopoulos (2002) utilized the more common dual-beam LDV (also called differential) for velocity difference measurements. This technique allows for measurement of the instantaneous velocity as well as velocity difference by receiving light from two cones within the measurement volume. The resolution achieved was 3 times the smallest scales of the flow. The resolution of this and the dual-parallel beam techniques are limited by finite size of the receiving cone and laser beams diameters.

## 1.2.2 Lagrangian acceleration measurement

Interest in Lagrangian acceleration measurement has been growing with the advent of some new optical particle tracking technologies and the increased computational and storage capacities of modern computers and digital signal processors. Due to the complexity of the measurements, very little information exists about the acceleration structure in turbulent flows. Published techniques include indirect measurement via the isotropy assumption by measuring the fourth-order velocity structure functions (Hill and Thoroddsen 1997), as well as direct studies using DNS (Vedula and Yeung 1999), particle tracking velocimetry techniques (Virant and Dracos 1997; LaPorta et al. 2001; Voth et al. 1998, 2002), particle image velocimetry (PIV) (Christensen and Adrian 2002), and LDV (Lehmann et al. 2002).

DNS is a useful tool for studies utilizing instantaneous pressure values as well as the difficult-to-measure particle acceleration. Vedula and Yeung (1999) used the technique to observe the Eulerian spatial structure of acceleration in homogeneous turbulence simulated up to  $R_\lambda = 230$ . The Reynolds number restrictions of such studies hinder their ultimate usefulness since Reynolds number effects separate them from most practical real flows.

Significant progress has been made in this subject using variants of particle tracking velocimetry (PTV). In particular, improved two-dimensional photodetectors have allowed important advances in measuring three-dimensional particle trajectories. Virant and Dracos (1997) presented PTV in the more traditional sense using CCD cameras as photodetectors for measurements of particle trajectories. The most impressive work utilizing particle tracking has been done by a group at the Laboratory of Atomic and Solid State Physics at Cornell University (LaPorta et al. 2001; Voth et al. 1998, 2002). This group has utilized instrumentation developed for the study of high-energy particle physics to obtain resolved particle trajectories in quasi-homogeneous mixing flows. Two silicon strip detectors are used to obtain two-components of particle position each. The measurement region was projected onto the strips such that each strip represented about  $7.8\mu\text{m}$ . The position could be interpolated to about an order of magnitude better than that. Though these studies have yielded some of the best data ever obtained for resolved particle trajectories, the technique is primarily limited to somewhat homogeneous flows with small mean velocities where particle residence times are large.

PIV has successfully been used to evaluate two components of particle acceleration (Christensen and Adrian 2002). Similar to stereo-PIV methods for gradient measurements, these measurements require two PIV systems to work in together. Polarization is used to discriminate the light from two different dual-cavity Nd-YAG lasers which are double-pulsed some tens of microseconds apart due to the much large shutter times of the cameras used. This arrangement was used to study mean two-dimensional channel flow. Unfortunately, the system was unable to resolve the out-of-plane motions necessary for studying mean three-dimensional flows.

In the current study, LDV is chosen primarily due to its exceptional resolution in the near-wall region. Previous work has shown the potential for estimating instantaneous particle accelerations using LDV. The differential LDV technique can be directly extended to make acceleration measurements by simply adjusting the signal processing. In work reported by Lehmann et al. (2002), the authors compared three signal processing methods for estimating particle accelerations and used one of the techniques in a flow situation. The results validated that LDV could successfully be extended to acquire acceleration measurements in turbulent flows. Of particular interest in the current study is the role of the correlation between the fluctuating velocity and fluctuating acceleration in the Reynolds stresses transport (RST) equations. This term is chosen for two reasons, first because it appears directly in the RST equations as a combination of up-to-now difficult to measure terms. Second because the correlation results in low uncertainties

relative to the individual uncertainties of the velocities and the accelerations, since the random noise content will not result in any net correlation.

### 1.3 Structure of the dissertation

The dissertation is organized in four additional chapters following the current one. Chapter 2 describes the instrumentation designed, the associated uncertainties, and the techniques used to validate the newly-developed ‘comprehensive’ LDV (CompLDV) instrumentation. In chapter 3, the problem of signal processing for LDV is tackled to identify methods available and quantify their effectiveness for estimating burst frequency and rate-of-change of frequency as well as data processing techniques for the extraction of time-delay correlations and frequency spectra from non-equidistantly-sampled LDV data. Chapter 4 contains the results obtained using the newly-developed CompLDV instrumentation for turbulent boundary layer measurements in both mean-2-D and 3-D flows. Finally chapter 5 wraps up the discussion of the results by stating the conclusions of the study. Appendices follow that outline some of the developments of the CompLDV program including the computer-based real-time three-component LDV data acquisition and processing system described in appendix A.

### 1.4 References

Agui, J.H. and Andreopoulos, Y., 2002 “A new laser vorticity probe--LAVOR: Its development and validation in turbulent boundary layer,” *Exp. in Fluids*, Vol. 34, No. 2, pp. 192-205.

Andreopoulos, Y. and Honkan, A. 2001 “An experimental study of the dissipative and vortical motion in turbulent boundary layers,” *J. Fluid Mech.*, Vol. 439, pp. 131-163.

Christensen, K.T. and Adrian, R.J. 2002 “The velocity and acceleration signatures of small-scale vortices in turbulent channel flow,” *J. Turb.*, Vol. 3, paper 023.

Durbin, P.A. and Petterson Reif, B.A. 2001 *Statistical Theory and Modeling for Turbulent Flows*, Wiley, New York.

Durst, F., Melling, A. and Whitelaw, J. H. 1981 *Principles and Practice of Laser-Doppler Anemometry, Second Edition*, Academic Press, London.

Hill, R.J. and Thoroddsen, S.T. 1997 “Experimental evaluation of acceleration correlation for locally isotropic turbulence,” *Physical Rev. E*, Vol. 55, No. 2, pp. 1600-1606.

Honkan, A. and Andreopoulos, Y. 1997 “Vorticity, strain-rate and dissipation characteristics in the near-wall region of turbulent boundary layers,” *J. Fluid Mech.*, Vol. 360, pp. 29-96.

Hu, H., Saga, T., Kobayashi, T., and Nubuyuki, T., 2002 “Simultaneous measurements of all three components of velocity and vorticity vectors in a lobed jet flow by means of dual-plane stereoscopic particle image velocimetry,” *Phys. of Fluids*, Vol. 14, No. 7, pp. 2128-2138.

Hu, H., Saga, T., Kobayashi, T., Taniguchi, N., and Yasuke, M. 2001 “Dual-plane stereoscopic particle image velocimetry system set-up and its application on a lobed jet mixing flow,” *Exp. Fluids*, Vol. 31, pp. 277-293.

Kähler, C. J., Scholz, U., and Ortmanns, J. 2006 “Wall-shear-stress and near-wall turbulence measurements up to single pixel resolution by means of long-distance micro-PIV,” *Exp. Fluids* **41**, pp. 327-241.

Kähler, C.J., Stanislas, M., and Kompenhans, J. 2002 “Spatio-temporal flow structure investigation of near-wall turbulence by means of multiplane stereo particle image velocimetry,” *12<sup>th</sup> Intl. Symp. on Appl. of Laser Tech. to Fluid Mech.*, July 12-15, Lisbon, Portugal, paper 29.3.

Kholmyansky, M., Tsinober, A., and Yorish, S. 2001 “Velocity derivatives in the atmospheric surface layer at  $R_\lambda = 104$ ,” *Phys. of Fluids*, Vol. 13, no. 1, pp. 311-314.

LaPorta, A, Voth, G.A., Crawford, A.M., Alexander, J. and Bodenschatz, E. 2001 “Fluid particle accelerations in fully developed turbulence,” *Nature*, Vol. 409, pp. 1017-1019.

Lehmann, B., Nobach, H., and Tropea, C. 2002 “Measurement of acceleration using the laser-Doppler technique,” *Meas. Sci. Technol.* **13**, 1367-1381.

Meneveau, C. and Katz, J. 2000 “Scale-invariance and turbulence models for large-eddy simulation,” *Annu. Rev. Fluid Mech.*, Vol. 32, pp. 1-32.

Morton, B.R. 1984 “The generation and decay of vorticity,” *Geophys. Astrophys. Fluid Dynamics*, Vol. 28, pp. 277-308.

Mullin, J.A. and Dahm, W.J.A. 2004 “Direct experimental measurements of velocity gradient fields in turbulent flows via high-resolution frequency-based dual-plane stereo PIV (DSPIV),” *12<sup>th</sup> Intl. Symp. on Appl. of Laser Tech. to Fluid Mech.*, July 12-15, Lisbon, Portugal, paper 16.1.

Mullin, J.A. and Dahm, W.J.A. 2006 “Dual-plane stereo particle image velocimetry measurements of velocity gradient tensor fields in turbulent shear flow. I. Accuracy assessments” *Phys. Fluids*, **18**, pp. 035101-1 to 035101-18.

Pope, S.B. 2000 *Turbulent Flows*, Cambridge University Press, Cambridge, U.K.

Sagaut, P. 2001 *Large Eddy Simulation for Incompressible Flows. An Introduction* Springer, Heidelberg.

Santiago, J.G., Wereley, S.T., Meinhart, C.D., Beebe, D.J., and Adrian, R.J., 1998 “A particle image velocimetry system for microfluidics,” *Exp. in Fluids*, Vol. 25, pp.316-319.

Schetz, J.A. 1993 *Boundary Layer Analysis*, Prentice Hall, Upper Saddle River, NJ.

Simpson, R.L. 2003 Class notes from AOE 6154: Turbulent Shear Flows, Virginia Tech, Spring Semester.

Somandepalli, V.S.R. and Mungal, M.G. 2004 “A novel technique to improve near-wall resolution in PIV using cylindrical lenses: DMPIV,” *12<sup>th</sup> Intl. Symp. on Appl. of Laser Tech. to Fluid Mech.*, July 12-15, Lisbon, Portugal, paper 8.5.

Tao, B. Katz, J., and Meneveau, C. 2000 “Geometry and scale relationships in high Reynolds number turbulence determined from three-dimensional holographic velocimetry.” *Phys. of Fluids*, Vol. 12, No. 5, pp. 941-944.

Tarau, T., Stepaniuk, V.P., and Otugen, M.V., 2002 “Evaluation of a new laser gradient probe,” *40th Annual AIAA Aerospace Science Meeting and Exhibit*, Jan. 14-17, Reno, NV, AIAA 2002-0688.

Tennekes H and Lumley JL. 1972 *A First Course in Turbulence*, The MIT Press, Cambridge.

van der Bos, F., Tao, B., Meneveau, C. and Katz, J. 2002 “Effects of small-scale turbulent motions on the filtered velocity gradient tensor as deduced from holographic particle image velocimetry measurements,” *Phys. Fluids*, Vol. 14, pp. 2456-2474.

Vedula, P. and Yeung, P.K. 1999 “Similarity scaling of acceleration and pressure statistics in numerical simulations of isotropic turbulence,” *Phys. Fluids*, Vol. 11, pp. 1208-1220.

Virant, M and Dracos, T. 1997 “3D PTV and its application on Lagrangian motion,” *Meas. Sci. Technol.* **8**, pp. 1539-1552.

Voth, G.A., LaPorta, A., Crawford, A.M., Alexander, J. and Bodenschatz, E. 2002 “Measurement of particle accelerations in fully developed turbulence,” *J. Fluid Mech.*, Vol. 469, pp. 121-160.

Voth, G.A. Satyanarayan, K., and Bodenschatz, E. 1998 “Lagrangian acceleration measurements at large Reynolds numbers,” *Phys. Fluids*, Vol. 10, pp. 2268-2280.

Wallace, J.M. and Foss, J.F. 1995 “The measurement of vorticity in turbulent flows,” *Annu. Rev. Fluid Mech.* Vol. 27, pp. 469-514.

Wang, T. and Sen, S., 1999 “Development of a miniature six-wire vorticity-temperature probe,” *30th AIAA Fluid Dyn. Conf.*, June 28-July1, Norfolk, VA, AIAA-99-3519.

Yao, S., Tong, P., and Ackerson, B. J., 2001 “Proposal and testing for a fiber-optic-based measurement of flow vorticity: *Applied Optics*, Vol. 40, No. 24, pp. 4022-4027

Zhang J., Tao B., Katz J. 1997 “Turbulent flow measurement in a square duct with hybrid holographic PIV,” *Exp Fluids* **23**, No. 5, pp. 373–381.

Zhu, Y. and Antonia, R.A., 1996 “Spatial resolution of a 4-X-wire vorticity probe,” *Meas. Sci. Technol.* **7**, pp. 1492-1497.

## **2 Instrumentation and apparatus**

### **2.1 Advanced turbulent flow instrumentation development**

In this chapter the recent work that has been done to advance the state-of-the-art for laser-Doppler velocimetry (LDV) is discussed. These recent improvements have motivated the development of a novel instrument that combines several of these concepts. The designs of the advanced laser-Doppler instruments used for this study are discussed including the uncertainties which drove the design and the practical considerations needed.

### **2.2 Recent work**

Several recent developments have significantly increased the capabilities of the LDV technique. These include methods for estimating the particle acceleration (Lehmann et al. 1990, Lehmann and Helbig, 2000, Lehmann, Nobach, and Tropea 2002 and Nobach, Kinzel, and Tropea 2005), obtaining sub-measurement volume particle position resolution (Czarske et al. 2001, 2002, and 2003), processing very closely-spaced-in-time Doppler bursts (Nobach 2002a), the ability to store vast amounts of burst data to be processed offline using high-speed PC-based digitizers (see appendix A), and robust, efficient estimation of signal time-delay correlation and spectra for non-evenly sampled data (Benedict, Nobach, and Tropea 2000, Nobach 2002b).

#### **2.2.1 Laser-Doppler acceleration measurement**

Previous work has shown the power of LDV for estimating instantaneous particle accelerations. The differential LDV technique can be directly extended to make acceleration measurements by simply adjusting the signal processing. In work reported by Lehmann et al. (2002), the authors compared three methods for estimating particle accelerations from linearly-chirped Doppler signals and validated one of the techniques in a flow situation. The acceleration extraction capabilities of the comprehensive LDV (CompLDV) developed for the present study are derived from the work discussed by Lehmann et al. (2002). The primary concerns addressed in previous work have been in signal processing, particle lag, and beam alignment (Lehmann et al. 2002, Nobach et al. 2005). Signal processing methods discussed in those works and expanded upon in Chapter 1. The key aspect of particle lag was examined by Lehmann et al. (2002). In that work the authors showed that the same relative lag effects are present for acceleration as for velocity—the first-order system-type time constant for either the velocity or acceleration is given as

$$\tau = \frac{d_p^2 \left( \rho_p + \frac{1}{2} \rho_f \right)}{18\mu} \quad (2.1)$$

where the time constant is  $\tau$ ,  $d_p^2$  is the particle diameter,  $\rho_p$  is the particle density,  $\rho_f$  is the fluid density, and  $\mu$  is the fluid viscosity. It then follows that a particle which can faithfully follow the meaningful frequencies for the velocity will do the same for the accelerations. For 0.6  $\mu\text{m}$  diameter DOP particles in air at lab conditions, we compute a time constant of 1  $\mu\text{s}$  indicating that Lagrangian fluctuations out to 160kHz are attenuated by no more than 3dB.

Both the works of Lehmann et al (2002) and Nobach et al. (2005) mention the importance of minimizing aberrations which result in variation of the fringe space. These anomalies cause additional uncertainties and result in chirp signals systematically in error with the linear acceleration/chirp Doppler equation. Nobach et al. (2005) also mentions a device for analyzing the quality of the fringe pattern utilizing a traversable solid particle on a stepper motor. The methods for extracting the Doppler chirp and for optimizing the LDV system for these measurements are still research topics and are addressed in part in the current work.

## 2.2.2 Enhanced-spatial-resolution laser-Doppler velocimetry

The sub-measurement-volume resolution in LDV is a topic that a few researchers have addressed in earnest in recent years (Czarske, Büttner, and Razik 2002; Büttner and Czarske 2003; Pfister, Büttner, and Czarske 2005; Czarske, J. 2001; Büttner and Czarske 2001). The methodologies for achieving enhanced spatial resolution includes measurement volume size reduction by employing limited coherency light (Büttner and Czarske 2001), using a ‘tilted’ fringe pattern measuring nearly the same velocity component (Büttner and Czarske 2003), and by employing interference fringe patterns with calibrated spatial variations (Czarske, Büttner, and Razik 2002; Pfister, Büttner, and Czarske 2005; Czarske, J. 2001). The advantages of achieving the enhanced spatial resolution are many. In particular, very small spatial scales of motion may potentially be resolved, flows that rapidly change in space may be characterized very precisely, broadening effects due to the finite measurement volume size may be greatly reduced, spatial resolution may be enhanced in long optical access systems, and of interest in the present study, the precise position information may be used to track relative particle trajectories for estimation of velocity gradient measurements. Of the high-resolution methods mentioned, the only reported efforts have been one-component velocity and position resolution until the current work. Thus, an important aspect of the current work is extending these methods and developing new ones to enable three components of simultaneous velocity and position measurement that will allow for full-vector velocity and position measurements.

### 2.2.3 Velocity gradient laser-Doppler measurements

As discussed in the introduction, velocity gradient measurement has been realized, at least to a limited degree, with LDV in previous work. Two methods have been employed for these measurements, a parallel beam method (Ötügen, M.V., Su, W-J., and Papadopoulos, G. 1998; Tarau, T., Stepaniuk, V.P., and Ötügen, M.V., 2002; and Yao, S., Tong, P., and Ackerson, B. J., 2001) and a dual-receiving-cone method (Agui, J.H. and Andreopoulos, Y., 2002). Each of these techniques was validated in flow situations, although to-date no significant results have been reported. The parallel beam method was considered in early applications for the current project and the results from that study are discussed in following sections.

### 2.2.4 Laser-Doppler signal processing

A detailed review of the aspects of laser-Doppler signal processing and non-equidistantly sampled velocity spectral estimation as well as the contributions from this work is reserved for chapter 1 to follow.

## 2.3 Comprehensive laser-Doppler velocimetry

The goal of the comprehensive laser-Doppler velocimetry (CompLDV) program is to produce *novel* results for turbulence structural quantities never before measured in wall-bounded turbulent flows. The CompLDV was designed to leverage the technologies mentioned in section 2.1 to enable near-wall, non-intrusive, spatio-temporally resolved instantaneous measurements of all components of velocity, acceleration, and velocity gradients in high Reynolds number laboratory flows. The power of such a measurement system is illustrated by the abundance of useful measurement quantities which may be realized. Table 2.1 lists some of the quantities of primary interest which may be measured or inferred from the data.

To be useful for interpretation, each of these measurements is needed at the lowest-possible uncertainties. Thus, the overwhelming driver for system design was obtaining low-uncertainty, unbiased measurements of the desired quantities. Despite the design uncertainties driving many parts of the system, some aspects of the final design were not predicted by simple uncertainty analyses. The design process, including formal uncertainty analysis as well as practical implementation considerations, for obtaining the optimal CompLDV configuration is described to follow.

**Table 2.1 CompLDV measurement quantities**

- Instantaneous direct measurements:
  - 3 components of velocity
  - 3 components of particle position
  - 3 components of acceleration
- Instantaneous calculated quantities:
  - Reynolds stress tensor
  - Triple product tensor
  - Velocity gradient tensor
  - Vorticity tensor
  - Rate-of-strain tensor
  - Reynolds stress gradient tensor
  - Acceleration gradient tensor
  - Velocity-acceleration fluctuation tensor
  - Dissipation
  - Skin friction velocity
- Additional time-averaged quantities:
  - Velocity-pressure gradient fluctuation tensor
  - Laplacian of Reynolds stress tensor

### 2.3.1 General Uncertainty Estimation

Measurement uncertainties are the most important specifications for any practical measurement system. In the process of designing an instrument, the limiting factors for realizable uncertainties in conjunction with the operation criteria form the envelopes for the design. The uncertainties dictate the usefulness and applicability of the instrument and indicate the limit of the depth at which the user may interpret the results obtained. In this section, a review of the methods for estimating uncertainties is given. Useful texts covering aspects of the subject include those by Doebelin (2003) or Bendat and Piersol (1992).

Consider a measurement system with  $N$  orthogonal independent variables,  $x_i$  affecting the final measurement result,  $M$ . The measurement result may be written as a function of each of these variables,

$$M = f(x_1, x_2, \dots, x_N) \quad (2.2)$$

The sensitivity of  $M$  to any variable  $x_i$  is then

$$\frac{\partial M}{\partial x_i} = \frac{\partial f(x_1, x_2, \dots, x_N)}{\partial x_i} \quad (2.3)$$

Likewise, a Taylor series expansion around  $x_k$  for a constant state for all other variables is given as

$$M(x_k + \delta x_k) = M(x_k) + \left. \frac{\partial M}{\partial x_k} \right|_{x_i, \text{fixed}} \delta x_k + O(\delta x_k^2) \quad (2.4)$$

or

$$\delta M_k = M(x_k + \delta x_k) - M(x_k) = \left. \frac{\partial M}{\partial x_k} \right|_{x_i, \text{fixed}} \delta x_k + O(\delta x_k^2) \quad (2.5)$$

Owing to the orthogonality of the independent variables, the ‘distance’ from the expected measurement at  $M(x_i)$ ,  $i=1, 2, \dots, N$  may be given by the perturbations of  $M$  as projected onto each of the variables such that

$$(\delta M)^2 = \sum_{i=1}^N (\delta M_i)^2 \quad (2.6)$$

Finally, by linearizing the measurement function around the expected state,  $x_i$ , by employing the first-order approximation given in equation (2.5), the familiar uncertainty relation is obtained

$$(\delta M)^2 = \sum_{i=1}^N \left( \left. \frac{\partial M}{\partial x_i} \right|_{x_i, \text{fixed}} \delta x_i \right)^2 \quad (2.7)$$

The challenge of estimating the uncertainties is determining the contributions, both the sensitivities and expected values for the perturbations, for each of the  $x_i$ . The sensitivity derivatives,  $\frac{\partial M}{\partial x_i}$ , may be estimated analytically when possible or numerically in jitter

analysis. The jitter analysis is necessary when an explicit function for  $M$  is unattainable. In jitter analysis, a known perturbation for the variable of interest is input into the system while all other variables remain at a known state. The change in the output of the measurement system will then give the sensitivity derivative to first-order approximations by finite difference. The estimated sensitivity to the variable  $x_k$  in the jitter analysis is then

$$\frac{\partial M}{\partial x_i} \approx \frac{M(x_1, x_2, \dots, x_k + \Delta x_k, \dots, x_N) - M(x_1, x_2, \dots, x_k, \dots, x_N)}{\Delta x_k} \quad (2.8)$$

The jitter analysis is particularly useful in the case when complex computer reduction schemes are used, allowing a simple yet accurate estimation of the sensitivity of the output to perturbations in the input quantities.

With the best estimates for the sensitivities to each variable, the system uncertainties may be estimated knowing the expected perturbation magnitudes for each variable. Each variable itself is also governed by the uncertainty relation in equation (2.7), such that a recursive relationship exists. The uncertainties in each of the independent variables may be determined in several different ways. In the case of a COTS instrument sub-system, the manufacturer may quote uncertainties for the measurement obtained, and calibrations may be used to verify these against a standard. Likewise, as in the case for the sensitivity derivatives, analytical or jitter analyses may be done.

When designing an instrument, it is desired to manipulate the sensitivities and expected perturbations to obtain the optimal system uncertainty. The lowest possible uncertainties are always desired, but limited by the current state-of-the-art technology, implementation constraints, and costs. Therefore, the designer must then make decisions on the values of system parameters that satisfy constraints and result in the optimal uncertainties. The

most efficient solution to the problem is to use the so-called method of equal effects (Doebelin 2003) to determine the desired uncertainties for each system variable. The method of equal effects states that a well-designed measurement system will obey

$$\delta M_1 = \delta M_2 = \dots = \delta M_N \quad (2.9)$$

such that the overall uncertainty will be

$$\delta M = \sqrt{N} \delta M_i \quad (2.10)$$

This relation arises due to the importance of relative magnitude effects in equation (2.7). If any contributions are disproportionate, they will dominate the total uncertainty, and reducing the values of the less uncertain terms will result in no meaningful reduction in total uncertainty. Thus, in an existing measurement system or one to be designed, attacking the most uncertain elements in the system is crucial.

In the CompLDV designs to be discussed, these uncertainty principles were applied numerous times. With experience, more accurate estimates of the uncertainty drivers for these relatively-complex systems were determined and quantified. This has allowed for a progression of the CompLDV instrument that resulted in successively lower uncertainties with each augmentation and iteration.

### 2.3.2 Preliminary specifications for the CompLDV

A primary aspect of the CompLDV project is instrumentation research. In this way, the constraints on the design are not an *a priori* goal for system uncertainties, but rather to obtain the lowest uncertainties possible given the facility dimensions and allotted budget. The desired measurements in the near-wall regions of 2D and 3D turbulent boundary layers included time- and space-resolved velocity, acceleration, and velocity gradient measurements. The statistical moments and spectral distributions of these quantities, both auto- and cross-correlated were the desired final output for analysis. Non-intrusive laser-Doppler-based methods were the only ones considered to obtain these measurements due to the high spatial and temporal resolution of these techniques as well as the ability to obtain measurements in very close proximity to solid boundaries. Finally, the facilities being used dictated that the probe have a working distance of over 100 mm so that high Reynolds number measurements are possible in thick boundary layers.

### 2.3.3 The CompLDV design process

The path to reaching the current CompLDV system design has involved many intermediate steps. Several hardware configurations have been designed, tested, and modified. Many analyses for achieving the optimal design have been accomplished. To follow are descriptions of the three primary measurement systems developed to satisfy the goals of the CompLDV program.

#### 2.3.3.1 The Rate-of-strain and Vorticity (ROSVOR) LDV

The goal of the ROSVOR probe was to realize fine-spatial-resolution instantaneous measurements of the complete rate-of-strain and vorticity tensors in practical high Reynolds number complex turbulent flows. This probe did not measure velocities or accelerations, as it was developed based upon the parallel beam probe design of Ötügen et al. (1998). This system utilized a parallel beam spacing of 1.2mm to measure a single component of velocity difference. Good agreement was reported for work by Ötügen et al. for rotating wire tests and a laminar test flow involving the viscous circumferential flow between concentric cylinders, for which an exact solution exists. Several fundamental and practical limitations exist for this probe design that was determined in this research, including the necessary spacing between parallel beams that makes resolution of the smallest turbulence scales unachievable, the improbability of achieving good signals from multiple channels, the ambiguities introduced by a finite-light receiving cone, and the necessarily bulky design of a 9-component system.

### 2.3.3.2 Operating Principles

The basic idea of the ROSVOR LDV is to collect and beat together (i.e., optically mix coherent, Doppler shifted light) the instantaneous Doppler signals produced by micron-sized particles that pass through pairs of volumes on laser beams of  $20\ \mu\text{m}$  diameter spaced  $100\ \mu\text{m}$  apart. (Durst et al., 1981, panel 3.26). Thus, the measured Doppler beat frequency  $f_D$  from light scattered from a pair of volumes is directly proportional to the difference in that measured velocity component for a given pair of volumes, U, V, or W. For example, for the U component, by using one beam passing through a point and 3 different Bragg frequency-shifted beams passing at volumes  $\Delta x$ ,  $\Delta y$  and  $\Delta z$  away from the first beam measurement volume, one can obtain identifiable beat frequency signals for  $\Delta U/\Delta x$ ,  $\Delta U/\Delta y$ , and  $\Delta U/\Delta z$ , including the sign. Figure 2.1 is a schematic showing 4 polarized single color parallel incident laser beams that pass at an angle of  $45^\circ$  through the transparent floor of the Virginia Tech Boundary Layer Wind Tunnel. Note the Doppler-shift equation

$$f_D = \frac{1}{2\lambda} (\hat{k}_s - \hat{k}_o) \cdot \Delta \vec{V} \quad (2.11)$$

where  $\lambda$  is the wavelength of the laser light,  $\hat{k}_o$  is the unit vector direction of incident beams,  $\hat{k}_s$  is the unit vector direction of received scattered light, and  $\Delta \vec{V} = \Delta U \hat{i} + \Delta V \hat{j} + \Delta W \hat{k}$  is the velocity-difference between a given pair of measurement locations. For the orthogonal velocity component system depicted in Figure 2.1, signal receiving optics in the direction  $\hat{k}_{sy}$  at  $45^\circ$  below horizontal collects  $\Delta V/\Delta x, \Delta V/\Delta y, \Delta V/\Delta z$  data on the V or y-direction component of velocity, while  $\hat{k}_{sx}$  at  $45^\circ$  above horizontal collects  $\Delta U/\Delta x, \Delta U/\Delta y, \Delta U/\Delta z$  data on the U or x-direction component of velocity. Each set of signal receiving optics consists of a collecting lens, mirrors to fold the beam paths to make the system more compact, an array of 4 precisely located pinholes to collect magnified images from the four  $20\ \mu\text{m}$  diameter laser measurement volumes, and a photomultiplier tube (labeled PM Tube in Figure 2.1) for detection of the beat frequencies between pairs of these 4 beams. A second color system,

with the same components as the U-measuring incident and receiving optics, is located in the yz plane and measures  $\Delta W / \Delta x, \Delta W / \Delta y, \Delta W / \Delta z$ .

A key requirement of this concept is that one particle is in each of the 8 beams within the  $100 \mu\text{m}$  measurement volume at the same time to produce the nine necessary beat signals coincidentally. For most dual-beam laser-Doppler velocimetry applications, the seeding density is much lower than this, since multiple-particles in the volume reduce the quality of the signals (Nobach 2002). This requirement is one of the fundamental difficulties of implementing the ROSVOR LDV since optical mixing does not occur in the measurement volume as in the dual-beam system but occurs on the face of the detector and only when light from two or more particles heterodyne. It then becomes highly-improbable to receive high signal-to-noise ratio (SNR) signals from several measurement directions simultaneously.

### 2.3.3.3 Detail description of the ROSVOR LDV

This system is comprised of optical table components, a probe system, and signal conditioning and processing components.

#### 2.3.3.3.1 *Optical table components*

The INNOVA 90-5C argon-ion laser and fiber-coupling components are mounted on an optical table. With an etalon installed, the laser is run in multi-line mode. A prism is used to separate the lines and high-quality mirrors select and redirect the 514.5 nm green and 488 nm blue. Two additional mirrors then steer these beams into Newport single-mode fiber couplers (model F-91-C1). The light is then launched into  $4 \mu\text{m}$  diameter single-mode polarization-preserving Alcoa-Fujikura optical fibers (SM8-P-4/125-ST/NY-9000) and transmitted to the probe.

#### 2.3.3.3.2 *The probe system*

The probe system transmits laser beams and receives the scattered light from the measurement volume. To develop this probe a ‘proof-of-concept’ module was first designed, built and tested. This prototype serves as the  $\Delta V$  system in the final apparatus.

##### 2.3.3.3.2.1 **Prototype module.**

The prototype module was built to prove the conceptual design of this probe. It includes all of the principal functions of the complete system, but can only measure a single velocity component (i.e., three gradients,  $\Delta V / \Delta x, \Delta V / \Delta y, \Delta V / \Delta z$ ). Figure 2.2 depicts the  $\Delta V$  module. The task of creating four parallel beams with the same polarization, center-to-center spacing of  $100 \mu\text{m}$ , and waist diameters of  $20 \mu\text{m}$  is non-trivial. In order to reduce the beam travel within the transmitting system of the probe it is desired to keep the initial beam spacing at a minimum, otherwise the act of condensing the beam spacing may take several meters due to the combined requirements of waist diameter and beam

spacing. To solve this, light from the optical table is transmitted to the incident light probe by a single optical fiber. After exiting the fiber, the light is collimated using a 6mm focal-length plano-convex lens to a diameter of 1mm. This light then passes through an acousto-optical modulator (Bragg cell) which is mounted on a rotation stage for adjustment, resulting in two useful beams that travel in the plane parallel to the optics support plate and frequency shifting ones of these beams by 30 MHz. These beams are made parallel by cylindrical lens A (Figure 2.1) with a focal length of 250mm—the parallel spacing of these beams is on the order of 1mm. The beams then pass through a second Bragg cell also mounted on a rotation stage, splitting the two primary beams again, now a vertical plane with first order frequency shifting of 40 MHz. Thus, there are at that point 4 primary beams with frequency shifts of 0, +30, -40, and -10 MHz from the original wavelength. To fold the system into a compact design, these beams are retro-reflected using a right-angle prism. Cylindrical lens B (Figure 2.1), 130mm focal length, which is rotated 90° relative to cylindrical lens A is used to make the beams parallel in the vertical plane at a spacing of about 0.7mm. A ‘reverse’ Keplerian beam expander is then used to condense the beam spacing by an order of magnitude and focus the waists. The beams first pass the 750mm focal length plano-convex lens A, followed by a second right angle prism to retro-reflect the beams toward the measurement volume. The final, focusing plano-convex lens B, 76mm focal length, makes the beams parallel and focuses the beam waists to about 20  $\mu\text{m}$  in the measurement volume with an effective length of 0.5mm, located 85mm axially from the center of plano-convex lens B. It should be noted that since all the beams have the same polarization, the scattered light will have optimal mixing qualities.

To receive the scattered light from the measurement volume, a stand-alone system was created. This system consists first of a 50mm diameter, 120mm focal length plano-convex lens. The distance from the measurement volumes is chosen to ensure a magnification of 2 in the focused image. The light collected by this lens is redirected with two 25.4 mm diameter mirrors used to fold the light path. This light is focused onto a plane containing the pinholes necessary for discriminating the proper regions of the measurement volume. The pinhole array chosen, with its dimensions, is shown in Figure 2.3. This array was made in 0.125 mm thick stainless steel shim stock painted black. The holes were made using a focused multi-line laser beam with 7.8 W of output and traversed from pinhole-to-pinhole with a fine resolution (2.5  $\mu\text{m}$ ) manual two-axis stage. The pinhole array was installed into an alignment system in the probe which allowed adjustments in the plane of the pinholes and rotation around the axis axial to the received light. Finally, the light passes about 10cm past the pinholes and produces beats on the face of the photomultiplier tube.

A photograph of the prototype module is given in Figure 2.4.

#### 2.3.3.3.2.2 Complete nine-component system.

The complete probe system is shown schematically in Figure 2.5. This system consists of two modules identical to the transmitting light optics described for the prototype module above, along with three scattered-light receiving systems very similar to the receiving

system already described, an aluminum truss structure to accommodate light collection and reflection above the tunnel roof, and a three-axis heavy-duty traverse system.

Two transmitting optical systems—one transmitting 514.5nm light, the other 488nm light—are used to orient two sets of four parallel beams, crossing each set in the measurement volume. As mentioned the optics for these systems are identical to the transmitting optics described for the prototype system. To align these two systems with each other, they are mounted on three-axis manual micrometer-drive stages.

To receive the nine components of the rate-of-strain tensor, it is necessary to view the measurement volume from three different angles as described by the Doppler equation (2.11). In this way, the receiving system for measuring  $\Delta V$  gradients is identical to that used in the prototype system, (with the addition of a dichroic filter to receive only green light), but for measuring  $\Delta U$  and  $\Delta W$ , light must be received from above the tunnel. It was decided to construct a stiff, lightweight truss structure from 1.59 mm web aluminum angle to support only the collection lens and a mirror for each component above the tunnel. For both  $\Delta U$  and  $\Delta W$ , plano-convex lenses of 50 mm diameter and 350 mm focal length were chosen in order to give a  $2\times$  magnification of the image. The mirrors above the tunnel reflect the light to the modules humor on the base-plate of the probe corresponding to the proper component. These modules each consist of two 50.8 mm diameter mirrors, a dichroic filter allowing only the proper color of light to pass, a pinhole array alignment apparatus identical to the one previously described, and a photomultiplier tube.

To traverse the probe, a custom lead-screw type stepper motor-driven positioning system was designed and constructed using motorized stages from Velmex, Inc, ball bearing slides from Del-Tron, Inc., and custom made parts. This system is shown supporting the probe in Figure 2.5. With the 1 mm/turn lead-screw in the y-axis, theoretical step resolutions of  $2.5 \mu\text{m}$  are achievable, sufficient for accurately assessing the position of the measurement volume relative to the tunnel wall. The motors are controlled with a model VP 9000 three-axis stepper motor controller from Velmex, Inc., which is interfaced to a PC running LabView software using the RS232 serial port.

#### **2.3.3.4 Signal conditioning and processing.**

The ROSVOR LDV presents the need to acquire and process the frequency information of nine independent Doppler bursts at one instant with very low uncertainty in frequency. While commercial laser-Doppler frequency domain processors are not limited in the maximum number of coincident channels, this is a relatively costly solution (\$10-45k/channel). Furthermore, these systems are not re-programmable to allow custom signal processing, as may be necessary in determining particle accelerations (Lehmann and Helbig, 2000, Lehmann, Nobach, and Tropea, 2002). Considering the somewhat recent advances in computing capabilities along with newly available high speed analog-to-digital converter data acquisition cards (or A/D boards), it was determined that the best solution to this signal processing problem was a completely PC-based one. Using National Instruments NI 5112 100 MS/s A/D boards, coincident measurements may be

made at a fraction of the cost (<\$1200/channel). In addition, the signal processing algorithms may be custom-configured using the LabView graphical instrument programming suite. A detailed description for the National Instruments-based LDV data acquisition and processing system is given in Appendix A. This system was used to obtain most of the extensive measurement of Byun (2005) documenting the structure of the near-body flow separations of a symmetric bump.

The analog signal conditioning electronics, all from Minicircuits, Inc., serve four purposes, as follows: amplification of the PM tube signal using model ZFL-500LN-BNC, high pass filtering of this signal to remove the signal pedestal using model BHP-25, downmixing to acceptable bandwidths with a model ZAD-6 frequency mixer, and low-pass filtering of the downmixed signal with model BLP-5. It is desired to downmix the signals to the lowest magnitude frequencies near zero in order to reduce the needed bandwidth. A crystal-controlled oscillator was used in the RF downmixer corresponding to a frequency near the Bragg frequency shift of a given channel. This limited the frequency drift to <100ppm for shifts of 12.5 MHz, 32.5 MHz, and 42.5 MHz.

### 2.3.3.5 Rotating wire calibration of the prototype system

As both a calibration and a proof of concept, a wire mounted on a moving wheel was used to generate velocity gradients within the measurement volume of the prototype system described in section 3.2.1. Analysis of this system yields that the velocity gradient along the wire is given as  $\Delta V = 2\pi f \Delta r$  where  $f$  is the rotation frequency of the wheel and  $\Delta r$  is the center-to-center spacing of the beams ( $100 \mu m$ ). The relationship between the Doppler frequency and the velocity difference is given through the Doppler equation (2.11) with  $\hat{k}_{sv}$  and  $\hat{k}_o$  as defined in Figure 2.1. The velocity-difference equation reduced

to  $\Delta V = \frac{f_D}{2.749} m/s$ . Since the radius of the wheel does not affect the velocity difference,

the wire was attached directly to the shaft of a high speed AC motor. The speed of the motor was controlled by a Variac controller and was measured instantaneously by the measured time between subsequent bursts. The motor itself was mounted to a three-axis micrometer-driven manual stage to allow proper alignment in the measurement volume. For these tests 200 mW of total laser power was used in the 514.5 nm line with an etalon installed. The wire cut the beams corresponding to  $\Delta V / \Delta z$  in the configuration. An empirical study was done to determine the appropriate wire diameter for the calibration. Wires of nominal diameters of  $12 \mu m$ ,  $50 \mu m$ ,  $125 \mu m$ , and  $250 \mu m$  were tested. These experiments revealed that all wires gave the same numerical results, but the larger wires required no additional alignment between speed adjustments due to their extra rigidity and increased scattering of light. Thus the  $250 \mu m$  wire was chosen for the calibrations.

The results of the calibration are shown in Figure 2.6. The random, root-mean-square deviation of the data from the expected line is 0.641 mm/s from the true values. Note that no bias is seen in the data. The random deviation may be attributed to a couple of factors. First, small vibrations in the calibration rig due to the high rotation rate of the shaft may have led to variations in the specular reflection from the wire. Thus, since the beams have

a finite diameter ( $20 \mu\text{m}$ ), the distance between the primary sources of the scattered light may vary instantaneously from  $100 \mu\text{m}$ ; i.e., values may range between 60 and  $140 \mu\text{m}$ . However, due to the nearly Gaussian intensity distribution of the beams, the center of the measurement volume is most-likely to contribute to the signal. An additional source of broadening which is related to reference beam systems is described by Durst, Melling, and Whitelaw (1981) in panel 12.11. This source of Doppler broadening arises from the collection of light at multiple angles since the collection lens has a finite aperture size. The broadening in the Doppler frequency is related as

$$\delta f_D = \frac{2\Delta V}{\lambda} \cos \varphi \delta \varphi \quad (2.12)$$

where  $\varphi$  is the half-angle between the incident light direction and the received light direction, in this case,  $45^\circ$ . This equation will reduce to  $\delta f_D = f_D \delta \varphi$  for  $\varphi = 45^\circ$ . The angle  $\delta \varphi$  is given as  $\delta \varphi = \tan^{-1} \frac{r_L}{d_M}$  where  $r_L$  is the collecting lens radius and  $d_M$  is the

distance from the collecting lens to the measurement volume. Evaluating the Doppler broadening equation (2.12) with  $r_L = 25.4\text{mm}$  and  $d_M = 180\text{mm}$ , as used in the calibration,  $\delta f_D = 0.141 f_D$ , indicating a significant amount of random uncertainty.

It is appropriate to compare the magnitude of the velocity gradient uncertainty to the magnitude of values expected in possible flow applications to assess the performance of the instrument. Consider the semi-logarithmic mean velocity profile region of a mean two-dimensional flat-plate turbulent boundary layer. In this region of the flow, significant evidence exists that the production of turbulent kinetic equals the dissipation rate (Pope 2000). From this fact, the dissipation rate may be written as  $\varepsilon = \frac{u_\tau^3}{\kappa y}$ , where  $u_\tau$  is the skin-

friction velocity given by the wall-strain-rate and the viscosity,  $\kappa$  is the log-layer slope constant, usually taken as 0.41, and  $y$  is position coordinate normal to the flat plate. For high Reynolds numbers, the dissipation may be considered to be only affected by the smallest scales of turbulence, which is assumed to be locally isotropic in two-dimensional flow. Thus, using the instantaneous continuity equation with the definition of local isotropy and the definition of dissipation rate, it is possible to obtain the following equation for isotropic dissipation rate

$$\varepsilon = \frac{15\nu}{2} \overline{\left(\frac{du}{dy}\right)^2} \quad (2.13)$$

where  $u$  is the instantaneous streamwise velocity fluctuation. Now consider  $y^+ \equiv \frac{y u_\tau}{\nu} y^+ = 40$  in the log-layer of a two-dimensional flat-plate turbulent boundary layer with a momentum thickness Reynolds number,  $\text{Re}_\theta = 7300$  and skin friction velocity  $u_\tau \approx 1.0 \text{ m/s}$  (Ölçmen, Simpson, and George 2001). One may expect to find instantaneous velocity gradients of  $17,520 \text{ s}^{-1}$  at three standard deviations from the mean value. The mean value is found by the log-law equation given as  $\frac{\partial U^+}{\partial y^+} = \frac{1}{\kappa y^+}$  where  $U^+ \equiv U / u_\tau$ .

This leads to a value of 4 000 1/s. Multiplying both of these values by the 100 $\mu$ m beam spacing, assuming a Gaussian distribution about the mean, the expected range for the velocity differences to be measured in a mean two-dimensional flow at  $y^+ = 40$  becomes  $-1.35 \text{ m/s} < \Delta u < 2.15 \text{ m/s}$ . Thus the root-mean-square uncertainty from the calibration is 0.018% of the expected span of velocity differences.

### 2.3.3.6 Concluding Remarks on the ROSVOR LDV

The ROSVOR LDV was designed for multi-component velocity-gradient measurements in turbulent flows. Calibration data obtained with wire-wheel measurements were presented that show low differential velocity uncertainties. Unfortunately, however, difficulties in practical implementation of this technique in flow situations preclude its application for the present study. Several problems are present, including very bulky probe hardware and the necessity of optical access in two tunnel walls and excessive lines of sight. When applying the prototype (with more accommodating dimensions and lines of sight) in a flow situation, it was not possible to obtain signals with sufficient signal-to-noise ratio to obtain useful measurements. The likely problem was the inability to obtain seeding with the optimal concentration and particle diameter for sufficient intensity from the heterodyning scattered light. It was also determined that this implementation was not optimal since velocity and acceleration measurements were not possible.

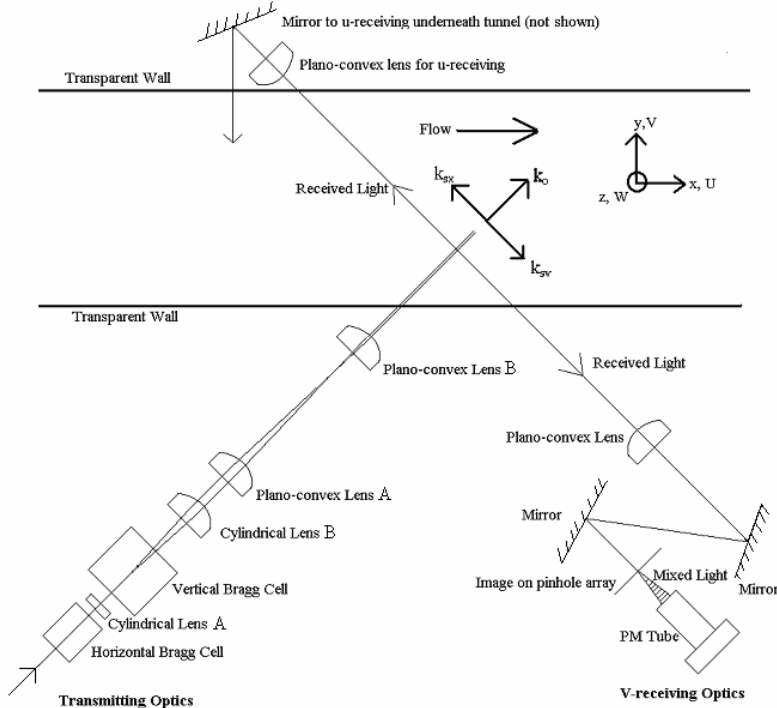


**Figure 2.1. Schematic of the optical arrangement for measuring the gradients of the ‘U’ and ‘V’ velocities; the components for measuring ‘W’ gradients are not shown since they do not lie in the same plane, although the arrangement is identical to that of the ‘U’ s**

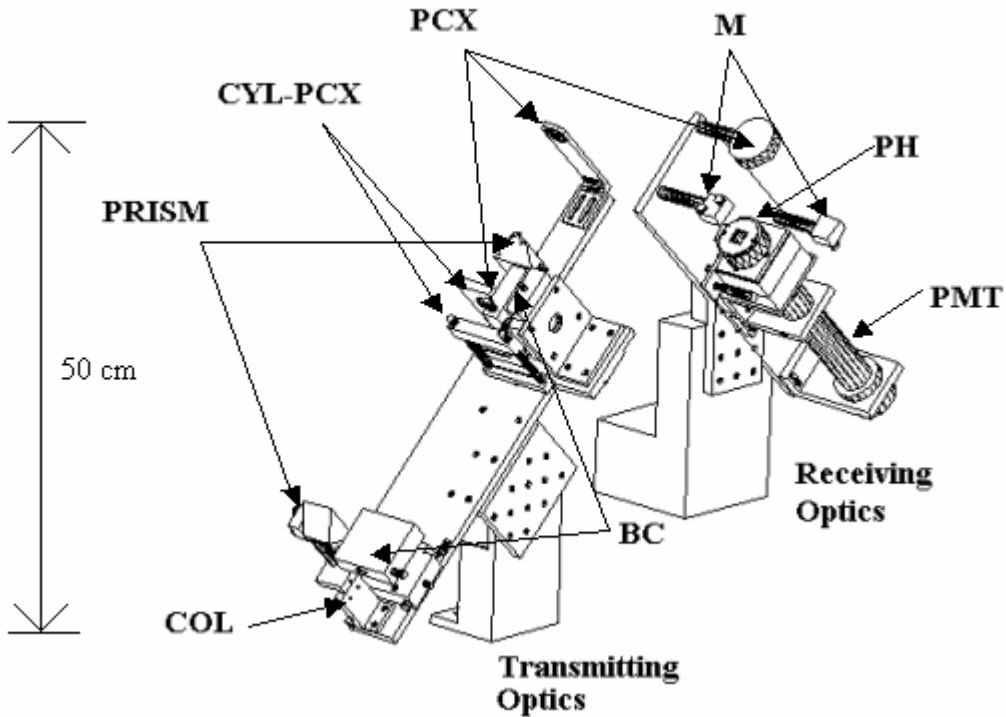


Figure 2.2. Schematic illustrating the components of the  $\Delta v$  prototype system. Each component is labeled as follows: PCX: plano-convex lens, M: mirror, PH: pinhole array and alignment apparatus, PMT: photomultiplier tube, CYL-PCX: cylindrical plano-convex lens, PR

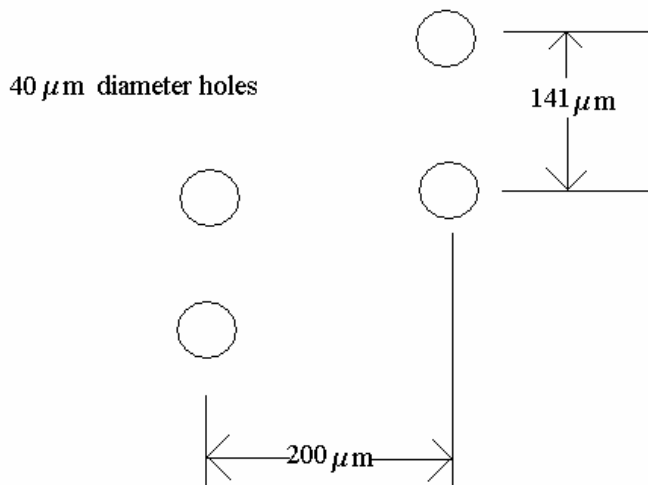


Figure 2.3. Orientation and dimensions of the pinhole array used to spatially filter the image of the measurement volume.

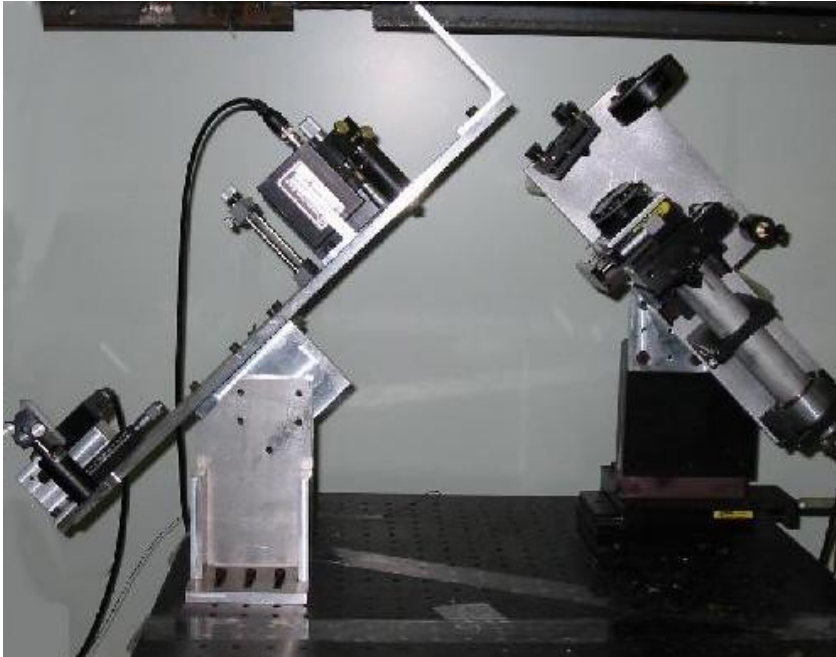


Figure 2.4. Photograph of the Prototype ROSVOR system.

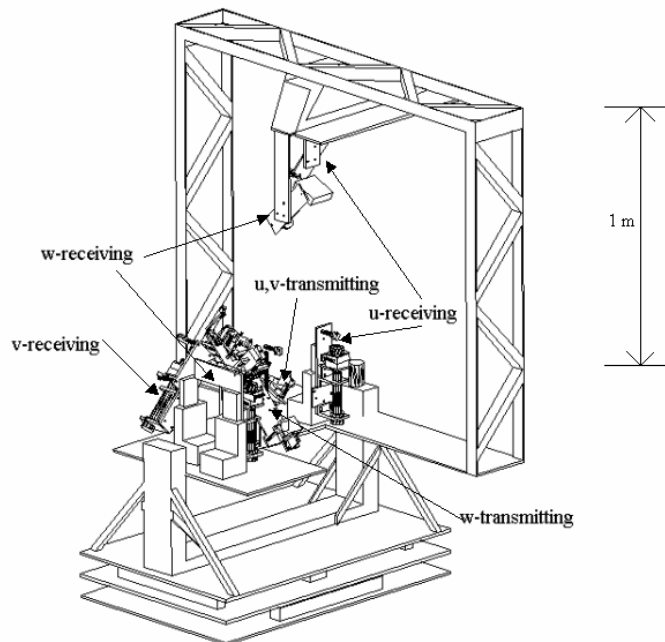
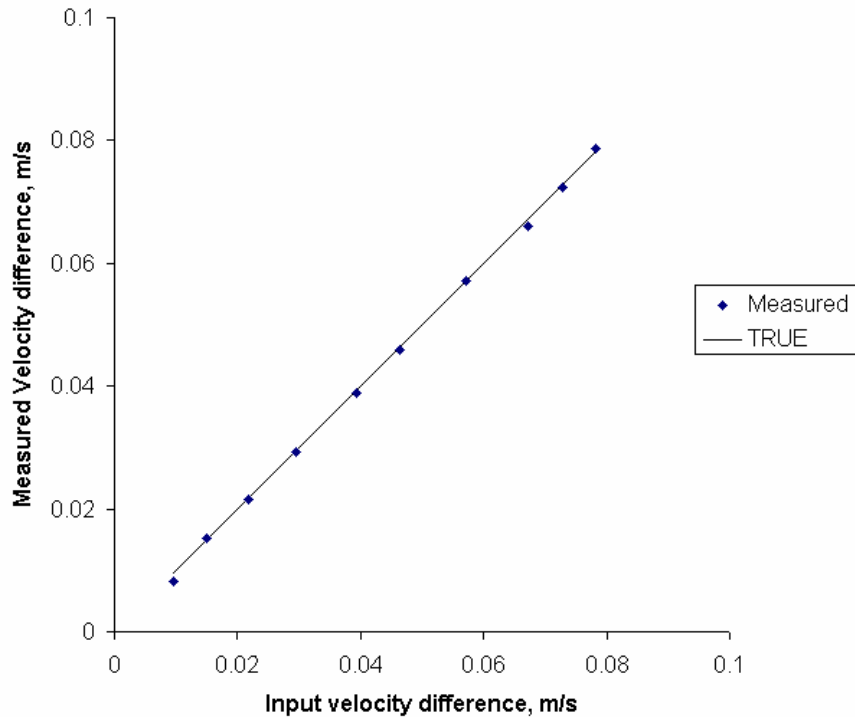


Figure 2.5. Schematic of the complete ROSVOR LDV. Note the gross features of the design: base-plate mounted onto the heavy-duty three-axis traverse, two identical transmitting system three receiving systems mounted to base-plate, truss structure mounted to the base plate with two sets of receiving lens and mirror systems for  $\Delta u$  and  $\Delta w$ .



**Figure 2.6. Plot of the calibration of the prototype ROSVOR LDV.**

### 2.3.3.7 The Dual-beam-mode Comprehensive LDV

Building upon the lessons from the ROSVOR LDV and considering some additional advances in LDV technology, the ‘comprehensive’ LDV (CompLDV) probe concept was developed to meet the goals of the study. By incorporating the advancements in particle position measurement (Czarske et al. 2002) along with the proven acceleration Doppler measurement technique (Lehmann et al. 2002), the CompLDV measures fully-resolved second order trajectories of seed particles following the turbulent flows of interest. Utilizing the DAQ capabilities already developed in-part for the ROSVOR LDV, it was determined that high repetitions of these trajectories were possible and could likely result in gradient measurements if four such trajectories were measured within the Kolmogorov scales.

#### 2.3.3.7.1 Basic CompLDV Principles of Operation

The CompLDV technique combines advanced LDV techniques to simultaneously measure three components of velocity, acceleration and crossing position of a sub-micron seed particle following the local motions in test flows. The quantities measured allow a good approximation—to second order—for the trajectory of each particle crossing the volume:

$$\bar{x}(t) = \bar{x}_0 + \bar{V}(t - t_0) + \frac{\bar{a}}{2}(t - t_0)^2 \quad (2.14)$$

where  $\bar{x}(t)$  is the time-dependent three-dimensional particle trajectory,  $\bar{x}_0$  is the position vector at  $t = t_0$ ,  $\bar{V}$  is the velocity vector at  $t = t_0$ , and  $\bar{a}$  is the acceleration at  $t = t_0$ . With this information, the rate of strain tensor may be estimated by a linear fit to the velocity field measured from four or more particles. This will be discussed in detail in section 2.3.3.9.4.2.

A technique for obtaining spatial resolution within LDV measurement volumes, already briefly discussed, was developed by Czarske et al. (2002). This technique utilizes two measurements of the same component of velocity to achieve particle position resolution two orders of magnitude smaller than the measurement volume diameter, at absolute scales unobtainable for any other spatially-resolving flow velocity measurement technique with a dynamic velocity range approaching that of LDV. The method can be easily understood looking at the Doppler equation for differential LDV,

$$U_{\perp} = f_D d \quad (2.15)$$

where  $U_{\perp}$  is the velocity of the particle perpendicular to the fringes,  $f_D$  is the Doppler frequency and  $d$  is the interference fringe spacing. Figure 2.7 gives a schematic of the basic geometry of such a LDV measurement volume. Now consider the case when two parallel measurement volumes are overlapped, the ratio of the Doppler equations for the two systems becomes

$$\frac{U_1}{U_2} = \frac{f_{D1} d_1}{f_{D2} d_2} = 1 \quad (2.16)$$

since  $U_1 = U_2$  for parallel measurement volumes. It follows then that

$$\frac{f_{D1}}{f_{D2}} = \frac{d_2}{d_1} \quad (2.17)$$

Now if the fringe spacing is non-uniform along the measurement volume, as is possible when beams are crossed off waist (Miles 1996), then the ratio of the two Doppler frequencies is a function of the crossing position within the measurement volume. Also, if the fringe spacings vary monotonically along the measurement volume, as is the case if one set of fringes are converging while the other is diverging as illustrated schematically in Figure 2.8, there will exist a monotonic function,  $q$ , such that

$$\frac{f_2}{f_1} = \frac{d_1(x'_{cross})}{d_2(x'_{cross})} = q(x'_{cross}) \quad (2.18)$$

where  $x'_{cross}$  is the particle crossing position measured axially along the measurement volume, as in Figure 2.7. The function  $q(x')$  is a constant for a given beam alignment and may be calibrated by measuring the fringe spacing along the measurement volume. Using the instantaneous measurements of the Doppler frequency ratios, the calibration may be interpolated to find the particle crossing position.

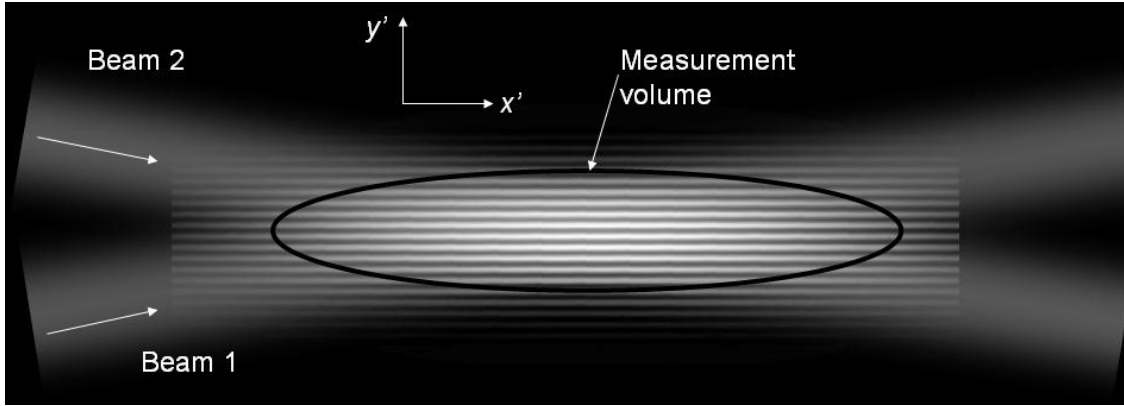


**Figure 2.7. Schematic of the intersection of two coherent laser beams forming an interference fringe pattern.**

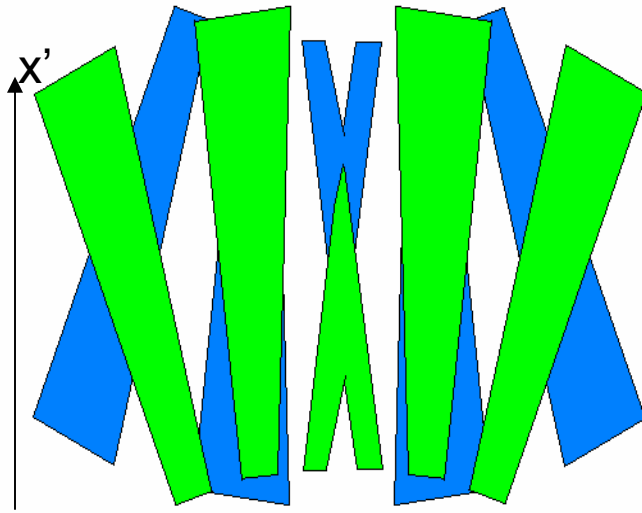


**Figure 2.8. Schematic of overlapping fringe sets with varying fringe spacings along the measurement volume beam-bisector.**

Analysis of the interference fringe patterns formed by pairs of Gaussian-intensity distribution light beams has been examined by Miles (1996). Of interest in this application is the special case when a pair of laser beams has waists that are spaced equal distances from the center of the beam overlap region. In this case, an axial variation of fringe spacing occurs for which Miles (1996) derived the following expression:

$$d(x') = \frac{\lambda}{2 \sin \theta} \left( 1 + \frac{x' \cos^2 \theta (x' \cos^2 \theta - x'_w)}{x'^2_R \cos^2 \theta - x'_w (x' \cos^2 \theta - x'_w)} \right) \quad (2.19)$$

where  $x'$  is measured along the centerline of the measurement volume,  $x'_w$  is the distance between the waist of the beam and the center of the measurement volume,  $\theta$  is the angle of the intersection of the beams,  $\lambda$  is the nominal wavelength of the light, and  $x'_R$  is the

Rayleigh number of the beams as given by  $x'_R = \frac{\pi \omega_0^2}{\lambda}$  with  $\omega_0$  being the radius of the

beam at the waist. A schematic example of such an interference fringe pattern arising from two Gaussian beams is given in Figure 2.9. While deviations from this model situation may occur in practice, this equation may be employed by the instrument designer to achieve optimal fringe variations to satisfy the position resolution needs.

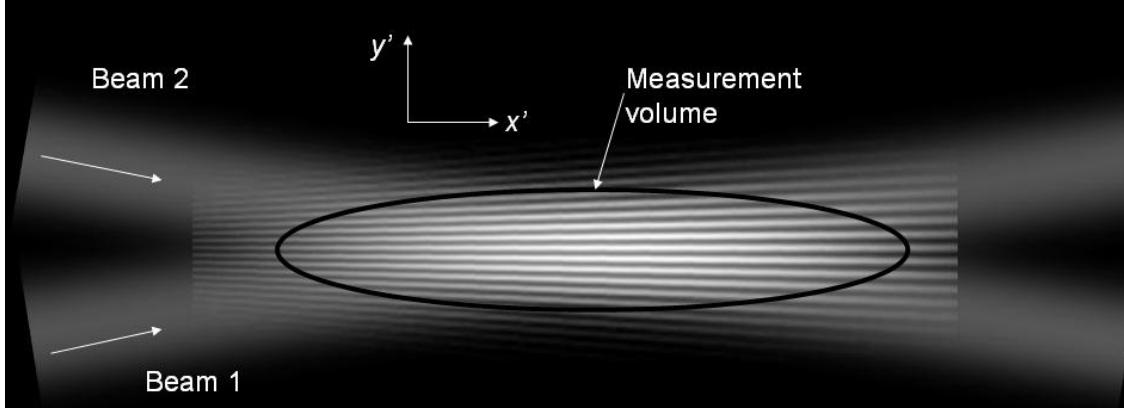


**Figure 2.9. Schematic of the off-waist intersection of two coherent laser beams forming interference fringes with  $\frac{\partial d}{\partial x'} > 0$ .**

The principle for acceleration extraction is also based upon the Doppler model for the differential LDV. Taking the time-derivative of equation (2.15) yields

$$\frac{df_D}{dt} = \frac{1}{d} \left( \frac{dU_{\perp}}{dt} - \frac{1}{d} \frac{d(d)}{dt} f_D \right) \quad (2.20)$$

Thus the rate of change of the Doppler frequency is proportional to the Lagrangian acceleration. In order to find the acceleration of each particle, the rate-of-change of frequency or chirp rate is determined using the power spectral density distribution in the orthogonal frequency-chirp-rate space. This PSD map is computed from individual burst signals by way of the discrete chirp Fourier transform (DCFT)—further details of the signal processing will be presented in the following chapter.

To interpret the chirp rate results, one must take into account the effects of the fringe gradients—both in the longitudinal and transverse directions of the measurement volume. By differentiating equation (2.15), this is quantified as

$$\left. \frac{\partial f}{\partial t} \right)_{\text{FringeGradient}} = - \frac{U_{\perp}}{d(x'_{\text{cross}})^2} \frac{Dd}{Dt} \quad (2.21)$$

where  $\frac{Dd}{Dt} = U_{\parallel} \frac{\partial d}{\partial x'} + U_{\perp} \frac{\partial d}{\partial y'} + U_z \frac{\partial d}{\partial z'}$ . The quantity in equation (2.21) can be calculated at low uncertainties since the uncertainties for all velocity components are low and the fringe gradients are constant. Note that in equations (2.18) and (2.21), the fringe space itself is only considered a function of the direction  $x'$ , yet fringe gradients in the  $y'$  and  $z'$  directions are also considered for the chirp rate correction. This is explained due to the scaling of quantities making up the total derivative of the fringe spacing passed by the

particle in equation (2.21). Since the contributions to the chirp rate due to fringe gradient perpendicular to the fringes themselves scale on the square of the Doppler velocity,  $U_{\perp}$ , very small values of  $\frac{\partial d}{\partial y'}$  can contribute significantly to the value of  $\left. \frac{\partial f}{\partial t} \right)_{\text{FringeGradient}}$ .

Further since a stress-like term,  $U_{\parallel}U_{\perp}$ , is required to correlate to result in a longitudinal fringe gradient contribution to  $\left. \frac{\partial f}{\partial t} \right)_{\text{FringeGradient}}$ ,  $\frac{\partial d}{\partial y'}$  can be more than an order of magnitude smaller than  $\frac{\partial d}{\partial x'}$  and still be significant.

### 2.3.3.7.1.1 Optical probe design

The fiber optic probe-hardware for the CompLDV generation 1 (CompLDV1) program was designed based upon the proven technology of the laser-Doppler probe designed by Ölçmen and Simpson (1995). This system couples the minimum number of optical components to a reliable alignment system that is simple and precise to adjust. A schematic of the probe is shown in Figure 2.10. This probe consists of three identical transmitting optics heads and a single receiving optical system. The transmitting and receiving optics are discussed in detail in the sections to follow.

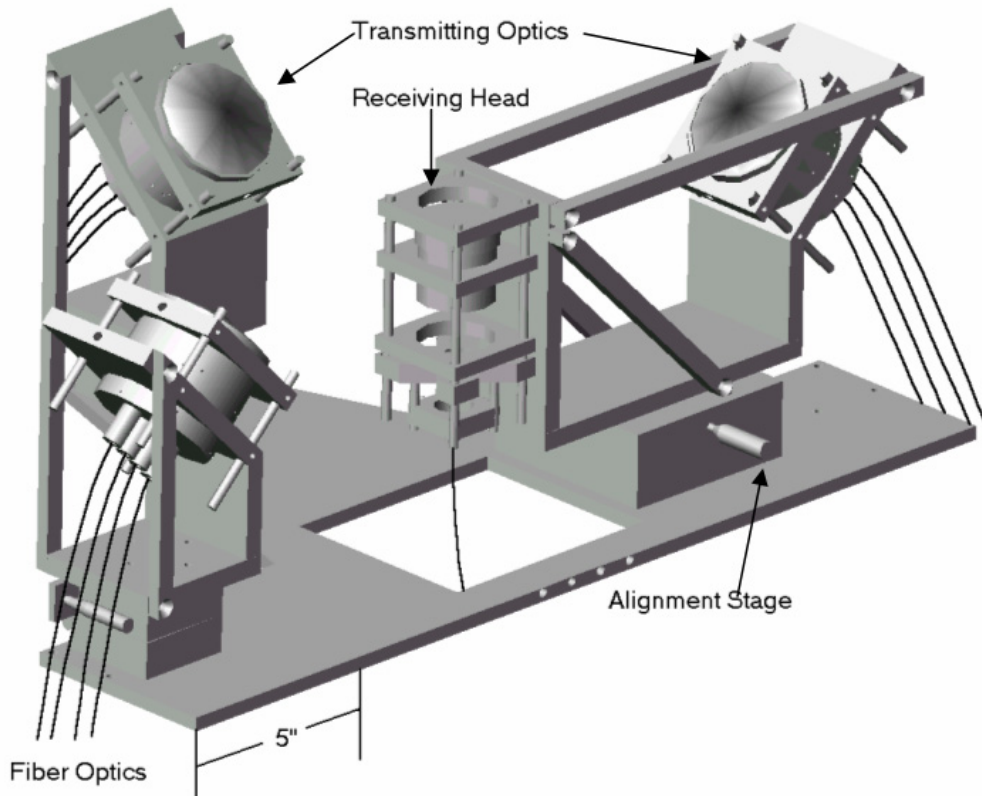
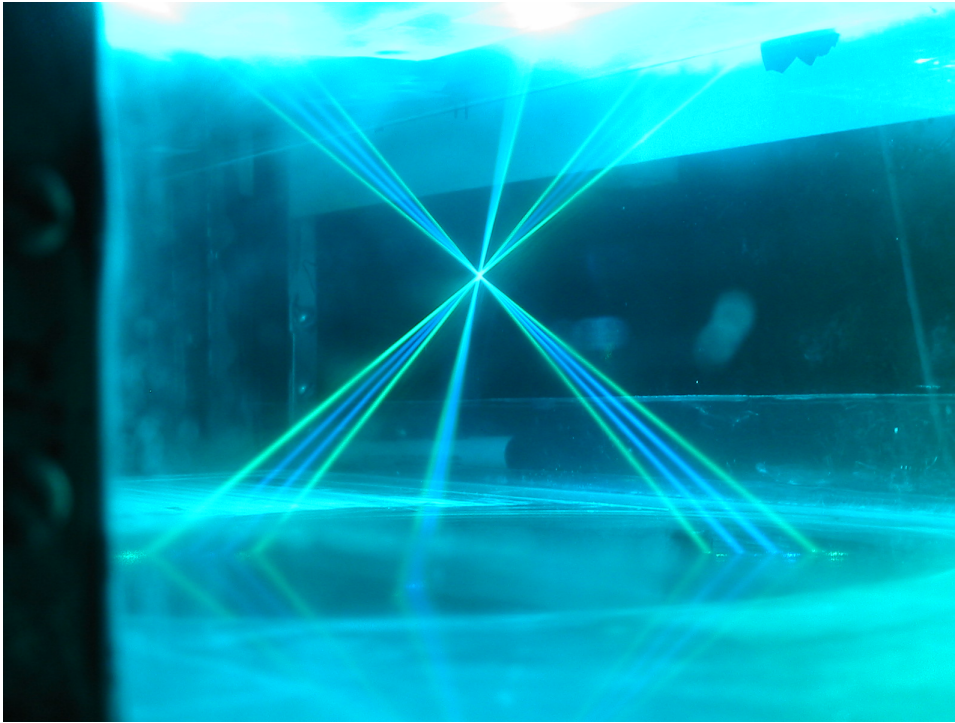


Figure 2.10. Schematic of the comprehensive LDV generation 1 probe.



**Figure 2.11. Photograph of the comprehensive LDV laser beams in a test flow.**

#### 2.3.3.7.1.1.1 Incident Optics

As a direct extension of the design by Czarske et al. (2002) for achieving high particle position resolution, the problem at hand calls for the formation of 6 measurement volumes using 12 beams that have variable fringe spacing along the length of the measurement volume. **Two overlapping measurement volumes are used for each component of velocity—one with converging fringes and another with diverging fringes.** To help understand the geometry of such a system of 12 beams, a photograph of the beam orientations for one iteration of the design is given in Figure 2.11.

In this design, the Doppler position technique was specified for each of the three position components. Since the variable fringe spacing is used to extract information about the position of particles within the measurement volume, it is necessary to have measurement volumes which lie along three linearly independent directions in order to get three components of position. In the geometric description to follow, the optical coordinate system refers to an orthogonal Cartesian system with directions conveniently chosen according to the planes in which beam bisectors lie. To obtain all the necessary position measurement directions, two overlapping measurement volume axes are aligned perpendicularly to another pair of two overlapping measurement volume axes within the optical  $x$ - $y$  plane. To get a component in the optical  $z$ -direction an additional two measurement volumes are arranged in the optical  $y$ - $z$  plane. These directions were also chosen to allow measurement of three independent velocity components. The components of velocity that are directly measured are represented in the optical coordinate system as follows:

$$\begin{aligned}
\bar{U}_{1,2} \Big|_O &= \frac{1}{\sqrt{2}} \hat{i}_o - \frac{1}{\sqrt{2}} \hat{j}_o \\
\bar{U}_{3,4} \Big|_O &= -\frac{1}{\sqrt{2}} \hat{i}_o - \frac{1}{\sqrt{2}} \hat{j}_o \\
\bar{U}_{5,6} \Big|_O &= \frac{1}{\sqrt{2}} \hat{j}_o - \frac{1}{\sqrt{2}} \hat{k}_o
\end{aligned} \tag{2.22}$$

where  $U_{i,i+1}$  represents the pairs of co-bisector measurement volumes and the subscript  $O$  denotes the optical coordinate system. A simple set of linear equations can be used to extract three orthogonal components of velocity from these measured values. Later implementations of this probe configuration utilized velocity measurement directions slightly different by rotating the individual incident optics head  $45^\circ$  about the transmitting lens optical axis. Also, the optical coordinate system was rotated  $45^\circ$  about the y-axis (axis normal to the wind tunnel floor). This modification was used to avoid a singularity in the operating range for the position measurement. Since equation (2.16) requires non-zero velocities to be valid, typical normal-to-wall and out-of-plane velocities were too small relative to the streamwise velocities to allow for effective position measurements given the geometry originally specified. The solution to this problem was to ensure that each head measured a significant component of the streamwise velocity. The resulting velocity measurement directions in the tunnel coordinates were

$$\begin{aligned}
\bar{U}_{1,2} \Big|_T &= \frac{1}{\sqrt{2}} \hat{i}_T - \frac{1}{2} \hat{j}_T - \frac{1}{2} \hat{k}_T \\
\bar{U}_{3,4} \Big|_T &= \frac{1}{\sqrt{2}} \hat{i}_T + \frac{1}{2} \hat{j}_T - \frac{1}{2} \hat{k}_T \\
\bar{U}_{5,6} \Big|_T &= \frac{1}{2} \hat{i}_T - \frac{1}{2} \hat{j}_T + \frac{1}{\sqrt{2}} \hat{k}_T
\end{aligned} \tag{2.23}$$

This configuration was used to acquire the data reported by Lowe and Simpson (2006).

The design requirements for the specification of lenses include a few key factors. The probe must traverse 6.5-7 inches above the wall for measurements in high Reynolds number flows. This determines the focal length of the focusing lens, an achromatic lens chosen to minimize spherical and chromatic aberrations, at the exit of the transmitting head to be about  $7\sqrt{2}in \approx 250mm$ .

It was desired that the position of particles crossing the measurement volume be determined to the same level of precision as by Czarske et al (2002). From the validation experiment in that work, a RMS position uncertainty of  $1.6 \mu m$  was surmised. In that paper, it is shown that the uncertainty of position is inversely proportional to the slope of the calibration function for the fringe spacing, i.e.,  $\delta x' \propto \frac{dq}{dx'}$ . The mean gradient for the calibration quotient reported by Czarske et al. then became the benchmark for the optical design. Therefore, to replicate this success, one should create a measurement volume with a calibration quotient gradient,  $\frac{\partial q}{\partial x'}$ , that is greater than or equal to the magnitude of

that used by Czarske et al. The data given by Czarske et al. for the calibration quotient is presented in Figure 2.12. From this plot, one may calculate that the average value of  $\frac{\partial q}{\partial x'}$  is  $0.231 \text{ mm}^{-1}$ .

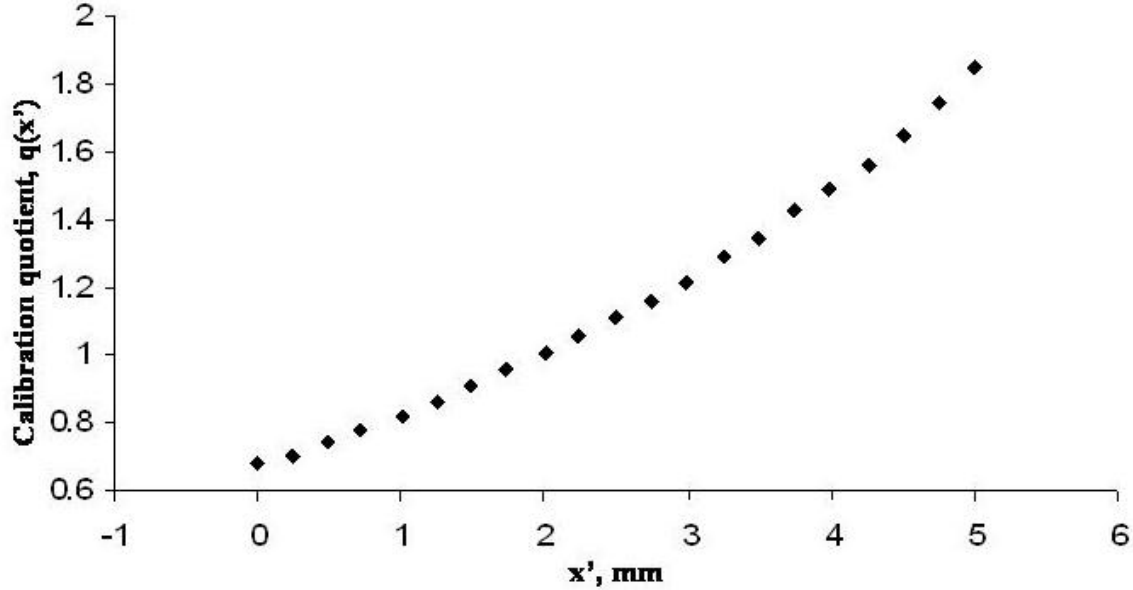


**Figure 2.12. Example of fringe calibration function from the published data of Czarske et al. (2002).**

Equation (2.19) must be considered along with the Gaussian beam radius equation to find the combination of the values of  $\theta$ ,  $x'_w$ , and  $\omega_0$  that will produce a measurement volume of the desired size with the maximal fringe gradient. The Gaussian beam radius equation as a function of the propagation location,  $z$ , relative to the waist is given as

$$\omega(z) = \omega_0 \left[ 1 + \left( \frac{\lambda z}{\pi \omega_0^2} \right)^2 \right]^{\frac{1}{2}} \quad (2.24)$$

To determine the desired measurement volume size, several considerations were taken into account. First, since the position of the particle was to be determined to good precision, it is not necessary to minimize the size of the measurement volume. On the other hand, a smaller measurement volume will concentrate more laser power and thus will generally produce stronger signals. A larger measurement volume is desired from the standpoint of signal processing since more frequency resolution can be obtained for a signal of longer duration. Finally, the measurement volume must be large enough to result in good relative uncertainties of the particle position to the measurement volume diameter. With these considerations, a  $200 \mu\text{m}$  diameter measurement volume was chosen as a reasonable compromise.

To find the location of the measurement volume relative to the waist of each beam, one must first decide upon a waist radius for the incident beams. This should be done considering equation (2.19). However, to implement this equation it is necessary to input the location of the waist relative to the middle of the measurement volume as well as the angle of beam intersection. Both of these values are dependent upon the position variable of equation (2.24). Thus, it is necessary to find these parameters iteratively. Examining equation (2.19) numerically, one sees that for beams which cross a few millimeters from the waist at relatively small angles, the difference in the fringe spacing over a  $200 \mu\text{m}$  measurement volume is somewhat insensitive to the waist parameter for waist radii less than  $20 \mu\text{m}$ . Since the magnitude of the fringe gradient does slightly increase for smaller waist radii, a  $10 \mu\text{m}$  waist was chosen for further study. Working with the waist radius of  $10 \mu\text{m}$ , the input diameter for the collimated beam is found using the following equation:

$$d = \frac{4\lambda f}{\pi\omega} \quad (2.25)$$

Using the necessary parameter values, the input diameter of the beam is found to be about 8mm. Implementing equation (2.25) again will determine the focal length of the collimating lens considering the diameter of the fiber optic emitting the beam ( $4 \mu\text{m}$ ). The collimating lens focal length is found to be 50 mm.

Knowing the desired beam waist, one may solve equation (2.24) to determine the distance between the waist and the diameter at which the beam is  $200 \mu\text{m}$ . This calculation yields a distance of 6.4 mm, giving the value of  $x'_w$ .

Due to commercially-available lens focal-lengths and desires for constraining the volume of the probe head, the minimum beam angles that allowed space for the necessary optics support hardware were determined given the focal distance. An intersection angle of  $4^\circ$  was chosen to allow center-to-center spacing of the closest beams to be 17.5 mm. The outer set of beams was chosen to cross at  $10^\circ$  angles of intersection.

A review of the optical specifications is given in Table 2.2.

**Table 2.2. Optical specifications for the first CompLDV.**

<b>Transmitting lens focal length</b>	250 mm
<b>Transmitting lens diameter</b>	76.2 mm
<b>Collimating lens focal length</b>	50 mm
<b>Collimating lens diameter</b>	25 mm
<b>Fiber optic diameter</b>	$4 \mu\text{m}$
<b>Focused beam diameter</b>	$20 \mu\text{m}$

The parameters chosen for the incident optics yield the information concerning the measurement volume specifications, as is given in Table 2.3. From the initial and final design fringe spacing, the average value of the gradient of the calibration parameter,  $q$ , is found to be  $0.800 \text{ mm}^{-1}$ . This value is about 240% greater than that used by Czarske et al. (2002), giving confidence in the optical specifications.

**Table 2.3. Specifications of the measurement volume for the first CompLDV.**

<b>Measurement Volume Diameter, <math>\mu\text{m}</math></b>	200
<b>Fringe space range for inner beams, <math>\mu\text{m}</math></b>	[6.99—6.74]
<b>Fringe space range for outer beams, <math>\mu\text{m}</math></b>	[2.95—3.05]
<b>Calibration parameter gradient, <math>\text{mm}^{-1}</math></b>	0.800
<b>Calibration parameter gradient, <math>\text{mm}^{-1}</math>, Czarske et al. (2002)</b>	0.233

The transmitting optics head hardware included #6-80 thread-per-inch adjustment screws for aligning each laser beam and additional adjustments for each of the incident optics heads needed to align the 3 different sets of measurement volumes. Each transmitting optics head is mounted to 2-axis adjustment stages in the horizontal plane along with vertical-movement pivot stages. The manual micrometer-drive stages allow fine adjustments over a range of 0.5" in each direction.

#### 2.3.3.7.1.1.2 Receiving Optics

In this laser-Doppler system, the receiving optics are used to define the measurement volume extent in the horizontal directions. The size of the cone from which light is received is a function of the receiving lens focal length and the diameter of the fiber into which light is coupled. To specify the receiving lens, then, one should decide upon the appropriate object distance from the lens to the measurement volume and the diameter of the measurement volume itself.

The receiving fiber chosen was a 100  $\mu\text{m}$  diameter-core multi-mode fiber. As mentioned previously, the measurement volume diameter was chosen to be 200  $\mu\text{m}$ ; thus, a magnification factor,  $m$ , is defined  $m \equiv \frac{\omega_{\text{fiber}}}{\omega_{\text{meas}}} = \frac{\text{image}}{\text{object}} = \frac{100}{200} = 0.500$ . Previous

experience has shown that the most efficient light receiving system is a pair of achromatic lenses, one lens that will collect scattered light and collimate it toward the receiving fiber and a second to focus the collimated scattered into the fiber. This combination helps balance any spherical aberrations of a single-lens system by employing each of the lenses at the preferred infinite conjugate ratio (ratio between the object and image distances). In addition to the required magnification, there are three considerations for choosing the focal length and diameter of the receiving lenses. First, the focal length of the outer collecting lens must be large enough to allow proper clearance of the probe hardware. Second the lenses should be as large as possible to increase the collection efficiency. However, the lenses' diameters and the focal length of the focusing lens must be chosen to satisfy the numerical aperture of the receiving fiber. The numerical aperture is a measure of the effective collection angle of an optical element and is defined as the sine of the maximum half-angle of the cone of light that optic can accept times the refractive index in which the vertex of the cone exists. In the

case of a lens working on a free-space beam, this turns out to be  $NA = \frac{r}{\sqrt{f^2 + r^2}}$  where

$r$  is the lens radius and  $f$  is the lens focal length. In the case of the optical fiber, the numerical aperture is given by the manufacturer as a specification. The multimode fibers used have a numerical aperture of 0.27. This requirement fully constrains the maximum useful radius of the lens system once the focal length of the collection lens is specified. In the case of the CompLDV receiving system, the collection lens focal length was chosen as 200 mm to allow ample clearance of the hardware and the wind tunnel. This choice immediately constrains the focal length of the focusing lens to 100mm. These focal lengths were also chosen for their commercial availability. Applying the numerical aperture formula to the focusing lens, setting it equal to the fiber numerical aperture yields a maximum lens radius of 28 mm. Since lenses of these focal lengths are commercially available in diameters of 50.8 mm, this was the specification.

To mount the receiving optics, a cage assembly similar to the receiving systems in the laser-Doppler probe designed by Ölçmen and Simpson (1995) is specified. To accomplish simple alignment of these optics, adjustments are supplied for focusing the lens and positioning the multi-mode receiving fiber. Tube-style lens mounts accommodate the 50.8 mm (2") diameter receiving lenses and have the capability of adjustable focus with a range of 25.4 mm (1"). To focus the image directly onto the fiber, a 2-axis fine traverse is used in the horizontal plane. Using an ST-style fiber optic connector the receiving fiber is mounted directly to the traverse component. This mechanism has a 2 mm range in both axes. In practice, these adjustments have proven very effective and easy-to-use.

#### 2.3.3.7.1.1.3 Optical table

A schematic of the optical table configurations used for the CompLDV systems are given in Figure 2.13 and Figure 2.14. The argon-ion lasers (Coherent Innova I90C-5) were run in multiline mode with no etalon such that all wavelength lines were emitting and the coherence length of single wavelengths was about 20mm. The multimode light was first focused using a pair of achromatic lenses, one with a focal length of about 100 mm and another with about 50 mm focal length. By optimizing the diameter of the beam at the point of fiber optic coupling, the efficiency of the coupling system is maximized. Prior to chromatic separation via a dispersion prism, the polarization of the multiline beam is rotated 90° from vertical to horizontal using a mica half-wave plate in a rotating mount. This step is necessary to minimize reflective losses at the prism since such light with horizontal polarization will nearly satisfy the Bragg condition of zero-reflectance upon entering the prism. The beam is steered upon the table using front surface protected aluminum mirrors with 98% or greater reflectivity. The mirrors are mounted on kinematical mounts with two-degree of freedom angular adjustments. After passing through the dispersion prism, the light is given ample distance to separate to allow the desired wavelengths to be 'picked off'. The 476.5nm, 488nm, and 514.5 nm lines are chosen due to the optical power that is achievable for these lines using a standard argon ion laser. Note that in Figure 2.13, only the 488nm and 514.5nm lines are used, as this was the first configuration for the CompLDV setup. In that configuration, additional mica

half-wave plates are used to adjust the beam polarization prior to being split with a polarizing beam-splitting cube. The power balance between the two split beams is dependent upon the input beam polarization. In the later implementations utilizing the 476.5nm line, these beam-splitting components were omitted since a sufficient number of beams could result without splitting. This three-wavelength optical table configuration is illustrated in Figure 2.14. With the required number of beams, mirrors are used to direct the individual beams of the desired wavelengths into acousto-optical modulators (Bragg cells) with varying carrier frequencies. These devices are used to impart a velocity to the interference fringes in the measurement volume by heterodyning light of very slightly different wavelengths. This fringe velocity solves the zero-velocity ambiguity that can occur for static fringes. In this way, a zero-velocity particle will result in a Doppler signal frequency equal to the carrier frequency of the Bragg cell. Only when particles are moving at the fringe velocity will ambiguities again arise, but such a condition is out of the realm of possibility for the fringe spacings and flow velocities expected. The Bragg cell carrier frequencies chosen also allow frequency-domain separation of the signals from different measurement volumes of the same color. The Bragg cells and corresponding radio frequency (RF) drivers are purchased from Intra-Action in carrier frequencies of 30, 40, 50, 60, and 80 MHz. The desired output from the Bragg cells is a pair of beams of equal intensity, one at the original frequency of the laser and the other shifted in frequency (positive or negative) by the carrier frequency of the Bragg cell. The powers in the beams are adjusted in two ways: first the Bragg cell is mounted on a horizontal rotation stage that allows angular adjustment of the device; and second the power of the Bragg cell carrier signal is adjusted. To maximize the efficiency of this process, first the mechanical adjustment is used to maximize the intensity of the first-order shifted beam (the one shifted by the Bragg cell carrier frequency). Next, the power of the carrier signal is adjusted electronically via a potentiometer knob on the Bragg cell driver unit. This adjustment allows much finer and predictable balance of the power instead of simply adjusting the angular direction of the Bragg cell. After exiting the Bragg cell the beams are allowed distance to separate sufficiently and are steered into the fiber optic coupling units. These units are obtained from Newport (model F-91-C1 coupler, FPH-CA6 ST-style fiber optic chuck, and M-20X objective lens) and consist of a 20X objective lens for focusing the beam to approximately the diameter of the fiber optic and a 5 degree-of-freedom precision fiber optic alignment system. Using these couplers, coupling efficiencies of 45-60% are achieved.

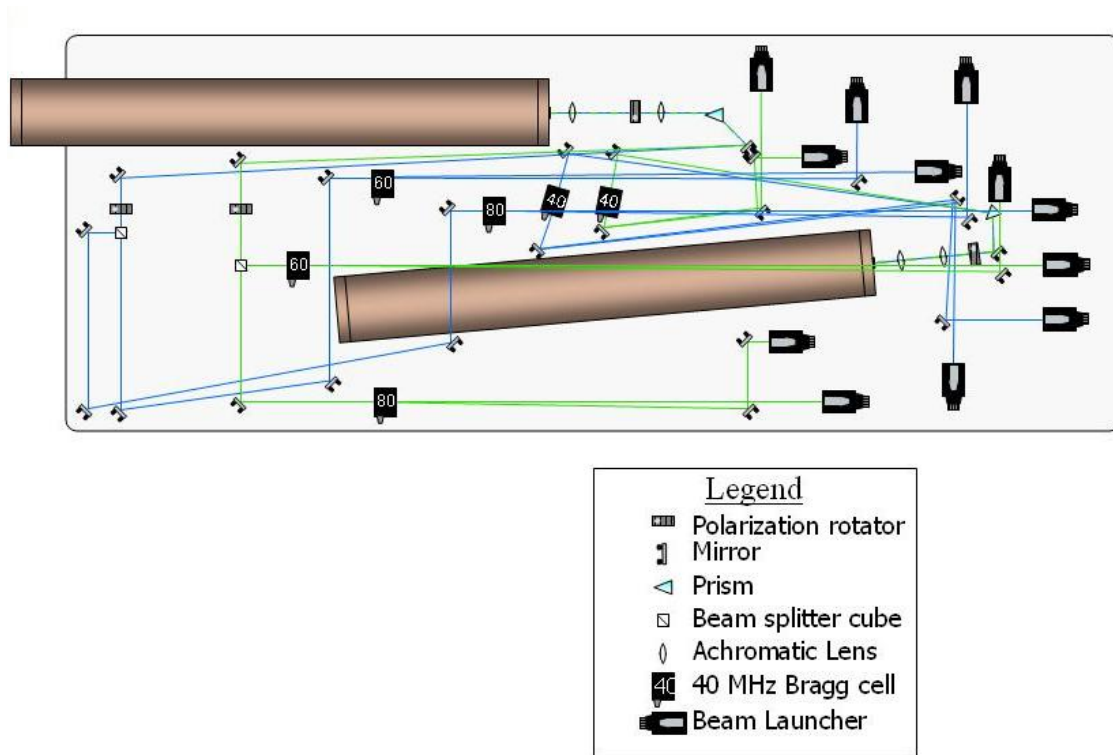


**Figure 2.13.** Schematic of the optical table configuration used for the first ComplDV optical system. Schematic is credited to Devin Stewart.

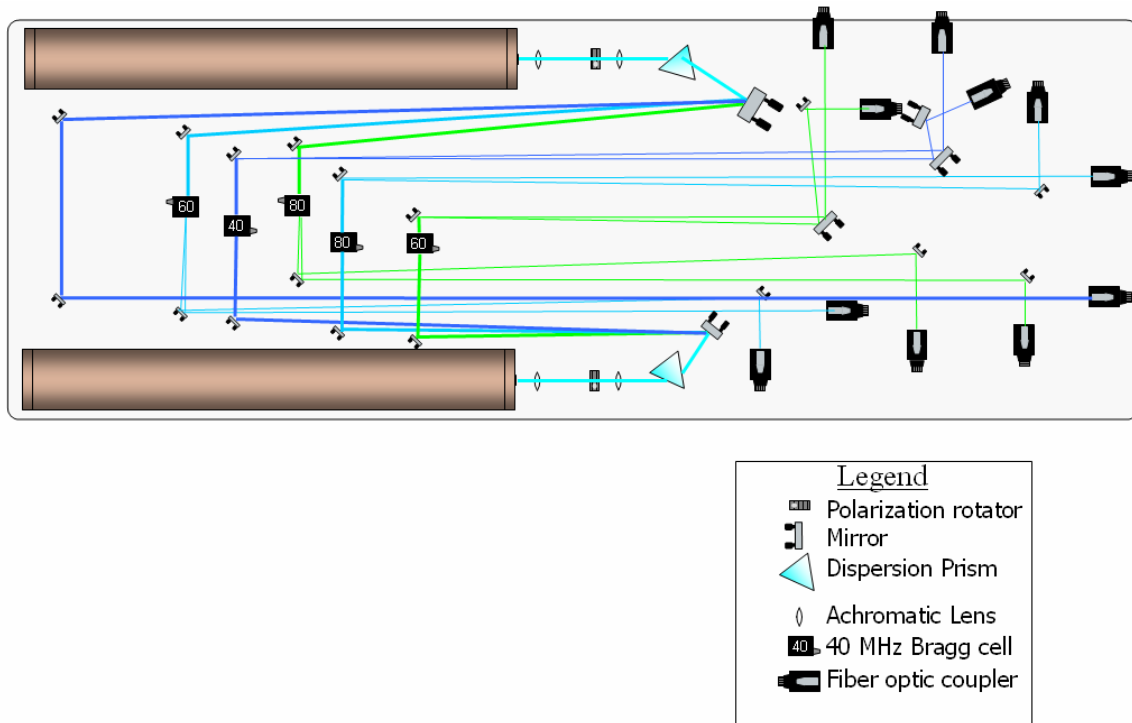


**Figure 2.14.** Schematic of the optical table configuration used for the three-color ComplDV optical systems.

### 2.3.3.7.1.2 Data Acquisition System and Signal Conditioning

The signal processing complexity and the rate of particle arrivals for the CompLDV makes real-time frequency-domain processing infeasible. For this reason, data acquisition units acquire and record *all* of the time-series data for a given location in space and over the sampling duration. Due to the bandwidth of the Doppler signals for obtaining all the signals on two channel of analog-to-digital conversion, very high sampling frequencies are necessary. Therefore, the data acquisition specified was chosen for maximum throughput of data and storage capabilities.

#### 2.3.3.7.1.2.1 A/D Converter Card

In choosing an A/D device for this application, two requirements are of high importance: the sampling rate of the device and the onboard storage capabilities. The sampling frequency limits the maximum Doppler frequency that may be measured due to the Nyquist criterion. On the other end of the frequency spectrum, the onboard storage capacity limits the lowest observable frequencies for a given sampling rate.

The CompLDV utilizes Bragg frequencies up to 80 MHz, requiring sampling at no less than 160 MS/s. One must add to this the potential Doppler shift of the signal up to 10 MHz for flows in the Virginia Tech Boundary Layer Wind Tunnel with fringe spacings of the CompLDV1. Thus, a minimum sample rate is 170 MS/s. Commercial devices with the order of sampling capabilities sample at 250 MS/s, giving practical bandwidths of 100 MS/s. Due to the ease of application and the efficiency of data transfer, a PCI-board from Strategic Test (model UF.258) was chosen. This device samples one channel at 500 MS/s or two simultaneous channels at 250 MS/s on a single card with a resolution of 8 bits. At the maximum sampling rate, continuous data samples of 0.54 s may be obtained, which adequately defines low frequency flow phenomena.

#### 2.3.3.7.1.2.2 DAQ Computer

The DAQ computer used was a standard top-end PC. Both immediate and long-term storage of raw burst data is achieved on high capacity IDE hard disks. During data acquisition, measurement run times are limited by the transfer rates between the PCI A/D card and the IDE hard disks. To reduce this bottle neck, pairs of RAID disks running in the striping (0) mode have been used, however, the non-portability of such pairs of disks led to using single IDE disks. The portability is an important issue, as the processing-intensive data must be transported to other computers to free-up resources on the DAQ computer so that measurements are not delayed.

#### 2.3.3.7.1.2.3 Signal Conditioning

The light gathered by the receiving system exits the multimode optical fiber into the chromatic separation optics (Figure 2.15). That light is collimated and passes through successive filters that direct a maximum amount of monochromatic light to three photomultiplier tubes (PMTs). Dichroic filters from Omega Optical are used to separate

the light of different wavelengths. The first dichroic (model XF-2039) is a narrow band blocking filter that reflects light in the region of 485-497nm. The only wavelength reflected by this filter is the 488nm blue signal that then passes through an interference filter to further protect against cross-talk before being focused upon the PMT face. Next, the remaining light consisting primarily of 476.5 nm and 514.5 nm burst signals pass a second dichroic filter (model XF-2010) with a single transition in the wavelengths of interest. This filter is essentially a long-pass filter allowing light above 505nm in wavelength to pass while reflecting shorter wavelengths. The 476.5nm and 514.5nm signals then each pass through narrow-pass interference filters to avoid cross talk and are focused upon the PMT faces. The efficiency of this separation process is acceptable, with the dichroic filters sending more than 80% of the light in the correct directions. The interference filters contribute a loss of 40-50% of the light signal in order to sharply limit unwanted wavelengths from reaching the PMT faces.

The voltage signals which the DAQ system record originate as current signals from the PMTs. The PMTs used are Hamamatsu model R4124, high frequency response (low single electron transit time) tubes. The very low current signals leaving the PMT anodes are converted to voltage signals using the input impedance of the low noise, high bandwidth, high gain RF amplifiers (Sonoma Instruments Model 315, 10kHz-1GHz response, 355V/V gain). These amplifiers have 50 Ohm impedance which limits the filtering effects that can occur before current-to-voltage conversion. To use the optimal amount of the amplifiers dynamic range, the PMT high voltage power supply is set to a value of about -520V, yielding signals of  $O([-10mV \ 500mV])$  from the amplifier. Since the DAQ unit used has only two input channels, the three PMT signals must be combined to two channels for compatibility. To do this, the Bragg frequencies of each of the channels is considered, since the electronic filters that will allow combination of the signals must be specified based upon these frequencies. The pre-combining filters are necessary to avoid the addition of noise from spectral regions of the channels that are known to have no useful signals. In the case of the 488nm channel, the Bragg cell carrier signals used are 60MHz and 80MHz. The 476.5 nm has Bragg cell carrier frequencies of 30MHz and 40MHz, allowing ample separation of these channels so that filtering may be used to condition the signals prior to combining. The amplified signal of the 476.5nm channel is filtered using a Mini-Circuits brand BLP-50 low pass filter that has a cut-off frequency of 55MHz. The 488nm channel is filtered with a 55 MHz high pass filter from KR Electronics model 2290-55. Next the signals are combined using a Mini-Circuits model ZSC-3-1 power combiner. The 514.5nm channel continues to the digitizer card independently. Prior to digitization both the electronic channels are passed through anti-aliasing filters (Mini-Circuits model BLP-100) with cut-off frequencies of 108MHz. This value is chosen over any greater frequency up to the Nyquist to allow for ample roll-off of the anti-aliasing filter to develop. The practical rule-of-thumb for such an anti-aliasing cut-off is 2.56 divided by the sampling frequency rather than 2 as defined by the Nyquist criterion (Doebelin 2001).

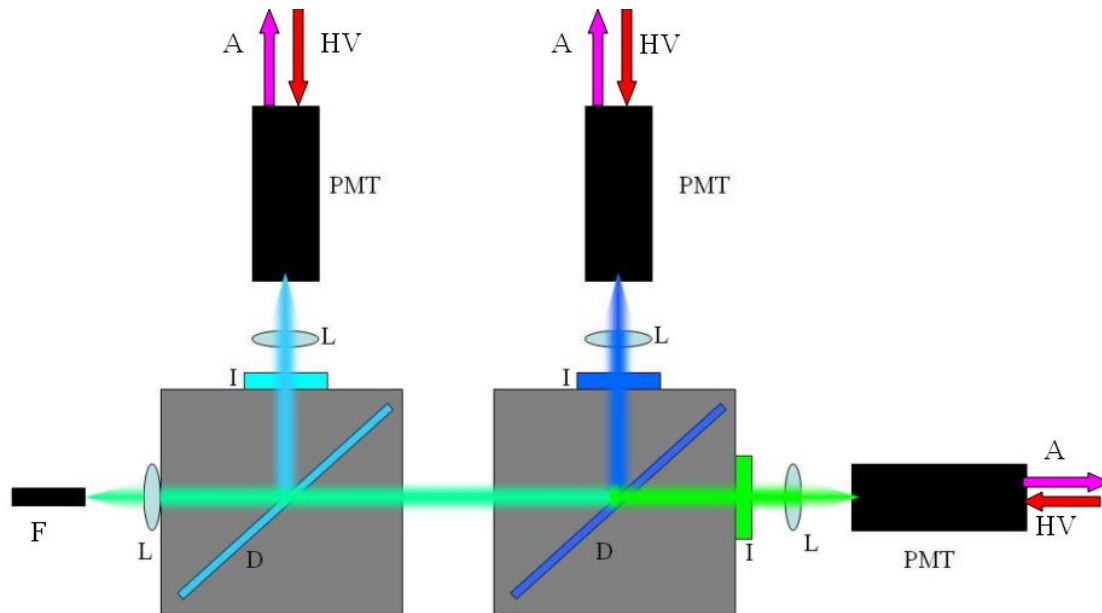


**Figure 2.15. Diagram of the light separation and detection optics and photonics. F, multimode fiber optic transmitting received light; L, 19mm focal length lens; D, dichroic filter; I, interference narrow bandpass filter; PMT, photomultiplier tube; A, anode signal out; HV, high voltage in.**

### 2.3.3.7.2 Uncertainty analysis

Uncertainties for the CompLDV generation 1 probe were analyzed in both the design and operation phases. The sources of uncertainty for the CompLDV technique are very similar to those for any LDV technique, including Doppler frequency uncertainties due to inherent electronic and photonic noise, uncertainties in the exact geometry of the interference fringe field, and beam propagation-direction uncertainties as discussed in section 2.3.3.7.2.3. The uncertainties due to random noise in the signal are manifest as random uncertainties that broaden the results and limit the dynamic range of the instrument. In contrast, the uncertainties in the propagation-direction and fringe field are systematic uncertainties that produce biases in the data and must be mitigated as much as possible. A discussion of the quantification of the CompLDV1 uncertainties follows.

#### 2.3.3.7.2.1 Random uncertainties of fundamental quantities

As already mentioned, the random uncertainties in fundamental measurement quantities arise primarily from the uncertainties in the measurement of the Doppler frequencies due to noise. The effects of noise on the signal frequency estimation are discussed in detail by Shinpaugh et al. (1992) and to follow in chapter 1. A typical estimate for the RMS uncertainty in Doppler frequency measured for typical noise-levels encountered in a back-scatter LDV configuration is  $\delta f = 0.1/T$  where  $T$  is the duration of the Doppler burst. To quantify the effects of this frequency uncertainty, we consider the uncertainties in the Doppler velocity as determined by the dual-beam LDV Doppler equation (2.15),

$$\delta U = \sqrt{(d\delta f)^2 + (f\delta d)^2} \quad (2.26)$$

In a typical LDV system, the second term  $\delta d$  is often omitted since it is assumed that the fringe field is homogeneous and the fringe spacing is known; however, in the CompLDV this term must be retained since the fringe space for any measurement is determined by the particle crossing position along the beam bisector. In the case of the CompLDV1, then, the position and velocity uncertainty are intrinsically linked.

For the purpose of analysis, let us consider the fringe space profiles to vary in a linear manner and only along the beam bisector directions. For the small measurement volumes considered (about  $200 \mu m$  in diameter), this is an excellent assertion, as Figure 2.16 shows in the plot of equation (2.19) for a length of  $200 \mu m$ , beam waist diameter of  $20 \mu m$ , wavelength of  $514.5 nm$ , full-angle of bisection of  $10^\circ$ , and off-waist crossing distance of  $6 mm$  which are typical parameters for the outer sets of beams for the CompLDV1. The first-order Taylor-series expansion around  $x' = 0$  yields

$$d(x') = \frac{\lambda}{2 \sin \theta} \left[ 1 - x' \left( \frac{x_w}{x_R^2 + x_w^2 / \cos^2 \theta} \right) \right] \equiv d_0 (1 - Ax') \quad (2.27)$$

The relative error between this result and the exact equation (2.19) is plotted in Figure 2.17. With confidence in this approximation, we may now further develop our analytical model for the uncertainties in the velocity and position for the CompLDV1. Using equation (2.27) for the fringe space variation and equation (2.18) to obtain the functional relationship between frequency and fringe spacing, the bisector-direction position measured by a pair of overlapping measurement volumes sensing the same velocity component is

$$x' = \frac{f_1 d_{01} - f_2 d_{02}}{A_1 f_1 d_{01} - A_2 f_2 d_{02}} \quad (2.28)$$

where the subscripts 1 and 2 index the overlapping measurement volumes. Applying equation (2.7) to equation (2.28), assuming only random uncertainties in the frequencies,  $f_1$  and  $f_2$ , one may obtain the uncertainty relationship for the position:

$$\delta x' = \frac{(A_1 - A_2)}{(A_1 f_1 d_{01} - A_2 f_2 d_{02})^2} \sqrt{(d_{01} f_1 d_{02} \delta f_2)^2 + (d_{01} f_2 d_{01} \delta f_1)^2} \quad (2.29)$$

If we now consider the case when  $x' = 0$ , so that  $f_1 d_{01} = f_2 d_{02} = U_\perp$  according to analysis leading to equation (2.18), equation (2.29) simplifies drastically to

$$\delta x' = \frac{\sqrt{2}}{A_1 - A_2} \frac{\delta U_0}{U_0} \quad (2.30)$$

where  $U_0$  is a velocity measured from a particle crossing the fringes at  $x' = 0$ . To get a first-estimate for the relative uncertainty term in equation (2.30), we may use equation (2.26) without considering the fringe uncertainty for the moment. In this case,

$$\frac{\delta U_0}{U_0} = \frac{d_0 \delta f}{U_0} = \frac{d_0 \delta f}{d_0 f} = \frac{\delta f}{f} \quad (2.31)$$

The duration of the burst,  $T$ , also known as the transit time is given as

$$T = D / \|\vec{U}\| \quad (2.32)$$

where  $D$  is the length (or width) of the measurement volume where the particle crosses. We now consider the approximate relationship between the Doppler frequency and the transit time for the case when the velocity vector is aligned with the measured velocity,  $U_0$ ,

$$T = \frac{D}{fd_0} \quad (2.33)$$

where we may now define the number of fringes crossed as  $N_f = \frac{D}{d_0}$ . Finally, we may

evaluate all that we have discussed in equation (2.31) to obtain

$$\frac{\delta U_0}{U_0} = \frac{\delta f}{f} \approx \frac{0.1}{T} \frac{T}{N_f} = \frac{1}{10N_f} \quad (2.34)$$

For a worst-case estimate, we will consider the CompLDV1 measurement volume with the fewest fringes for the evaluation of equation (2.34). In this case, Table 2.3 gives the nominal fringe space as  $6.86 \mu\text{m}$  leading to a total of 29 fringes in the widest part of the measurement volume. The relative RMS uncertainty in the velocity is then 0.34%. As per the discussion in section 2.3.3.7.4.1, we must analyze two cases of the fringe gradients,  $A_1$  and  $A_2$ . Again referring to Table 2.3,  $A_1 = -182.2 \text{m}^{-1}$  and  $A_2 = 166.7 \text{m}^{-1}$ . We first consider the design case where both sets of fringes vary in space. Evaluating equation (2.30) yields  $\delta x' = 13.8 \mu\text{m}$  or  $\delta x' / D = 6.9\%$  for RMS uncertainty values. The case discussed in section 2.3.3.7.4.1 takes  $A_2 = 0$  for optical implementation reasons, and the resulting position uncertainties are  $\delta x' = 26.4 \mu\text{m}$  or  $\delta x' / D = 13.2\%$  for RMS uncertainty values. A summary of the instantaneous uncertainties for 20:1 odds are given in Table 2.4 where the ‘original system’ refers to the case when both of the overlapping fringe patterns have significant fringe spacing variations and the ‘modified system’ refers to the case when the outer beams form parallel fringes and only the inner beams result in a varying fringe pattern.

With these uncertainties it is now possible to evaluate the fringe space uncertainty appearing in equation (2.26). We may obtain an uncertainty equation for the instantaneous fringe space estimate using equation (2.27) as  $\delta d = d_0 A \delta x'$ . Using the values obtained above  $\delta d / d_0 = A \delta x' \approx 0.25\%$  for the case with two sets of varying fringes or  $\delta d / d_0 = A \delta x' \approx 0.48\%$  for one parallel fringe set and the other varying along the bisector. Finally, we may evaluate the normalized velocity uncertainty where we consider the case of a particle crossing the measurement volume at  $x' = 0$  such that

$$\frac{\delta U}{U_0} = \sqrt{\left(\frac{\delta f}{f}\right)^2 + \left(\frac{\delta d}{d_0}\right)^2} \quad (2.35)$$

Using this equation applied to the case of two sets of varying fringes, the RMS uncertainty in the instantaneous velocity for the measurement volume formed by the outer set of beams is  $\frac{\delta U}{U_0} = 0.29\%$  while for the inner set it is  $\frac{\delta U}{U_0} = 0.42\%$ . In the case of

one parallel fringe set and one varying, the parallel fringe set is the outer pair of beams and will have no significant random uncertainty contributions from the fringe term and

results in a RMS velocity uncertainty of  $\frac{\delta U}{U_0} = 0.15\%$  while the velocity uncertainty for the inner pair that does have varying fringe spacing is  $\frac{\delta U}{U_0} = 0.59\%$ . One may consider the possibility of using both of the velocity measurements by taking an average of the two. This will result in a total uncertainty of  $\frac{\delta U}{U_0} = \frac{1}{\sqrt{2}} \sqrt{\left(\frac{\delta U}{U_0}\right)_1^2 + \left(\frac{\delta U}{U_0}\right)_2^2}$ .

Unfortunately, in both of these cases, the inequity of the uncertainties in the two estimates results in a greater uncertainty for the mean than for the uncertainty from the outer beams.

The development for the uncertainty in the acceleration is similar to the velocity uncertainty. The dual-beam LDV acceleration equation (2.20) may be used to obtain the acceleration uncertainty

$$\delta A \approx \sqrt{(d\delta\gamma)^2 + (\gamma\delta d)^2} \quad (2.36)$$

where  $\gamma \equiv \frac{\partial f}{\partial t}$  and  $A$  is the Doppler acceleration measured. The uncertainty in estimating the chirp parameter  $\gamma$  is considered in detail in the chapter to follow, but two key bits of information are needed for the present analysis. First, it is shown in the next chapter that the appropriate signal parameter that scales the uncertainties in any estimator that approaches the Cramer-Rao lower bound defining the lowest possible estimation variance for a given model signal (Albrecht et al. 2004) is the square of the spectral line width given by the burst duration as  $(\Delta f)^2 = 1/T^2$ . While in the case of the velocity, we may establish an approximated relationship between the burst duration and the velocity, no such relationship exists between the burst duration and the acceleration. This matter complicates the normalization of the acceleration uncertainties and reveals an important point about this uncertainty—that the acceleration uncertainty is more-closely related to the velocity magnitude than the acceleration value. The second key bit of information from chapter 1 is the value of the RMS uncertainty for the chirp parameter estimation for typical noise levels,  $\delta\gamma \approx 1/T^2$ . Equation (2.36) may be evaluated further by including the estimate for the chirp parameter uncertainty and normalizing by the measured acceleration  $A_0 \equiv \gamma d_0$  to obtain

$$\frac{\delta A}{A_0} = \sqrt{\left(\frac{1}{\gamma T^2}\right)^2 + \left(\frac{\delta d}{d_0}\right)^2} \quad (2.37)$$

Unfortunately, at this point we still have a dependency in the chirp parameter, which is not surprising in light of the earlier discussion. To remedy this, let us first disregard the second term in equation (2.36) due to the fringe space uncertainty and next let us use a different normalization parameter,  $A_U \equiv \|\vec{U}\|/T = D/T^2$ , which yields:

$$\frac{\delta A}{A_U} = \frac{d_0}{D} = \frac{1}{N_f} \quad (2.38)$$

This very concise form reveals the close relationship between the velocity magnitude and the acceleration uncertainty. A good estimate for the acceleration uncertainty is obtained using the number of fringes in the measurement volume due to the outer beams,

$$\frac{\delta A}{A_U} = 1.5\%.$$

The beam geometries may be used to determine the uncertainties in the Cartesian tunnel coordinate system as described by the directions in equation (2.23). The 20:1 velocity uncertainties for the original ComplDV1 system are given as

$$\delta \left\{ \begin{array}{l} U / \|\vec{U}\| \\ V / \|\vec{U}\| \\ W / \|\vec{U}\| \end{array} \right\} = \left\{ \begin{array}{l} 0.56 \\ 0.72 \\ 0.63 \end{array} \right\} \% \text{ while the acceleration uncertainties are } \delta \left\{ \begin{array}{l} A_x T / \|\vec{U}\| \\ A_y T / \|\vec{U}\| \\ A_z T / \|\vec{U}\| \end{array} \right\} = \left\{ \begin{array}{l} 1.47 \\ 1.89 \\ 1.66 \end{array} \right\} \%.$$

For the modified ComplDV1 system with one-set of parallel fringes per transmitting

$$\text{head, the 20:1 velocity uncertainties are } \delta \left\{ \begin{array}{l} U / \|\vec{U}\| \\ V / \|\vec{U}\| \\ W / \|\vec{U}\| \end{array} \right\} = \left\{ \begin{array}{l} 0.29 \\ 0.36 \\ 0.32 \end{array} \right\} \% \text{ while the acceleration}$$

uncertainty estimates are the same as the original system configuration.

**Table 2.4. 20:1 Uncertainties in instantaneous measurement quantities for a single measurement head in the ComplDV1.**

Quantity	Original system	Modified system
$\delta x'$	27.0 $\mu m$	51.7 $\mu m$
$\delta x' / D$	13.5%	25.9%
$\frac{\delta U}{U_0}$	0.57%	0.29%
$\frac{\delta A}{A_U}$	2.9%	2.9%

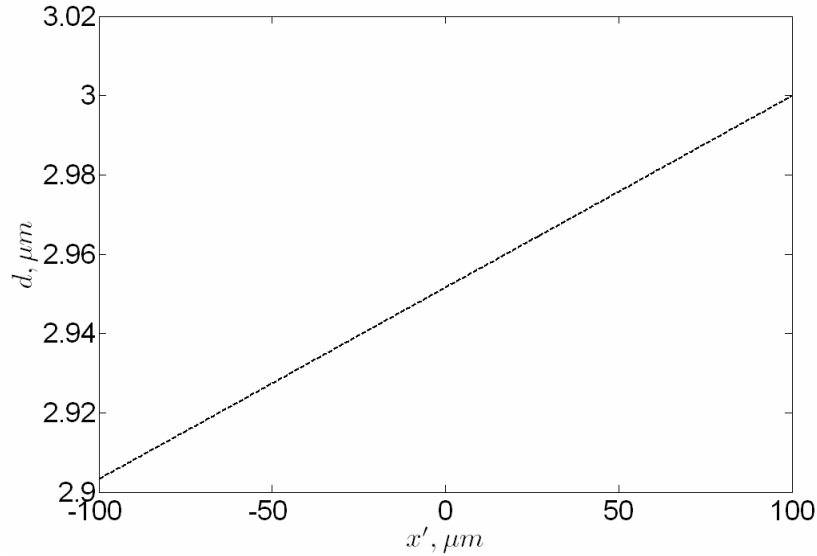


**Figure 2.16. Predicted fringe variation from Gaussian beam propagation due to off-waist crossing of beams with parameters for the CompLDV1.**

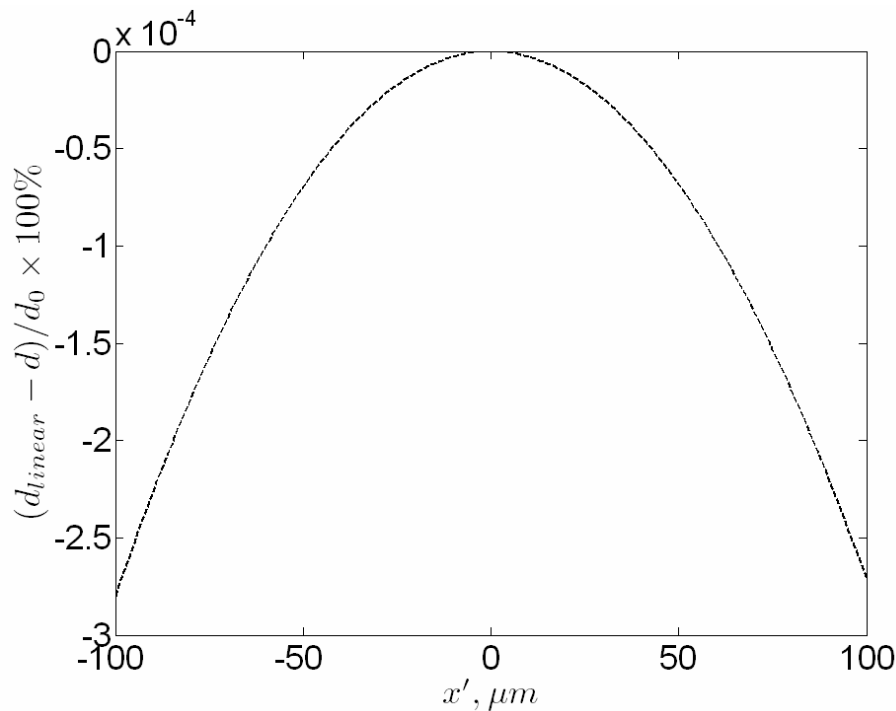


**Figure 2.17. Relative truncation error of equation (2.27) compared to the exact equation (2.19) where  $d_0 \equiv \frac{\lambda}{2 \sin \theta}$ .**

#### 2.3.3.7.2.2 Velocity Statistics Uncertainties

The instantaneous velocity uncertainty values were used to determine the uncertainties in the velocity statistics throughout a boundary layer profile. Data in the 2D flat-plate

turbulent boundary layer (TBL) at  $Re_\theta = 7600$  were used to give the statistical variations of the velocities to allow an uncertainty assessment. Since the uncertainty of a measurement set depends upon the true distribution of the quantity sampled, this simulation takes the variation in the turbulence intensities into account. This dependency is easily seen for the estimation of the statistical mean, where the standard error of the mean for the variable  $x$  is given as  $S_x = \frac{\sigma(x)}{\sqrt{n}}$  where  $\sigma(x)$  is the standard deviation of  $x$ ,

and  $n$  is the total number of samples for  $x$ . Note that this statistical error value occurs even when  $x$  is sampled without any inherent uncertainties. The addition of uncertainties in the sampling of  $x$  increases the total uncertainty in the statistical quantity.

Series of values for each velocity component were produced with mean values and standard deviations given by the profile data. Gaussian probability distribution functions were used for all the simulated velocity distributions. No cross-correlations or higher-order moment values were introduced to the simulated data sets so that any such statistics measured would indicate an uncertainty in that value. The uncertainties for the velocity statistics up to triple-products (third-moments of velocities) non-dimensionalized by the wall friction velocity in the 2D flat plate TBL are plotted in Figure 2.18-Figure 2.23. These values may be taken as the uncertainty values for the statistical quantities estimated using the CompLDV1.

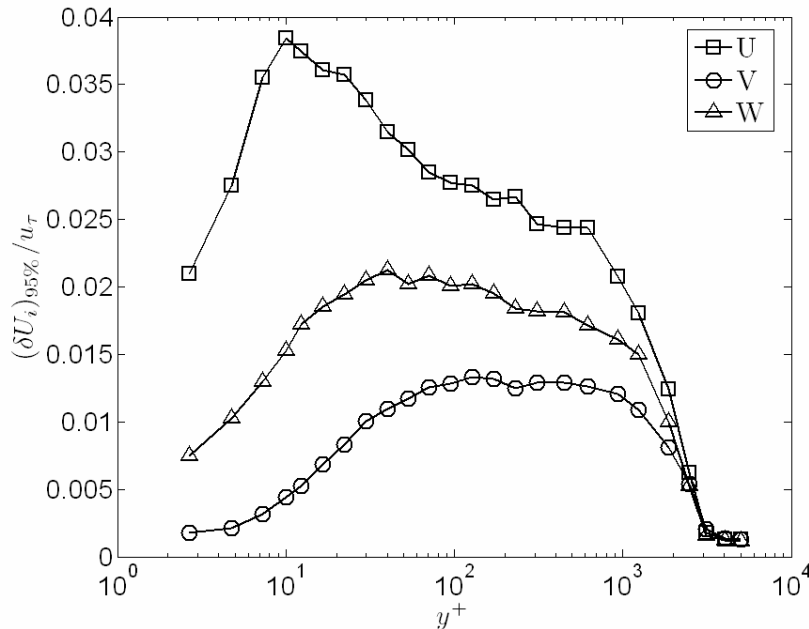


**Figure 2.18. 20:1 uncertainties in the mean velocities throughout a 2D flat plate turbulent boundary layer profile non-dimensionalized on the wall friction velocity.**

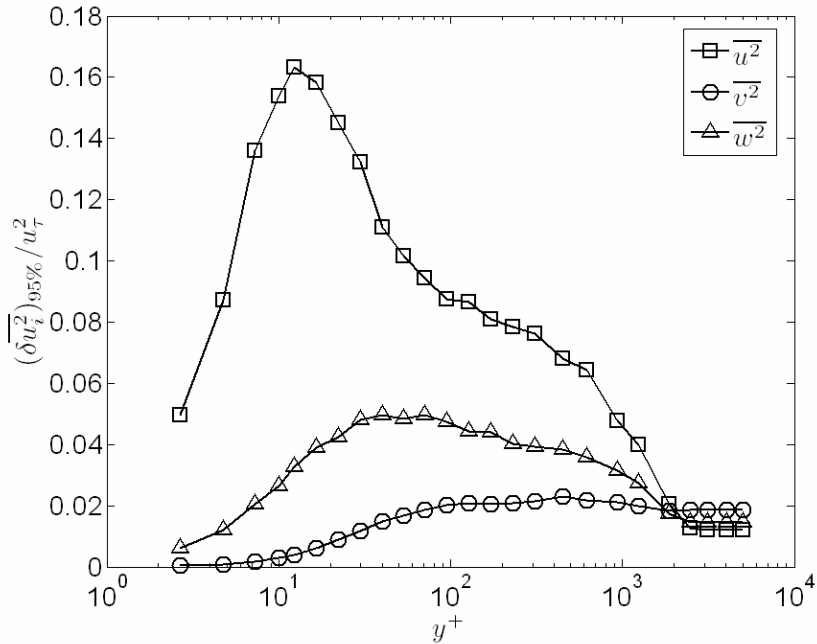


**Figure 2.19.** 20:1 uncertainties in the Reynolds normal stresses throughout a 2D flat plate turbulent boundary layer profile non-dimensionalized on the wall friction velocity.

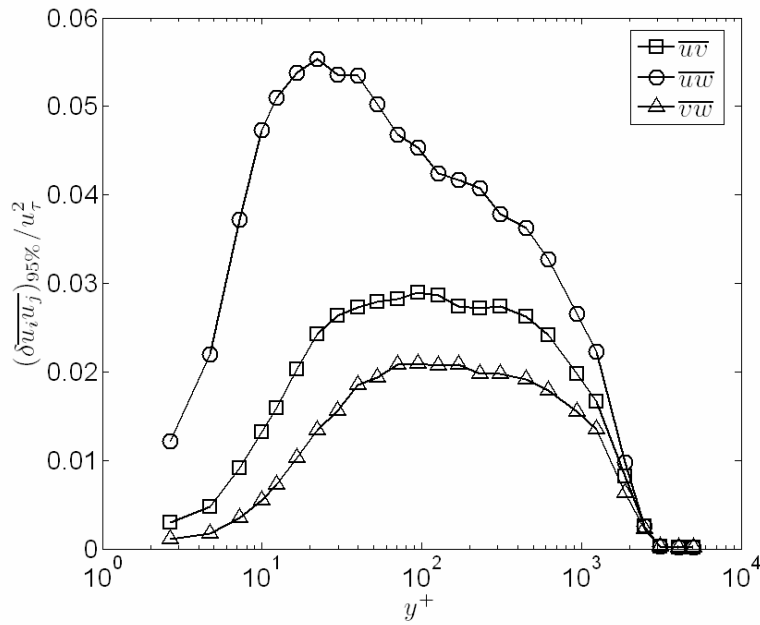


**Figure 2.20.** 20:1 uncertainties in the Reynolds shear stresses throughout a 2D flat plate turbulent boundary layer profile non-dimensionalized on the wall friction velocity.

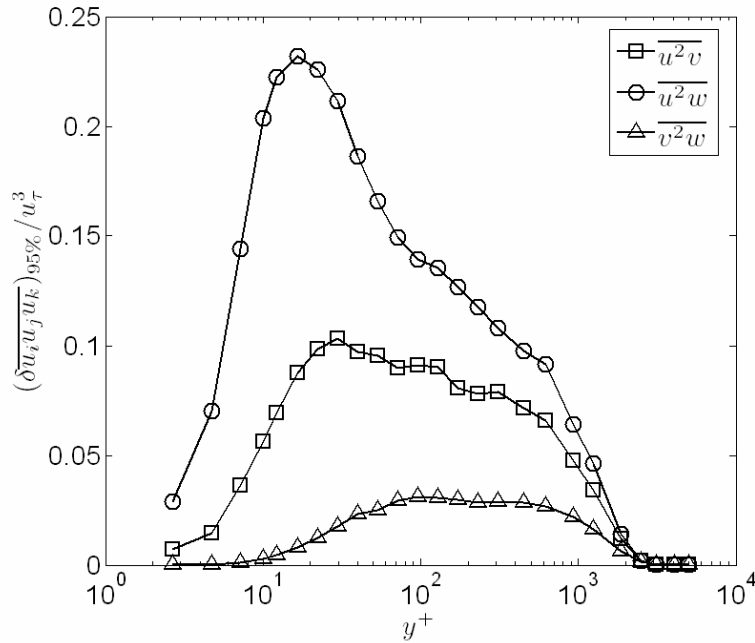


**Figure 2.21.** 20:1 uncertainties in velocity triple-products throughout a 2D flat plate turbulent boundary layer profile non-dimensionalized on the wall friction velocity.

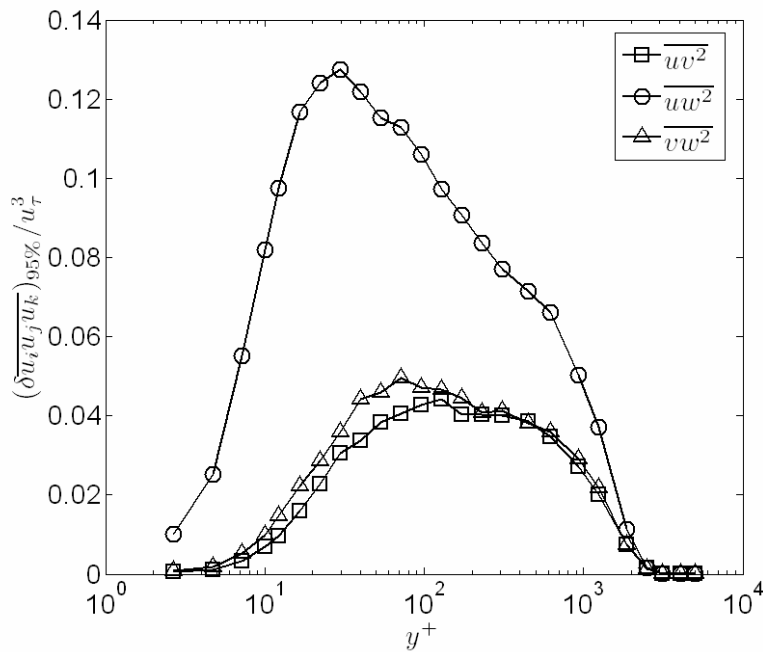


**Figure 2.22.** 20:1 uncertainties in velocity triple-products throughout a 2D flat plate turbulent boundary layer profile non-dimensionalized on the wall friction velocity.

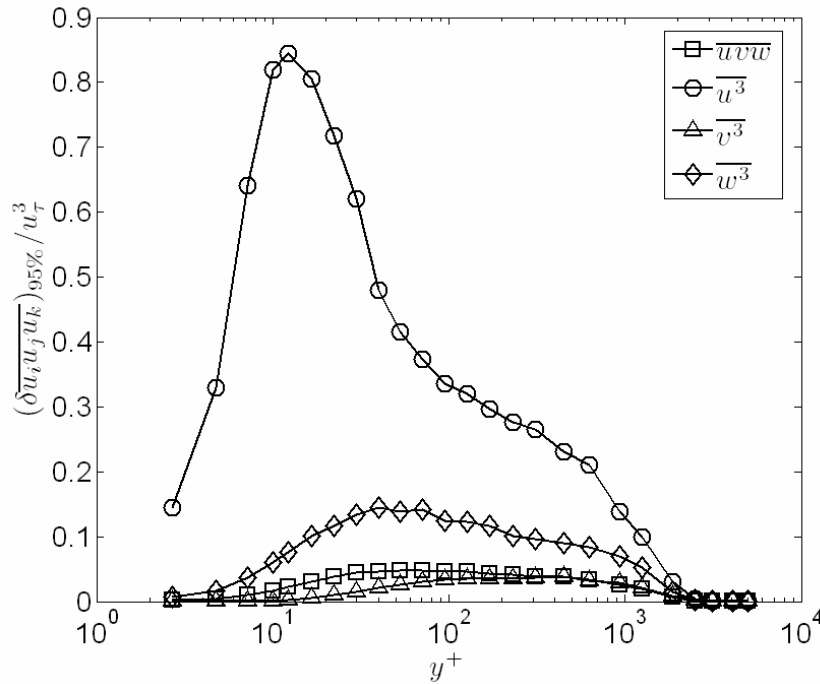


**Figure 2.23. 20:1 uncertainties in velocity triple-products throughout a 2D flat plate turbulent boundary layer profile non-dimensionalized on the wall friction velocity.**

### 2.3.3.7.2.3 Beam angle measurement

One of the most critical tasks in the setup of a multi-component LDV system is the measurement of the beam angles. In the current study, the beam angles are measured by measuring the locations of each beam in two horizontal planes. From this it is possible to estimate beam propagation unit vectors. The procedure for making these planar measurements is to position the probe at a height such that the center of the measurement volume is positioned on a paper that is fixed to the surface of the glass window used for measurements. A reference line corresponding to the x-axis of wind tunnel is drawn using drafting triangles and squares aligned with the wind tunnel side walls so that beam vectors may be represented in the tunnel coordinate system. It is important to use low laser power when measuring beam angles to avoid burning the paper used for locating the beams and to avoid the health hazards of over-exposure to the laser beams. During this procedure, the operator should be wearing laser goggles to protect his/her eyes from the laser flare through the paper. A fine-point pencil is used to make the location of the measurement volume on the paper. Next the probe is moved a distance vertically to allow for a second measurement of the planar beam positions. This vertical motion is known very well thanks to the high precision traverse with a linear encoder. At the second height, typically 50mm or greater from the first height, the location of the center of each beam is located on the paper. After all beams are marked with the pencil, the paper is removed from the wind tunnel and placed on a flat surface for obtaining the coordinates of the marks made. A pair of dial calipers with divisions down to 0.001" (25.4  $\mu\text{m}$ ) is used to measure the coordinates of each beam.

The geometry of the beam vector measurements for a single measurement volume is given in Figure 2.24. The Cartesian beam unit vectors are formed simply as

$$\hat{b}_i \Big|_T = \frac{1}{\sqrt{(\Delta x)^2 + (\Delta y)^2 + (\Delta z)^2}} (\Delta x \hat{i} + \Delta y \hat{j} + \Delta z \hat{k}) \quad (2.39)$$

where  $\Delta x$ ,  $\Delta y$ , and  $\Delta z$  are the differences between those coordinate directions from one planar measurement to the next and the subscript  $T$  indicates tunnel coordinates. For a pair of beams forming a measurement volume, the Doppler measurement direction is determined using the beam unit vectors as

$$\bar{m} = (\hat{b}_1 \times \hat{b}_2) \times (\hat{b}_1 + \hat{b}_2) \quad (2.40)$$

The uncertainty for the measurement vector is a function of the uncertainty in each of the position measurements used in equation (2.39). Due to the cumbersome algebra, the uncertainties for the measurements have been propagated using a Monte Carlo simulation. The individual measurements in the  $x$ - $z$  plane were given a 20:1 uncertainty of 0.005'' (254  $\mu\text{m}$ ) while an uncertainty of 0.0005'' (25.4  $\mu\text{m}$ ) is considered in the vertical measurements due to high resolution of the vertical traverse. The uncertainty computed is the angle made between the true measurement vector and the simulated measured one. The resulting 20:1 uncertainty from the simulation is  $\pm 0.97^\circ$  for a 50mm separation between the measurement planes. For 75 mm of separation between the planes, the uncertainty reduces to  $\pm 0.68^\circ$ .

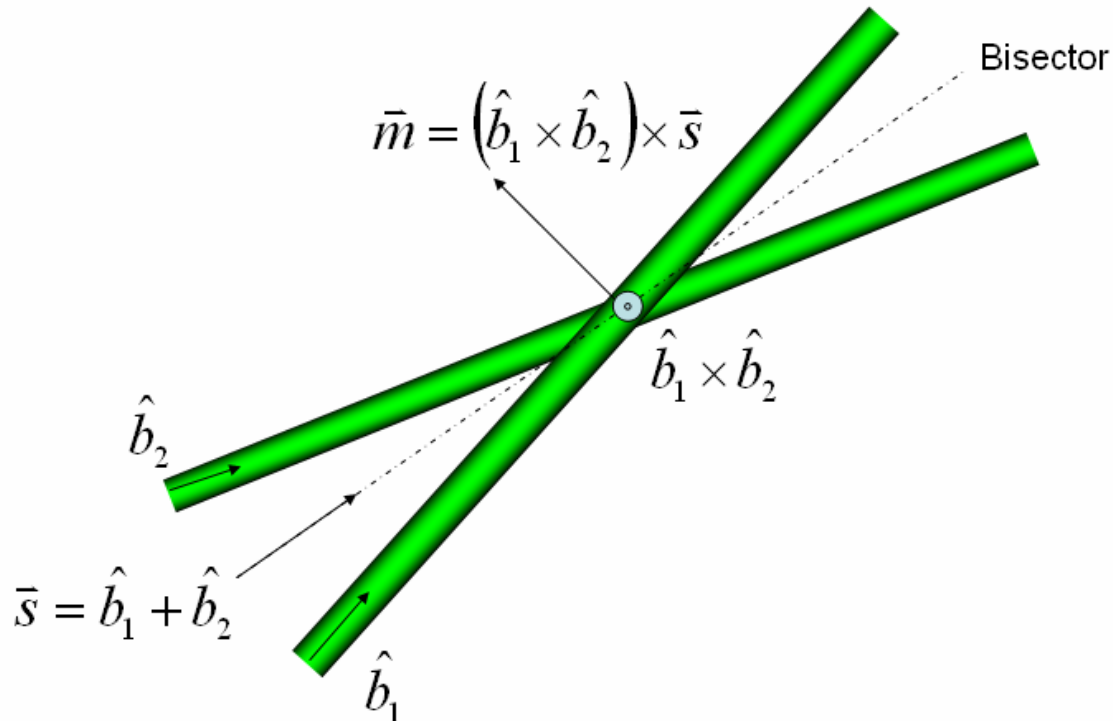


**Figure 2.24. Geometry of the beam and measurement vectors for a pair of interfering beams forming a measurement volume.**

### 2.3.3.7.3 Calibration

Two calibration procedures were used for estimation of the fringe spacing within the measurement volume—a wire on a rotating wheel and a uniform flow. The wire/wheel calibration procedure is similar to the one described by Czarske et al. (2002) and allows for accurate positioning of the wheel plane within the measurement volume to estimate fringe spacing. The uniform flow calibration was implemented as an attractive means of calibration since the scatterer used was an actual particle. Both these methods are described in more detail to follow.

#### 2.3.3.7.3.1 Wire/wheel calibration

In the wire/wheel calibration, a 4  $\mu\text{m}$  diameter tungsten wire affixed radially to a rotating wheel is used as a light-scattering object with a well-known position and velocity. For the wheel, a 4" diameter commercial optical beam chopper (Thor Labs model MC1000) was used which has a frequency drift less than 100 ppm at rotational frequencies up to 100Hz. The wire/wheel configuration is depicted schematically in Figure 2.26. To traverse the wire/wheel within the measurement volume, a 5-axis precision positioning system was specified. A photograph of the calibration rig is given in Figure 2.27. It is not possible to calibrate each of the measurement volumes while keeping the wheel in the same orientation since two of the measurement volumes lie in a plane orthogonal to the plane in which the other four lie. Thus the entire calibration rig was mounted on a rotation stage. In order to attempt to define a reference position, it was decided that the wheel should be positioned such that the wire crossing point lies at the center of rotation for the rotation stage. If this condition is accurately met, one may rotate from one pair of measurement volumes to the next while remaining at the reference position. The rotation stage chosen for this task is a Parker Daedal model 30006 stage with angular readout resolution of 0.002°. This stage has a 1.75" diameter center through-hole to allow the scattered light to pass to the receiving optics directly below. To position the wheel at the proper point in the horizontal plane, two stages are mounted offset from the center of the rotation stage. To traverse the wheel along the measurement volume bisectors, an Oriel Mike encoder-driven translation stage was mounted to a second model 30006 rotation stage used to set the wheel plane perpendicular to the beam bisector. The Mike encoder system afforded positioning resolution of 1  $\mu\text{m}$  for the wheel along the measurement volume major axis.

Three significant sources of uncertainty exist in determining the speed of the wire in the optical fringe coordinates. One is the radial location of the measurement volume along the wheel. This uncertainty may be mitigated to a fraction of the measurement volume diameter by traversing the wheel edge to intersect the measurement volume and observing the transition which occurs in the photomultiplier signal amplitude. A second uncertainty involves the angles made between the beam bisectors and the line between the center of the wheel and the crossing point. If this angle is 90°, then the velocity measured will be  $U_{\text{wire}} = 2\pi fr$  where  $f$  is the frequency of rotation of the wire and  $r$  is the radius of the measurement volume location; however, if the angles are different from 90° this speed must be multiplied by the cosine of the difference. Since the maximum speed

will be encountered when the angle is  $90^\circ$ , the probe may be positioned relative to the wheel to maximize the Doppler frequency. This second uncertainty is somewhat tolerable due to the relative insensitivity of the measured velocity with angular error (i.e., cosine near zero abscissa). The most important source of uncertainty, as determined upon practical implementation, is the radial variation of the wire velocity. Since the wire spans the entire measurement volume, signals from a range of velocities contribute to the Doppler signal measured. Furthermore, the primarily specular mode of scattering due to the wire can bias certain locations of the wire over others due to inhomogeneities along the wire such as kinks. Considering the velocity variation along the wire, the ranges of velocities possible are given as  $\Delta U_{\text{wire}} = 2\pi f \Delta r$  where  $\Delta r$  is the width of the measurement volume. At first glance, one would suggest that this error could be minimized by simply reducing the frequency of rotation, however, while this reduces the wire speed variation, the relative variation to the mean wire speed is unaffected,  $\frac{\Delta U_{\text{wire}}}{U_{\text{wire}}} = \frac{\Delta r}{r}$ . Instead, the

only fix for the problem is the use of a very large wheel such that the wire motion approaches pure translation. To quantify this uncertainty in the case of the CompLDV, the measurement volume diameter is about  $200 \mu\text{m}$  while a typical wheel radius for calibrations is  $95\text{mm}$ , yielding a velocity variation of 0.2% along the wire within the measurement volume. Since the fringe space measured is directly proportional to the velocity of the scatterer, it follows that the fringe space uncertainty due to the wire velocity variation is  $\frac{\delta d(x')}{d(x')} = \frac{\Delta U_{\text{wire}}}{U_{\text{wire}}} = \frac{\Delta r}{r} \approx 0.002$ . As noted in section 2.2.3.1.1.1, the

variation of the fringe spacing over the entire length of the measurement volume is about 3%, so an uncertainty of 0.2% in the calibration velocity immediately results in an uncertainty of nearly 10% relative to the expected fringe space range. If one were to assume a linear variation of the fringe spacing with distance, this uncertainty translates to about a  $20 \mu\text{m}$  uncertainty in the observed wire position.

#### 2.3.3.7.3.1.1 Practical implementation

In the course of implementing the wire/wheel calibration, several problems were encountered, limiting the effectiveness of the method. By far, the biggest uncertainty contributor was the radial variation of velocity along the wire. The specular nature of the scattering made the signal quality very dependent upon alignment of the wire within the measurement volume. It was observed that stronger signals occurred with different orientations of the wire since facets and kinks on the wire length resulted in preferred-direction specular reflections. Making the situation more acute was the fact that it was not possible to receive the signals from the same specular reflection site along the entire measurement volume since the LDV system was not moved along with the wire. The result was a variation of preferred scattering locations and thus a strong variation of the sensed wheel velocity. Also experienced during practical implementation was the challenge of determining the reference position to define the fringe spacing variation in universal coordinates for each measurement volume. While the system design allowed for ample adjustment to keep the measurement volume location near the center of rotation, no reliable methods for ensuring that the wheel radius remained constant upon rotation

were discovered. Instead, the problem was solved using a combination of wheel and flow calibrations wherein fringe spacings were measured for each system simultaneously by measuring the Doppler frequencies of particles of uniform velocity within the core of a wind tunnel. In light of the wire speed variation already discussed, it was decided in later studies to completely forego the wire/wheel calibrations in favor of flow calibrations where particle scatterers were used yielding a more concise technique.

#### 2.3.3.7.3.1.2 Wire/wheel results

Figure 2.25 is an example of a wire/wheel calibration acquired. It was noted in many of the calibrations the systematic wave-like deviations from linearity as seen in Figure 2.25. The explanation offered here is that due to the specular reflections from the wire and the reciprocating method of translation caused by the linear traverse motor, a cyclical variation in the prevalent wheel velocity occurred. Since even the precision translation stages being used would still have some very small amount of wobble, as the orientation of the wire changed slightly, the specular reflection would also and a different area of the wire could become the dominant scatterer for the constant light-receiving direction.

#### 2.3.3.7.3.1.3 Concluding remarks for the wire/wheel technique

The wire/wheel calibration technique was specified based upon published success with the technique for a similar application. Precision equipment was used for all aspects of positioning and wheel rotation rate control. The limiting factor to employing such a technique is the finite dimensional of a rotating wire that spans the entire measurement volume with a linear velocity gradient. This systematic uncertainty in the wire velocity along with the inconsistency in wire scattering location makes the technique unsuitable for sub-micron determination of fringe spacing variation.

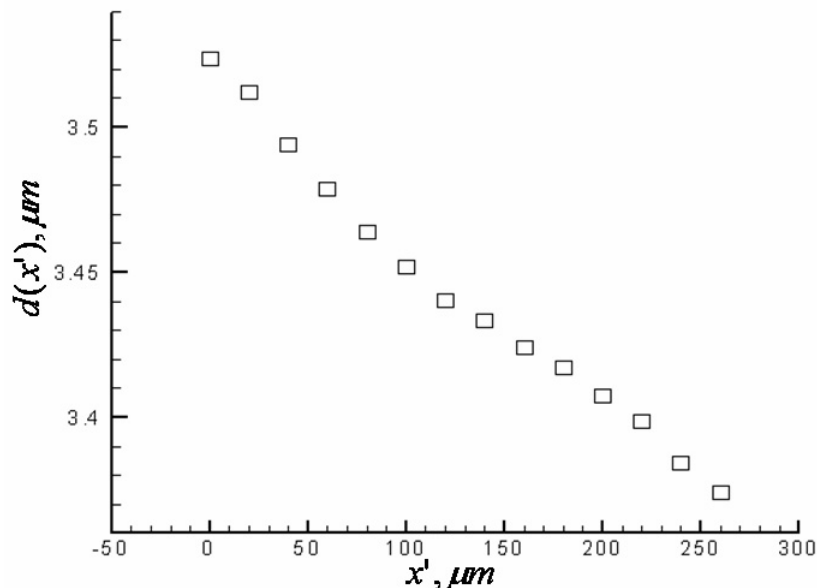


**Figure 2.25. Example of the results from the wire/wheel calibration.**

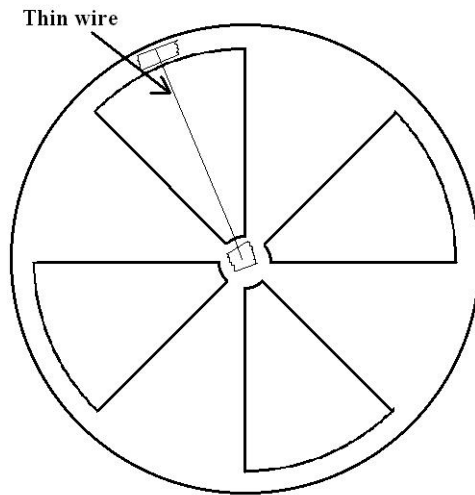


**Figure 2.26.** Schematic depicting the  $4\ \mu\text{m}$  diameter tungsten wire affixed to the optical chopper wheel.

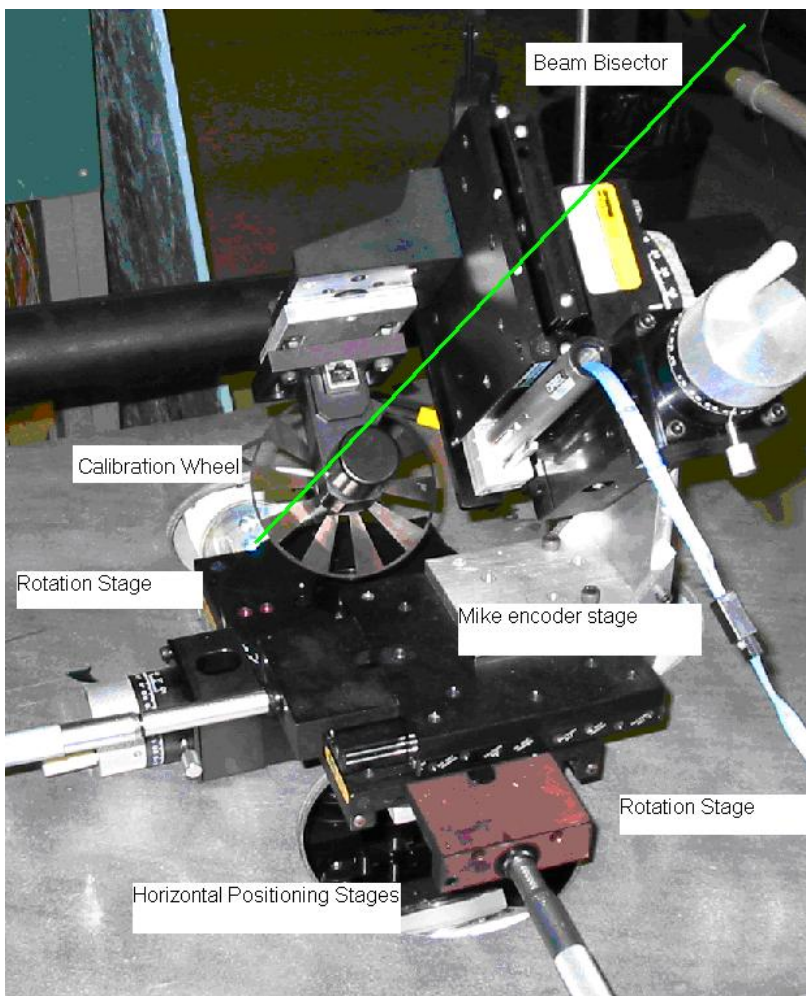


**Figure 2.27.** Photograph of the calibration rig.

### 2.3.3.7.3.2 Freestream Calibration

The freestream calibration technique utilizes the well-defined inviscid steady uniform flow in the core of a wind tunnel as a calibration flow. While no position information is available since the flow is uniform, two important bits of information may be obtained from this calibration. First, the average fringe space is determined at approximately the same uncertainty as the uncertainty in the core velocity value, which is measured using a Pitot-static probe at precisely the location of the measurement volume. Second, using coincident data, maps of the way that each fringe spacing value changes relative to the fringe spacing of the other measurement volumes are possible.

Since this technique is used for calibration, a further discussion of the uncertainties involved is necessary. First note, that since the quantities being measure are all mean-quantities, a properly-converged set of data will yield little if any uncertainties due to random errors. This indicates that any small-amplitude unsteadiness that may occur in the facility will have no effect on the quality of the calibration given a sufficient record-length of data. It is then the case that systematic errors are the remaining factors. There are two sources of such uncertainties in this technique. One is the measurement of the mean velocity at the location of the measurement volume. As mentioned this is done using a Pitot-static probe. The dynamic pressure is sensed by differencing the two lines of this probe using a Dwyer electronic digital display pressure transducer. The resolution of this device is  $\pm 0.01$  inches of water or about 0.5% of the freestream dynamic pressure. The second source of uncertainty is the measurement of the beam angles. The beam angles determine the contributions of the freestream velocity to the measured Doppler velocity. An analysis of the beam angle measurement technique is given in an independent section to follow. From that analysis, the uncertainty in the velocity measurement vector for any measurement volume is approximately  $0.7^\circ$  with this angle being the angle made between the measured Doppler velocity vector and the true Doppler velocity vector. The component of the freestream velocity (in the  $x$ -direction in tunnel coordinates) that results in the Doppler velocity measured is given as

$$U_{\perp} = \cos \theta_1 U_{\infty} \quad (2.41)$$

where  $\theta_1$  is the angle of projection between the Doppler measurement vector and the  $x$ -axis and  $U_{\infty}$  is the freestream velocity. The uncertainty in the estimated value of the Doppler velocity is

$$\frac{\delta U_{\perp}}{U_{\infty}} = \sqrt{(\sin \theta_1 \delta \theta_1)^2 + \left( \cos \theta_1 \frac{\delta U_{\infty}}{U_{\infty}} \right)^2} \quad (2.42)$$

Considering equation (2.42), an estimate for the systematic uncertainty in the mean Doppler velocity measured is 1.1% of the freestream velocity for the worst case of  $60^\circ$  angle between the measurement direction and the freestream, but improves as the measurement direction coincides with the freestream velocity direction to 0.25%.

Example Doppler frequency data obtained with this technique are given in Figure 2.28 and Figure 2.29. These data were obtained with an overlapping pair of measurement volumes (with the same beam bisector and Doppler measurement directions). A scatter

plot of the data is presented with the abscissa as the ratio between the coincident frequency measurement values for the two head. From these data, the absolute value of the fringe spacing may be determined as well as the relative variation of the fringe spacing for overlapping measurement volumes, as in Figure 2.29. This information is all that is needed to estimate velocities in any flow, however additional information is needed for the function,  $q(x')$  to allow for measurements of the particle position.

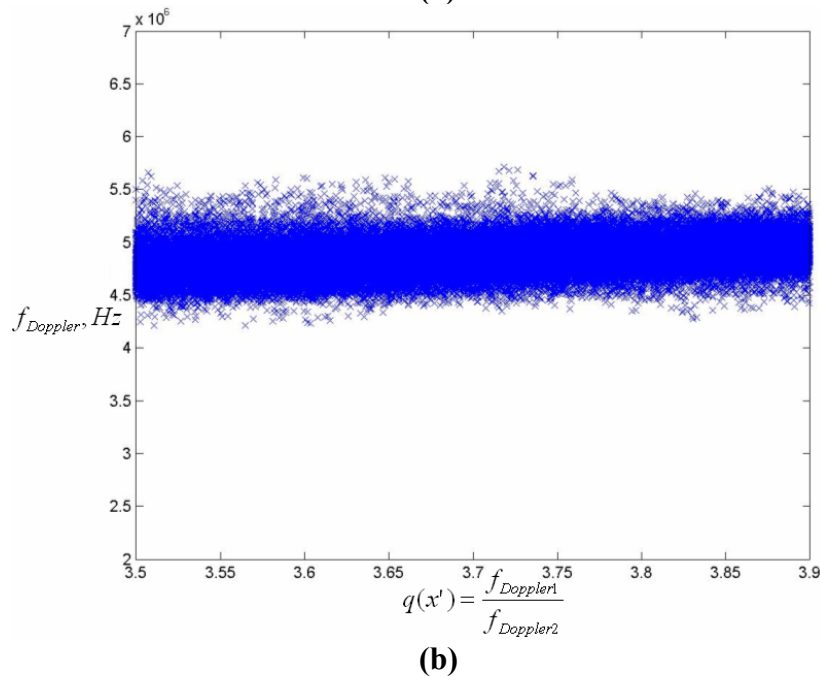
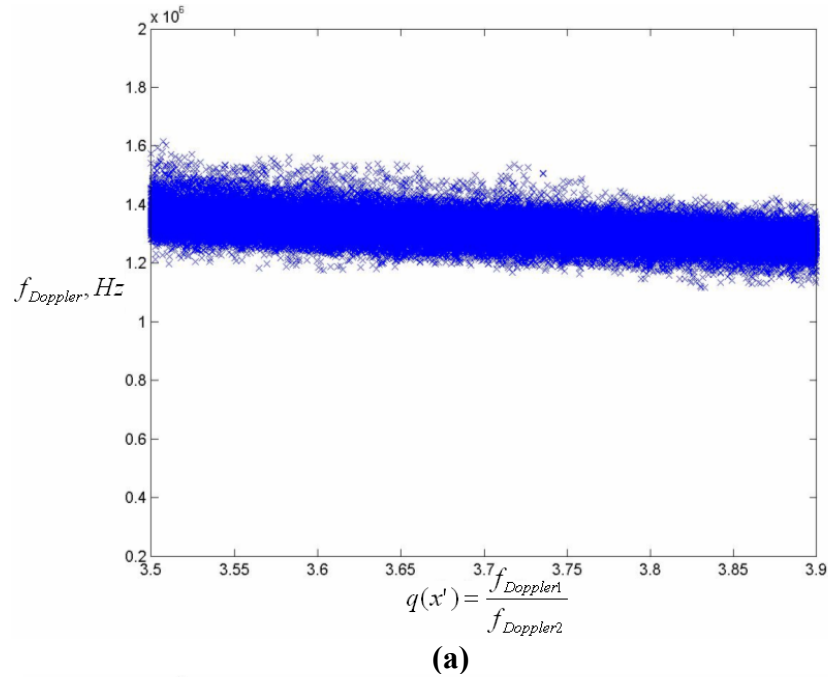
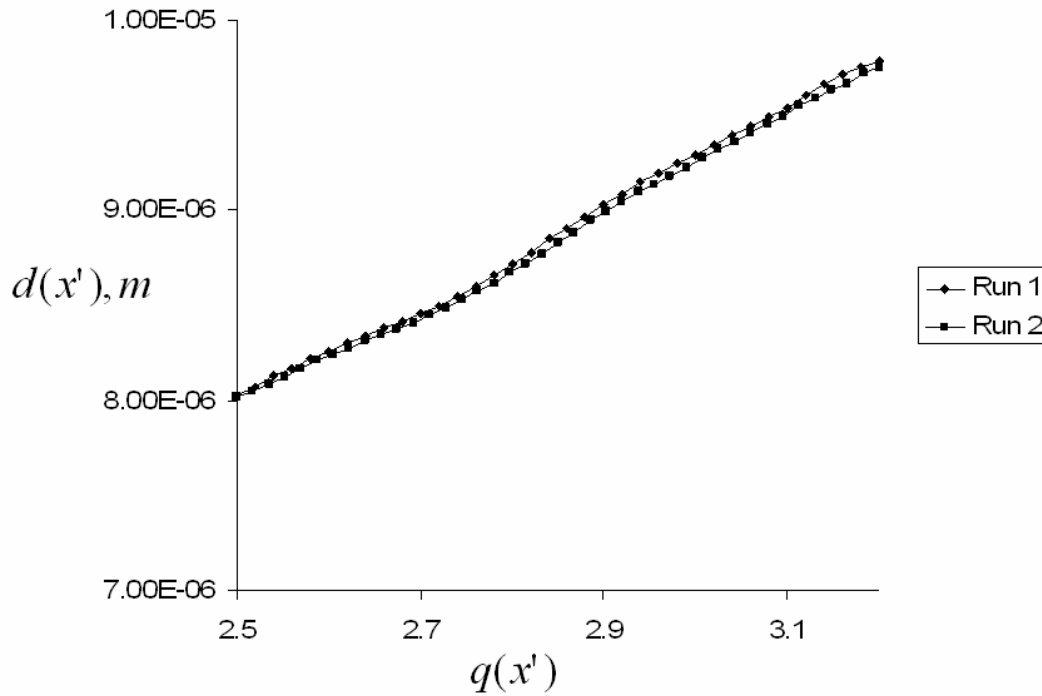
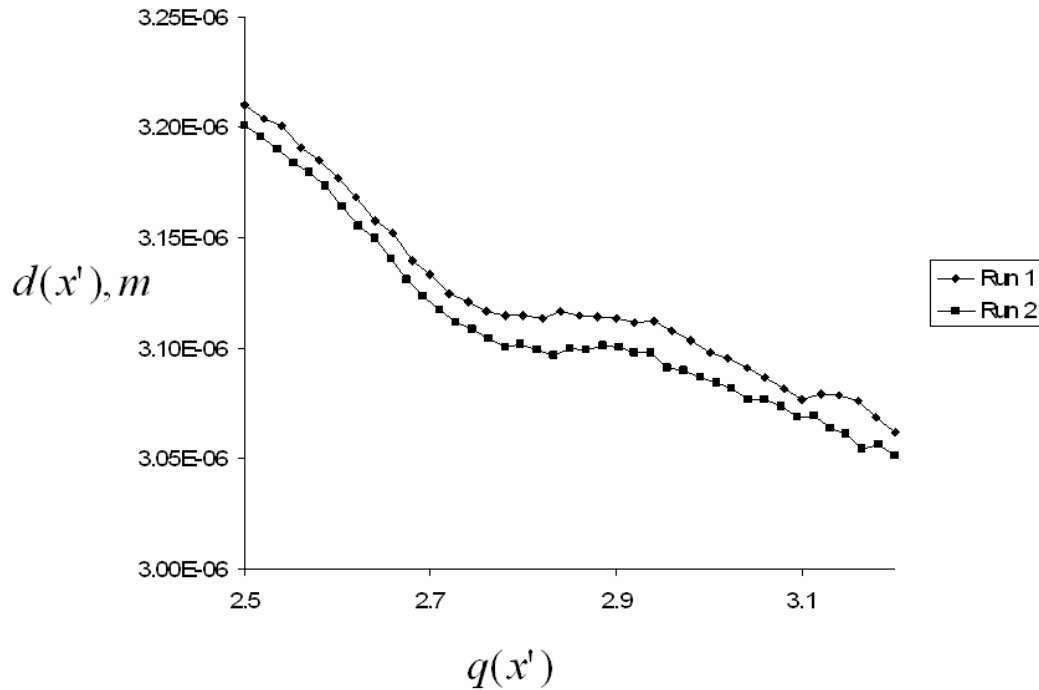


**Figure 2.28. Scatter plot of instantaneous Doppler frequency measurements versus the ratio between these Doppler frequencies for (a) inner and (b) outer overlapping measurement volumes sharing a single bisector direction.**



(a)



(b)

**Figure 2.29.** Plot of mean fringe space measurements versus the ratio between these Doppler frequencies for (a) inner and (b) outer overlapping measurement volumes sharing a single bisector direction for two different runs. Exhibits the repeatability of the technique. Note the range of scales on the ordinates.

#### ***2.3.3.7.4 Some notes on implementing the first generation CompLDV***

During the course of implementing the design of the CompLDV1, several practical aspects warranted changes to the original specifications. Many of these aspects were determined based upon experience with equipment and components and the real-world behavior of these sub-systems. A couple of the major aspects that were addressed for improvement are discussed to follow.

##### **2.3.3.7.4.1 Changes to the interference pattern**

A highly-magnified depiction of a typical interference pattern for a cross-section of a dual-beam LDV measurement volume is given in the photograph in Figure 2.30. In this figure, we note the generally-Gaussian intensity distribution in the vertical direction of the photograph and clearly-defined fringes that appear superimposed on the Gaussian intensity pattern. Each CompLDV1 head has two beams positioned on the outer portions of the transmitting lenses that have a short Rayleigh length of  $610 \mu\text{m}$ . These beams have a large diameter as they pass through the transmitting lens and since these beams are not centered within that lens, under go a highly non-axisymmetric refraction. The result of this condition is a complex interference of wave-fronts that occur in off-focus beam cross-sections. This condition has been documented in photographs such as the one in Figure 2.31. At least two interference patterns are evident in this photograph—one coming from the intersection of two laser beams manifest as the horizontal lines in the picture and another interference pattern identical in both of the superimposed beams that is distributed circumferentially around the beam. Clearly, the latter interference is undesirable as it is complex and distinctly non-Gaussian and results in significant signal broadening.

For the CompLDV1, the solution for the complex off-focus intensity pattern in the outer-beams was to eliminate the off-waist focusing for those beams. By reducing the size of the collimated beams for the outer pair to about 2 mm by changing the focal length of the collimating lenses, a Gaussian intensity pattern is achieved. This change unfortunately compromises the predicted uncertainties in the particle position for the CompLDV1 as already discussed, but when practically implemented it acts to reduce these uncertainties due to the high degree of signal broadening due the fringe pattern in Figure 2.31.

A second advantage to the parallel fringe sets for the CompLDV1 is that complete velocity vectors may be measured with only three-signals. In the case of 6 sets of fringes with converging/diverging patterns, all six signals are necessary for the measurement of the velocity vector. With the sets of parallel fringes, the CompLDV1 can function optically just as a conventional dual-beam mode LDV. This can be useful for high-frequency spectral studies, as the use of only one signal per laser wavelength significantly increases the signal-to-noise ratio and thus the probability of receiving valid signals and this leads to higher data rates. The measurements reported by Lowe and Simpson (2006) were acquired with the 3-component parallel fringe sub-system of the CompLDV1.

#### 2.3.3.7.4.2 Conversion from a two-wavelength to a three-wavelength system

One of the advantages of using Argon-ion ( $\text{Ar}^+$ ) lasers at the prototype level is the number of usable wavelength lines available. In the case of the CompLDV1 probe, the initial design calls for a two-wavelength system (for instance see the photograph in Figure 2.11) that utilizes the two-strongest lines from the  $\text{Ar}^+$  laser—the 488nm and 514.5nm lines. It may be easily shown that the addition of incoherent signals on the same wavelength of light decreases the modulation depth of the signal and the signal-to-noise ratio with it. This is evident since the intensity signals from the signal pedestals will add due to the mean-square nature of this quantity and there is essentially an increase in background (un-modulated) light. The problem is further exacerbated by the fact that the shot noise from the PMTs is proportional to the square-root of the intensity measured. The only way to mitigate the problem is to superimpose as few fringe patterns of the same wavelength as possible. The solution for the CompLDV1 was to include the 476.5nm line in addition to the two primary lines already mentioned. Despite the relatively lower power on this third line, the net result is a significant increase in signal-to-noise ratios for each of the measurement volumes. The other advantage for this is, when using two lasers, each interference pattern receives all the light from a single laser line. This reduces the complexity of the optical table components since the polarizing beam-splitting cubes and corresponding half-wave retardation plates are not necessary in the three-wavelength CompLDV1.

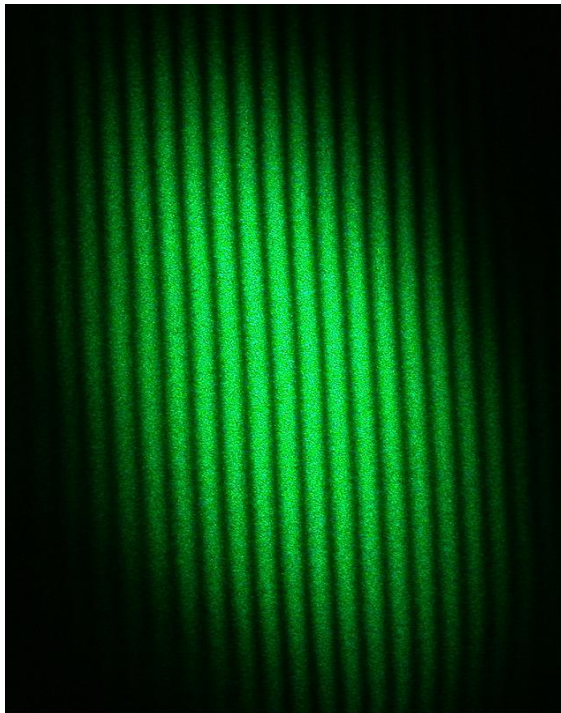


**Figure 2.30. Photograph of a highly-magnified fringe pattern in the cross-section of a dual-beam LDV measurement volume.**

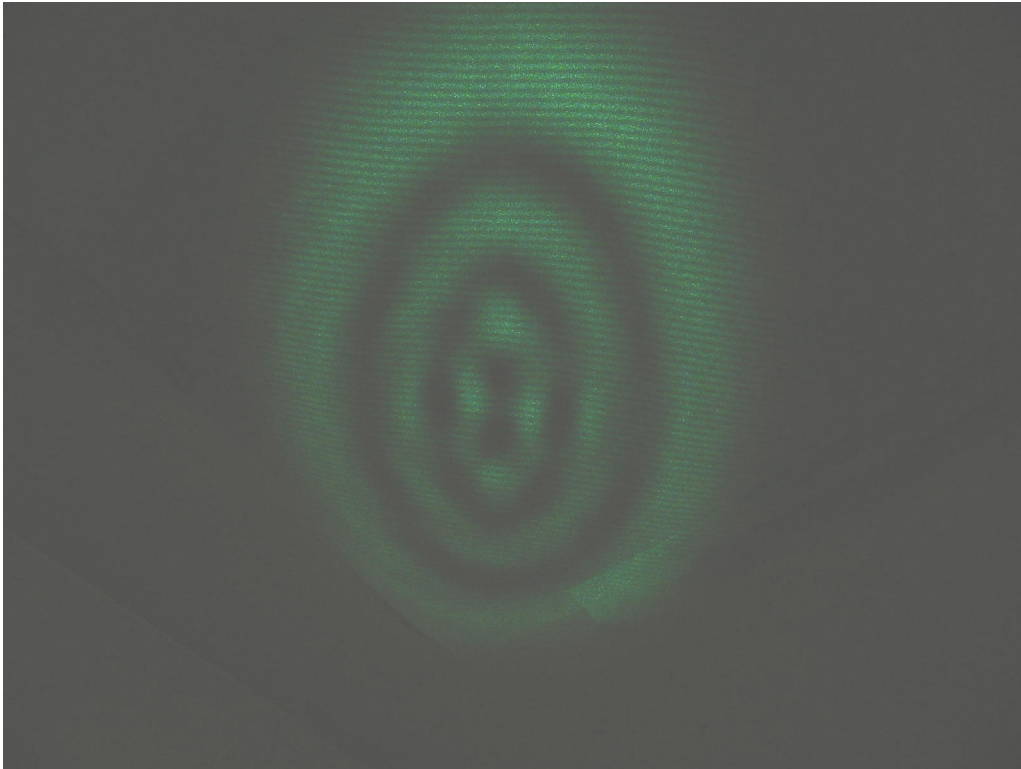


**Figure 2.31.** Photograph of the fringe image obtained for the design waist condition.

### 2.3.3.7.5 Validation of the first generation CompLDV

#### 2.3.3.7.5.1 Plate and cone viscometer measurements

The plate and cone viscometer arrangement is frequently used in many rheometric applications to determine the viscous properties of fluids. It is also frequently used for biological applications such as subjecting cells to high laminar shear stresses to simulate the effects of hypertension (Grad and Einav 2000). Though these applications exist, the purpose of this experiment is to utilize the well-known flow behavior in this device as a validation test for the position resolution of the CompLDV.

Figure 2.32 is a schematic of the plate and cone arrangement. A simple analysis reveals the physics of the primary flow in the gap. By the no-slip condition, fluid directly adjacent to either the plate or cone must move at the speed of the surface. Thus the shear rate between the two boundaries is

$$\frac{\partial U_{\theta}}{\partial y} = \frac{\omega r}{r \tan \alpha} = \frac{\omega}{\tan \alpha} \approx \frac{\omega}{\alpha}, \quad (2.43)$$

where  $y$  is normal to the wall,  $\omega$  is the angular velocity of the cone relative to the plate, and  $\alpha$  is the angle between the cone face and the plate. The most interesting result from this analysis is that the shear rate is independent of radial position in the flow.

The secondary flow in the plate and cone viscometer is described in detail by Sdougos et al. (1984). In this research, the laminar flow regime is examined experimentally and

modeled mathematically through an expansion of the Navier-Stokes equations. Results revealed that the appropriate scale factor for the flow was a Reynolds number-type term,

$$\tilde{R} = \frac{\omega r^2 \alpha^2}{12\nu}, \quad (2.44)$$

where  $\omega$  is the angular velocity of the cone,  $\alpha$  is the angle between the cone and the plate,  $r$  is the local radius of the cone, and  $\nu$  is the kinematic viscosity of the fluid filling the small gap. This term is proportional to the ratio of the centrifugal force to viscous force on the fluid particles—the two primary forces acting in the flow. Sdougos et al. showed that the onset of secondary flow occurs for values of  $\tilde{R}$  greater than about 0.01. Turbulent transition is observed for  $\tilde{R} > 4$  and the laminar velocity field analysis begins to breakdown for  $\tilde{R} > 1$ . Sdougos et al. also analyzed and measured the near-plate flow angle for various values of  $\tilde{R}$ . The primary flow predicts concentric streamlines, but the study reveals flow angles that deviate monotonically with  $\tilde{R}$  up to  $50^\circ$  from concentricity before  $\tilde{R} \approx 1$ . The analytic result for the near-plate deviation from concentricity is

$$\phi = \tan^{-1} \left[ \frac{U_r}{U_\theta} \right] = \tan^{-1} [-0.8\tilde{R} + O(\tilde{R}^3)], \quad (2.45)$$

which holds for  $\tilde{R} \leq 0.5$ . Since the normal to surface flow is found to be very small, i.e.,  $\frac{V}{U_r} = O(\alpha)$ , the secondary flow will have little impact on the information desired in the current work.

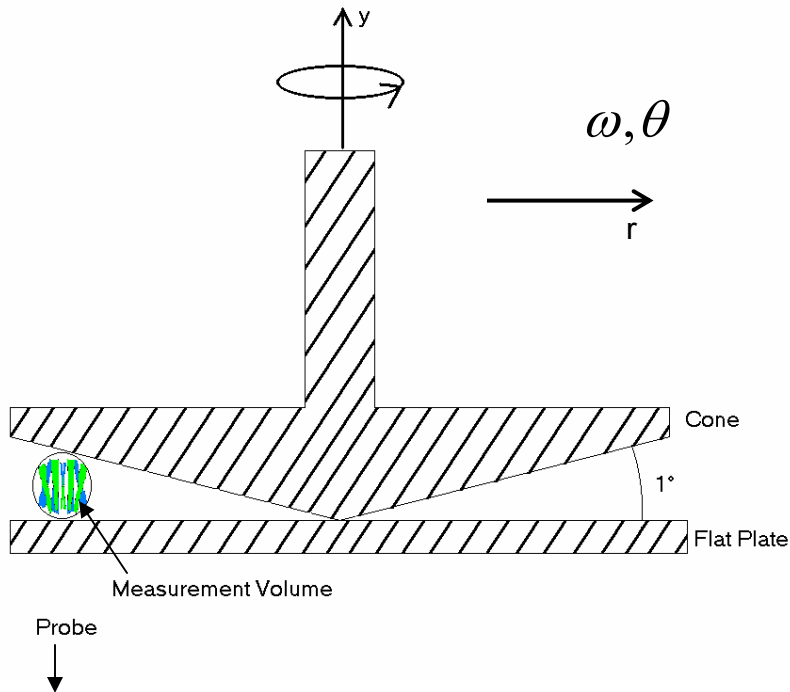


**Figure 2.32. Schematic of the plate and cone viscometer arrangement.**

### 2.3.3.7.5.1.1 Experimental Description

#### 2.3.3.7.5.1.1.1 Plate and cone device

A simple, previously existing, custom-made plate and cone device was used in the experiment. The cone outer diameter is about 8 cm with a  $1^\circ$  cone angle. A shaft extends above the cone into two rotational bearings set into a brass housing just larger than the cone. The cone was gauged to rotate with a surface wobble less than  $13 \mu\text{m}$ . The apex of the cone was removed so that the inner 4.75 mm diameter is flat. The cone was then recessed into the housing  $85 \mu\text{m}$  such that the virtual position of the apex was placed on the plate to within  $\pm 13 \mu\text{m}$ . This modification was made to reduce the wear between the cone apex and the plate, which could cause uncertainty in apex position much greater than  $\pm 13 \mu\text{m}$ . To accommodate laser measurements near the cone surface, the cone was polished and chrome-plated. This step greatly reduced the flare from the cone surface so that the burst SNR was in an acceptable range.

To rotate the cone, two methods were used. In initial tests, a high-speed electric grinder (26000 RPM @ 120 VAC) was regulated by a Variac power control. The grinder was linked to the cone shaft using a flexible PVC tube intended to isolate the vibrations of the grinder. The Variac controller allowed adjustment of the rotation rates from about 600 to 8000 RPM. To detect the rotation rate, a simple optical tachometer was implemented. Reflective tape was placed on the hexagonal grinder chuck nut and a light source was directed onto the nut. A silicon photodiode detector was positioned to receive the reflected light. The frequency of the light pulses captured by the photodiode was measured with a digital counter and the rotation rate was determined as  $f = f_{\text{photodiode}} / 6$ . In later tests, an 1800 RPM AC motor was used with no variable power controls. The rotation of this motor was found to be very constant based upon measurements made with a rotational encoder affixed to an exposed section of the side of the cone.

The plate used was an optical BK7 glass window 6.35 mm thick. The surfaces of the window were coated with a semi-hard dielectric anti-reflective coating which reduces laser flare for the near-plate measurements to be made.

#### 2.3.3.7.5.1.1.2 Oil flow visualization technique

The oil flow visualization technique was used to diagnose the flow in the plate and cone viscometer. Black plastic film was carefully attached to the glass plate to observe the wall shear. Care had to be taken that no bubbles in the film occurred since the gap between the plate and cone was so small. The oil mixture consisted of about 10 parts kerosene to 3-4 parts  $\text{TiO}_2$  with just a couple drops of oleic acid. The visualizations were repeated until the flow structure was clearly distinguishable from the oil mixture application lines.

### 2.3.3.7.5.1.1.3 Instrumentation

The first generation CompLDV was used to acquire velocity and position measurements. For the purpose of the first experiments discussed, only pairs of overlapping measurements volumes were operated simultaneously, allowing separate tests for each pair since the primary flow varies only in one direction (normal to the plate). By positioning the probe volume so that the local azimuthal velocity would lie in the plane of the four beams, a linear variation of the velocity with the measurement volume axial coordinate  $x'$  would result despite that the measured velocity component and coordinate were rotated  $45^\circ$  about the radial axis with respect to the local azimuthal velocity.

### 2.3.3.7.5.1.2 Results

#### 2.3.3.7.5.1.2.1 Oil Flow Visualization

A photograph of the oil flow visualization is given in Figure 2.33. The cone was revolving at about 1600 RPM for the oil flow. The flow visualizations of Sdougos et al. reveal very similar flow angles for the near-plate region. The oil collected in the center of the picture arises from the inward flow at the wall. The centrifugal forces push the flow outward near the cone; therefore, by continuity, flow near the plate must be toward the center. From these results it was concluded that the flow within this device was accurately represented by the laminar analysis of Sdougos et al.

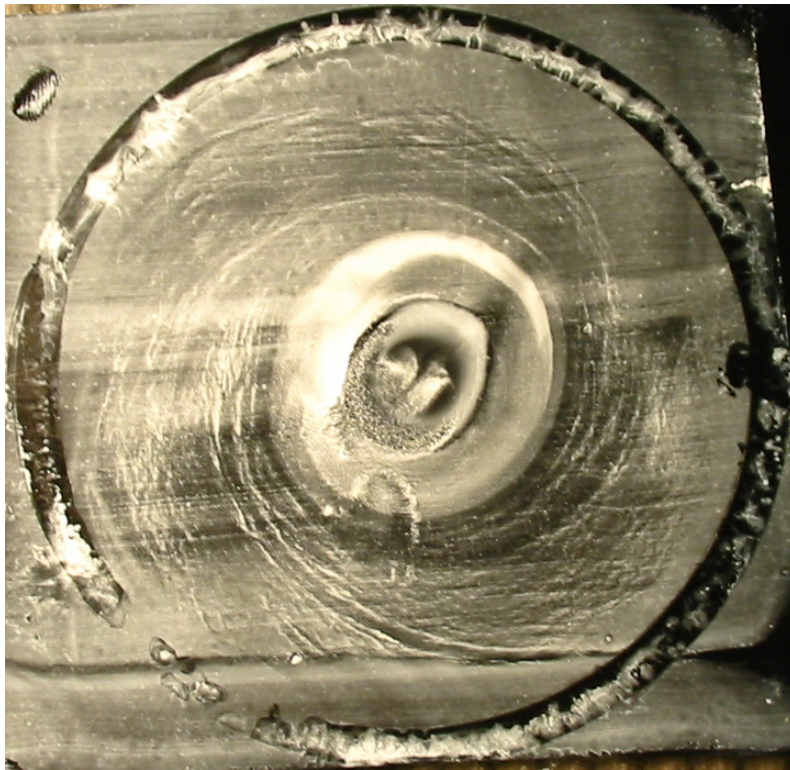


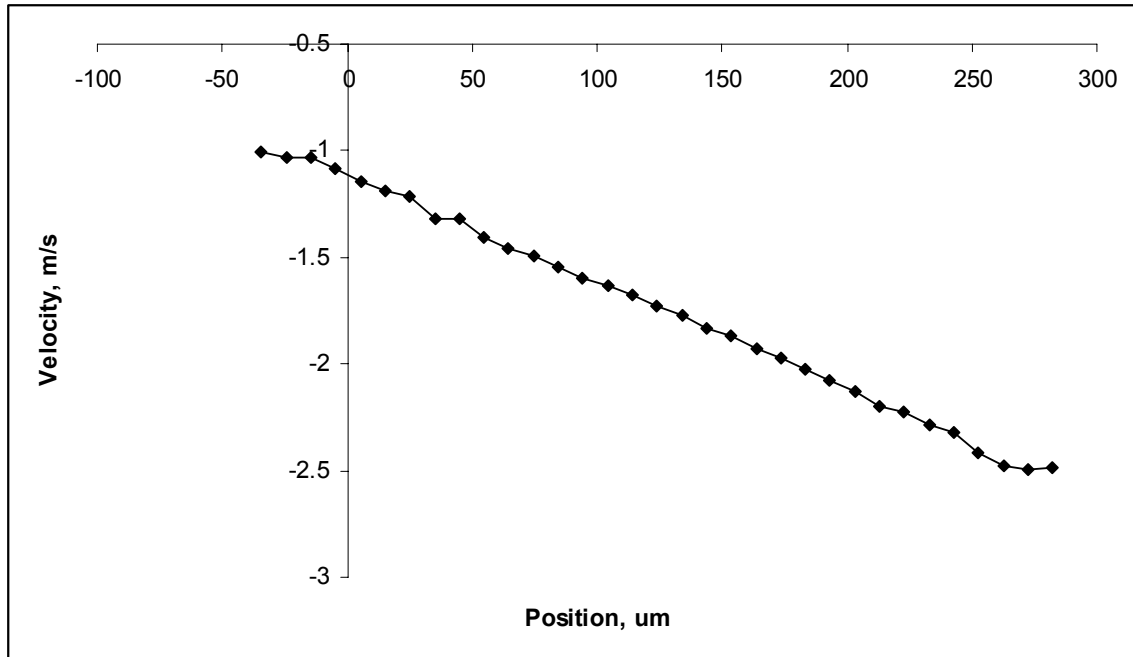
**Figure 2.33. Oil flow visualization photograph for cone angular rate of 1600 RPM.**

### 2.3.3.7.5.1.2.2 *Velocity profile measurements*

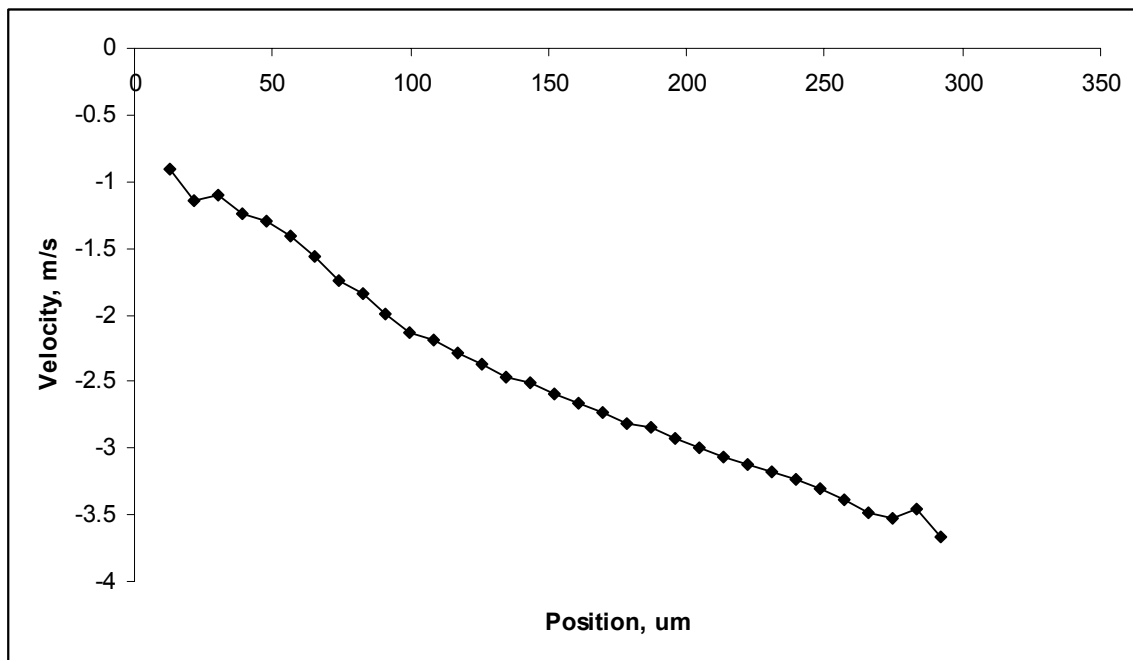
#### 2.3.3.7.5.1.2.2.1 Single-velocity-component measurements for the original CompLVD1 configuration

Measurements were taken for each of three measurement volume pairs in the CompLDV1 for the original interference configuration with pairs of converging/diverging fringes. The signal pairs are distinguished by their carrier frequencies imparted by frequency shifting using Bragg cells. To discuss the results, the different measurement volume pairs will be referenced using the carrier frequency for each pair, i.e., '40MHz', '60 MHz', and '80 MHz'. In each case the measurement volume was positioned such that the azimuthal velocity direction lay in the plane of the four beams forming the fringe patterns. The measurement volume was positioned radially at about 75% of total radius to avoid unwanted three-dimensionality arising from cone edge effects. The measurement volume was positioned vertically near the center of the local gap (with a predicted height of about  $525 \mu\text{m}$ ), so that no flare from the plate or cone was validated as particle velocity measurements. For each measurement volume pair about 20,000 validated Doppler bursts were acquired.

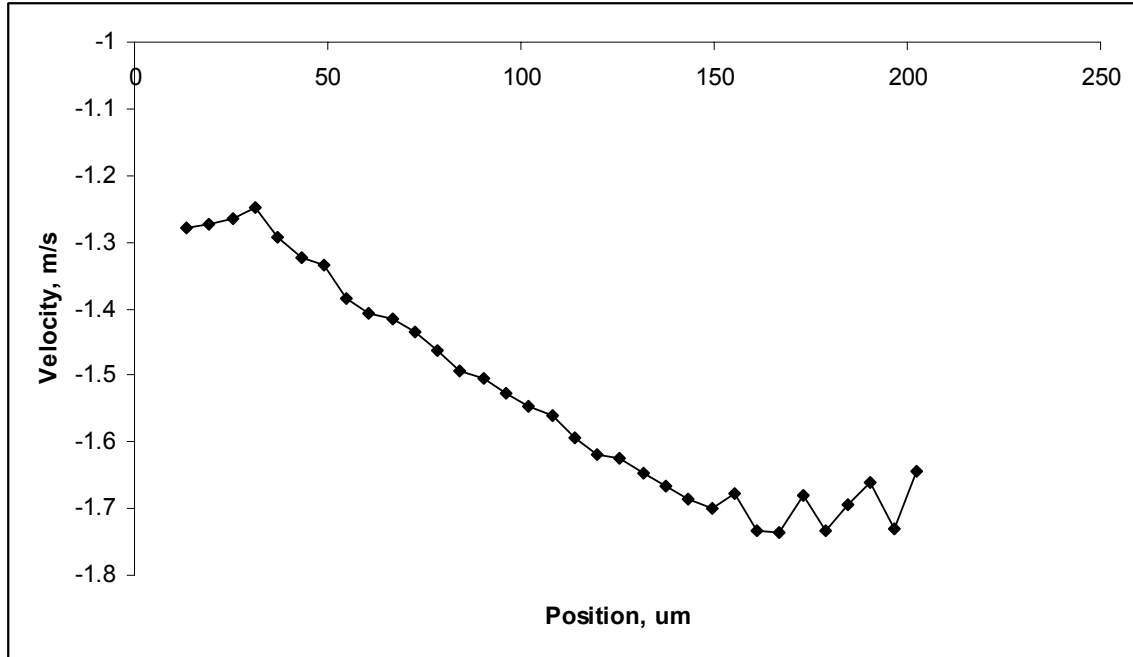
Due to the scatter in the instantaneous measurements, statistics were compiled. In Figure 2.34 the mean velocity is plotted versus position as calculated from calibrations inputting the calibration quotient. The RMS velocities are plotted in Figure 2.35 for each channel. Since the flow is laminar, one would expect RMS values to be very near zero. Though they are not zero, it is interesting to note they each plot exhibits nearly the same constant value for RMS velocity near the center of the measurement volume. This proves that the RMS value is not a function of revolution rate for this range of angular velocities. The oil flows discussed earlier exhibited laminar flow structure and a constant RMS velocity with angular velocity further supports the lack of turbulence. A second possible explanation for the high RMS velocity would be virtual turbulence due to the instrumentation. The instrument itself has a built-in check for how accurately particle velocities are being measured since two totally independent measurements are made for each particle velocity. In this experiment, the RMS difference between two independent measurements was 0.15, 0.05, and 1.1 mm/s for the three sets of fringe patterns. This uncertainty is much too small to explain the amount of turbulence measured. Flow unsteadiness due to a 4% variation in the angular speed and small surface imperfections may have contributed to some of the scatter in the data.



(a)

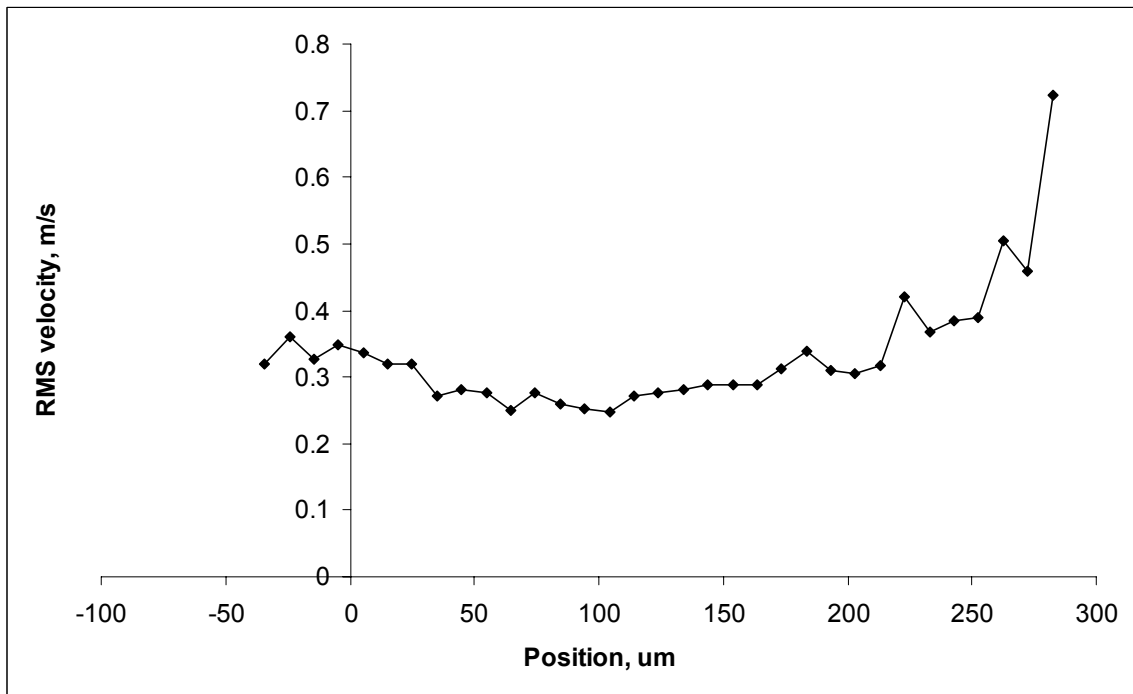


(b)

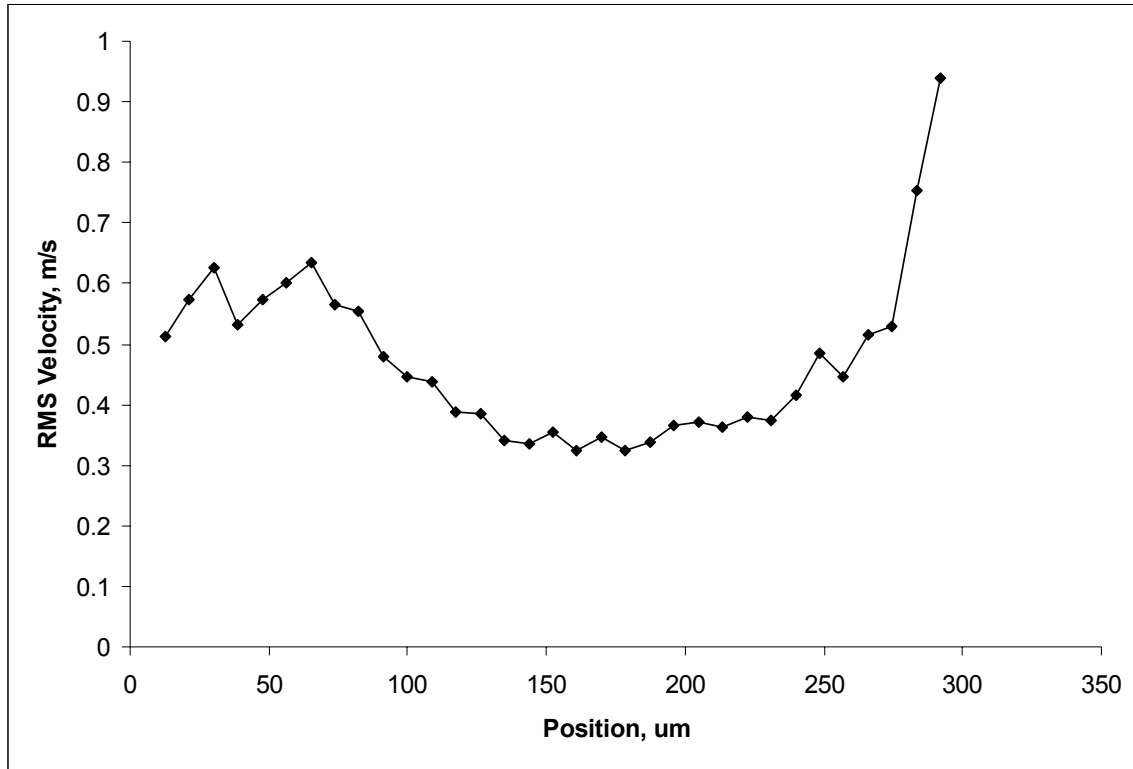


(c)

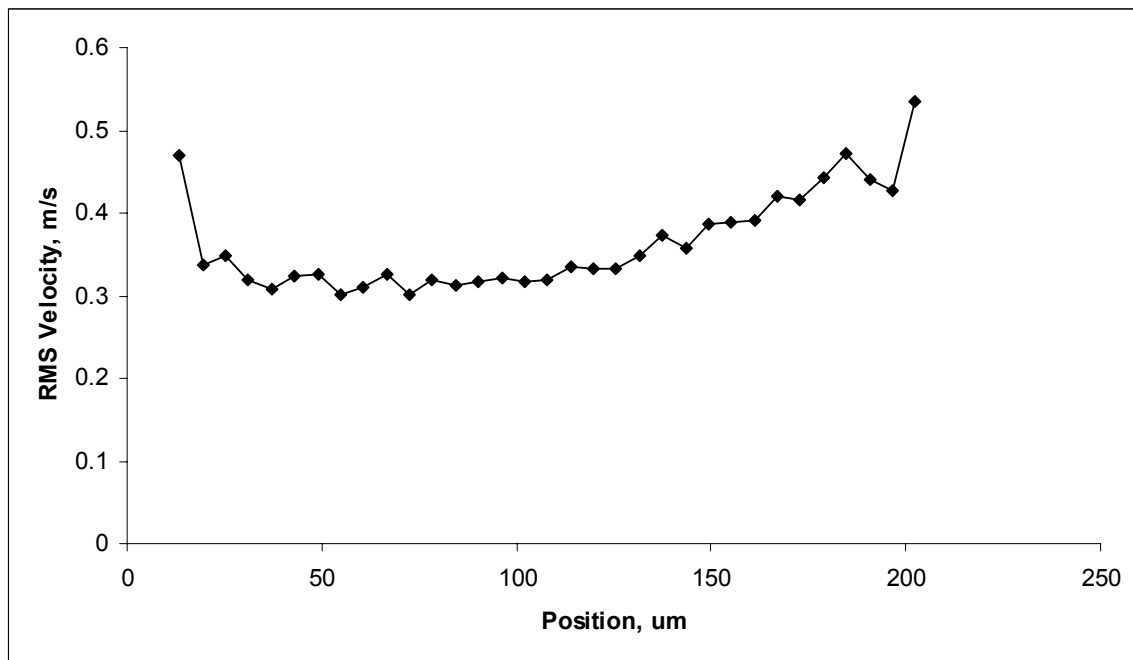
Figure 2.34. Mean velocity as a function of position along the measurement volume for a) 40 MHz volumes @ 2200 RPM, b) 60 MHz volumes @ 3400 RPM, and c) 80 MHz volumes @ 1500 RPM.



(a)



(b)



(c)

**Figure 2.35.** RMS velocities as a function of position along the measurement volume for a) 40 MHz volumes @ 2200 RPM, b) 60 MHz volumes @ 3400 RPM, and c) 80 MHz volumes @ 1500 RPM.

### 2.3.3.7.5.1.2.2.2 Three-velocity component measurements with the modified CompLDV1

The modified version of the CompLDV1 with a single converging fringe set and a parallel fringe set for each transmitting head was used to acquire data on the plate and cone flow. For these measurements the grinder motor previously used was replaced by an 1800 RPM A/C motor that has been used for LDV calibration in the past. A rotational encoder consisting of equally-spaced stripes of black-and-white was placed on the outer edge of the cone. To measure the rotation rate, a Helium-Neon (HeNe) laser was coupled into a multimode fiber optic and the output was focused to a spot on the exposed encoder. A basic photodiode was used to measure the light signal fluctuations as the dark and light areas of the encoder passed through the laser beam. The transitions measured by the photodiode could easily be detected and simple counting procedures could be used to estimate the rotation rate of the cone several times per revolution. There was no measurable deviation of the drive motor through the full rotation or with time so that the 1800 RPM revolution rate could be taken as constant within experimental uncertainties. For this rotation rate, the Reynolds number parameter,  $\tilde{R} = 0.434$  at the outer edge of the cone. For the measurements, the CompLDV1 probe volume was positioned at a radius of 28.42mm where the cone tangential velocity was 5.357m/s. At this location the Reynolds number parameter was  $\tilde{R} = 0.242$ , which is below the transitional regime according to Sdougos et al. (1984). For these measurements, the theoretical velocity gradient is given

by equation (2.43) as  $\frac{\partial U_\theta}{\partial y} \approx \frac{\omega}{\alpha} = 10,800s^{-1}$ . However, the setup for the plate and cone

device used was not ideal in that tapes were used to secure the brass housing to the glass plate and this acted to raise the apex of the cone from the plate surface. The modified expression for the velocity gradient in this case is

$$\frac{\partial U_\theta}{\partial y} = \frac{\omega r}{r \tan \alpha + y_0} \quad (2.46)$$

where  $y_0$  is the displacement of the apex of the cone from the plate. While an estimate for  $y_0$  is possible by measurement of the approximate thickness of the tape used, it is also possible to measure the velocity gradient using several measurements of the volume-averaged velocity statistics within the gap. The volume-averaged statistics for the tangential velocity at several points within the gap are plotted in Figure 2.36. From these data the actual tangential velocity gradient was determined to be  $\frac{\partial U_\theta}{\partial y} = 6,261s^{-1}$  which

leads to a value  $y_0 = 360\mu m$  for the apex displacement in equation (2.46). This value of apex displacement is very reasonable and consistent with the experimental set-up.

The instantaneous measurements of the three velocity components, tangential, radial, and normal-to-wall, are plotted as a scatter plot in Figure 2.37. In these plots, each discernable cloud of data represents a separate position of the center of the measurement volume. It is clear that the data for the tangential velocities are aligned with the mean profile. The secondary flow measurements indicate that the flow contains both the zeroth-order predicted flow as well as secondary contributions similar to those described by

Sdougos et al. (1984). To analyze the quality of the instantaneous measurements, the velocities and positions measured were sorted by position so that the amount of scatter in the velocity could be interpreted as broadening and transformed to position uncertainties as  $\delta y = \delta U / \frac{\partial U_\theta}{\partial y}$ . Doing this, the average 20:1 uncertainty in the position for the center portion of the measurement volume, presuming all the uncertainty in the profile measurement is due to position uncertainties, is about  $37 \mu m$ .

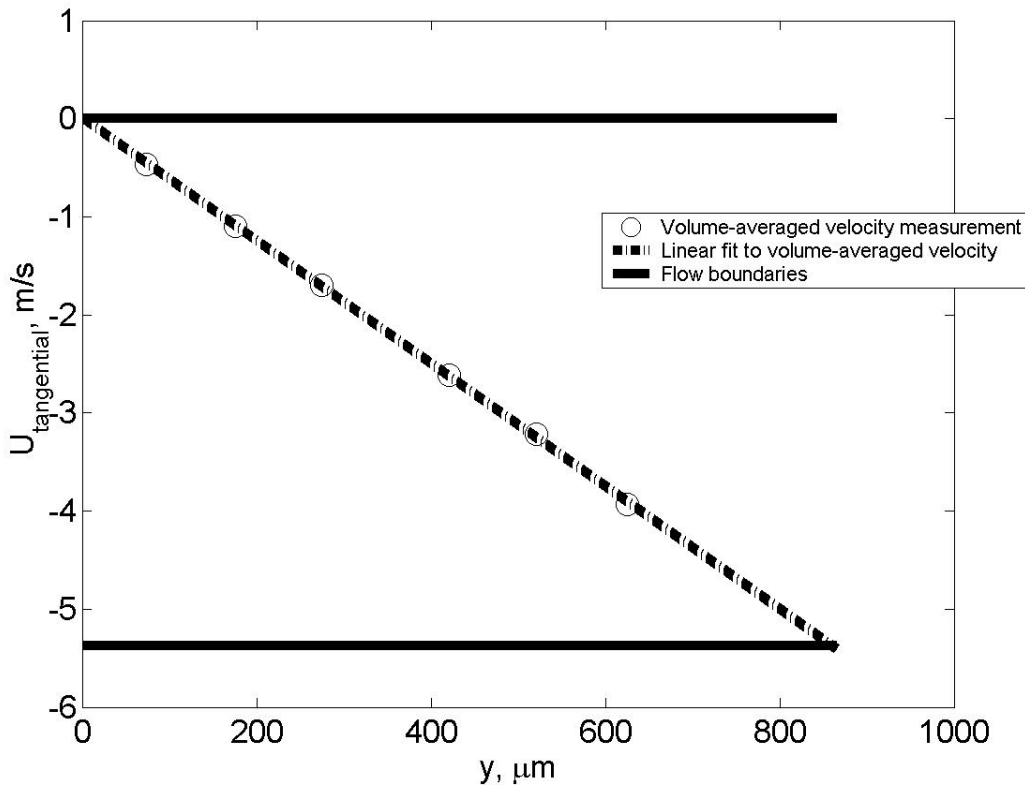
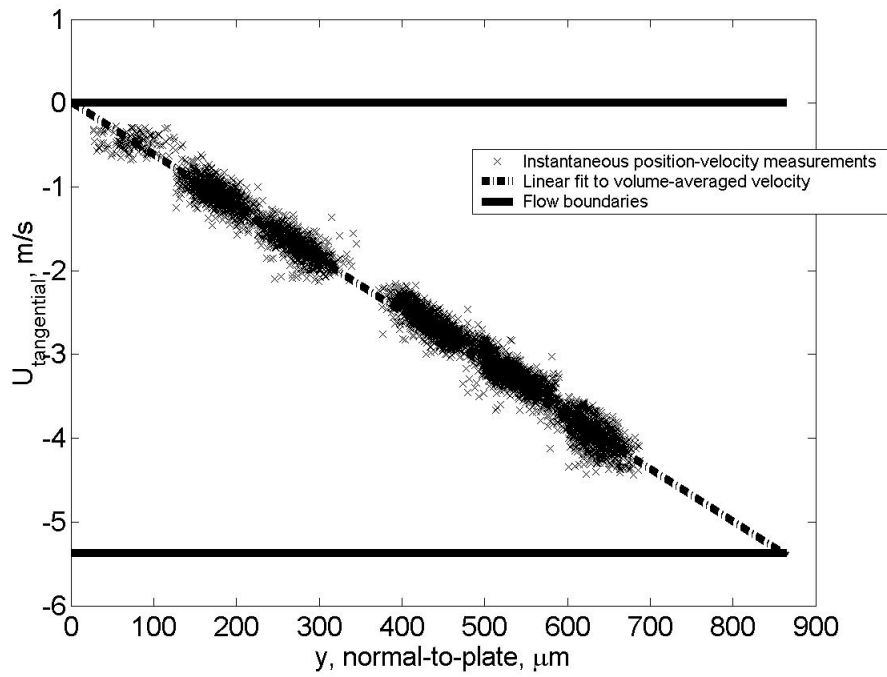
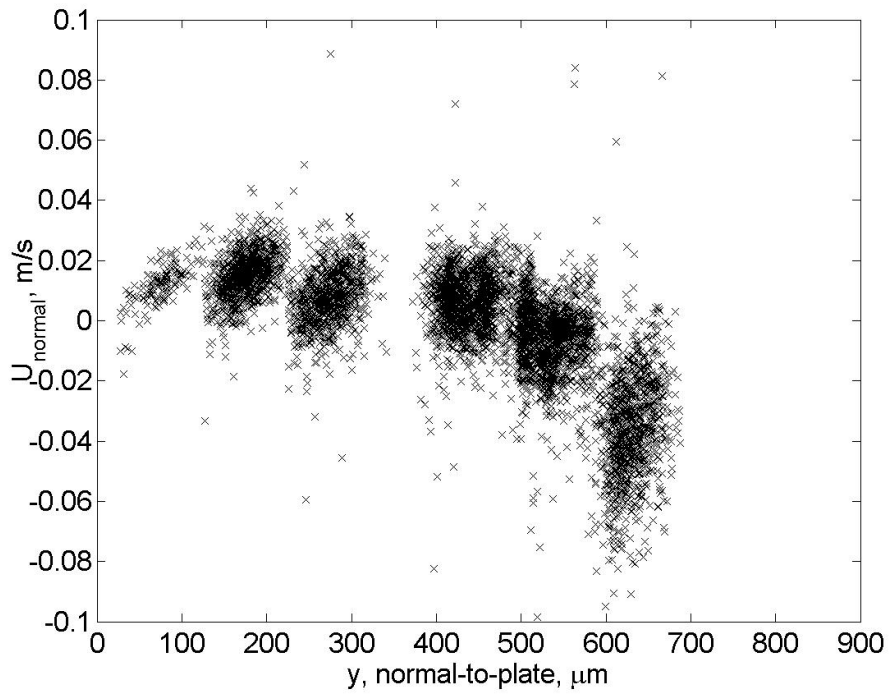


**Figure 2.36. Volume-averaged statistics for the plate and cone flow measured by the modified CompLDV1.**



(a)



(b)

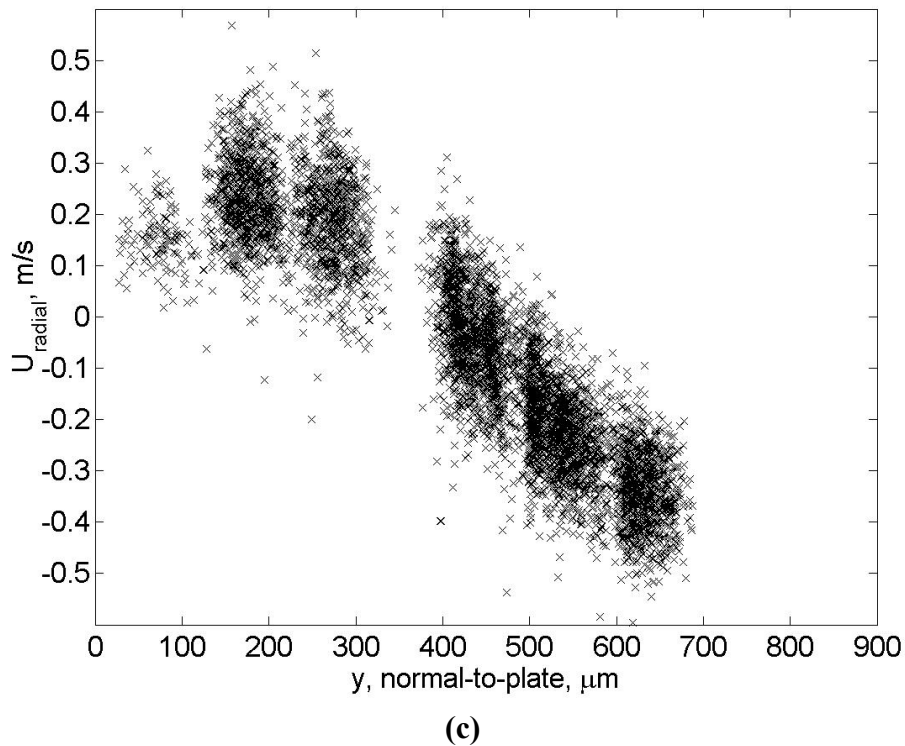


Figure 2.37. Scatter plots of the instantaneous measurements of (a) tangential, (b) normal-to-plate, and (c) radial velocities for the plate and cone flow measured with the modified CompLDV1.

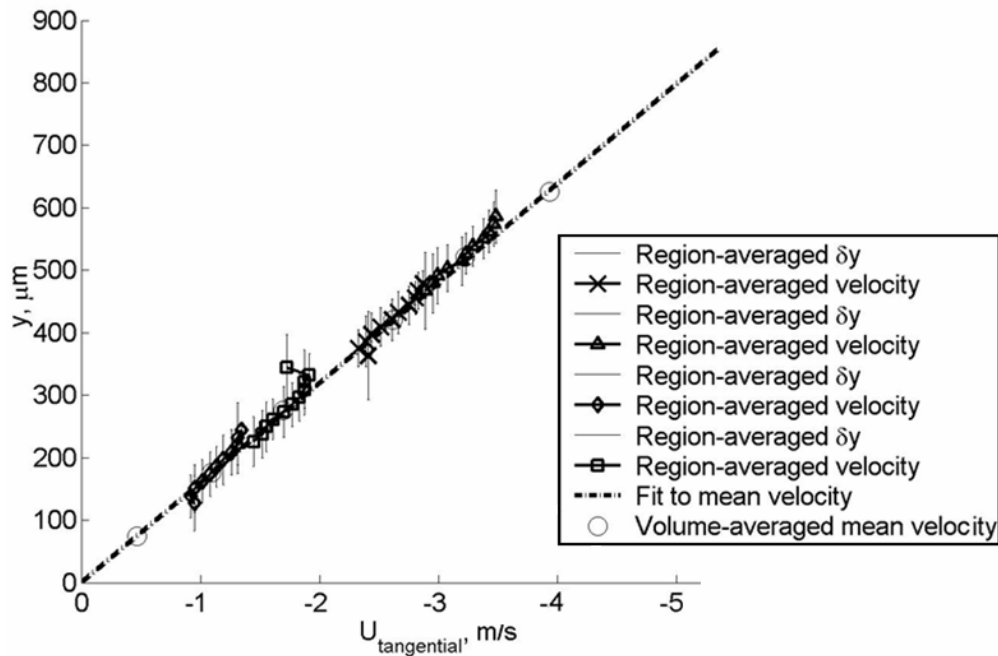


Figure 2.38. Statistics of velocity/position data from the plate and cone flow measured with the modified CompLDV1.

### 2.3.3.7.5.1.3 Concluding remarks for the plate and cone measurements

The laminar flow in the small gap of a plate and cone viscometer was used to validate the CompLDV1 particle velocity and position measurement technique. Visualization for the flow being measured was compared to the data of Sdougos et al. (1984), indicating that laminar plate and cone flow could be assumed. It was found that the RMS error of position determination was of the order predicted by the uncertainties, assuming that no unforeseen unsteadiness exists in the plate and cone flows examined. The position-resolution capabilities of the CompLDV1 concept were verified by these experiments, and give confidence in the application of this concept to turbulent flows.

### 2.3.3.8 Second generation CompLDV: 24"-Access CompLDV

The second generation CompLDV (CompLDV2), also known as the 24"-access CompLDV was developed as a side-wall-entry, long-access system for flows in which through-the-floor access is limited. This system was co-developed by the author, his advisor and Qing Tian. The CompLDV2 was based-largely upon the CompLDV1 technology, but with extended probe access without significantly increased uncertainties in any quantity measured. Qing Tian has further-developed and used the system extensively and the reader is referred to his dissertation for further information (Tian 2006).

### 2.3.3.9 Third generation CompLDV

The framework for realizing a comprehensive instrument for studying the structure of near-wall turbulent flows was formed during the development of the first two generations of the CompLDV already discussed. During this work many aspects of conventional LDV were significantly improved by implementing new technologies. Among these improvements have included the development of

- completely PC-based burst acquisition methods
- low-uncertainty adaptive signal processing
- much-improved signal-to-noise ratio signals by optimal optics design and low noise detection and electronics
- high valid burst rates due to easily-obtainable, nearly-monodisperse seeding
- sub-measurement-volume particle position resolution
- particle acceleration sensing

During the course of implementing these improvements, much was learned about the nature of the uncertainties encountered in the advanced measurements. As the first generations were primarily combinations of parallel ideas discussed but never fully integrated in the literature, the third generation makes use of the experience gained to produce a laser instrument which is significantly different from previously designs. These differences are explained to follow.

### ***2.3.3.9.1 Motivation for a new design: previous uncertainties***

The primary driver for a new design of the CompLDV was to reduce the uncertainties in the position and acceleration measurements. These measurements set this instrument apart from many other flow diagnostics. In the previous design, the position uncertainty was determined experimentally to be about  $\pm 15$  microns RMS. The velocities were measured at about  $\pm 0.8\%$  uncertainties and the acceleration at about  $\pm 1.6\%$  of the instantaneous velocity divided by the particle transit time both at 20:1 odds. The uncertainties encountered were excessive for velocity gradient estimation, and it was desired to reduce the uncertainties on the acceleration as well.

### ***2.3.3.9.2 Theory of operation***

In the third generation CompLDV (CompLDV3), the key uncertainty drivers were determined so that the optimal design could be achieved. The two most important measurement volume parameters were the number of fringes across the volume and the percent change in fringe spacing along the beam bisector, both should be maximal. There were three challenges in obtaining the maximum values for these parameters:

1. The maximum number of fringes occurs at large intersection angles—this is difficult to produce with single transmitting lenses.
2. Spherical aberrations introduce significantly non-Gaussian beam profiles with the combination of moderate intersection angles and large fringe gradients as discussed concerning Figure 2.31
3. When a particle moves along the beam bisector, it experiences the large fringe gradient and position resolution is greatly hindered.

To avoid these problems, two important design decisions were made. The first was the elimination of large transmitting lenses. Instead, each beam was given a focusing lens so that any combination of intersection angle and off-waist focusing was possible without aberration effects. Second, the problem of position determination in the convection direction was solved. It was decided to replace the Doppler method for positions in the convection direction with an intensity-based method. By focusing a thin (10 to 20 micron thick) light sheet within the center of the measurement volume, the time at which a particle passes this known position is determined. Now since the convection direction is not constant, and since near wall flow angles are primarily in the  $x$ - $z$  plane, the probe would be rotated so that the mean flow vector in the  $x$ - $z$  plane is normal to the light sheet. In this way, the convection of particles along the beam bisectors is limited significantly, and there is a method for determining the particle position in the mean convection direction.

To determine the optimal design, the constraints of the system were considered. Since aberration effects were eliminated, the primary constraint was the particle diameter; that is, a limit on how small the fringe spacing may be to still achieve good visibility. Given the known particle size of  $0.6 \mu\text{m}$ , guidelines given by Durst, Melling, and Whitelaw (1976, plate 4.18) were used to obtain that the fringe spacing should not be less than 1 micron. This resulted in an angle of intersection of about  $28^\circ$  by applying the geometric

fringe space equation,  $d = \frac{\lambda}{2 \sin \theta}$ . The only other desired attribute of the system was that it uses as few beams as possible to reduce complexity. The only way to achieve this goal was to make use of all information in a concise way. Since we need only measure 3 linearly-independent velocity/acceleration measurements and 2 linearly-independent Doppler position measurements, then we should be able to make a system which has exactly 5 measurement volumes. A solution to the resulting coupled system of equations is needed to determine the velocities and positions from five Doppler frequencies. To develop this system of equations, the very good model that the fringe spacing varies linearly along the beam bisector according to equation (2.27) is employed. Equation (2.47) illustrates the system of equations which must be solved

$$\begin{aligned}
 d_i(y'_i) &= \frac{\lambda_i}{2 \sin \phi_i} + \frac{dd_i}{dy'_i} y'_i + O(y'^2_i) \\
 f_i(t) &= U_{\perp}(t) / d_i[y'_i(t)] \\
 U_{\perp} &= f_i d_i \approx f_i \left( \frac{\lambda_i}{2 \sin \phi_i} + \frac{dd_i}{dy'_i} y'_i \right)
 \end{aligned}$$

$$\begin{bmatrix}
 a_1 & b_1 & c_1 & f_1 e_1 \frac{dd_1}{dy'_1} & f_1 g_1 \frac{dd_1}{dy'_1} \\
 a_2 & b_2 & c_2 & f_2 e_1 \frac{dd_2}{dy'_1} & f_2 g_1 \frac{dd_2}{dy'_1} \\
 a_3 & b_3 & c_3 & f_3 e_2 \frac{dd_3}{dy'_2} & f_3 g_2 \frac{dd_3}{dy'_2} \\
 a_4 & b_4 & c_4 & f_4 e_2 \frac{dd_4}{dy'_2} & f_4 g_2 \frac{dd_4}{dy'_2} \\
 a_5 & b_5 & c_5 & f_5 e_2 \frac{dd_5}{dy'_2} & f_5 g_2 \frac{dd_5}{dy'_2}
 \end{bmatrix}
 \begin{Bmatrix}
 U_{Local} \\
 V \\
 W_{Local} \\
 y_L \\
 z_L
 \end{Bmatrix}
 =
 \begin{Bmatrix}
 d_1 f_1 \\
 d_2 f_2 \\
 d_3 f_3 \\
 d_4 f_4 \\
 d_5 f_5
 \end{Bmatrix}
 \quad (2.47)$$

In this system of equations,  $a_i$ ,  $b_i$ ,  $c_i$ ,  $e_i$ , and  $g_i$  are all geometric constants that depend upon the beam directions, the  $d_i$  are the fringe spacings, the  $f_i$  are the measured Doppler frequencies,  $y'_1$  and  $y'_2$  are the Doppler position measurement directions lying along the two independent beam bisectors for interfering beams,  $U_{\perp}$  is the Doppler velocity,  $U_{Local}$ ,  $V$ , and  $W_{Local}$  are the Cartesian velocities,  $\lambda$  is the wavelength of the light, and  $\phi$  is the half-angle of intersection for fringe-forming beam pairs (the same for each measurement volume).

The geometry of the LDV optical arrangement was driven by the uncertainties to be discussed in the section 2.3.3.9.4. A simulation of equations (2.47) was implemented to propagate the expected Doppler frequency uncertainties through that system. Several geometric candidates were tested with the primary goal of achieving low uncertainties in the Doppler position measurements,  $y_L$  and  $z_L$ . Since the beam intersection angle was decided based upon optimal fringe visibility, this parameter and thus the center-of-volume fringe spacing was not modulated. Also, the analysis of section 2.3.3.7.2.1 has

shown the importance of employing maximal fringe gradients to minimize the position uncertainties, and that analysis is still qualitatively correct in the CompLDV3 design. The magnitude of the fringe gradient along the bisector increases greatly with decreasing beam waist, so the minimum practical waist was chosen at  $20\ \mu\text{m}$  diameter. Since it was desired to have good position resolution relative to the total measurement volume size, a value of  $200\ \mu\text{m}$  was chosen for the measurement volume diameter. A smaller diameter would result in a small range of resolved positions while a much larger diameter would reduce signal-to-noise ratio and limit how closely the measurement volume may approach the wall. With the waist diameter and the desired measurement volume diameter, Gaussian beam propagation may be used to obtain the relative separation between the beam waist and the measurement volume, which is found to be about 6mm. Equation (2.27) may be used with this information to obtain the fringe gradients to be input in to equations (2.47).

The geometry chosen is two transmitting heads, one with 6 beams and the other with 4. Figure 2.39 is a schematic head-on view of the two heads with notation for the pairs of beams that interfere to form fringes. From the 6-beam head, two-pairs of  $514.5\text{nm}$  beams cross and form fringes that converge along the bisector direction since their waists are positioned beyond the measurement volume. The other two beams from this head are  $476.5\text{nm}$  in wavelength and form a diverging fringe set by crossing the beams after the waists. The 4-beam transmitting head emits only  $488\text{nm}$  laser light and has one converging fringe set and one diverging fringe set. These combinations of fringe gradient senses are carefully chosen to achieve the lowest possible uncertainties in the position measurement.

A schematic three-dimensional view of the two transmitting heads oriented properly is given in Figure 2.40. The normal to the plane through which the beams in both heads emit is  $45^\circ$  from vertical and the included angle between those normal vectors is  $90^\circ$ . A side-view photograph of the system is given in Figure 2.41 and a photograph of the beams transmitting through a test window in a wind tunnel illuminated with seeding particles is given in Figure 2.42.

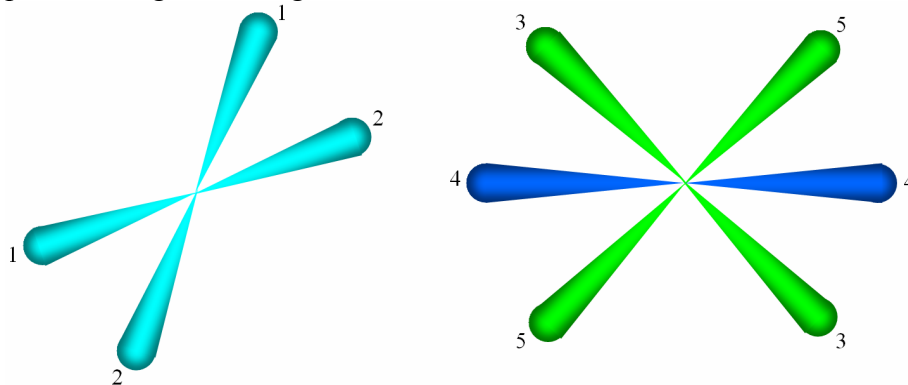


**Figure 2.39. Schematic of the head-on view of the blue and green/purple transmitting heads. Pairs of beams with the same label interfere to form fringes. Converging fringe sets in measurement volume: 1, 3, 5; Diverging fringe sets in measurement volume: 2, 4.**

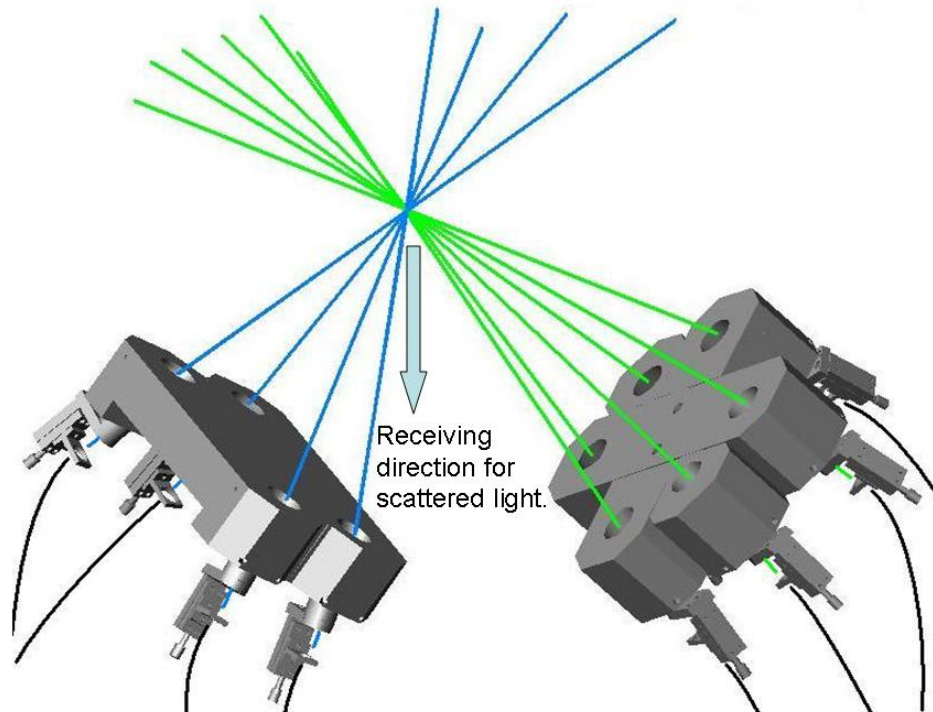


**Figure 2.40. Schematic of the probe geometry.**

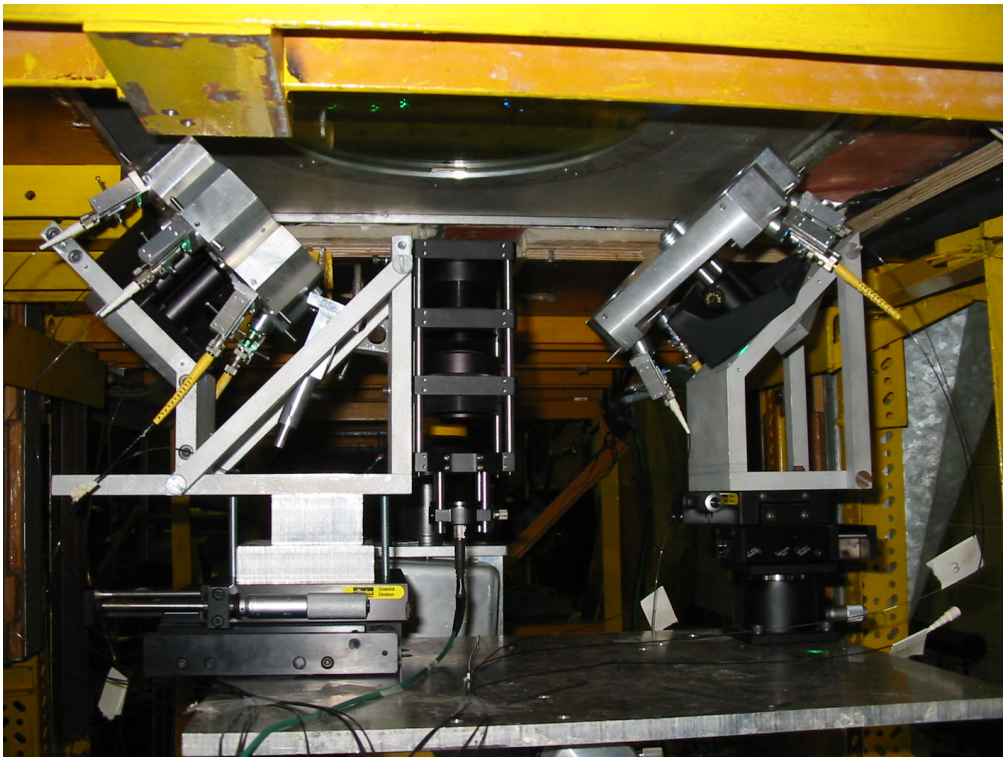


**Figure 2.41. Photograph of CompLDV generation 3 configuration.**

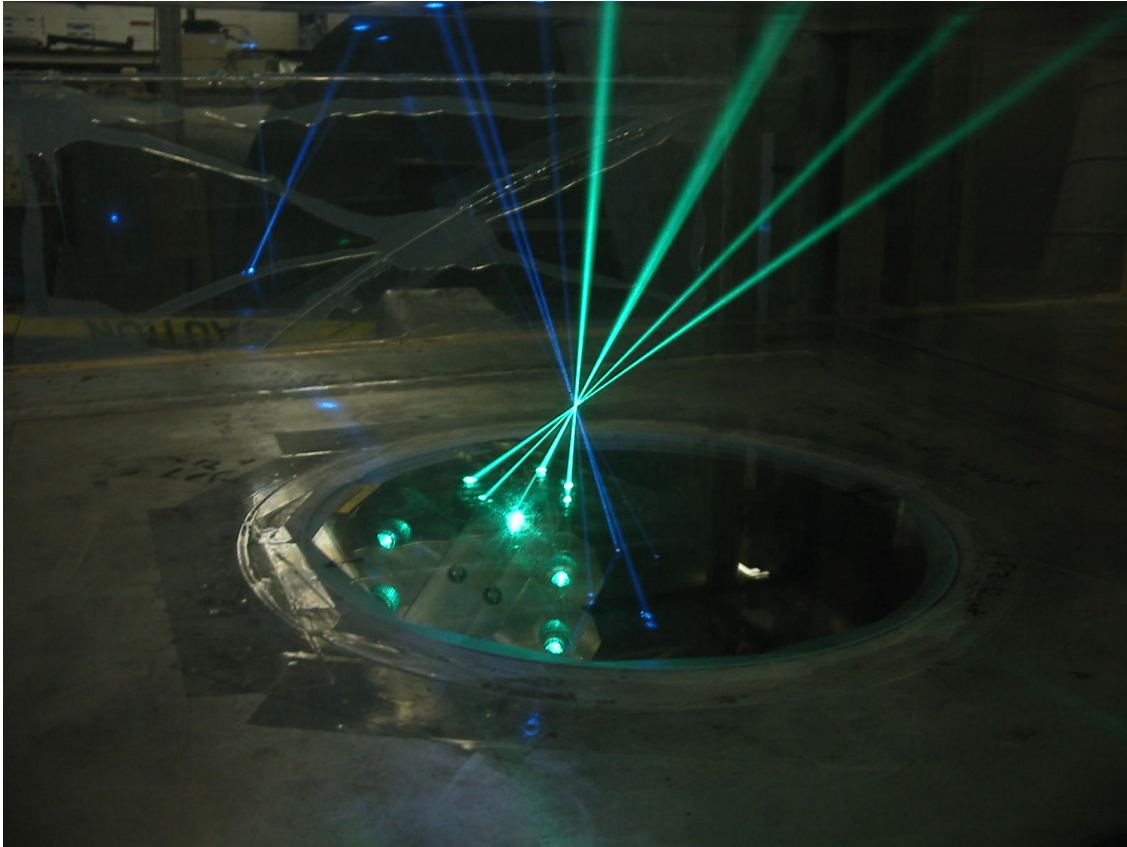


**Figure 2.42. Photograph of laser beam configuration for the CompLDV3.**

### ***2.3.3.9.3 Hardware Implementation***

The hardware developed and described for the CompLDV1 was used as a basis for much of the hardware in the CompLDV3. The same optical table configuration already discussed and given schematically in Figure 2.14 was used. Also, precisely the same light separation and measurement instruments from Figure 2.15 as well as the original data acquisition system were employed. While the receiving optics for the CompLDV3 were adapted directly from the CompLDV1, the incident optics were newly designed with more-capable alignment mechanisms and the key improvement of an independent lens system for each transmitting laser beam.

### ***2.3.3.9.4 Uncertainty analysis***

The uncertainties for the CompLDV3 have been analyzed based upon the optics, geometry, and noise levels of the system. The first step in determining the uncertainties for statistical quantities measured using the CompLDV3 was to estimate uncertainties in the instantaneous measurements of velocity and position. To do this, a Monte Carlo uncertainty simulation was run to propagate the known Doppler frequency uncertainties as determined by the FFT signal processing simulations through the CompLDV3 system of equations (2.47) relating the Doppler frequency measurements to the geometry and desired physical quantities.

For the simulation, a single representative velocity vector was utilized— $\vec{U} = (18\hat{i} + 0.01\hat{j} - 0.5\hat{k})\text{m/s}$ , and a position measured from the center of the volume was used— $\vec{x} = (0\hat{i} + 150\hat{j} - 50\hat{k})\mu\text{m}$ . Note that the simulation was run for a range of other velocity-position sets and they produce the same quantitative results when the velocities are normalized by the magnitude of the input velocity. The geometric constants,  $a_i$ ,  $b_i$ ,  $c_i$ ,  $e_i$ , and  $g_i$ , are all given from the CompLDV3 design as are the fringe space gradients as determined by from the analysis of Miles (1996). From this information, the expected Doppler frequencies,  $f_i$ , were determined. The work of Shinpaugh et al. (1992) as well as the current work has quantified the expected uncertainties in Doppler frequency estimates using digital signal processing techniques. From this work, the uncertainty levels for the lowest signal-to-noise ratio that allows reliable Doppler frequency estimates ( $SNR_f = 18\text{-}20\text{dB}$ ) was used,  $\delta f = 0.1/T$  where  $T$  is the Doppler signal duration. The Monte Carlo simulation sampled 20,000 frequencies around the nominal values determined from the given velocity and position vector. The PDFs of the frequencies sampled were Gaussian with standard deviations of magnitude  $\delta f = 0.1/T$ . The signal duration was determined using the transit time of the particle estimated as  $T \approx D/|\vec{U}|$  where  $D$  is the diameter of the measurement volume, nominally  $200\mu\text{m}$ . In the simulation,  $T = 11\mu\text{s}$ . For coordinate system reference, the CompLDV3 is designed to operate with the mean  $U$  flow velocity being approximately aligned with the  $x$ -axis of the optical coordinate system which is defined by the normal to the plane of the laser light sheet. The statistics for the simulated velocities and positions propagated through equations (2.47), which give the representative uncertainties for the quantities, are given in Table 2.5. Note that the uncertainties in the velocity components are exceptional compared with other measurement systems used for similar measurements. For instance, the particle-image velocimetry (PIV) technique for direct measurements of the velocity gradient tensor described by Mullin and Dahm (2006) exhibits 2-4% uncertainties for in-plane velocity components and 6-8% for the out-of-plane velocity component for 20:1 odds. For the CompLDV3 the stream-wise velocity component is measured at an uncertainty that is 25% lower than for the span-wise and normal-to-wall values and each is less than 0.2% uncertainty at 20:1 odds. The 20:1 absolute uncertainties in the  $y$ - and  $z$ -particle positions are each about  $5.8\mu\text{m}$  for all velocity magnitudes. Although Czarske et al. (2002) report an uncertainty smaller than this in their work with a similar LDV technique, the probe implemented therein has limited general applicability since it operates in a forward scatter mode which requires optical access on both sides of the flow facility. This difference results in stronger signals and reduces the frequency uncertainty considerably if noise sources are properly managed. For practical back-scattering systems such as the CompLDV3, the frequency metric used is typical (Albrecht et al. 2003). Otherwise, the incident optical arrangement of the CompLDV3 is seen to be superior to the one discussed by Czarske et al. (2002), since despite a factor of 10 improvement in the frequency estimation variance in that work, the particle position uncertainty is only 50% lower. The acceleration uncertainties were shown in section 2.3.3.7.2.1 to vary proportionally to the velocity uncertainties due to similar functional dependencies. The

resulting uncertainties are given in Table 2.5 and are seen to be much lower than those for the CompLDV1 from section 2.3.3.7.2.1.

**Table 2.5. 20:1 uncertainties for instantaneously-measured velocities and positions as determined by the sensitivities from equations (2.47) for these quantities.**

Term	Uncertainty
$\delta U / \ \vec{U}\ $	0.075%
$\delta V / \ \vec{U}\ $	0.11%
$\delta W / \ \vec{U}\ $	0.12%
$\delta x / D$ Entire volume used	0.6%
$\delta x / D$ Narrow light sheet used	0.2%
$\delta y / D$	2.9%
$\delta z / D$	2.9%
$\delta A_x T / \ \vec{U}\ $	0.38%
$\delta A_y T / \ \vec{U}\ $	0.56%
$\delta A_z T / \ \vec{U}\ $	0.61%

The x-position uncertainty was determined in an independent simulation of the process for estimating the particle arrival time. To estimate the arrival time, a fit of the low-frequency data for the burst envelope is performed. The non-high-pass-filtered electronic burst signal is analyzed. The digitized data are low-pass-filtered to remove the broadband noise and narrowband Doppler signals. The resulting signal is primarily comprised of the signal contributions from the burst envelope. The model for the low-passed signal is then the Gaussian window. A least-squares quadratic is fit to the logarithm of the filtered data with the intention of finding the position of maximum signal, where the first time derivative of the model function is zero. The time at which this occurs is estimated as being the arrival time. This time is compared with the input arrival time and their difference times the input velocity gives the position uncertainty, i.e.  $\delta x = U \delta t$ . For the simulations run, two cases were considered—one in which the signal from the measurement volume ( $200\mu m$  diameter) was used to find the arrival time and another where the signal from the narrower light sheet ( $20\mu m$  width) is used. The resulting 20:1 uncertainties are about  $1.2\mu m$  and  $0.4\mu m$  for the entire measurement volume and the narrow light sheet methods, respectively.

#### 2.3.3.9.4.1 Velocity Statistics Uncertainties

The same procedure discussed in section 2.3.3.7.2.2 was used to estimate the uncertainties for the velocity statistics in the CompLDV3. The uncertainties for the velocity statistics up to triple-products (third-moments of velocities) non-dimensionalized by the wall friction velocity in the 2D flat plate TBL are plotted in Figure 2.43-Figure 2.48. These values may be taken as the uncertainty values for the statistical quantities estimated using the CompLDV3.

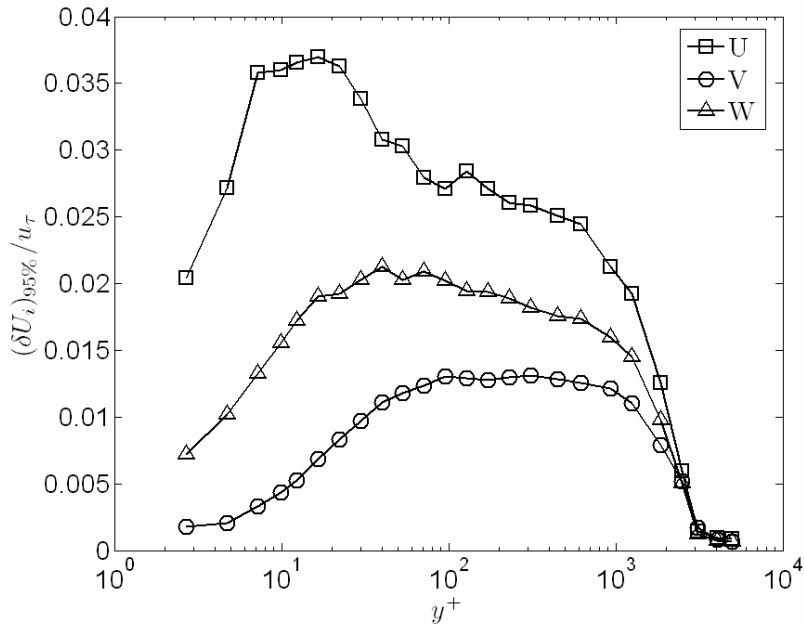


**Figure 2.43.** 20:1 uncertainties in the mean velocities throughout a 2D flat plate turbulent boundary layer profile non-dimensionalized on the wall friction velocity.

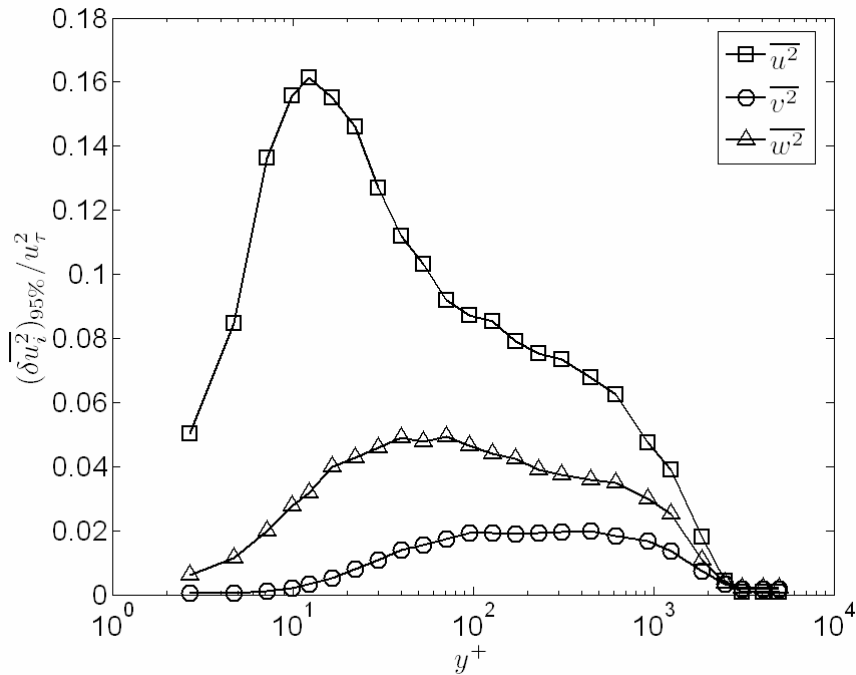


**Figure 2.44.** 20:1 uncertainties in the Reynolds normal stresses throughout a 2D flat plate turbulent boundary layer profile non-dimensionalized on the wall friction velocity.

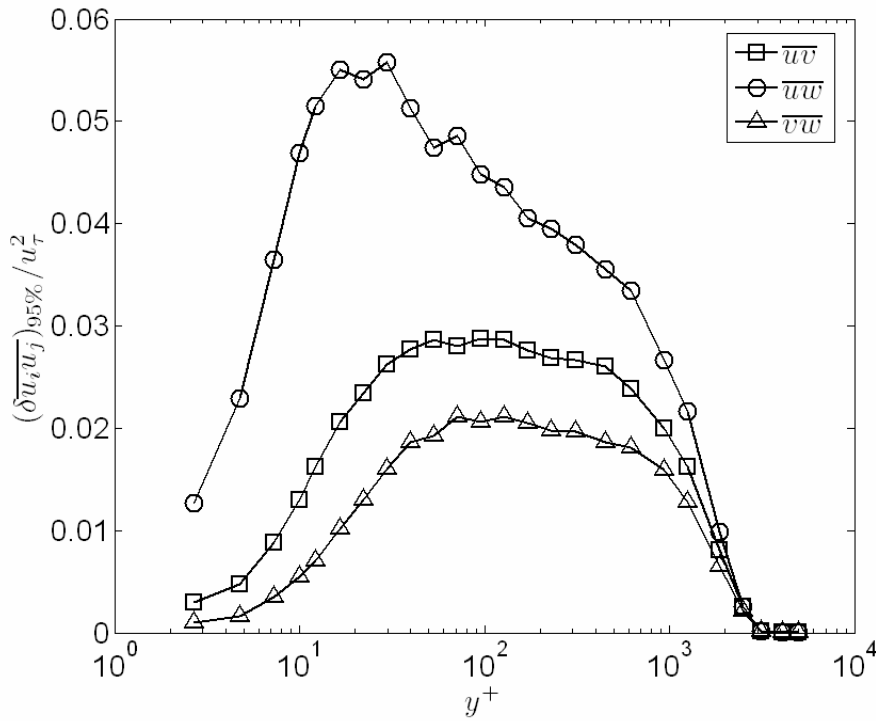


**Figure 2.45.** 20:1 uncertainties in the Reynolds shear stresses throughout a 2D flat plate turbulent boundary layer profile non-dimensionalized on the wall friction velocity.

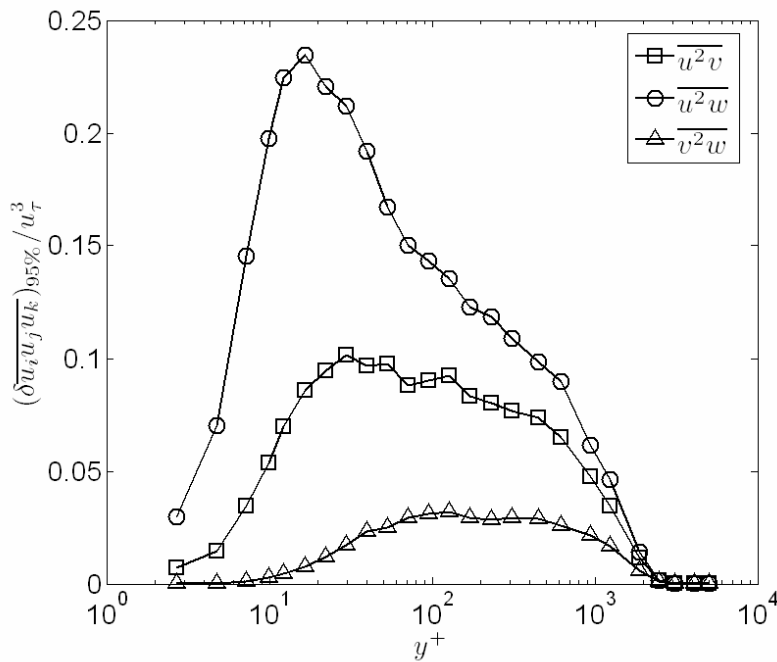


**Figure 2.46.** 20:1 uncertainties in velocity triple-products throughout a 2D flat plate turbulent boundary layer profile non-dimensionalized on the wall friction velocity.

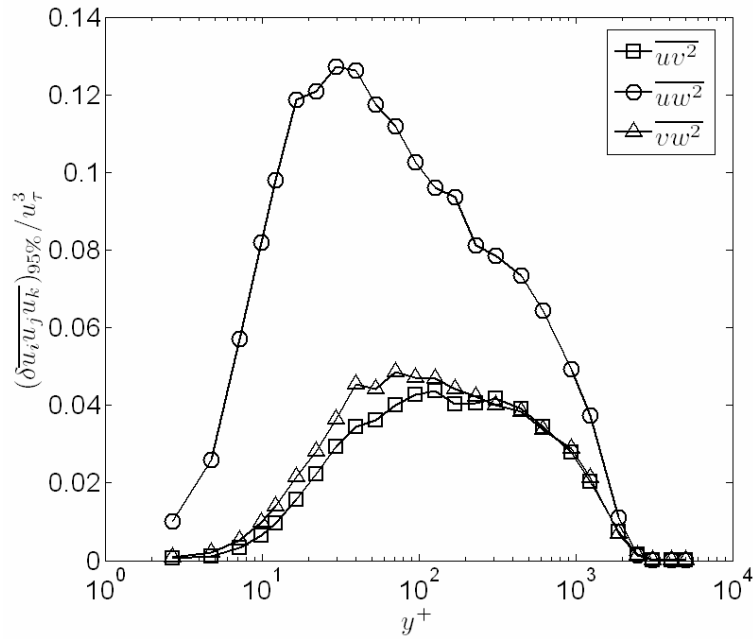


**Figure 2.47.** 20:1 uncertainties in velocity triple-products throughout a 2D flat plate turbulent boundary layer profile non-dimensionalized on the wall friction velocity.

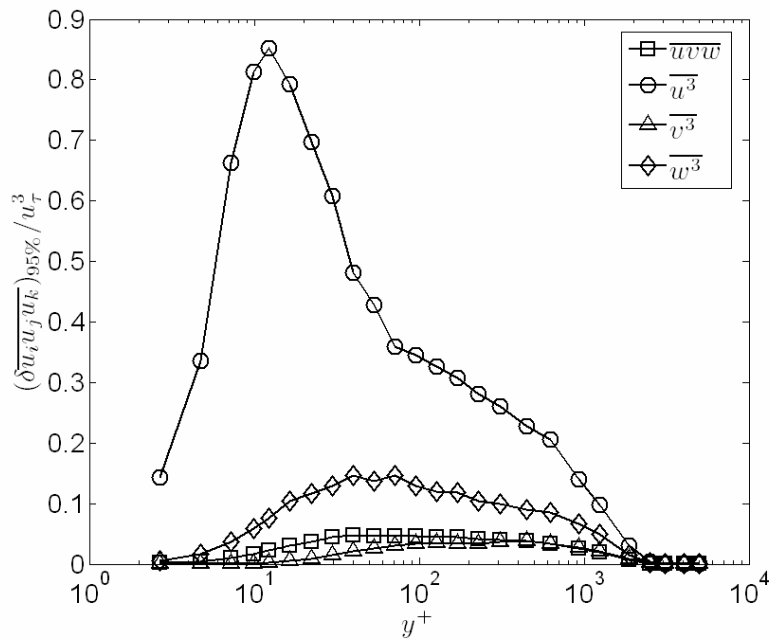


**Figure 2.48.** 20:1 uncertainties in velocity triple-products throughout a 2D flat plate turbulent boundary layer profile non-dimensionalized on the wall friction velocity.

### 2.3.3.9.4.2 Velocity Gradient Estimation and Uncertainties

The problem of estimating velocity gradients from CompLDV3 data is posed as follows:

*Given the velocities and relative positions of  $N$  particles ( $N \geq 4$ ), determine the velocity gradient tensor that is consistent with the data within experimental uncertainties and the constraints imposed by coherent turbulence scales.*

The geometry of the problem is shown schematically in Figure 2.49. The particles arrive randomly in space and time. The statistics of the arrivals depend on the turbulence level as well as the velocity gradients across the volume (Albrecht et al. 2004). In the case of zero turbulence and velocity gradient, the arrival time statistics follow a Poisson (exponential) distribution while the particles are uniformly distributed in space. The probability distribution function (PDF) of the measurement-volume validation weights the arrival position so that the measured positions are not uniformly distributed. The extrapolated volume is aligned approximately with the mean flow direction in the case that turbulent flow angles are relatively small.

For a typical situation, consider a region of fluid convecting with some time- and space-local centroid velocity in the 2D flat-plate TBL at  $y^+ = 100$ . In this case, the mean-stream-wise velocity,  $U^+ \approx 16.25$ , and the mean secondary flow velocities are very small. At this height in the TBL of interest, the Reynolds normal stresses are given approximately as  $\overline{u^{2+}} \approx 5$ ,  $\overline{v^{2+}} \approx 1$ ,  $\overline{w^{2+}} \approx 3$ . Now consider the case when the region of flow moves with a centroid velocity such that each of the velocity components has a fluctuation equal to one standard deviation from the mean. In this case the centroid velocity vector is  $\bar{U}^+ = 18.5\hat{i} + 1.0\hat{j} + 1.7\hat{k}$ . The location of the leading edge of the region of fluid after it has convected over a time of  $t^+ = 10$  is a distance of  $x^+ = 185$ ,  $y^+ = 10$ ,  $z^+ = 17$ . Now superimpose the nominally spherical measurement volume with the region of convecting fluid. Some sub-region of the fluid volume will convect through this superimposed volume and the particles seeding the flow will result in scattered light signals measured by the CompLDV3. Over the time  $t^+ = 10$  several particles will pass through the measurement volume resulting in velocity and position measurements. The particle paths are extrapolated to form the description of the fluid motion that is shown schematically in Figure 2.49. Noting the scales of the problem, the length of the region of fluid for which measurements are made will be about  $x^+ = 180$ . However, since the time-scales are so small, it is not expected that significant fluctuations in the secondary velocities will exist such that the region of fluid interrogated will have dimensions in the  $y$ - and  $z$ -directions on the order of the measurement volume diameter. The result is that the region for which

flow velocities are known has a very large aspect ratio:  $AR \equiv \frac{\Delta x^+}{\sqrt{\Delta y^+ \Delta z^+}}$ . This geometry

imbalance the sensitivities of the gradient-measurement directions to the position and velocity uncertainties in the measurements. That is, since small differences are measured in the  $y$ - and  $z$ -directions, the gradients in these directions become more sensitive to the inherent uncertainties in measuring these positions and the velocities. The challenge at hand is, then, to determine an effective way to handle this geometry that results in useful gradient measurements in the  $y$ - and  $z$ -directions.

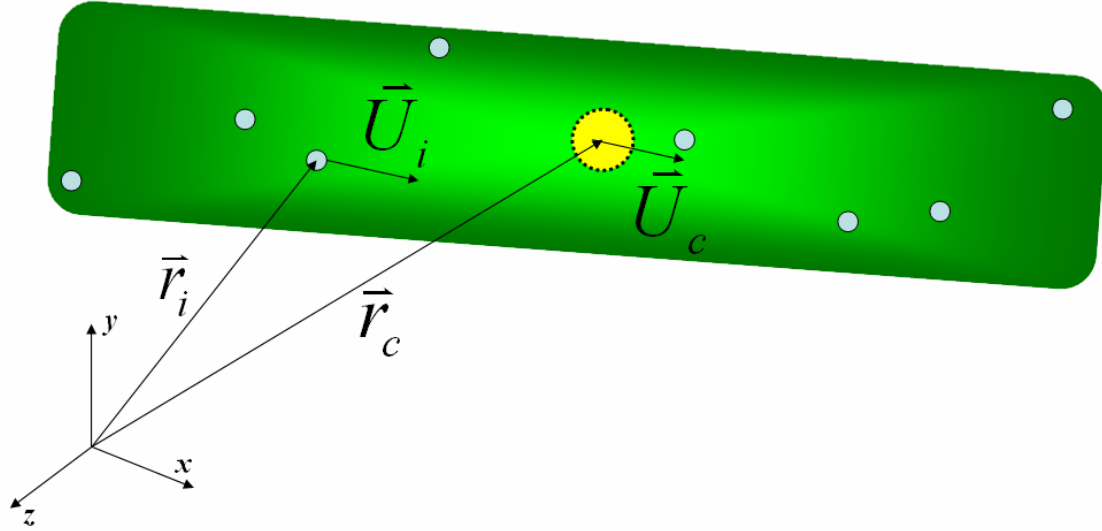


**Figure 2.49.** Schematic of an instance for the CompLDV3 extrapolated measurement volume containing several particles with estimated velocities and positions.  $\vec{r}_i$  is the position vector of the  $i^{\text{th}}$  particle,  $\vec{U}_i$  is the velocity vector of the  $i^{\text{th}}$  particle,  $\vec{r}_c$  is the position vector of the centroid of the  $N$  particles considered for velocity gradient tensor estimation, and  $\vec{U}_c$  is the centroid velocity vector for the  $N$  particles.

#### 2.3.3.9.4.2.1 Direct estimation

We begin by considering the case in which four particles are used for direct estimation of the velocity gradient tensor by solution of a fully-constrained system of equations. For the computation, we consider four particles, each with their own set of states as given by the trajectory of the  $i^{\text{th}}$  particle by Taylor expansion:

$$\vec{x}_i(t) = \vec{x}_{0i} + \vec{U}_{0i}(t - t_{0i}) + \frac{\vec{a}_{0i}}{2}(t - t_{0i})^2 + O[(t - t_{0i})^3] \quad (2.48)$$

where  $\vec{x}_i$  is the position of the  $i^{\text{th}}$  particle at time  $t$ ,  $\vec{x}_{0i}$  is the position of the  $i^{\text{th}}$  particle at time  $t_0$ ,  $\vec{U}_{0i}$  is the velocity of the  $i^{\text{th}}$  particle at time  $t_0$ , and  $\vec{a}_{0i}$  is the acceleration of the  $i^{\text{th}}$  particle at time  $t_0$ . The Latin subscripts to follow will indicate the particle in question.

Next, let us consider the expansion of the velocity component  $U$  in a Cartesian coordinate system around point  $\vec{x}_{0i}$  and time  $t_0$ :

$$U_i(t, \vec{x}_i) = U_{0i} + \nabla U_{0i} \cdot (\vec{x}_i - \vec{x}_{0i}) + \left. \frac{\partial U}{\partial t} \right|_{0i} (t - t_{0i}) + O\left[(t - t_{0i})^2, [(\vec{x}_i - \vec{x}_{0i}) \cdot \hat{i}]^2, [(\vec{x}_i - \vec{x}_{0i}) \cdot \hat{j}]^2, [(\vec{x}_i - \vec{x}_{0i}) \cdot \hat{k}]^2\right] \quad (2.49)$$

The quantity desired from the exercise appears directly in equation (2.49),  $\nabla U_{0i}$ , so dropping the higher-order terms yields

$$\nabla U_{0i} \cdot (\bar{x}_i - \bar{x}_{0i}) = U_i(t, \bar{x}_i) - U_{0i} + \frac{\partial U}{\partial t} \Big|_{0i} (t - t_{0i}) \quad (2.50)$$

The first problem that arises is that it is not possible to measure the velocity of the same particle at two instances in time and space. This indicates that both terms,  $U_i(t, \bar{x}_i)$  and  $U_{0i}$ , may not be measured for the same particle. Since, however, all the particles are passing within the same domain and sufficiently close to one-another such that truncation errors are manageable, it is possible to consider a velocity  $U_0$  and acceleration  $\bar{a}_0$  that occurs at a position  $\bar{x}_0$  at time  $t_0$  that is used as a reference for all the expansions. Further, if we assume that the velocity gradient field holds for all the particles that pass within some acceptable duration of time, we can re-write equation (2.49) as

$$U_i(t, \bar{x}_i) = U_0 + \nabla U_0 \cdot (\bar{x}_i - \bar{x}_0) - \frac{\partial U}{\partial t} \Big|_{0i} (t - t_{0i}) + HOT \quad (2.51)$$

and likewise equation (2.50) is written

$$\nabla U_0 \cdot (\bar{x}_i - \bar{x}_0) = U_i(t, \bar{x}_i) - U_0 - \frac{\partial U}{\partial t} \Big|_{0i} (t - t_{0i}) \quad (2.52)$$

One additional simplification may be made to equation (2.52) by evaluating it at the time  $t_0$  to eliminate the unsteady term:

$$\nabla U_0 \cdot [\bar{x}_i(t_0) - \bar{x}_0] = U_i(t_0, \bar{x}_i) - U_0 \quad (2.53)$$

The next issue with equation (2.53) is that it gives only a single relation for three quantities in this case (nine in the full tensor case considering other velocity components). To remedy this, three values of the particle subscript  $i$  must be used, such that four particles are needed in total. To use the particles as such, we may obtain an estimate of the velocity,  $U_i(t_0, \bar{x}_i)$ , by expanding this velocity in time around the arrival time for that particle:

$$U_i(t_0, \bar{x}_i) = U_{0i}(t_{0i}, \bar{x}_{0i}) + (\bar{a}_{0i} \cdot \hat{i})(t_0 - t_{0i}) + O[(t_0 - t_{0i})^2] \quad (2.54)$$

To clarify the subscripts in equation (2.54), the terms  $t_{0i}$ ,  $\bar{x}_{0i}$ ,  $U_{0i}$ , and  $\bar{a}_{0i}$  are the measured arrival time, position at the arrival time, velocity at the arrival time and acceleration at the arrival time, respectively. Equation (2.53) and (2.54) may next be combined to form:

$$\nabla U_0 \cdot [\bar{x}_i(t_0) - \bar{x}_0] = U_{0i}(t_{0i}, \bar{x}_{0i}) - U_0 + (\bar{a}_{0i} \cdot \hat{i})(t_0 - t_{0i}) \quad (2.55)$$

Finally, equation (2.55) may be written more explicitly by substituting for  $\bar{x}_i(t_0)$  using equation (2.48):

$$\nabla U_0 \cdot \left[ (\bar{x}_{0i} - \bar{x}_0) + \bar{U}_{0i}(t_0 - t_{0i}) + \frac{\bar{a}_{0i}}{2}(t_0 - t_{0i})^2 \right] = U_{0i}(t_{0i}, \bar{x}_{0i}) - U_0 + (\bar{a}_{0i} \cdot \hat{i})(t_0 - t_{0i}) \quad (2.55a)$$

Let us now expand the dot product in the left-hand side of (2.55a):

$$\begin{aligned} & \left. \frac{\partial U}{\partial x} \left[ \Delta x_i + U_{0i}(t_0 - t_{0i}) + \frac{\bar{a}_{x0i}}{2}(t_0 - t_{0i})^2 \right] + \frac{\partial U}{\partial y} \left[ \Delta y_i + V_{0i}(t_0 - t_{0i}) + \frac{\bar{a}_{y0i}}{2}(t_0 - t_{0i})^2 \right] \right. \\ & \left. + \frac{\partial U}{\partial z} \left[ \Delta z_i + W_{0i}(t_0 - t_{0i}) + \frac{\bar{a}_{z0i}}{2}(t_0 - t_{0i})^2 \right] = \Delta U_i + \bar{a}_{x0i}(t_0 - t_{0i}) \right. \end{aligned} \quad (2.56)$$

We can now obtain a system of three equations for the relationship given in equation (2.53) for four particles. The measurements for the particle with arrival time  $t_0$  are represented in equation (2.53) and to follow without a Latin subscript.

$$\begin{aligned} & \left[ \begin{array}{c} \Delta x_1 + U_{01}(t_0 - t_{01}) + \frac{\bar{a}_{x01}}{2}(t_0 - t_{01})^2 \\ \Delta x_2 + U_{02}(t_0 - t_{02}) + \frac{\bar{a}_{x02}}{2}(t_0 - t_{02})^2 \\ \Delta x_3 + U_{03}(t_0 - t_{03}) + \frac{\bar{a}_{x03}}{2}(t_0 - t_{03})^2 \end{array} \right] \left[ \begin{array}{c} \Delta y_1 + V_{01}(t_0 - t_{01}) + \frac{\bar{a}_{y01}}{2}(t_0 - t_{01})^2 \\ \Delta y_2 + V_{02}(t_0 - t_{02}) + \frac{\bar{a}_{y02}}{2}(t_0 - t_{02})^2 \\ \Delta y_3 + V_{03}(t_0 - t_{03}) + \frac{\bar{a}_{y03}}{2}(t_0 - t_{03})^2 \end{array} \right] \left[ \begin{array}{c} \Delta z_1 + W_{01}(t_0 - t_{01}) + \frac{\bar{a}_{z01}}{2}(t_0 - t_{01})^2 \\ \Delta z_2 + W_{02}(t_0 - t_{02}) + \frac{\bar{a}_{z02}}{2}(t_0 - t_{02})^2 \\ \Delta z_3 + W_{03}(t_0 - t_{03}) + \frac{\bar{a}_{z03}}{2}(t_0 - t_{03})^2 \end{array} \right] \left\{ \begin{array}{c} \frac{\partial U}{\partial x} \\ \frac{\partial U}{\partial y} \\ \frac{\partial U}{\partial z} \end{array} \right\} \\ & = \left\{ \begin{array}{c} \Delta U_1 + \bar{a}_{x01}(t_0 - t_{01}) \\ \Delta U_2 + \bar{a}_{x02}(t_0 - t_{02}) \\ \Delta U_3 + \bar{a}_{x03}(t_0 - t_{03}) \end{array} \right\} \end{aligned} \quad (2.57)$$

Or to simplify things further, we may drop the acceleration term by assuming first-order particle trajectories to obtain

$$\begin{aligned} & \left[ \begin{array}{ccc} \Delta x_1 + U_{01}(t_0 - t_{01}) & \Delta y_1 + V_{01}(t_0 - t_{01}) & \Delta z_1 + W_{01}(t_0 - t_{01}) \\ \Delta x_2 + U_{02}(t_0 - t_{02}) & \Delta y_2 + V_{02}(t_0 - t_{02}) & \Delta z_2 + W_{02}(t_0 - t_{02}) \\ \Delta x_3 + U_{03}(t_0 - t_{03}) & \Delta y_3 + V_{03}(t_0 - t_{03}) & \Delta z_3 + W_{03}(t_0 - t_{03}) \end{array} \right] \left\{ \begin{array}{c} \frac{\partial U}{\partial x} \\ \frac{\partial U}{\partial y} \\ \frac{\partial U}{\partial z} \end{array} \right\} \\ & = \left\{ \begin{array}{c} \Delta U_1 \\ \Delta U_2 \\ \Delta U_3 \end{array} \right\} \end{aligned} \quad (2.58)$$

Finally, equation (2.57) or (2.58) may be solved for the velocity gradients by obtaining the inverse of the matrix on the left-hand side and doing a left-multiply of this inverse with both sides of equation (2.58).

#### 2.3.3.9.4.2.1.1 Quantification of performance of the direct estimation procedure

The first step to finding the uncertainties that will result for equation (2.58) should be to validate that given ideal inputs, the system of equations will result in a stable solution when there are no uncertainties for the velocities and positions. To do this, a MATLAB simulation was written with inputs for the velocity components, mean velocity gradients, and range of y- and z-positions possible. For the simulation, a representative set of data for the 2D flat plate turbulent boundary layer was input at  $y^+ = 100$  and  $Re_\theta = 7300$  in the boundary layer research wind tunnel, as listed in Table 2.6. Particle arrivals were

staggered uniformly at times of  $[0, 25, 50, 75] \mu\text{s}$  for the four particles. The  $y$ - and  $z$ -positions were uniformly sampled within a  $200 \mu\text{m}$  diameter volume. Since no turbulence is input, any resulting variation in the velocity gradients is determined to be in error. For this simulation, a very small amount of variance in the velocity gradients was observed—on the order of the machine precision. Also, with 10,000 samples the mean velocity gradient values input were computed within  $13 \times 10^{-12}\%$  of the mean  $y$ -gradient. Some of these values are listed as Case 0 in Table 2.7. The conclusions from this exercise are that the method for estimating the velocity gradients is stable and converges to the proper mean value.

Five cases were run to explore the variance in the velocity gradients that may result from uncertainties in the velocities and particle positions. These cases are numbered 1-5 in Table 2.7. Note once again that there is no turbulence input into the simulations, all variances arise from the Gaussian uncertainties in the velocity and positions from 10,000 simulation samples. A few interesting observations are made from these data. First, the  $x$ -direction gradient variance is consistently lower than the  $y$ - and  $z$ -positions. This is an inherent property of the CompLDV3 operation geometry since the method is based upon extrapolation of the particle paths before or after the particle velocities and positions are measured while crossing the  $200 \mu\text{m}$  diameter measurement volume. The resulting extrapolated measurement volume has a typical aspect ratio of about 10 (length in  $x$ -direction divided by typical width along  $y$ - or  $z$ -directions). Such an aspect ratio is reasonable compared with, although greater than, the coherent structure length-scale ratios in the near-wall turbulent boundary layer (Simpson 1989; Jeong et al. 1997), but strongly affects the gradient estimation variance. The effect of this aspect ratio on the uncertainties for the final result is evident in a couple of ways. First, since the linear system of equations (2.58) is fully coupled among the position-direction components, the imbalance in these components results in potential for great uncertainties. A metric for this is the matrix inverse condition number that may be defined by

$$1/\kappa \equiv \left( \frac{\|A\|}{\|A^{-1}\|} \right)^{-1} \quad (2.59)$$

where  $1/\kappa$  is the metric, and the matrix  $A$  is the position matrix on the far left-hand-side of equations (2.58) for the current application. This metric is unity for a well-conditioned matrix which may be confidently inverted, and becomes decreasingly small for ill-conditioned matrices (Golub and Van Loan 1996). The average matrix inverse condition number for the simulation run with no uncertainties (Case 0 in Table 2.7) was 0.03, much less than unity. Even in the case of a structured grid, it is clear that gradients taken over smaller distances will require more resolution in the constituent values of velocity and positions used to compute these to achieve the same levels of uncertainties as those gradients taken over larger differences. Thus, one may expect to see greater uncertainties in a similar aspect ratio volume even for a structured grid in the span-wise and normal-to-wall directions compared with the stream-wise direction.

From the results for Cases 1-5, we see variances arising fully from random, incoherent Gaussian-distributed uncertainties. Larger variances in the span-wise and normal-to-wall directions compared to the stream-wise direction are consistently observed. For each case, the ratios of the span-wise or normal-to-wall direction gradient variance to the

stream-wise gradient variance are about 120-150. To make the magnitudes of these values clearer, they are compared to the 2D flat-plate turbulent boundary layer results of Honkan and Andreopoulos (1997) in viscous wall scaling. To note is that the variance for the  $x$ -direction derivative from the simulation is much smaller than the measurement variance in the 2D turbulent boundary layer indicating that this derivative may be confidently measured with the CompLDV3. In contrast, for the most realistic case for the uncertainties in the system as determined by the simulations discussed in previous sections, Case 5, the  $y$ - and  $z$ -direction derivative variances are on the order of the measurement value for both cases. This indicates that the measurement uncertainties are perhaps too great to directly estimate the velocity gradients with confidence using this technique with no corrections.

The propagation of the measurement uncertainties through to the velocity gradients is further-examined by looking at the histograms of the velocity gradients computed in Case 5. For comparison, the histograms for the simulated velocity gradient measurements for the  $x$ ,  $y$ , and  $z$ -direction gradients normalized by the measured standard deviations are plotted together in Figure 2.50. One may immediately note the similarity in these distributions. They each have high kurtosis,

$$\kappa = \frac{\overline{u^4}}{(\overline{u^2})^2} \quad (2.60)$$

with values of about 23, 22, and 16 for the stream-wise, normal-to-wall, and span-wise-direction velocity gradients respectively, indicating that the distributions are ‘peaky’ compared with the Gaussian case with a value of 3. For such distributions, the ‘tails’ of the histograms persist at higher probabilities than the comparable Gaussian distribution with the same standard deviation.

An additional simulation was done in which turbulence-like fluctuations of the velocities and velocity gradients were input to be representative of the 2D flat plate TBL at  $y^+ = 100$  and  $Re_\theta = 7500$ . The probability distributions for the turbulence were all taken to be Gaussian with statistics values given in Table 2.9. The data of Honkan and Andreopoulos (1997) were used as estimates for the velocity gradient variances. The ranges of  $y$ - and  $z$ -positions were based upon experimentally determined ranges for the CompLDV3. Using these ranges, the uncertainties were adjusted to obtain similar results as those of the CompLDV3 measurements are listed in comparison with other benchmark measurements in Table 2.10. Again, the stream-wise direction gradient variance is considerably smaller than the normal-to-wall and span-wise variances, as expected. The estimated variance for the stream-wise gradient is about 1.85 times greater than the value input. However, the normal-to-wall direction gradient was 23.7 times greater than the input value and the span-wise direction gradient was found to be 16 times greater than that input. The three resulting histograms for the  $U$ -gradients are plotted in Figure 2.51. We do see a fair preservation of the Gaussian-distributed input gradients for the  $x$ -direction estimation, with a kurtosis value of  $\kappa = 6.4$ . But the other gradient components considered are similar to those in Figure 2.50 and exhibit large values of kurtosis of about  $\kappa = 15$ .

Case 6 in Table 2.7 and Table 2.8 is the analogous case to the turbulence-like statistics simulation with the same input uncertainties and mean velocities and gradients. That case differs from Cases 1-5 in that the  $y$ - and  $z$ -positions are sampled with Gaussian statistics with a standard deviation of  $50\mu\text{m}$  as determined from empirical histograms obtained with the CompLDV3 of the  $y$ - and  $z$ -position differences among particles. The statistics are comparable to the case with turbulence-like input statistics, except the  $x$ -direction gradient exhibits a large kurtosis of  $\kappa = 23$ , which is comparable with the other gradient directions.

It is clear from table 5, that the direct estimation procedure for the velocity-gradient measurements is not sufficient for reliable measurements of the variances of velocity-gradient terms without the development of large corrections. This has led to the development of an alternative approach to estimating the velocity gradients described to follow.

**Table 2.6. Parameters for the velocity gradient uncertainty simulations at  $\text{Re}_\theta = 7500$  and  $y^+ = 100$ .**

$\text{Re}_\theta$	7500
$y^+$	100
$u_\tau$	1 m/s
$\frac{\overline{\partial U}}{\partial y}$	$1478 \text{ s}^{-1}$
$\overline{U}$	16.25 m/s

**Table 2.7. Velocity gradient uncertainty simulation cases and results.**

Case	$\delta x$	$\delta y$	$\delta z$	$\delta U$	$\left(\frac{\overline{\partial U}}{\partial y}\right)_{\text{Computed}}$	$\left[\left(\frac{\partial u}{\partial x}\right)^2\right]_{\text{Computed}}$	$\left[\left(\frac{\partial u}{\partial y}\right)^2\right]_{\text{Computed}}$	$\left[\left(\frac{\partial u}{\partial z}\right)^2\right]_{\text{Computed}}$
0	0	0	0	0	$1478 \text{ s}^{-1}$	$7.23 \text{ E} - 23 \text{ s}^{-2}$	$5.0 \text{ E} - 20 \text{ s}^{-2}$	$7.1 \text{ E} - 21 \text{ s}^{-2}$
1	0	$1\mu\text{m}$	$1\mu\text{m}$	0	$1477 \text{ s}^{-1}$	$62 \text{ s}^{-2}$	$8.9 \text{ E} 3 \text{ s}^{-2}$	$7.3 \text{ E} 3 \text{ s}^{-2}$
2	0	0	0	0.5%	$1470 \text{ s}^{-1}$	$2.1 \text{ E} 5 \text{ s}^{-2}$	$2.7 \text{ E} 7 \text{ s}^{-2}$	$2.4 \text{ E} 7 \text{ s}^{-2}$
3	0	$30\mu\text{m}$	$30\mu\text{m}$	0	$1211 \text{ s}^{-1}$	$5 \text{ E} 4 \text{ s}^{-2}$	$4.9 \text{ E} 6 \text{ s}^{-2}$	$4.7 \text{ E} 6 \text{ s}^{-2}$
4	0	0	0	0.2%	$1482 \text{ s}^{-1}$	$3.5 \text{ E} 4 \text{ s}^{-2}$	$4.3 \text{ E} 6 \text{ s}^{-2}$	$4.1 \text{ E} 6 \text{ s}^{-2}$
5	$4\mu\text{m}$	$6\mu\text{m}$	$6\mu\text{m}$	0.2%	$1430 \text{ s}^{-1}$	$3.6 \text{ E} 4 \text{ s}^{-2}$	$4.5 \text{ E} 6 \text{ s}^{-2}$	$3.8 \text{ E} 6 \text{ s}^{-2}$
6	$4\mu\text{m}$	$10\mu\text{m}$	$10\mu\text{m}$	0.38%	$664 \text{ s}^{-1}$	$2.1 \text{ E} 5 \text{ s}^{-2}$	$3.1 \text{ E} 8 \text{ s}^{-2}$	$2.6 \text{ E} 8 \text{ s}^{-2}$

**Table 2.8. Velocity gradient uncertainty simulation results in viscous wall scaling.**

Case	$\left[ \overline{\left( \frac{\partial u}{\partial x} \right)^2} \right]^+$ <i>Computed</i>	$\left[ \overline{\left( \frac{\partial u}{\partial y} \right)^2} \right]^+$ <i>Computed</i>	$\left[ \overline{\left( \frac{\partial u}{\partial z} \right)^2} \right]^+$ <i>Computed</i>
<b>1</b>	<b>1.7E-8</b>	<b>2.4E-6</b>	<b>2.0E-6</b>
<b>2</b>	<b>5.7E-5</b>	<b>7.3E-3</b>	<b>6.5E-3</b>
<b>3</b>	<b>1.3E-5</b>	<b>1.3E-3</b>	<b>1.3E-3</b>
<b>4</b>	<b>9.5E-6</b>	<b>1.2E-3</b>	<b>1.1E-3</b>
<b>5</b>	<b>9.8E-6</b>	<b>1.2E-3</b>	<b>1.0E-3</b>
<b>6</b>	<b>5.7E-5</b>	<b>8.4E-2</b>	<b>7.1E-2</b>
<b>Typical real flow at <math>y^+=100</math> (Honkan and Andreopoulos 1997)</b>	<b>1.3E-3</b>	<b>3.8E-3</b>	<b>5.6E-3</b>

**Table 2.9. Velocity gradient simulation with statistical variations given by the expected results in the 2D flat-plate TBL at  $Re_\rho = 7500$  and  $y^+=100$ .**

Input variables	Input values
$U$	16.25 m/s
$\overline{u^2}$	$5m^2 / s^2$
$\overline{v^2}$	$1.3m^2 / s^2$
$\overline{w^2}$	$2.5m^2 / s^2$
$\frac{\partial U}{\partial y}$	$1478s^{-1}$
$\left[ \overline{\left( \frac{\partial u}{\partial x} \right)^2} \right]^+$	0.0013
$\left[ \overline{\left( \frac{\partial u}{\partial y} \right)^2} \right]^+$	0.0038
$\left[ \overline{\left( \frac{\partial u}{\partial z} \right)^2} \right]^+$	0.0056
$\delta x$	$4\mu m$
$\delta y$	$10\mu m$
$\delta z$	$10\mu m$
$\delta U$	0.38%
Standard deviation of probability distribution of y- and z-positions (a statement of measurement volume size)	$50\mu m$
<b>Output variables</b>	<b>Output values</b>

$\overline{\left(\frac{\partial u}{\partial x}\right)^{2+}}$	0.0024
$\overline{\left(\frac{\partial u}{\partial y}\right)^{2+}}$	0.09
$\overline{\left(\frac{\partial u}{\partial z}\right)^{2+}}$	0.08

**Table 2.10. Comparison of velocity gradient measurements at  $y^+=100$  for three bodies of work in the 2D flat plate turbulent boundary layer.**

Lowe 2006	Klebanoff 1955	Honkan and Andreopoulos 1997
$\overline{\left(\frac{\partial u}{\partial x}\right)^{2+}} = 0.0013$	$\overline{\left(\frac{\partial u}{\partial x}\right)^{2+}} = 0.0013$	$\overline{\left(\frac{\partial u}{\partial x}\right)^{2+}} = 0.0013$
$\overline{\left(\frac{\partial u}{\partial y}\right)^{2+}} = 0.0955$	$\overline{\left(\frac{\partial u}{\partial y}\right)^{2+}} = 0.0021$	$\overline{\left(\frac{\partial u}{\partial y}\right)^{2+}} = 0.0038$
$\overline{\left(\frac{\partial u}{\partial z}\right)^{2+}} = 0.0955$	$\overline{\left(\frac{\partial u}{\partial z}\right)^{2+}} = 0.0021$	$\overline{\left(\frac{\partial u}{\partial z}\right)^{2+}} = 0.0056$
$\overline{\left(\frac{\partial v}{\partial x}\right)^{2+}} = 0.0012$	$\overline{\left(\frac{\partial v}{\partial x}\right)^{2+}} = 0.00062$	$\overline{\left(\frac{\partial v}{\partial x}\right)^{2+}} = 0.0023$
$\overline{\left(\frac{\partial v}{\partial y}\right)^{2+}} = 0.0907$	$\overline{\left(\frac{\partial v}{\partial x}\right)^{2+}} = 0.001$	$\overline{\left(\frac{\partial v}{\partial y}\right)^{2+}} = 0.0032$
$\overline{\left(\frac{\partial v}{\partial z}\right)^{2+}} = 0.0893$		$\overline{\left(\frac{\partial v}{\partial z}\right)^{2+}} = 0.0055$
$\overline{\left(\frac{\partial w}{\partial x}\right)^{2+}} = 0.0017$		$\overline{\left(\frac{\partial w}{\partial x}\right)^{2+}} = 0.0034$
$\overline{\left(\frac{\partial w}{\partial y}\right)^{2+}} = 0.1310$		$\overline{\left(\frac{\partial w}{\partial y}\right)^{2+}} = 0.0063$
$\overline{\left(\frac{\partial w}{\partial z}\right)^{2+}} = 0.1208$		$\overline{\left(\frac{\partial w}{\partial z}\right)^{2+}} = 0.0064$

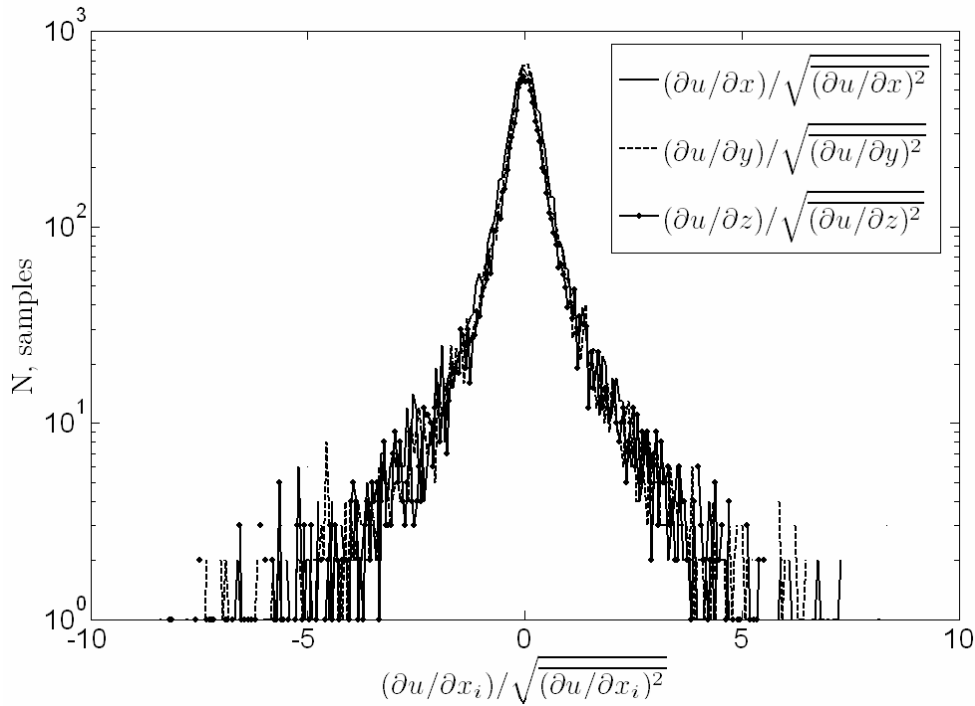


**Figure 2.50.** Normalized histogram illustrating the similarity of histograms for each of the three gradients considered.

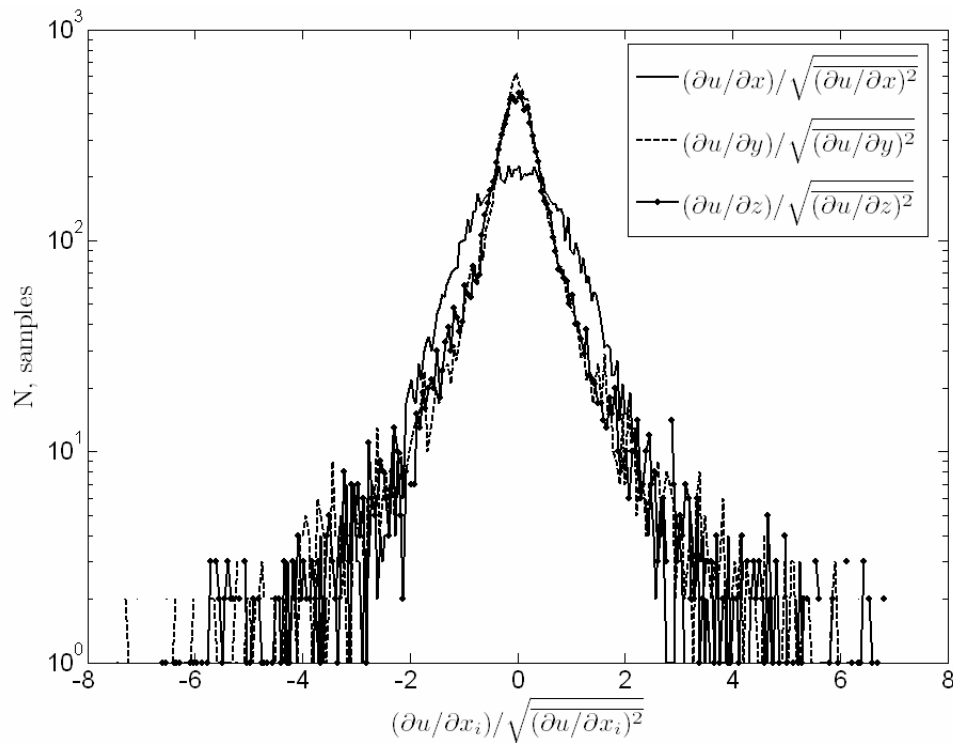


**Figure 2.51.** Normalized histogram for each of the three gradients considered when a Gaussian distribution of velocity gradients are simulated with variances given by Honkan and Andreopoulos (1997).

## 2.3.3.9.4.2.2 Least-squares estimation of velocity gradients

A second technique for estimating the velocity gradients is developed based upon an over-constrained system for the  $N$ -particles that cross the measurement volume within the allowable time  $t$ . To construct a least-squares cost function, some model for the distribution of the measured quantities must be assumed. In this case, we desired a coherent-structure-based model for the velocity field observed over a short record of time. The model assumed is a swirling structure aligned with the free-stream direction and with a relatively large extent in space for that direction. The near-wall coherent structures in the 2-D TBL such as the quasi-streamwise vortex of Robinson (1991) have been observed to be consistent with this model. Further from the wall, it is still observed that the stream-wise ‘legs’ of ‘crescent-shaped’ structures are really those that contribute to dissipation of the turbulence energy in the Reynolds stresses as the legs stretch and the vorticity within is intensified. The existence of these elongated dissipative structures gives credence to a technique that utilizes a long-narrow region of fluid as the basis for obtaining resolved velocity gradients. A simple structure of the velocity distribution is assumed such that the nine Cartesian-components of the velocity gradient tensor are modeled as constant within the observed region of flow.

To implement the model chosen, we refer again to Figure 2.49. The centroid velocity and position of the  $N$  particles may be readily computed from the data. In the case that the velocity field assumed is exact and the measurements are without uncertainty, then, a velocity gradient field which is consistent with the measurements will result in the following relationship:

$$\begin{aligned} U_i &= U_c + [(\bar{r}_i - \bar{r}_c) \cdot \bar{\nabla}] U_c \\ V_i &= V_c + [(\bar{r}_i - \bar{r}_c) \cdot \bar{\nabla}] V_c \\ W_i &= W_c + [(\bar{r}_i - \bar{r}_c) \cdot \bar{\nabla}] W_c \end{aligned} \quad (2.61)$$

where  $\bar{r}_i$  is the position vector of the  $i^{\text{th}}$  particle,  $\bar{U}_i = U_i \hat{i} + V_i \hat{j} + W_i \hat{k}$  is the velocity vector of the  $i^{\text{th}}$  particle,  $\bar{r}_c$  is the position vector of the centroid of the  $N$  particles considered for velocity gradient tensor estimation, and  $\bar{U}_c = U_c \hat{i} + V_c \hat{j} + W_c \hat{k}$  is the centroid velocity vector for the  $N$  particles. Equations (2.61) may also be thought of as the 3-D Taylor-series expansions for the velocity components truncated for velocity derivatives of order 2 and greater (although one may refine velocity estimates using the CompLDV3 acceleration measurements to enhance the order of the method). In the CompLDV3 measurements, uncertainty exists both for the measurements obtained as well as for the model equations (2.61). To mitigate this, redundant measurements for several particles are used along with equations (2.61) to construct objective cost functions that must be minimized by successive guesses for the velocity-gradient tensor. The cost function chosen is a least-squares error function developed from equation (2.61):

$$\begin{aligned}
\Phi_U &= \sum_{i=1}^N \left\{ U_c + [(\bar{r}_i - \bar{r}_c) \cdot \bar{\nabla}] U_c - U_i \right\}^2 \\
\Phi_V &= \sum_{i=1}^N \left\{ V_c + [(\bar{r}_i - \bar{r}_c) \cdot \bar{\nabla}] V_c - V_i \right\}^2 \\
\Phi_W &= \sum_{i=1}^N \left\{ W_c + [(\bar{r}_i - \bar{r}_c) \cdot \bar{\nabla}] W_c - W_i \right\}^2
\end{aligned} \tag{2.62}$$

where  $\Phi_U, \Phi_V, \Phi_W$  are the cost functions that are minimized to obtain the velocity gradient estimates. Note that in this implementation, the velocity components are decoupled except in the convection that is hidden in the calculation of the position vectors:

$$\bar{r}_i = U_i(t_0 - t_A)\hat{i} + [y_i + V_i(t_0 - t_A)]\hat{j} + [z_i + W_i(t_0 - t_A)]\hat{k} \tag{2.63}$$

where  $t_A$  is the arrival time for the  $i^{\text{th}}$  particle,  $t_0$  is the time at which the centroid information is computed, and  $y_i$  and  $z_i$  are the position-components directly-measured by the CompLDV3. It is taken that the arrival time measurement for the burst occurs when the particle is at the location  $x_i=0$ , which is an excellent assertion considering the overall length of the volume under consideration.

In a similar manner as with the four-particle technique, the least-squares technique was tested to ensure that the optimization scheme would result in the proper velocity gradient tensor with no uncertainties input. A simulation technique was implemented in which particle inter-arrival times were sampled from the exponential Poisson distribution with a mean particle rate of 20,000 particle arrivals per time unit. The same representative point at  $y^+=100$  in the 2D flat-plate turbulent boundary layer was used for mean velocities and mean velocity gradients as given in Table 2.6, but no turbulence was input. Simulations with 6 and 7 particles used in the least-squares optimization were carried out. The results from these two simulations are listed in Table 2.11. It is reiterated, that no turbulence is entered either within the velocities or the gradients—all deviations from zero-variance are due to uncertainties in the technique. A comparison between these results and those in Table 2.8 for the four-particle method reveals a much-reduced level of variance in the estimated velocity gradients. In particular, the variance for the  $y$ - and  $z$ -direction gradients are reduced by approximately two orders of magnitude when one compares Case 6 in table Table 2.8 to either case in Table 2.11 since each of these cases have the same level of input uncertainty in the velocities and positions. Based upon the promising results of this simulation, the method was applied to actual data in the 2D flat-plate TBL to obtain real-flow results discussed to follow in chapter 4.

**Table 2.11. Uncertainty simulations for the least-squares velocity gradient estimation method.**

Case	1	2
<b>Inputs</b>		
$U$	16.25 m/s	16.25 m/s
Number of particles	7	6
$\overline{\frac{\partial U}{\partial y}}$	1478.2 s <sup>-1</sup>	1478.2 s <sup>-1</sup>
$\delta x$	4 $\mu\text{m}$	4 $\mu\text{m}$
$\delta y, \delta z$	10 $\mu\text{m}$	10 $\mu\text{m}$
$\delta U, \delta V, \delta W$	0.38% of $\ \bar{U}\ $	0.38% of $\ \bar{U}\ $
Data rate	20 kHz	20 kHz
<b>Outputs</b>		
$\left. \overline{\frac{\partial U}{\partial y}} \right)_{\text{Computed}}$	1407.3 s <sup>-1</sup>	1390.2 s <sup>-1</sup>
$\left. \overline{\left( \frac{\partial u}{\partial x} \right)^2} \right)_{\text{Computed}}$	2E-7	3E-7
$\left. \overline{\left( \frac{\partial u}{\partial y} \right)^2} \right)_{\text{Computed}}$	1.8E-4	2.7E-4
$\left. \overline{\left( \frac{\partial u}{\partial z} \right)^2} \right)_{\text{Computed}}$	1.7E-4	2.7E-4
$\kappa \left[ \overline{\left( \frac{\partial u}{\partial x} \right)^2} \right]$	5.6	6.5

$\kappa \left[ \overline{\left( \frac{\partial u}{\partial y} \right)^2} \right]$	4.4	5.7
$\kappa \left[ \overline{\left( \frac{\partial u}{\partial z} \right)^2} \right]$	4.4	4.9

### 2.3.3.9.4.3 Calibration of third generation CompLDV

Just as with the CompLDV1, a calibration is necessary to determine the fringe pattern so that the Doppler frequencies may be interpreted properly. Following the discussions of section 2.3.3.7.2.1, the fringe field for each measurement volume has been parameterized by two constants of alignment. The two parameters are the same ones in equation (2.27)—the fringe spacing at the center of the measurement volume ( $d_0$ ) and the normalized fringe gradient,  $A \equiv \frac{1}{d_0} \frac{d[d(x')]}{dx'}$ .

#### 2.3.3.9.4.3.1 Center fringe spacing calibration

The center fringe spacing may be determined in a simple and robust manner by making laser-Doppler measurements within the inviscid core of the facility being used. Measurements of the mean velocity at this location are made using a Pitot-static probe and an electronic pressure transducer. In a manner as quickly as possible, the CompLDV3 is used for measurements at nearly the same location. The mean Doppler frequencies and the beam geometries may be used to determine the center fringe spacing,  $d_0$ . Note that due to the Gaussian nature of the beams and the fact that a small portion of the longitudinal extent of the measurement volume is ‘viewed’ by the receiving optics, the mean frequencies measured are truly indicative of the center-of-volume fringe spacing for fringe gradients that approximately follow the variations in equation (2.27) (i.e., approximately constant gradients). The issue of alignment of the CompLDV3 volume and the Pitot-static probe is eased by the configuration of the laser beams. To align, the operator wears laser-protection goggles so that the measurement volume region may be viewed and the Pitot-static probe is carefully positioned so that the beams from both transmitting heads are reflected away approximately equally. This achieves a spatial confidence about the order of the width of the Pitot-static probe itself, which is quite sufficient for the only-large-scale variations that are characteristic of an inviscid core.

#### 2.3.3.9.4.3.2 Fringe gradient calibration

The calibration of the fringe gradients is more difficult in that the spatial-extent of the measurement volume is very small and only dynamic targets are useful for fringe characterization. The wheel method for calibration for the CompLDV1 has been discussed along with its limitations. The width of the wire spanning the measurement

volume simply results in too many possibilities for irresolvable systematic errors such that no number of independent calibrations will increase the fidelity of the technique. For this reason, a particle or point-like scatterer is necessary to fully resolve the fringe variations in an unbiased manner.

With the need of a point-like scatterer established, the most-obvious candidate experiment would be a particle-seeded flow. The requirements for the flow must be that it is well-understood, that it have large spatial variations at least one mean velocity component, and that those spatial variations in the velocity are repeatable. The plate and cone viscometer flow was first considered for this application after the relatively successful applications of the device as discussed in section 2.3.3.7.5.1. The application of the CompLDV3 to this flow, however, proved difficult, as flare from the cone-surface was problematic and would not allow sufficient range of traverse within the gap so that the flow gradients could be characterized effectively. It is surmised that this problem arose due to the large intersection angles of all the beams for the CompLDV3 that results in beams striking the cone-surface within the receiving line-of-sight at relatively large distances between the cone and the measurement volume. This problem resulted in low signal-to-noise ratios that could only be remedied by increasing the parameter  $y_0$  in equation (2.46). As will be shown in section 2.3.3.9.4.4, this results in significant secondary flow in the operation of the plate and cone device and drastically reduces its effectiveness as a calibration tool.

The next ‘well-understood’ flow that is accessible to the Turbulent Boundary Layer Research Group (TBLRG) that contains velocity gradients on the orders needed is the 2D flat-plate turbulent boundary layer on the floor of the Boundary Layer Research Wind Tunnel (BLWT). This flow is attractive in a few ways. First, the BLWT facility is extremely reliable and results in very repeatable measurements from day to day. Second, the CompLDV3 is capable of very near-wall measurements, meaning that it is possible to make measurements in the region of the flow where viscous forces dominate and where lower-Reynolds number direct-numerical simulations (DNS) exist to corroborate CompLDV3 data. Third, extensive measurements exist for this flow in addition to the DNS that indicate that law-of-the-wall and the parameters defining it are well-founded. The most-obvious drawback to this approach is that the flow is turbulent, and with the highest intensities of anywhere in the boundary layer profile occurring just above the wall. This means that extensive amounts of data are needed to truly define the mean velocities at several points within the measurement volume. Nonetheless, the advantages discussed are sufficient to make the method attractive, and applications of this technique show that the flow is effective for these purposes.

The method of calibration is to find the combination of 5 values for the measurement volume fringe gradients that result in the most continuous velocity profile that is also consistent with the viscous sublayer law-of-the-wall where the velocity gradient approaches the constant value given by the wall shear. A couple of methods may be used to determine the value of the velocity gradient at the wall for the 2D flat-plate TBL. The work of DeGraaff and Eaton (2000) has shown that the wall-friction velocity,  $u_\tau$ , may be

determined effectively in this particular flow by a fit of the logarithmic region of the boundary layer profile to the law-of-the-wall in that region:

$$u / u_\tau = \frac{1}{\kappa} \ln \frac{yu_\tau}{\nu} + B \quad (2.64)$$

where  $\kappa$  and  $B$  are constants given by Coles' as  $\kappa = 0.41$  and  $B=5.0$ . Lowe and Simpson (2006) have also reported data that indicates a small difference between this fitted value and the value obtained by a fit to data in the sublayer using the rigorous equation there (Rotta 1962; Tang 2004; Durst et al. 1995)

$$U = \frac{\tau_{wx}}{\mu} y + \frac{1}{2\mu} \left. \frac{\partial P}{\partial x} \right)_{wall} y^2 + C_U y^4 \quad (2.65)$$

where  $U$  is the stream-wise mean velocity,  $\tau_{wx}$  is the stream-wise wall shear stress,  $\mu$  is the dynamic viscosity of the fluid,  $\left. \frac{\partial P}{\partial x} \right)_{wall}$  is the wall pressure gradient (zero in this case)

and  $C_U = f \left\{ \frac{\partial^3 (\overline{uv})}{\partial y^3} \right\}$ . This is observed to yield reliable shear stress estimates for  $y^+ < 9$

(Tang 2004). Many researchers in the TBLRG has used this technique successfully in low-speed smooth wall 2-D and 3-D flows (Ölçmen et al., 2001a). Since the fit to the sublayer data is done on the mean velocity, volume-averaged conventional LDV data may be used to obtain the sublayer profile in flows where viscous scales allow for direct fits to equation (2.65).

In the present work, a 2D flat-plate TBL at  $Re_\theta = 5930$  was used for a calibration case. In this case, the volume-averaged statistics for the near-wall region could be used both for a fit to equation (2.65) as well as in the logarithmic region as a fit to equation (2.64). Considering the values of wall shear for both these cases, a value of  $u_\tau \approx 0.78$  well-represents both equations (2.65) and (2.64) for the data. To obtain the velocities and positions for each CompLDV burst acquired, we must solve equations (2.47). To obtain an initial solution for this equation in terms of wind tunnel coordinates, with the  $x$ -axis aligned with the free-stream velocity, equation (2.27) is evaluated with the values for the design parameters used to align beams. Solving the system in equations (2.47) then yields an estimate for the velocities and positions. It is possible to organize the data in bins according to the position estimated and obtain statistics for the velocities measures. The mean stream-wise velocities resolved by the CompLDV3 before calibration in the 2D flat-plate TBL of interest are plotted in Figure 2.52. In this plot, there is clear discontinuity in both the values of the stream-wise mean velocities and their derivatives. The goal of the calibration is then to find a multiplicative constant for the measured-positions that results in a continuous profile and a wall velocity gradient that approaches the predicted value. Adjustment of the calibration constant yields the calibrated data in Figure 2.53 that is considerably more continuous in both the velocity values and the gradients. Furthermore, the values of the wall velocity gradient approaches the value measured using independent methods.

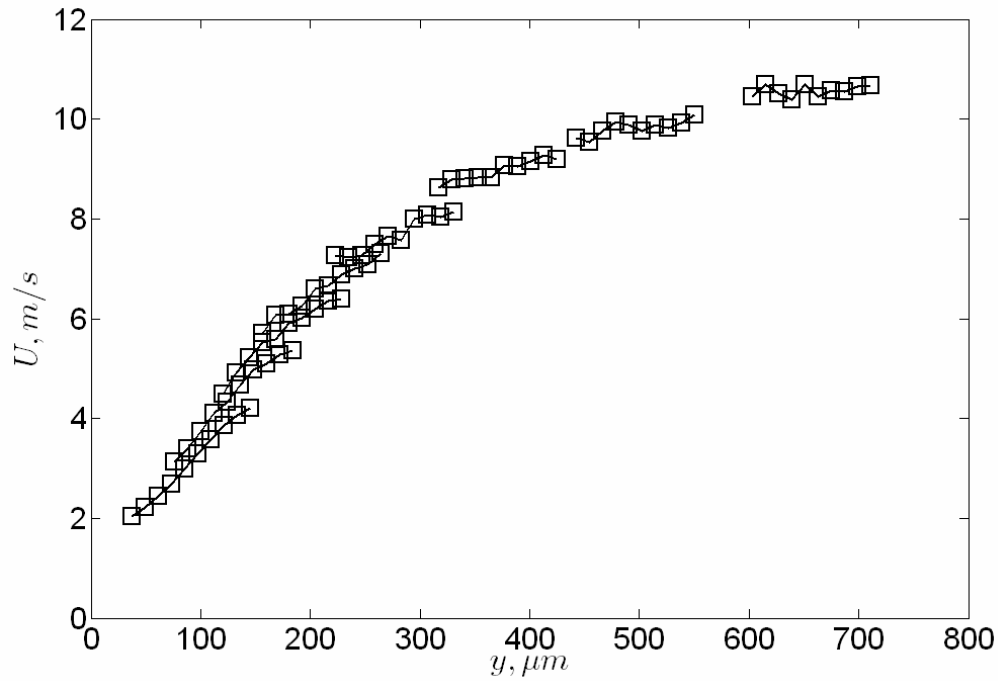


Figure 2.52. Sub-measurement volume resolution measurements in a 2D flat plate turbulent boundary layer with assumed fringe gradients.

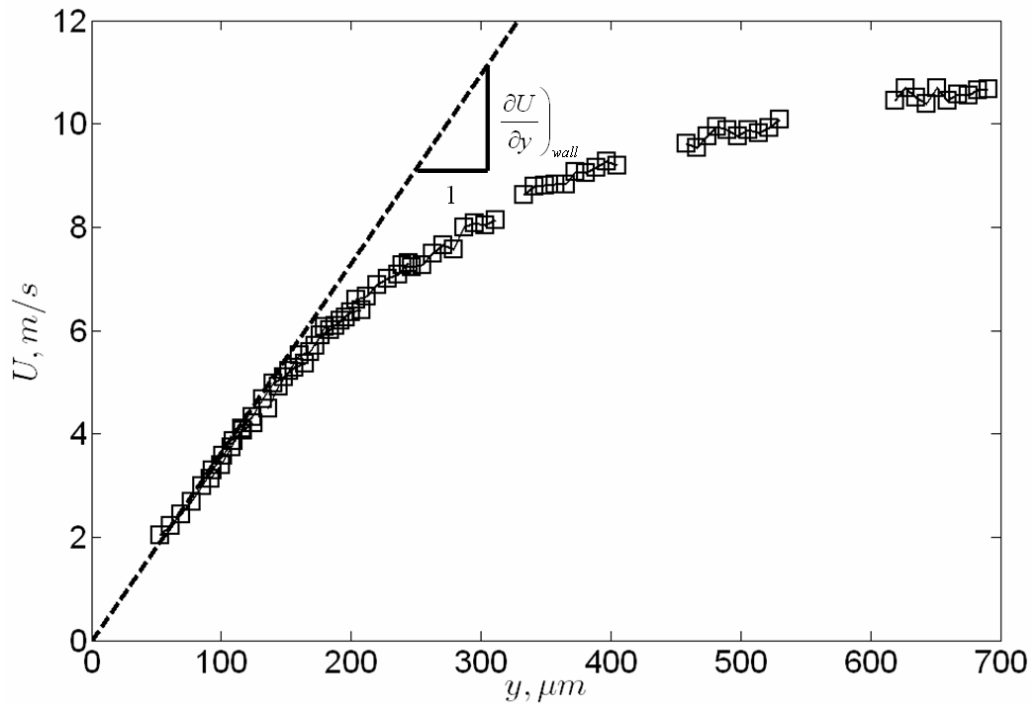


Figure 2.53. Sub-measurement volume resolution measurements in a 2D flat plate turbulent boundary layer with calibrated fringe gradients.

#### 2.3.3.9.4.4 Validation of the third generation CompLDV

In a similar manner as the CompLDV1, the plate and cone viscometer flow is used as a validation experiment for the CompLDV3. In applying the CompLDV3 to this flow, considerable interference from the surface of the cone was encountered that limited the region of the flow that could be interrogated. This interference precluded the use of the flow device for calibrations since the region of flow that could be measured was too small to get a high-confidence measurement of the velocity gradient. In order to obtain measurements, the housing for the rotating cone was displaced from the plate such that the cone apex was a considerable distance from the stationary glass plate. The measurements to be discussed show considerable secondary flow that further make the flow measured unsuitable for calibrations but effective as a validation case.

The flow parameters for the profile measured are given in Table 2.12. The angular speed of the cone has been verified in previous experiments already discussed. The distance between the apex and the measurement point was measured using the stepper motors of the  $x$ - $z$  probe traverse by carefully visually aligning the measurement volume on the apex of the cone. The linear-profile azimuthal velocity gradient was determined by a linear fit to the mean volume-averaged velocity statistics plotted in Figure 2.54. From this fit, the gap height is also determined, which indicates that the additional space added between the cone housing and the glass plate was about 1.46mm, which is consistent with the thickness of the two pieces of reinforced double-sided tape used to displace and secure the housing.

The three-orthogonal velocity components determined from the volume-averaged statistics for the CompLDV3 are plotted in Figure 2.55, non-dimensionalized using the gap height and the cone azimuthal velocity. As already mentioned, the extra displacement of the cone apex has caused the significant secondary flow to arise as is evident by the radial mean-velocity profile. One original hope for the current measurements was to quantify the random uncertainty in the position estimation to validate the quality of those measurements. To obtain these estimates, the flow interrogated must be free of turbulence so that there is a one-to-one correspondence between velocity and position. Unfortunately, there appears to be turbulence in the current flow most likely arising from instabilities due to the large gap between the apex of the cone and the plate. The volume-averaged Reynolds stresses corrected for velocity gradient broadening as described by Durst et al. (1995) are plotted in Figure 2.56. Since both the azimuthal and radial mean velocities exhibit significant gradients in this region of the flow, the azimuthal and radial normal stresses were corrected as

$$\Delta \overline{u_i^2} = \frac{d^2}{12} \left( \frac{\partial U_i}{\partial y} \right)^2 \quad (2.66)$$

where  $\Delta \overline{u_i^2}$  is the correction to be subtracted from the normal stress  $\overline{u_i^2}$ ,  $d$  is the effective diameter of the measurement volume (determined as 100  $\mu\text{m}$  in the CompLDV3 volume-averaged data), and  $\frac{\partial U_i}{\partial y}$  is the mean velocity gradient of the in the same velocity

component as the normal-stress being corrected. Since both the radial and azimuthal velocities vary considerably, it is also necessary to correct the shear-stress value that involves those velocities. The appropriate correction in that case is

$$\overline{\Delta u_i u_j} = \frac{d^2}{12} \left( \frac{\partial U_i}{\partial y} \right) \left( \frac{\partial U_j}{\partial y} \right) \quad (2.67)$$

At maximum, the velocity gradient broadening-corrected data exhibit a turbulence intensity (defined here as  $\sqrt{\overline{u_\theta^2}} / (U_\theta)_{cone}^2 \times 100\%$ ) of about 2.5%—high enough to be considered at least transitional.

Despite that this device may not be used effectively to give an estimate for the position uncertainties, it is still useful as a flow with large velocity gradients yet relatively low turbulence intensities. This becomes useful for testing the sub-measurement volume profile-resolution capabilities of the CompLDV3 since volume-averaged data are available. The mean azimuthal velocities resolved by positioning the center of the CompLDV3 volume at five vertical locations are plotted in Figure 2.57. The profile measured is very continuous and exhibits very little scatter among the data points except near the edges of the measurement volume. The mean radial velocities for these five locations are plotted in Figure 2.58, exhibiting that the CompLDV3 has true resolution capabilities in multiple velocity-directions. This is even further demonstrated in Figure 2.59 in which the sub-measurement volume profiles of flow angle are plotted. Since the flow angle is continuously changing, no rotation of the data may found to make the flow purely one-dimensional. It is noted here that the CompLDV3 is truly sensing the rapid change of flow angle within the measurement volume at each point.

**Table 2.12. Parameters for the CompLDV3 measurements in the plate and cone flow.**

$f_{cone}$	<b>1800RPM</b>
$\omega_{cone}$	<b>188.5rad/s</b>
<b>Gap height, <math>y_{max}</math></b>	<b>1.92mm</b>
$r$	<b>26.2mm</b>
$(U_\theta(r))_{cone}$	<b>4.93m/s</b>
$\partial U_\theta / \partial y$	<b>2565s<sup>-1</sup></b>

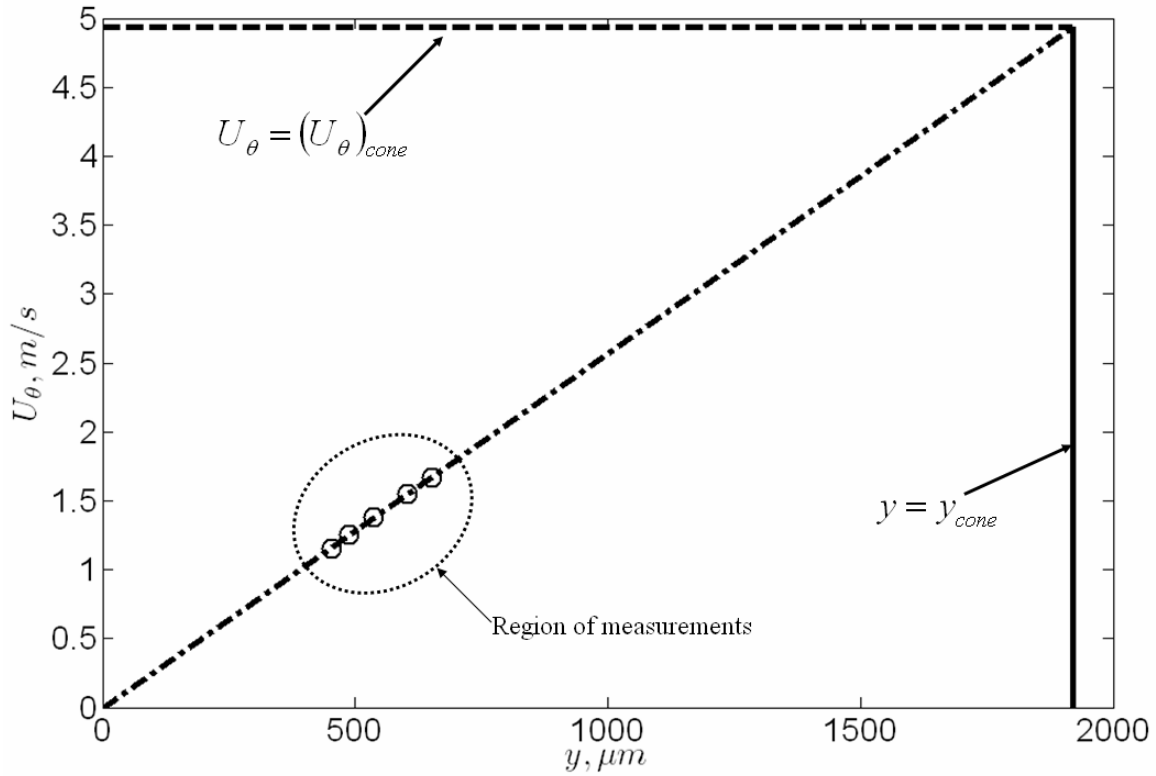


**Figure 2.54. Volume-averaged mean azimuthal velocities in the plate and cone flow as measured with the ComplDV3.**

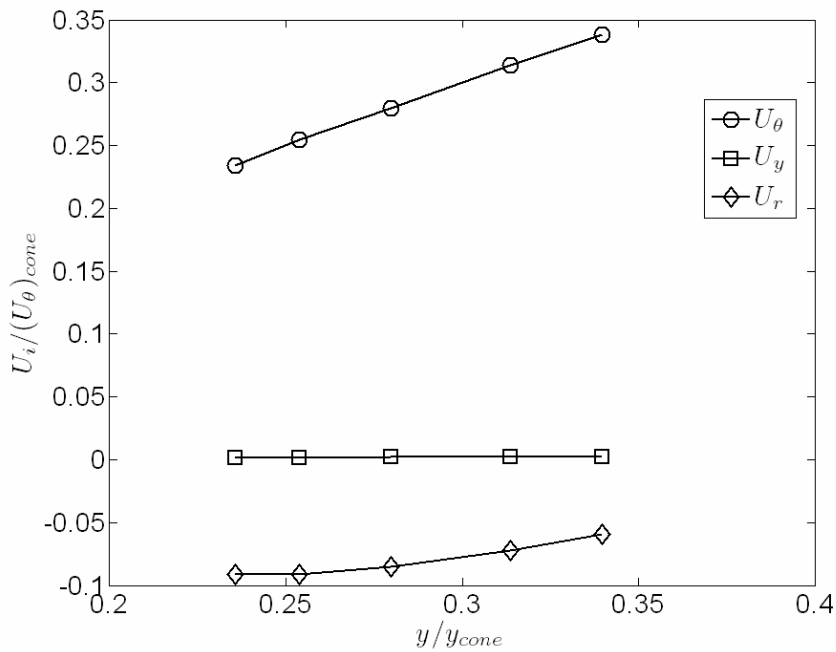


**Figure 2.55. Volume-averaged mean velocities normalized by the local cone velocity and measured gap-height for the plate and cone flow with the ComplDV3.**

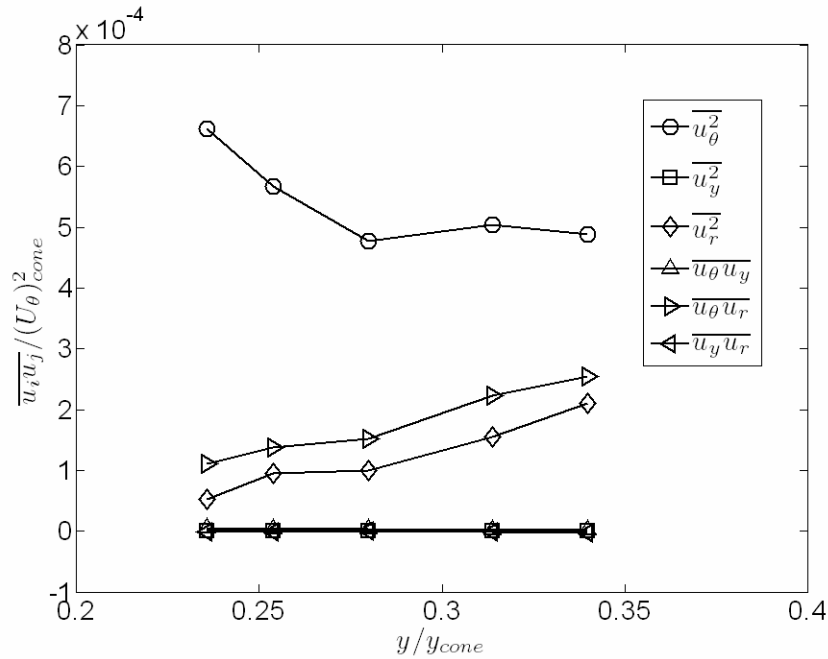


**Figure 2.56. Volume-averaged Reynolds stresses normalized by the local cone velocity and measured gap-height for the plate and cone flow with the ComplDV3.**

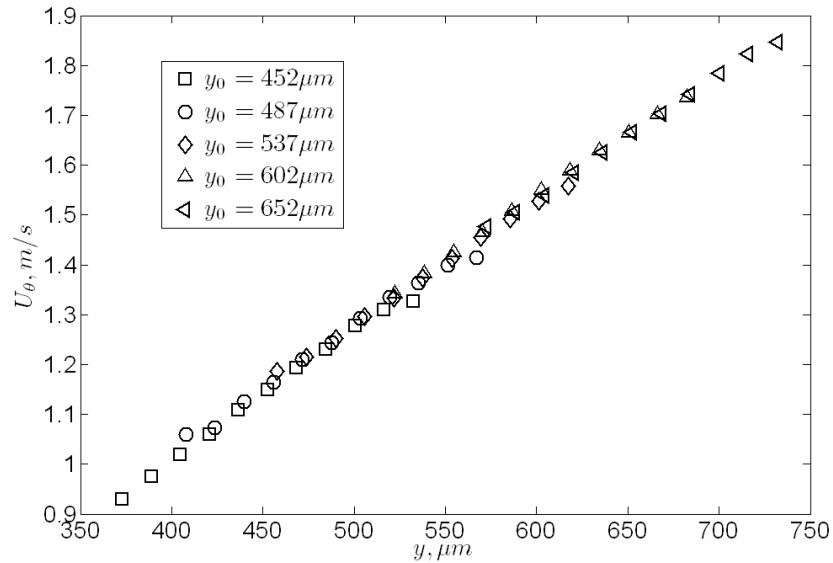


**Figure 2.57. Sub-measurement-volume resolved mean azimuthal velocity measurements in the plate and cone flow using the ComplDV3.**

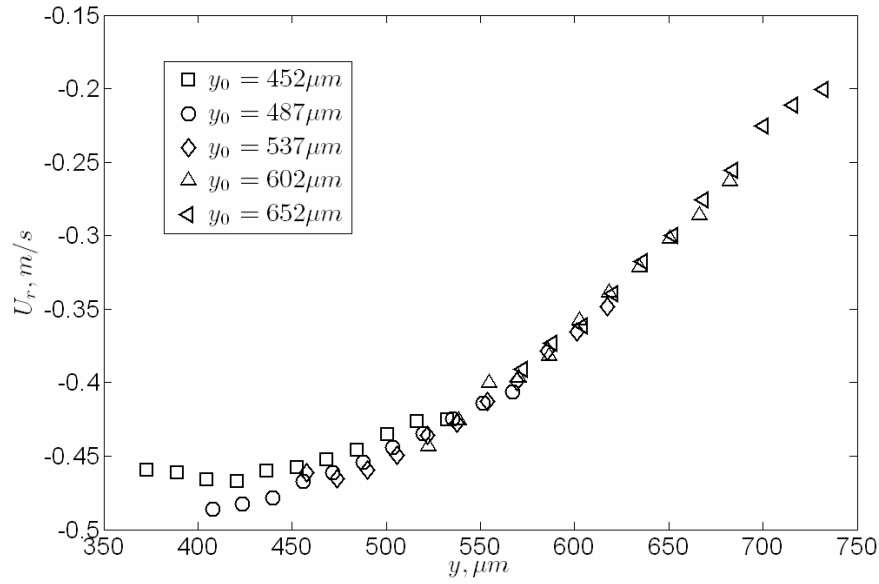


**Figure 2.58. Sub-measurement-volume resolved mean radial velocity measurements in the plate and cone flow using the ComplDV3.**

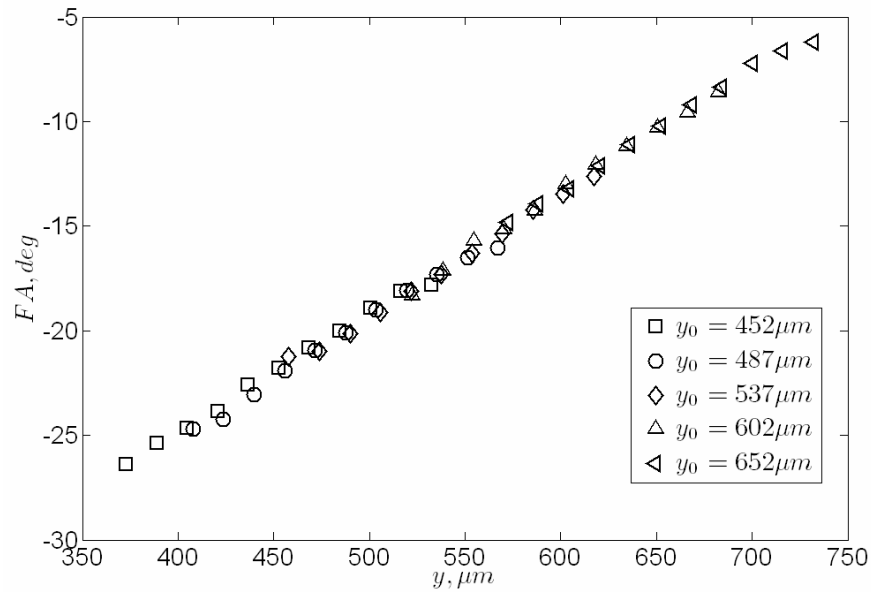


**Figure 2.59. Sub-measurement-volume resolved mean flow-angle measurements in the plate and cone flow using the ComplDV3.**

## 2.4 Facilities and apparatus

### 2.4.1 Measurement facilities

Measurements were acquired in the Department of Aerospace and Ocean Engineering Boundary Layer Research Wind Tunnel (BLWT) and Small Boundary Layer Wind Tunnel (SBLWT). These facilities have been described by previous authors (Devenport and Simpson 1990, Ölçmen 1995, Simpson 2001, and Bennington 2003). Other information about the BLWT facility is available online at <http://www.aoe.vt.edu/research/facilities/bllab.php>. For most measurements, both tunnels were operated at 27.5m/s nominal freestream velocity. The upper walls in both tunnels were set to achieve a zero-pressure gradient flow in the vicinity of the measurement region. Once this pressure gradient was set for the smooth, bare tunnel configuration, it remained in that setting while test elements (isolated roughness elements or wing-body junction) were placed in the flow. In the case of the Reynolds number study for the smooth wall, constant pressure boundary layer, the streamwise pressure gradient was eliminated for each Reynolds number.

### 2.4.2 Flow Seeding

In order to make optical measurements in flows, particles must be introduced to serve as light scattering sites. An optimal particle scatters a large amount of light while following the flow at all the significant fluctuation frequencies. In the case of translucent particles, the theories of Rayleigh and Mie Scattering can be used to predict the amount of light scattered by a spherical particle given the wavelength of light, the diameter of the particle, and the ratio of indices of refraction from flow medium to the particle medium (Albrecht et al. 2003). As discussed in section 2.2.1, the degree to which a particle follows the flow may be estimated using a first-order lag model of equation (2.1) as discussed by Lehman, Nobach, and Tropea (2002). For the liquid DOP particles that exhibit approximately  $0.6 \mu\text{m}$  mean diameters and very little deviation from this size, we compute a time constant of  $1 \mu\text{s}$  indicating that Lagrangian fluctuations out to 160kHz are attenuated by no more than 3dB.

More sophisticated treatments of particle dynamics in two-phase flows have been considered by several authors as reviewed by McLaughlin (1994). His discussion includes the effects of particle rotation, which is driven by vorticity in the flow. For the flows studied herein, the vorticity is greatest near the wall, but as McLaughlin notes from the previous work of Goldman et al. (1967a, b), the presence of the wall reduces the particle rotation from the zeroth-order-analysis maximum of one-half the vorticity. To briefly examine the effects of particle rotation, we consider the effect that vorticity may have on the Doppler signals measured using an extreme case of particle angular velocity equals one-half the viscous sublayer vorticity in a flat-plate turbulent boundary layer (i.e., the maximum mean vorticity in a flat-plate turbulent boundary layer). Since the LDV senses the velocity of a particle as a Doppler shift in the laser light being scattered by that particle, the varying translational velocities across a particle with non-zero angular

velocity results in a broadening of the spectral distribution of Doppler frequencies. Although particle scattering theories may be used to give precise contributions of light scattered from the regions of the particle surface, we will consider for the moment that the broadening results from equal contributions from two points on opposite sides of the particle sphere that lie on the axis with the largest velocity gradient. Consider the velocities resulting in scattering to be given as

$$U_2 = U_0 + \frac{\partial U}{\partial y} \frac{d}{2}$$

$$U_1 = U_0 - \frac{\partial U}{\partial y} \frac{d}{2}$$
(2.68)

where  $U_{1,2}$  are the velocities at the top (2) and bottom (1) of the particle,  $U_0$  is the velocity at the center and  $d$  is the diameter of the particle. Reverting back to the bounding case in the viscous sublayer of a flat-plate turbulent boundary layer, we may relate all the quantities in equations (2.68) by scaling them using the viscosity and the wall friction velocity (and denoting variables using this scaling with the superscript '+'):

$$U_2^+ = U_0^+ + \frac{d^+}{2}$$

$$U_1^+ = U_0^+ - \frac{d^+}{2}$$
(2.69)

or

$$U_2^+ - U_1^+ = d^+ \tag{2.70}$$

Thus the amount of broadening in the velocity measured due to particle rotation is approximated by equation (2.70). Applying the viscous sublayer relationship,  $U^+ = y^+$ , to normalize equation (2.70) by the center velocity of the particle, we obtain

$$\frac{U_2^+ - U_1^+}{U_0^+} = \frac{U_2 - U_1}{U_0} = \frac{d^+}{y^+} = \frac{d}{y} \tag{2.71}$$

which gives the magnitude of the rotational velocities relative to the particle center velocity. For the particle diameters used and considering the current operational limits of

the CompLDV, the maximum value of  $\left. \frac{U_2 - U_1}{U_0} \right)_{\max} = \left. \frac{d}{y} \right)_{\max} \approx 0.01$  is obtained for the

nearest-to-wall data. While this value is larger than random velocity uncertainties for the CompLDV3, it is still not significantly lower than these uncertainties and an attempt to estimate flow vorticity based upon Doppler peak broadening may result in high relative uncertainties in the vorticity measured and the estimates would become increasing poorer as the vorticity decreases. In the same way, this simple analysis bounds the possible uncertainties in the measured particle velocity due to particle rotation and exhibits that rotation does not contribute a significant amount uncertainty for all but the most-extreme cases of extremely high vorticity.

A liquid particle aerosol made with DOP has been used as flow seeding for some time by the TBLRG. The aerosol is generated with a Laskin-nozzle-style seeder that is passed through a heat-exchanger that first vaporizes and then condenses the aerosol in a controlled manner. The heat-exchanger unit known as the VAP/CON was devised and

tested by Liu et al. (1966). The original unit in use in this research group was built by Baker (1986). The VAP/CON unit (Figure 2.60) consists of a manifold that distributes the input of polydisperse DOP aerosol evenly into four stainless-steel tubes. Near the entrance of the tubes, heating tapes increase the temperature at the outer surface of the tubes to about 770°F as measured by a simple thermocouple probe. This temperature may be adjusted using Variac A/C voltage regulators. The high temperature in the first section of the tubes raises the temperature of the aerosol above the vapor point of DOP so that a DOP-laden gas results. This mixture is then cooled through the remainder of the stainless steel tubes with heat transfer from the fluid mixture to the tubes and the DOP condenses onto solid nucleation sites naturally present in the supply air. Since all the DOP/air mixture undergoes the same controlled cooling process at a constant flow-rate, the particles that result are highly uniform. The condensed DOP particles in the supply air exit the stainless steel tubes to a second manifold that recombines the streams to a single line that leads to the test facility.

To measure the performance of the VAP/CON unit, Dan Neuhart from the NASA Langley Research Center conducted tests on the particle size statistics using a TSI model 3321 Aerosol Particle Sizer Spectrometer at the facilities used by the TBLRG. While this particle sizer does not detect the presence of particles smaller than 0.3  $\mu\text{m}$  and cannot measure the size of particles smaller than 0.523  $\mu\text{m}$ , the statistics of the larger particles in the aerosol are well-gauged.

Particle distributions are best described by the log-normal distribution where the natural-log of the sample magnitude follows the Gaussian distribution. The primary statistics of interest for these measurements include the geometric mean particle diameter and the geometric standard deviation. The geometric mean is defined as

$$\bar{d}_g = \left( \prod_{i=1}^N d_i \right)^{1/N} \quad (2.72)$$

where  $d_i$  is the particle diameter measurement of the  $i^{\text{th}}$  sample. The geometric standard deviation is likewise given as

$$s_g = \exp \left[ \frac{\sum_{i=1}^N (\ln d_i - \ln \bar{d}_g)^2}{N} \right]^{1/2} \quad (2.73)$$

Several cases were considered for the particle sizing that included modulations of the supply-air pressure to the Laskin nozzle as well as varying the VAP/CON temperature. A sample normalized concentration histogram of particle diameter for the closest-case to the one used for aerodynamic measurements in the present work with a Laskin nozzle supply-air pressure of 16 psi and VAP/CON outer surface temperature of 768°F is plotted in Figure 2.61. The ordinate in this case is normalized such that the varying bin-widths in diameter do not bias the interpretation of the data. For this seeding case, an estimate for the geometric mean particle diameter is 0.61  $\mu\text{m}$  with a geometric standard deviation of 1.12. This may be interpreted to give one-standard deviation particle diameter bounds as

$\frac{\overline{d}_g}{s_g} < d_p < \overline{d}_g s_g$  or  $0.54\mu\text{m} < d_p < 0.68\mu\text{m}$ , a very narrowly-distributed range of particle diameters for both light-scattering and aerodynamic considerations. It is noted that the particle statistics do not change significantly with supply-air pressure when the VAP/CON is operated at around 770°F outer surface temperature. To emphasize the utility of the VAP/CON unit, Figure 2.62 is the normalized concentration histogram for the case with 15 psi supply-air pressure for the Laskin nozzle without the VAP/CON unit. Clearly, the complete histogram is even more truncated on the low-end than for Figure 2.61, and the distribution of larger-particles is more-pronounced. In this case the particle distribution statistics reflect the increase of polydisperse particle sizes, with a one-standard deviation range of  $0.57\mu\text{m} < d_p < 0.93\mu\text{m}$  about the geometric mean of  $\overline{d}_g = 0.728\mu\text{m}$ . For all the CompLDV boundary layer tests, the VAP/CON unit was used to improve the signal-to-noise ratio of the signals and give confidence in the fluid dynamic results.

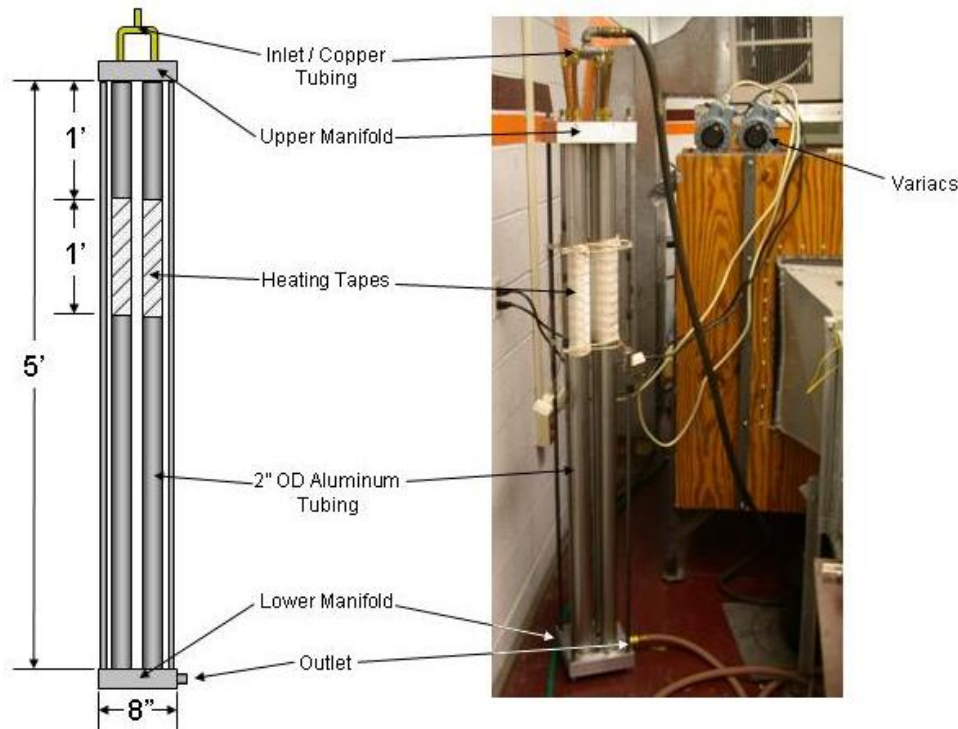


**Figure 2.60. The VAP/CON monodisperse aerosol generator (figure due to Devin Stewart).**

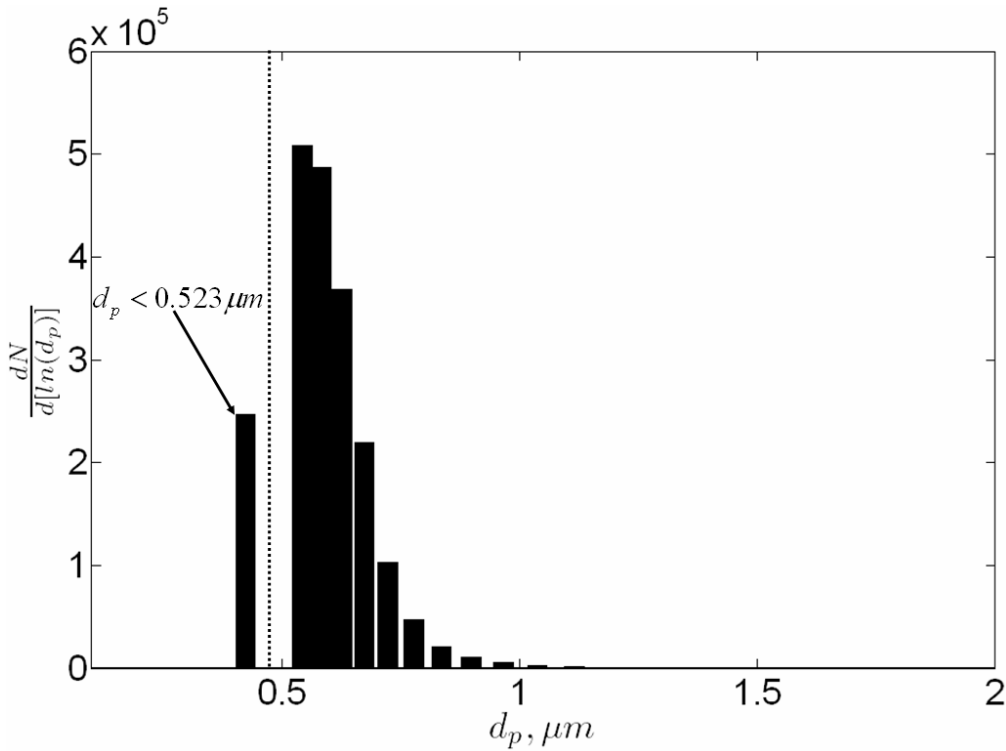


**Figure 2.61. Normalized concentration histogram of the DOP particle diameter distribution for a Laskin nozzle supply air pressure of 16 psi and a VAP/CON outer surface temperature of 768°F.**

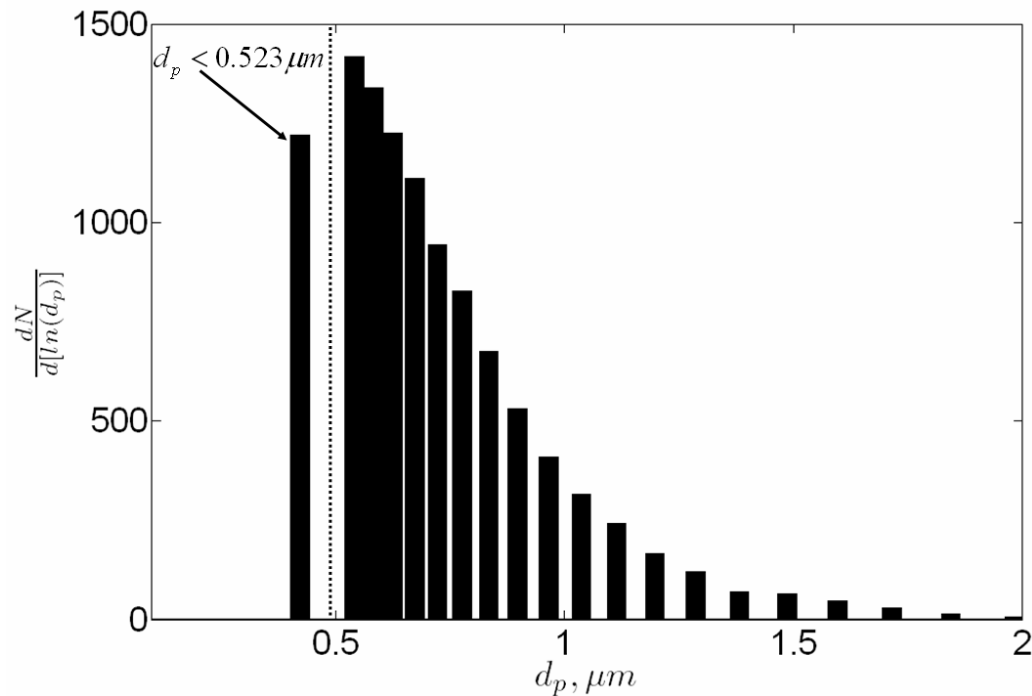


**Figure 2.62. Normalized concentration histogram of the DOP particle diameter distribution for a Laskin nozzle supply air pressure of 15 psi without VAP/CON unit.**

## 2.5 References

- Adrian, R. J. 1991 "Particle-imaging techniques for experimental fluid mechanics," *Ann. Review Fluid Mech.*, Vol 23, pp.261 - 304.
- Adrian, R. J. 1999 Comments at Workshop on "Turbulence Measurements for LES," Chicago, IL, Oct. 4-5.
- Agui, J.H. and Andreopoulos, Y., 2002 "A new laser vorticity probe--LAVOR: Its development and validation in turbulent boundary layer," *Exp. in Fluids*, Vol. 34, No. 2, pp. 192-205.
- Andreopoulos, Y. and Honkan, A. 1996 "Experimental techniques for highly resolved measurements of rotation, strain, and dissipation-rate tensors in turbulent flows," *Meas. Sci. and Technol.*, vol. 7, pp. 1462 - 1476.
- Baker, D. 1986 "A Report on the Vaporization/Condensation Aerosol Generator Built at Virginia Tech." Internal report.
- Bendat, J.S. and Piersol, A.G. 2000 *Random Data: Analysis and Measurement Procedures*, Third Ed., Wiley-Interscience.
- Benedict, L.H., Nobach, H., and Tropea, C. 2000. "Estimation of turbulent velocity spectra from laser-Doppler data," *Meas. Sci. Tech.* **11**, pp. 1089-1104.
- Bennington, J.L. 2004 "Effects of various shaped roughness elements in two-dimensional high Reynolds number turbulent boundary layers," *M.S. Thesis*, August, Department of Aerospace and Ocean Engineering, Virginia Polytechnic Institute and State University.
- Buettner, L. and Czarske, J. 2001 "A multimode-fibre laser-Doppler anemometer for highly spatially resolved velocity measurements using low-coherence light," *Meas. Sci. Technol.* **12**, pp. 1891-1903.
- Büttner, L. and Czarske, J. 2003, "Spatial resolving laser-Doppler velocity profile sensor using slightly tilted fringe systems and phase evaluation," *Meas. Sci. Technol.* **14**, pp. 2111-2120.
- Byun, G. 2005, "Structure of three-dimensional separated flow on symmetric bumps," *Ph.D. Dissertation*, September, Department of Aerospace and Ocean Engineering, Virginia Polytechnic Institute and State University.
- Czarske, J. 2001, "Laser-Doppler velocity profile sensor using a chromatic coding" *Meas. Sci. Technol.* **12**, pp. 52-57.

Czarske, J., Büttner, L., and Razik, T. 2002, “Boundary layer velocity measurements by a laser-Doppler profile sensor with micrometre spatial resolution” *Meas. Sci. and Technol.* **13**, 1979-1989.

DeGraaff, D.B. and Eaton, J.K. 2000 “Reynolds-number scaling of the flat-plate turbulent boundary layer,” *J. Fluid Mech.*, Vol. 422, pp. 319-346.

Devenport, W.J. and Simpson, R.L. 1990 “Time-dependent and time-averaged turbulence structure near the nose of a wing-body junction,” *J. Fluid Mech.*, Vol. 210, p.23-55.

Doebelin, E. 2001 *Measurement Systems: Application and Design*. 4<sup>th</sup> edition. McGraw-Hill, New York, 836.

Durst, F., Jovanovic, J., and Sender, J. 1995 “LDA measurements in the near wall region of a turbulent pipe flow,” *J. Fluid Mech.* **295**, 305.

Durst, F., Melling, A. and Whitelaw, J. H. 1976 *Principles and Practice of Laser-Doppler Anemometry*, First Edition, Academic Press, London.

Durst, F., Melling, A. and Whitelaw, J. H. 1981 *Principles and Practice of Laser-Doppler Anemometry*, Second Edition, Academic Press, London.

Elsner, J. W. and Elsner, W. 1996 “On the measurement of turbulence energy dissipation,” *Meas. Sci. and Technol.*, vol. 7, pp. 1334 - 1348.

Fouras, A. and Soria, J. 1998 “Accuracy of out-of-plane vorticity measurements derived from in-plane velocity field data,” *Experiments in Fluids*, Vol. 25, pp 409 - 430.

Goldman, A.J., Cox, R.G., and Brenner, H. 1967a “Slow viscous motion of a sphere parallel to a plane wall—I. Motion through a quiescent fluid,” *Chem. Engng. Sci.* Vol. 22, 637-651.

Goldman, A.J., Cox, R.G., and Brenner, H. 1967b “Slow viscous motion of a sphere parallel to a plane wall—2. Couette flow,” *Chem. Engng. Sci.* Vol. 22, 653-660.

Golub, G.H. and Van Loan, C.F. 1996 *Matrix Computations, 3rd edition* Johns Hopkins University Press.

Grad, Y. and Einav, S. 2000 “Spectral and instantaneous flow field characteristics of the laminar to turbulent transition in a cone and plate apparatus” *Exp. in Fluids*, no. 28, pp. 336-343.

Grant, I. 1997 “Particle image velocimetry: a review,” *Proc. Inst. Mech. Engrs.*, Vol. 211, Part C, pp. 55 -76.

Honkan, A. and Andreopoulos, Y. 1997 "Vorticity, strain-rate and dissipation characteristics in the near-wall region of turbulent boundary layers," *J. Fluid Mech.*, Vol. 350, pp. 29-96.

Jeong, J., Hussain, F., Schoppa, W., and Kim, J. 1997 "Coherent structures near the wall in a turbulent channel flow," *J. Fluid Mech.*, Vol. 332, pp. 185-214.

Klebanoff, P.S. 1955 "Characteristics of turbulence in a boundary layer with zero pressure gradient," *NACA Report 1247*.

Kuhl, D. and Simpson, R. 2000 "Near-wall investigation of a streamwise vortex pair" **10th Inter.Symp. Appl. Laser Techniques to Fluid Mech.**, Lisbon, Portugal, July.

Lecerf, A., Renou, B., Allano, D., Boukhalfa, A., and Trinité, M. 1999 "Stereoscopic PIV: validation and application to an isotropic turbulent flow," *Exp. in Fluids*, Vol. 26, pp 107 - 115.

Lehmann, B., Helbig, J., and Hassa, C. 1990 "LDA method to measure the acceleration of particles and the curvature radii of particle trajectories," *5<sup>th</sup> Intl. Symp. on Appl. of Laser Techniques to Fluid Mech. and Workshop on the Use of Computers in Flow Measurement*, July, Lisbon, Portugal.

Lehmann, B. and Helbig, J. 2000 "Local Acquisition of Mean and Turbulent Fluid Acceleration in Highly Turbulent Flow by the Means of Laser-Doppler Velocimetry," paper 17.2, *10<sup>th</sup> Inter. Symp. Appl. Laser Techniques to Fluid Mech.*, Lisbon, Portugal, July.

Lehmann, B., Nobach, H., and Tropea, C. 2002 "Measurement of acceleration using the laser-Doppler technique," *Meas. Sci. and Technol.*, Vol. 9, pp. 1367-1381

Liu, B., Whitby, K., and Yu, H. 1966 "A Condensation Aerosol Generator For Producing Monodispersed Aerosols in the Size Range, 0.036 $\mu$  to 1.3 $\mu$ ." *Journal de Recherches Atmosphériques*. Vol. 2, pp. 397-406.

Lowe, K.T. and Simpson, R.L. 2006 "Measurements of velocity-acceleration statistics in turbulent boundary layers," *Int. J. Heat and Fluid Flow*, Vol. 27, No. 4, pp. 558-565; also in *4<sup>th</sup> Intl. Symp. on Turb. Shear Flow Phenom.*, June 27-29, 2005, Williamsburg, VA, USA, Vol. 3, pp. 1043-1048.

Luff, J.D., Drouillard, T., Rompage, A.M., Linne, M.A., and Hertzberg, J.R. 1999 "Experimental uncertainties associated with particle image velocimetry (PIV) based vorticity algorithms," *Experiments in Fluids*, Vol. 26, pp 36 - 54.

Lumley, J.L. 1992 "Some Comments on turbulence," *Phys. Fluids A*, 4, pp.203 - 211.

McLaughlin, J.B. 1994 "Numerical computation of particles-turbulence interaction," *Int. J. Multiphase Flow*, Vol. 20, Suppl., pp. 211-232.

- Mullin, J.A. and Dahm, W.J.A. 2006 “Dual-plane stereo particle image velocimetry measurements of velocity gradient tensor fields in turbulent shear flow. I. Accuracy assessments” *Phys. Fluids*, **18**, pp. 035101-1 to 035101-18.
- Miles, P.C. 1996 “Geometry of the fringe field formed in the intersection of two Gaussian beams.” *Appl. Optics*, Vol. 35, No. 30, pp. 5887-5895.
- Nobach, H. 2002a "Analysis of dual-burst laser-Doppler signals", *Meas. Sci. Technol.* **13**, pp. 33-44.
- Nobach, H. 2002b “Local time estimation for the slotted correlation function of randomly sampled LDA data,” *Exp. Fluids* **32**, pp. 337-345.
- Nobach, H., Kinzel, M., and Tropea, C. 2005, “Measurement of Lagrangian acceleration in turbulent flows using the laser-Doppler technique,” *Optical Methods of Flow Investigation in Proc. SPIE* , Vol. 6262, paper 626201.
- Ölçmen, S.M. and Simpson, R.L., 1995, “A 5-velocity-component laser-Doppler velocimeter for measurements of a three-dimensional turbulent boundary layer,” Invited Paper, *Meas. Sci. Tech.*, **6** pp. 702-7156. Highlighted in *Aerospace America: The Year in Review*, Fluid Dynamics, pp. 20-21, Dec. 1995 issue; also paper 4.2, *Seventh Int’l Symp. on Appl. of Laser Tech. to Fluid Mech.*, 11-14, July, 1994, Lisbon, Portugal.
- Ölçmen, S., Simpson, R., and George, J. 2001a “Some Reynolds number effects on two and three-dimensional turbulent boundary layers,” *Exp. in Fluids*, Vol. 31, pp 219-228.
- Ölçmen, S., Simpson, R., and Goody, M. 2001b “An Experimental Investigation of Two-Point Correlations in Two-and Three-Dimensional Turbulent Boundary Layers,” *Flow, Turbulence and Combustion*, Vol. 66, pp 85-112.
- Ötügen, M.V., Su, W-J., and Papadopoulos, G. 1998, “A new laser-based method for strain rate and vorticity measurements,” *Meas. Sci. Technol.* **9**, pp. 267-274.
- Pfister, T., Büttner, L., and Czarske, J. 2005, “Laser-Doppler profile sensor with sub-micrometre position resolution for velocity and absolute radius measurements of rotating objects,” *Meas. Sci. Technol.* **16**, pp. 627-641.
- Pope, S. 2000 *Turbulent Flows*, Cambridge University Press, p. 157.
- Robinson, S.K. 1991 “Coherent motions in the turbulent boundary layer,” *Ann. Rev. Fluid Mech.*, Vol. 23, pp. 601-639.
- Rodi, W. 1999 Personal Communication.

Rotta, J.C. 1962 "Turbulent boundary layers in incompressible flow," in *Prog. in Aeronautical Sciences*, Vol. 2, ed. Ferri, A., Küchemann, D., and Sterne, L.H.G., pp. 1-220.

Sdougos, H.P., Bussolari, S.R., and Dewey, C.F. 1984, "Secondary flow and turbulence in a cone-and-plate device" *J. Fluid Mech.*, vol. 138, pp. 379-404.

Sheng, J. and Meng, H. 1998 "A genetic algorithm particle pairing technique for 3D velocity field extraction in holographic particle image velocimetry," *Exp. in Fluids*, Vol. 25, pp 461 - 473.

Shinpaugh, K.A., Simpson, R.L., Wicks, A.L., Ha, S.M., and Fleming, J.L. 1992 "Signal-processing techniques for low signal-to-noise ratio laser-Doppler velocimetry signals," *Experiments in Fluids*, Vol. 12, pp 319-328.

Simpson, R.L. 1989 "Turbulent Boundary Layer Separation," *Ann. Rev. Fluid Mech.* 21, pp. 205-234.

Spalart, P. 1988, "Direct simulation of a turbulent boundary layer up to  $Re_\theta = 1410$ ," *J. Fluid Mech.*, Vol. 187, pp. 61-98.

Tang, G. 2004 "Measurements of the Tip-gap Turbulent Flow Structure in a Low-speed Compressor Cascade," *Ph.D. Dissertation*, April, Department of Aerospace and Ocean Engineering, Virginia Polytechnic Institute and State University.

Tarau, T., Stepaniuk, V.P., and Otugen, M.V., 2002 "Evaluation of a new laser gradient probe," *40th Annual AIAA Aerospace Science Meeting and Exhibit*, Jan. 14-17, Reno, NV, AIAA 2002-0688.

Tian, Q. 2006 "Near Wall Behavior of Vortical Flow around the Tip of an Axial Pump Rotor Blade," *Ph.D. Dissertation*, Fall Semester, Department of Aerospace and Ocean Engineering, Virginia Polytechnic Institute and State University.

Yao, S., Tong, P., and Ackerson, B. J., 2001, "Proposal and testing for a fiber-optic-based measurement of flow vorticity." *Applied Optics*, vol. 40,no. 24, pp. 4022-4027.

Zhang, J., Tao, B., and Katz, J. 1997 "Turbulent flow measurements in a square duct with hybrid holographic PIV," *Experiments in Fluids*, Vol. 23, pp 373 -381.

Zhu, Y. and Antonia, R.A. 1996 "The spatial resolution of hot-wire arrays for the measurement of small-scale turbulence," *Meas. Sci. and Technol.*, vol. 7, pp. 1349 - 1359.

## 3 Signal processing

### 3.1 Laser-Doppler Burst Processing

In order to take advantage of newly available digitization and PC-storage capabilities, the laser-Doppler signals which are stored must be analyzed thoroughly and efficiently. The current application is demanding in that signals are needed in rapid succession for gradient estimation and high frequency spectra. To further compound the challenge, we wish in this study to measure particle accelerations which are an order of magnitude more difficult to estimate compared to velocities. Much effort in the study has been in determining the lowest-uncertainty and most robust algorithms for obtaining the frequency, rate-of-change of frequency, and arrival time for each burst of sufficient signal-to-noise ratio (SNR) while making the minimum allowable SNR to be as low as possible so that the maximum number of bursts is accepted.

#### 3.1.1 Signal description

An adequate model for a laser-Doppler burst from a single, small particle is given as

$$s(t) = A \exp\left[-\frac{\beta}{2}(t-t_0)^2\right] \cos[\phi(t)] + n(t) \quad (3.1)$$

where  $A$  is the signal amplitude,  $\beta$  is the Gaussian window parameter analogous to the variance,  $t_0$  is the center-arrival time of the burst,  $\phi(t)$  is the phase of the signal and  $n(t)$  is the noise. For the case when the interference fringes are parallel throughout the measurement volume, the particle velocity is equal to the fringe spacing,  $d$ , times the frequency of the signal described by equation (3.1),  $U = df = \frac{d}{2\pi} \frac{d\phi(t-t_0)}{dt}$ . Likewise,

the particle acceleration is given as  $a = \frac{dU}{dt} = d \frac{df}{dt} = \frac{d}{2\pi} \frac{d^2\phi(t-t_0)}{dt^2}$ . The Taylor series expansion of the velocity of a particle as it passes the measurement volume is

$$U(t) = U_0 + \left. \frac{dU}{dt} \right|_{t=t_0} (t-t_0) + O[(t-t_0)^2] \quad (3.2)$$

For the small transit times, much smaller than the Kolmogorov time scales, the first-order approximation is sufficient. Thus, we need only estimate the velocity and acceleration at the time  $t=t_0$ . We see then that at similar Taylor expansion of the phase evolution of the signal yields dependencies only on the first two-orders,

$$\phi(t) = \phi_0 + 2\pi f_0(t-t_0) + \left. \pi \frac{df}{dt} \right|_{t=t_0} (t-t_0)^2 + O[(t-t_0)^3] \quad (3.3)$$

Thus two parameters for the way the signal changes in addition to the constant phase are necessary to describe the signal. The model signal used in this study is thus simplified from equation (3.1) as

$$s(t) = A \exp\left[-\frac{\beta}{2}(t-t_0)^2\right] \cos\left[\phi_0 + 2\pi f_0(t-t_0) + \pi \frac{df}{dt}\bigg|_{t=t_0} (t-t_0)^2\right] + n(t) \quad (3.4)$$

The time-series for an example signal is given in Figure 3.1.

The noise in a laser-Doppler signal,  $n(t)$ , arises from shot noise inherent in the photomultiplier. This noise is proportional to the square-root of the photocathode current, is broadband and follows Poisson statistics (Albrecht et al. 2003, Coates 1972). This means that the noise level is dependent upon the signal level, which is time dependent. If we consider the *noise-free* instantaneous signal level as follows:

$$\hat{s}(t) \propto A \exp\left[-\frac{\beta}{2}(t-t_0)^2\right] \quad (3.5)$$

Then the noise will be represented as

$$n(t) \propto A \exp\left[-\frac{\beta}{4}(t-t_0)^2\right] \quad (3.6)$$

Thus the signal-to-noise ratio,  $SNR(t) = \hat{s}(t) / n(t)$  is given as

$$SNR(t) \propto \exp\left[-\frac{\beta}{4}(t-t_0)^2\right] \quad (3.7)$$

This is not a new result and has been recognized in the literature (Lehmann et al. 2002). However, many simulation studies of LDV signals are done with constant Gaussian noise which theoretically results in a worst-case, but also results in a bias by over-accentuating the center of the signal. Figure 3.2 illustrates the difference in burst SNR given by the two techniques. There is significant degradation of the SNR for a burst with constant noise at  $|t\sqrt{\beta}| > 1$ , while the same drop in is not seen until about  $|t\sqrt{\beta}| > 2$  for the Gaussian model. Evidence for this model is seen in Figure 3.3, a spectrogram for a real LDV burst which contains two Doppler frequencies is given. The deepest red indicates a region of high power while cooler colors are low power. With the passage of the particle comes an increased amount of broadband noise which is not constant throughout the burst. Note that background light from scattering surfaces and grazing particles do cause a small constant amplitude noise component, but this is insignificant compared with the shot noise within the burst.

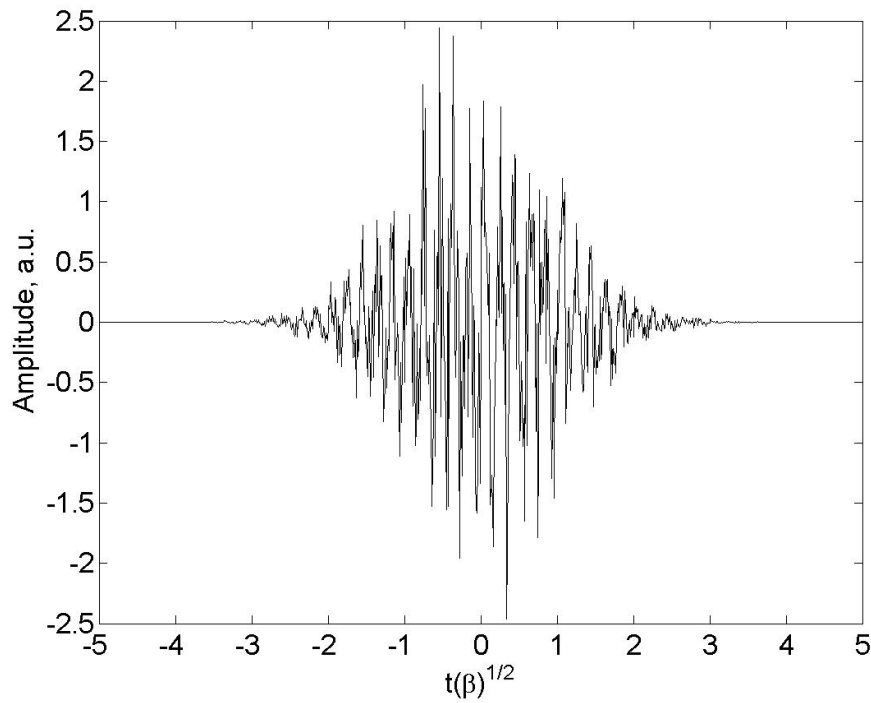


**Figure 3.1. Model burst with noise.**

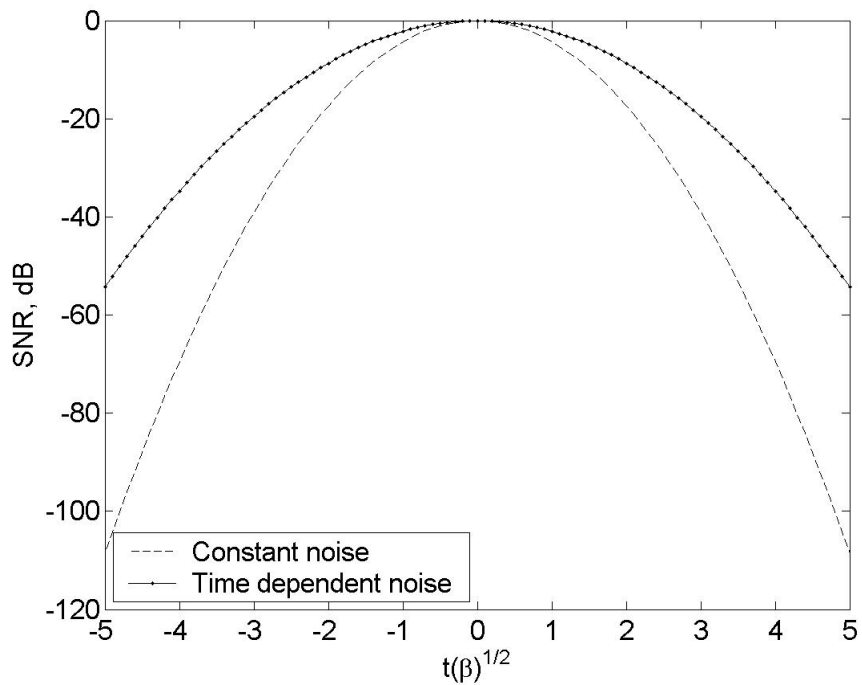
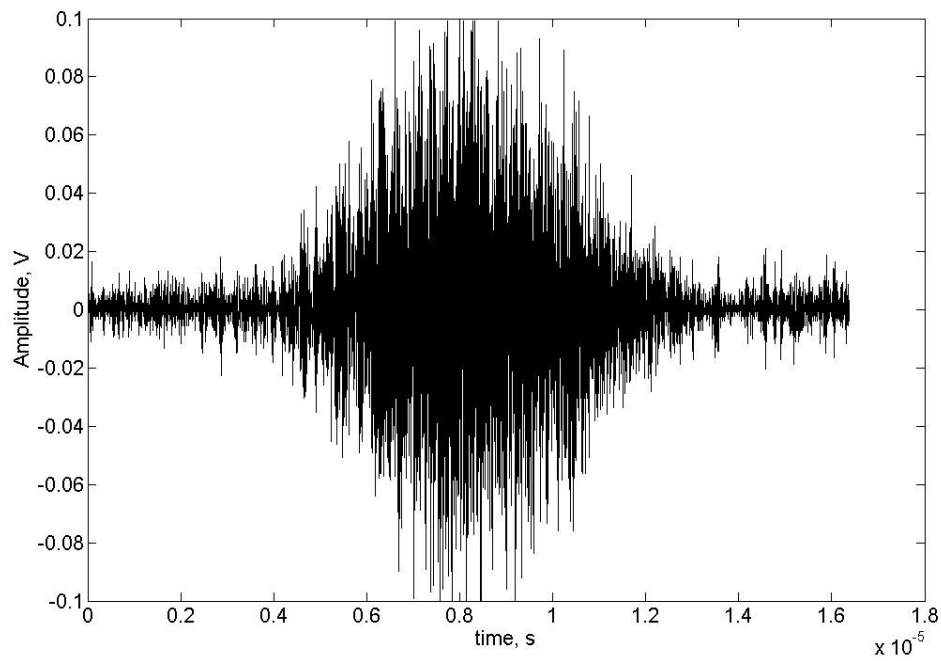
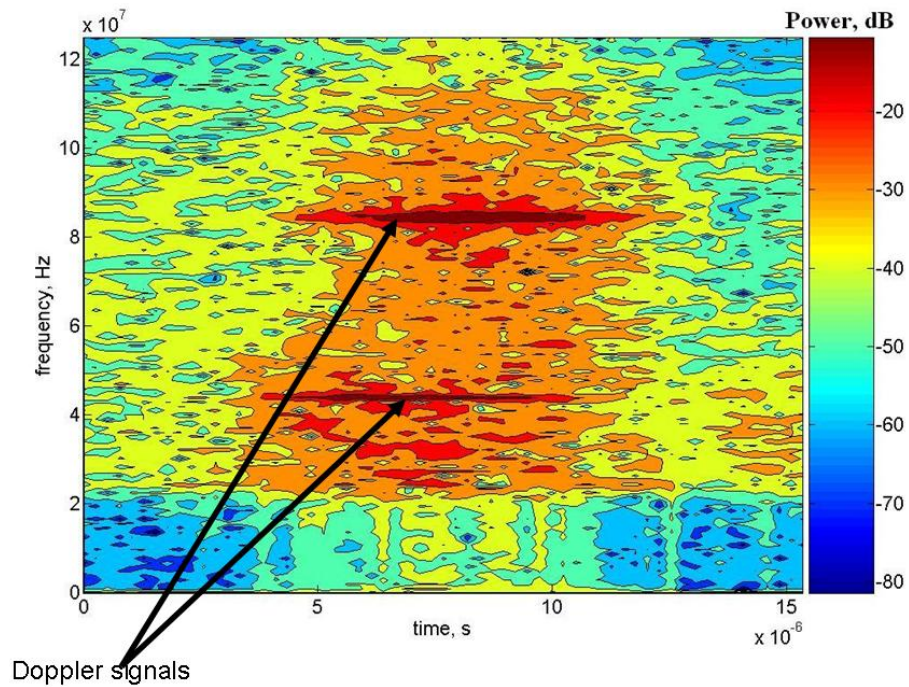


**Figure 3.2. Comparison of the SNR for signals with constant noise levels versus noise levels that vary in time as a Gaussian.**



(a)



(b)

**Figure 3.3. (a) Time series and (b) spectrogram of an LDV burst containing two Doppler signals. Note that the noise is not constant amplitude throughout the signal but varies with time.**

There are several fundamental challenges for processing laser-Doppler signals, the most significant of which are

- the signals are transient and brief
- the arrival time of the signal is random and unknown *a priori*
- the most probable inter-arrival time is *zero*
- the burst-to-burst SNR is fluctuating and relatively low

These issues are well-discussed throughout the literature and were recently all considered in a single work by Albrecht et al. (2002). The first two bullets underscore the need for an excellent burst recognition algorithm. The third point affects the way we must validate the bursts and indicates the necessity for separating closely spaced bursts for proper processing. The final point is the most difficult to overcome. First, it requires that the signals be validated so that the estimated SNR is likely to result in actual data. Second, the SNR is the limiting factor in the variance of signal parameter estimation due to the Cramer-Rao lower bound (Shinpaugh et al. 1992, Lehmann, Nobach, and Tropea 2002).

In the following sections the methods chosen for handling the abovementioned challenges will be discussed. These include aspects of signal recognition, signal discrimination in the presence of multiple signals, and frequency- and time-frequency domain processing.

### 3.1.2 Burst Recognition and Envelope Estimation

To achieve the lowest uncertainty and highest efficiency frequency-domain or time-frequency-domain processing of non-stationary signals such as LDV bursts, it is essential to have a good estimate of the burst envelope parameters before applying computationally-intensive processing techniques. Knowing a working estimate of the burst envelope parameters allows centering of the burst in the processing window. It also allows one to identify a time-domain cut-off for processing where the burst levels are obscured by noise; thus, creating the optimal case of a matched time-window processor (see Albrecht et al. 2002). Nobach (2002a) noted the power of burst envelope estimations for separation of dual-burst signals which are inevitable in the high-seed concentration cases of the CompLDV. Furthermore, signal characterization techniques such as the FFT or those discussed by Lehmann, Nobach, and Tropea (2002) will perform best when the burst is centered in the processing window. Finally, robust frequency- and time-frequency-domain processing is expensive, so only high-confidence burst signals should be passed to such a processor. The challenge set forth is in determining a robust and computationally inexpensive method for characterizing the burst envelope before detailed processing commences.

The Hilbert transform is often the chosen method for obtaining the window function of burst signals (e.g. Nobach 2002a and Lehmann, Nobach, and Tropea 2002). The magnitude of the so-called analytical signal obtained with the Hilbert transform yields the instantaneous window of the real signal. The problem with this technique is that it requires the same amount of time to compute as the FFT—if one already has the FFT representation of the signal *a priori*. Otherwise, the optimal computation of the Hilbert

transform requires computation of *two* FFTs. Also, the result must be low-pass filtered since instantaneous noise will distort the signal envelope from the analytical signal. It was thought that this method, though robust, was not the most efficient available for the problem.

The proposed solution to the burst recognition and envelope estimation problem involves a digital algorithm for inexpensively determining the burst envelope parameters. The digital algorithm takes advantage of the nearly Gaussian nature of the signal to robustly identify burst signals. By identifying this known pattern in the data, *a priori* knowledge is used to enhance the quality of the measurements. Details of the algorithm are discussed to follow.

### 3.1.2.1 Details of the process

#### 3.1.2.1.1 Pedestal Retention

In the case that large amplitude white noise is persistent on the LDV channels, it may prove more reliable for signal detection to retain the pedestal of the signal. It is commonly taken as practice that LDV signals should be high-pass filtered to remove the pedestal of the signal prior to processing. There are several arguments for doing this, such as the high-passed signal more optimally uses digitizer bits and signal processing is typically carried out on zero-mean signals. The argument for not filtering, however, is that the burst pedestal presents the highest-fidelity method for identifying the occurrence of a particle crossing the measurement volume. This is because the power within that low-frequency signal is many orders of magnitude greater than any noise component within the signal, and usually some factor more powerful than even the Doppler signal itself.

To retain the pedestal of a burst which is Bragg shifted to RF frequencies, one must use an RF amplifier with sufficient low-frequency response. The Sonoma Instruments model 315 amplifier being used has a flat response from 10 kHz to 1 GHz, allowing even relatively long duration burst pedestals to be preserved. The other detail with retaining the pedestal information is involved with the digitizing. To use the most possible digitizer bits, it is necessary to shift the waveform so that the zero-voltage bit is at some negative bit. This is possible to do with the manual settings of the Strategic Test UF.258 digitizer card used. The automatic bit distribution is from -128 to +128 with 0 corresponding to nominally zero-differential voltage. The manual settings allow one to set the zero-differential voltage to approximately bit -80. Then if the burst ranges from, say, 0V to 0.7V, the digitizer may be set with a range of 1V and the waveform will usurp most of the bits available.

#### 3.1.2.1.2 Digital Detection Algorithm

As mentioned, the biggest concerns with the detection algorithm were low computational cost with high fidelity of detection. It is sought to use the burst data in a manner which is

linear computationally. This precludes the use of general frequency-domain techniques like the FFT. Thus, a purely algebraic algorithm is specified, as described to follow.

### 3.1.2.1.2.1 RMS Power Characterization

The short-time RMS of a signal  $s$  is

$$RMS_T = \frac{1}{T} \int_0^T s(t)^2 dt \approx \frac{1}{N} \sum_{i=0}^N s(t_i)^2 \quad (3.8)$$

where  $T$  is the duration of the signal being averaged,  $N=Tf_s$  where  $f_s$  is the sampling rate of the digitizer. It is not a novel idea to detect burst signals based upon the RMS power of the waveform over some time (see Qui et al. 1994 for a discussion of burst detection methods). However, with a high fidelity burst envelope or pedestal, this type of metric can be quite useful. In the current algorithm, the signal is first divided into blocks and the RMS of that block computed. Figure 3.4 is a semi-logarithmic plot of a region of signal in which the burst time-series is plotted along with two-times the RMS signal power. In this signal the pedestal has been retained. The RMS values of the signal are computed every 256 burst samples in this case, though this should be adapted when flow conditions drastically change such as very near a wall. One may see that the results faithfully follow the burst envelope as detected by the eye. **This step requires  $2N$  operations where  $N$  is the number of time-series samples to be searched for bursts.**

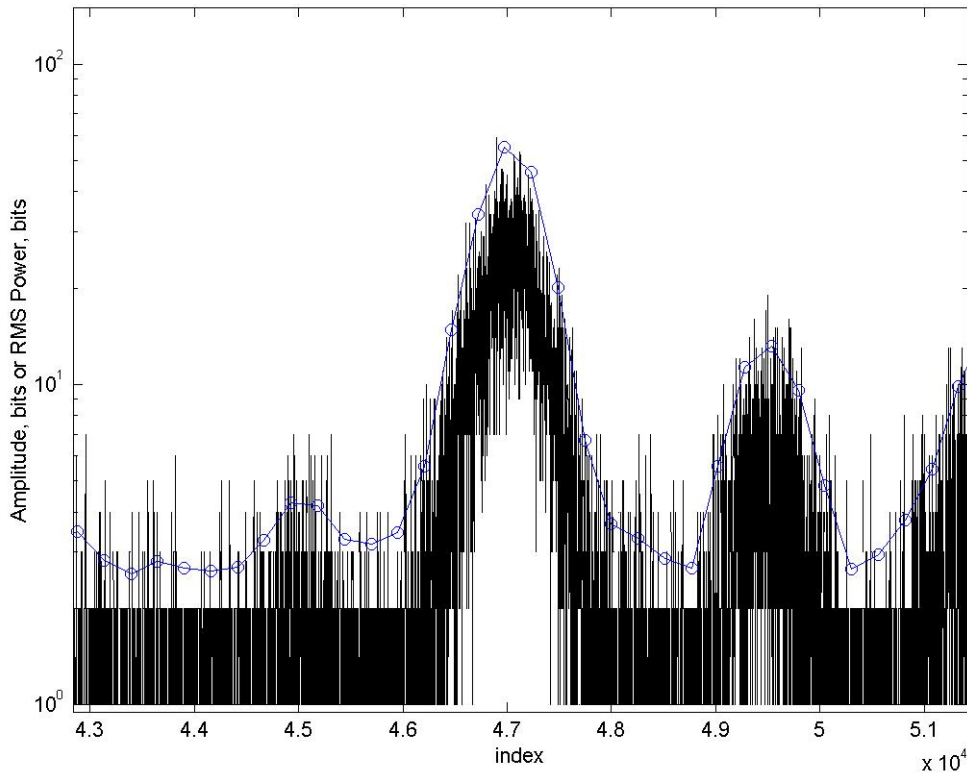


**Figure 3.4. Burst amplitude (black) and 2x the RMS power (blue circles) for a typical LDV signal snippet.**

### 3.1.2.1.2.2 Parabolic fitting

To better identify the center of the burst and distinguish the bursts from noise spikes, parabolic fitting of the logarithm of the RMS power is used. This offers the possibility of identifying the burst envelope parameters relating to the Gaussian model case,

$$e(t) = \exp\left[-\frac{\beta}{2}(t-t_0)^2\right] \quad (3.9)$$

including the burst center time,  $t_0$ , and decay parameter,  $\beta$ , analogous to the variance in a normal distribution. A least-squares parabola is fit to every five adjacent points in the RMS power signal, stepping one RMS power data point each new parabola. If the parabola fit is concave down and occurring such that the center is within the five points, the correlation coefficient,

$$R_{xy} = \frac{\overline{xy}}{\sqrt{\overline{x^2}}\sqrt{\overline{y^2}}} \quad (3.10)$$

is computed. This “goodness of fit” parameter is then used as an additional metric for burst recognition by multiplying the correlation coefficient raised to the fourth-power by the RMS power of the central point of the fit. The fit parameters are further refined such that one obtains the center time of the burst and the Gaussian decay parameter; this information is saved for burst envelope identification. Note that this step may result in multiple maxima per burst if the burst duration is mismatched with the number of samples used to obtain the RMS power distribution. Ideally, no more than 10-12 RMS power points should span one burst to ensure proper parabola fitting. Figure 3.5 is a plot of the new burst recognition metric including the correlation coefficient weighting. **This step requires less than N operations.**

### 3.1.2.1.2.3 Peak detection and thresholding

The peak detection and thresholding step involves determining where the burst detection metric exhibits maxima and which of these are above a threshold. The threshold value is user-set and may be determined quickly by processing data snippets to judge the success of the threshold level. In this step, the bursts which pass the detection criteria are identified and information is stored indicating their locations and decay parameters. This step requires  $0.012N$  operations, negligibly contributing to the computational costs.

**The total cost for the burst detection is then about  $3N$ . Since this is a linear cost and the search for an event in an array is inherently linear in itself, it is much more computationally efficient than any non-linear technique such as frequency-domain detection.**

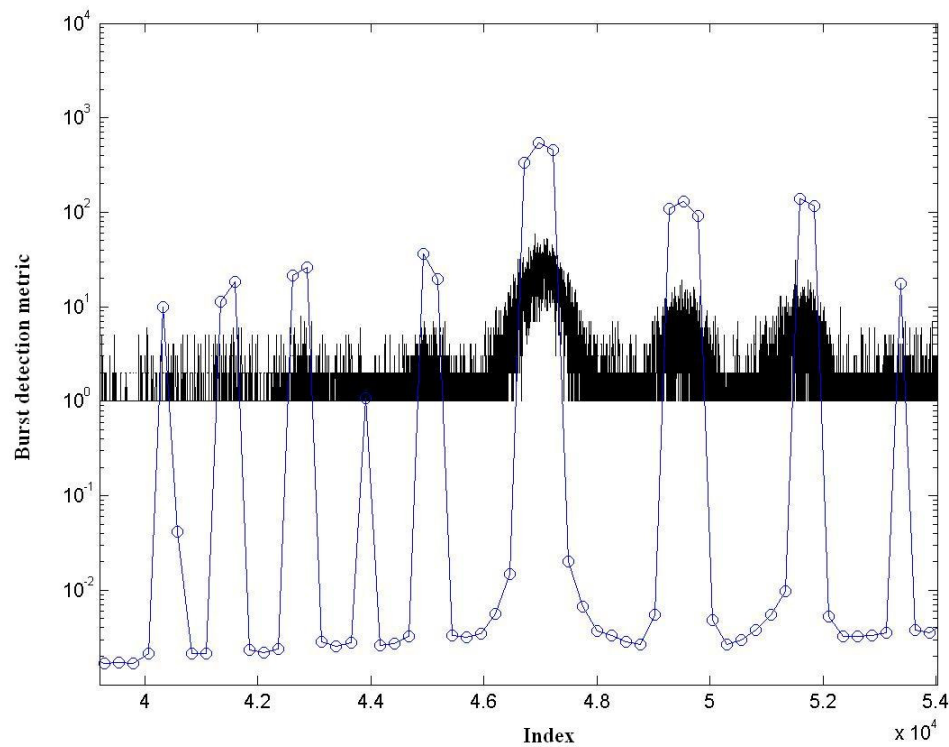


**Figure 3.5. Final burst detection metric versus sample index.**

### 3.1.2.1.3 Dual burst processing

Since the CompLDV experiences very high burst rates, the probability of closely spaced or overlapping bursts is high. To properly process these signals, we must identify those bursts and go about separating them in some way. Knowing the burst envelope parameters allows one to devise an efficient way to do just that.

Figure 3.6 is an example of the semi-logarithmic time-series of a dual burst event. The first parabola of the RMS power is noticeably distorted by the second burst, but the large amplitude will ensure that it passes validation; thus, the processor must know to identify this event as a dual burst event for proper processing. The two burst envelope parameters allow one to easily identify these events. The  $1/e^2$  definition may be used to define the ‘edge’ of the burst and the decay parameters and burst center times may be used to determine the presence of overlap. Figure 3.7 and Figure 3.8 are time-series and frequency-domain plots of the same dual burst event. In Figure 3.7, the first burst is centered in the window while the second burst is centered in Figure 3.8. The fitted burst envelope is exaggerated in duration in the case of some dual bursts, an example being made in Figure 3.7. This is acceptable because it increases the probability of the burst being processed as a dual burst.

To separate the bursts from one-another, the envelopes are used yet again. In Figure 3.7 and Figure 3.8, the blue plots are the original data while the red plots signify the

separated signals. In each processing window, the burst envelope is used as an absolute boundary such that if the signal extends beyond the instantaneous envelope value, it is set to the envelope value. Also the signal is cut so that no data occur below zero. Functionally, the following is occurring

$$\tilde{s}(t) = \begin{cases} s(t), 0 \leq s(t) \leq e(t) \\ e(t), s(t) > e(t) \\ 0, s(t) < 0 \end{cases} \quad (3.11)$$

Where  $s(t)$  is the measured signal,  $e(t)$  is the Gaussian envelope fit to the RMS signal, and  $\tilde{s}(t)$  is the processed signal. The result of the separation is quite dramatic, both in the time- and frequency-domains. Figure 3.8 in particular illustrates a greatly improved behavior in the semi-logarithmic burst spectrum. The red plot shows a frequency spike that is nearly parabolic, as predicted for the Gaussian-windowed sinusoid. The less dramatic results in Figure 3.7 are due to an over-prediction of the burst duration which may be corrected by adding a step in the process that notes that a burst follows that one closely in time, thus only the leading edge of the burst should be used for envelope determination.

Nobach (2002a) discusses a simple validation scheme which is derived from signal simulations. We must test to see that the bursts may truly be separated, if not, they must be discarded due to large bias in the frequency estimate. For two bursts at arrival times  $t_{01}$  and  $t_{02}$  with nominal decay parameters,  $\beta$ , the validation criteria should be

$$|t_{02} - t_{01}| \sqrt{\beta} > 2 \quad (3.12)$$

The cost of the burst separation algorithm is very modest. Compared to any frequency-domain processing done on these bursts, the linear separation schemes will be trivial.

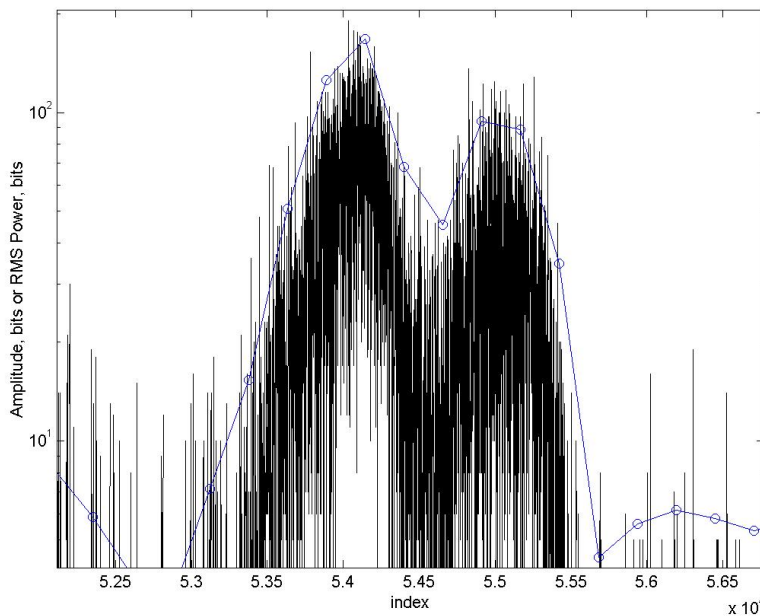


**Figure 3.6. Semi-logarithmic amplitude of burst time-series for a dual burst, along with the RMS power metric.**

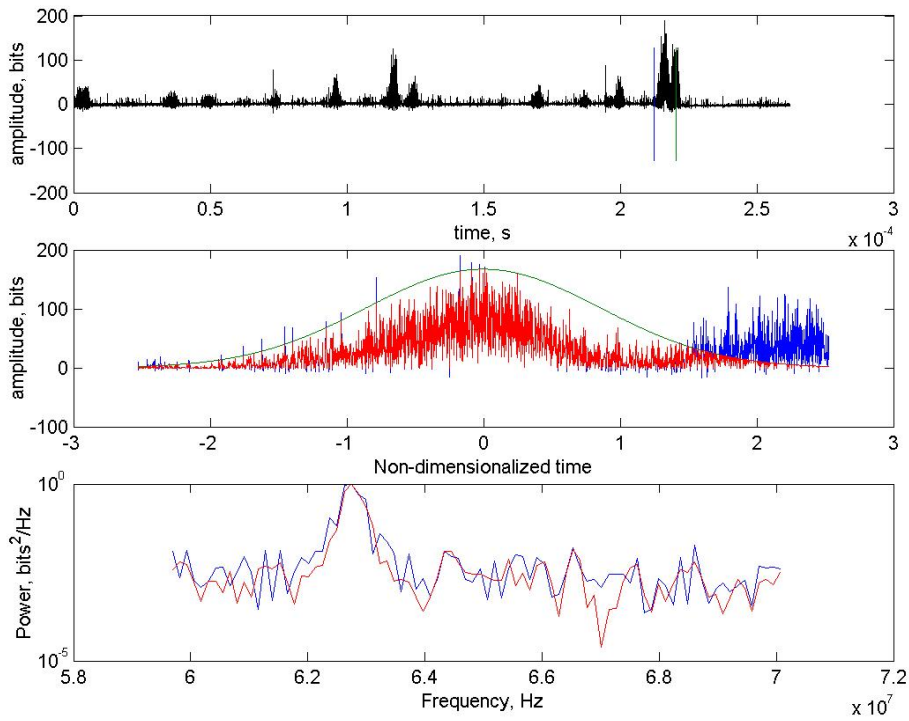


**Figure 3.7. First burst in the dual burst pair example.**

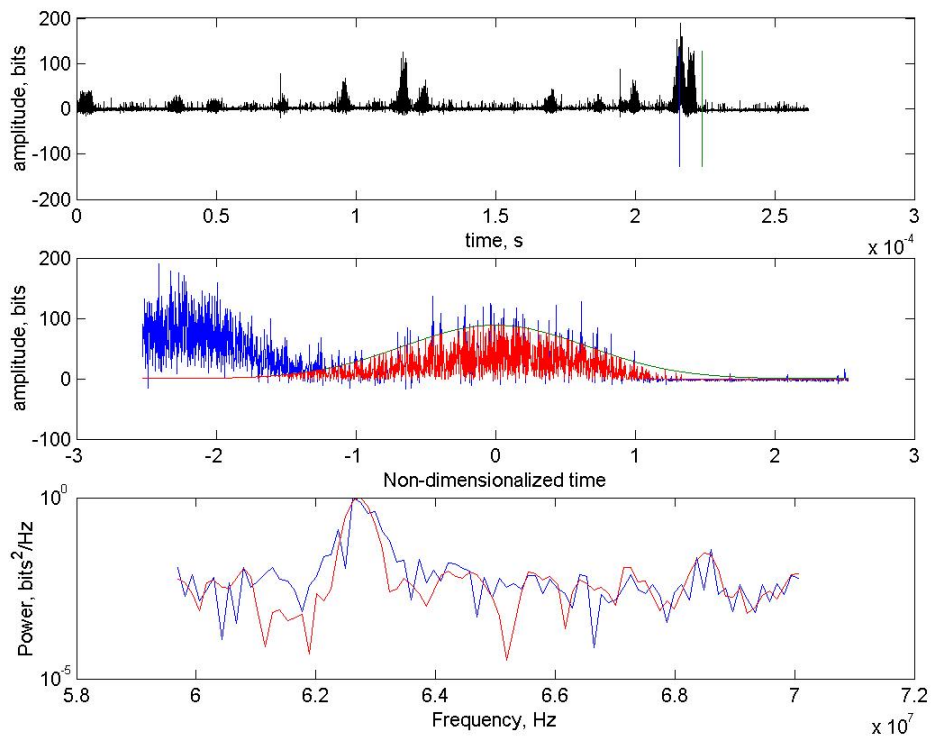


**Figure 3.8. Second burst in the dual burst pair example.**

### 3.1.2.1.4 Processing for Signal Phase Parameters

#### 3.1.2.1.4.1 The Cramer-Rao Lower Bound

With a confident identification of the burst using the recognition algorithms described and adequate separation of closely spaced bursts, processing for determining the burst phase parameters is possible. These parameters, as discussed, are the average frequency,  $f_0$ , and the chirp parameter,  $\gamma = \left. \frac{df}{dt} \right)_{t=t_0}$ . Many options exist for estimating the signal

phase and chirp for laser-Doppler bursts. As mentioned, however, the best unbiased estimator for any signal is given by the *Cramer-Rao Lower Bound* (CRLB), the theory of which is discussed by Whalen (1971) and Albrecht et al. (2002). Therefore, we must be aware of the limits imposed by the CRLB and seek an estimator which approaches this level of fidelity.

##### 3.1.2.1.4.1.1 Formulation for CRLB

The computation of the CRLB is based upon the model signal to be processed. The measured signal is taken as equation (3.1) with the model signal,

$$\hat{s}(t) = A \exp\left[-\frac{\beta}{2}(t-t_0)^2\right] \cos[\phi(t)] \quad (3.13)$$

Assuming a Gaussian noise distribution, the so-called Fisher information matrix is computed for a discrete signal at times  $[t_1, t_2, \dots, t_k]$  as

$$J_{ij} = \frac{1}{\sigma_n^2} \sum_{k=1}^N \frac{\partial \hat{s}(t_k)}{\partial \theta_i} \frac{\partial \hat{s}(t_k)}{\partial \theta_j} \quad (3.14)$$

where  $\sigma_n^2$  is the variance of the noise and  $\theta$  is a vector of the signal parameters, in our case,  $\theta = [A \ \beta \ \gamma \ f_0 \ \phi_0]^T$ . Note that it is assumed that  $t_0$  is known and is zero. The pertinent expressions for the partial derivatives are

$$\begin{aligned} \frac{\partial \hat{s}}{\partial A} &= \Gamma \sin \Phi \\ \frac{\partial \hat{s}}{\partial \beta} &= -\frac{A}{2} t^2 \Gamma \sin \Phi \\ \frac{\partial \hat{s}}{\partial \gamma} &= A \pi t^2 \Gamma \cos \Phi \\ \frac{\partial \hat{s}}{\partial f_0} &= 2 A \pi t \Gamma \cos \Phi \\ \frac{\partial \hat{s}}{\partial \phi_0} &= A \Gamma \cos \Phi \end{aligned} \quad (3.15)$$

Where  $\Gamma = \exp\left(-\frac{\beta}{2} t^2\right)$  and  $\Phi = \pi(\gamma t^2 + 2f_0 t) + \phi_0$ . The CRLB is directly related to the Fisher information matrix such that the diagonal of the inverse of equation (3.14) gives

the CRLB for each parameter. It is then possible, to compute the CRLB for representative signal parameters.

To generalize the signal variance estimates, Shinpaugh et al. (1992) illustrated the usefulness of the proper normalization for the variance and a more pertinent definition of the SNR. It is shown that the CRLB for the simpler case of the constant frequency burst will collapse for all signal parameters when the frequency and chirp variance is normalized using the spectral line width of the Fourier transformed signal,  $\delta f = 1/T$  where  $T$  is the duration of the sampling period, and the SNR is modified by multiplying with the number of signal samples,  $N$ . The expression for the SNR used by Shinpaugh et al. (1992) is

$$SNR_1 = N(SNR) = N \frac{\sigma_{signal}^2}{\sigma_n^2} \quad (3.16)$$

or in decibel form

$$SNR_1)_{dB} = 10 \log_{10} \left( N \frac{\sigma_{signal}^2}{\sigma_n^2} \right) \quad (3.17)$$

where  $\sigma_{signal}^2$  is the mean-square of the model signal given by equation (3.13) and  $\sigma_n^2 / N$  is one-half the noise variance per spectral line in the spectral vicinity of the signal. The  $SNR_1$  formulation is particularly meaningful because the noise metric is representative of the narrowband noise that directly affects signal parameter estimation. Heuristically speaking, it is only the narrowband noise that degrades spectral estimates because broadband noise may be filtered before processing.

#### 3.1.2.1.4.1.2 Results for CRLB

Although equations (3.14) and (3.15) indicate that the CRLB is dependent upon absolute values of the signal parameters, it was found that it is very insensitive to *phase* parameters and the signal amplitude when the results were normalized and indexed with  $SNR_1$ . The Gaussian window parameter,  $\beta$ , was chosen such that the burst decayed to the  $e^{-2}$  value at the edge of the window. This may be stated in a relationship between the period,  $T$ , and  $\beta$  as  $\beta = 8/(T/2)^2$ . For reference, the exact signal parameters used for the CRLB reported are given in Table 3.1, although it is reiterated that the CRLB obtained is generally applicable for a signal following the model of equation (3.14).

The parameters of interest to our measurements are the minimum variance (or similarly, the standard deviation) for the frequency and the chirp. Figure 3.9 is a plot of the CRLB for the frequency standard deviation normalized by the spectral line width,  $\delta f = 1/T$ . Figure 3.10 is a plot of the CRLB for the standard deviation of the chirp parameter normalized by  $(\delta f)^2$ . Table 3.2 lists the values of the CRLB at various levels of  $SNR_1$ . For reference on the  $SNR_1$  scale, a practical lower limit for the value of  $SNR_1$  allowing estimates to approach the CRLB variance was shown by Shinpaugh et al. (1992) to be about 20dB. Below this value, the signal parameters could not be estimated. More will be

said to follow concerning the minimum  $SNR_1$  for unbiased estimates of the chirp parameter.

**Table 3.1. Signal parameters for the reported Cramer-Rao Lower Bound.**

Parameter	Value
Sampling frequency, $f_s$	250 MS/s
$N$	8192
$T$	32.77 $\mu$ s
$\delta_{SL}$	30.5 kHz
$A$	1 arbitrary unit
$f_0$	3.06 MHz
$\gamma$	7.45E8 Hz <sup>2</sup>
$\phi_0$	0
$\beta$	1.49E10 Hz <sup>2</sup>

**Table 3.2. The Cramer-Rao Lower Bound for the signal parameters in Table 3.1.**

$SNR_1$	$\sigma_\gamma / \delta_{SL}^2$	$\sigma_{f_0} / \delta_{SL}$	$SNR_1$	$\sigma_\gamma / \delta_{SL}^2$	$\sigma_{f_0} / \delta_{SL}$
0	7.990821	0.919593	36	0.126646	0.014575
2	6.347335	0.730459	38	0.100598	0.011577
4	5.041867	0.580224	40	0.079908	0.009196
6	4.004897	0.460888	42	0.063473	0.007305
8	3.181203	0.366097	44	0.050419	0.005802
10	2.526919	0.290801	46	0.040049	0.004609
12	2.007203	0.230991	48	0.031812	0.003661
14	1.594378	0.183483	50	0.025269	0.002908
16	1.26646	0.145746	52	0.020072	0.00231
18	1.005985	0.11577	54	0.015944	0.001835
20	0.799082	0.091959	56	0.012665	0.001457
22	0.634733	0.073046	58	0.01006	0.001158
24	0.504187	0.058022	60	0.007991	0.00092
26	0.40049	0.046089	62	0.006347	0.00073
28	0.31812	0.03661	64	0.005042	0.00058
30	0.252692	0.02908	66	0.004005	0.000461
32	0.20072	0.023099	68	0.003181	0.000366
34	0.159438	0.018348	70	0.002527	0.000291

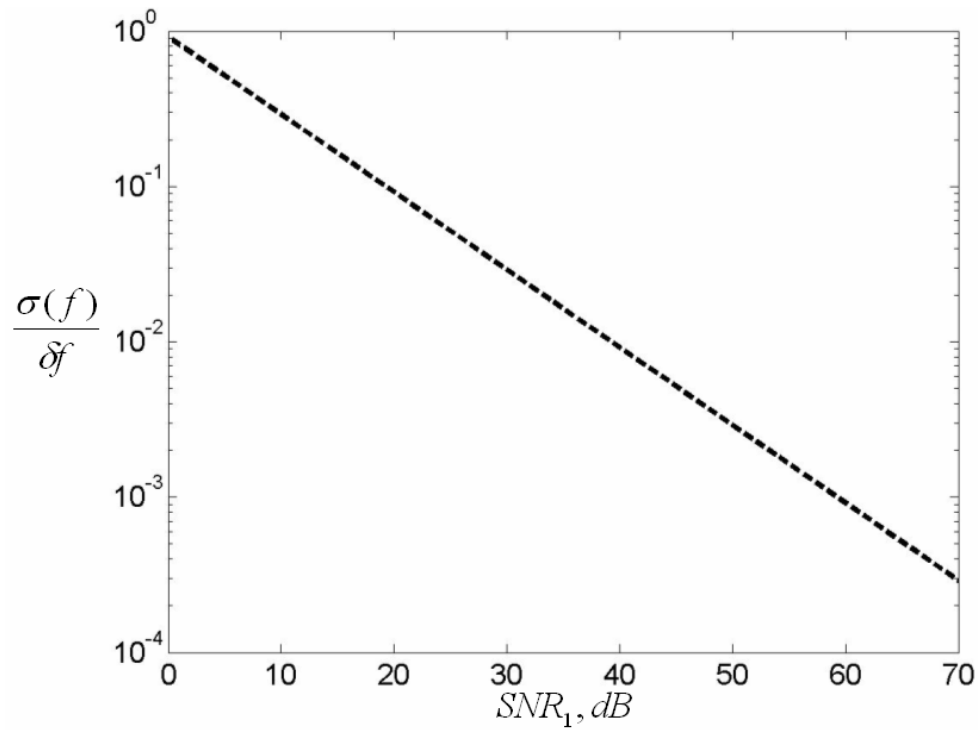


**Figure 3.9.** The Cramer-Rao Lower Bound for the standard deviation in frequency for the signal described by equation (3.14).

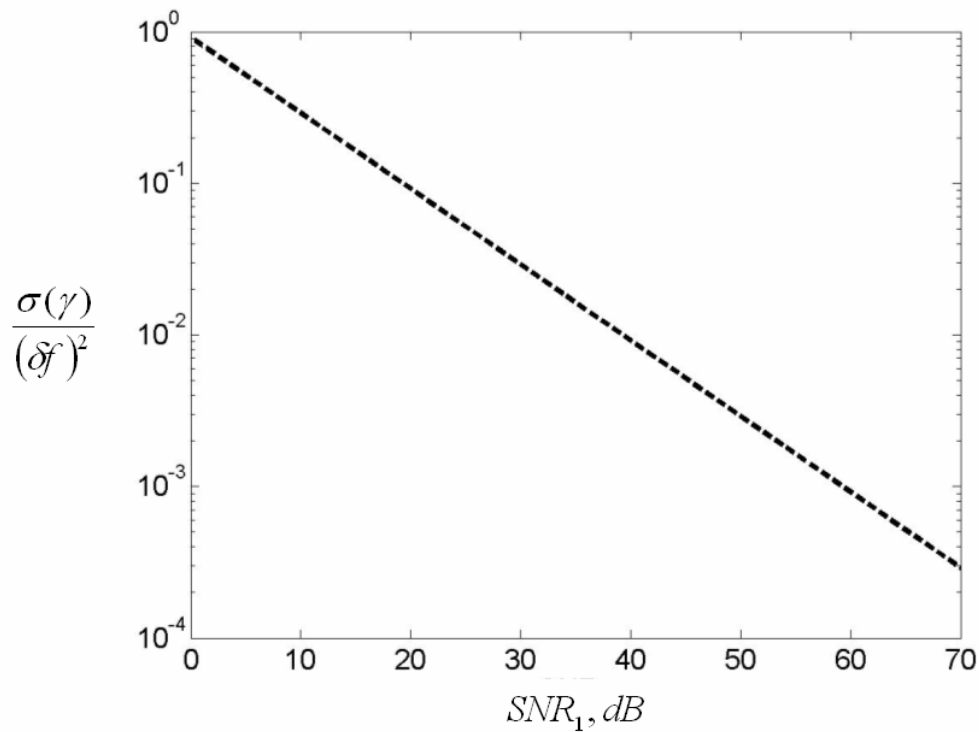


**Figure 3.10.** The Cramer-Rao Lower Bound for the standard deviation in chirp for the signal described by equation (3.14).

### 3.1.2.1.4.2 Processing options

The options for signal processing for laser-Doppler bursts have been discussed extensively in the literature by Shinsaugh et al. (1992) and more recently by Albrecht et al. (2002). Many techniques used for general signal processing applications have been considered for obtaining the burst frequency, chirp, and time-frequency information. These include spectral analysis via Fourier transforms; correlation-domain analysis; time-frequency analysis by quadrature demodulation, wavelet transforms, spectrograms (or short-time Fourier transforms), and Wigner-Ville transforms; the discrete chirp Fourier transform and many model-based parametric techniques which optimize the model parameters to best fit the signal. In the following section the literature will be briefly reviewed for these techniques and considerations for this specific application will be discussed.

#### 3.1.2.1.4.2.1 Spectral Analysis

The work by Shinsaugh et al. (1992) extensively explores the use of the fast Fourier transform (FFT) for estimating the spectra of Doppler bursts. In this method, the presence of a burst is first identified through signal recognition and then is centered into a processing window. The signal is transformed using the discrete Fourier transform (DFT),

$$X_k = \frac{1}{N} \sum_{j=1}^N x_j \exp(-ik(2\pi j)/N) \quad (3.18)$$

where  $X_k$  is the DFT of the discrete signal,  $x_j$  at sampled at times  $t_j$ , and  $k$  is the spectral line number. The FFT is an efficient implementation of the DFT which results in  $N \log_2 N$  number of floating point operations, instead of the  $N^2$  operations implied by direct implementation of (3.18). The discrete frequency domain power spectrum of a burst is estimated as

$$S_k = X_k X_k^* \quad (3.19)$$

Note that when the expected value of (3.19) is obtained for a stationary signal, the autospectrum will result.

To determine the Doppler frequency, the spectrum is considered in the expected frequency range. The signal will result in a large amount of power being concentrated around the Doppler frequency, as is shown in slices of constant time in the spectrogram in Figure 3.3. The final frequency estimate is determined by interpolation using the spectral lines adjacent to the maximum power spectral line. There are two effective ways of interpolating the spectra that are worth mentioning. First, since the Gaussian burst transforms as a Gaussian curve in the frequency domain when the chirp is small (see Albrecht et al. 2002 and Lehmann et al. 2002), a three-point Gaussian interpolation is appropriate. This is equivalent to a parabolic fit to the logarithm of the power spectral peak near the Doppler frequency such that,

$$f_D = \delta_{SL} \left( k + \frac{\ln\left(\frac{S_{k-1}}{S_{k+1}}\right)}{2 \ln\left(\frac{S_{k+1}S_{k-1}}{S_k^2}\right)} \right) \quad (3.20)$$

where  $k$  is the spectral line number of the maximum value in the power spectrum. A second interpolation scheme which is very effective is the centroid fit which is given as

$$f_D = \delta_{SL} \left( \frac{\sum_{p=k-j}^{k+j} p S_p}{\sum_{p=k-j}^{k+j} S_p} \right) \quad (3.21)$$

where  $j$  is an odd number (typically  $j=1$ ) which will allow sufficient interpolation of the Doppler peak.

An additional option for enhancing the capabilities of the DFT in estimating the signal is via zero-padding. Since the resolution of the spectral lines is limited by the period over which the signal was sampled, one may reduce the spectral line width by artificially extending the sampling period by appending zeros to the signal. Of course, no additional information is added to the signal, so the theoretical bandwidth of the signal (or the amount of information the signal is capable of conveying) is unaltered. However, the technique is effective at interpolating the spectrum which may allow for more refined estimates of the Doppler frequency. An example of a power spectrum obtained using the DFT for a signal without zero-padding is compared with the DFT for the same signal but zero-padded with  $N$  zeros is given in Figure 3.11.

Shinpaugh et al. (1992) tested the performance of the spectral interpolation schemes and zero-padding using signal simulations of bursts with constant Doppler frequencies. The results indicate that the FFT technique does *approach* the CRLB for values of  $SNR_1$  greater than about 20 dB. Below this value the signal and noise peaks become inseparable and unbiased estimation is prohibited. In the case of the centroid interpolation, the zero-padding technique is ineffective in improving the signal estimation variance. However for the Gaussian interpolation scheme, zero-padding is very effective for  $SNR_1 > 30$  dB. For low  $SNR_1$  the Gaussian and centroid interpolations performed very similarly, but the centroid interpolation out-performs the Gaussian interpolation at higher values of  $SNR_1$  when no zero-padding is used. If signals are high fidelity and processing time allows, the Gaussian interpolation with zero-padding is preferred.

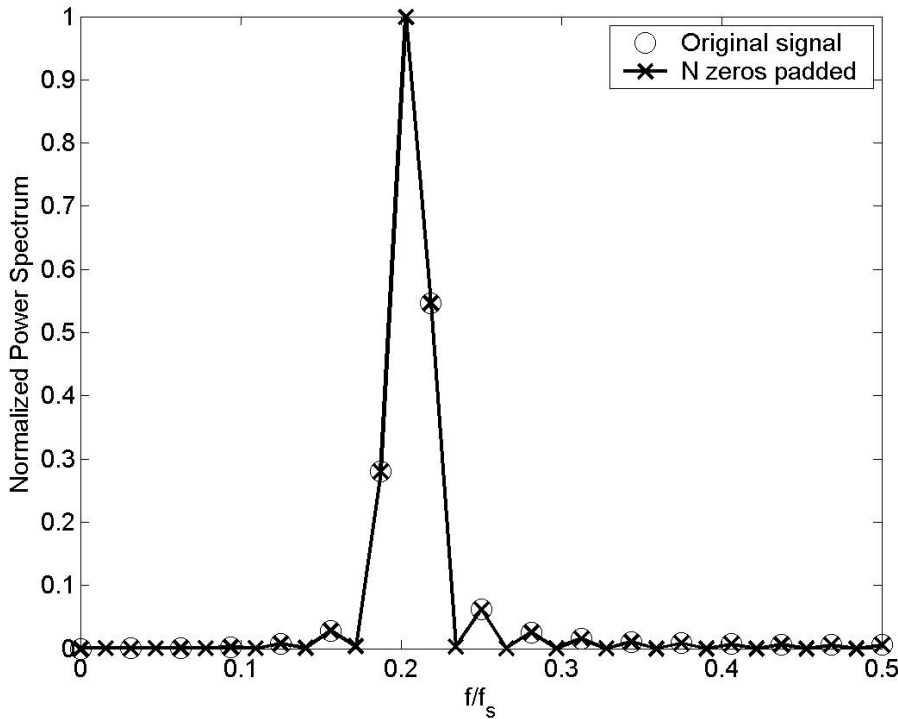


**Figure 3.11. Spectrum of a signal with and without zero-padding.  $f_s$  is the sampling frequency of the signal.**

#### 3.1.2.1.4.2.1.1 DFT Spectral analysis for time-varying frequency

The implementation of the FFT-based spectral analysis for signals with non-constant frequencies was considered by Lehmann et al. (2002). The scheme is based upon finite difference of the Doppler frequency as estimated in two parts of the signal. The concept is shown graphically in Figure 3.12. For a chirp signal with a constant rate-of-change of frequency, the chirp is then given by

$$\gamma = \frac{f_{D2} - f_{D1}}{t_2 - t_1} \quad (3.22)$$

where the subscripts represent the appropriate portion of the burst.

Since the burst amplitude is modulated, it is necessary to amplitude equalize the signal to avoid biasing the center of the burst. The signal envelope is removed using the empirical value of the window function as estimated using the Hilbert transform. The amplitude equalized signal is related as follows:

$$\hat{x}_k = \frac{x_k}{|x_k + iH\{x_k\}|} \quad (3.23)$$

where  $H\{x_k\}$  is the discrete Hilbert transform of the signal and  $x_k + iH\{x_k\}$  is the so-called analytical signal for  $x_k$ . Note that the Hilbert transform may be computed using the inverse FFT given the DFT of  $x_k$  by the following modifications to  $X_k$  (Whalen 1971),

$$\hat{X}_k = \begin{cases} X_k, & k = 0 \\ 2X_k, & 1 \leq k < N/2 \\ 0, & N/2 \leq k < N \end{cases} \quad (3.24)$$

The Hilbert transform is then

$$H\{x_k\} = \text{Im}\left[F^{-1}\{\hat{X}_k\}\right] \quad (3.25)$$

where  $F^{-1}\{\hat{X}_k\}$  is the inverse Fourier transform of  $\hat{X}_k$ .

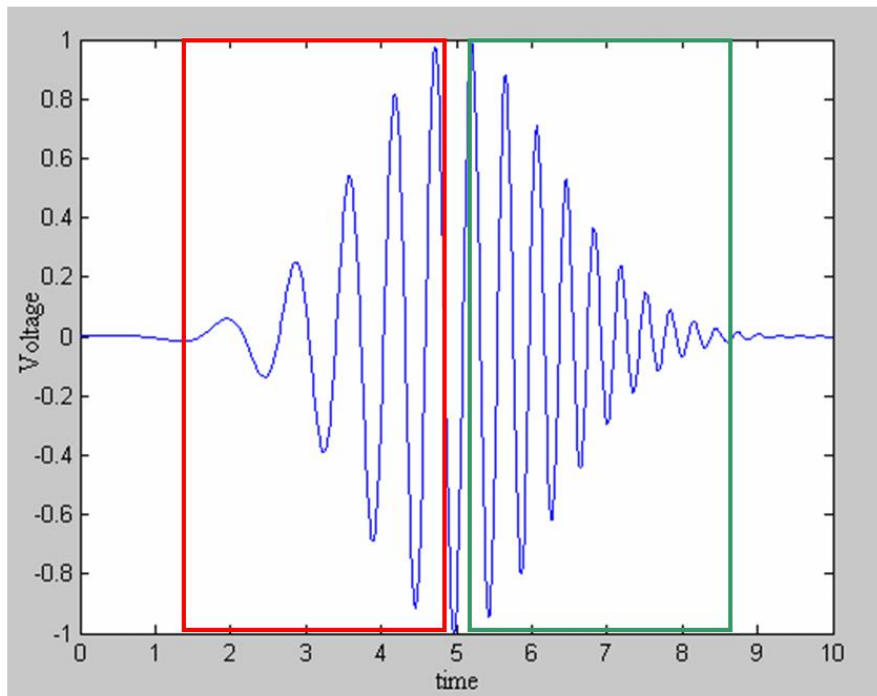


**Figure 3.12. Illustration of a chirped burst and two nominal processing zones.**

Given the amplitude-equalized signal split into two parts, the average Doppler frequency for each part is determined. Since any contribution from constant amplitude noise will decrease the SNR near the signal edges, a window function is applied to the signal. Lehmann et al. (2002) considered both the Hanning window,

$$w_k = \frac{1}{2} \left[ 1 + \cos\left(\frac{2\pi k}{N}\right) \right] \quad (3.26)$$

as well as the Gaussian window,

$$w_k = \exp\left[-\xi \left(\frac{k}{N-1} - \frac{1}{2}\right)^2\right] \quad (3.27)$$

where the authors used  $\xi = 40$ . For further reference to the characteristics of window functions, the definitive work by Harris (1978) is very informative.

In the study by Lehmann et al. (2002), the authors considered the effects of the processing window width and window choice for varying amounts of noise and signal chirp. The simulations indicated that separating the burst signal into the first 2/3rds and

last 2/3rds resulted in approximately the lowest combination of variance in the midpoint frequency estimation as well as the chirp estimation. Further, they indicated that a reduced bias and measurement variance could be achieved using the Gaussian window compared to the trigonometric Hanning window. The most likely explanation for this is that the Gaussian window behaves favorably under Fourier transformation such that the spectral peak of the signal is also Gaussian. Knowing a decent model for the spectral peak shape allows one to more-effectively interpolate the spectral peak. Of course, in the case of large chirp, the Gaussian spectral approximation fails; this magnitude of frequency change is, in general however, out of the realm of expected values for these measurements.

To benchmark the performance of similar algorithms which were implemented in the current system, signal simulations of chirped Doppler bursts with noise were performed. The signal parameters for the simulation were the same as the ones used by Lehmann et al. (2002) and are given in Table 3.3. Eight cases were considered as outlined in Table 3.4. It was sought to examine the impact of zero-padding, interpolation function, and mid-point frequency estimation scheme used. For each noise level the signal was processed 5000 times, each time with an independently realized Gaussian noise time series. The results for the study are shown in Figure 3.13-Figure 3.16. Note that in the cases in which zero-padding was employed, the spectral line width was still calculated based upon the sampling period of the actual signal before zero-padding. There are a few interesting features from the simulations that deserve mention. First, the zone of non-biased estimation occurs at  $SNR_1 \approx 20dB$  for the midpoint frequency when the entire burst is used. However, for the cases in which the burst is separated into parts in order to compute the parameters, the break occurs at  $SNR_1 \approx 24dB$ . It is also seen from these simulations that the chirp rate estimator RMS error fails to approach the CRLB. This failure is attributed to the loss of amplitude information when the envelope of the signal is removed to avoid biases (Lehmann et al. 2002). However, for the techniques tested, for both the frequency and the chirp rate it is found that the Gaussian spectral peak interpolation scheme is the superior technique. For expected noise levels in the 20-40 dB range, case 2 with no zero-padding is seen to perform as well case 3 utilizing zero-padding. Since zero-padding requires more processing power, this knowledge is quite useful for reducing processing time.

**Table 3.3. Signal parameters for the chirped burst simulation.**

Parameter	Value
Sampling frequency, $f_s$	1 S/s
$N$	256
$T$	255 s
$\delta_{SL}$	0.0078 Hz
$A$	1.3 arbitrary units
$f_0$	0.04 Hz
$\gamma$	0.00015 Hz <sup>2</sup>
$\phi_0$	1.2 rad

**Table 3.4. Processing cases for the chirped burst simulation study. Note: “Whole burst” means that the mid-point frequency was estimated from power spectrum of entire burst; “Average” means mid-point frequency was estimated by averaging the frequency determined from the two portions of the burst.**

Case	Description
1 Whole burst	Signal length N, centroid interpolation
2 Whole burst	Signal length N, Gaussian interpolation
3 Whole burst	Signal length 2N, Gaussian interpolation
4 Whole burst	Signal length 2N, centroid interpolation
1 Average	Signal length N, centroid interpolation
2 Average	Signal length N, Gaussian interpolation
3 Average	Signal length 2N, Gaussian interpolation
4 Average	Signal length 2N, Centroid interpolation

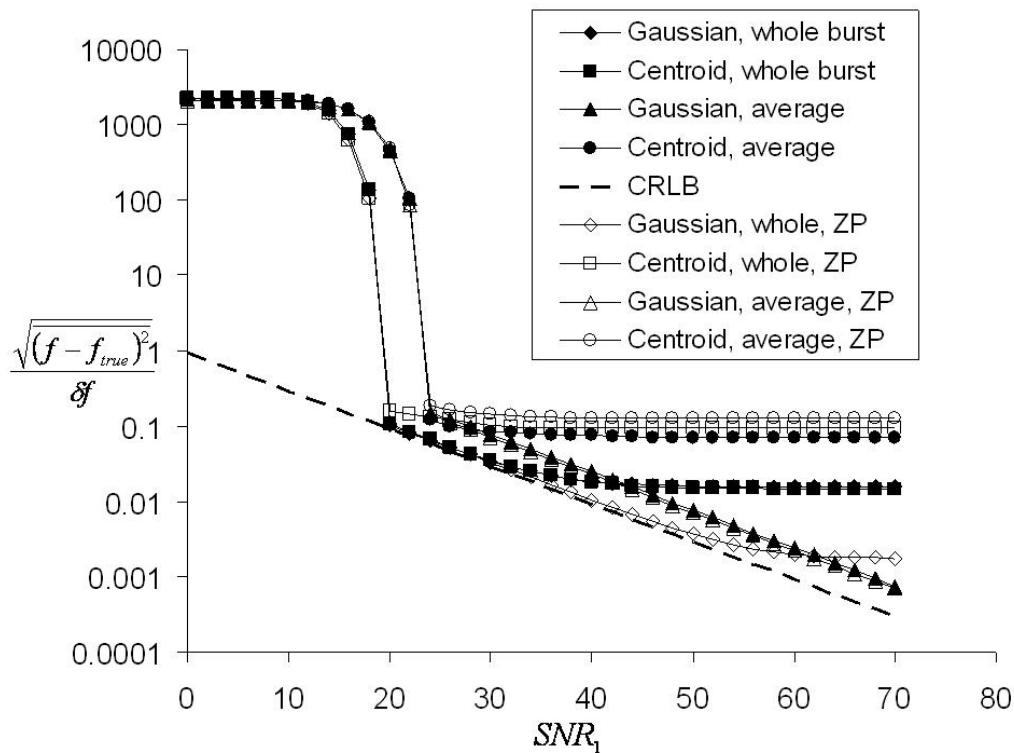


**Figure 3.13. RMS error in midpoint frequency calculations for signal simulations of a chirped burst with noise. Gaussian, Gaussian frequency interpolation; Centroid, Centroid frequency interpolation; whole, entire burst used for computing single DFT; average, burst broken into two parts to form two power spectral densities and frequency result determined by average; ZP, N zeros padded.**

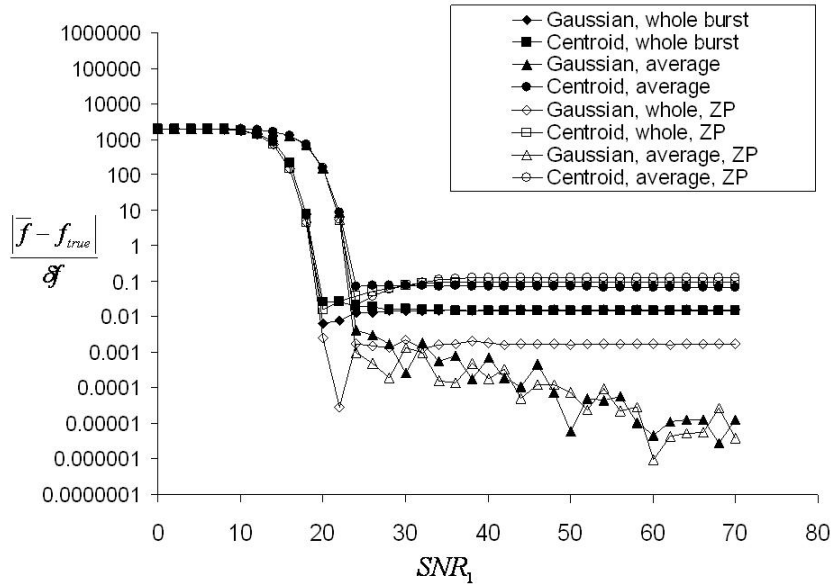


**Figure 3.14.** Bias of the frequency measurement for the parameters of signal 1. Gaussian, Gaussian frequency interpolation; Centroid, Centroid frequency interpolation; whole, entire burst used for computing single DFT; average, burst broken into two parts to form two power spectral densities and frequency result determined by average; ZP, N zeros padded.

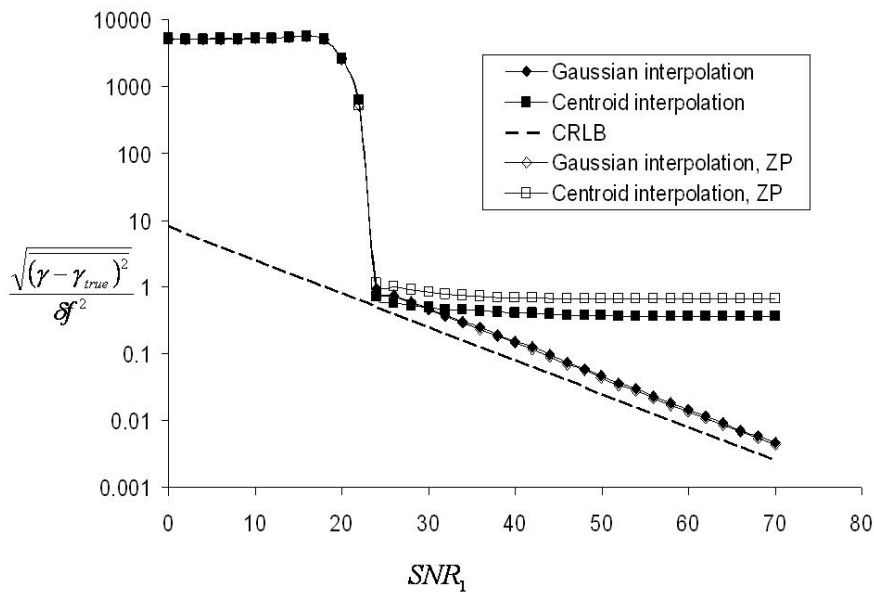


**Figure 3.15.** RMS chirp rate error from signal simulations of a chirped burst with noise for . Gaussian, Gaussian frequency interpolation; Centroid, Centroid frequency interpolation; ZP, N zeros padded.

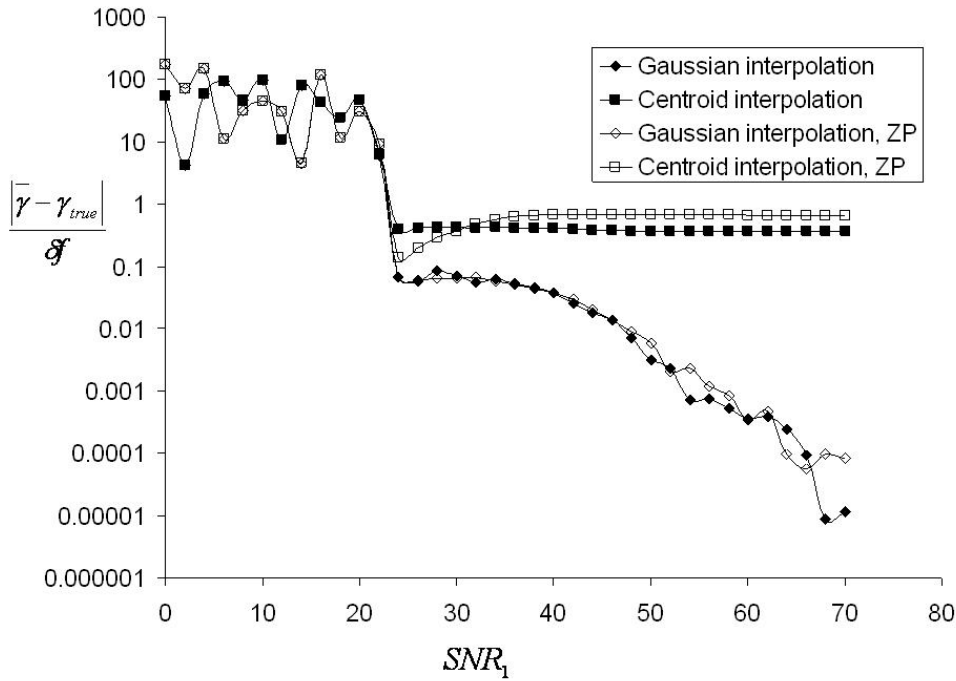


**Figure 3.16. Bias in the chirp rate. Gaussian, Gaussian frequency interpolation; Centroid, Centroid frequency interpolation; ZP, N zeros padded.**

#### 3.1.2.1.4.2.2 Correlation Domain Processing

The correlation domain processing is a technique for determining the Doppler frequency of a burst signal by analysis the time-delay correlation of the measured signal. This technique is most-often used by commercial processors to leverage the favorable noise response of the time-delay correlation functions. The correlation between signals  $a(t)$  and  $b(t)$  is written as

$$R_{ab}(\tau) = \frac{1}{T} \int_{-T/2}^{T/2} a(t-\tau)b(t)dt \quad (3.28)$$

where  $R_{ab}$  is the time-delay correlation of the signals. When  $a=b$  the correlation is known as the autocorrelation, otherwise it is the cross-correlation of the signal. An important note here is in the analysis of the noise when the expected value of  $R_{ab}$  is obtained. In this case we can represent the signals  $a$  and  $b$  as the sum of the desired signals  $s_a$  and  $s_b$  and the unwanted noise  $n_a$  and  $n_b$ . Making the substitution into (3.28) we obtain

$$R_{ab}(\tau) = \frac{1}{T} \int_{-T/2}^{T/2} [s_a(t-\tau)s_b(t) + n_a(t-\tau)s_b(t) + s_a(t-\tau)n_b(t) + n_a(t-\tau)n_b(t)]dt \quad (3.29)$$

In the case that  $a \neq b$ , then presumably the noise for each signal has resulted from separate stochastic processes and are thus unrelated. The resulting correlation will then only contain components from the first time within the integrand such that

$$E[R_{ab}(\tau)] = E\left[\frac{1}{T} \int_{-T/2}^{T/2} [s_a(t-\tau)s_b(t)] dt\right] \quad (3.30)$$

In the more common case as in typical laser-Doppler velocimetry signals when only a single measurement of a Doppler signal exists, the autocorrelation of the signal will be

$$E[R_{aa}(\tau)] = E\left[\frac{1}{T} \int_{-T/2}^{T/2} [s_a(t-\tau)s_a(t) + n_a(t)^2] dt\right] \quad (3.31)$$

Thus the autocorrelation will only contain noise contributions at zero-delay. The frequency of the signal may then be determined by any of several methods, including counting signal periods or fit to model signals.

Implementing this technique has similar costs as the FFT, but is not the preferred method for this study. As discussed by vanMaanen (1999), while the correlation technique will effectively separate signal from noise in a stationary signal, Doppler signals are transient, finite, and non-stationary. In this way, it is not possible to find the expected value of the autocorrelation and so noise will still be present throughout the correlation estimate. While it is possible to eliminate broadband noise to improve correlation estimates, ultimately it is the narrowband noise which may not be filtered that contaminates the correlation (vanMaanen 1999). Since the algorithms for frequency extraction from correlation signals are less general and robust than the FFT-based algorithms and since the chirp rate was also desired, the correlation technique was not considered for this study.

#### 3.1.2.1.4.2.3 Quadrature Demodulation

The quadrature demodulation technique (QDT) is a very power method for obtaining efficient estimates of the phase evolution of signals. The method utilizes the analytical signal, defined as

$$S(t) = r(t) + ic(t) = A(t)e^{i\phi(t)} \quad (3.32)$$

where  $r$  and  $c$  form an orthogonal quadrature pair such that

$$\int_{-T/2}^{T/2} r(t)c(t) dt = 0 \quad (3.33)$$

If both  $r$  and  $c$  are known, then the signal the time-varying amplitude,  $A(t)$ , and phase,  $\phi(t)$  may be determined as the magnitude and argument, respectively, of  $S(t)$ . In many cases, the quadrature pair of a signal is not measurable, so the Hilbert transform is used to determine  $c(t)$ .

As discussed by Lehmann, Nobach, and Tropea (2002), this technique offers great promise for determining the desired parameters of the signal phase. A succinct description of the performance of this estimation technique for signals in the presence of noise is given by Czarske (1999). The drawback of the QDT, however, is the requirement for high signal-to-noise ratio signals for performance that approaches the CRLB. Using the data from the work by Lehmann, Nobach, and Tropea (2002), the limiting noise level for which the CRLB-level variance is achieved is about  $SNR_f = 41 dB$ . In the LDV systems

utilized for this work, such signal-to-noise ratios could not be achieved on a regular basis and thus the power of the QDT may not be tapped.

#### 3.1.2.1.4.2.4 Discrete chirp Fourier transform

The discrete chirp Fourier transform (DCFT) is a method for examining signals with quadratic phase evolutions. The transform is directly analogous to the Fourier transform, but with an additional phase term for the chirp rate,

$$CF[s(t)](l, m) = \sum_{k=0}^{N-1} s_k e^{-i\left(\pi m \left(\frac{k-N/2}{N}\right)^2 + 2\pi l \frac{k-N/2}{N}\right)} \quad (3.34)$$

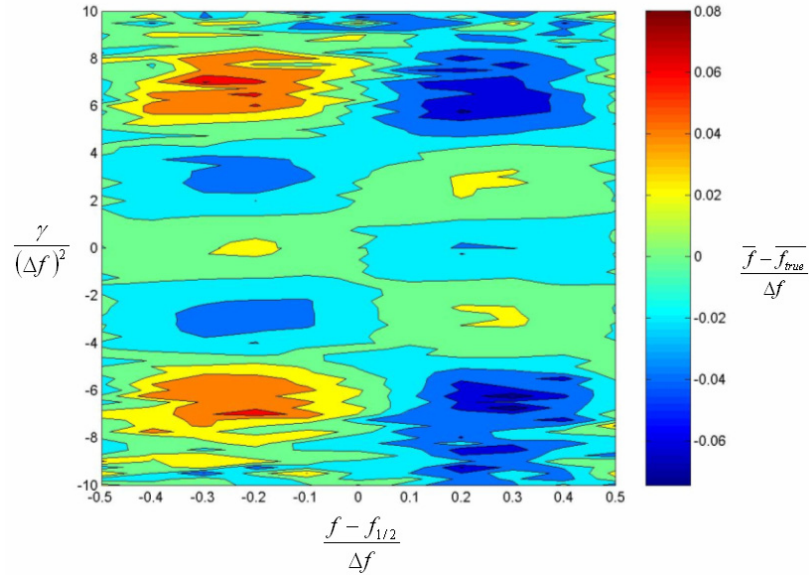
where  $l$  is the frequency spectral line number and  $m$  is the chirp spectral line number. Just as the discrete Fourier transform is limited in its frequency range by the Nyquist criterion, the chirp rate range is limited by a similar parameter,  $\gamma_{\max} = \frac{1}{4} f_s^2$ . Another observation

for the technique is the relation of the chirp line width,  $\delta\gamma = \left(\frac{f_s}{N}\right)^2$ . This parameter has

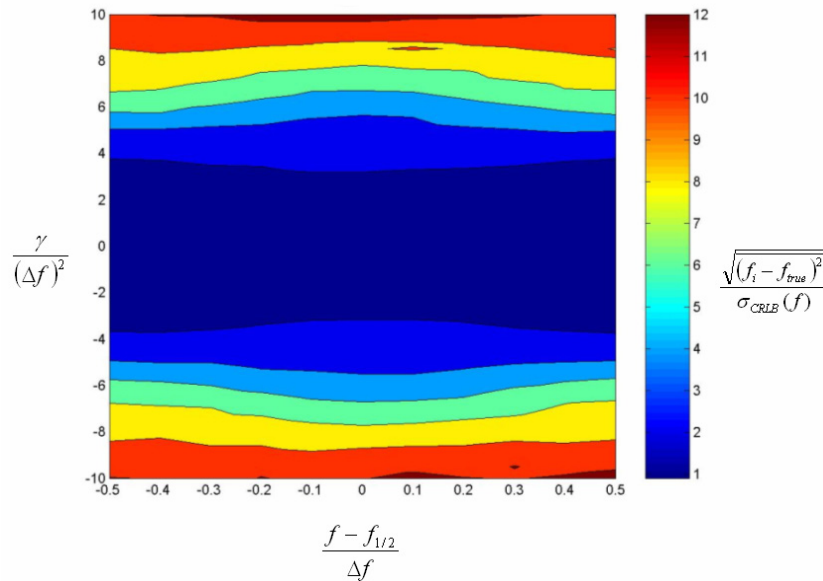
been shown in an above section to scale the uncertainties for the chirp estimation. It should be noted at this point that the chirp line width is a large value for typical Doppler signals in turbulent flows. A typical set of values for  $f_s$  and  $N$  is 250 MS/s and 4096 samples respectively. This results in a chirp line width of 3.7 GHz/s, with typical resolutions being some fraction of this number.

The primary interest in the DCFT is to extend the application of the acceleration estimation to lower values of signal-to-noise ratio. This presumption is due to the very robust operation of the DFT techniques for estimation of Doppler frequencies from low SNR signals, and the similarity between the DCFT and DFT techniques. An algorithm for achieving this was developed to implement the DCFT for LDV burst signals. In this algorithm, a combination of the DFT and DCFT is used to bound the value of the frequency and then resolve both the frequency and chirp rate to nearly the lowest-possible uncertainties. First the DFT is computed for the burst centered in the processing window. Gaussian interpolation is used around the Doppler frequency peak, giving an estimate of the frequency for the case when the chirp rate is zero. Next the DCFT is computed at the three spectral lines adjacent to Doppler frequency peak estimate (i.e., along the  $l$  index in equation 3.34) and along the range of realizable chirp rates (i.e., the  $m$  index in equation 3.34). Next, the maximum power spectral density value in the two-dimensional map is determined. Finally, two interpolations around this value of  $(l, m)$  are done. Since at significant chirp rates the frequency estimate from the DFT can be highly uncertain as seen in Figure 3.17, a new estimate for the Doppler frequency is determined by interpolating along the spectral lines using Gaussian interpolation. In Figure 3.17 and similar figures to follow, on the abscissa  $f_{1/2}$  refers to the frequency equally between adjacent spectral lines. Referring to Figure 3.17, note that at chirp rates above 3 chirp line widths, significantly higher RMS errors than the Cramer-Rao lower bound exist and bias errors become more predominate. To refine the chirp rate estimate, two interpolation

methods are considered, a parabolic interpolation and a centroid interpolation. These methods were chosen because it was observed that the power spectral densities are much more diffuse in the chirp domain than in the frequency domain where the Gaussian interpolation is perfectly suited for the Gaussian-windowed signals.



(a)



(b)

**Figure 3.17. Simulation results for the DFT with Gaussian interpolation to determine the frequency of a Gaussian windowed LDV burst over a cycle of one frequency spectral line and several chirp lines. (a) Contours of frequency bias errors normalized by the spectral line width. (b) Contours of RMS errors for the estimated frequency normalized by the Cramer-Rao Lower Bound.**

To examine the behavior of the DCFT/DFT algorithm in response to burst signals containing noise, signal simulations similar to the ones discussed in the spectral analysis section were executed. Both methods of chirp domain interpolation discussed above were considered to determine which may be better suited for the application. As with the previous simulations, the desired results were the estimator biases and variances for the frequency and chirp rate for given noise levels. Figure 3.18 is a plot of the chirp rate variance with  $SNR_1$  for the DCFT along with the finite difference spectral techniques discussed previously. Two important aspects are immediately evident. First, as expected the DCFT converges to give unbiased estimations at the same value of  $SNR_1$  as for the FFT for frequency estimation. Second, the DCFT results in RMS errors approaching the CRLB more closely than the finite difference method. To further study the response of the DCFT to signals with different frequency and chirp rates, a range of both those parameters were considered for the representative level of  $SNR_1=24dB$ . Signals with a chirp-rate of 1.47 in chirp spectral lines and a sweep of frequencies across a single spectral line were investigated at the constant value of  $SNR_1$ . The results are presented in Figure 3.19-Figure 3.22 with frequency spectral line units on the abscissa and normalized units on the ordinate. The important note from these plots is that the signal estimator approaches the Cramer-Rao lower bound to within about 5-40% for all cases, indicating a high fidelity estimator. Particularly useful in visualizing the effectiveness of this algorithm over the unrefined DFT-based techniques is comparison of Figure 3.17 to Figure 3.23. These two figures are exactly analogous; however Figure 3.23 utilizes the DCFT for determining both the frequency and chirp rate jointly. Since the modulation of the Doppler frequency peak due to a variable frequency is accounted in the model signals in the DCFT, the quality of the midpoint frequency estimation is not affected by the chirp rate.

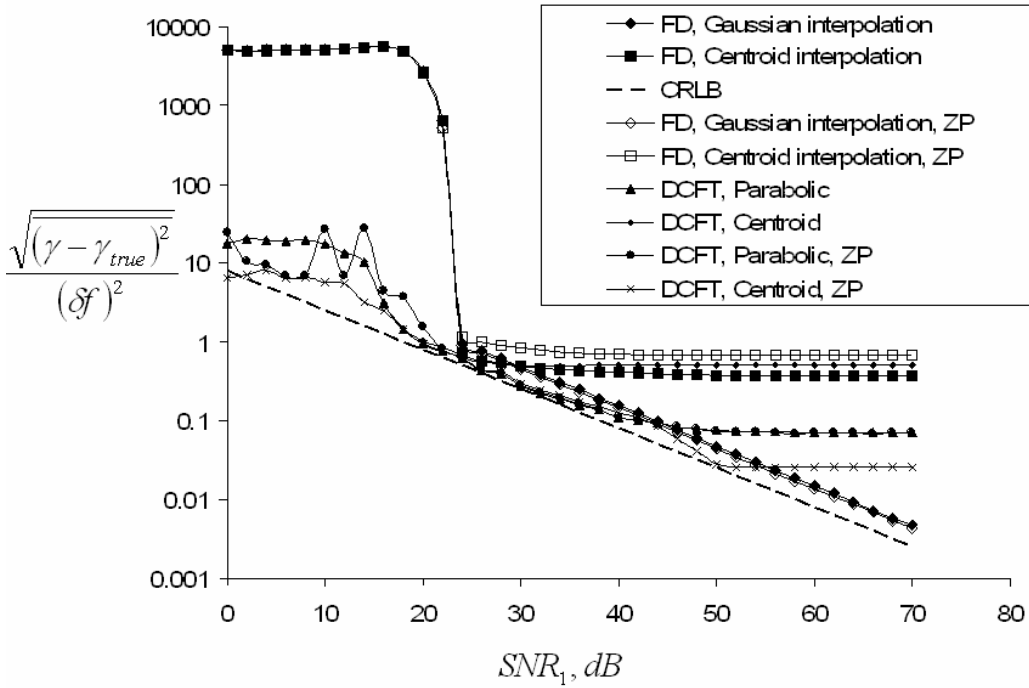


**Figure 3.18.** Uncertainty of estimated Doppler frequency chirp ( $\gamma$ ) as a function of normalized signal-to-noise ratio,  $SNR_I$  for finite difference methods (FD) and discrete chirp Fourier transform methods (DCFT). CRLB: Cramer-Rao lower bound, ZP: 2-times zero-padding, Parabolic: Parabolic interpolation of chirp power distribution, Centroid: centroid interpolation of chirp power distribution.

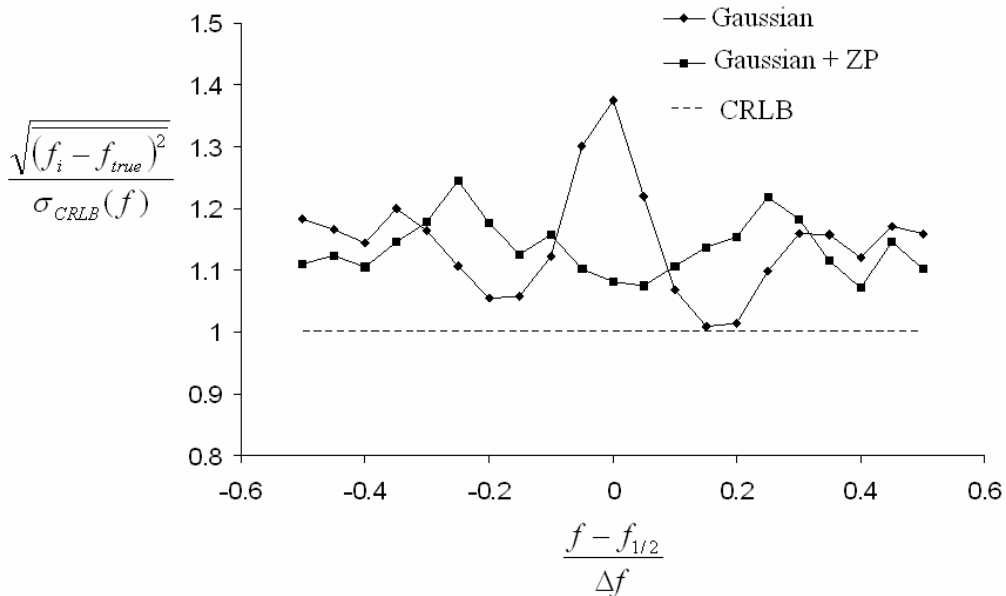


**Figure 3.19.** Relative frequency estimator RMS error over a frequency sweep with  $SNR_I=24$ dB. Gaussian, Gaussian interpolation of spectral lines in frequency domain; Gaussian + ZP, Gaussian interpolation of spectral lines in frequency domain with  $N$  zeros padded; CRLB, Cramer-Rao Lower Bound.

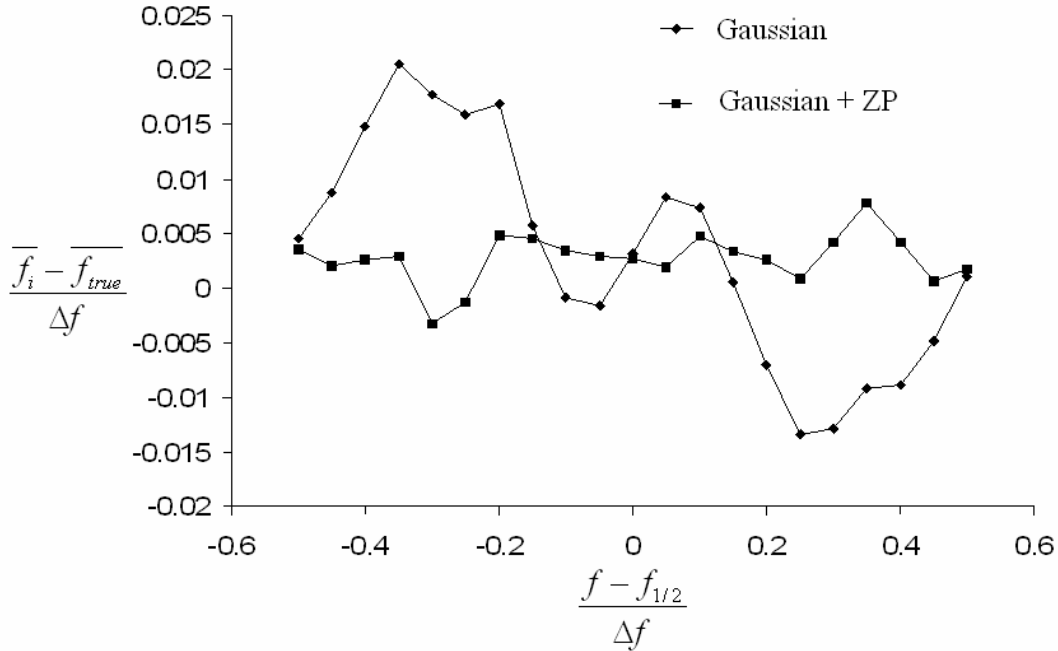


**Figure 3.20. Relative frequency estimator bias error over a frequency sweep with  $SNR_f=24\text{dB}$ . Gaussian, Gaussian interpolation of spectral lines in frequency domain; Gaussian + ZP, Gaussian interpolation of spectral lines in frequency domain with  $N$  zeros padded.**

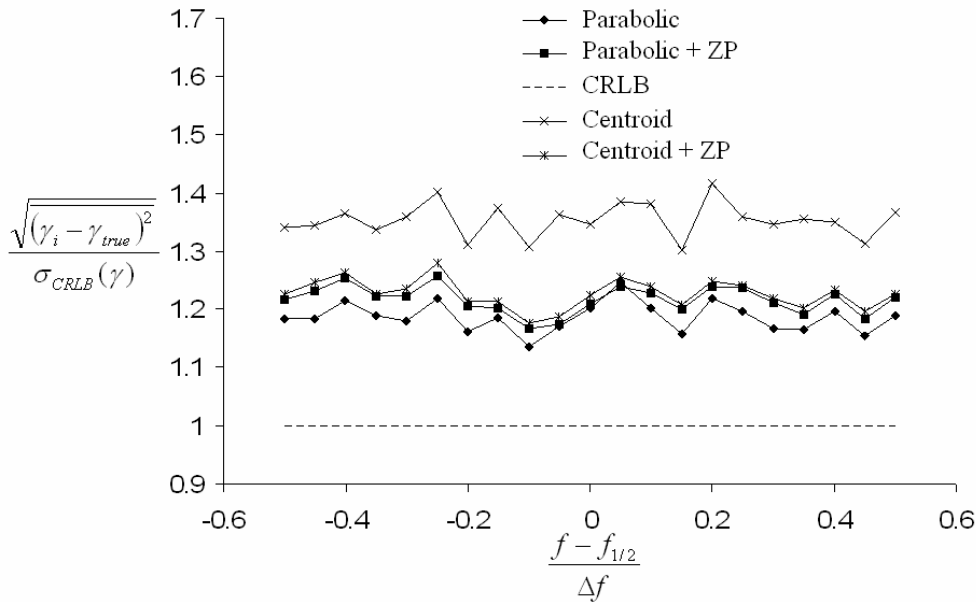


**Figure 3.21. Relative chirp rate estimator RMS error over a frequency sweep with  $SNR_f=24\text{dB}$ . Parabolic, Parabolic interpolation of chirp lines; Parabolic + ZP, Parabolic interpolation of chirp lines with  $N$  zeros padded. Centroid, Centroid interpolation of chirp lines; Centroid + ZP, Parabolic interpolation of chirp lines with  $N$  zeros padded; CRLB, Cramer-Rao Lower Bound.**

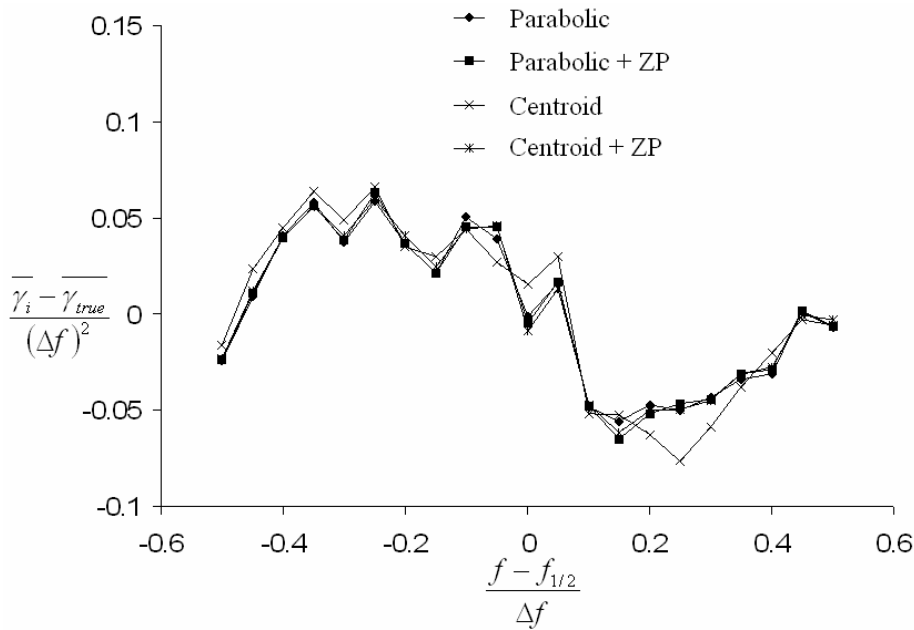
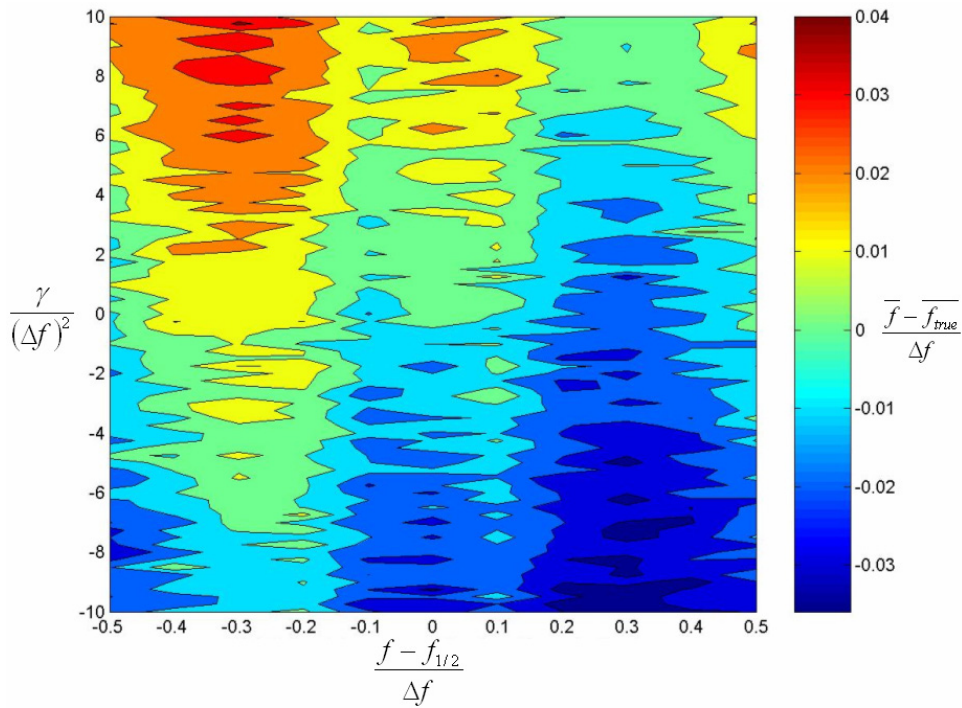


**Figure 3.22. Relative chirp rate estimator bias error over a frequency sweep with  $SNR_f=24\text{dB}$ . Parabolic, Parabolic interpolation of chirp lines; Parabolic + ZP, Parabolic interpolation of chirp lines with  $N$  zeros padded. Centroid, Centroid interpolation of chirp lines; Centroid + ZP, Parabolic interpolation of chirp lines with  $N$  zeros padded; CRLB, Cramer-Rao Lower Bound.**



**(a)**

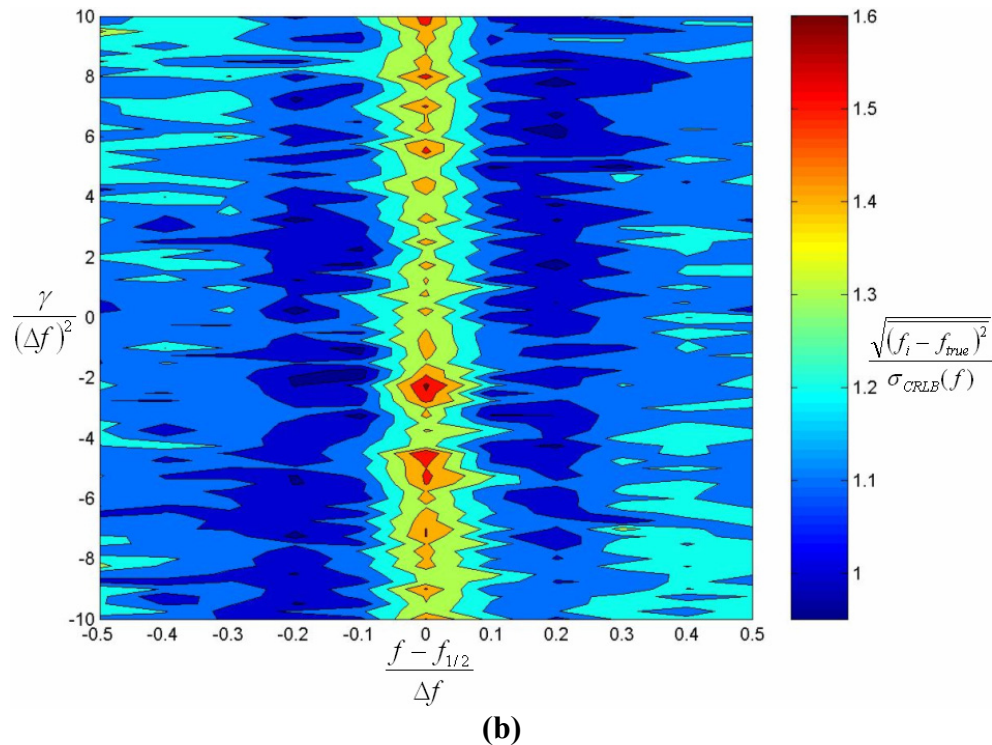


**Figure 3.23. Simulation results for the DFT/DCFT combination technique with Gaussian interpolation to determine the frequency of a Gaussian windowed LDV burst over a cycle of one frequency spectral line and several chirp lines. (a) Contours of frequency bias errors normalized by the spectral line width. (b) Contours of RMS errors for the estimated frequency normalized by the Cramer-Rao Lower Bound.**

#### 3.1.2.1.4.2.5 General time-frequency analysis

The time-frequency analysis is a challenging and well-researched field. Both these points are evident when examining a review of the available techniques by Boashash 1992. The challenge of the time-frequency analysis is inherent in the nature of problem: time and frequency are conjugate variables and thus subject to Heisenberg's uncertainty principle. This principle states that the uncertainty in time and frequency are related such that  $\delta f \delta t = C$  where  $C$  is a constant (Døssing 1998). In this way, we may either know the frequency with low uncertainty by sacrificing the time uncertainty or vice-versa. This makes time-frequency analysis very useful for applications where signal bandwidth is very large such as voice analysis. To utilize the analysis in an effective way for low-bandwidth LDV signals, we must choose the technique which optimizes the combination of frequency and time uncertainties to achieve the desired measurement for the signal.

The general time-frequency analysis tools available are many (see Boashash 1992 for a review). A few popular time-frequency techniques include the spectrogram (or short-time Fourier transform), the wavelet analysis, and the Wigner-Ville transform. Each of these is a linear transform that attempts to capture the non-stationary events through adapting either the kernel of the transform integral (Wigner-Ville), the width of the processing

window (spectrogram), or both (wavelet). Researchers have implemented each of these techniques for laser-Doppler signals to obtain time-frequency information from the signals.

Lehmann (1998) implemented both the spectrogram and the Wigner-Ville transform to examine LDV signals from oscillating droplets. His research indicated that the cross-product terms inherent in the Wigner-Ville transform made the method unusable even for moderate amounts of noise in the signal. The spectrogram method was used successfully in the study by Lehmann (1998) to make estimates of the time-frequency variation of the signals due to the robustness of the discrete Fourier transform in the presence of noise. Unfortunately, the relative bandwidths encountered in the signals for the study by Lehmann (1998) were very large and not typical for those encountered in turbulence measurements. The broadening of the spectral peak which occurs when the spectrogram is used severely limits the quality of the frequency estimates. This is seen using Figure 3.13 as an example. Even if a high level of  $SNR_1$  is achieved for the short-duration processing window, the scaling of the error with the spectral line width makes ‘instantaneous’ frequency estimates highly uncertain. Small variations in signal frequency are undetectable, being lost in the estimator variance.

The wavelet transform has also been examined for implementation in Doppler signal analysis (Nobach and vanMaanen 2001). The wavelet transform has a varying resolution of time and frequency such that low frequencies are measured precisely but with high uncertainty in the time at which they occurred and high frequencies events are measured precisely in time but with high frequency uncertainty. The result is that the relative frequency uncertainty is constant for all frequencies or conversely the relative time uncertainty is constant for all signal periods. The motivation for developing this technique for LDV signal processing was improved estimations of the burst arrival time. Since the burst duration itself is smaller than the smallest time scales in the flows in interest in the current work, this additional refinement beyond the envelope estimates from the burst recognition algorithms was unnecessary. Presently, no researchers have implemented the wavelet transform for analysis of the performance of wavelets for Doppler frequency time-variation. It is expected that due to the small bandwidth of the signals of interest, this technique will yield unsatisfactory results much like the spectrogram.

### 3.1.3 Validation of the complete burst processor

The individual algorithms discussed above for determining the location and duration of burst, estimating frequency and chirp rate and validating the burst were coded into a comprehensive processor. In order to validate the operation of these algorithms as implemented together in the processing code, sample burst signals with arrival time-values from and LDV dataset at  $y^+=181$  in a 2D constant pressure boundary layer were used. Furthermore, the mean-square velocity fluctuations were matched with the velocity data at the same point such that,  $\overline{u^2} = 4.7m^2/s^2$ ,  $\overline{v^2} = 1.4m^2/s^2$ ,  $\overline{w^2} = 2.4m^2/s^2$ . The velocity signals generated were single-tone sinusoids, with a frequency of 100Hz to allow simple comparison in the time series between input and estimated velocities. No

accelerations were input. The velocities were transformed to the non-orthogonal optical coordinates so realistic Doppler frequencies were used to generate the bursts at the appropriate time-indices. For each burst, the phase was randomly varied to eliminate any processor preference for such a characteristic. To simulate the effects of noise, the bursts were introduced with constant-amplitude Gaussian noise such that  $SNR_I=34dB$ —this value was chosen due to its proximity to the values encountered in flow situations. A time-series snippet comparing the input to the output velocities for the  $U$  channel is given in Figure 3.24. The mean-square estimates obtained with the processed results were 0.18%, -0.21%, and -0.18% in error for  $\overline{u^2}$ ,  $\overline{v^2}$ ,  $\overline{w^2}$ , respectively. In addition, the velocity-acceleration correlations found were each on the order of  $100m^2/s^3$ , or about 1-2% of the maximum value in the 2D flat plate boundary layer flow for which these data were simulated.

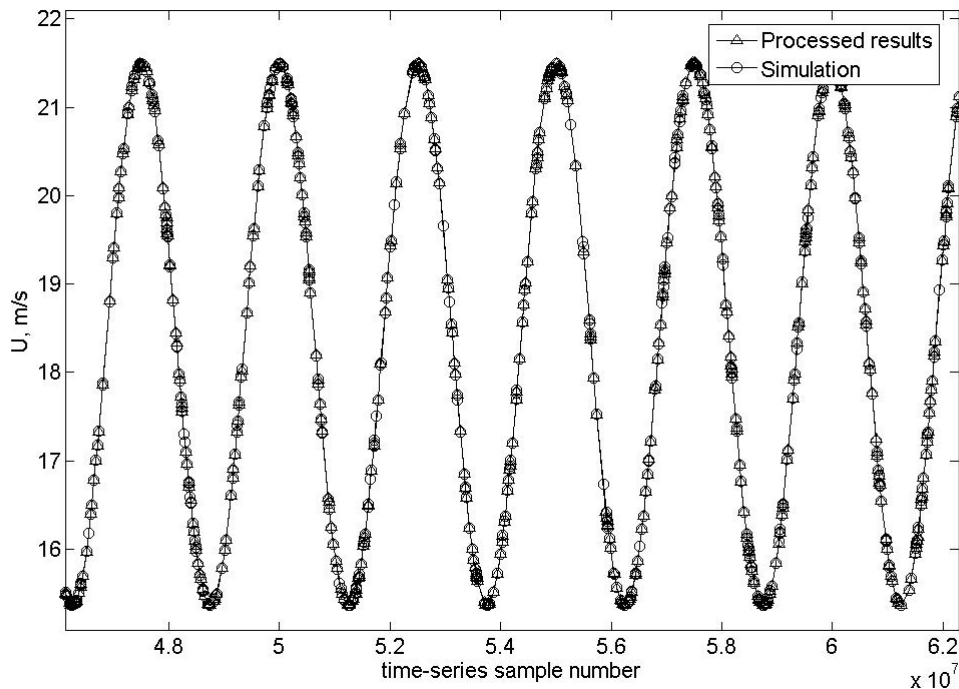


Figure 3.24. Comparison of the simulated  $U$  signal with the one processed using the CompLDV processing algorithms.

### 3.2 Spectral Analysis for Non-equidistantly Sampled Data

The subject of time-delay correlation and spectral estimation for signals arising from laser-Doppler measurements has been visited by numerous researchers since the advent of single-burst frequency estimation. An excellent review of this work up to the current state-of-the-art is given by Benedict, Nobach and Tropea (2000). The problem at hand is to efficiently and robustly estimate the time-delay correlation of a signal which is

sampled at a random time distribution. This time distribution follows Poisson statistics such that the probability of encountering a given arrival time,  $\Delta t$ , is given as

$$P(\Delta t) = \frac{N}{T} \exp\left(-\frac{N\Delta t}{T}\right) \quad (3.35)$$

where  $N$  is the number of Doppler measurements and  $T$  is the period of time for acquisition (see Benedit, Nobach, and Tropea 2000 or vanMaanen 1999 for a more detailed discussion of the arrival time phenomena). An example of such a distribution is given in Figure 3.25. The result of the Poisson arrival time distribution is that there are many data points with instantaneous ‘sampling rates’ greater than the mean rate,  $N/T$ , but also some instantaneous sampling rates much lower than the mean rate.

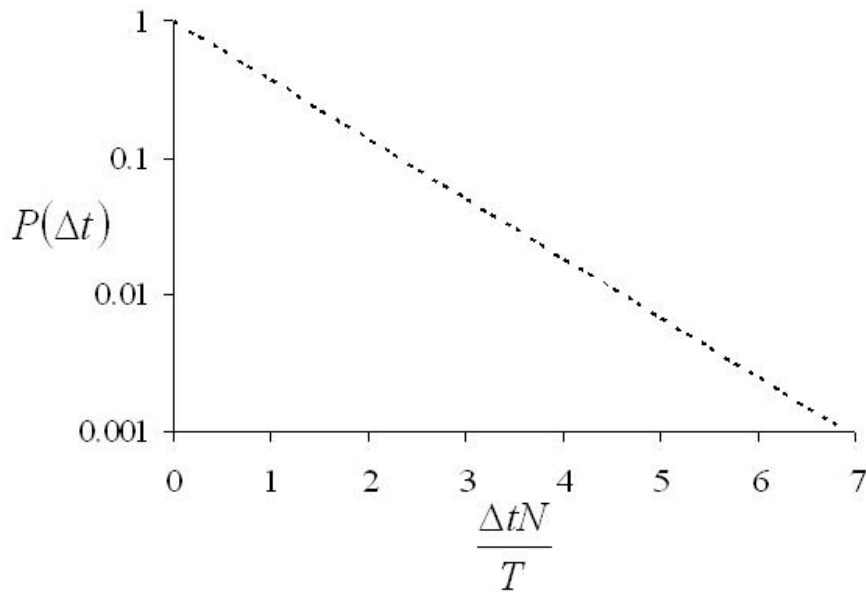


**Figure 3.25. Graphical depiction of the Poisson arrival time statistics for particle-laden flows.**

### 3.2.1 Methods for estimating time-delay and frequency-domain information from LDV data

Three classifications of methods exist for computing the frequency content of LDV signals. These are

1. Direct transform methods
2. Evenly-sampled time-series reconstruction via signal interpolation
3. Slot correlation

Of these methods, only 2. and 3. offer viable estimates as Benedict, Nobach, and Tropea (2000) show by comparison. The direct transform methods suffer from significant bias and high estimation variance which worsens with increasing noise levels. Signal reconstruction may be done by any interpolation scheme desired. However, due to the random nature of the arrival time, higher-order schemes fail since adjacent data-points that are used to interpolate intermediate values have unknown relationships. The result is that high-order interpolation results in progressively greater low-pass filtering and bias of the spectral results. The most successful of these interpolation schemes has been the

zeroth-order sample-and-hold. This method has the benefit of being very quick and simple to program and process data, but still results in low-pass filtering of the data. The frequency content of a signal which has been sample-and-hold processed will exhibit first-order system-type attenuation with the cut-off frequency being  $\frac{N}{2\pi T}$  (Adrian and Yao 1987). Corrections for the auto- and cross-correlations resulting from the sample-and-hold signals have been derived by Nobach, Müller, and Tropea (1998) and Müller, Nobach, and Tropea (1998) respectively. These methods significantly increase the viability of the sample-and-hold estimators for frequencies nearing the mean particle rate.

The third estimation scheme is a very robust statistical technique for obtaining the time-delay correlation functions for laser-Doppler data. The basic slot correlation of signals  $u(t_i)$  and  $v(t_j)$  is given by

$$R_{uv}(n\Delta\tau) = \frac{\sum_{i=1}^N \sum_{j=1}^N u_i v_j b_n(t_i - t_j)}{\sum_{i=1}^N \sum_{j=1}^N b_n(t_i - t_j)} \quad (3.36)$$

where

$$b_n(t_i - t_j) = \begin{cases} 1 & \text{for } \left| \frac{t_i - t_j}{\Delta\tau} - n \right| < 1/2 \\ 0 & \text{otherwise} \end{cases}$$

This is the basic algorithm which Benedict, Nobach, and Tropea (2000) credit to Mayo et al. (1974). Three important improvements have been made for this algorithm, known as the methods of fuzzy slotting, local normalization, and local time estimation. The fuzzy slotting technique was first proposed by Nobach, Müller, and Tropea (1998) as an improvement over the slotting technique of Mayo et al. (1974). The algorithm given by equation (3.36) was modified such that the weighting parameter,  $b_n(t_i - t_j)$  was no longer digital but could be distributed according to the proximity of the sample to the two nearest adjacent bins. The result is the fuzzy slotting condition,

$$b_n(t_i - t_j) = \begin{cases} 1 - \left| \frac{t_i - t_j}{\Delta\tau} - n \right| & \text{for } < 1 \\ 0 & \text{otherwise} \end{cases} \quad (3.37)$$

This significantly reduces the variance for the slotting methods and makes it much more attractive for general use. vanMaanen, Nobach, and Benedict (1999) published a short communication wherein they exhibit the usefulness of the fuzzy slotting scheme along with that of the local normalization scheme. The merging of these two techniques resulted in an even lower estimator variance. The local normalization is given by

$$\hat{R}_{uv}(n\Delta\tau) = \frac{\sum_{i=1}^N \sum_{j=1}^N u_i v_j b_n(t_i - t_j)}{\sqrt{\sum_{i=1}^N \sum_{j=1}^N u_i^2 b_n(t_i - t_j)} \sqrt{\sum_{i=1}^N \sum_{j=1}^N v_j^2 b_n(t_i - t_j)}} \quad (3.31)$$

where  $\hat{R}_{uv}(n\Delta\tau)$  is now the time-delay correlation coefficient with  $\hat{R}_{uv}(0) = 1$ . Finally, the local time estimation technique was developed by Nobach (2002b) to obtain the proper location of time-delay bins given sample sets that may be non-homogeneously distributed within the bins. In this case, the integer bin number,  $n$ , is replaced such that the correlation coefficient,  $\hat{R}_{uv}(\tau_n)$ , is defined at bin delay  $\tau_n$  as given by

$$\tau_n = \frac{\sum_{i=1}^N \sum_{j=1}^N (t_i - t_j) b_n(t_i - t_j)}{\sum_{i=1}^N \sum_{j=1}^N b_n(t_i - t_j)} \quad (3.32)$$

The local time estimation is very useful particularly at the smallest time delays where finite transit time limits the minimum inter-arrival time. Note that in each of these statistical slotting techniques, the general form of the equations allows a non-unity weighting of the  $i^{\text{th}}$  sample by some  $w_i$  and/or analogous weighting for the  $j^{\text{th}}$  sample. Since it has been shown by work in the past that the commonly-corrected velocity-data rate bias is very small for three-component LDV systems, no necessity for non-unity weighting exists for the present study.

A caveat of the local time estimation is that the resulting correlation function is still unevenly sampled, albeit to a much lesser degree than the original signal. Nobach (2002) suggests that interpolation of the correlation values to evenly sampled delays gives good results, especially since the shift of the bin location is very small. With this newly re-sampled correlation function, the spectral method of choice is the discrete transform with variable windowing developed by Tummers and Passchier (1996)

$$\hat{S}(f_i) = 2\Delta\tau \sum_{n=1}^L W_n \hat{R}_{uv}(n\Delta t) (\cos(2\pi f_i n\Delta t) + i \sin(2\pi f_i n\Delta t)) \quad (3.33)$$

where  $W_n$  is the variable window chosen to be a Tukey-Hanning window such that

$$W_n = \begin{cases} 1/2 + 1/2 \cos(\pi f_i n\Delta t / \kappa) & \text{for } |f_i n\Delta t| < \kappa \\ 0 & \text{otherwise} \end{cases} \quad (3.34)$$

where Benedict, Nobach, and Tropea (2000) suggest a value of  $\kappa = 6$ .

For a continuous spectral distribution as with turbulence, adjacent bin smoothing may be used to reduce the scatter in the frequency-domain data. In this technique, the power-spectral values for two adjacent estimates are averaged and replaced with a single estimate at their average frequency. This technique was used in the results section to obtain smooth estimates of the power spectra for all three-velocity components and corresponding cross-spectra.

### 3.2.2 Slot correlation validation

It was desired to validate the implementation of the slot correlation algorithms just discussed so that the flow data to be processed could be analyzed confidently. To this end, the slot correlation with fuzzy slotting, local normalization, and local time estimation was used to compute the cross-correlation between known sample sets. The

sets were constructed using an even sample set and then interpolating for time-indices taken from an actual LDV file at  $y^+=181$  in a 2D flat plate turbulent boundary layer flow. The signals entered include a sine-cosine pair, the auto-correlation of a sine function, and the cross and auto-correlations of Gaussian noise with unit standard deviations. The sampling frequency for the original signal was taken as the mean burst frequency from the LDV data, 9563.3 Hz. The frequency for the sine-cosine pair was 100 Hz.

The time-delay (cross) correlation is defined as

$$R_{uv}(\tau) = \frac{1}{2T} \int_{-T}^T u(t+\tau)v(t)dt \quad (3.38)$$

In the case of the cross-correlation between the sine and cosine functions with frequency,  $2\pi f = \omega$ ,

$$R_{\sin(\omega t)\cos(\omega t)}(\tau) = \frac{1}{2T} \int_{-T}^T \sin[\omega(t+\tau)]\cos(\omega t)dt = \frac{1}{2} \sin(\omega\tau) \quad (3.39)$$

The autocorrelation is given as

$$R_{\sin(\omega t)\sin(\omega t)}(\tau) = R_{\cos(\omega t)\cos(\omega t)}(\tau) = \frac{1}{2} \cos(\omega\tau) \quad (3.40)$$

In the other case of the random noise content the auto- and cross- correlations become, respectively

$$\begin{aligned} R_{uu}(\tau) &= \delta(\tau = 0) \\ R_{uv}(\tau) &= 0 \end{aligned} \quad (3.41)$$

The delay-space results for the first case described analytically by equation (3.39) are shown graphically in Figure 3.26 and Figure 3.27. The agreement between the cross-correlation derived from the evenly-sampled data and the LDV-time-series data is very good. To quantify the agreement, the RMS error and correlation coefficient were computed. The RMS error divided by the amplitude of the correlation was found to be 0.0076%. The correlation coefficient was computed as 0.9998. The sinusoid autocorrelation case is presented in Figure 3.28 and Figure 3.29 with equal levels of correlation between the input and computed correlations.

To obtain the Gaussian noise, two methods were employed. In the first method, a regularly sampled set was first obtained and then linearly interpolated to obtain the noise at the times from the LDV time-series list. Unfortunately, this method results in filtering and introduces very short time correlations evident in Figure 3.30 and Figure 3.31 in which similar data were used to obtain the time-delay correlations using the slotting technique as well as direct estimation from the evenly sampled data (Figure 3.32). Note that to obtain the evenly sampled data, the LDV-like data were evenly sample-and-hold interpolated. To remedy the filtering, a second method was used in which a Gaussian random number was generated for each point in the LDV time-series list. It is impossible to rigorously compare this plot to the regularly-sampled case since it will contain aliased values for regular samples. However, from the results of the slot correlation (Figure 3.33 and Figure 3.34), we see much reduced correlations near zero delay indicating that the

noise was found to be uncorrelated at non-zero values of the autocorrelation. Figure 3.35 also exhibits favorable behavior for the cross-correlation of two independently realized noise time-series with the same LDV arrival time distribution. Thanks to these simulation data, much confidence in the slot correlation algorithms used was obtained.

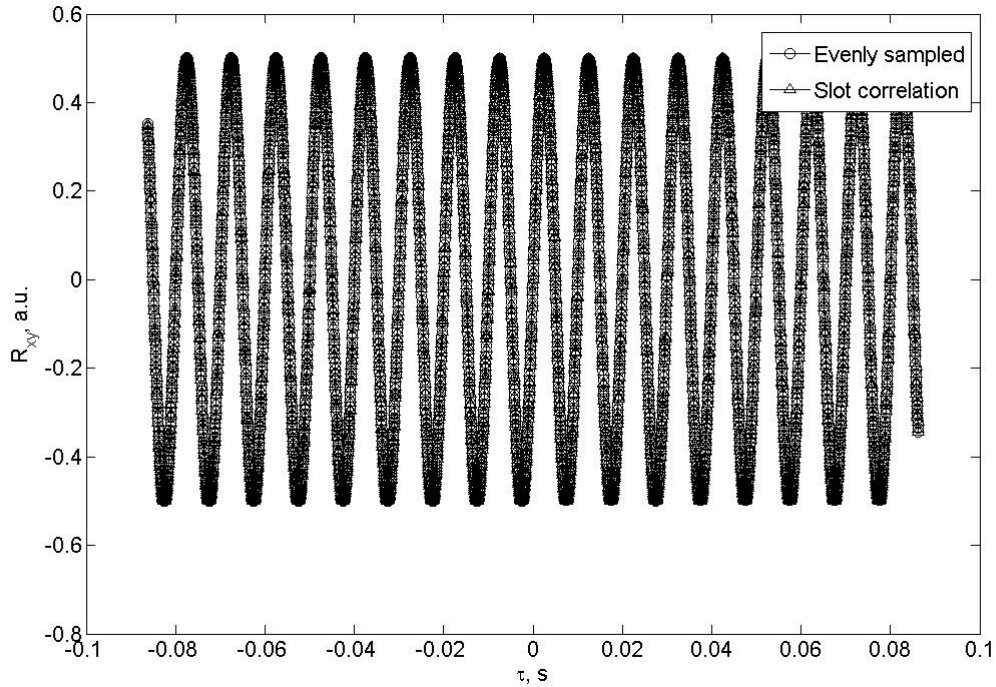


**Figure 3.26.** Cross-correlation of sine-cosine pair.

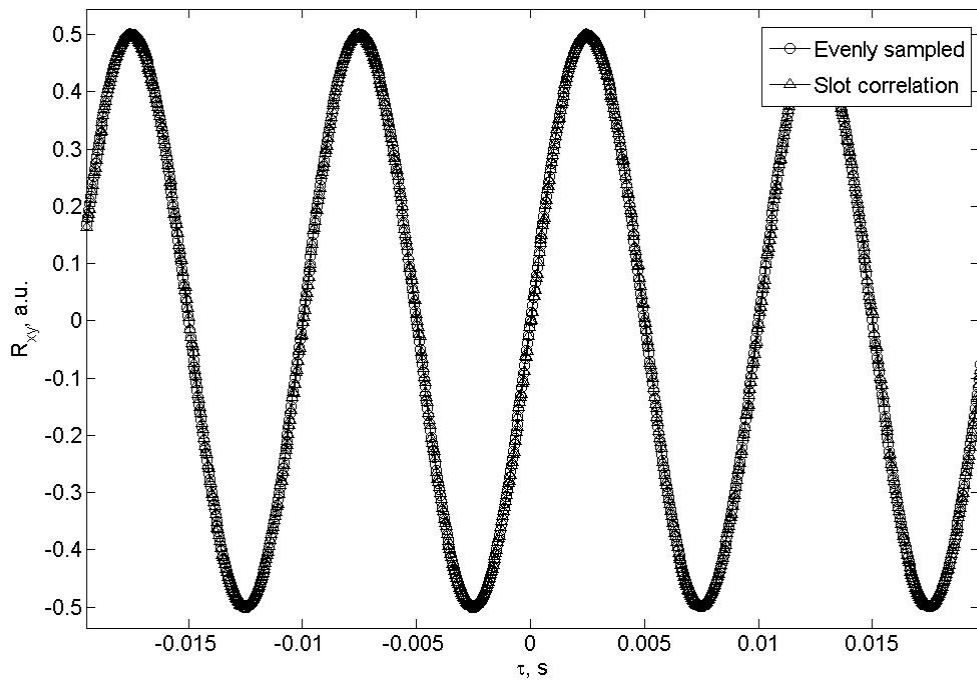


Figure 3.27. Cross-correlation of sine-cosine pair near zero delay.

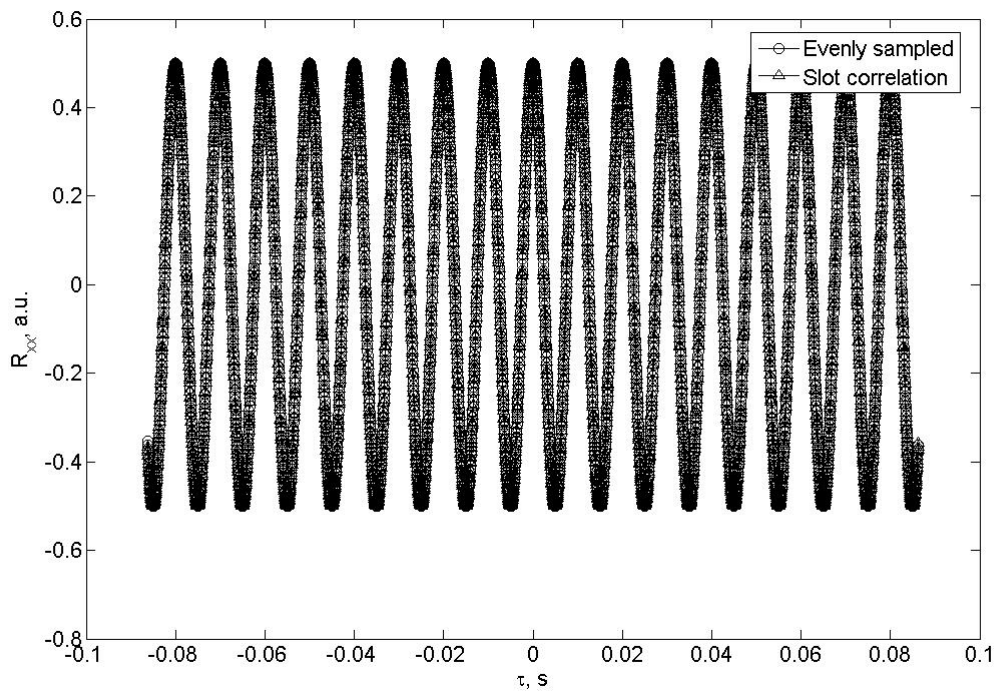


Figure 3.28. Autocorrelation of sine.

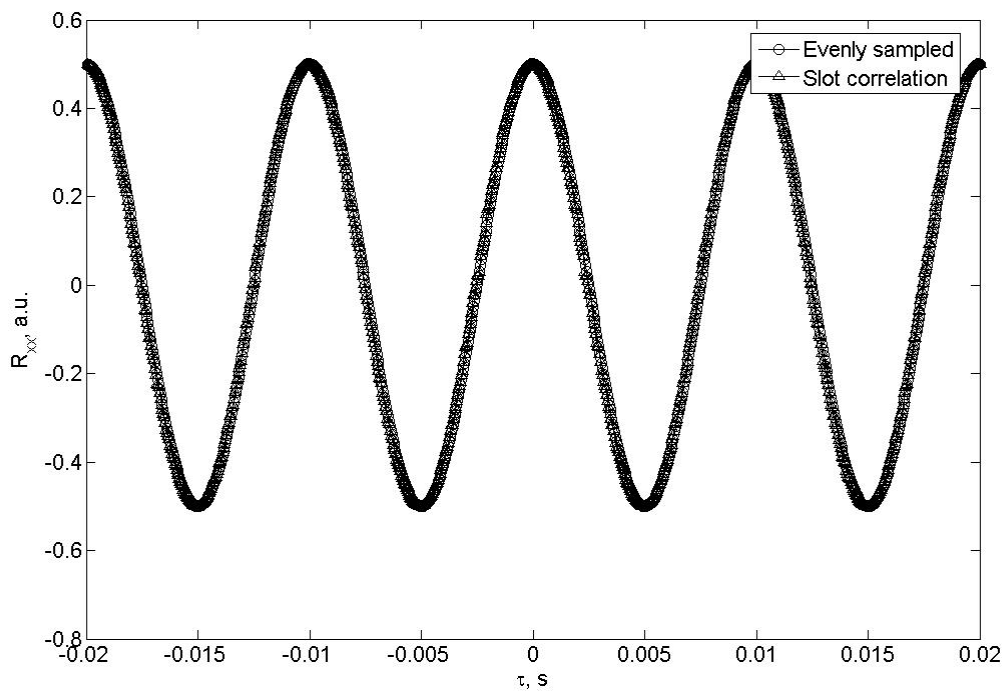


Figure 3.29. Autocorrelation of sine near zero delay.

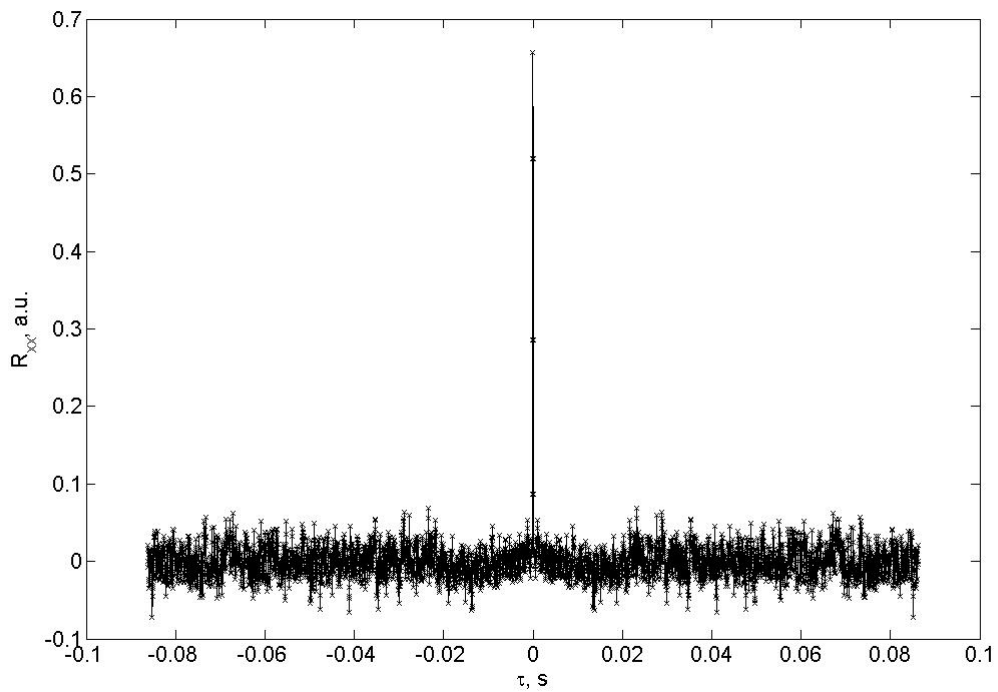
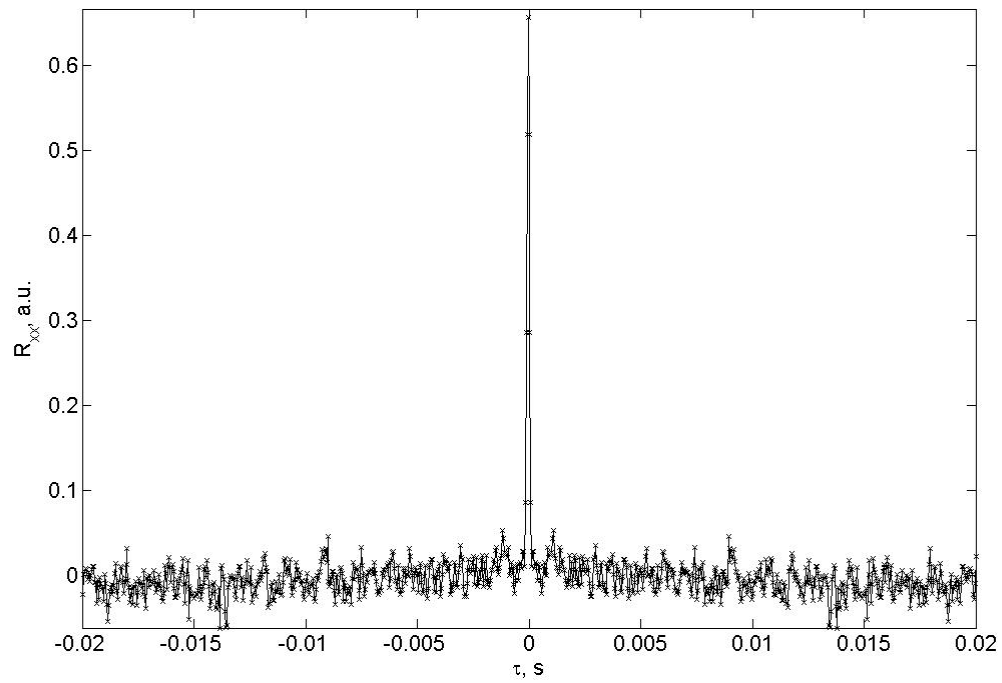
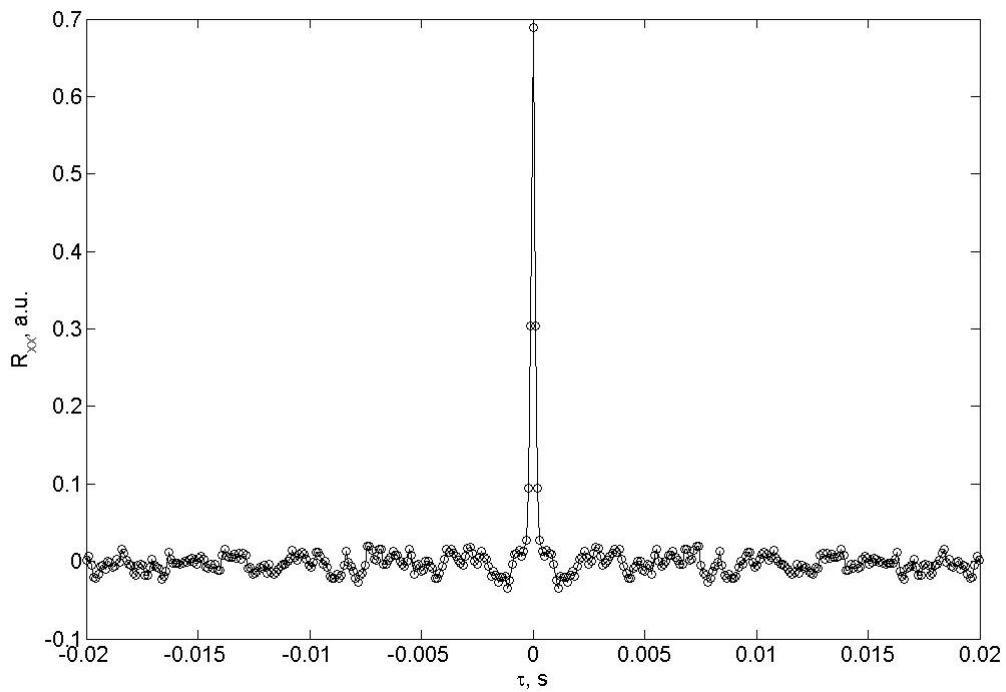


Figure 3.30. Autocorrelation of Gaussian noise as computed with the slot correlation with linear interpolation.



**Figure 3.31.** Autocorrelation of linearly interpolated Gaussian noise near zero delay as computed with the slot correlation.



**Figure 3.32.** Autocorrelation of regularly sampled data obtained from linearly interpolated Gaussian noise.

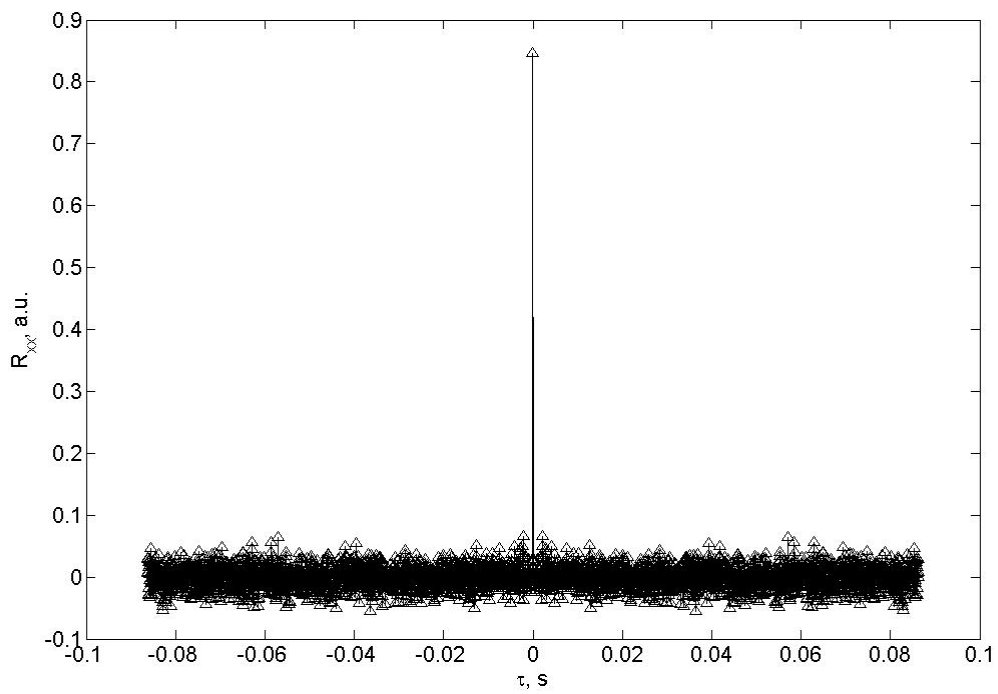


**Figure 3.33. Autocorrelation of Gaussian noise with no interpolation as computed with the slot correlation.**

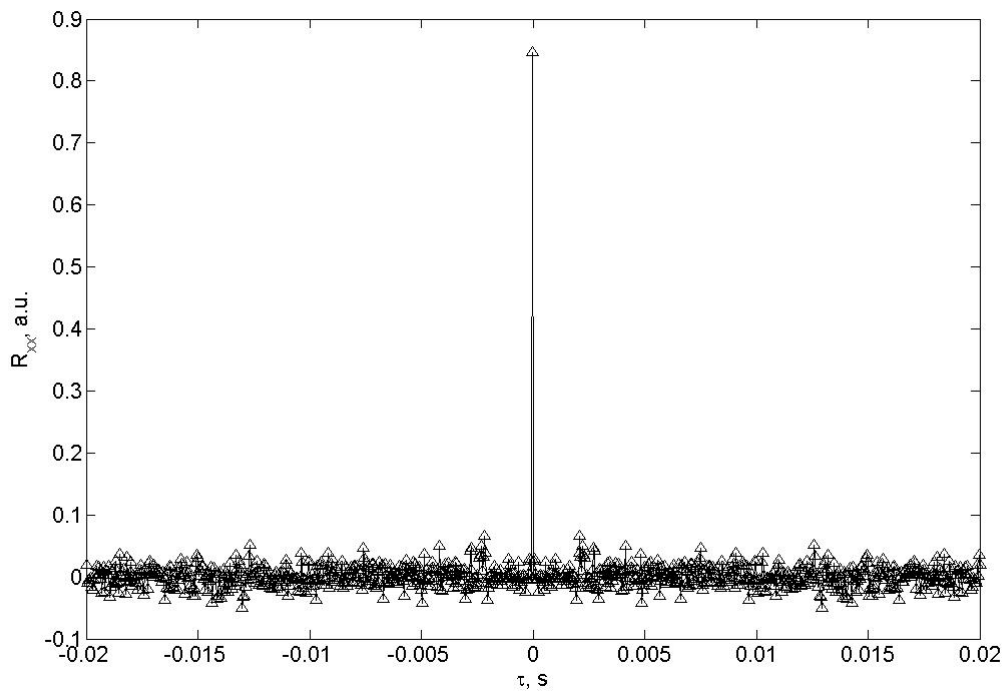


**Figure 3.34. Autocorrelation of Gaussian noise with no interpolation near zero delay as computed with the slot correlation.**

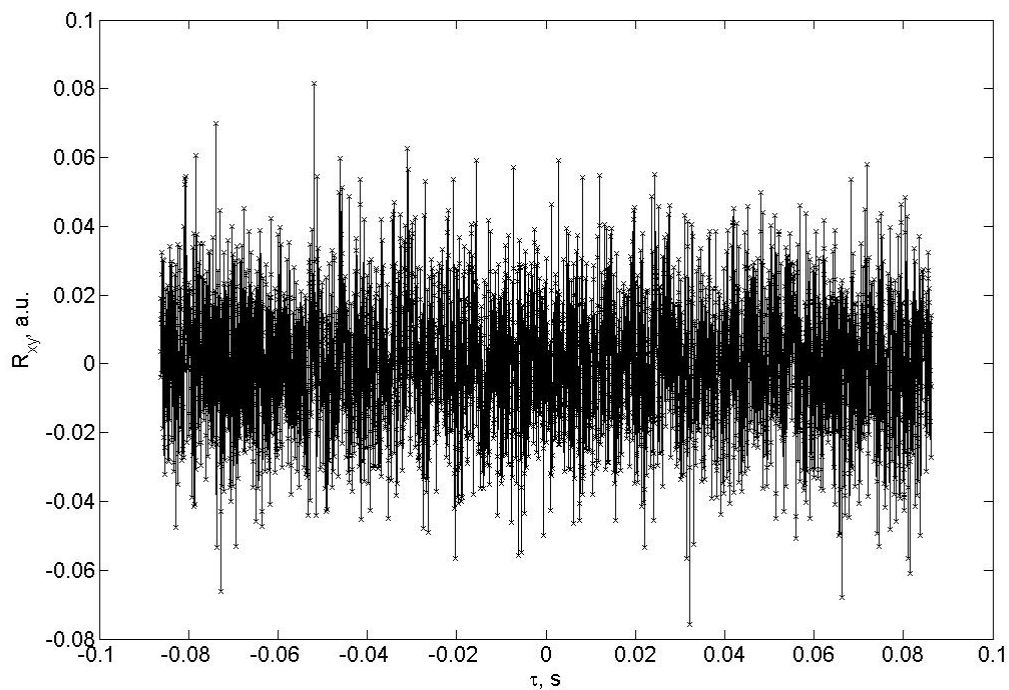


**Figure 3.35. Cross-correlation of two Gaussian noise signals with no interpolation as computed with the slot correlation.**

### 3.3 References

Adrian, R.J. and Yao, C.S. 1987, "Power spectra of fluid velocities measured by laser-Doppler velocimetry," *Exp. Fluids* **5**, pp. 17-28.

Albrecht, H.-E., Borys, M. Damaschke, N., and Tropea, C. 2002 *Laser-Doppler and Phase Doppler Measurement Techniques* Springer-Verlag, New York.

Benedict, L.H., Nobach, H., and Tropea, C. 2000. "Estimation of turbulent velocity spectra from laser-Doppler data," *Meas. Sci. Tech.* **11**, pp. 1089-1104.

Boashash, B. 1992, *Time-Frequency Signals Analysis: Methods and Applications*, Halsted Printing.

Coates, P.B. 1972, "Photomultiplier noise statistics," *J. Phys. D: Appl. Phys.*, Vol. 5, 915-930.

Czarske, J. W. 2001, "Statistical frequency measuring error of the quadrature demodulation technique for noisy single-tone pulse signals," *Meas. Sci. Tech.* **12**, pp. 597-614.

Døssing, O. 1998 “Uncertainty in time/frequency domain representations: How accurately can we know when and how often?” *Sound and Vibration*, January, pp. 14-24.

Harris, F.J. 1978, “On the use of windows for harmonic analysis with the discrete Fourier transform,” *Proc. IEEE*, Vol. 66, No. 1, pp. 51-83.

Lehmann, B., Nobach, H., and Tropea, C. 2002, “Measurement of Acceleration Using the Laser-Doppler Technique,” *Measurement Science and Technology* 13, 1367-1381.

Lehmann, P. 1998, “Determination of Doppler frequencies and characteristic frequency modulation phenomena in laser-Doppler signals,” *Proc. 9<sup>th</sup> Int. Symp. On Appl. Of Laser Techn. To Fluid Mech.*, Lisbon, Portugal, July, paper 32.3.

Mayo, W.T. Jr., Shay, M.T., and Ritter, S. 1974, “Digital estimation of turbulence power spectra from burst counter LDV data,” *Proc. 2<sup>nd</sup> Int. Workshop on Laser Velocimetry, Purdue University*, pp. 16-26.

Müller, E., Nobach, H., and Tropea C. 1998, “Model parameter estimation from non-equidistant sampled data sets at low data rates,” *Meas. Sci. Technol.* 9, pp. 435–41.

Nobach, H. 2002a "Analysis of dual-burst laser-Doppler signals", *Meas. Sci. Technol.* 13, pp.33-44.

Nobach, H. 2002b “Local time estimation for the slotted correlation function of randomly sampled LDA data,” *Exp. Fluids* 32, pp. 337-345.

Nobach, H., Müller, E. and Tropea C. 1998, “Efficient estimation of power spectral density from laser-Doppler anemometer data,” *Exp. Fluids* 24 pp. 499–509.

Nobach, H. and vanMaanen, H.R.E. 2001, “LDA and PDA signal analysis using wavelets,” *Exp. Fluids* 30, pp. 613-625.

Qui, H-H., Sommerfeld, M., and Durst, F. 1994 “Two novel Doppler signal detection methods for laser-Doppler and phase Doppler anemometry,” *Measurement Science and Technology* 5, 769-778.

Shinpaugh, K.A., Simpson, R.L., Wicks, A.L., Ha, S.M., and Fleming, J.L. 1992, “Signal-processing techniques for low signal-to-noise ratio laser-Doppler velocimetry signals,” *Experiments in Fluids*, Vol. 12, pp 319-328.

Tummers, M.J. and Passchier, D.M. 1996, “Spectral estimation using a variable window nad the slotting technique with local normalization,” *Meas. Sci. Tech.* 7, 1541-1546.

vanMaanen, H.R.E. 1999, “Retrieval of turbulence and turbulence properties from randomly sampled laser –Doppler anemometry data with noise,” Dissertation, T.U. Delft, Netherlands.

vanMaanen, H.R.E., Nobach, H., and Benedict, L.H. 1999, "Improved estimator for the slotted autocorrelation function of randomly sampled LDA data," *Meas. Sci. Tech.* **10**, L4-7.

Whalen, A.D., 1971, *Detection of Signals in Noise*, Academic Press, New York.

## 4 Results

In this chapter, we examine results obtained using the CompLDV instrumentation in turbulent boundary layers. Several flows of fundamental interest have been examined and the measurements have yielded important results for better understanding these flows. The goals of this chapter are two-fold. First it is hoped that the reader gains an appreciation for the depth of information that is available when applying the CompLDV to turbulent flows. Second, the results give insight into flow phenomena that have only been fully-examined by DNS or in some cases not at all, and we wish to comment on these insights herein.

The information in this chapter is broken down into the different flows examined using the CompLDV. Within each of the flow cases, many different measurement quantities are considered, including measurement-volume-averaged velocity statistics, near-wall spatially-resolved velocity statistics, spectral results, velocity-acceleration statistics, Reynolds stress transport, and velocity gradient statistics. For each of these cases, previous work may be referenced that give representative results for similar flow cases, although many of the results to be presented are completely novel at the Reynolds numbers examined.

### 4.1 2D flat-plate turbulent boundary layers

The 2D flat-plate turbulent boundary layer (2DFPTBL) is the most-basic of TBL flows. In this flow a boundary layer is formed on the surface of a flat plate and the flow undergoes no mean pressure gradients in any direction. Analyses are possible in the near-wall region of the flow that lead to a few relationships that are thought to hold for all flat-plate TBLs. First, we may consider the momentum equation in the nearest-to-wall region.

Since all the flow velocities are zero directly on the wall, the convective terms are also zero there and in a flow without pressure gradients as in this one, the Navier-Stokes equations reduce to

$$\frac{1}{\rho} \left( \frac{\partial \tau_x}{\partial y} \right)_{y=0} = 0 \quad (4.1)$$

where  $\tau_x$  is the shear stress in the flow. The mean shear stress for this particular flow consists of the Newtonian viscous shear stress from the mean velocity gradient and the turbulent Reynolds shear stress from the Reynolds-averaged Navier-Stokes (RANS) equations:

$$\overline{\tau_x} = \mu \frac{\partial \overline{U}}{\partial y} - \overline{\rho uv} \quad (4.2)$$

Thanks to the no-slip condition, the turbulent stresses are necessarily zero at the wall, and the shear stress at the wall is exactly

$$\overline{(\tau_x)}_{wall} = \mu \left( \frac{\partial \overline{U}}{\partial y} \right)_{wall} \quad (4.3)$$

While this equation is valid directly on the wall, it is unclear how the contributions from the Reynolds shear stress will vary just above the wall. To further consider this, we may obtain the Taylor series expansions for the fluctuating velocities in the very near-wall region following the discussion by Simpson (2003) or Pope (2000):

$$\begin{aligned} u &= a_1 + b_1 y + c_1 y^2 + O(y^3) \\ v &= a_2 + b_2 y + c_2 y^2 + O(y^3) \\ w &= a_3 + b_3 y + c_3 y^2 + O(y^3) \end{aligned} \quad (4.4)$$

The constants  $a_1$ ,  $a_2$ , and  $a_3$  are all necessarily zero due to the no-slip condition and the non-penetration condition. Thanks to the no-slip condition also, the  $u$  and  $w$  velocities do not change anywhere on the surface so that

$$\left( \frac{\partial u}{\partial x} \right)_{wall} = \left( \frac{\partial u}{\partial z} \right)_{wall} = \left( \frac{\partial w}{\partial x} \right)_{wall} = \left( \frac{\partial w}{\partial z} \right)_{wall} = 0 \quad (4.5)$$

Now considering the continuity equation at the wall,

$$\left( \frac{\partial u}{\partial x} \right)_{wall} + \left( \frac{\partial v}{\partial y} \right)_{wall} + \left( \frac{\partial w}{\partial z} \right)_{wall} = 0 \quad (4.6)$$

we obtain the important result that

$$\left( \frac{\partial v}{\partial y} \right)_{wall} = 0 \quad (4.7)$$

This indicates that the term  $b_2$  in equations (4.4) is also zero to satisfy continuity at the wall. Then equation (4.4) to leading order becomes

$$\begin{aligned} u &\sim b_1 y \\ v &\sim c_2 y^2 \\ w &\sim b_3 y \end{aligned} \quad (4.8)$$

These results may now be used to estimate the near-wall variation of the Reynolds stresses as

$$\begin{aligned} \overline{u^2} &\sim \overline{b_1^2} y^2 \\ \overline{v^2} &\sim \overline{c_2^2} y^4 \\ \overline{w^2} &\sim \overline{b_3^2} y^2 \\ \overline{uv} &\sim \overline{b_1 c_2} y^3 \end{aligned} \quad (4.9)$$

We now see that  $\frac{\partial \overline{uv}}{\partial y} \sim y^2$  and thus changes slowly in the vicinity of the wall. This

important result indicates that there is a significant region of flow near the wall where only viscous shear stress exists. This region is known as the viscous sublayer and is characterized by a constant velocity gradient and thus a linear profile in the mean velocity.

It is now convenient to obtain the velocity and length scales that are indicative of this near-wall flow. As the discussion has indicated, this region of the flow is dominated by the wall shear and the action of the velocity gradient through the viscosity. An appropriate velocity scale based upon the wall shear may be proposed based upon dimensional analysis of the wall-shear and fluid density,

$$\tau_w \equiv \rho u_\tau^2 \quad (4.10)$$

Thus the wall friction velocity,  $u_\tau = \sqrt{\frac{\tau_w}{\rho}} = \sqrt{\nu \left( \frac{\partial U}{\partial y} \right)_{wall}}$ . The other parameter needed

for scaling is the viscosity, for which the kinematic viscosity is chosen to account for fluid density. The length scale for this region of the flow then becomes

$$\delta_\nu = \frac{\nu}{u_\tau} \quad (4.11)$$

The linear portion of the sublayer in dimensional terms is given as

$$U = y \left( \frac{\partial U}{\partial y} \right)_{wall} \quad (4.12)$$

We now apply the wall friction velocity and viscous length scale to obtain

$$U^+ = y^+ \quad (4.13)$$

where  $U^+ \equiv U/u_\tau$  and  $y^+ \equiv y/\delta_\nu$ .

The linear portion of the sublayer has been shown by Spalart (1988) as well as DeGraaff and Eaton (2000) to extend to approximately  $y^+=4$ , although it remains a good approximation for even larger values of  $y^+$ .

In another region where  $y^+$  is significantly greater than for the upper limits of the viscous sublayer, there exists a region in which a scaling transition must transpire, such that both viscous wall-scaling and outer flow boundary layer thickness scaling holds. Two prominent arguments exist for obtaining the correct functional relationships for this region due to von Kármán (1930) and Millikan (1938), but both are based upon dimensional analysis and the existence of a region where two length-scales are simultaneously valid. The analytical result for this region is a logarithmic variation in the velocity profile, given as

$$U^+ = \frac{1}{\kappa} \ln y^+ + B \quad (4.14)$$

where  $\kappa$  and  $B$  are empirical constants. Coles' values for these constants are most-often used for 2DFPTBLs,  $\kappa = 0.41$ ,  $B = 5.0$  (Coles 1956).

Beyond these fundamental developments for the mean velocity profile in the 2DFPTBL, significant work has been conducted to better-understand the turbulence structure in this flow. The pioneering work of Klebanoff (1956) in which he used hot-wires and all-analog equipment to obtain velocity time derivatives and two-point correlations that lead to robust estimates of velocity gradients throughout most of the 2DFPTBL at  $Re_\theta \approx 7300$  has stood the test of time as a standard reference for the turbulent kinetic energy (TKE) dissipation rate in this flow. A key conclusion from Klebanoff's work was that significant

anisotropies in the dissipation rate exist near the wall and must be modeled for proper computations. The low-Reynolds number 2DFPTBL direct numerical simulation (DNS) of Spalart (1988) revealed much about the behavior of this flow in the very-near-wall region, where the viscous-dominated flow is very similar for a wide-range of Reynolds numbers. Since the work of Spalart was a full simulation, direct estimates of the complete Reynolds stress transport budgets were obtained and the role of anisotropies in the turbulence structure was examined. In particular, valuable data for the velocity/pressure gradient correlation, a key term in the Reynolds stress transport that requires much effort from the modeling community (Pope 2000), was obtained. This term is responsible for distributing turbulence energy from the Reynolds stresses that are being produced by the mean velocity gradients to those normal-stress components that have no means of production. The results of Spalart indicate that in the log-layer, the velocity/pressure gradient correlations draw energy from the stream-wise normal-stress at twice the rate of the dissipation.

Similar studies to Klebanoff's were repeated with elaborate hot-wire arrangements by Balint et al. (1991) and Honkan and Andreopoulos (1997) among others. These studies measured all-nine components of the velocity gradient tensor in low Reynolds number turbulent boundary layer flows, but with probe-sizes that were several times the Kolmogorov length scales in the low Reynolds number flows. The data showed good agreement with the data of Spalart (1988) for a relatively small portion of the boundary layer that was reported, in the region of  $20 < y^+ < 80$ . The spectral distributions of the vorticity (enstrophy) were also examined and revealed a persistence of high-energy modes to higher wave-numbers than in the case of the velocity fluctuations.

#### 4.1.1 CompLDV Measurements

Four different Reynolds numbers for the 2DFPTBL have been measured using the CompLDV technologies. The parameters for the flows measured are given in Table 4.1.

**Table 4.1. Flow parameters for the 2DFPTBLs measured for the current study.**

$Re_\theta$	$U_\infty, \text{m/s}$	$u_\tau, \text{m/s}$	$\delta, \text{mm}$	$\theta, \text{mm}$	$\delta^*$	$H \equiv \delta^* / \theta$	$\delta_v, \mu\text{m}$	Instrument
4113	13.78	0.537	39.9	4.96	6.82	1.375	30.7	C3
5929	21.00	0.777	39.5	4.70	6.44	1.370	21.2	C3
7497	27.95	1.022	39.0	4.46	6.00	1.345	16.1	C3
6350	26.86	1.032	38.0	3.9	5.1	1.31	16.0	C1

##### 4.1.1.1 The near-wall region

As discussed in Chapter 2, the CompLDV3 has powerful position-resolution capabilities that enable a detailed examination of phenomena that change rapidly in space. One possibility for utilizing these capabilities is in obtaining sub-measurement-volume profiles of velocity statistics in the 2DFPTBLs being studied. In the plots to follow for the Reynolds-averaged velocity statistics, dimensional plotting has been used so that the reader may gain an appreciation for the spatial scales that are being resolved. In these plots, five vertical positions of the measurement volume are used to obtain all the results.

Each symbol on the plot represents about 10 microns of vertical distance in the flow, so that the spatial resolution of these statistics is on that order.

The near-wall position-resolved ComplDV3 data are very valuable for determining the skin friction. As discussed briefly in Chapter 2, the skin friction for smooth walls can be obtained by using the nearest-wall data for the parallel-to-wall velocities. Fitting these data to the rigorous viscous sublayer equations (Rotta 1962; Tang 2004; Durst et al. 1995)

$$\begin{aligned} U &= \frac{\tau_{wx}}{\mu} y + \frac{1}{2\mu} \left. \frac{\partial P}{\partial x} \right)_{wall} y^2 + C_U y^4 \\ W &= \frac{\tau_{wz}}{\mu} y + \frac{1}{2\mu} \left. \frac{\partial P}{\partial z} \right)_{wall} y^2 + C_W y^4 \end{aligned} \quad (4.15)$$

where  $U$  and  $W$  are mean velocities in the plane parallel to the wall,  $\mu$  is the dynamic viscosity of the fluid,  $\left. \frac{\partial P}{\partial x} \right)_{wall}$  and  $\left. \frac{\partial P}{\partial z} \right)_{wall}$  are the mean wall pressure gradients,  $C_U = f \left\{ \frac{\partial^3 (\overline{uv})}{\partial y^3} \right\}$ , and  $C_W = f \left\{ \frac{\partial^3 (\overline{vw})}{\partial y^3} \right\}$ . This is observed to yield reliable shear stress estimates for  $y^+ < 9$  (Tang 2004).

The fit of equation (4.15) for the nearest-wall data were used to obtain the skin-friction velocities in Table 4.1, and to obtain the wall velocity gradients plotted in Figure 4.1-Figure 4.3 for the three Reynolds numbers measured with the ComplDV3. As may be noted, there is excellent agreement between these nearest-wall data and the linear sublayer relationship equivalent to equation (4.13).

In addition to the mean-velocity position-resolved profiles, the Reynolds stresses are also resolved within the measurement volume. These results are given in Figure 4.4-Figure 4.9 for the normal and shear stresses for each of the Reynolds numbers measured with the ComplDV3. These measurements are the most-highly-spatially-resolved measurements for these quantities at these flow scales that exist anywhere to the author's knowledge.

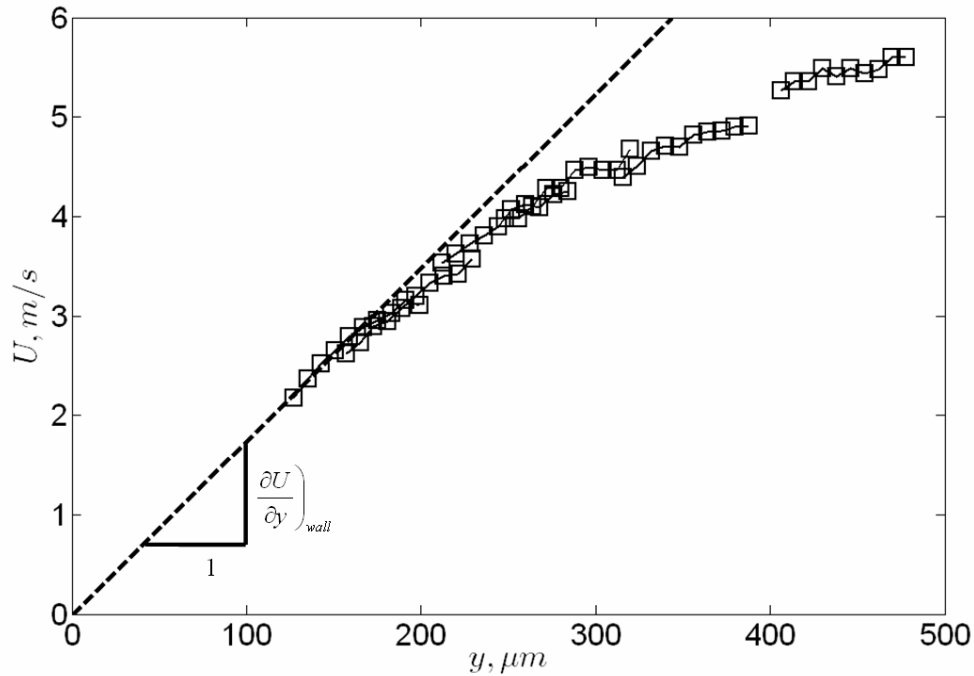


**Figure 4.1.** Resolved measurements of the stream-wise mean velocity in the 2DFPTBL at  $Re_\theta = 4113$ .

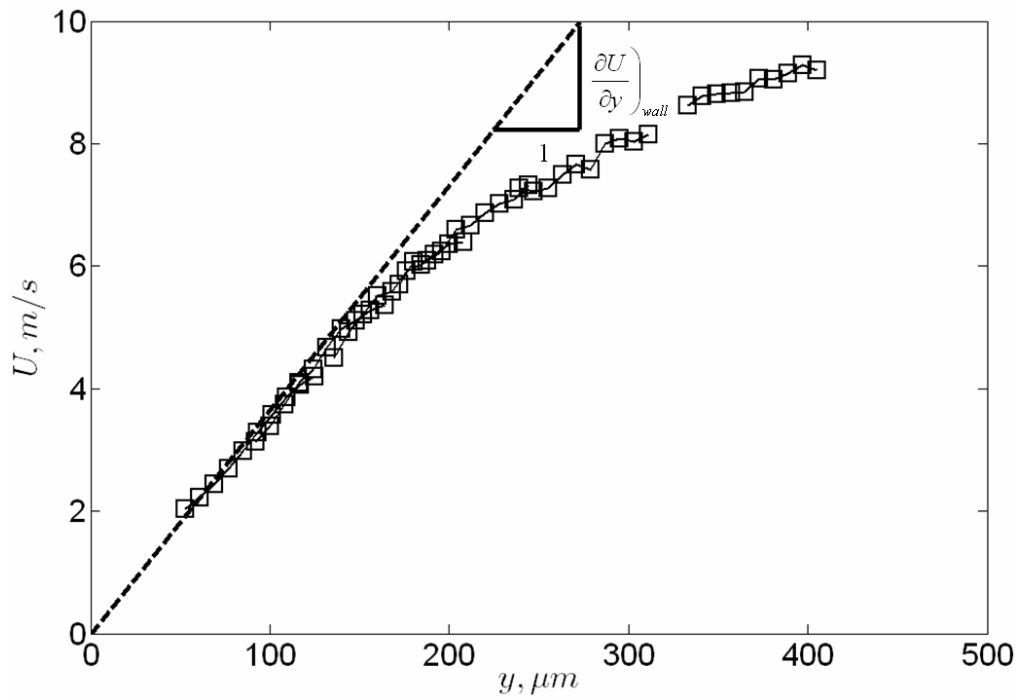


**Figure 4.2.** Resolved measurements of the stream-wise mean velocity in the 2DFPTBL at  $Re_\theta = 5929$ .

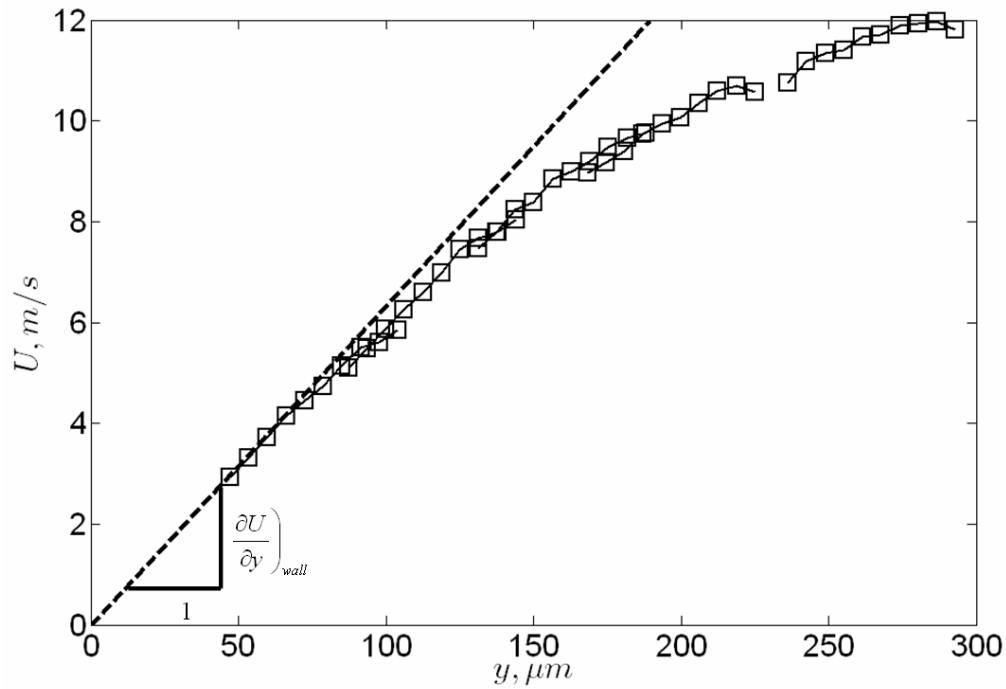


Figure 4.3. Resolved measurements of the stream-wise mean velocity in the 2DFPTBL at  $Re_\theta = 7497$ .

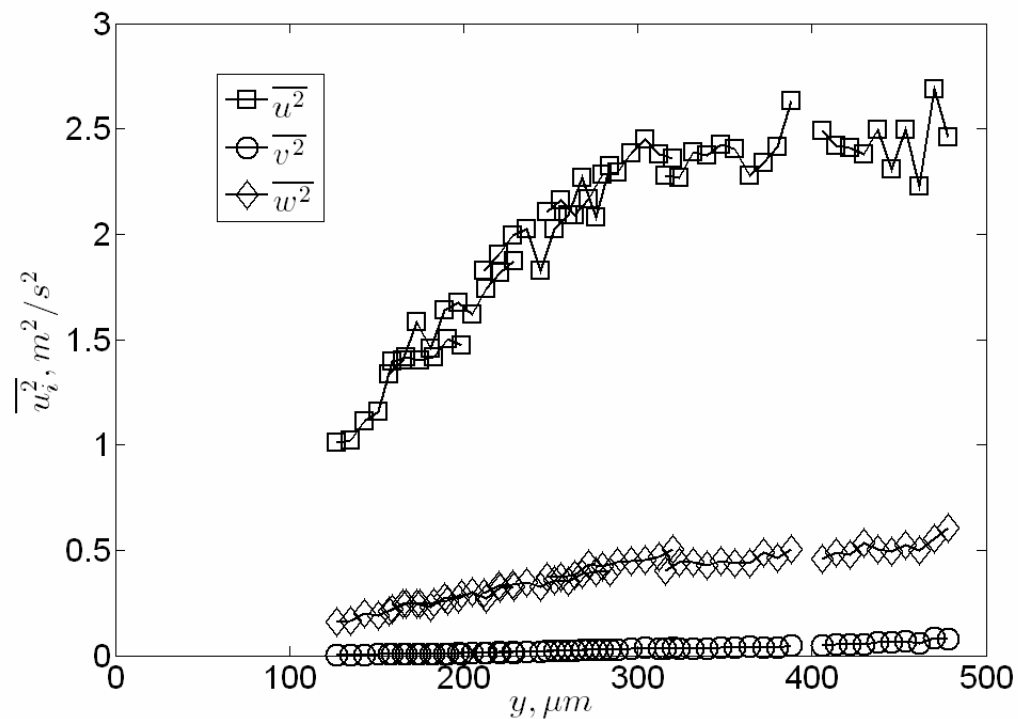


Figure 4.4. Resolved measurements of the Reynolds normal stresses in the 2DFPTBL at  $Re_\theta = 4113$ .

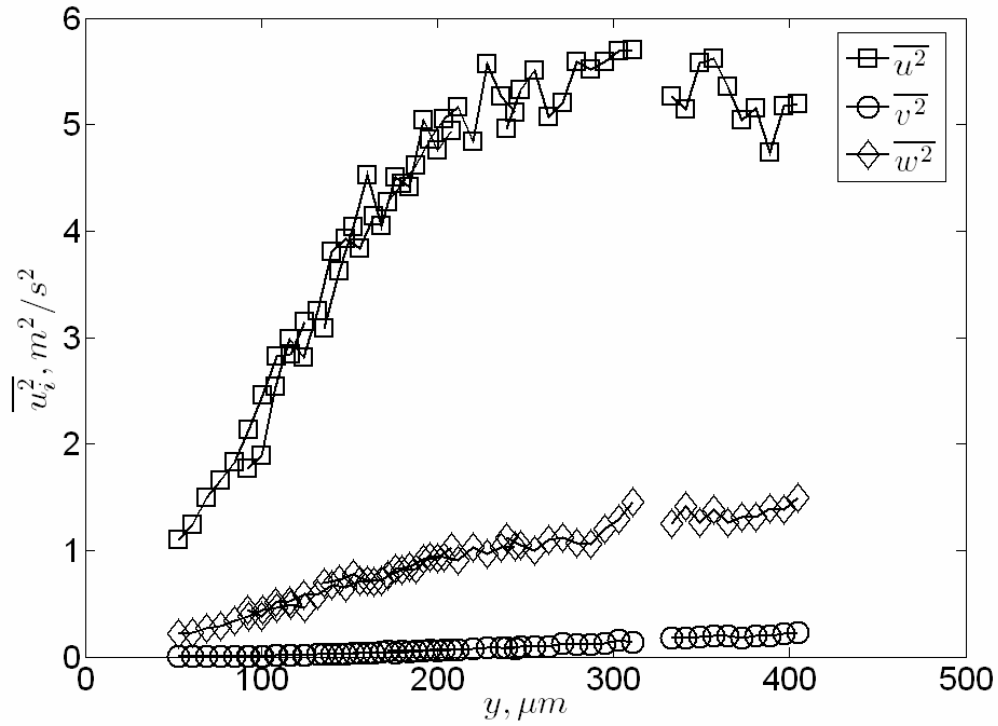


Figure 4.5. Resolved measurements of the Reynolds normal stresses in the 2DFPTBL at  $Re_\theta = 5929$ .

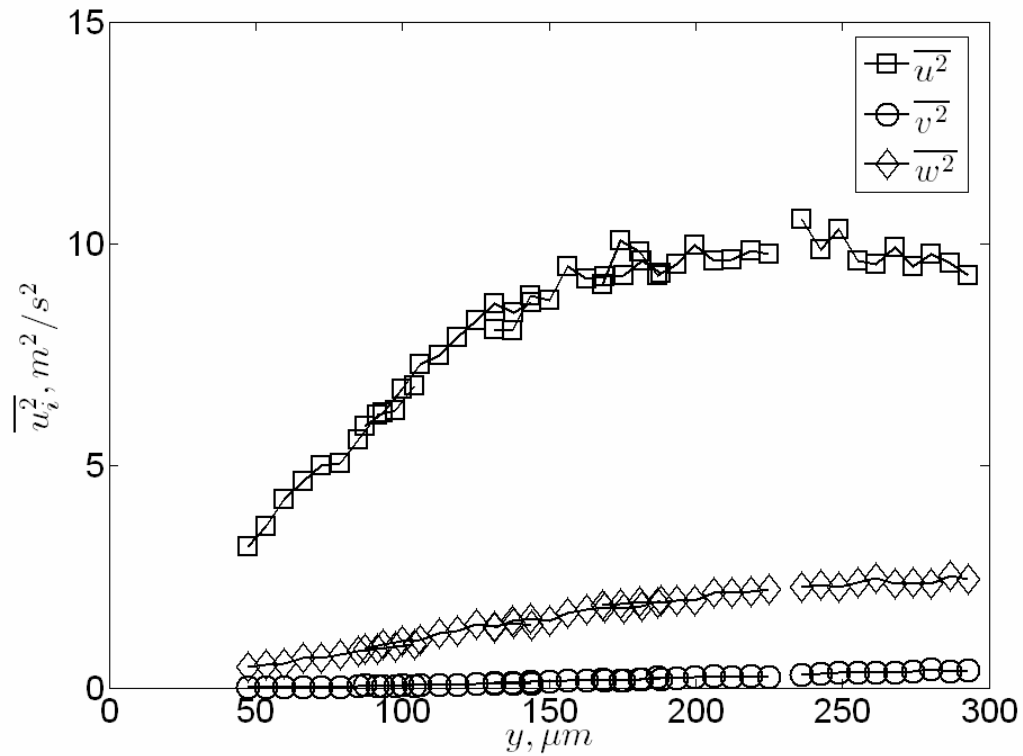
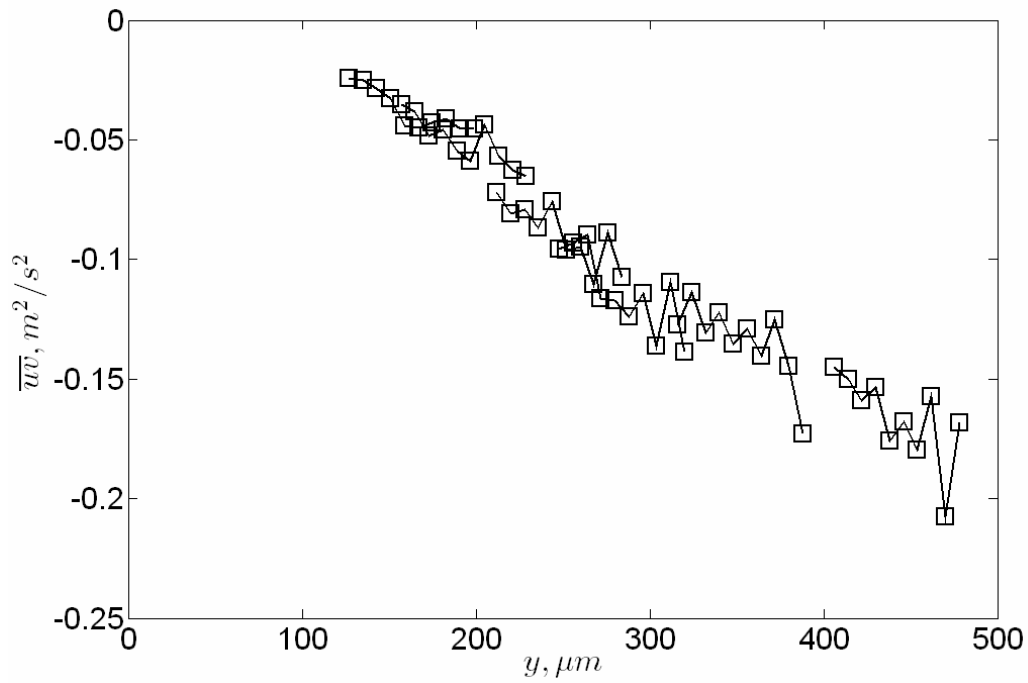
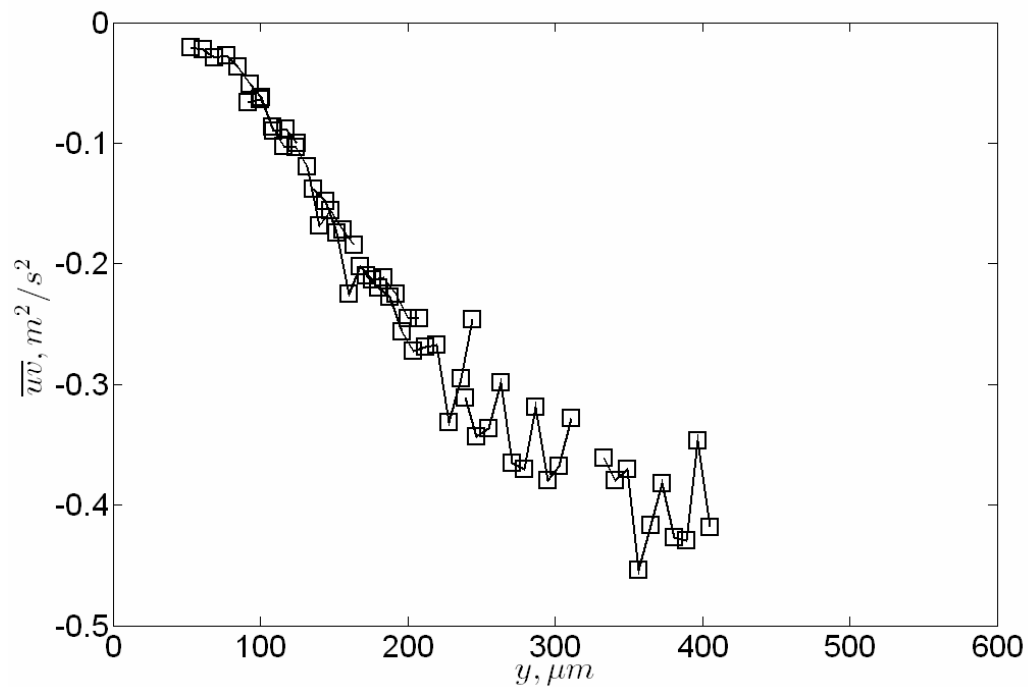


Figure 4.6. Resolved measurements of the Reynolds normal stresses in the 2DFPTBL at  $Re_\theta = 7497$ .



**Figure 4.7.** Resolved measurements of the Reynolds normal stresses in the 2DFPTBL at  $Re_\theta = 4113$ .



**Figure 4.8.** Resolved measurements of the Reynolds normal stresses in the 2DFPTBL at  $Re_\theta = 5929$ .

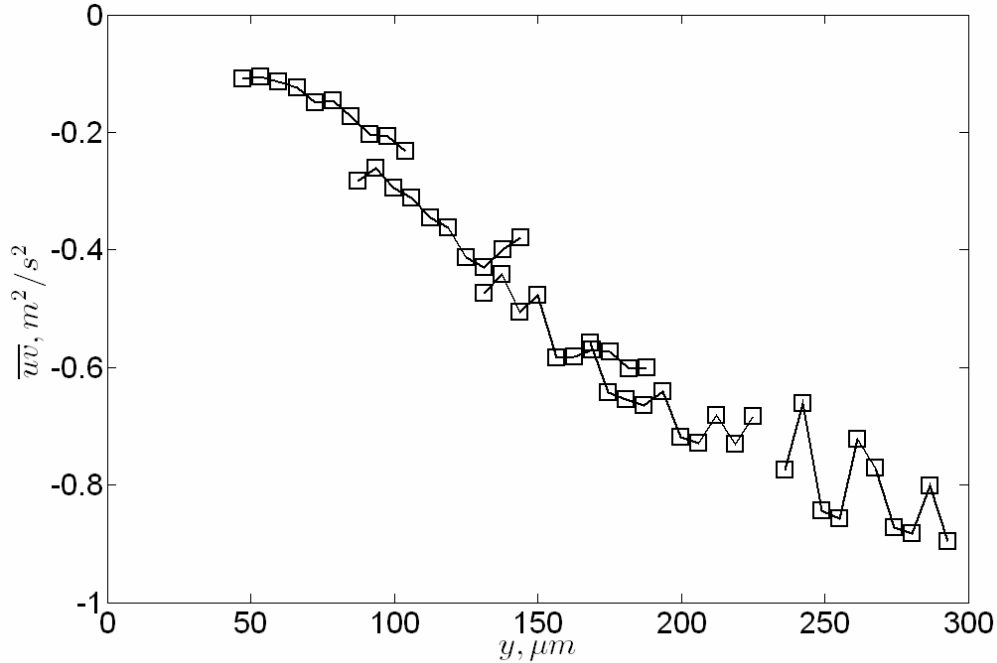


**Figure 4.9. Resolved measurements of the Reynolds normal stresses in the 2DFPTBL at  $Re_\theta = 7497$ .**

#### 4.1.2 Volume-averaged velocity statistics

To obtain full-profiles of data for comparisons to previous results, volume-averaged statistics were compiled. In the case of the CompLDV3 results to be presented, the option of limiting the spatial extent of the measurement volume existed due to the position resolution of the measurements. In order to get fully-converged statistics at all points, it was decided to limit the measurement volume diameter to about 100 microns, since this spatial range still contains a sufficient number of velocity estimations for converged statistics. By allowing volume-averaging, the aspect of velocity-gradient broadening must be considered and applied. In general, the velocity gradient broadening for a Reynolds stress term may be extended from the work of Durst et al. (1995) to obtain

$$\overline{\Delta u_i u_j} = \frac{d^2}{12} \frac{\partial U_i}{\partial y} \frac{\partial U_j}{\partial y} \quad (4.16)$$

where  $\overline{\Delta u_i u_j}$  is the apparent turbulence measured due to the velocity gradients. For all the volume-averaged measurements presented, this correction has been subtracted from the raw data to obtain the best-estimate for the velocity statistics.

The stream-wise velocity data are plotted on viscous wall-scaling in Figure 4.10. The data exhibit excellent agreement with this scaling out to very high values of  $y^+$ , as expected for these Reynolds numbers. A comparison to an independent data set of DeGraaff and Eaton (2000) for the stream-wise velocities is given in Figure 4.11—again with excellent agreement among the data sets. The Reynolds normal stresses are

compared in Figure 4.12-Figure 4.14. The Reynolds shear stress scales relatively well on wall variables as seen in Figure 4.15.

As many other researchers have noted, a failure of collapse among the Reynolds numbers for all except the nearest-wall data is evident in the peak-region of the stream-wise normal stress. In the present work, this is also seen to be the case in the span-wise normal stress which obeys similar near-wall functional relationships as discussed in section 4.1. To improve this situation, DeGraaff and Eaton have proposed the use of a mixed scaling

parameter,  $u_\tau U_\infty = \frac{\sqrt{C_f/2}}{u_\tau^2}$  for the stream-wise normal stress. The present data is plotted

with those of DeGraaff and Eaton in Figure 4.16 using the mixed scaling. Further, the span-wise normal stress is plotted with the same scaling in Figure 4.17. Both these plots exhibit excellent collapse of the data for  $y^+ < 50$ . This improvement has been achieved by recognizing the role of the Reynolds number in the peak-value of the Reynolds normal stresses parallel to the wall.

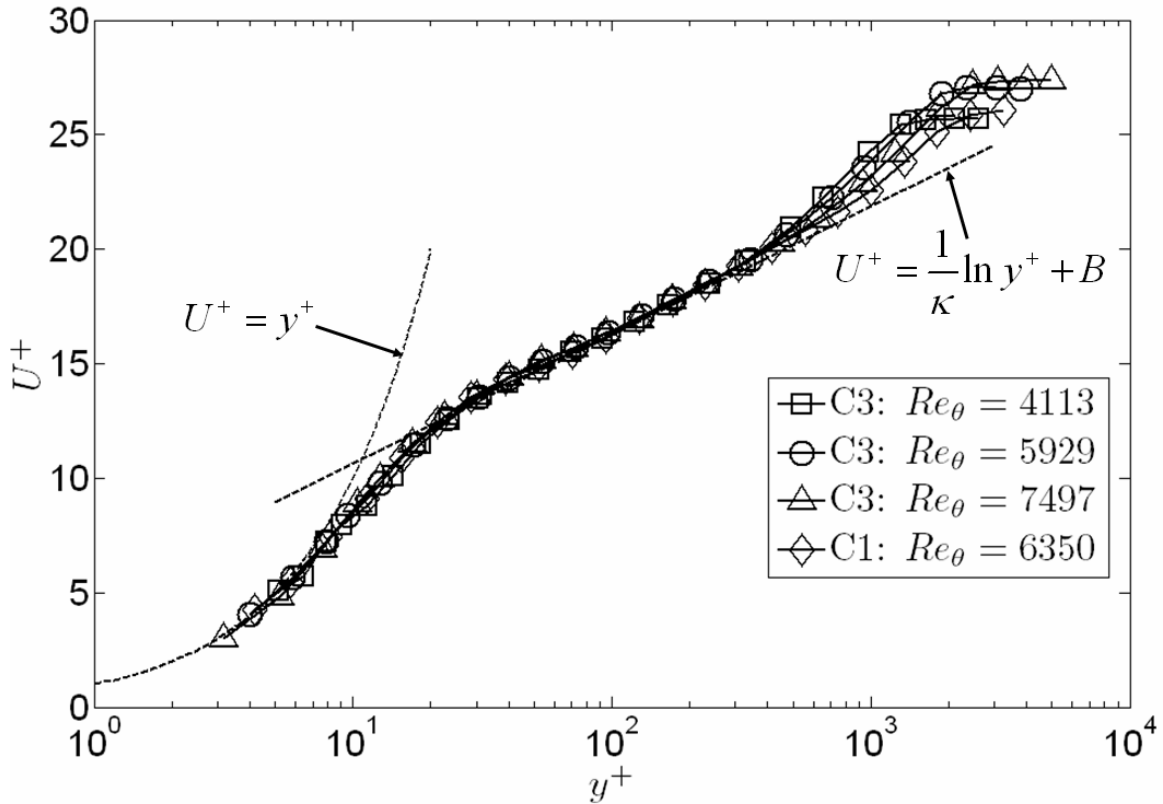


**Figure 4.10. Stream-wise mean velocities in the 2DFPTBL at four Reynolds numbers. C1: Measurements acquired with the ComplDV1; C3: Measurements acquired with the ComplDV3.**

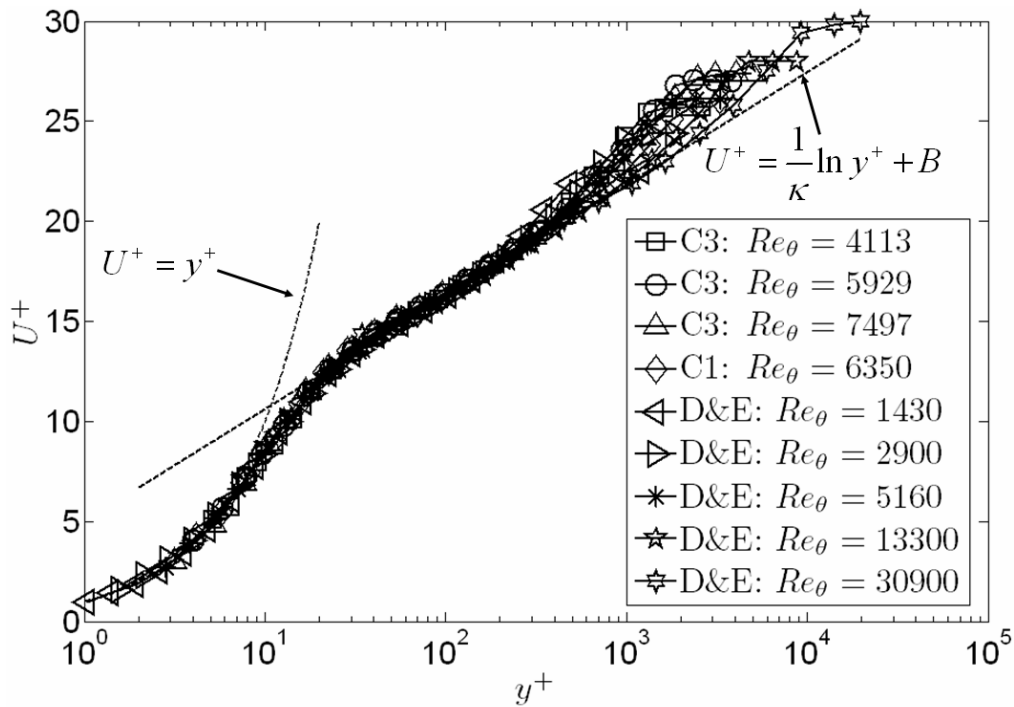


**Figure 4.11. Comparison of the stream-wise mean velocities in the 2DFPTBL compared to the results of DeGraaff and Eaton (2000). C1: Measurements acquired with the ComplDV1; C3: Measurements acquired with the ComplDV3; D&E: measurements reported by DeGraaff and Eaton (2000).**

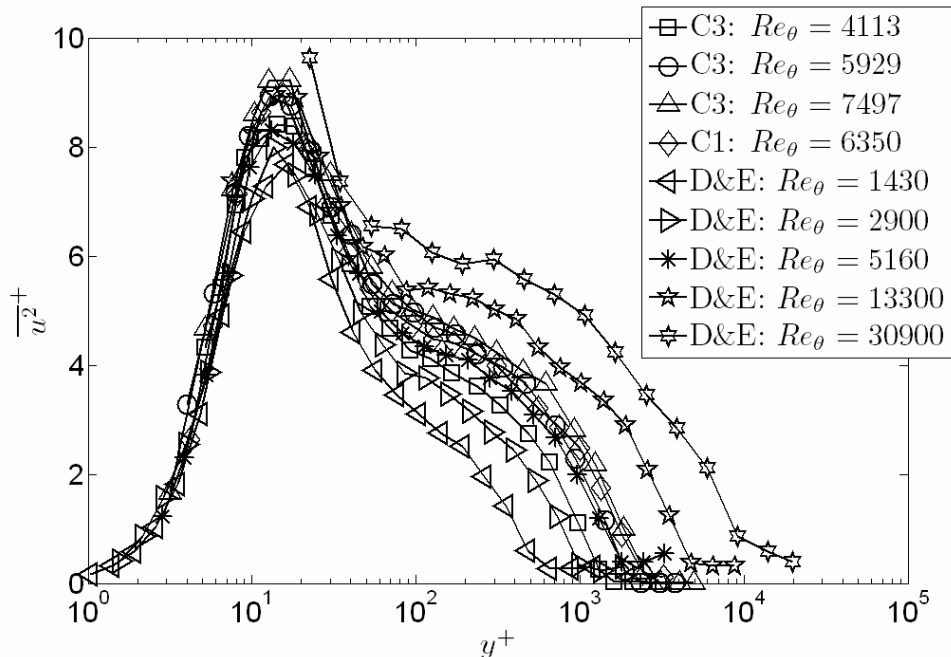


**Figure 4.12. Comparison of the stream-wise Reynolds stress in the 2DFPTBL compared to the results of DeGraaff and Eaton (2000). C1: Measurements acquired with the ComplDV1; C3: Measurements acquired with the ComplDV3; D&E: measurements reported by DeGraaff and Eaton (2000).**

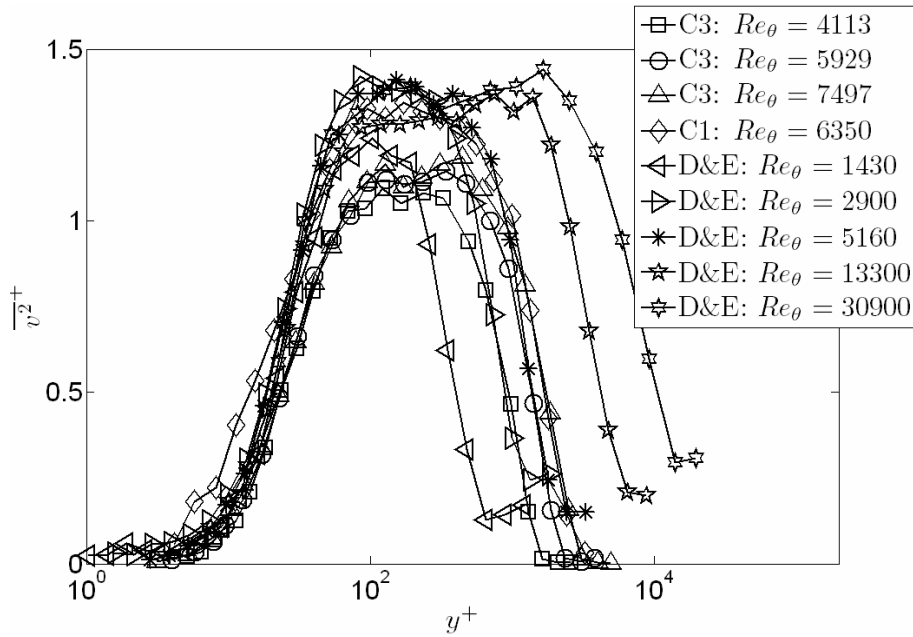


**Figure 4.13. Comparison of the normal-to-wall Reynolds stress in the 2DFPTBL compared to the results of DeGraaff and Eaton (2000). C1: Measurements acquired with the ComplDV1; C3: Measurements acquired with the ComplDV3; D&E: measurements reported by DeGraaff and Eaton (2000).**

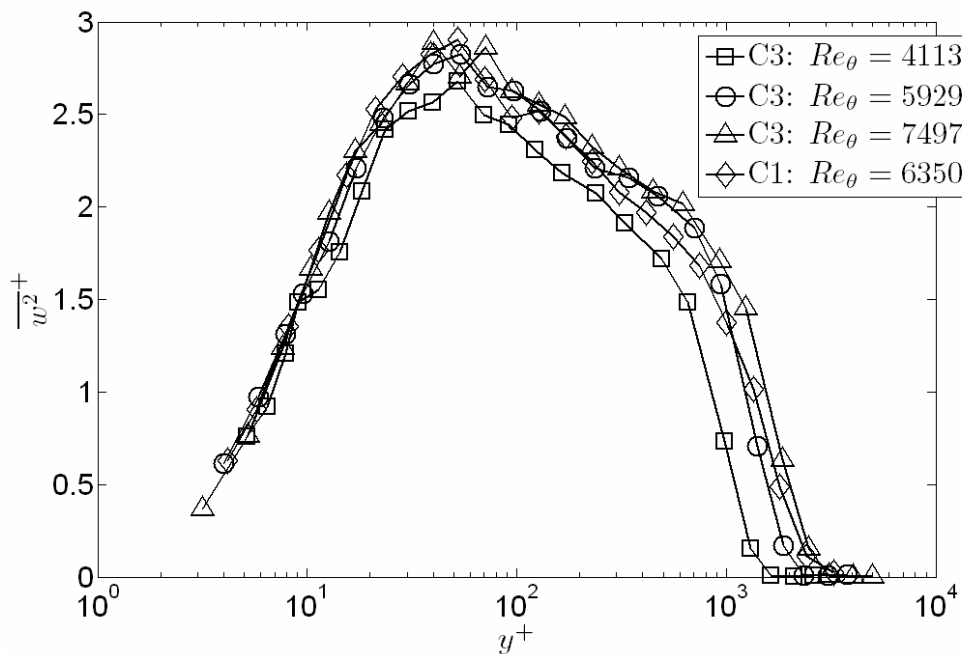


**Figure 4.14. Span-wise Reynolds stress in the 2DFPTBL at four Reynolds numbers. C1: Measurements acquired with the ComplDV1; C3: Measurements acquired with the ComplDV3.**

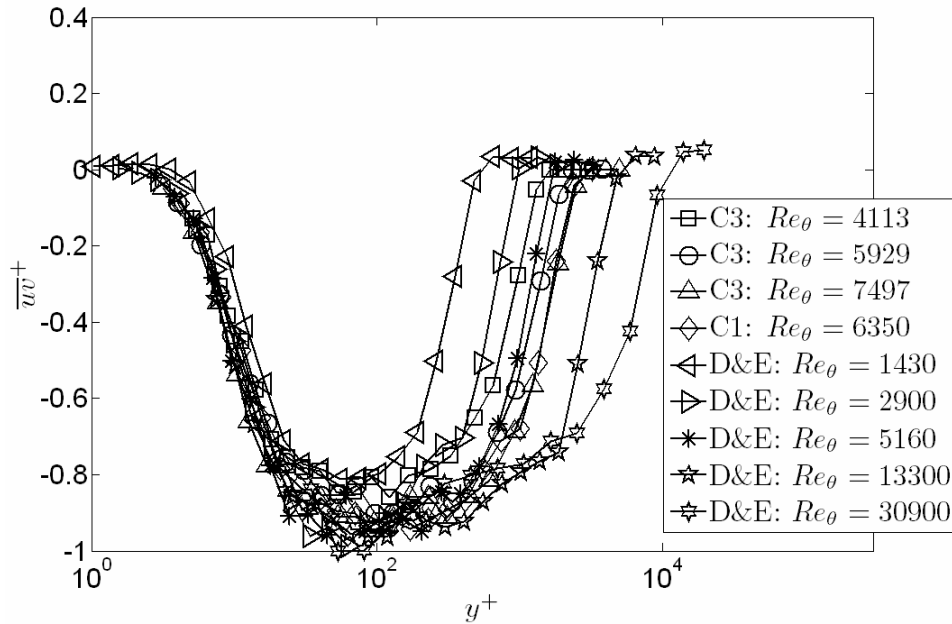


**Figure 4.15. Comparison of the Reynolds shear stress in the 2DFPTBL compared to the results of DeGraaff and Eaton (2000). C1: Measurements acquired with the CompLDV1; C3: Measurements acquired with the CompLDV3; D&E: measurements reported by DeGraaff and Eaton (2000).**

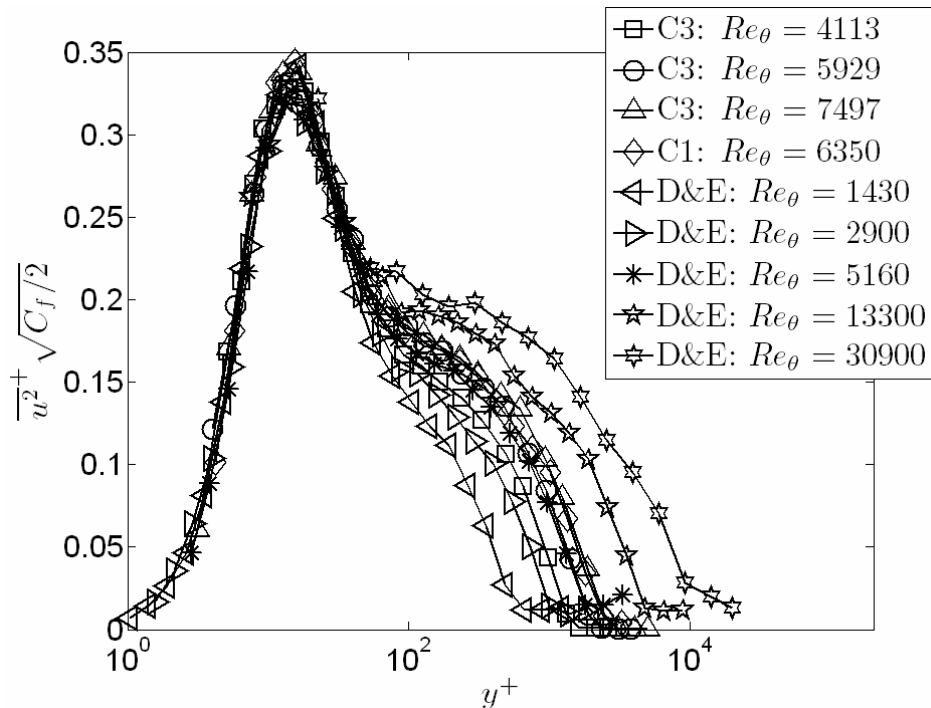


**Figure 4.16. Comparison of the stream-wise Reynolds normal stress in the 2DFPTBL compared to the results of DeGraaff and Eaton (2000) with mixed scaling to account for Reynolds number effects. C1: Measurements acquired with the CompLDV1; C3: Measurements acquired with the CompLDV3; D&E: measurements reported by DeGraaff and Eaton (2000).**

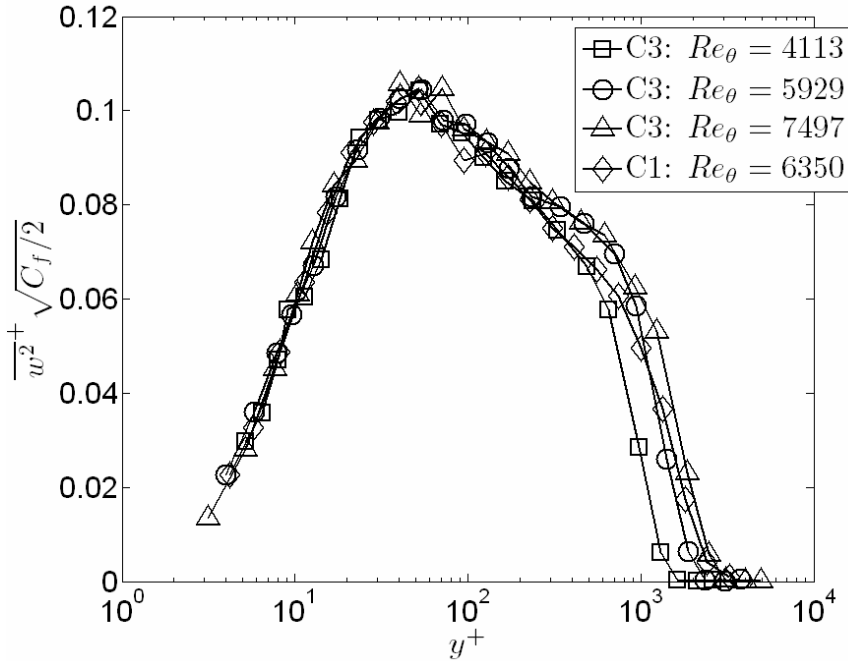


**Figure 4.17. Span-wise Reynolds normal stress in the 2DFPTBL with mixed scaling to account for Reynolds number effects. C1: Measurements acquired with the CompLDV1; C3: Measurements acquired with the CompLDV3; D&E: measurements reported by DeGraaff and Eaton (2000).**

### 4.1.3 Spectral analysis

Typical all-channel-coincident average data rates for the CompLDV systems in the log-layer and above range from 20-50kHz in the low-speed facilities used. These data give information content on a wide range of time-scales since contiguous sampling is done in lots of 0.54s and these lots of data contain information at frequencies even higher than the average data rate, as discussed in section 3.2. To analyze these data, spectral analysis is considered in this section by obtaining the auto- and cross-spectra of velocity fluctuations in the 2DFPTBL.

The velocity frequency spectrum may be defined as

$$E_{ij}(\omega) = \frac{1}{\pi} \int_{-\infty}^{\infty} R_{ij}(\tau) \exp(-i\omega\tau) d\tau \quad (4.17)$$

where  $R_{ij}(\tau)$  is the time-delay correlation of variables  $u_i$  and  $u_j$ ,  $\omega$  is the angular frequency, and  $\tau$  is the time-delay. The spectrum has the property that

$$\overline{u_i u_j} = \int_0^{\infty} |E_{ij}(\omega)| d\omega \quad (4.18)$$

so that the total energy in the spectrum equals the covariance of the fluctuations forming the spectrum.

The frequency content of velocity fluctuations may be interpreted to give several results. The most fundamental of these is the universal-equilibrium results of Kolmogorov (1991) that states that all fully-turbulent flows of sufficient Reynolds number contain a universal ‘inertial subrange’ for which the cascade of turbulence energy through the scales of motion is dominated entirely by the flow dissipation rate. Further, Kolmogorov asserted that in the same circumstances there must also exist a universal function for the cascade of turbulence energy in extremely high wave-numbers that is determined entirely by the viscosity and the dissipation rate. These postulates may be described as the condition of ‘local isotropy’ and form a universal similarity in the velocity spectra cascade for all turbulent flows of ‘sufficient Reynolds number’ and ‘sufficiently far from flow boundaries’. The result of these assertions is the famous Kolmogorov  $-5/3$  spectra:

$$E_{11}(\kappa_1) = C_1 \varepsilon^{2/3} \kappa_1^{-5/3} \quad (4.19)$$

where  $\kappa_1$  is the wave-number in the  $x_1$  direction and  $C_1$  is a ‘universal’ constant. For comparison to the frequency spectrum already discussed, Taylor’s hypothesis may be invoked as an approximation to convert the wave-number to a frequency by the following relationship

$$\kappa_1 \approx \frac{\omega}{2\pi U_1} \quad (4.20)$$

While the Kolmogorov relationship in equation (4.19) is one of the firmest foundations in all of turbulence research and is evoked often for the purpose of modeling and analysis, two key aspects limit its use in the turbulent boundary layer, particularly near-walls. First and foremost, the requirement of being ‘sufficiently far from boundaries’ is inherently violated through some region of the *boundary layer*. Second, the universality of equation (4.19) is in question as it has been discovered that it is likely no-flows are fully-turbulent by the strictest definition, as intermittency of dissipation occurs (see for example Pope 2000, pp. 255-262). While the later shortcoming results in small deviations from the predictions of local-isotropy and may be generally compensated by additional hypotheses, it nonetheless reveals the limitations of a ‘universal’ description in the field of turbulence research.

Despite the discrepancies resulting from internal intermittency just discussed, the concept of local-isotropy is still effective away from boundaries. The working-applicability of this concept was assessed in the outer-regions of turbulent boundary layers by Saddoughi and Veeravalli (1994). They explored the spectral distributions of all three simultaneously-measured velocity components in the outer-layer of very high Reynolds number 2DFPTBLs and found substantial evidence for local-isotropy over significant wave-number ranges, even in the presence of the inherently anisotropic mean shear stress.

Lumley (1967) has derived a power-law similar to the Kolmogorov spectrum but for cross-spectra for Reynolds shear stresses. The universal functional form follows when considering the dimensional scaling of the cross-spectrum with the mean strain rate and the dissipation rate in a wave-number range of overlap between the Kolmogorov scales and the strain rate scales. The result is

$$E_{12}(\kappa_1) = -C_{12} S \varepsilon^{1/3} \kappa_1^{-7/3} \quad (4.21)$$

where  $C_{12}$  is a ‘universal’ constant and  $S$  is the mean strain rate in the flow.

A frequency-based analog to the wave-number scaling of Perry et al. (1985) has been used to present the velocity spectral data for the first three cases in Table 4.1. This scaling is based upon a conceptual model for the coherent structures within the boundary layer. The idea presented is that of an attached-eddy concept where it is surmised that some region of the velocity spectrum is dominated by eddies with a size-scale on the order of the distance from the wall. Extensive data at three-different Reynolds numbers using this scaling is presented in Figure 4.18-Figure 4.29. Significant regions of the stream-wise Reynolds normal stress collapse for all three Reynolds numbers for heights above  $y^+ = 20$ . Regions of the Kolmogorov  $(-5/3)$  power law are present more apparently in the two higher-Reynolds-number cases than in the lowest Reynolds number case where the slope for the subrange is greater than  $(-5/3)$ . The  $(-1)$  slope in the plots is derived based upon the turbulence production due to the presence of a mean velocity gradient (Tchen 1953). A region within each of the stream-wise normal stress spectra exhibits a  $(-1)$  slope for the lower-frequencies. The span-wise normal stress spectra scale similarly as the stream-wise. The normal-to-wall spectra do not scale as well using these parameters, particularly nearer the wall.

The shear stress cross-spectra exhibit the  $(-7/3)$  slope for high frequencies, and the collapse of the data using the wall-scaling is excellent, which may be expected in a coherent-structure-based model since it is known that coherent structures are responsible for the shear stresses in this flow (Robinson 1991).

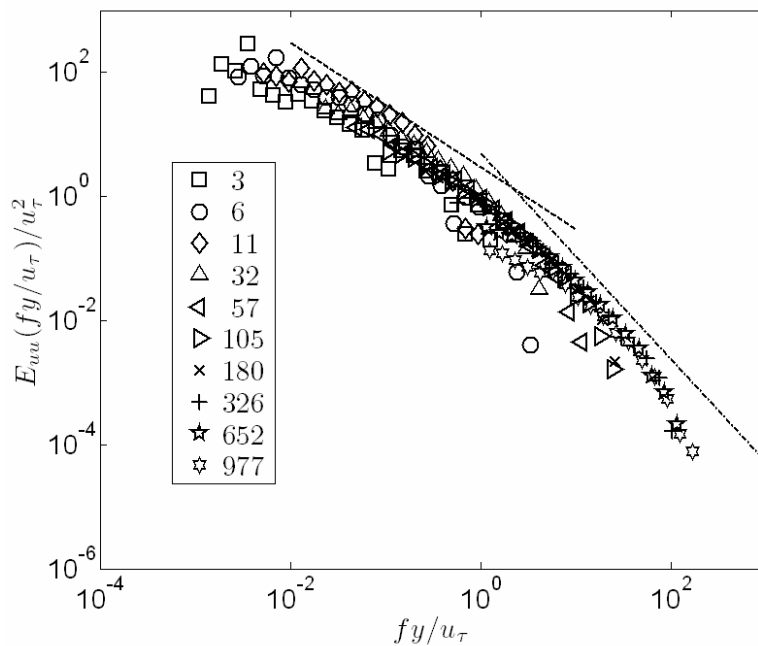


**Figure 4.18.** Energy spectra on viscous wall scaling for the stream-wise Reynolds normal stress in the 2DFPTBL at  $Re_\theta = 4113$ . The legend gives vertical locations in  $y^+$ . The lines in the plot are at slopes  $\sim f^{-1}$  and  $\sim f^{-5/3}$ .

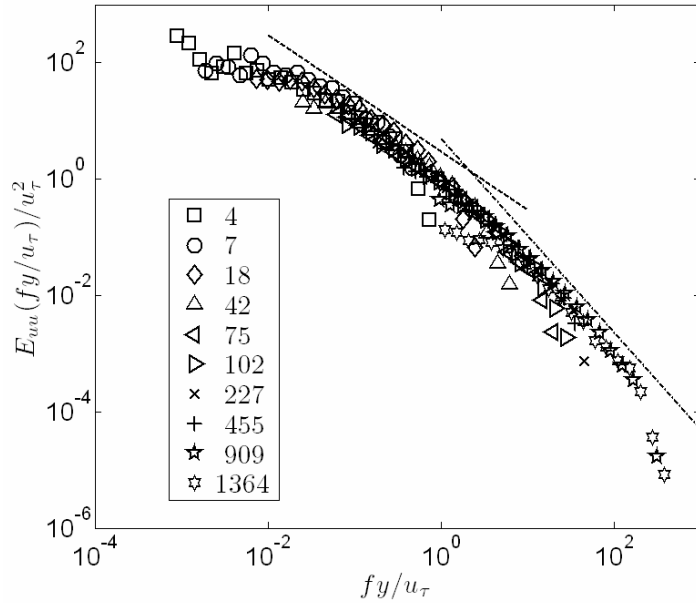


**Figure 4.19.** Energy spectra on viscous wall scaling for the stream-wise Reynolds normal stress in the 2DFPTBL at  $Re_\theta = 5929$ . The legend gives vertical locations in  $y^+$ . The lines in the plot are at slopes  $\sim f^{-1}$  and  $\sim f^{-5/3}$ .

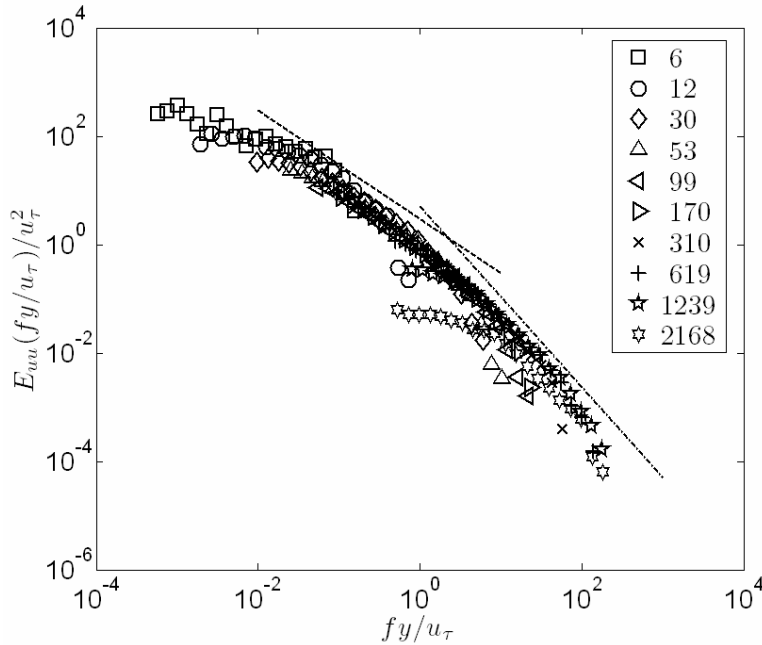


**Figure 4.20.** Energy spectra on viscous wall scaling for the stream-wise Reynolds normal stress in the 2DFPTBL at  $Re_\theta = 7497$ . The legend gives vertical locations in  $y^+$ . The lines in the plot are at slopes  $\sim f^{-1}$  and  $\sim f^{-5/3}$ .

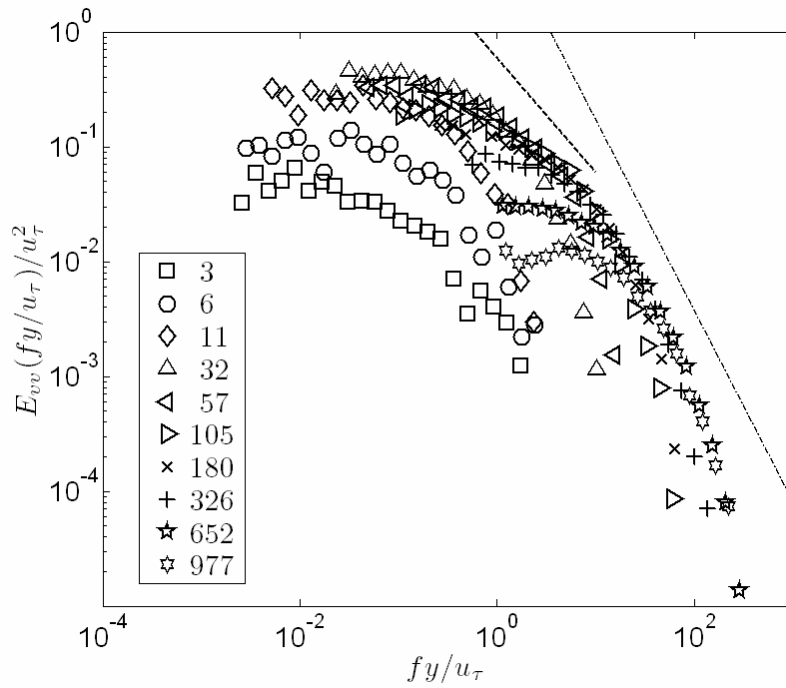


**Figure 4.21.** Energy spectra on viscous wall scaling for the normal-to-wall Reynolds normal stress in the 2DFPTBL at  $Re_\theta = 4113$ . The legend gives vertical locations in  $y^+$ . The lines in the plot are at slopes  $\sim f^{-1}$  and  $\sim f^{-5/3}$ .

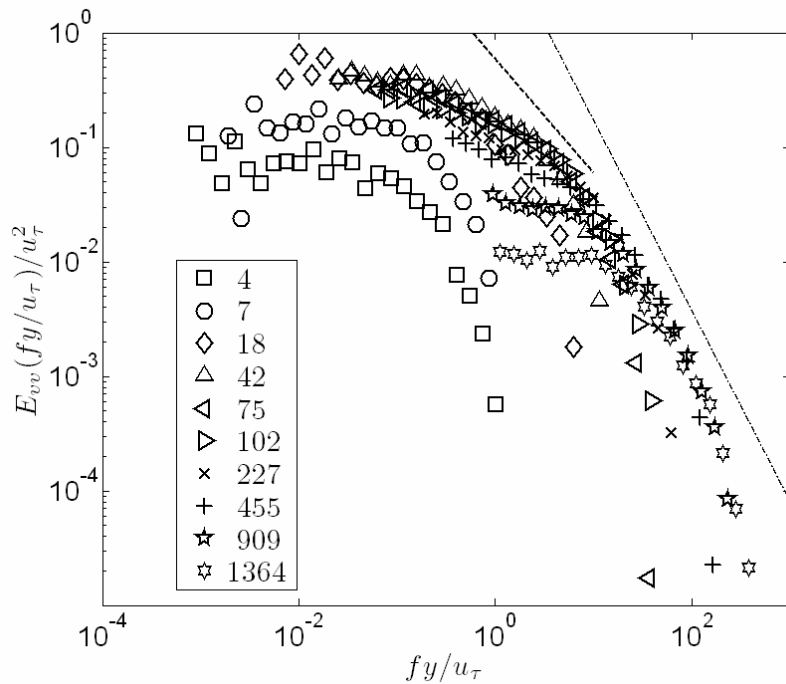


**Figure 4.22.** Energy spectra on viscous wall scaling for the normal-to-wall Reynolds normal stress in the 2DFPTBL at  $Re_\theta = 5929$ . The legend gives vertical locations in  $y^+$ . The lines in the plot are at slopes  $\sim f^{-1}$  and  $\sim f^{-5/3}$ .

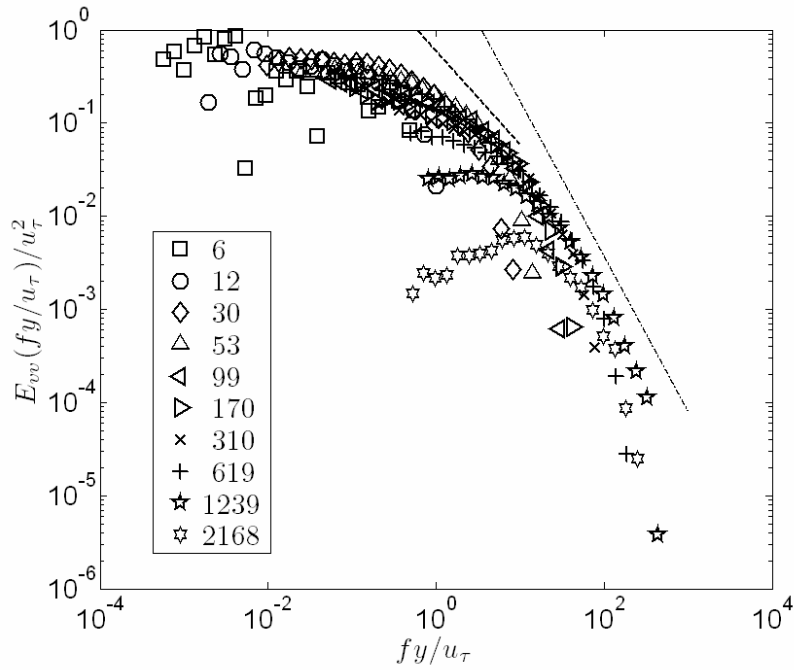


**Figure 4.23.** Energy spectra on viscous wall scaling for the normal-to-wall Reynolds normal stress in the 2DFPTBL at  $Re_\theta = 7497$ . The legend gives vertical locations in  $y^+$ . The lines in the plot are at slopes  $\sim f^{-1}$  and  $\sim f^{-5/3}$ .

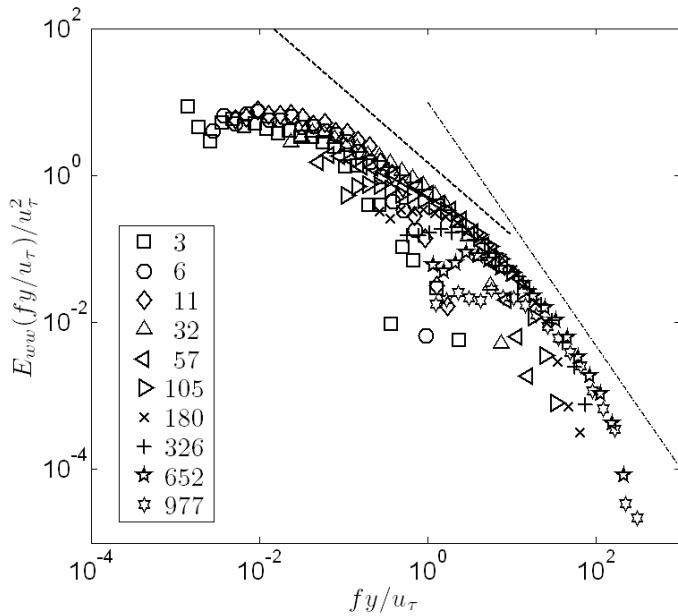


**Figure 4.24.** Energy spectra on viscous wall scaling for the span-wise Reynolds normal stress in the 2DFPTBL at  $Re_\theta = 4113$ . The legend gives vertical locations in  $y^+$ . The lines in the plot are at slopes  $\sim f^{-1}$  and  $\sim f^{-5/3}$ .

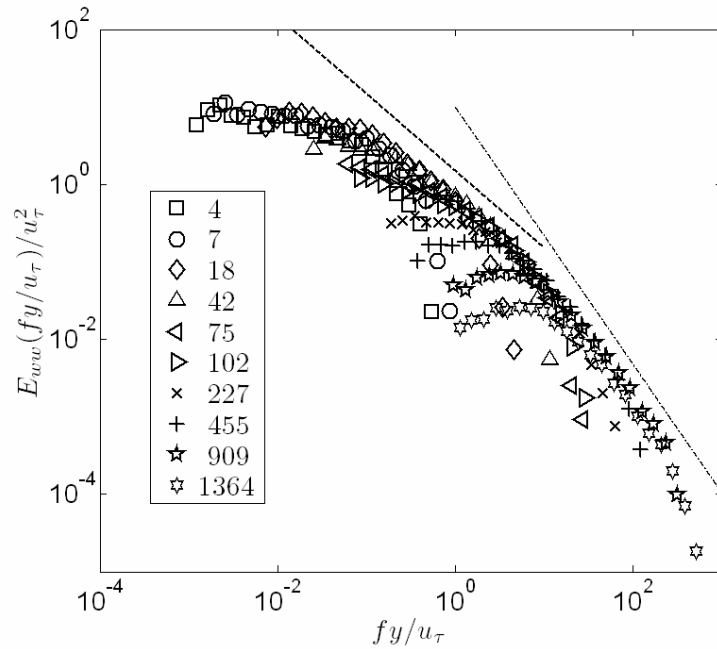


**Figure 4.25.** Energy spectra on viscous wall scaling for the span-wise Reynolds normal stress in the 2DFPTBL at  $Re_\theta = 5929$ . The legend gives vertical locations in  $y^+$ . The lines in the plot are at slopes  $\sim f^{-1}$  and  $\sim f^{-5/3}$ .

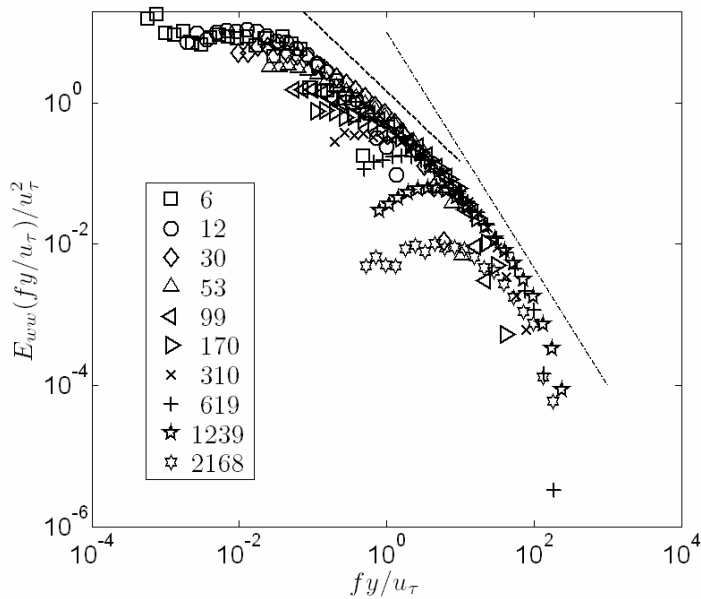


**Figure 4.26.** Energy spectra on viscous wall scaling for the span-wise Reynolds normal stress in the 2DFPTBL at  $Re_\theta = 7497$ . The legend gives vertical locations in  $y^+$ . The lines in the plot are at slopes  $\sim f^{-1}$  and  $\sim f^{-5/3}$ .

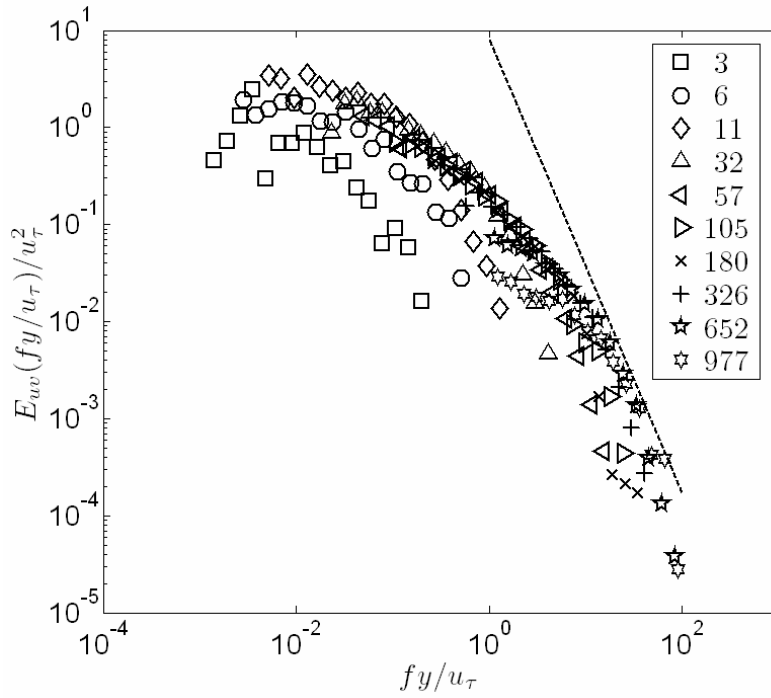


**Figure 4.27.** Energy spectra on viscous wall scaling for the Reynolds shear stress in the 2DFPTBL at  $Re_\theta = 4113$ . The legend gives vertical locations in  $y^+$ . The line in the plot is at a slope of  $\sim f^{7/3}$ .

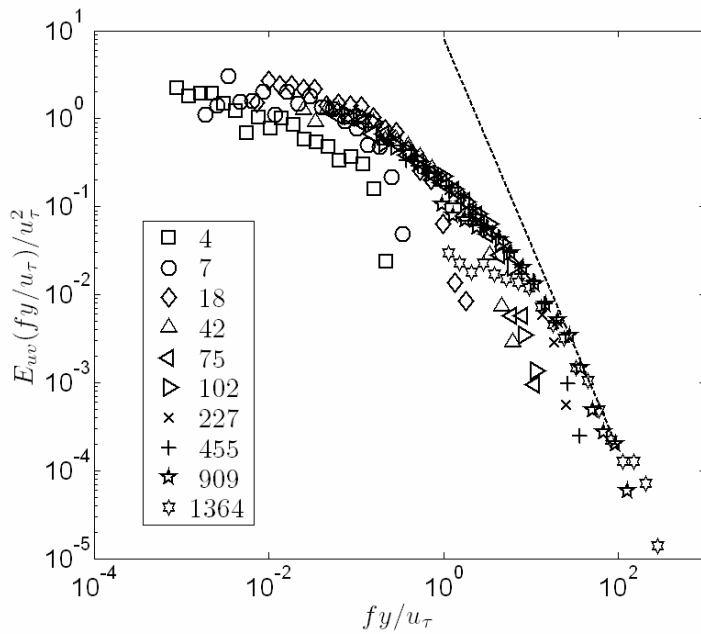


**Figure 4.28.** Energy spectra on viscous wall scaling for the Reynolds shear stress in the 2DFPTBL at  $Re_\theta = 5929$ . The legend gives vertical locations in  $y^+$ . The line in the plot is at a slope of  $\sim f^{7/3}$ .

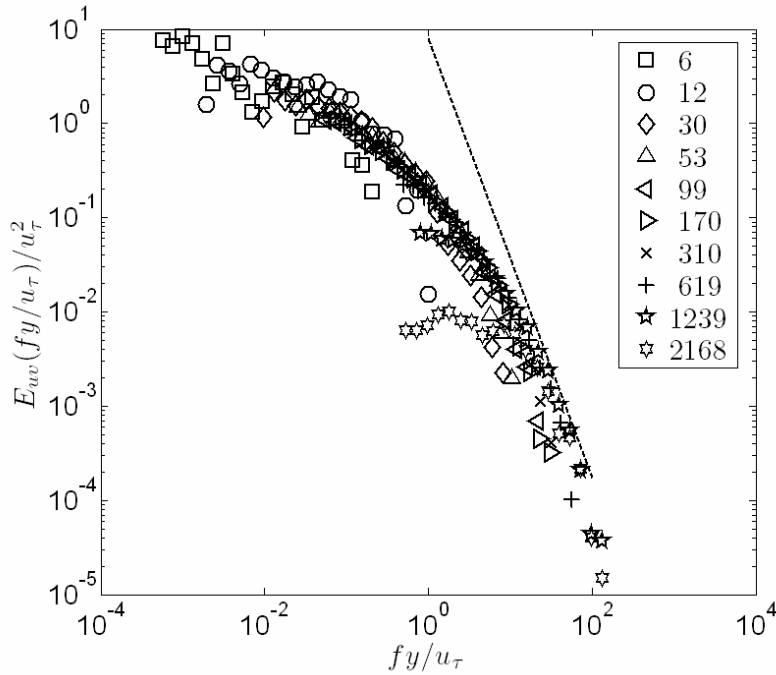


**Figure 4.29. Energy spectra on viscous wall scaling for the Reynolds shear stress in the 2DFPTBL at  $Re_\theta = 7497$ . The legend gives vertical locations in  $y^+$ . The line in the plot is at a slope of  $\sim f^{7/3}$ .**

#### 4.1.3.1 Reynolds shear stress coherency

The velocity spectral data may be used to obtain spectral coherency information. The coherency is a sort of correlation coefficient in the frequency domain and may be defined as

$$\gamma_{ij}^2 \equiv \frac{|E_{ij}|^2}{E_{ii}E_{jj}} \quad (4.22)$$

where no summing is employed. This information is quite rich, as Ha and Simpson (1993) and Saddoughi and Veeravali (1994) have discussed. The coherency function has a maximum range of  $[0 \ 1]$  and indicates what fraction of turbulence motion is being correlated to produce shear stresses in the frequency ranges measured.

The coherency data for the Reynolds shear stress,  $\overline{uv}$ , in the 2DFPTBL are given in Figure 4.30-Figure 4.32 for three Reynolds numbers. In frequency regions where the coherency is very low, it may be regarded that the turbulence energy in those regions is uncorrelated and simple modeling may be used to account for the energy there. This is particularly useful in large-eddy simulation (LES) studies, where a decision must be made as to what range of scales to simulate directly while leaving the remaining high wave-numbers to be modeled. The coherency data presented herein indicate that a significant amount of the shear-stress-producing motions happen at frequencies lower

than  $f\nu/u_\tau^2 \approx 0.1$  throughout the boundary layer. Unfortunately, this still indicates a large range of frequencies (wave-numbers) that exhibit significant coherency.

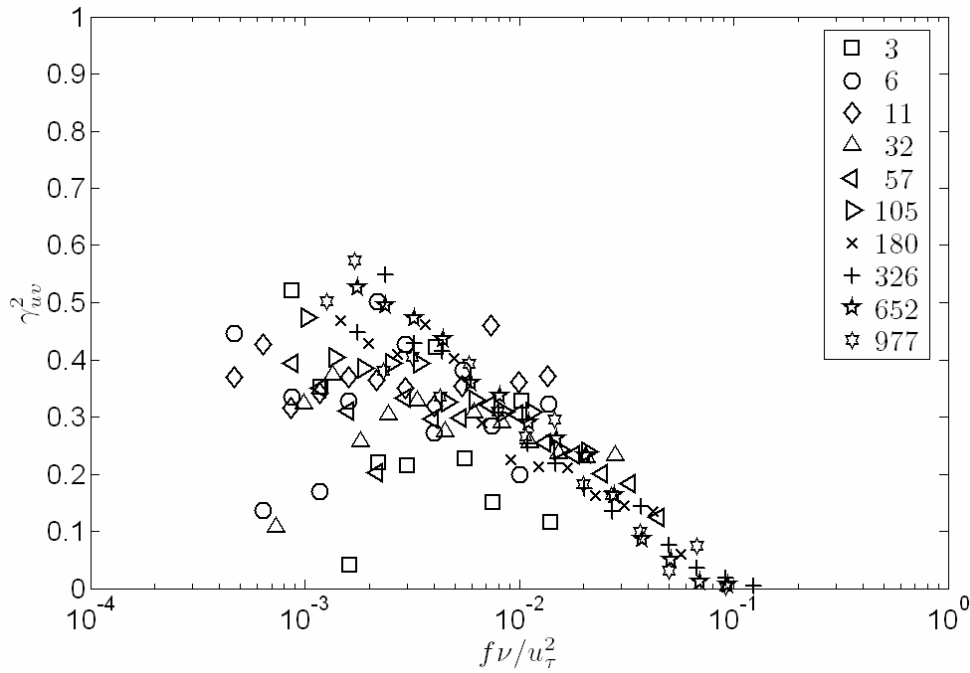


**Figure 4.30.** Coherency measurements for the Reynolds shear stress for the 2DFPTBL at  $Re_\theta = 4113$ . The legend gives vertical locations in  $y^+$ .

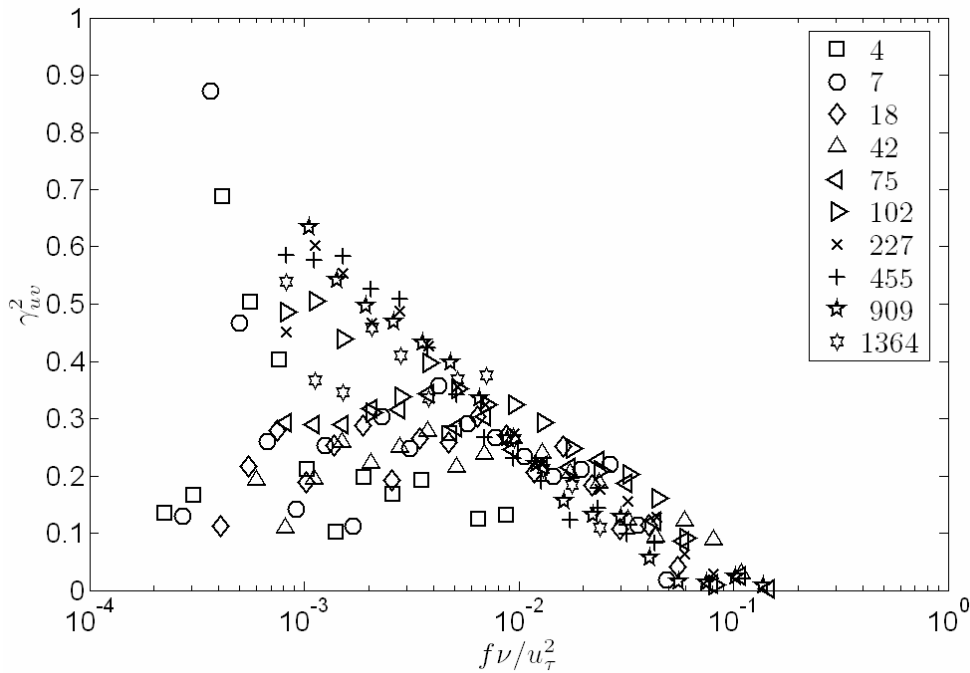


**Figure 4.31.** Coherency measurements for the Reynolds shear stress for the 2DFPTBL at  $Re_\theta = 5929$ . The legend gives vertical locations in  $y^+$ .

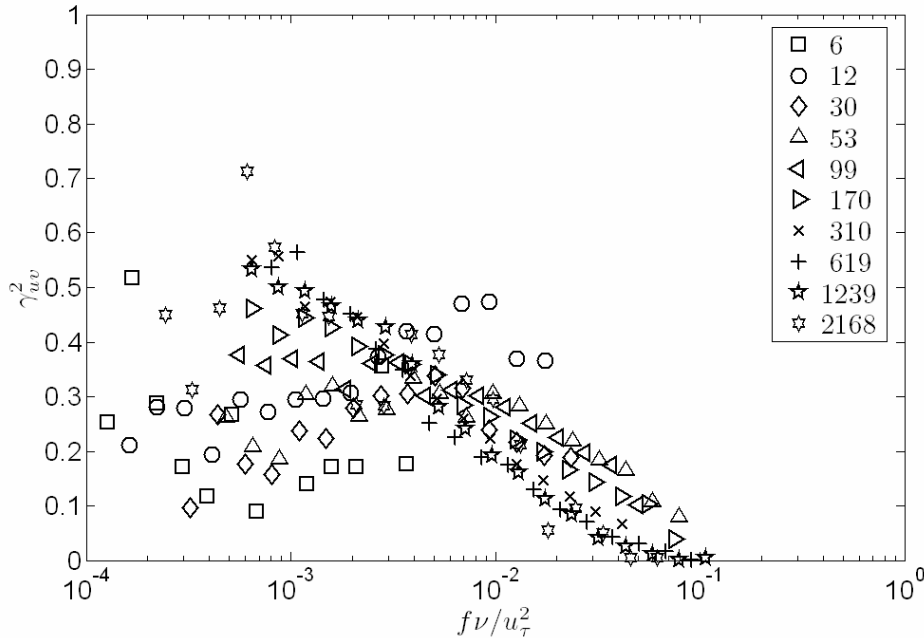


**Figure 4.32. Coherency measurements for the Reynolds shear stress for the 2DFPTBL at  $Re_\theta = 7497$ . The legend gives vertical locations in  $y^+$ .**

#### 4.1.4 Turbulence transport

Understanding the turbulence transport in shear flows is a key topic in fundamental research due to the immediate implications that these equations have on modeling for the Reynolds stresses. Although the most-obvious uses for the models of the turbulence structural (transport) terms is in Reynolds-averaged Navier-Stokes (RANS) solutions, other solution techniques benefit from the information obtained by studying Reynolds-averaged turbulence structure. For instance, wall functions that should obey RANS transport may be employed in LES to model the near-wall region of the filtered grid (Pope 2000 gives a brief description). Further, hybrid LES/RANS approaches have been developed and shown to be much more computationally efficient than LES and produce reasonable results (Labourasse and Sagaut 2002; Davidson and Dahlström 2004; Tessicini et al. 2005). Still further, RANS approaches remain the standard scheme employed by industry for computing complex engineering flows and design optimization. Improved knowledge for the behavior of Reynolds stress transport is the best hope in improving this efficient computation method.

With the present technique, two possibilities exist for obtaining Reynolds stress transport balances from the data sets. Since it is still impossible to obtain a direct measurement of the velocity/pressure gradient correlation within a flow, both methods rely upon the balance of information contained in transport equations. The Reynolds stress transport equation is repeated from chapter 1:

$$\frac{D\overline{u_i u_j}}{Dt} = P_{ij} + \Pi_{ij} + \nu \nabla^2 \overline{u_i u_j} - \varepsilon_{ij} - \frac{\partial \overline{u_i u_j u_k}}{\partial x_k} \quad (4.23)$$

where the production rate of the Reynolds stress tensor

$\overline{u_i u_j}$  is  $P_{ij} = -\overline{u_i u_k} \frac{\partial \overline{U_j}}{\partial x_k} - \overline{u_j u_k} \frac{\partial \overline{U_i}}{\partial x_k}$ , the velocity-pressure-gradient tensor is

$\Pi_{ij} = -\frac{1}{\rho} \overline{u_i} \frac{\partial p}{\partial x_j} + u_j \frac{\partial p}{\partial x_i}$  with  $p$  being the fluctuating static pressure, and the dissipation-

rate tensor is  $\varepsilon_{ij} = 2\nu \frac{\partial \overline{u_i}}{\partial x_k} \frac{\partial \overline{u_j}}{\partial x_k}$ . Also from chapter 1, an equivalent equation may be

derived that replaces some terms in equation (4.23) with velocity/acceleration fluctuation correlations:

$$\frac{1}{\rho} \overline{u_j} \frac{\partial P}{\partial x_i} + u_i \frac{\partial P}{\partial x_j} = -\left(\overline{a_i u_j} + \overline{a_j u_i}\right) - 2\nu \frac{\partial \overline{u_i}}{\partial x_k} \frac{\partial \overline{u_j}}{\partial x_k} + \nu \nabla^2 \overline{u_i u_j} \quad (4.24)$$

To follow, measurements from the CompLDV1 and CompLDV3 will be discussed that utilize both of these techniques for obtaining near-wall estimates of the turbulence structural parameters of equation (4.23).

#### 4.1.4.1 Velocity/acceleration correlations

In Chapter 1, the role of the fluctuating velocity-acceleration correlation has been examined in terms of Reynolds stress transport. The immediate power of such measurements is that combinations of terms in the Reynolds stress transport equations may be characterized by a single statistical measurement at one location in the flow—no gradients need be computed. The CompLDV technique allows through optimized optics design and signal processing measurement of the acceleration of particles as they pass through the measurement volume.

The measurements for the streamwise velocity–acceleration correlation profile in wall units are given in Figure 4.33. For comparison, the DNS data of Spalart (1988) for the same flow at  $Re_\theta = 1410$  and that of Abe et al. (2001) in a turbulent channel at  $Re_\tau = 640$  are plotted along with the current data. The measurements show agreement with the low Reynolds number DNS within experimental uncertainties, indicating little Reynolds number effects for this quantity when wall scaling is used. The near-wall differences that are seen may be attributed to combinations of uncertainties in the  $y$ -distance from the wall, the friction velocity, and the velocity–acceleration correlation. The relationship between coherent motions and the velocity–acceleration correlations is considered by decomposing the contributions from the in-plane quadrants. The major contributors to the Reynolds shear stress are the correlated motions known as sweeps which occur for  $u > 0$ ,  $v < 0$  and ejections occurring when  $u < 0$ ,  $v > 0$ . It is desired to relate the sweep and ejection motions in  $\overline{uv}$  of  $\overline{ua_x}$ . The results from the quadrant analysis are plotted in Figure 4.34. These results indicate that it is the sweep motions that dominate the velocity–acceleration correlation very near wall for  $y^+ < 10$ . For heights

above  $y^+ \approx 14$ , the contributions switch such that the ejections become dominant in producing the correlation, though the difference is approaching experimental uncertainties. An explanation of the mechanisms for these phenomena is proposed by considering the shape of the probability density functions for the streamwise velocities very near the wall. Figure 4.35 gives the skewness of the streamwise velocity histograms throughout the profile. It is seen that in the very near-wall region the histograms are positively skewed, indicating that the range of positive  $u'$  fluctuations is larger than the negative ones. This makes sense intuitively because there is a limit on the lowest velocity since the flow is always downstream, but the greatest possible velocities are related to the higher-momentum large-scale eddies sweeping toward the wall. Note also that the skewness of  $u'$  changes sign at the same location that the contributions from sweeps and ejections switch dominance. Heuristically, then, the large difference between the mean velocity very near the wall and the relatively infrequent high-speed sweeps leads to high local viscous shear that acts to limit the convection of momentum that has reached the wall and thus stabilize the mean shear rate in a Lagrangian sense.

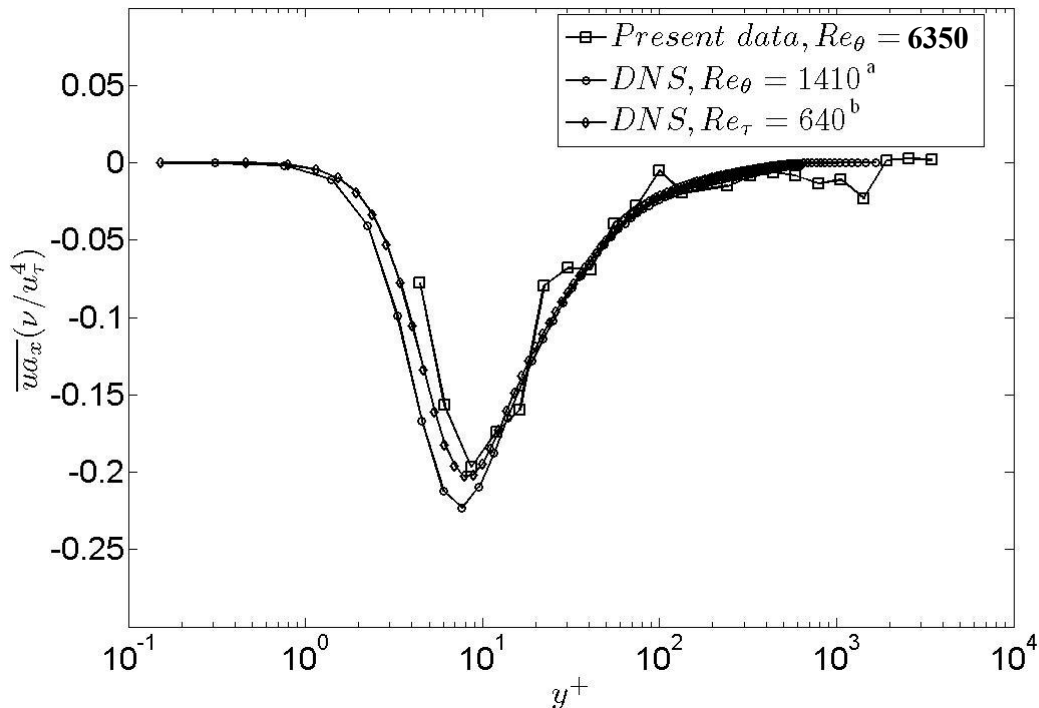


**Figure 4.33. Stream-wise velocity acceleration correlation for the 2D FPTBL at  $Re_\theta = 6350$  compared to the data of a) Spalart (1988) and b) Abe et al. (2001). Adapted from Lowe and Simpson (2006).**

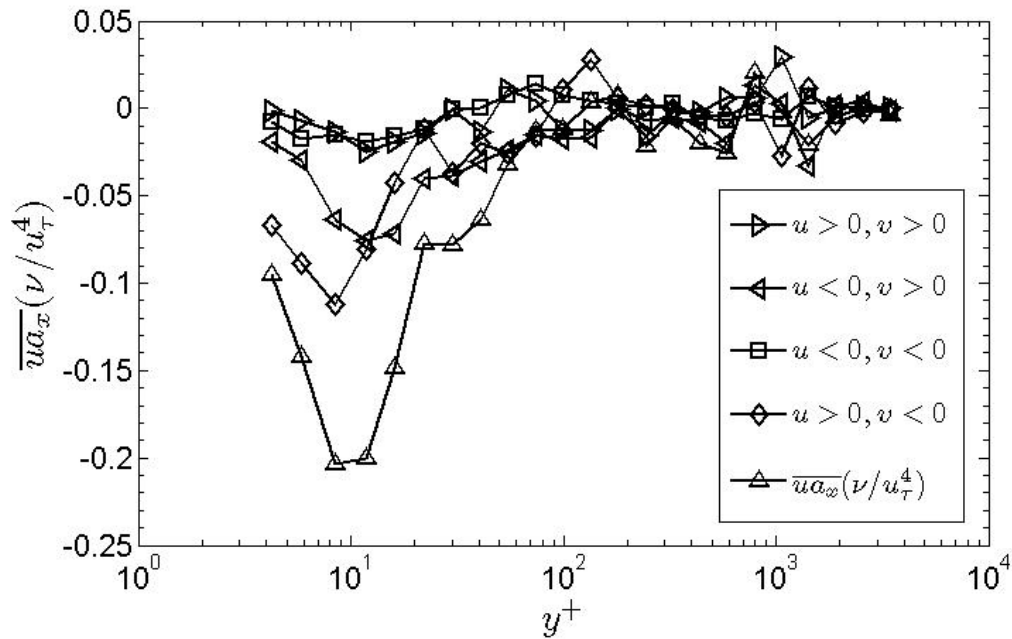


**Figure 4.34.** Velocity quadrant analysis of the streamwise velocity–acceleration correlation for the 2D FPTBL at  $Re_\theta = 6350$ . Adapted from Lowe and Simpson (2006).

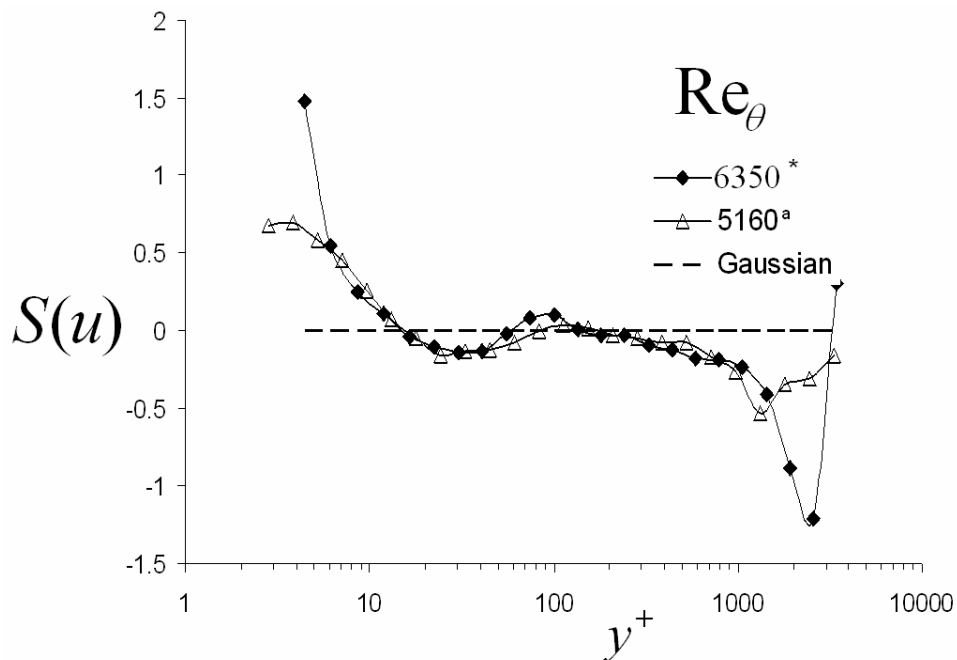


**Figure 4.35.** Skewness of the streamwise velocity fluctuation. (\*) Current data, (a) data of DeGraaff and Eaton (2000). The dashed line indicates the value for a Gaussian distribution. Adapted from Lowe and Simpson (2006).

The data for the 2DFPTBL at  $Re_\theta = 6350$  gives good estimates for the stream-wise velocity/acceleration correlation, as shown in Figure 4.33. For this flow and this component of the Reynolds stress,  $i = j = 1$ , the viscous diffusion term,  $D_{v11} = \nu \nabla^2 \overline{u^2}$ , reduces to  $D_{v11} = \nu (\partial^2 \overline{u^2} / \partial y^2)$  since derivatives in the stream-wise and span-wise directions are negligible compared with derivatives in the normal-to-wall direction. While in sections to follow, direct estimates of the dissipation rate from velocity gradient measurements will be considered, to estimate the dissipation rate for the current purposes, first the turbulent kinetic energy (TKE) dissipation rate is estimated by balance of the boundary layer approximation for the TKE transport equation:

$$U \frac{\partial k}{\partial x} + V \frac{\partial k}{\partial y} = P - \varepsilon + \nu \frac{\partial^2 k}{\partial y^2} - \frac{1}{2} \frac{\partial (\overline{u^2 v} + \overline{v^3} + \overline{w^2 v})}{\partial y} - \frac{1}{\rho} \frac{\partial \overline{vp}}{\partial y} \quad (4.25)$$

where  $k \equiv \frac{1}{2} (\overline{u^2} + \overline{v^2} + \overline{w^2})$  is the TKE and  $\varepsilon$  is the TKE dissipation rate. The CompLDV1 measurements afford direct estimation of all the terms in equations (4.25) except for the pressure diffusion,  $-\frac{1}{\rho} \frac{\partial \overline{vp}}{\partial y}$ . While spectral estimates of the TKE

dissipation rate are possible with the measurements made with the CompLDV1, DNS of Spalart (1988) indicate that the model of Lumley (1978),  $-\frac{1}{\rho} \overline{vp} \approx \frac{1}{5} (\overline{u^2 v} + \overline{v^3} + \overline{w^2 v})$  is

well-suited for the balance of equation (4.25) results in high-confidence estimates of the dissipation rate. The TKE transport budget for the current flow is given in Figure 4.36. All gradients were computed using central differencing. Given the TKE dissipation rate, one may estimate the dissipation rate of  $\overline{u^2}$ , by either assuming isotropy of the dissipation rate or else some model for accounting for the anisotropic dissipation. It was found that common models predict isotropic dissipation rates throughout the boundary layer above  $y^+ = 10$ , so the isotropic estimate,  $\varepsilon_{11} = \varepsilon_{22} = \varepsilon_{33}$  was used. The balance of equation (4.24), yielding estimates for the streamwise velocity/pressure gradient correlation is given in Figure 4.37. Note that the velocity–acceleration correlation data of Figure 4.33 have been spatially smoothed to result in more realistic estimates for the velocity/pressure gradient correlations reported in Figure 4.37. Comparing these results with those of Spalart (1988) reveals that the velocity–pressure gradient is greater near the wall compared with the lower Reynolds number DNS.

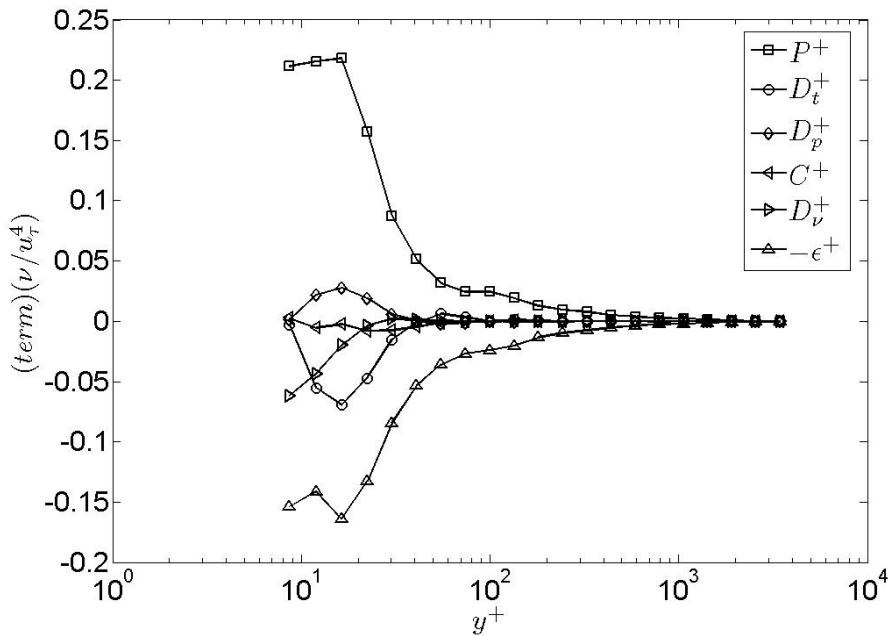


Figure 4.36. Transport budget for the turbulent kinetic energy in the 2D FPTBL at  $Re_\theta = 6350$ . Adapted from Lowe and Simpson (2006).

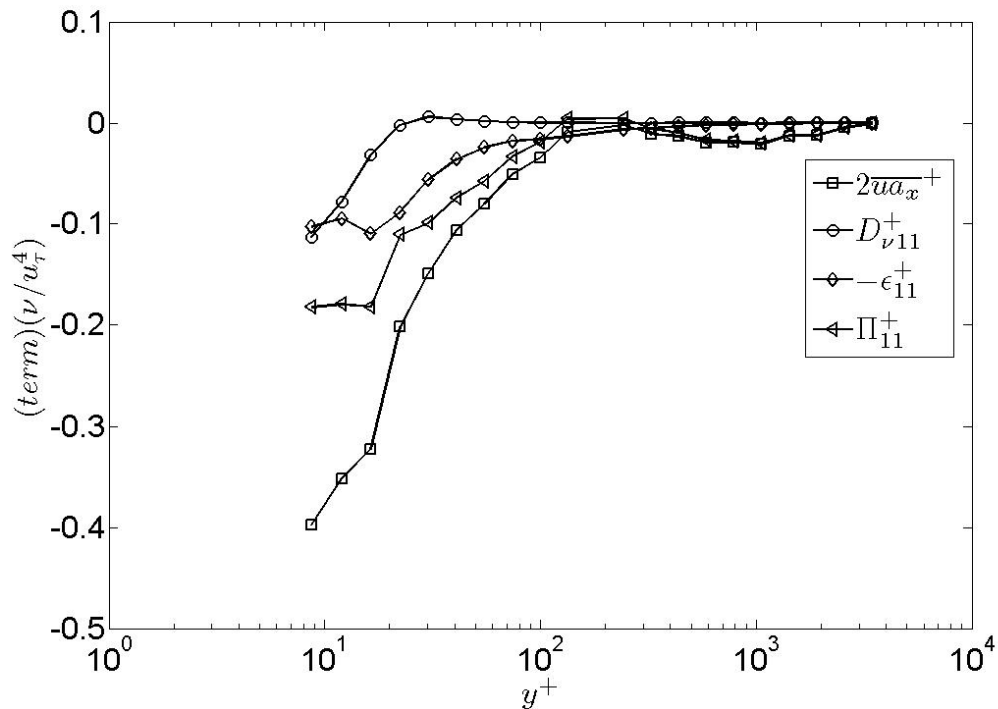


Figure 4.37. The balance of the stream-wise velocity-acceleration equation using isotropic dissipation estimates and measurements of the viscous diffusion and velocity-acceleration correlation in the 2D FPTBL at  $Re_\theta = 6350$ . Adapted from Lowe and Simpson (2006).

#### 4.1.4.2 Reynolds stress transport using dissipation rate estimates

It is possible using the capabilities of the CompLDV to obtain dissipation rate estimates within turbulent boundary layers. Two methods exist for obtaining these estimates—TKE dissipation rate estimates from velocity spectra and direct estimation using the velocity gradient tensor measurements. These methods are discussed in more detail to follow.

##### 4.1.4.2.1 Spectral dissipation rate estimates

Several methods exist for estimating the TKE dissipation rate from velocity spectral data. For spectral measurements that contain a sufficient range of scales to resolve the dissipative range such that the wave-numbers as high as  $k_1 = 1/\eta$  are measured where the

Kolmogorov length scale  $\eta \equiv (\nu^3 / \varepsilon)^{1/4}$ , isotropic relations give

$$\varepsilon = 15\nu \int_0^{\infty} k_1^2 E_{11}(k_1) dk_1 = \frac{15}{2} \nu \int_0^{\infty} k_1^2 E_{22}(k_1) dk_1 = \frac{15}{2} \nu \int_0^{\infty} k_1^2 E_{33}(k_1) dk_1 \quad (4.26)$$

Since most spectral data are acquired with single-point probes (as in this study), it is necessary to convert the frequency/time conjugate relationship to the wave-number/distance conjugate pair. This may be accomplished for high wave-number data sufficiently far from boundaries using Taylor's Hypothesis for frozen turbulence, as already discussed. Since relatively small scales of  $\eta$  are present throughout most of the 2DFPTBL flows measured, there was not a sufficient range of  $k_l$  obtained to directly apply equation (4.26).

Methods of fitting theoretical or model functions to spectral estimates may also lead to dissipation rate estimates. One possibility for this is using equation (4.19) for fits. One must identify the region of the spectrum in which the roll-off is approximately constant at  $k_l^{-5/3}$  and then the value of the dissipation is directly estimated from the scaling of the measurements given the value of the universal constant. In the present study, a method of fitting a model spectrum function that is consistent with the Kolmogorov (-5/3) spectrum is used. The Taylor's Hypothesis is employed to obtain wave-number distributions from the frequency spectra and the Pope (2000) model spectrum that consists of three-blended functions for the low-wave-number energy-containing range, the inertial subrange (-5/3 spectrum), and the dissipative range. Pope specifies his model in terms of the wave-number magnitude and the total-energy spectrum function:

$$E(\kappa) = C\varepsilon^{2/3} \kappa^{-5/3} f_L(\kappa L) f_\eta(\kappa \eta) \quad (4.27)$$

where  $\kappa = \sqrt{\kappa_1^2 + \kappa_2^2 + \kappa_3^2}$ ,  $C=1.5$ ,  $L \equiv k^{3/2} / \varepsilon$  and the blending functions are given as

$$f_L(\kappa L) = \left( \frac{\kappa L}{\sqrt{(\kappa L)^2 + c_L}} \right)^{5/3+p_0} \quad (4.28)$$

where  $c_L=6.78$  for  $p_0=2$  and

$$f_{\eta}(\kappa\eta) = \exp\left\{-\beta\left[(\kappa\eta)^4 + c_{\eta}^4\right]^{1/4}\right\} + c_{\eta} \quad (4.29)$$

where  $\beta = 5.2$  and  $c_{\eta} = 0.40$ . Each of these constants is determined using the extensive spectral data that exist in the field. To obtain the one-dimensional spectrum which may be of use in the current work, we may use isotropic assumptions inter-relating the wave-number directions to obtain

$$E_{11}(\kappa_1) = \int_{\kappa_1}^{\infty} \kappa^{-1} E(\kappa) \left(\frac{\kappa_1^2}{\kappa}\right) d\kappa \quad (4.30)$$

Of course this model may not perform well when the spectral distribution is significantly different from the model case, such as in the case of the very near wall data, but within the boundary layer it is a good approximation. This assertion is brought to point with an example of CompLDV3 spectral data fitted to Pope's spectra in Figure 4.38. These data were obtained in the 2DFPTBL at  $Re_{\rho} = 7497$  at the height  $y^+ = 619$  where the Kolmogorov length scale was found to be  $\eta = 61\mu m$ . This fit was accomplished by varying the Kolmogorov length scale to obtain the best correlation coefficient in the fit. The data points at the lowest and highest ends were disregarded for this fit since the low-end wave-numbers suffer uncertainties due to variable wavespeeds (Ahn and Simpson 1987) while the high-end wave-numbers are more uncertain due to large numbers of samples that are needed to obtain high confidence levels at such dynamic ranges. In implementing this fitting technique, it is found for the 2DFPTBL, which is known to have highly non-isotropic Reynolds stresses, that the dissipation length-scale parameter,  $L$ , is

best modified to  $L = \varepsilon^{-1} \left(\frac{3}{2} \overline{u^2}\right)^{3/2}$  to provide favorable fits to the energy-containing range

of  $E_{11}$ . This is exemplified in Figure 4.39 where the TKE has been used to compute  $L$ , instead of simply the stream-wise normal stress as in Figure 4.38.

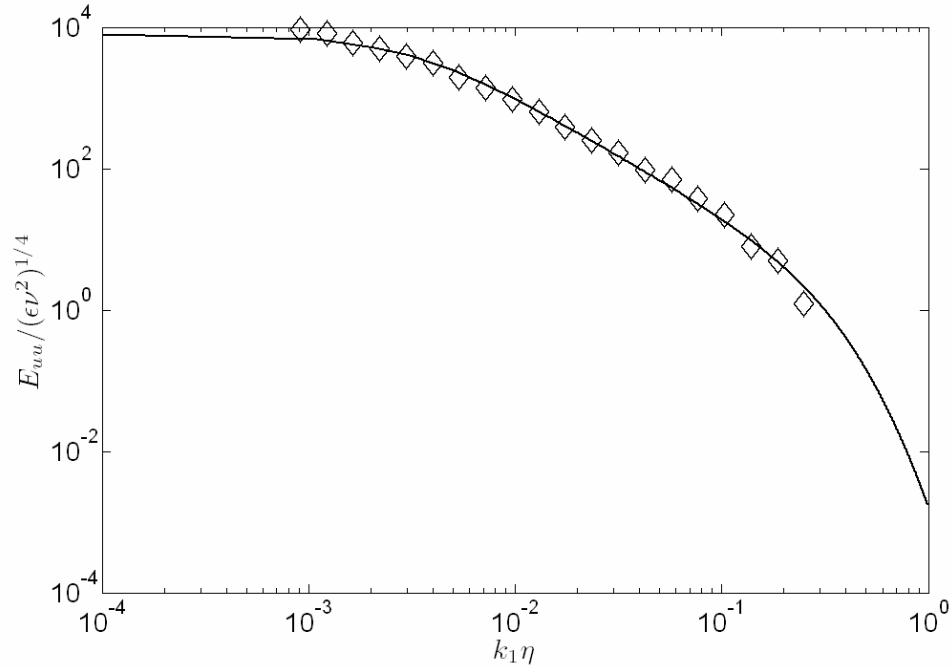


**Figure 4.38.** Fit to Pope's model for the stream-wise velocity auto-spectrum of the ComplDV3 from the 2DFPTBL at  $\text{Re}_\theta = 7497$  at  $y^+ = 600$  where  $\eta = 61 \mu\text{m}$  and

$$L = \left( \frac{3}{2} \overline{u^2} \right)^{3/2} / \varepsilon.$$

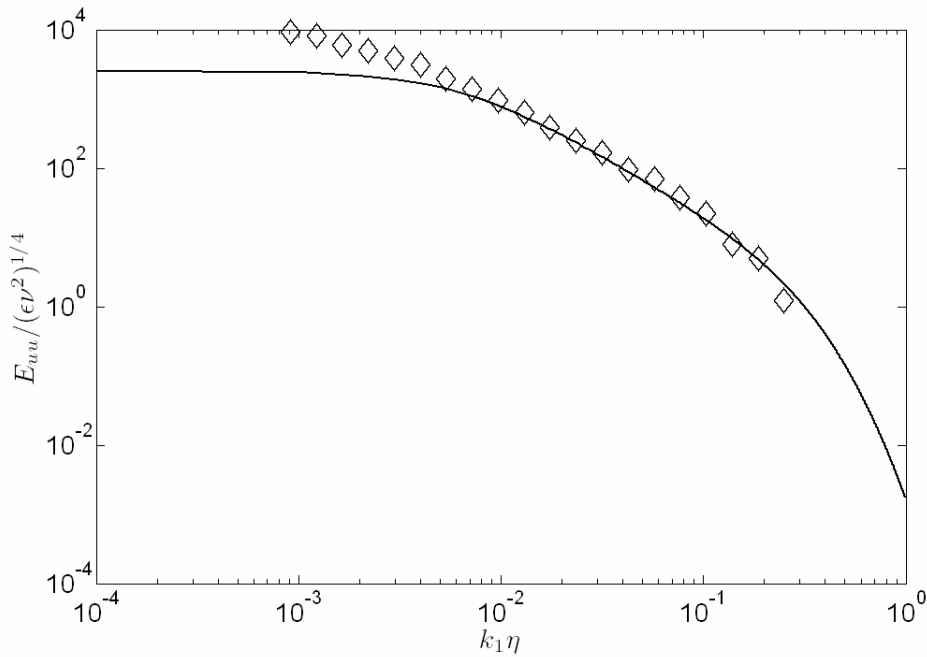


**Figure 4.39.** Same as Figure 4.38, but with  $L \equiv k^{3/2} / \varepsilon$ .

#### 4.1.4.2.2 *Direct dissipation rate estimates from the velocity gradient tensor*

The second method available from the CompLDV3 for estimating the dissipation rate is by direct evaluation of the dissipation rate from velocity gradient measurements. The technique for estimating the velocity gradient using particle velocity and position measurements was discussed in section 2.3.3.9.4.2.2. In that section, a least-squares method of extraction of velocity gradients was considered based upon the notion of a stream-wise-oriented turbulent motion with generally constant velocity gradients that convect frozen through the measurement volume. With the levels of uncertainty predicted for the CompLDV3, this technique was shown to work sufficiently-well using simulated data given at least 6-7 particles for the least-squares fit for estimating the velocity gradients. To determine a reasonable time-window that may be used, previous experimental information was used to obtain an estimate for the size and convection speed of the near-wall eddies. For the coherent structures in the near-wall region, it has been observed that the convective speed of eddies is about  $U_c / u_\tau \approx 14$  (Kline et al. 1967; Ahn and Simpson 1987) and typical active near-wall structures exist in very long dimensions of  $x^+ = 500$  or greater (Robinson 1991). In practice, this model for obtaining the velocity gradients requires some adaptation. First, it has been found that the stream-wise gradients (those that are obtained using the arrival time technique for determining the positions) give results much too small when such a large time-window is allowed. The effect at work there is filtering of the small-scales that contribute to the velocity gradients in this direction. The stream-wise and normal-to-wall gradients are estimated over small-scales in those directions, so the extended stream-wise window does not appear to attenuate those data. To remedy this problem of filtering, a shorter time-window of  $t^+ = 6$  is used and the results are much-improved. An example of these results is given in Figure 4.40 where spectral dissipation rate estimates are compared to the directly-estimated mean-square of the stream-wise gradient of the stream-wise velocity and to the TKE production computed from the Reynolds-averaged profile measurements. The comparison of the two dissipation rate measurements to the production measurements rests on the assumption of the isotropic relation,  $\varepsilon = 15\nu \overline{\left(\frac{\partial u}{\partial x}\right)^2}$ , but the direct comparison of the two estimates of dissipation rate to one-another is more rigorous since the spectral fitting discussed above seeks to directly estimate the term  $\overline{\left(\frac{\partial u}{\partial x}\right)^2}$ . The quality of the comparison for these two measurements of  $\overline{\left(\frac{\partial u}{\partial x}\right)^2}$  gives confidence in the gradient estimation scheme for stream-wise gradients.

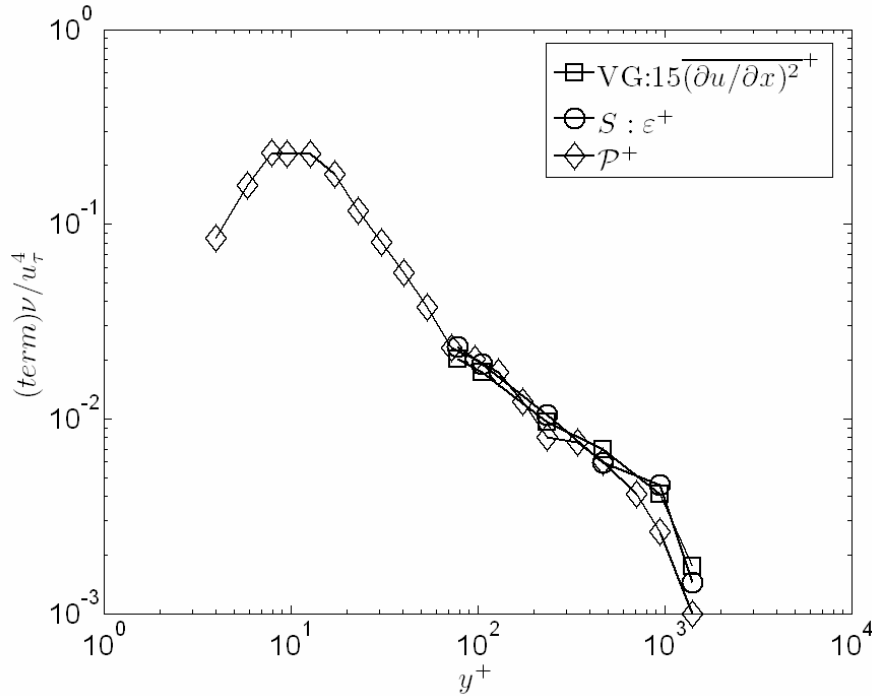


**Figure 4.40. Comparison of the dissipation estimate for the directly-estimated stream-wise velocity gradient in the stream-wise direction to the spectral dissipation rate estimates and the production for the 2DFPTBL at  $Re_\theta = 5929$ . VG, Directly-estimated dissipation rate from velocity gradients; S, Spectral-estimates of dissipation rate; Diamonds are TKE production computed from Reynolds-averaged statistics.**

In contrast to the stream-wise gradients, span-wise and normal-to-wall gradients exhibited values that level-off above the expected values by comparison to the production or DNS values for the non-isotropic dissipation rate. The raw data for the mean-square velocity gradients in a 2DFPTBL is given in Figure 4.41. It is clear from these data that the span-wise and normal-to-wall gradients of all velocity components are in significant error since the stream-wise gradient values have been verified by comparison to the expected results in Figure 4.40. The approach for correcting the situation is to apply a constant additive correction that is appropriate for each term. The premise for applying such a correction is that it is a white-noise floor that limits the minimum variance for these velocity gradients. Unfortunately, such a noise floor must be considered to vary from point-to-point since the flow parameters such as turbulence level are varying thusly,

and it is evident by the very low values that are measured for the term  $\overline{\left(\frac{\partial v}{\partial z}\right)^2}^+$  in the near-wall region that a constant correction is not perfect.

Future research will be conducted to predict this noise floor for each point based upon time-delay correlations and power spectral densities of the velocity gradients. The values of the time-delay correlation near zero-delay may be used with some model for the

variation to obtain new estimates for the auto-covariance at zero time-delay. As has been discussed already in section 3.2, the random noise content of the signal will be concentrated in the zero-delay sample (i.e., the auto-covariance), and with some assumption of the functional form for the time-delay correlation near zero-delay, the auto-covariance may be corrected. The power spectral density may be used in a similar manner to correct the value of the gradient variance, as it forms a Fourier transform pair with time-delay auto-correlation. In the case of the power spectral density, the random noise content will be assumed white since we have no information to indicate otherwise. It is known that the power spectral density of a turbulence quantity is continuous and as it approaches the high wave-numbers, it necessarily extends to zero due to the action of viscosity on the small scales. Then, the power spectral density may be used to indicate the portion of the high frequency spectrum where the spectral values cease to decrease and level-off. This noise-floor may be considered constant across the computed frequencies, integrated, and subtracted from the gradient variance.

For the current purposes, the assumption of a constant noise-floor for each gradient variance will be regarded to make the necessary corrections. The data from Figure 4.41 is corrected by subtracting constant noise-floor values from each of the terms at each point and the result is plotted in Figure 4.42. The goal in selecting these noise-floor values was to obtain mean-square velocity gradient estimates of the same order of magnitude as the stream-wise gradients for the normal-to-wall and span-wise values in the outer-portion of the boundary layer where locally-isotropic conditions exist. The amount that may be

subtracted is limited in some cases, most-notably for  $\overline{\left(\frac{\partial v}{\partial z}\right)^2}^+$ , by the values of these terms at the lower  $y^+$  region.

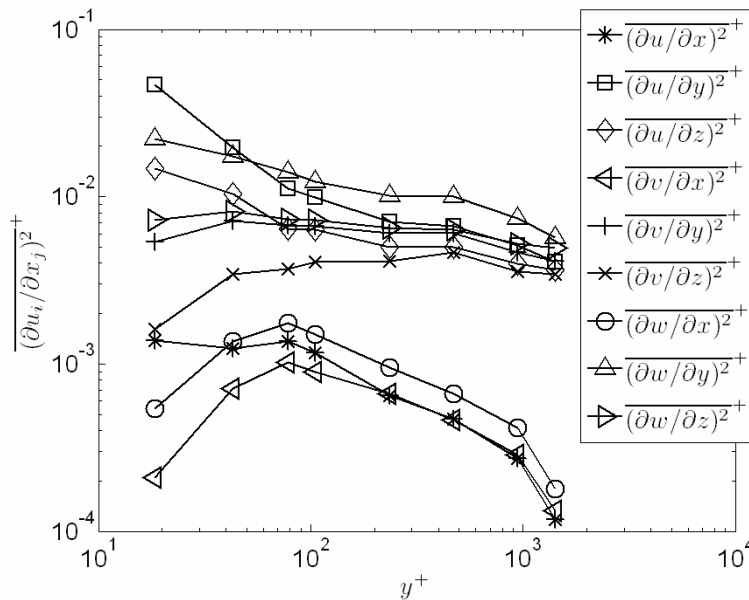


**Figure 4.41. Raw mean-square velocity gradient information for the 2DFPTBL at  $Re_\rho = 5929$ .**

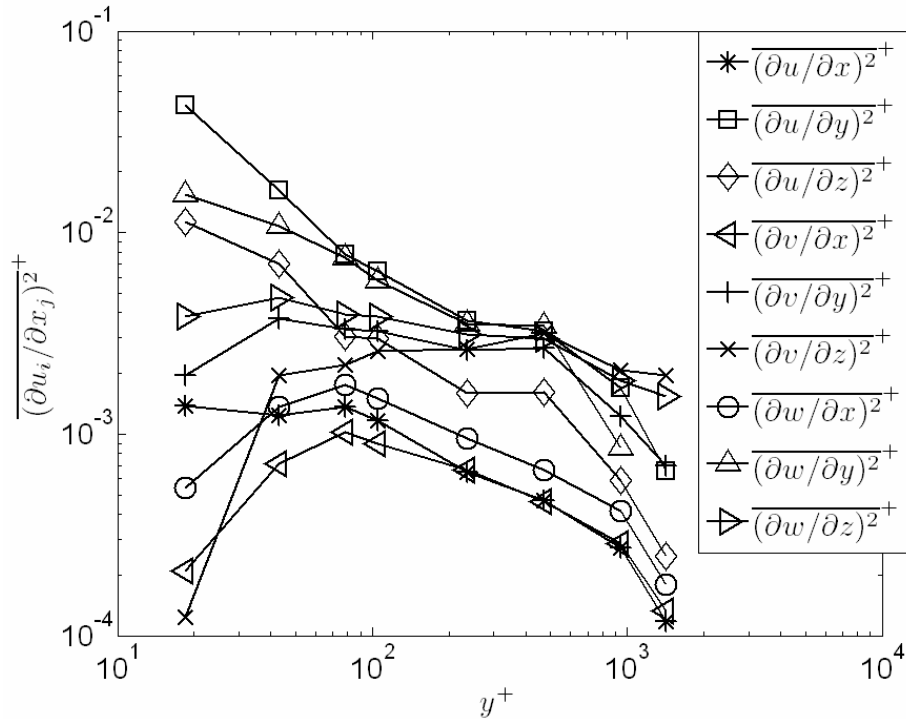


**Figure 4.42. Corrected mean-square velocity gradient information for the 2DFPTBL at  $Re_\theta = 5929$ .**

#### 4.1.4.2.3 Results for dissipation rate measurements

Both the methods just methods just discussed for estimating the dissipation rate throughout the 2DFPTBL have been applied to the CompLDV3 measurements. In this section, we compare the results for the TKE as well as Reynolds normal stress dissipation rates to the DNS results of Spalart (1988) for the low Reynolds number 2DFPTBL. In Figure 4.43 the TKE dissipation rate as measured by the spectral and velocity gradient methods are compared for the 2DFPTBL at  $Re_\theta = 5929$  and compared with the production of TKE for that profile as well as the dissipation rate data of Spalart. Analogous data are plotted for the higher Reynolds number 2DFPTBL in Figure 4.44. The underestimation of TKE dissipation rate in near-wall TBLs using single-point spectral data has been documented a number of times (Sandborn and Braun 1956; Balint et al. 1991). Surprisingly, the lower-Reynolds number case follows the spectral value for the lowest  $y^+$  value reported. In the higher-Reynolds number case, the velocity gradient dissipation rate data follows the production values of the TKE reasonably throughout the range of measurements. The distributions of the Reynolds normal stress dissipation rates measured with the velocity gradient technique are plotted in Figure 4.45 and Figure 4.46 for the lower-Reynolds number and higher-Reynolds number cases, respectively. To the author's knowledge, these measurements are the first of their kind at Reynolds numbers of this magnitude in turbulent boundary layers. To note is the persistence of anisotropy of the dissipation rate to values of  $y^+$  of about 100, since models such as the wall/isotropic

dissipation blending function of Lai and So (2000) give more-or-less isotropic predictions at  $y^+=10$ .

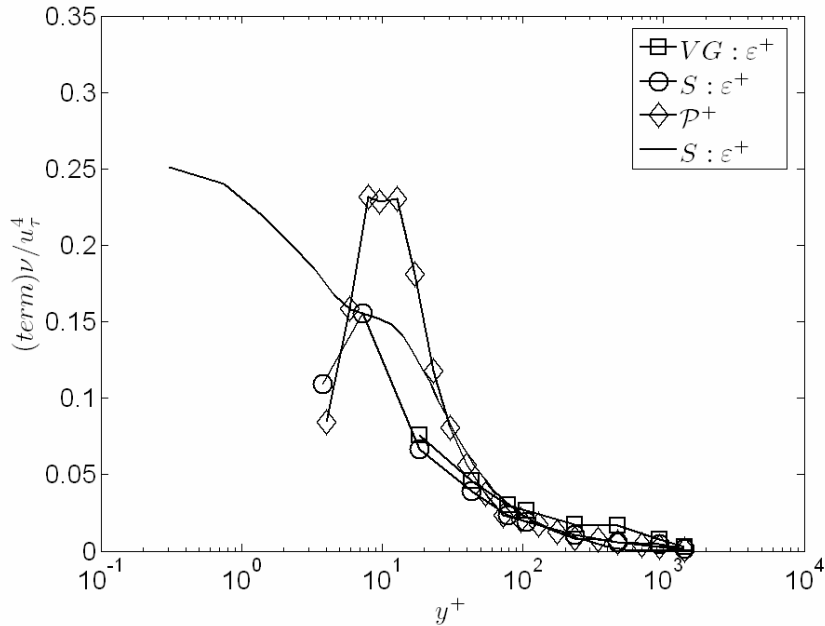


**Figure 4.43. Dissipation rate measurements for the 2DFPTBL at  $Re_\theta = 5929$ . VG, Direct estimation of velocity gradients; S, Spectral estimation with Taylor's Hypothesis; DNS, Low Reynolds number simulation data of Spalart (1988).**

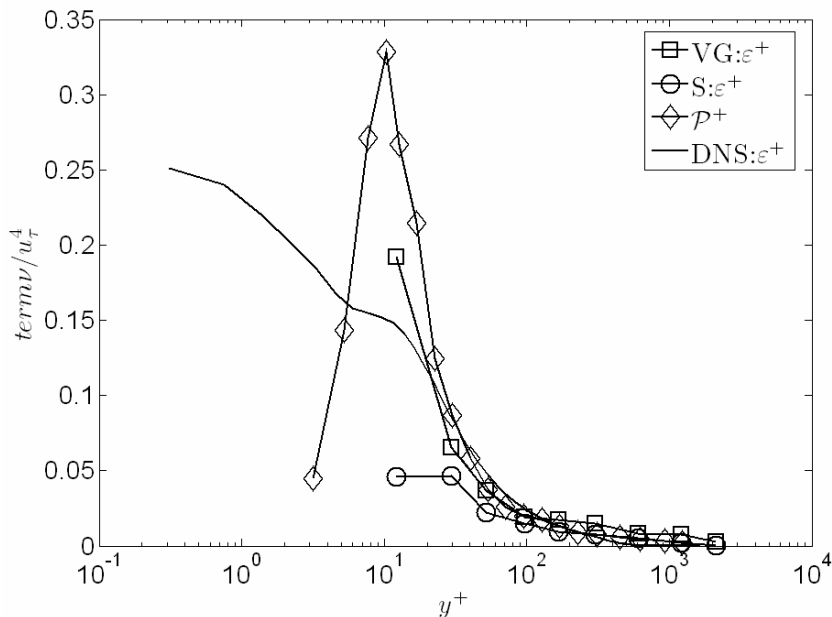


**Figure 4.44. Dissipation rate measurements for the 2DFPTBL at  $Re_\theta = 7497$ . VG, Direct estimation of velocity gradients; S, Spectral estimation with Taylor's Hypothesis; DNS, Low Reynolds number simulation data of Spalart (1988).**

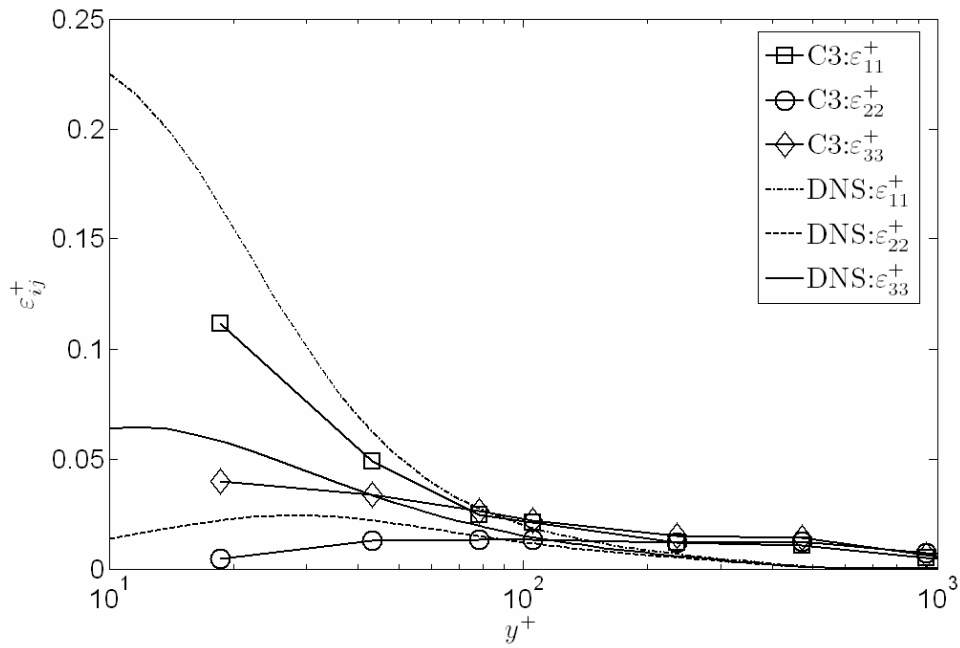


**Figure 4.45. Non-isotropic Reynolds stress dissipation rates measured in the 2DFPTBL at  $Re_\theta = 5929$ . C3, CompLDV3; DNS, Simulation data of Spalart (1988).**

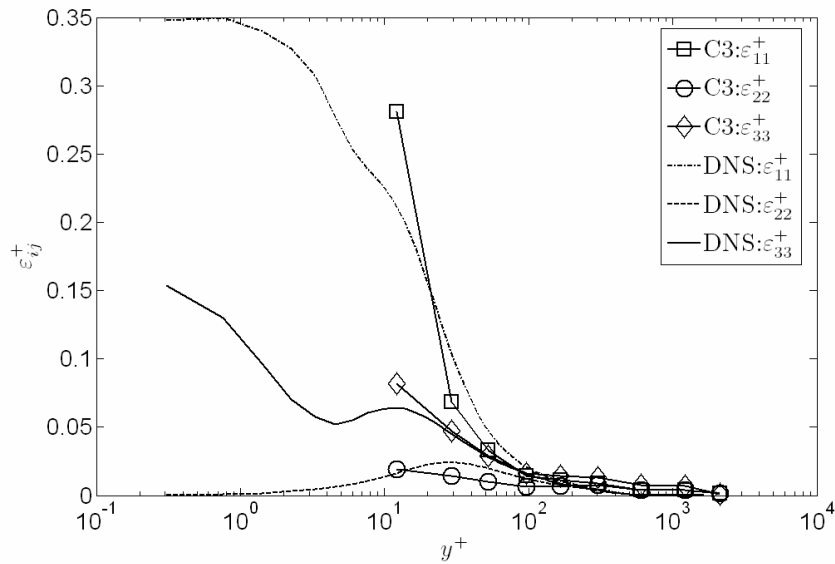
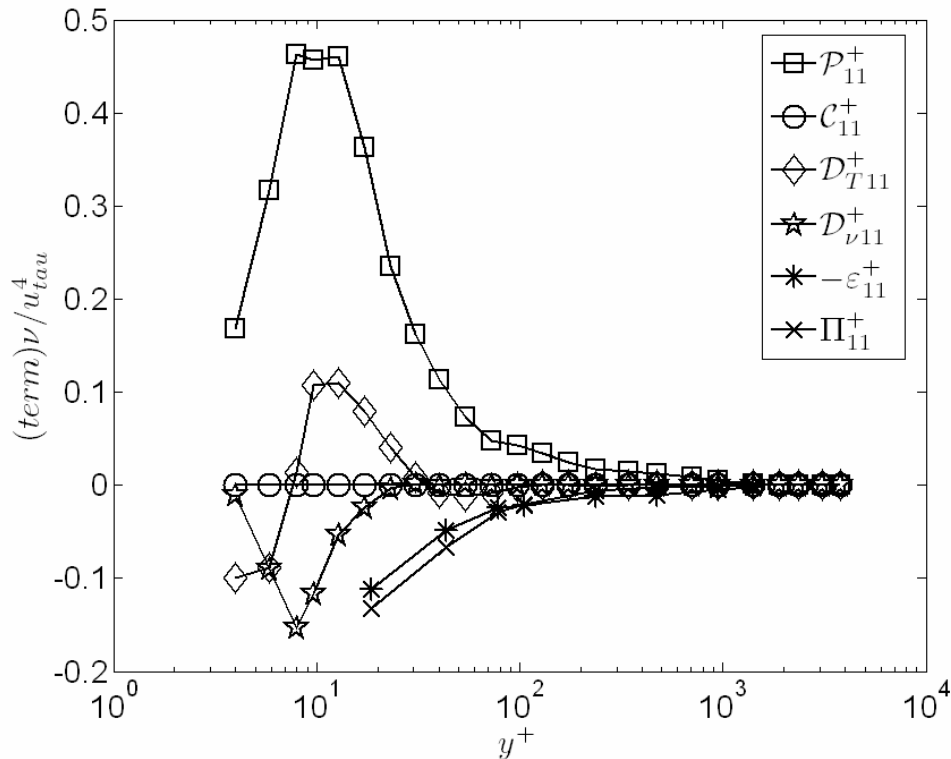


**Figure 4.46. Non-isotropic Reynolds stress dissipation rate measured in the 2DFPTBL at  $Re_\theta = 7497$ . C3, CompLDV3; DNS, Simulation data of Spalart (1988).**

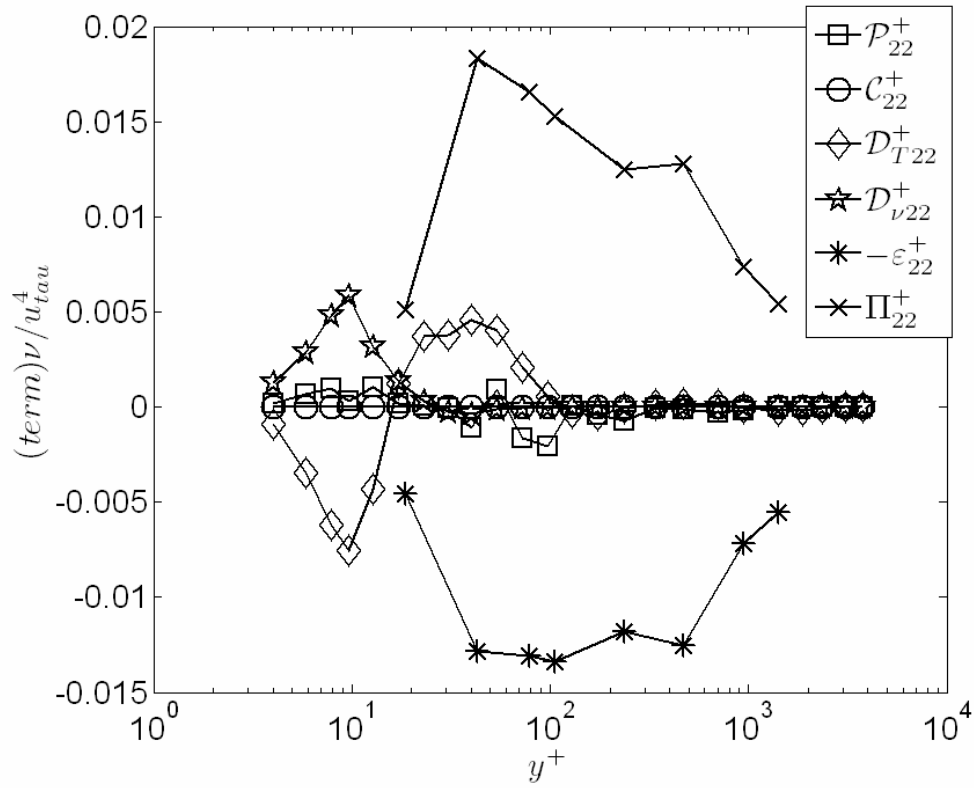
#### 4.1.4.2.4 Reynolds stress transport balances

The Reynolds stress transport balances have been estimated using the CompLDV3 data for the 2DFPTBL at two Reynolds numbers. For all terms involving gradients of Reynolds averaged quantities, central differencing was employed. To obtain the velocity/pressure gradient correlation the balance of equation (4.23) was obtained using the non-isotropic dissipation rates from direct velocity gradient measurements. In the case of the Reynolds shear stress, the statistics of the cross-products of velocity gradients have not yet been computed and the dissipation rate for the shear stress was taken as zero.

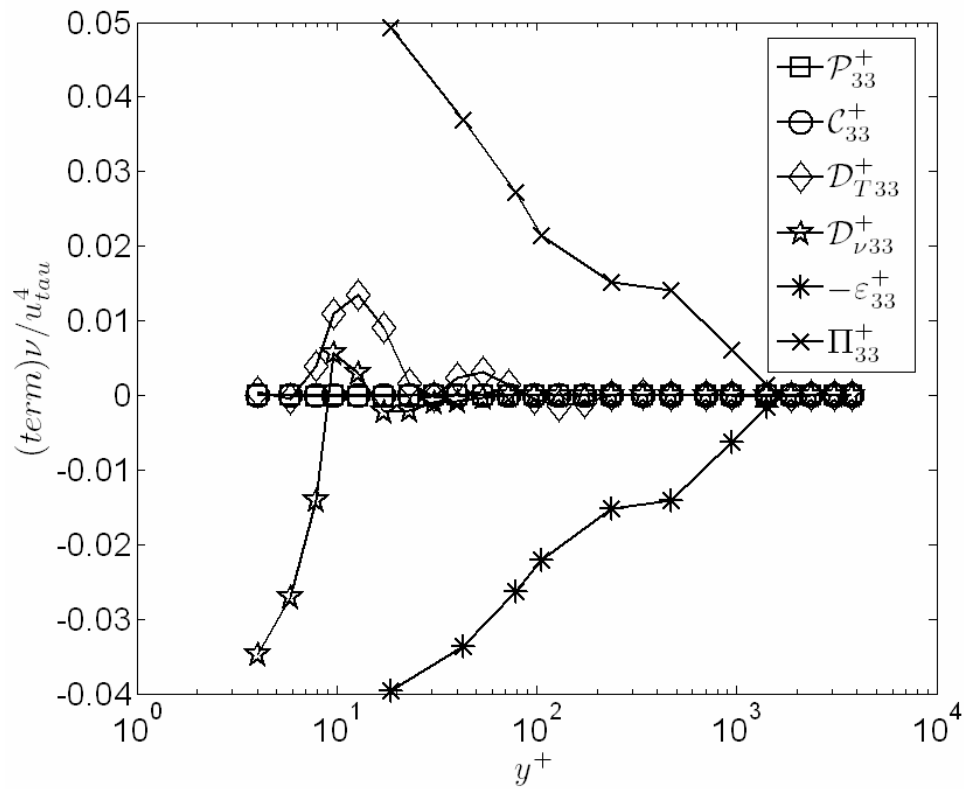
The transport rate budgets for each of the non-zero stresses in the flow and the TKE are plotted in Figure 4.47 and Figure 4.48 for the  $Re_\theta = 5929$  and  $Re_\theta = 7497$ , respectively. The importance of the velocity pressure gradient is again re-iterated based upon these data. The trends therein resemble the near-wall budgets of the DNS by Spalart (1988), although similar to the results in Figure 4.37, it appears that the velocity/pressure gradient correlation in the stream-wise normal stress plays an increasingly larger role with Reynolds number.



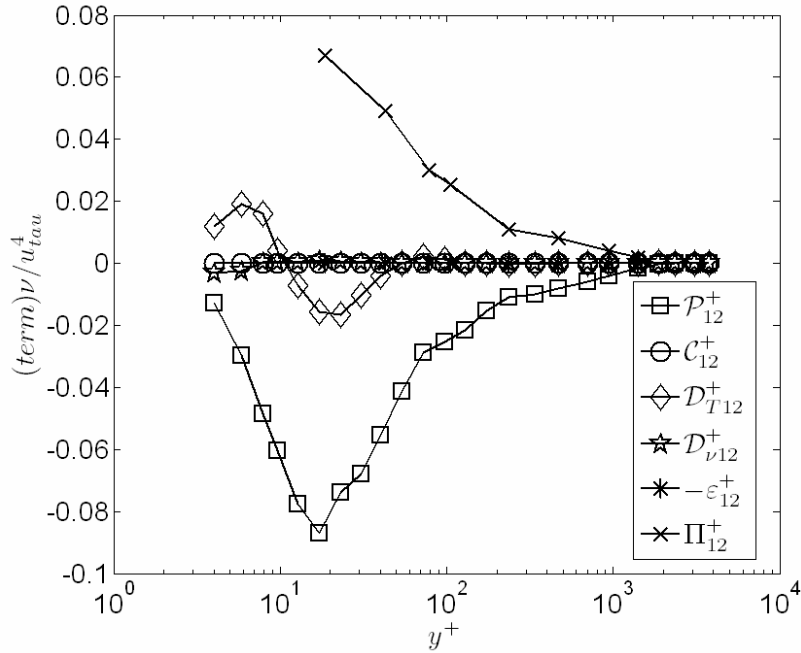
(a)



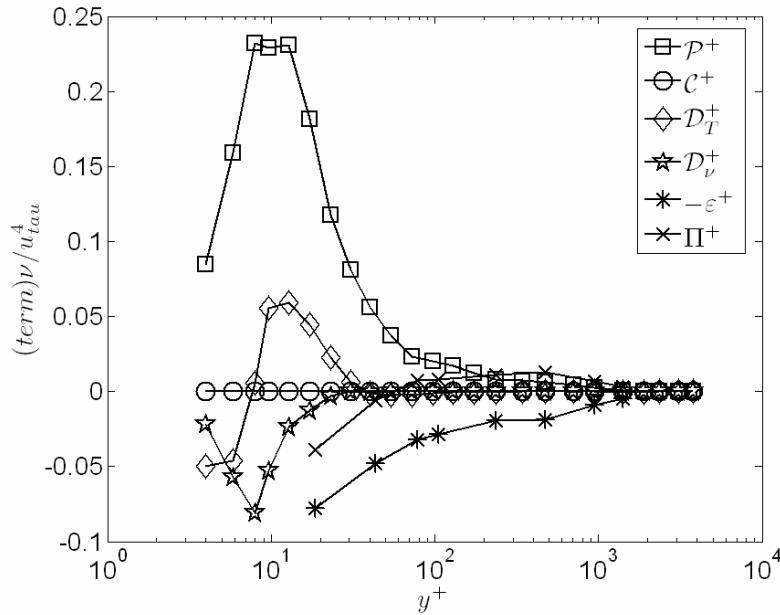
(b)



(c)

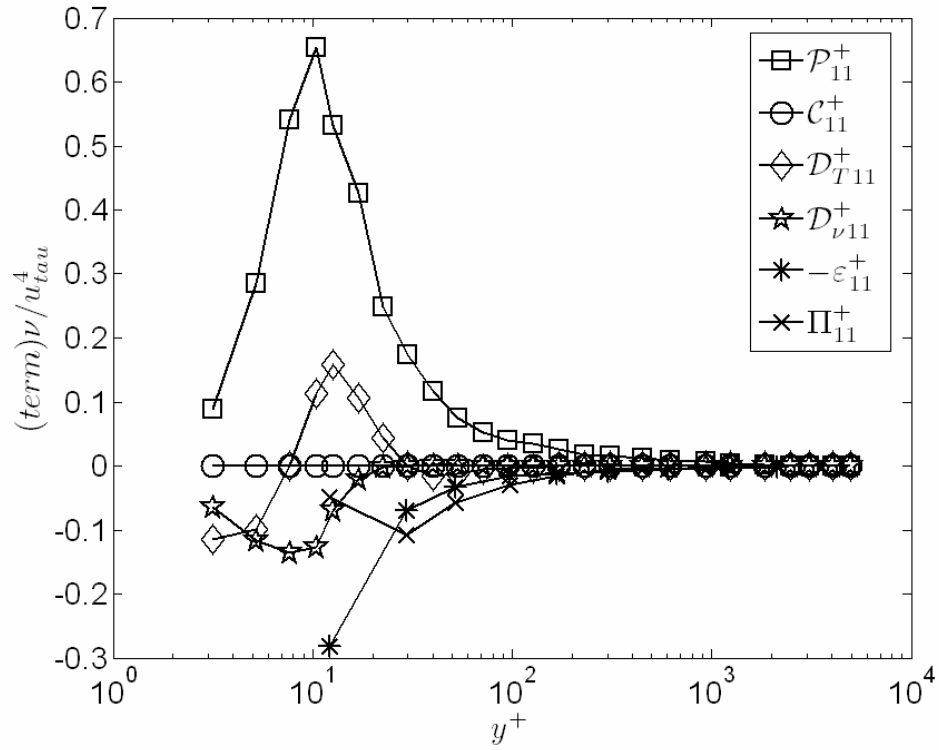


(d)

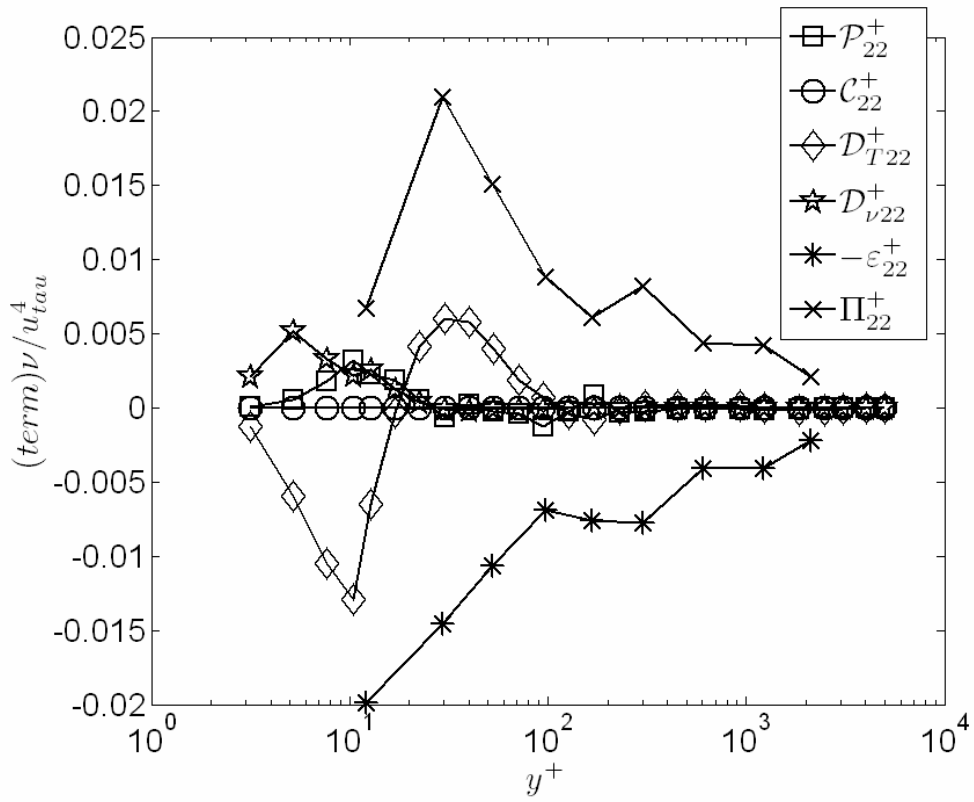


(e)

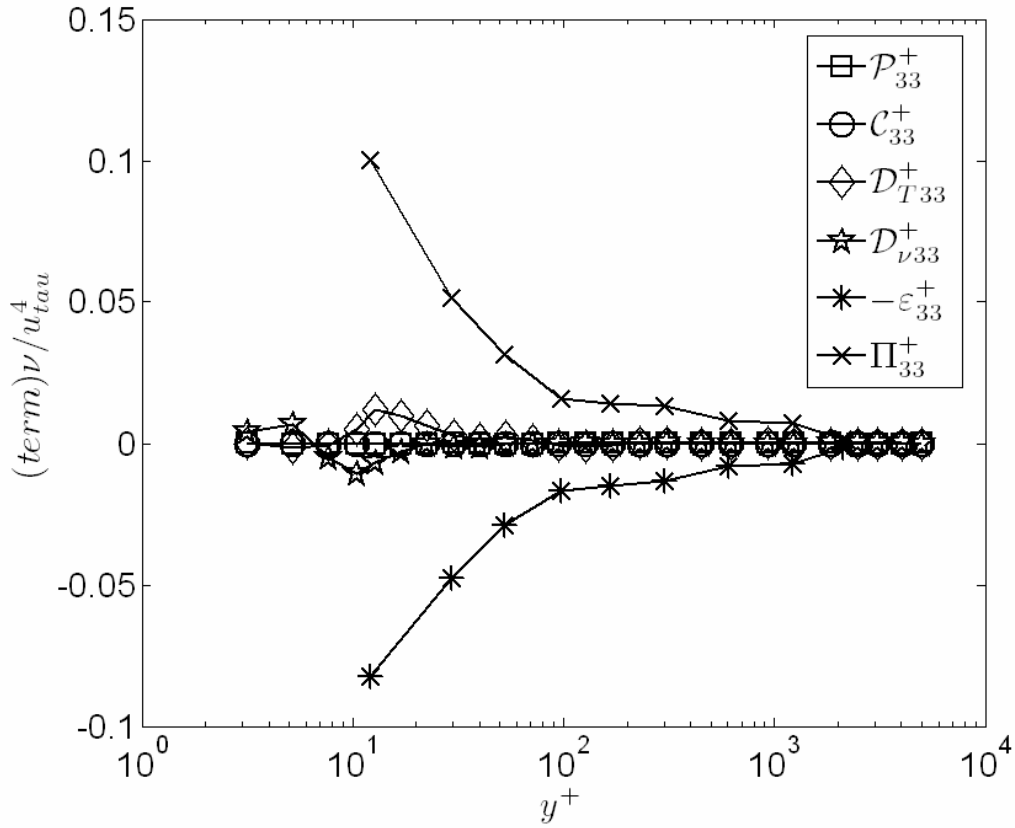
**Figure 4.47. Reynolds stress transport balances using the non-isotropic dissipation rates for the 2DFPTBL at  $Re_\theta = 5929$ . (a)  $\overline{u^2}^+$ , (b)  $\overline{v^2}^+$ , (c)  $\overline{w^2}^+$ , (d)  $\overline{uv}^+$ , (e)  $\frac{1}{2}(\overline{u^2}^+ + \overline{v^2}^+ + \overline{w^2}^+)$ .  $\mathcal{P}_{ij}$ =Production;  $\mathcal{C}_{ij}$ =Convection;  $\mathcal{D}_{vij}$ =Viscous diffusion;  $\mathcal{D}_{Tij}$ =Turbulent diffusion;  $\varepsilon_{ij}$ =Dissipation rate;  $\Pi_{ij}$ =Velocity/pressure gradient correlation.**



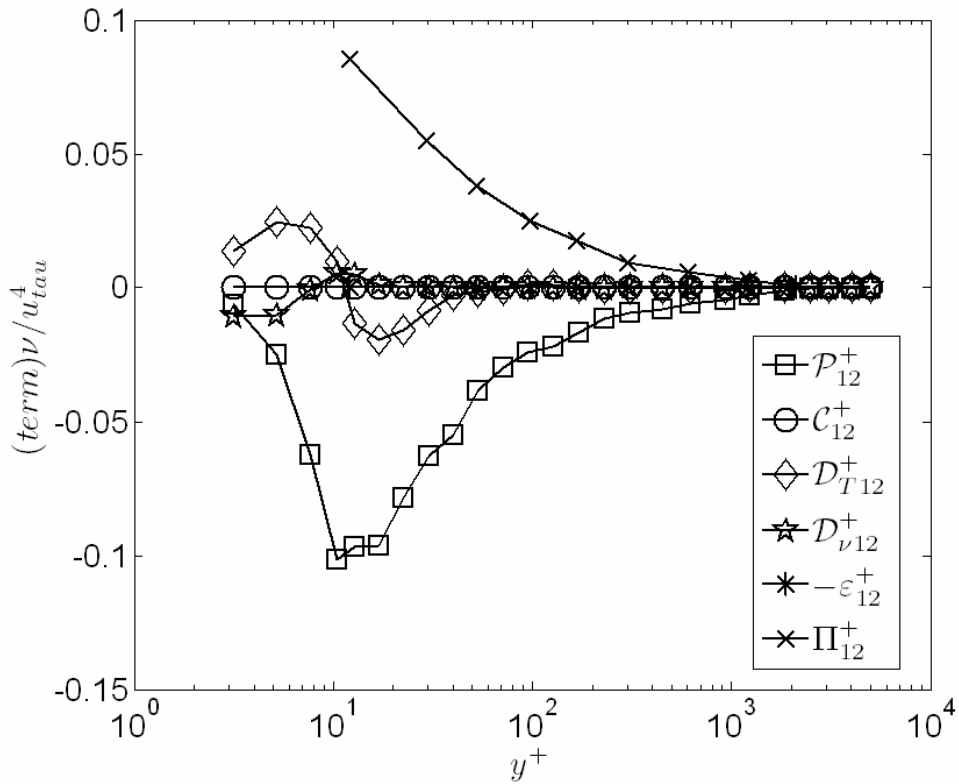
(a)



(b)



(c)



(d)

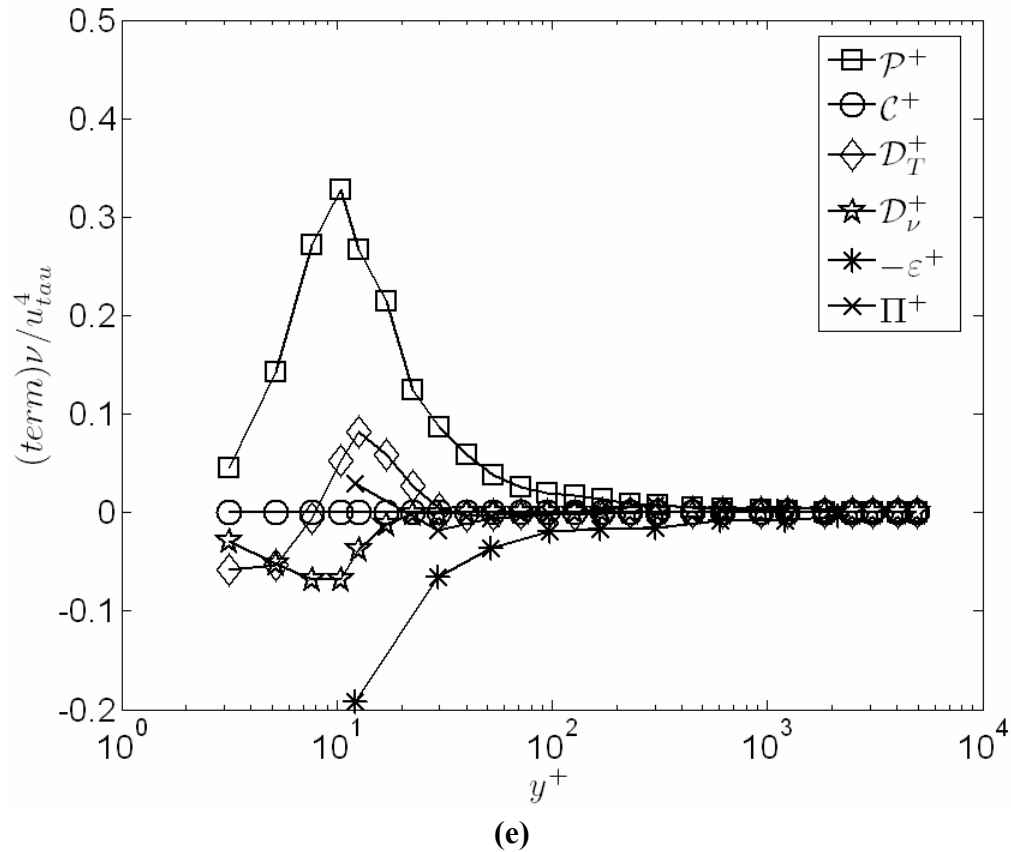


Figure 4.48. Same as Figure 4.47 for  $Re_\theta = 7497$ .

## 4.2 Isolated Protuberances

George (2005) has extensively studied the velocity statistics in the wakes of isolated cylindrical and axisymmetric Gaussian elements in hopes of a build-up approach for modeling distributed roughness made up of the same elements. These measurements have revealed intense action in both coherent and inactive motions shedding from the top of the cylindrical elements in addition to large downwash that leads to rapid reattachment of the flow. Bennington (2004) continued this study by expanding the portfolio of isolated elements for which detailed velocity statistics exist. This work exposed the importance of sharp edges on these elements in producing large TKE due to the abrupt separations that occur there.

The current study is an extension of the work done by George, further characterizing the turbulence structure in the wake of three isolated cylinders submerged in a 2DFPTBL at  $Re_\theta = 7497$ . The diameter of these cylinders were each 1.98mm with heights of  $k=0.38\text{mm}$ ,  $0.76\text{mm}$ , and  $1.52\text{mm}$ , corresponding to viscous roughness scales,  $k^+ \equiv \frac{ku_\tau}{\nu}$ , of  $k^+=23.5$ ,  $47.1$ , and  $94.1$ , respectively. In the discussions to follow, the Reynolds-averaged velocity statistics for profiles taken at locations of  $x/d=2.75$  on the

centerline of the cylinder ( $z/d=0$ ) will be compared with those of George (2005) to verify the consistency in the flows. To augment the current understanding of this flow, measurements of the velocity auto- and cross-spectra will be considered for the additional information about the frequency of motions that occur in the wakes of these elements.

### 4.2.1 Volume-averaged statistics

Just as discussed in section 4.1.2, the CompLDV3 probe-volume was limited to 100 microns in the vertical direction and all quantities were corrected for velocity gradient broadening to obtain the final statistics estimates. For normalization purposes, the 2DFPTBL value for the wall-friction velocity was used to compare with the data of George. This flow-field is characterized as being very-rapidly changing, in each direction due to the small sizes of the elements in each dimension. Considering this fact and the uncertainty inherent in locating the measurement positions relative to the cylindrical test element, the agreement in all the data is excellent. The velocity statistics data (mean velocities and Reynolds stresses) for the small cylinder,  $k^+=23.5$ , are plotted in Figure 4.49-Figure 4.51. These data agree well with the exception of the magnitude of the peak values for the span-wise normal stress,  $\overline{w^2}^+$ . This trend follows for the data for the medium-height cylinder,  $k^+=47.1$  (Figure 4.52-Figure 4.55) and the large cylinder,  $k^+=94.1$  (Figure 4.56-Figure 4.60). Despite the differences, the data from the two experiments are remarkably similar and give confidence in the further interpretation of CompLDV3 data.

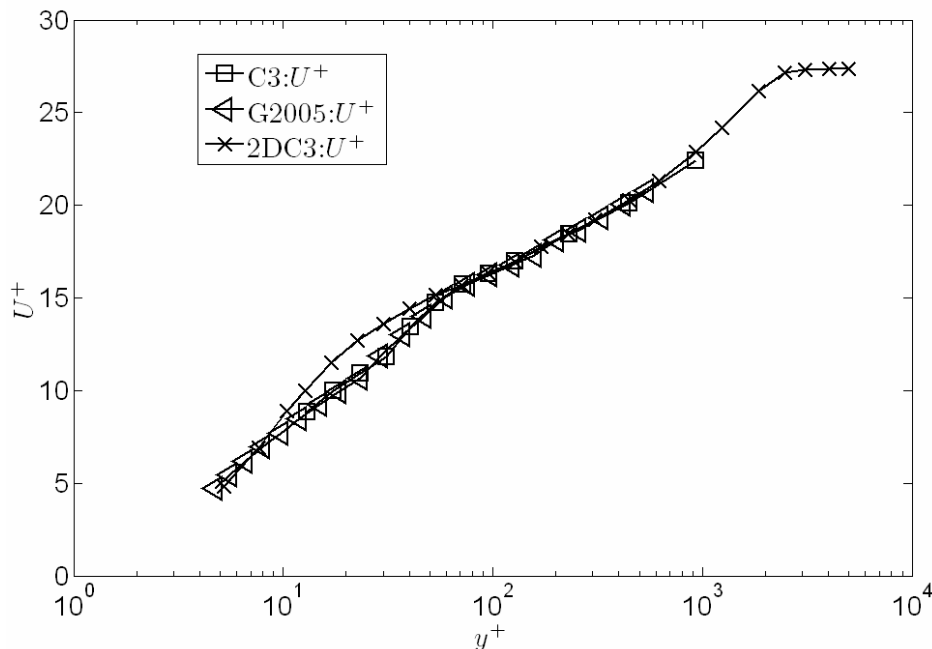


**Figure 4.49** Stream-wise mean velocity profile for the small isolated cylinder at the location  $x/d=2.75$ ,  $z/d=0$ . C3, CompLDV3 measurements; G2005, George (2005) measurements; 2DC3, 2DFPTBL measured with the CompLDV3.

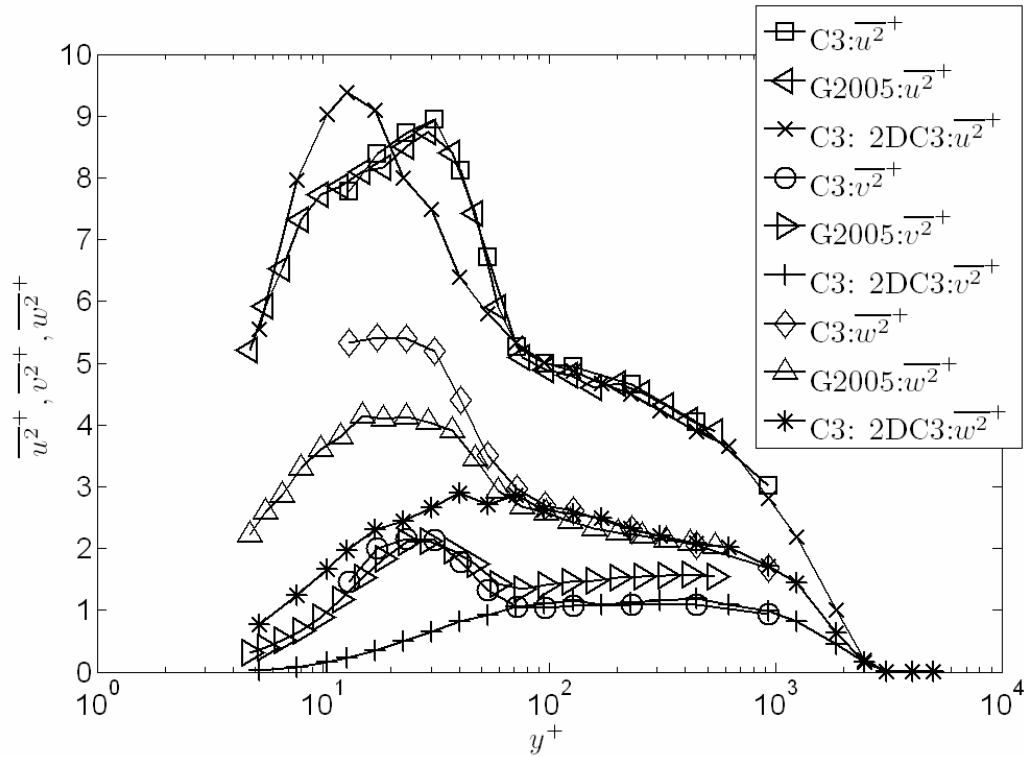


**Figure 4.50.** Reynolds normal stress profiles for the small isolated cylinder at the location  $x/d=2.75$ ,  $z/d=0$ . C3, ComplLDV3 measurements; G2005, George (2005) measurements; 2DC3, 2DFPTBL measured with the ComplLDV3.

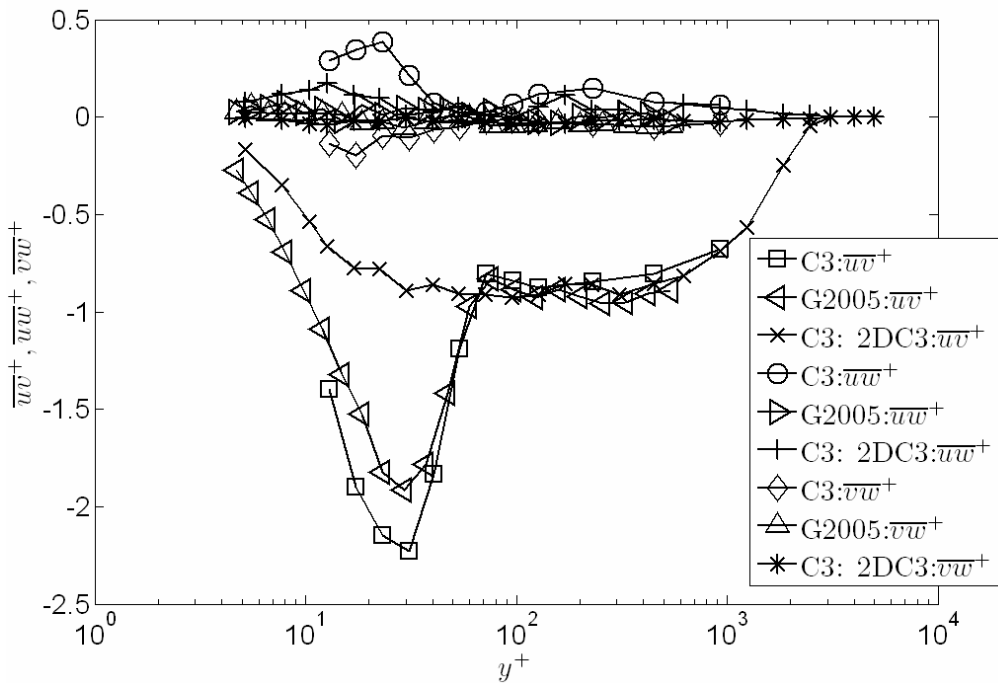


**Figure 4.51.** Reynolds shear stress profiles for the small isolated cylinder at the location  $x/d=2.75$ ,  $z/d=0$ . C3, ComplLDV3 measurements; G2005, George (2005) measurements; 2DC3, 2DFPTBL measured with the ComplLDV3.

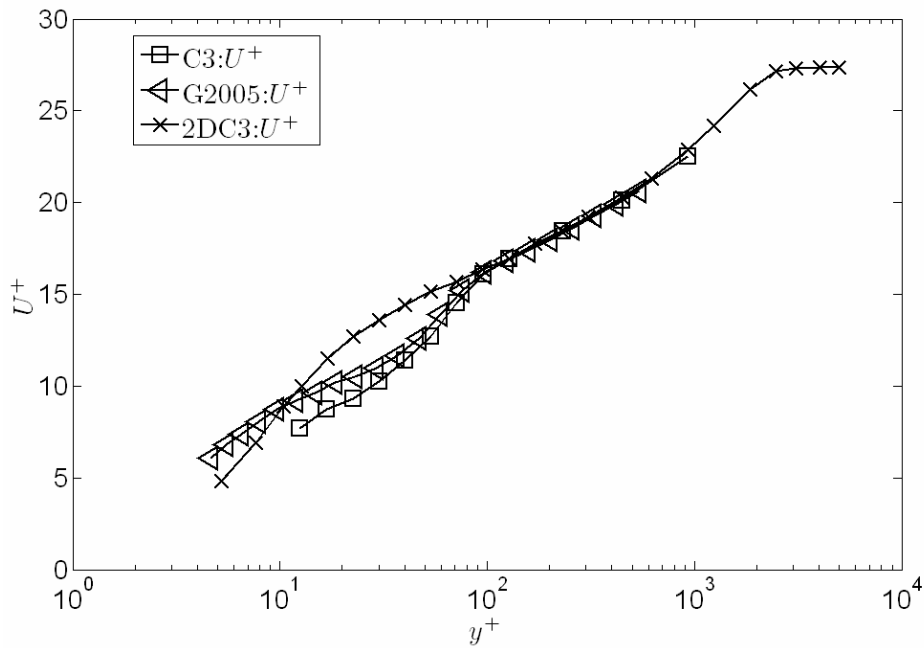


**Figure 4.52.** Stream-wise mean velocity profile for the medium-height isolated cylinder at the location  $x/d=2.75$ ,  $z/d=0$ . C3, CompLDV3 measurements; G2005, George (2005) measurements; 2DC3, 2DFPTBL measured with the CompLDV3.

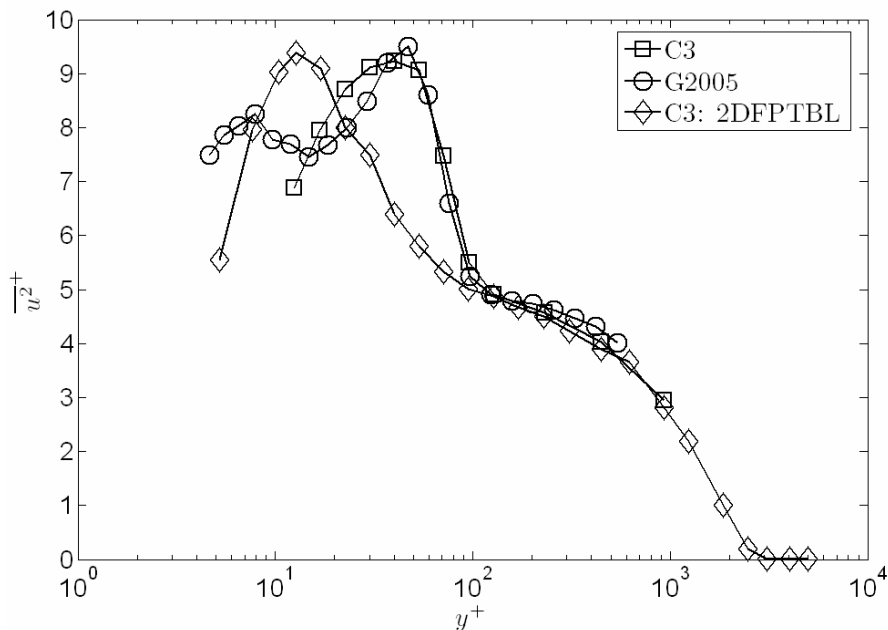


**Figure 4.53.** Stream-wise Reynolds normal stress profiles for the medium-height isolated cylinder at the location  $x/d=2.75$ ,  $z/d=0$ . C3, CompLDV3 measurements; G2005, George (2005) measurements; 2DC3, 2DFPTBL measured with the CompLDV3.

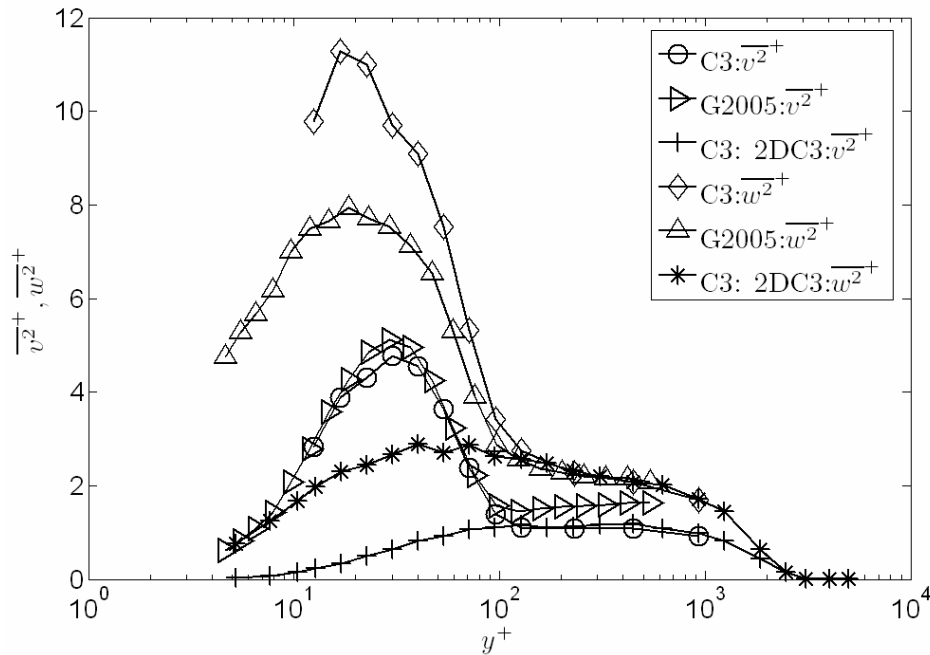


**Figure 4.54.** Span-wise and normal-to-wall Reynolds normal stress profiles for the medium-height isolated cylinder at the location  $x/d=2.75$ ,  $z/d=0$ . C3, ComplDV3 measurements; G2005, George (2005) measurements; 2DC3, 2DFPTBL measured with the ComplDV3.

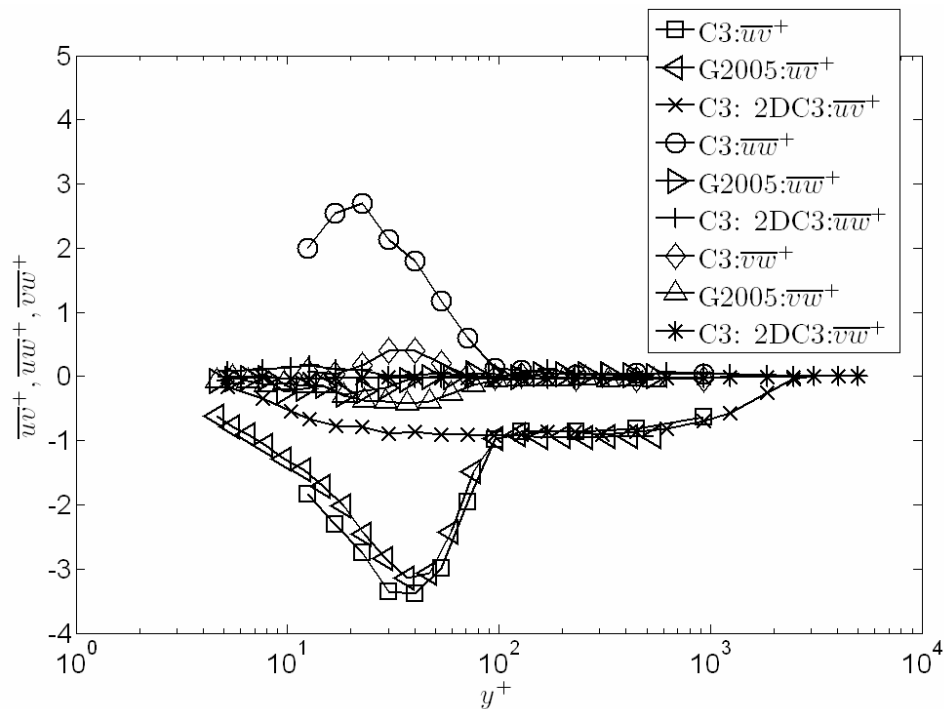


**Figure 4.55.** Reynolds shear stress profiles for the medium-height isolated cylinder at the location  $x/d=2.75$ ,  $z/d=0$ . C3, ComplDV3 measurements; G2005, George (2005) measurements; 2DC3, 2DFPTBL measured with the ComplDV3.

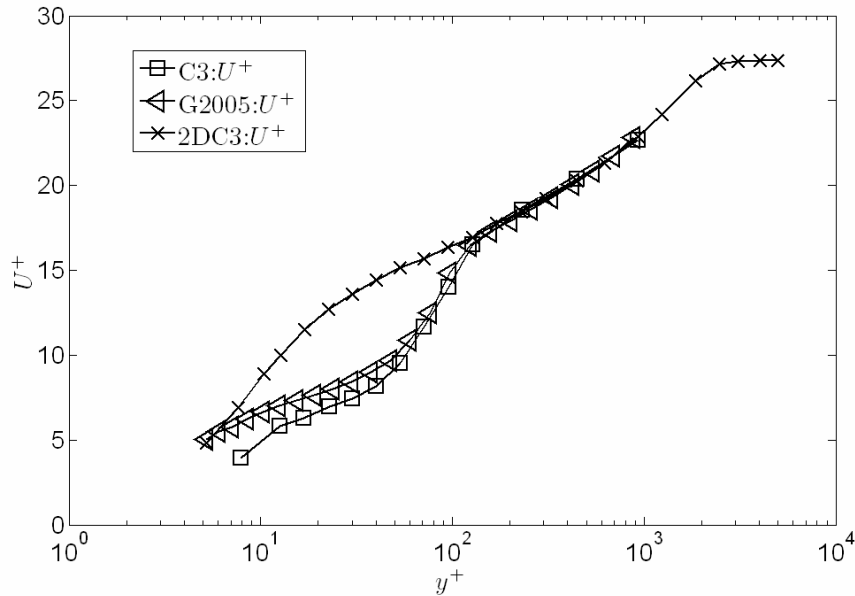


**Figure 4.56.** Stream-wise mean velocity profile for the large isolated cylinder at the location  $x/d=2.75$ ,  $z/d=0$ . C3, ComplLDV3 measurements; G2005, George (2005) measurements; 2DC3, 2DFPTBL measured with the ComplLDV3.

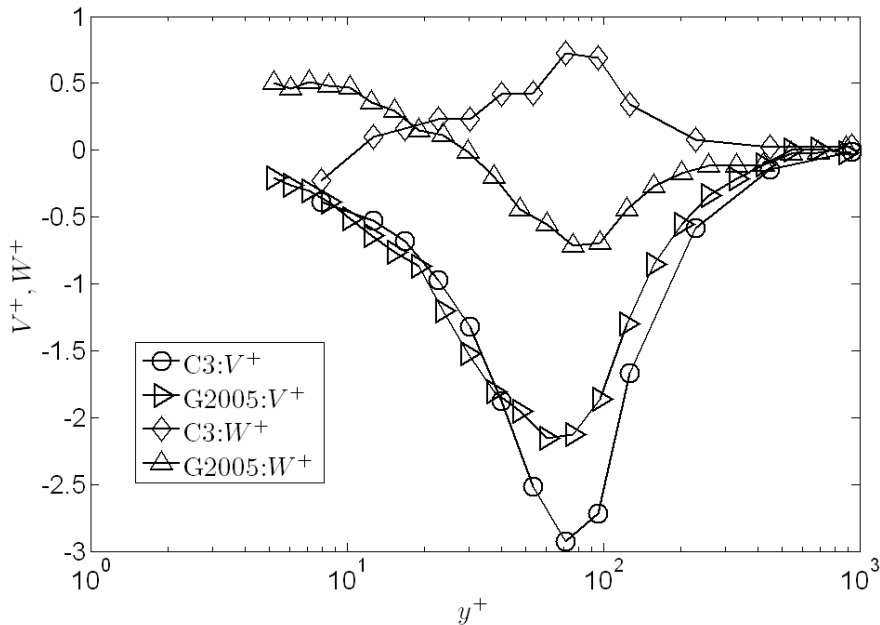


**Figure 4.57.** Normal-to-wall and span-wise mean velocity profiles for the large isolated cylinder at the location  $x/d=2.75$ ,  $z/d=0$ . C3, ComplLDV3 measurements; G2005, George (2005) measurements; 2DC3, 2DFPTBL measured with the ComplLDV3.

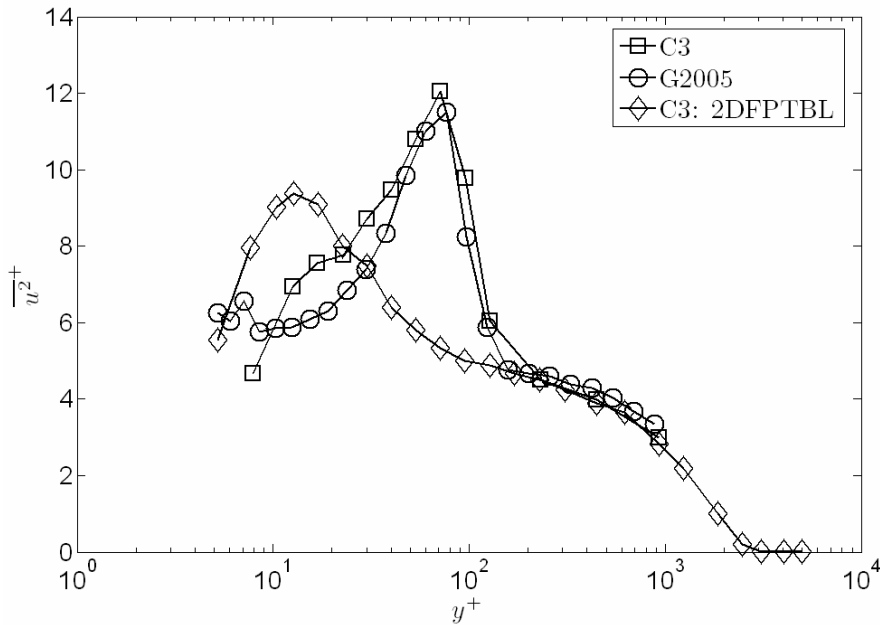


**Figure 4.58.** Stream-wise Reynolds normal stress profiles for the large isolated cylinder at the location  $x/d=2.75$ ,  $z/d=0$ . C3, CompLDV3 measurements; G2005, George (2005) measurements; 2DC3, 2DFPTBL measured with the CompLDV3.

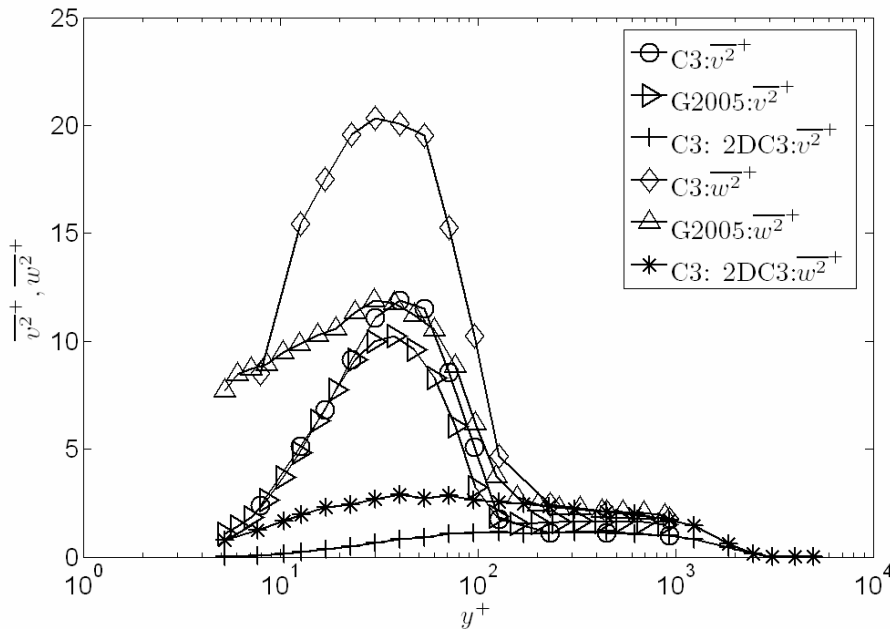


**Figure 4.59.** Normal-to-wall and span-wise Reynolds normal stress profiles for the large isolated cylinder at the location  $x/d=2.75$ ,  $z/d=0$ . C3, CompLDV3 measurements; G2005, George (2005) measurements; 2DC3, 2DFPTBL measured with the CompLDV3.

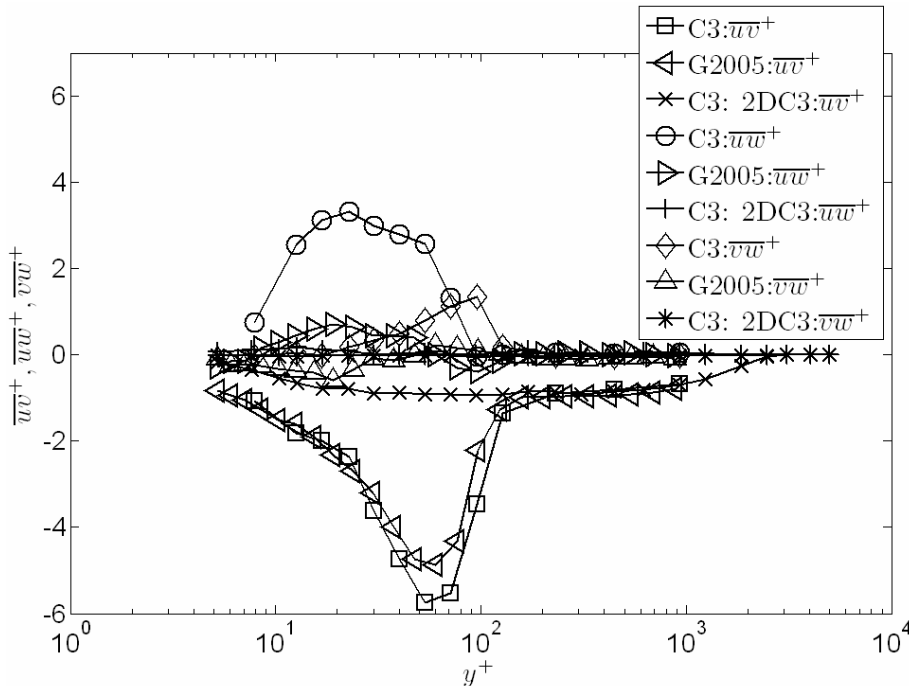


**Figure 4.60. Reynolds shear stress profiles for the medium-height isolated cylinder at the location  $x/d=2.75$ ,  $z/d=0$ . C3, ComplDV3 measurements; G2005, George (2005) measurements; 2DC3, 2DFPTBL measured with the ComplDV3.**

## 4.2.2 Spectral analysis

### 4.2.2.1 Small cylinder

The spectral distributions of the Reynolds stresses in the wake of the small isolated cylinder have been computed for the stream-wise location of  $x/d=2.75$  downstream from the center of the element. In order to achieve maximum data rates, the spatial-extent of the ComplDV3 volume was not significantly limited during post-processing and resulted in a diameter of about 200 microns. For this small cylinder, with a height of 381 microns, the relative extent of the measurement volume is significant. However, information about the scales of motion that occur downstream of this element are still useful for interpretation. Furthermore, it may be possible in future work to restrict the measurement volume to obtain spectral estimates at higher spatial resolutions, although at much-reduced data rates.

The velocity spectra have been normalized using the free-stream velocity and the height of the isolated cylinder. The normal-stress spectra are given in Figure 4.61-Figure 4.63. Shear stress cross-spectra and coherency are plotted in Figure 4.64 and Figure 4.65, respectively. Around the element height there is an enhancement of the high-frequency motions for the stream-wise normal stress and Reynolds shear stress that is most-likely linked to the large shear rate that occurs over the top of the element. As the flow abruptly encounters the cylinder, large velocity gradients occur perpendicular to the element height. Since a velocity gradient is in itself an inverse time-scale, the inverse of a large

gradient value is a very small time scale. Since the mean approach flow is in the streamwise direction, it is the streamwise velocity that reflects the enhancement of the high-frequency motion in the normal stresses. The instabilities in the shear layer that occurs after separation off the top of the cylinder result in coordinated motions that lead to the high shear stresses measured. The enhancement of the Reynolds shear stress in the high frequencies is also evident in Figure 4.64.

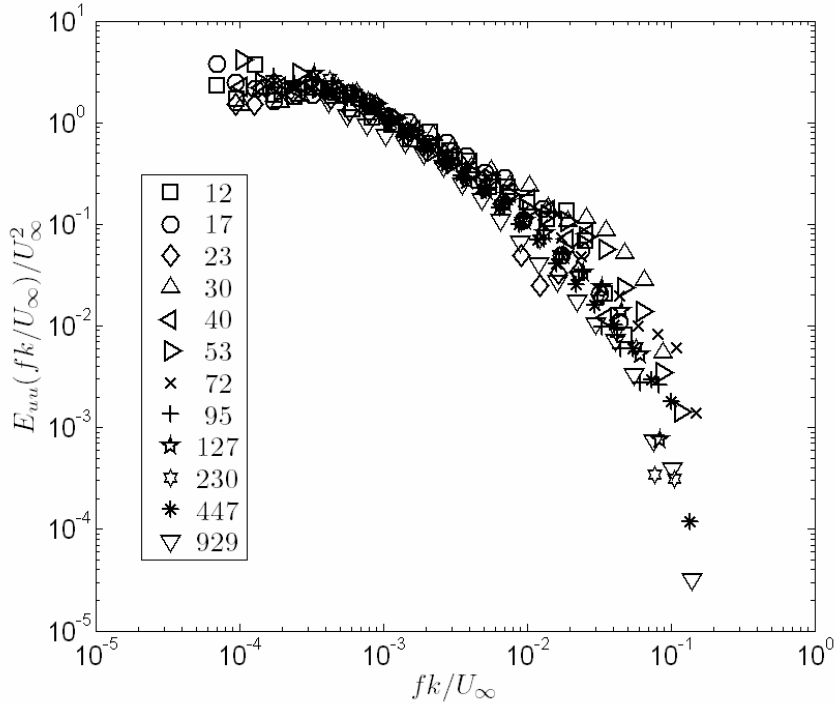


**Figure 4.61.** Auto-spectra of the stream-wise velocity fluctuations behind the small cylinder at the location  $x/d=2.75$ ,  $z/d=0$ . The legend gives the measurement height in  $y^+$ .

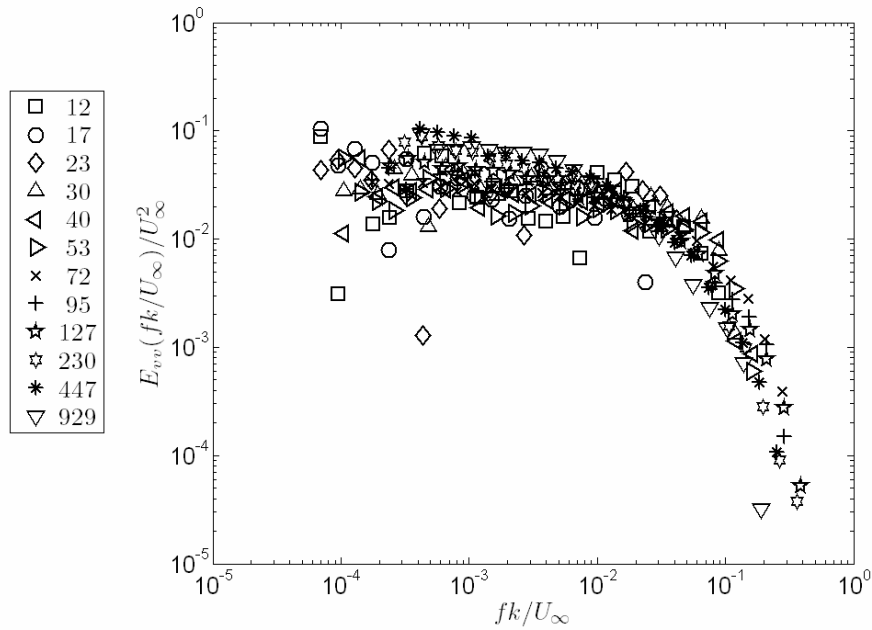


**Figure 4.62.** Auto-spectra of the normal-to-wall velocity fluctuations behind the small cylinder at the location  $x/d=2.75$ ,  $z/d=0$ . The legend gives the measurement height in  $y^+$ .

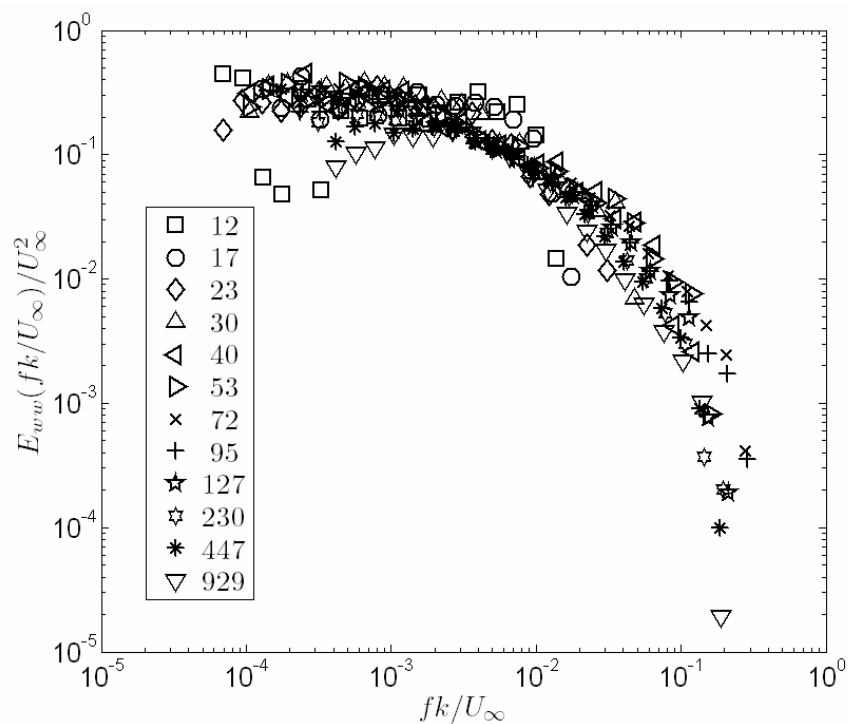


**Figure 4.63.** Auto-spectra of the span-wise velocity fluctuations behind the small cylinder at the location  $x/d=2.75$ ,  $z/d=0$ . The legend gives the measurement height in  $y^+$ .

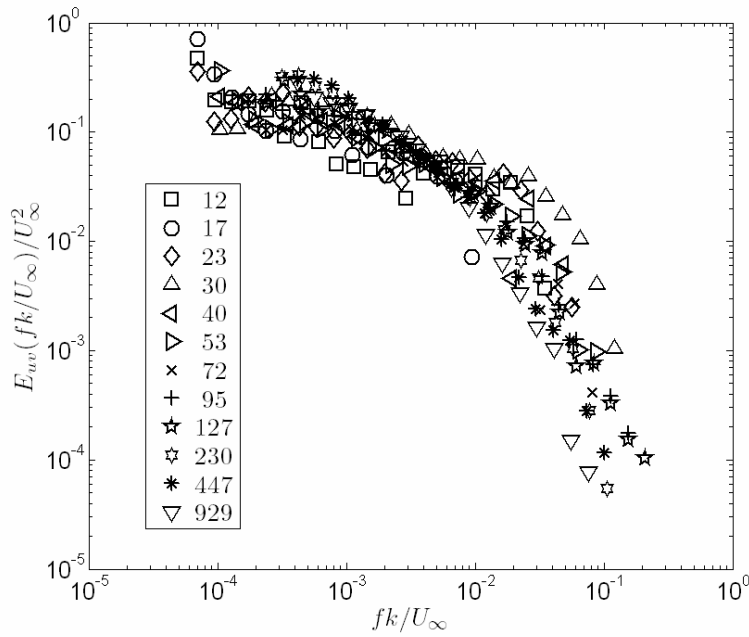


**Figure 4.64.** Cross-spectra of the Reynolds shear stress components,  $u'$  and  $v'$ , behind the small cylinder at the location  $x/d=2.75$ ,  $z/d=0$ . The legend gives the measurement height in  $y^+$ .

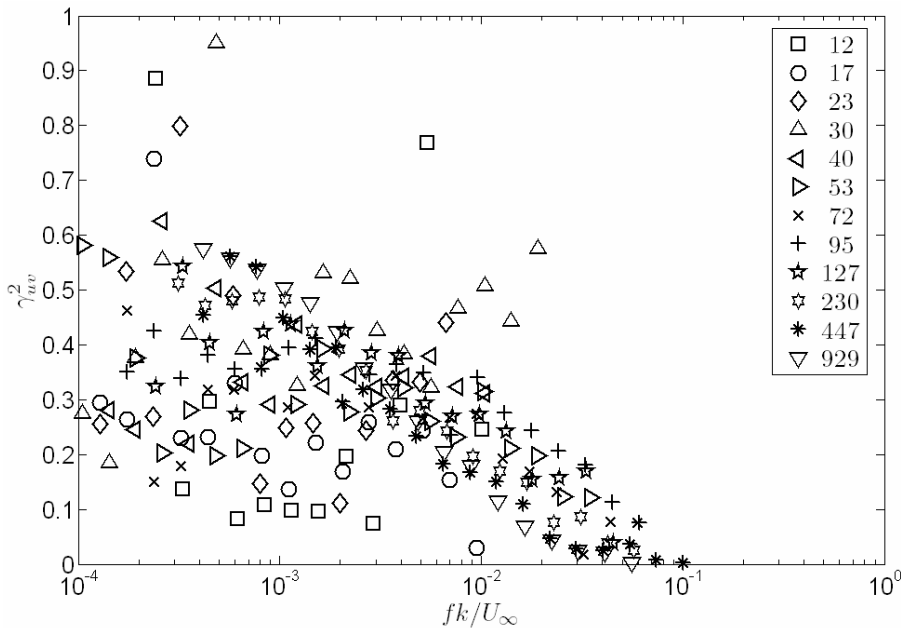


**Figure 4.65.** Spectral coherency between the Reynolds shear stress components,  $u'$  and  $v'$ , behind the small cylinder at the location  $x/d=2.75$ ,  $z/d=0$ . The legend gives the measurement height in  $y^+$ .

### 4.2.2.2 Medium-height cylinder

The spectral distributions of the Reynolds stresses in the wake of the medium-height isolated cylinder for the stream-wise location of  $x/d=2.75$  downstream from the center of the element are considered in this section. The concerns in the previous section about probe-volume dimensions still hold but are not as severe considering the cylinder height of 762 microns.

Again, the velocity spectra have been normalized using the free-stream velocity and the height of the isolated cylinder. The normal-stress spectra are given in Figure 4.66-Figure 4.68, while the shear-stress cross-spectra are given in Figure 4.69 with coherency of those fluctuations plotted in Figure 4.70. Again, evidence exists for the argument of the previous section concerning the behavior of the intense shear-layer just after separation from the top of the element. It is clearer for the present case that around the element height there is a definite enhancement of the high frequency motions in the stream-wise normal stresses as compared with the data much above the element. The vertical and span-wise normal stresses exhibit significant augmentation of the values of the velocity spectra in the same region, but for the most part these appear as a uniform scaling increase compared to the outer-flow data. The cross-spectra of the Reynolds shear stress exhibit substantial enhancement in the high-frequency ranges that again supports the notion of instabilities in the shear layer downstream of the element.

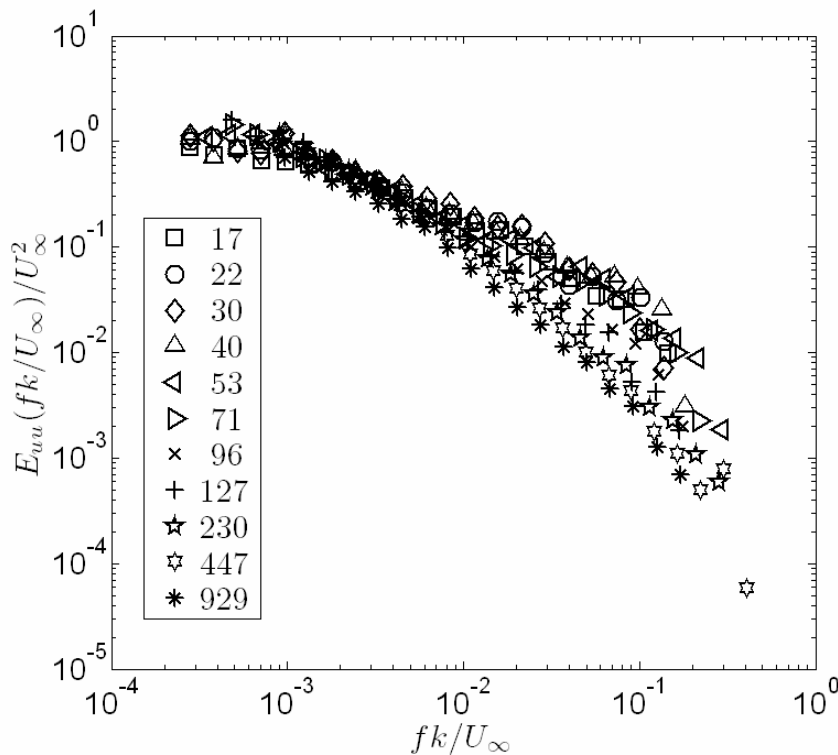


**Figure 4.66. Auto-spectra of the stream-wise velocity fluctuations behind the medium-height cylinder at the location  $x/d=2.75$ ,  $z/d=0$ . The legend gives the measurement height in  $y^+$ .**

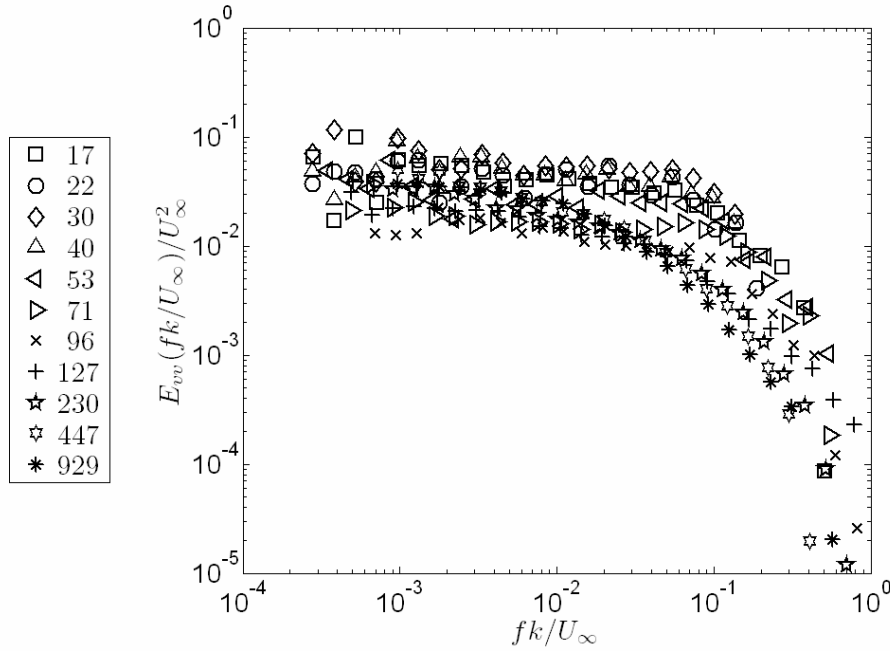


**Figure 4.67.** Auto-spectra of the normal-to-wall velocity fluctuations behind the medium-height cylinder at the location  $x/d=2.75$ ,  $z/d=0$ . The legend gives the measurement height in  $y^+$ .

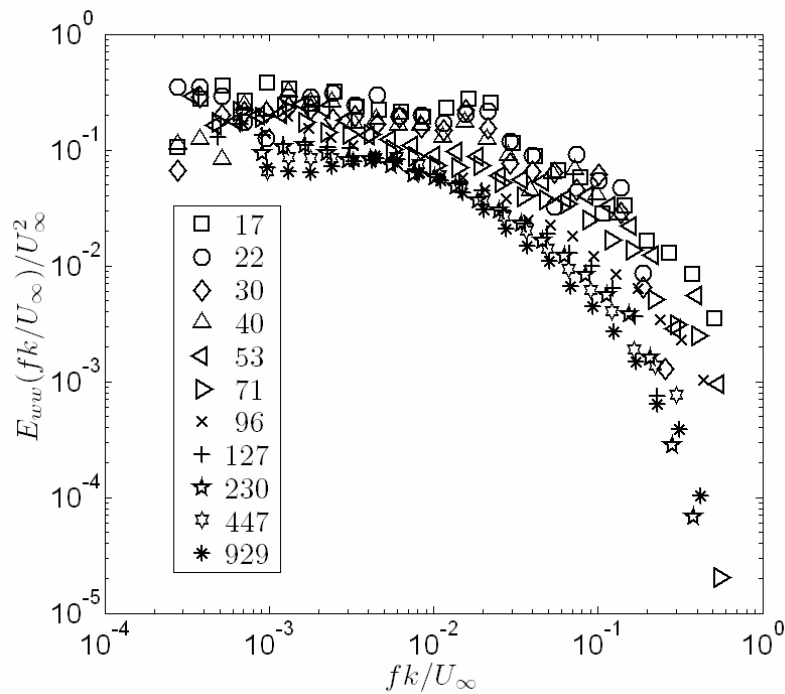


**Figure 4.68.** Auto-spectra of the span-wise velocity fluctuations behind the medium-height cylinder at the location  $x/d=2.75$ ,  $z/d=0$ . The legend gives the measurement height in  $y^+$ .

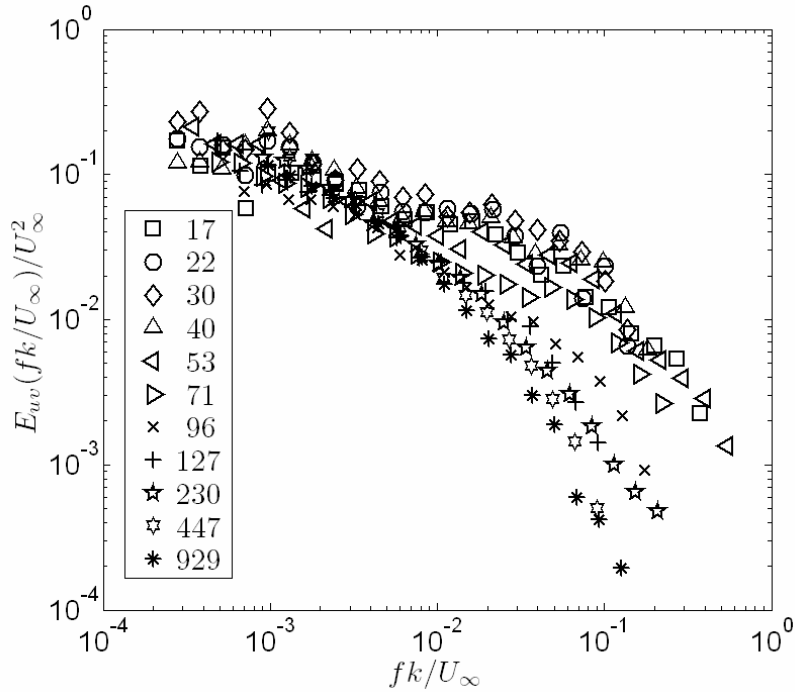


Figure 4.69. Cross-spectra of the Reynolds shear stress components,  $u'$  and  $v'$ , behind the medium-height cylinder at the location  $x/d=2.75$ ,  $z/d=0$ . The legend gives the measurement height in  $y^+$ .

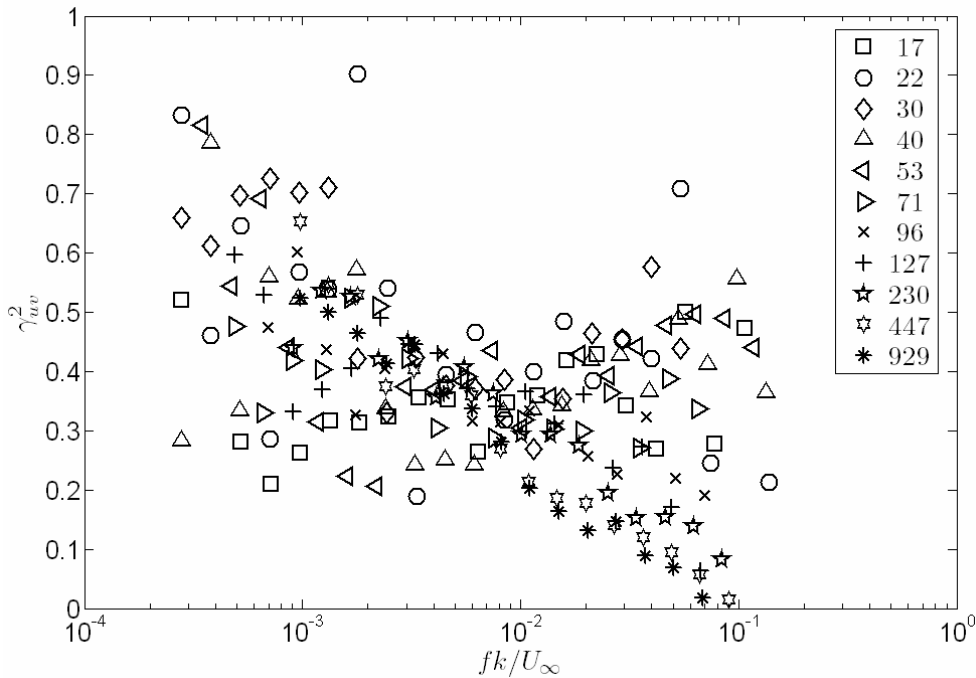
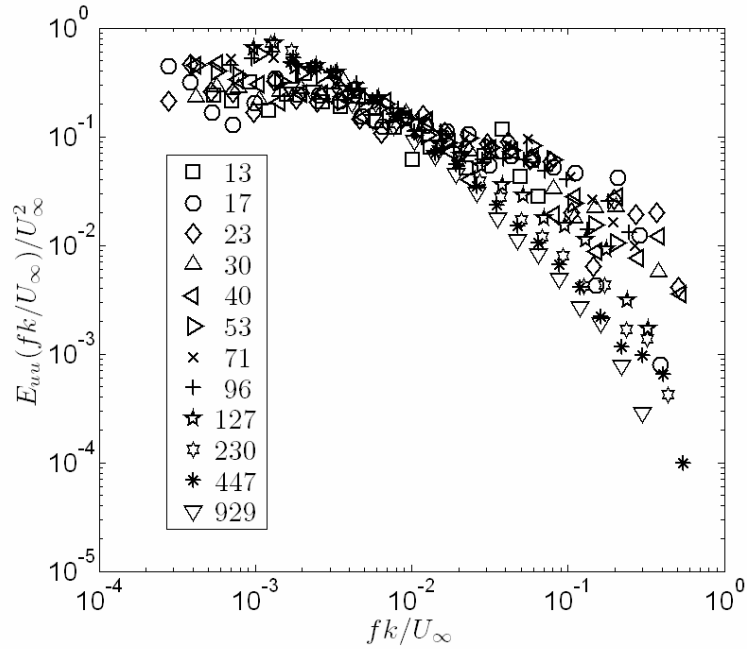


Figure 4.70. Spectral coherency between the Reynolds shear stress components,  $u'$  and  $v'$ , behind the medium-height cylinder at the location  $x/d=2.75$ ,  $z/d=0$ . The legend gives the measurement height in  $y^+$ .

### 4.2.2.3 Large cylinder

The normal-stress spectra for the large cylinder are given in Figure 4.71-Figure 4.73, while the shear-stress cross-spectra are given in Figure 4.74 with coherency of those fluctuations plotted in Figure 4.75. Very similar phenomena appear in the high frequencies of the stream-wise normal stress and Reynolds shear stress as discussed for the small and medium cylinders. Effects of the element on the Reynolds shear stress spectra appear out to  $y^+=230$ , more than twice the height of the cylinder.

An additional interesting feature appears in these data for the span-wise normal stress spectra. Energy is concentrated in the spectra around the element height at  $fk/U_\infty \approx 0.05$ . This is somewhat unexpected since the approach flow is fully-turbulent, and that may lead one to the conclusion that a deterministic occurrence in frequency is unlikely. The extensive velocity statistics data of George (2005) give some insight into this phenomenon. The large cylinder has a relatively-intense mean vortex, denoted by George as the roughness top vortex structure (RTVS) with its center of rotation at  $y^+=30$ . In the same region as the vortex center, there is an intense region of the shear stress  $\overline{uw}$  that is also aligned with the span-wise edge of the cylinder. This seems to indicate a vertical fluctuation of the vortex center location that delivers with it either positive stream-wise-momentum fluid from areas away from the element when it fluctuates toward the wall or negative-momentum fluid from the separated region behind the cylinder when the center of the vortex moves upward. It seems likely that the mechanism for this phenomenon is the interaction of the two legs of the RTVS on either side of the element. Since the frequency of this interaction is relatively high, it may be presumed that coherent structures of large stream-wise extent may establish a sufficiently stable flow for periods long enough to induce this unsteady motion.



**Figure 4.71.** Auto-spectra of the stream-wise velocity fluctuations behind the large cylinder at the location  $x/d=2.75$ ,  $z/d=0$ . The legend gives the measurement height in  $y^+$ .

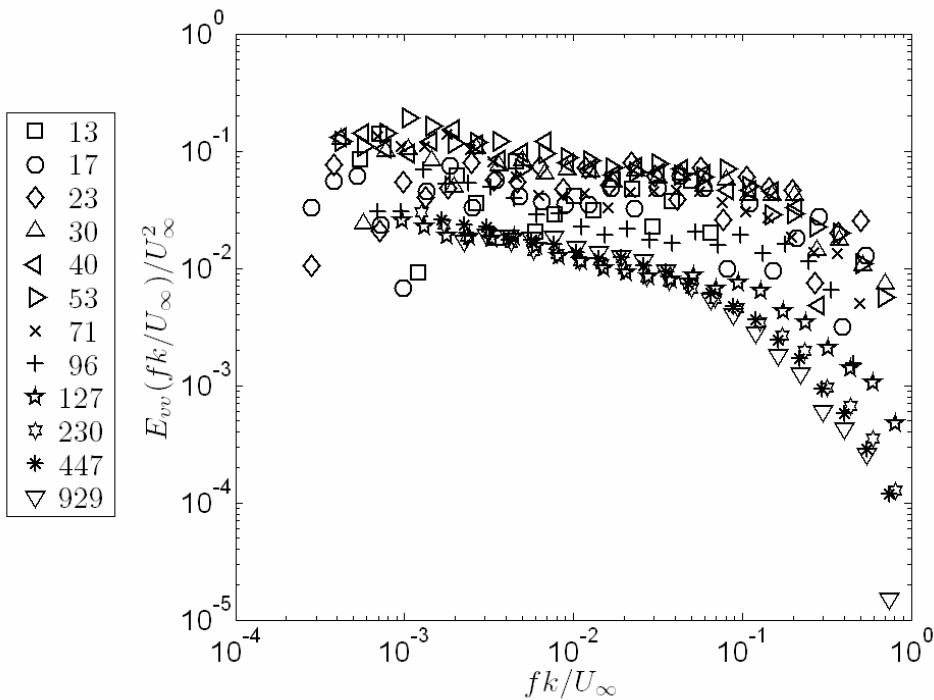


**Figure 4.72.** Auto-spectra of the normal-to-wall velocity fluctuations behind the large cylinder at the location  $x/d=2.75$ ,  $z/d=0$ . The legend gives the measurement height in  $y^+$ .

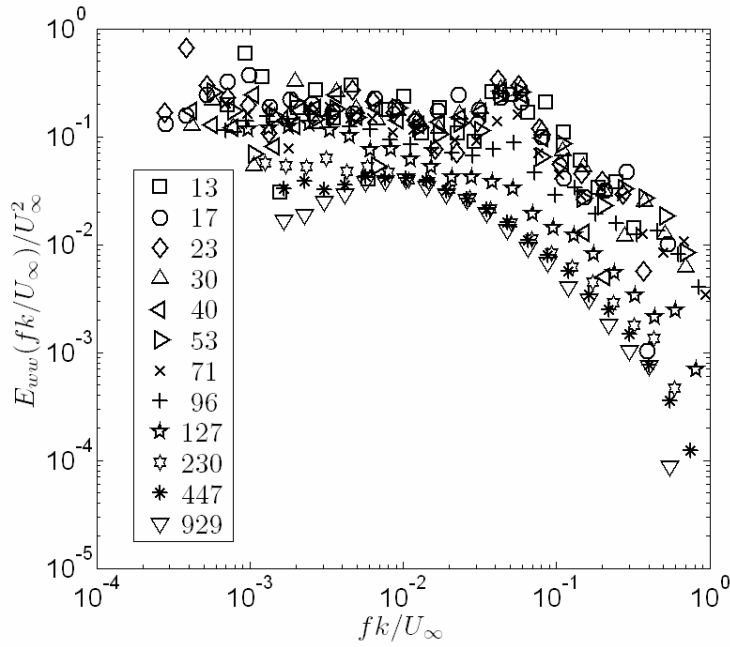


**Figure 4.73.** Auto-spectra of the span-wise velocity fluctuations behind the large cylinder at the location  $x/d=2.75$ ,  $z/d=0$ . The legend gives the measurement height in  $y^+$ .

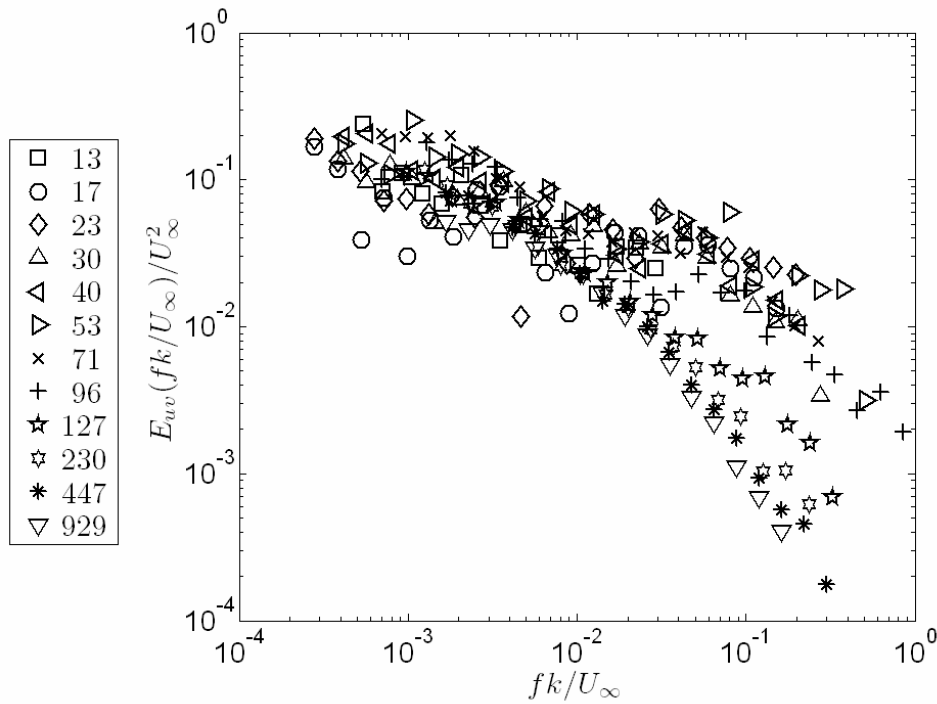


**Figure 4.74.** Cross-spectra of the Reynolds shear stress components,  $u'$  and  $v'$ , behind the medium-height cylinder at the location  $x/d=2.75$ ,  $z/d=0$ . The legend gives the measurement height in  $y^+$ .

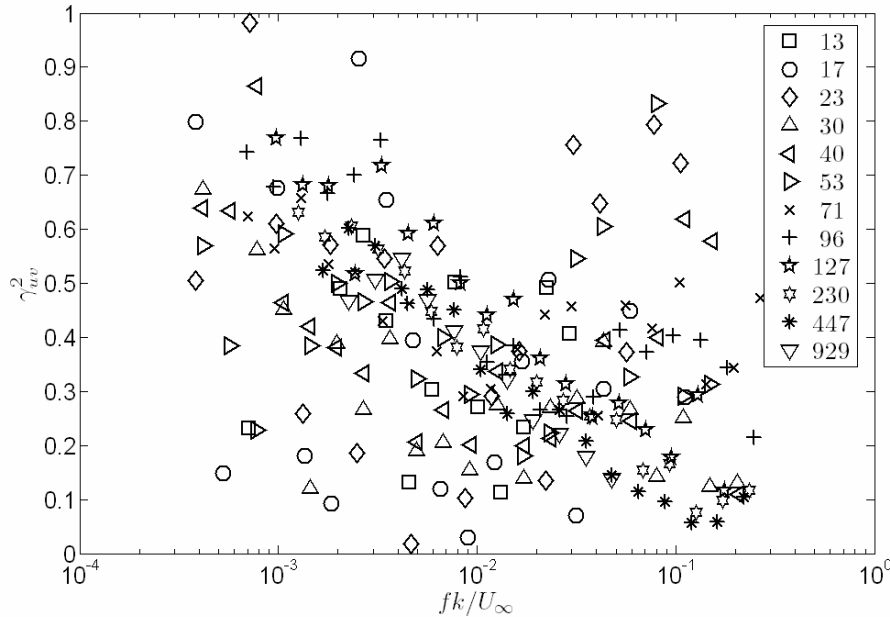


**Figure 4.75.** Spectral coherency between the Reynolds shear stress components,  $u'$  and  $v'$ , behind the medium-height cylinder at the location  $x/d=2.75$ ,  $z/d=0$ . The legend gives the measurement height in  $y^+$ .

## 4.3 3D Turbulent Boundary Layers

The attached turbulent boundary layer in the vicinity of a wing/body junction has been measured using the CompLDV3 technologies. The geometry of the wing is a 3:2 elliptical nose joined at the maximum thickness to a NACA 0020 airfoil with a maximum thickness of 7.17cm. This particular flow is well-studied by the TBLRG (Devenport and Simpson 1990; Ölçmen and Simpson 1995; Simpson 1996; Ölçmen et al. 2001a; 2001b; Simpson 2001; George 2005). The complex flow includes a meandering separated region very near the junction region of the wing, a highly-unsteady horseshoe vortex that is formed at the leading edge of the wing/body junction, and span-wise pressure gradients that generate stream-wise vorticity and strong three-dimensionality even outside of the attached vortex region.

### 4.3.1 Setup and oil-flow

The wing/body junction was installed into the Department of Aerospace and Ocean Engineering Boundary Layer Research Wind Tunnel in as nearly the same manner as possible to that done by previous researchers. To continue the same study as Ölçmen and Simpson (1995), the tunnel was set to a nominal freestream velocity of 27.5m/s such that the 2DFPTBL in the absence of the wing/body junction was at a Reynolds number of  $Re_\theta = 7497$  as documented in section 4.1.1.

The setup of the flow was initially tested for symmetry and consistency with previous experiments using oil-flow visualization. The procedures and oil-pigment formula described by Tian et al. (2004) were used. In Figure 4.76, a digital photograph of the oil-flow has been examined using a mechanical drawing program that allows precise gauging of the 2D positions of points in the photograph. To assess the symmetry of the flow, the perpendicular distance from the chord-line to the horseshoe vortex washout identified by the dark line absent of pigment from the oil-flow was measured at several stream-wise locations. An excellent symmetry was achieved within the spatial uncertainties of the oil-flow technique.

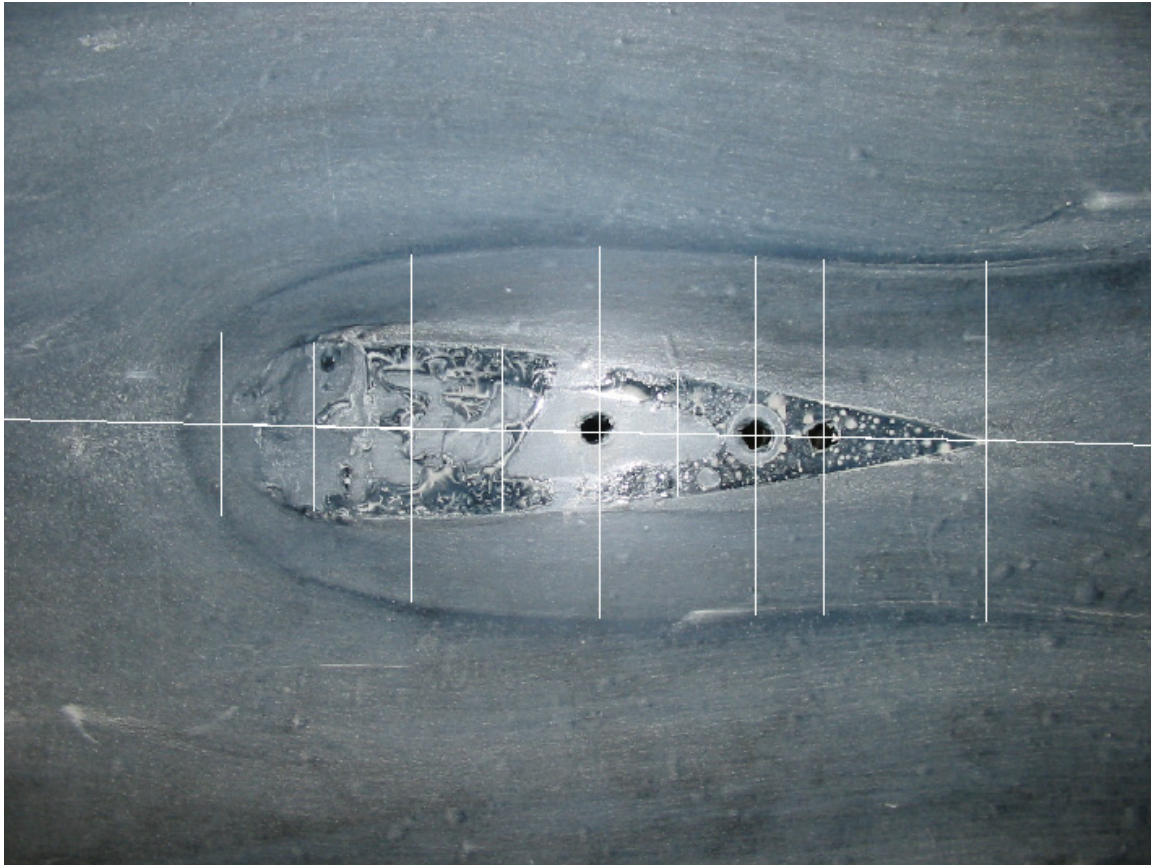


**Figure 4.76. Oil-flow visualization for the wind-tunnel floor in the vicinity of the wing junction. The lines on the plot were drawn using mechanical drawing software and are equal length from the chord-line of the wing. Credit goes to Joshua DeMoss for this figure.**

### **4.3.2 CompLDV3 data**

The CompLDV3 data were acquired at two stations that exhibit attached 3D TBL flows. The locations of the stations relative to the wing/body junction are shown in Figure 4.77, where stations 3 and 5 have been measured for the current study. At each of the stations, detailed, low-uncertainty conventional 3-component LDV data exist and stand as the

benchmark for the current results—all CompLDV3 velocity statistics results are compared to those of Ölçmen and Simpson (1995) for consistency.

As discussed in section 2.3.3.9, the CompLDV3 operates best when rotated to the approximate flow angle to be measured (see the geometry of  $\beta_{Probe}$  in Figure 4.77). With the previous data for these flows, it was possible to obtain these probe rotations *a priori*, although when measuring flows for the first time, a CompLDV3 profile may be done to obtain the mean velocities and flow angles for more subsequent, rotated measurements. The probe rotations used for measurements at station 3 were  $33.2^\circ$  for the near-wall data and  $20^\circ$  for the data further from the wall. For station 5 the near-wall data were taken with a probe rotation of  $25.2^\circ$  while an  $8^\circ$  rotation was used for the data further from the wall.

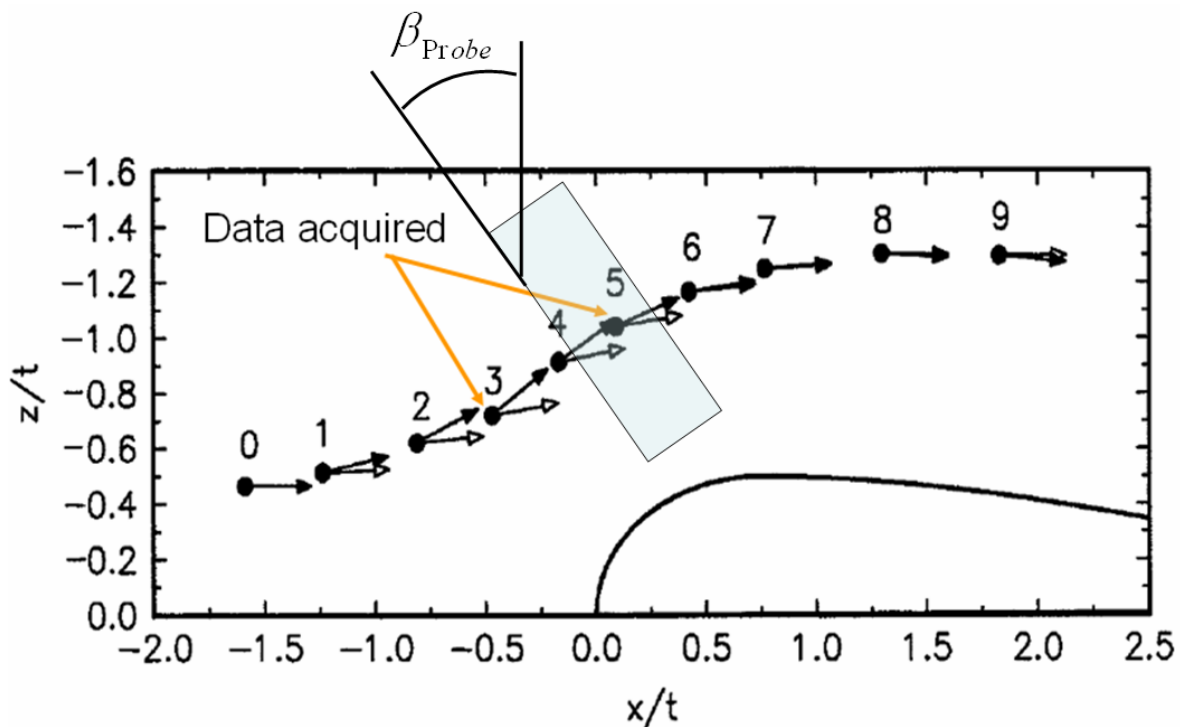


**Figure 4.77.** Plot of the 3D boundary layer measurements in the vicinity of the wind-tunnel floor near a wing junction. The filled arrow heads indicate the direction of the wall shear while the open arrows indicate the free-stream velocity direction. The box surrounding station 5 represents the CompLDV3 probe orientation with the length aligned with the projection of the beam bisectors of the two heads. This figure adapted from figure 1 in Ölçmen et al. (2001a) with kind permission of Springer Science and Business Media.

#### 4.3.2.1 Reynolds-averaged statistics

##### 4.3.2.1.1 The near-wall region

The CompLDV3 position resolution capabilities were used to obtain information in the near-wall regions of stations 3 and 5. The resolved measurements for station 3 are plotted in Figure 4.78-Figure 4.80 while station 5 data are given in Figure 4.81-Figure 4.84 . Again, as was mentioned in section 4.1.1.1, these are the most-spatially-resolved measurements ever obtained in these flows, with a resolution between each point of about 10 microns. As mentioned in section 2.3.3.9.4.4, the CompLDV3 is truly operating in a multi-dimensional manner as is evident in the plot of the flow angle for station 5, Figure 4.82. The CompLDV3 actually detects changes of flow angle occurring within the measurement volume.

These data were used to obtain estimates of the wall-shear stress by considering the velocity gradient of the resultant co-planar wall-velocity:  $Q \equiv \sqrt{U^2 + W^2}$  . The values obtained from these fits of the near-wall data gave wall-friction velocities of  $u_\tau = 1.05m/s$  and  $u_\tau = 1.20m/s$  for stations 3 and 5 respectively. In comparison, Ölçmen and Simpson (1995) report values of  $u_\tau = 0.957m/s$  and  $u_\tau = 1.15m/s$  for the same respective values. The volume-averaged data for the CompLDV3 to follow are normalized using the wall-friction values obtained in this study and are compared to the data of Ölçmen and Simpson (1995) using the wall friction values found in their study.

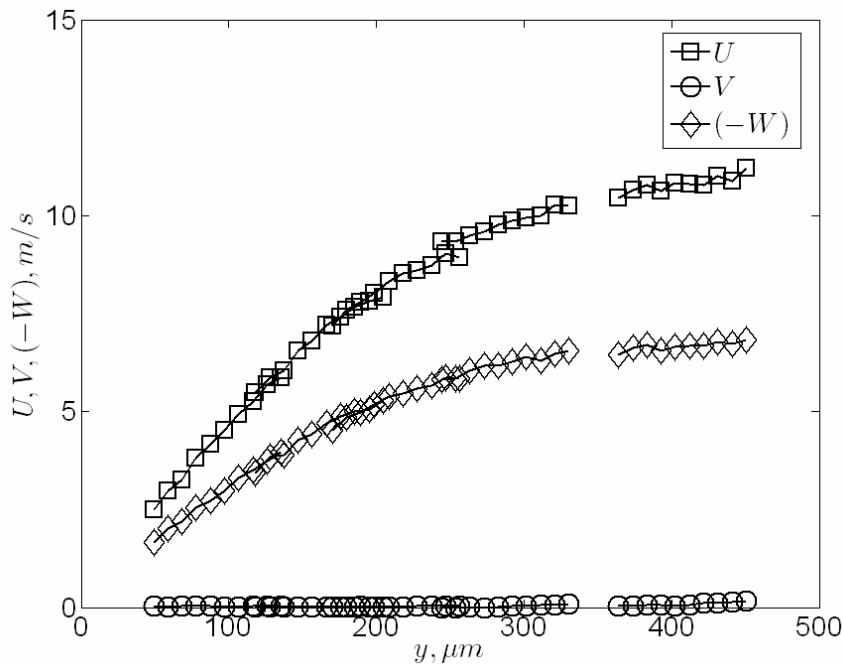


**Figure 4.78. Sub-measurement volume resolution mean velocities for the wing/body junction flow at station 3.**

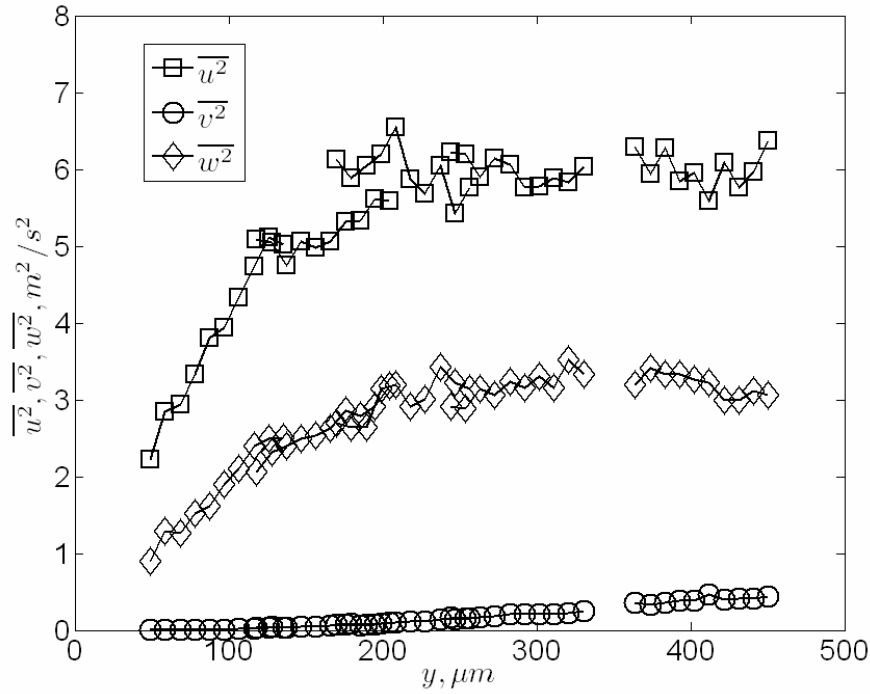


**Figure 4.79.** Sub-measurement volume resolution Reynolds normal stresses for the wing/body junction flow at station 3.

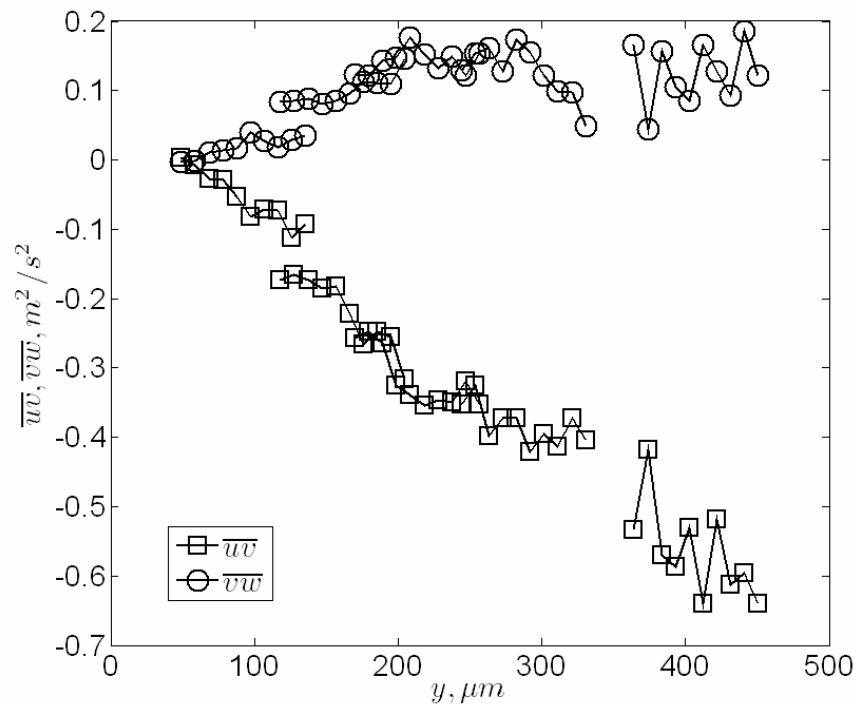


**Figure 4.80.** Sub-measurement volume resolution Reynolds shear stresses for the wing/body junction flow at station 3.

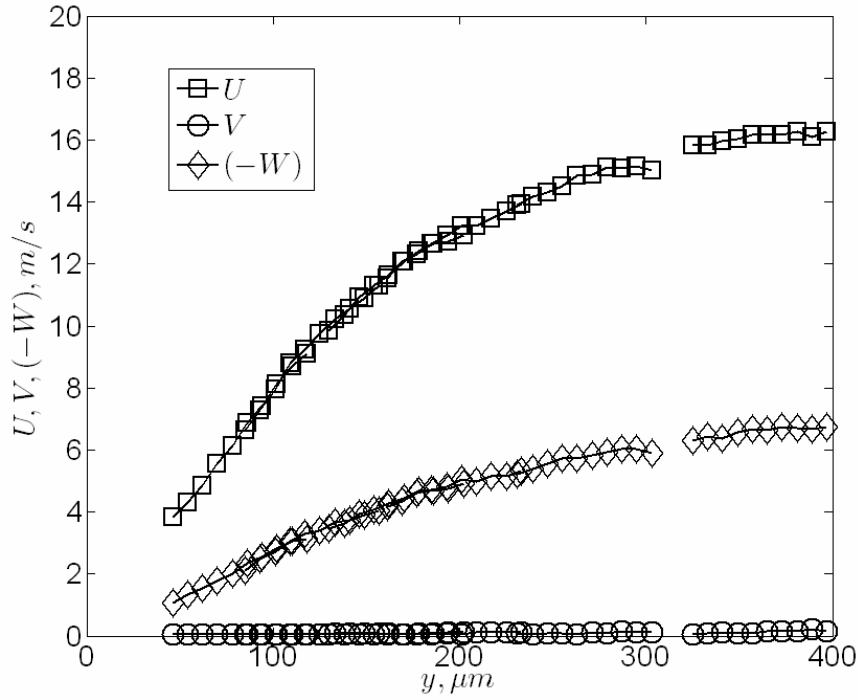


**Figure 4.81.** Sub-measurement volume resolution mean velocities for the wing/body junction flow at station 5.

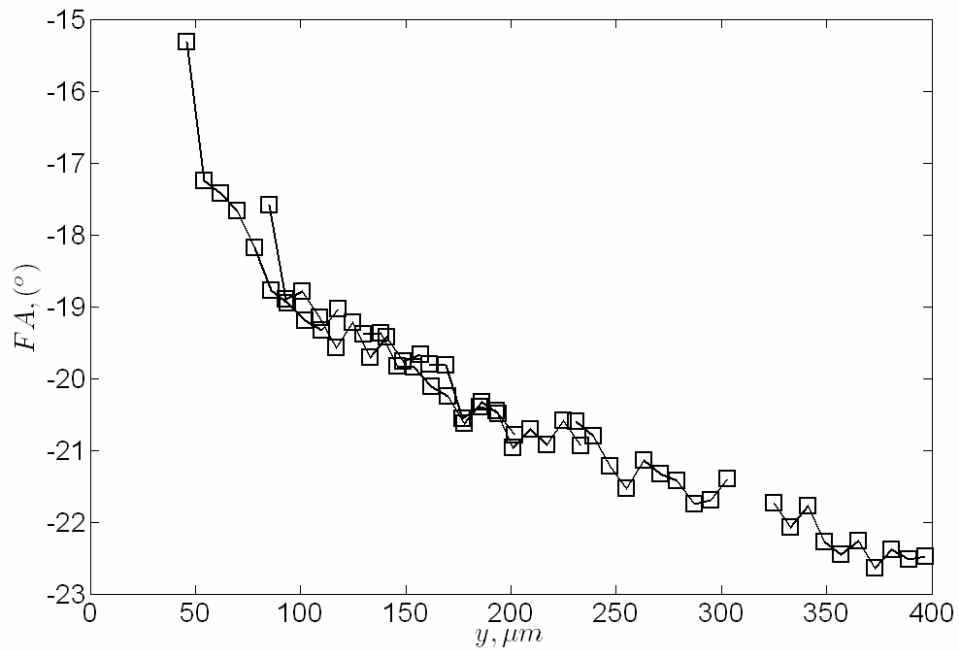


**Figure 4.82.** Sub-measurement volume resolution mean flow angle for the wing/body junction flow at station 5.

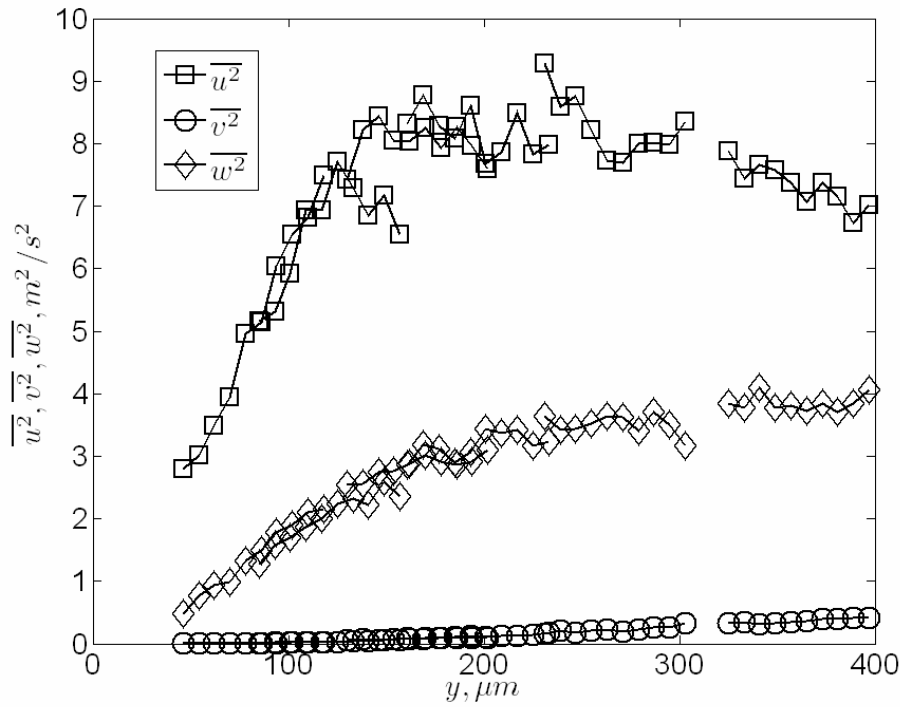


**Figure 4.83.** Sub-measurement volume resolution Reynolds normal stresses for the wing/body junction flow at station 5.

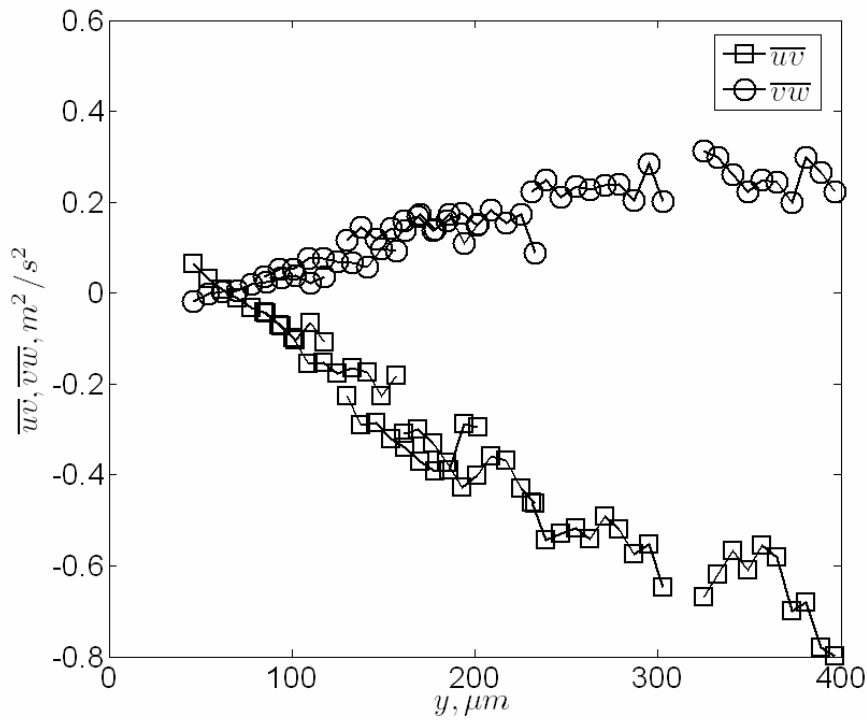


**Figure 4.84.** Sub-measurement volume resolution Reynolds shear stresses for the wing/body junction flow at station 5.

### 4.3.2.1.2 Volume-averaged statistics

The volume-averaged velocity statistics obtained with the CompLDV3 are compared to the results of Ölçmen and Simpson (1995) in Figure 4.85-Figure 4.88 for the data at station 3 and Figure 4.89-Figure 4.92 for station 5. Just as discussed in section 4.1.2, the CompLDV3 probe-volume was limited to 100 microns in the vertical direction and all quantities were corrected for velocity gradient broadening. Throughout the datasets, the agreement in the statistics is excellent between the current data and those of Ölçmen and Simpson (1995), despite the small discrepancy in the friction velocities.

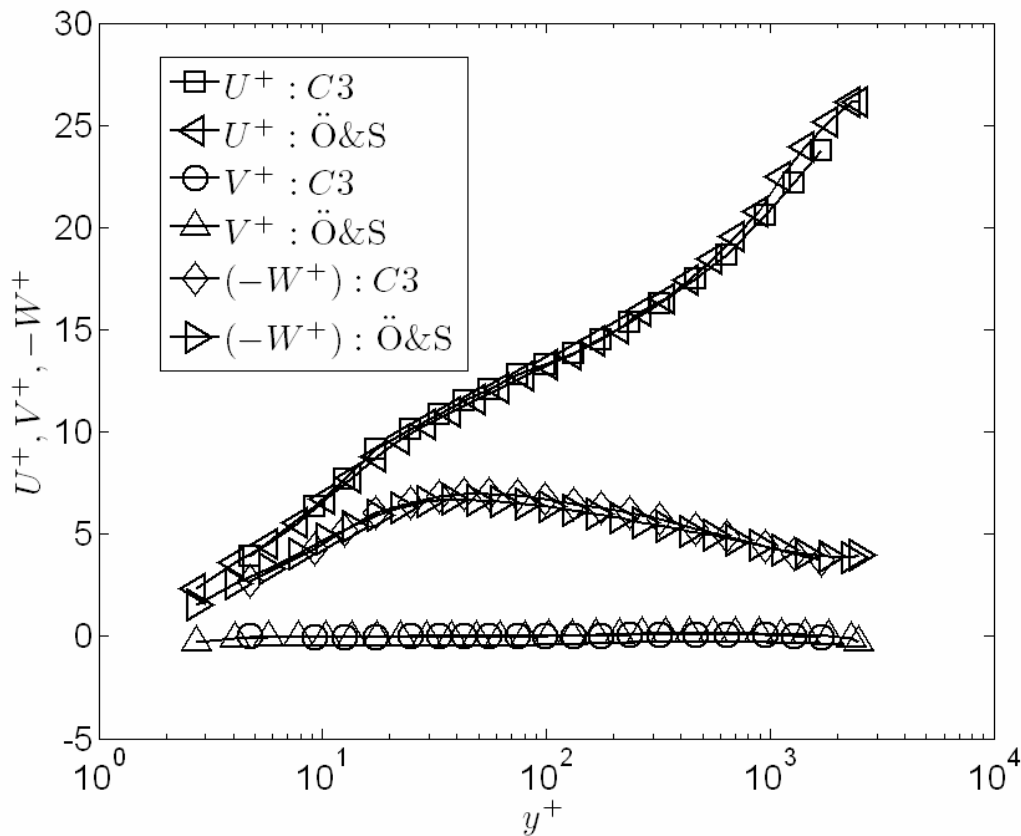


**Figure 4.85. Mean velocities for the wing/body junction flow at station 3. C3: CompLDV3; Ö&S: Ölçmen and Simpson (1995).**

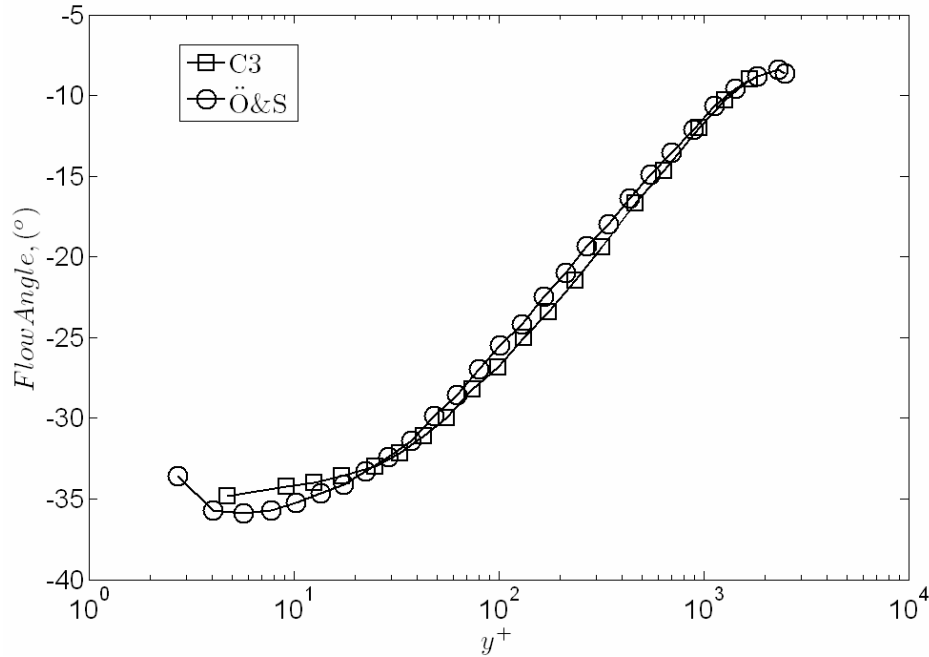


**Figure 4.86. Mean flow angle for the wing/body junction flow at station 3. C3: CompLDV3; Ö&S: Ölçmen and Simpson (1995).**

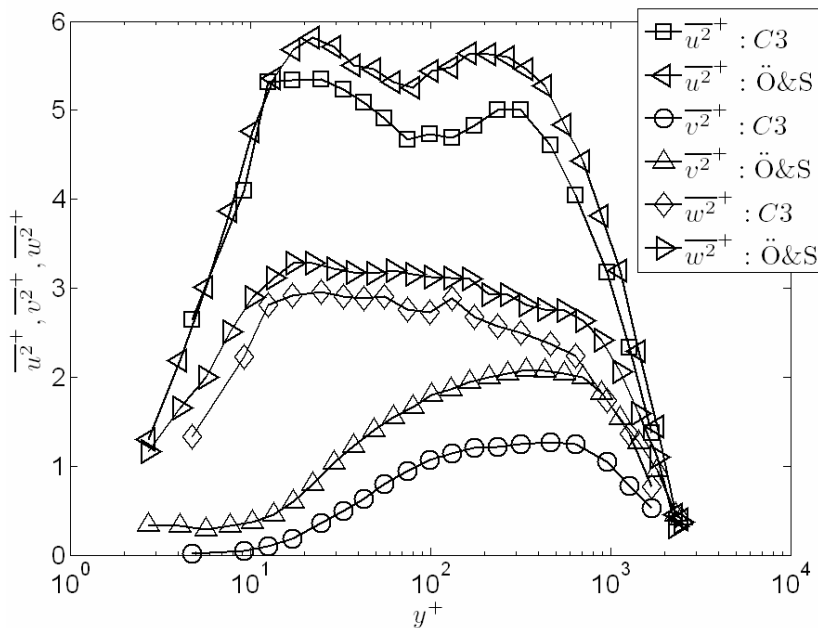


**Figure 4.87. Reynolds normal stresses for the wing/body junction flow at station 3. C3: CompLDV3; Ö&S: Ölçmen and Simpson (1995).**

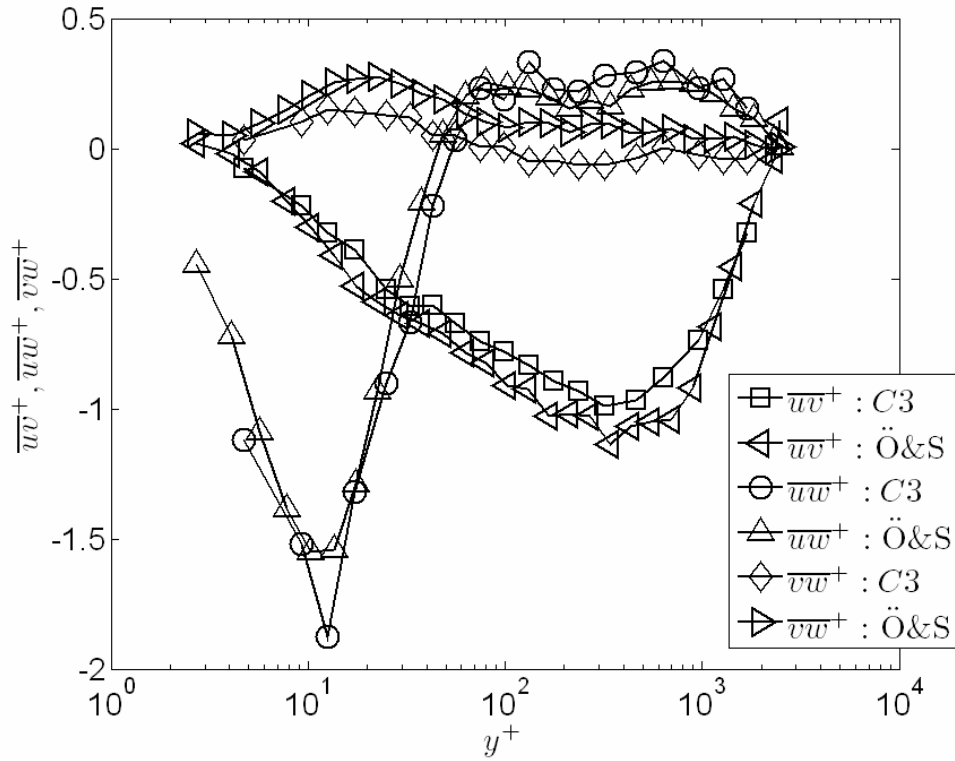


Figure 4.88. Reynolds shear stresses for the wing/body junction flow at station 3. C3: CompLDV3; Ö&S: Ölçmen and Simpson (1995).

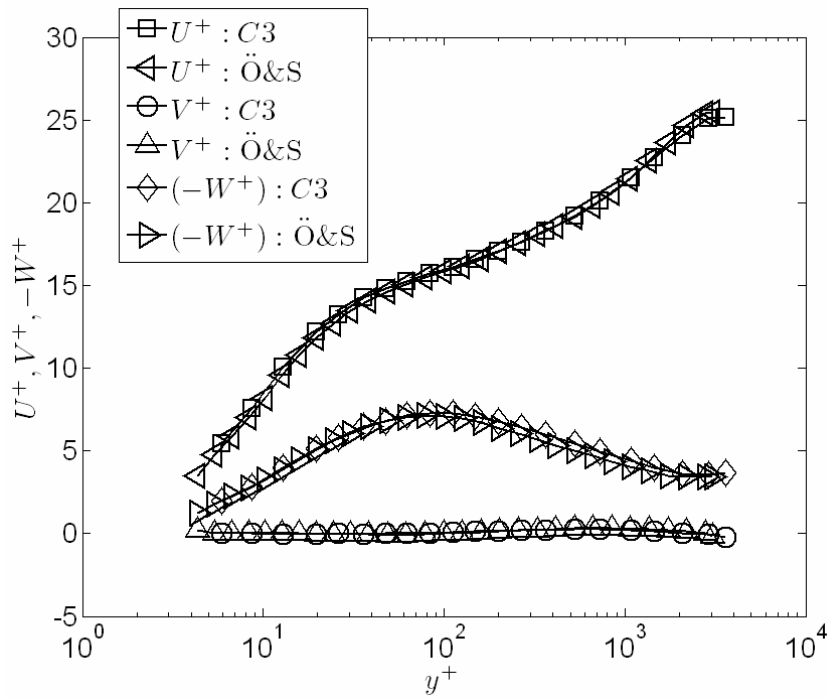
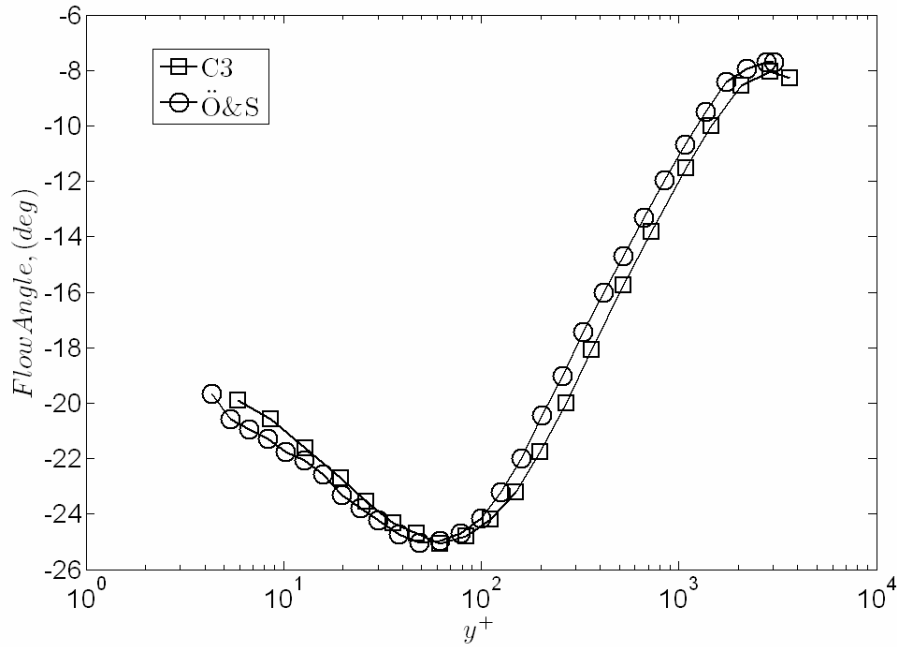
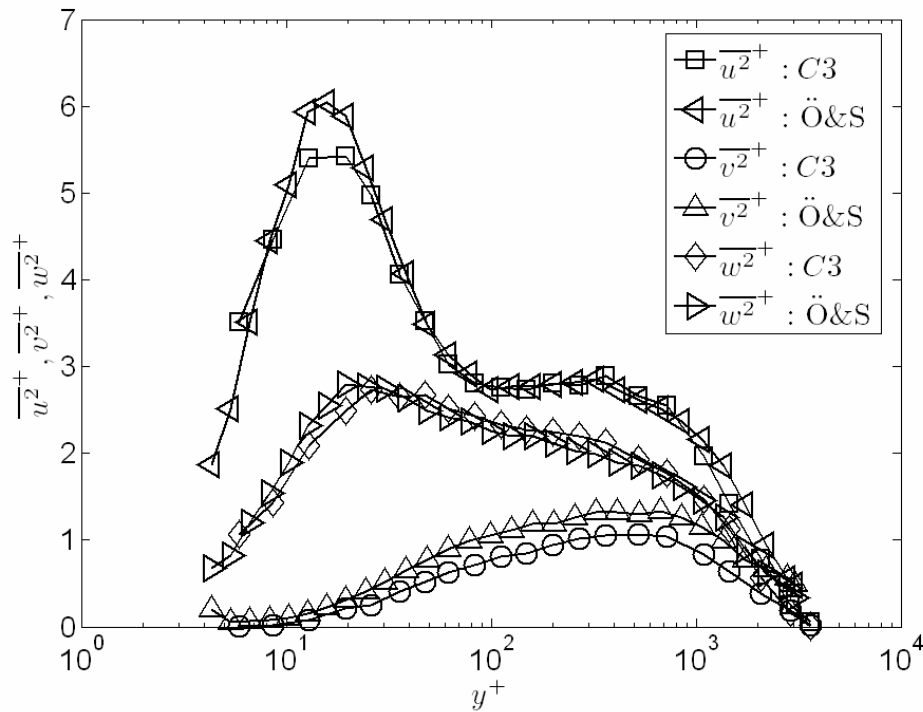


Figure 4.89. Mean velocities for the wing/body junction flow at station 5. C3: CompLDV3; Ö&S: Ölçmen and Simpson (1995).



**Figure 4.90. Mean flow angle for the wing/body junction flow at station 5. C3: CompLDV3; Ö&S: Ölçmen and Simpson (1995).**



**Figure 4.91. Reynolds normal stresses for the wing/body junction flow at station 5. C3: CompLDV3; Ö&S: Ölçmen and Simpson (1995).**

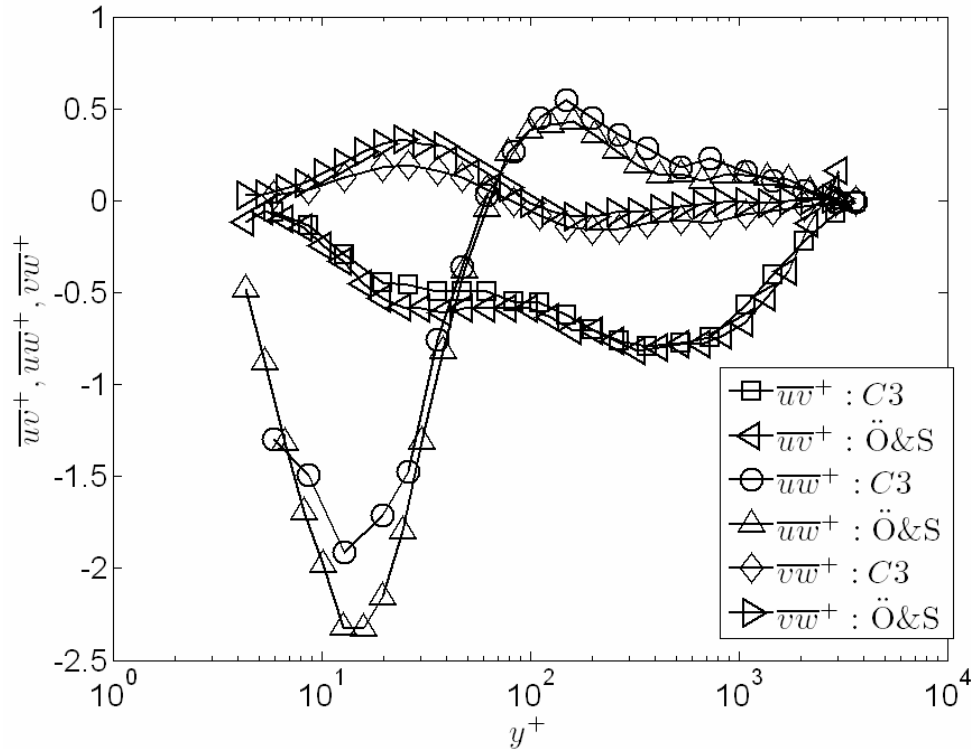


**Figure 4.92. Reynolds shear stresses for the wing/body junction flow at station 5. C3: CompLDV3; Ö&S: Ölçmen and Simpson (1995).**

#### 4.3.2.2 Spectral Analysis

The spectral analysis techniques of the CompLDV3 were also applied to the wing/body junction flow. The scaling of Perry et al. (1985) was again used to plot the data and proves to be a good scaling for both the profiles considered. The frequency spectra of the normal-stresses for station 3 are given in Figure 4.93-Figure 4.95 while the magnitude of the cross-spectra of the Reynolds shear stress  $\overline{uv}$  is plotted in Figure 4.96. Analogous plots for station 5 are given in Figure 4.98-Figure 4.101. The spectral distributions are extremely similar to those measured for the 2DFPTBL, and all show the expected ranges of power-laws including the Reynolds shear stress cross-spectra that show evidence of the  $(-7/3)$  power-law.

The coherency of  $\overline{uv}$  is plotted in Figure 4.97 for station 3 and in Figure 4.102 for station 5. The data for station 3 indicates a loss of coherency at non-dimensional frequencies even lower than in the 2DFPTBL and little scatter among the different coherency estimates in the higher frequencies. In contrast, station 5 exhibits a broader spread in these data at higher frequencies, which most-likely indicates the role of multiple scales of motion that determine the Reynolds stresses throughout the profile. In such a 3D flow where flow angles vary so dramatically throughout the profile, the existence of multiple scales is not unexpected due the different histories of eddies that pass that location as the instantaneous flow angle changes.

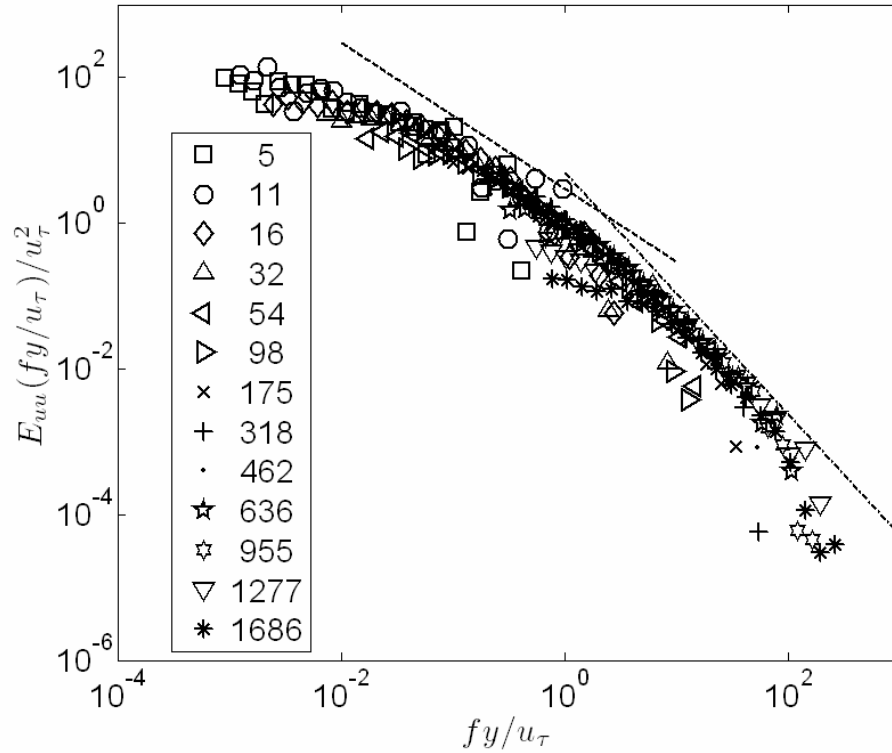


**Figure 4.93.** Auto-spectra of the stream-wise velocity fluctuations at station 3 in the WBJ flow with viscous wall scaling. The legend gives measurement positions in  $y^+$ . The lines in the plot are at slopes  $\sim f^{-1}$  and  $\sim f^{-5/3}$ .

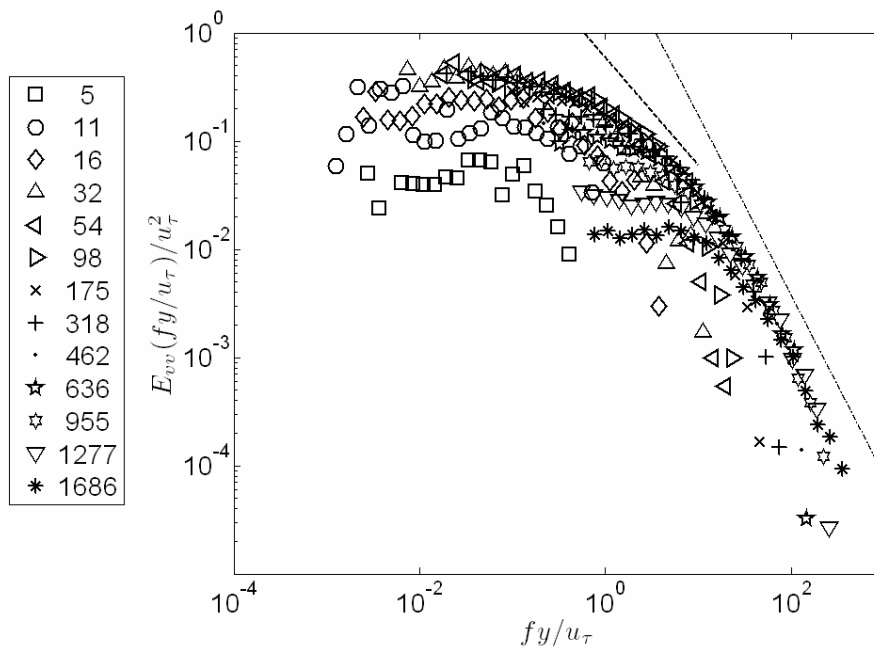


**Figure 4.94.** Auto-spectra of the normal-to-wall velocity fluctuations at station 3 in the WBJ flow with viscous wall scaling. The legend gives measurement positions in  $y^+$ . The lines in the plot are at slopes  $\sim f^{-1}$  and  $\sim f^{-5/3}$ .

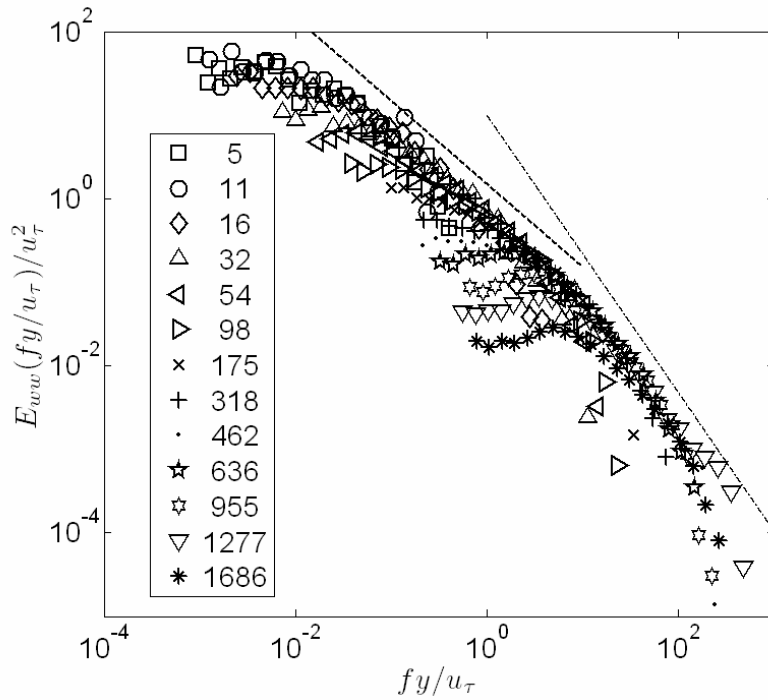


**Figure 4.95. Auto-spectra of the span-wise velocity fluctuations at station 3 in the WBJ flow with viscous wall scaling. The legend gives measurement positions in  $y^+$ . The lines in the plot are at slopes  $\sim f^{-1}$  and  $\sim f^{-5/3}$ .**

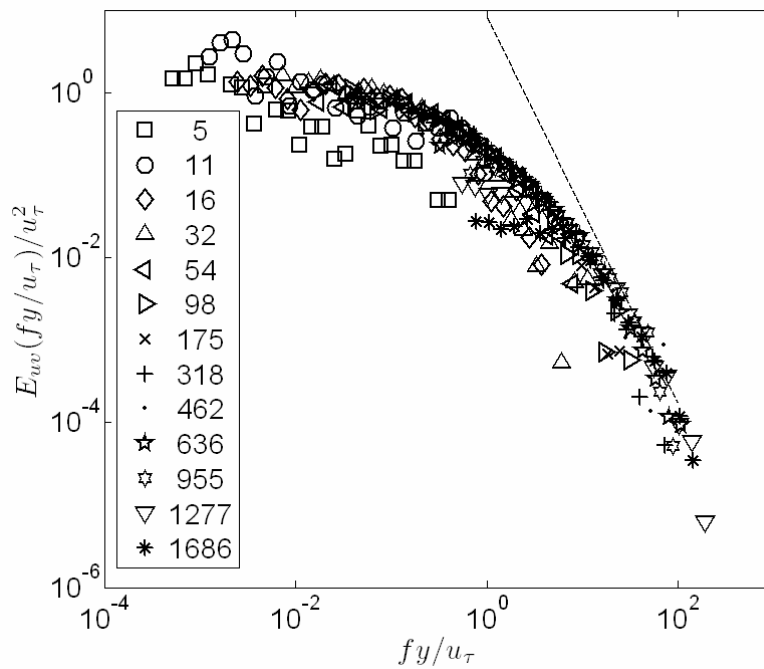


**Figure 4.96. Cross-spectra of the Reynolds shear stress components,  $u'$  and  $v'$ , at station 3 in the WBJ flow with viscous wall scaling. The legend gives measurement positions in  $y^+$ . The line in the plot is at a slope of  $\sim f^{-7/3}$ .**

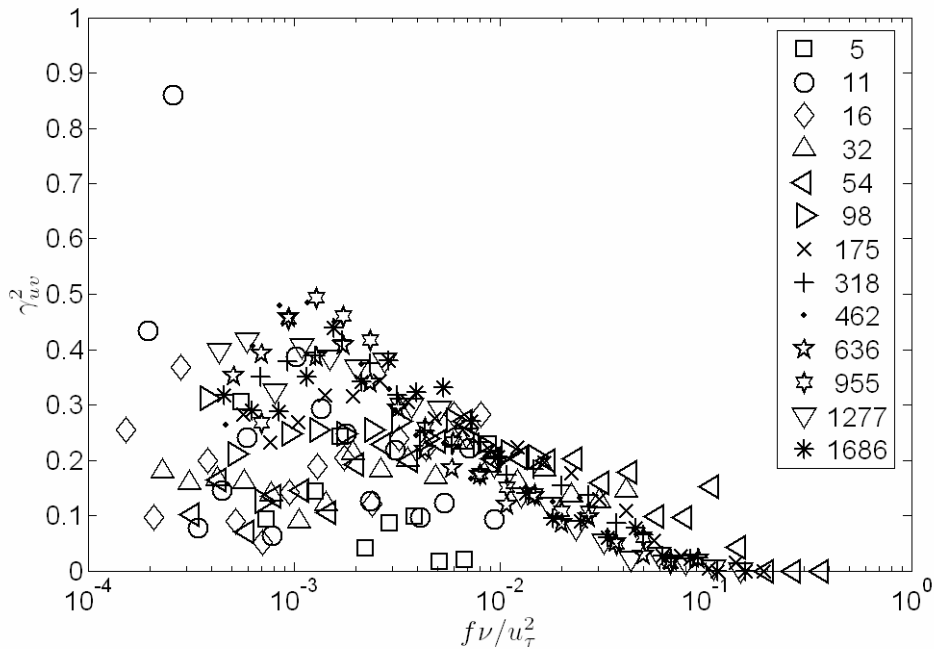


Figure 4.97. Coherency measurements for the Reynolds shear stress,  $\overline{uv}$ , at station 3. The legend gives vertical locations in  $y^+$ .

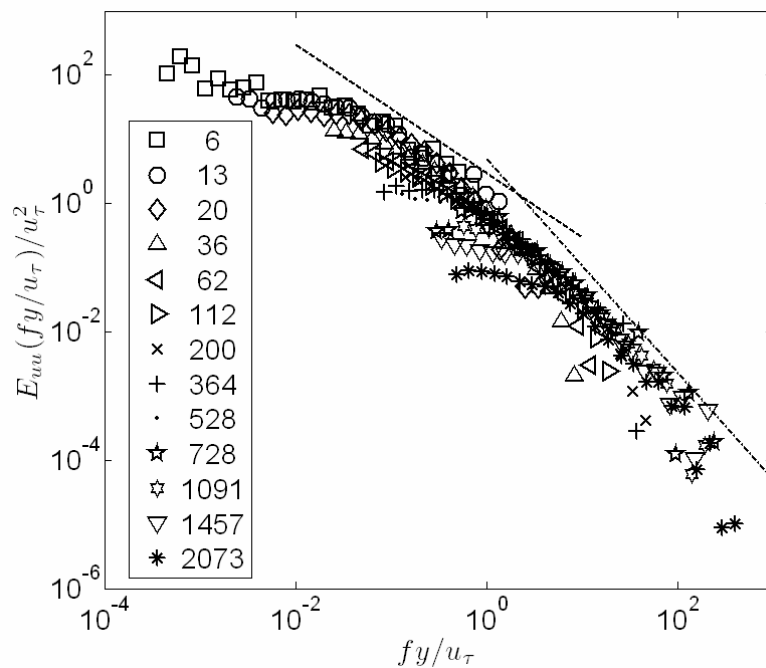
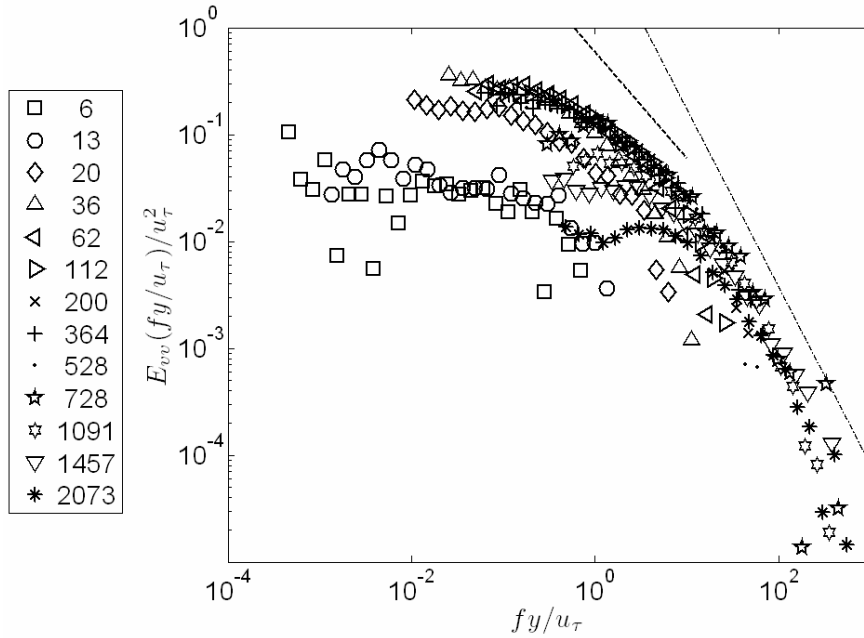
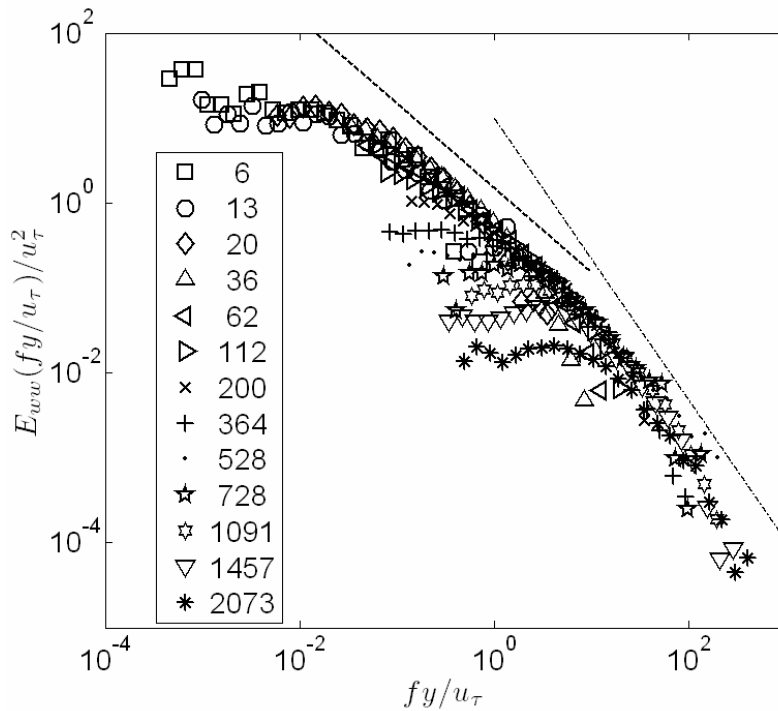


Figure 4.98. Auto-spectra of the stream-wise velocity fluctuations at station 5 in the WBJ flow with viscous wall scaling. The legend gives measurement positions in  $y^+$ . The lines in the plot are at slopes  $\sim f^1$  and  $\sim f^{5/3}$ .



**Figure 4.99.** Auto-spectra of the normal-to-wall velocity fluctuations at station 5 in the WBJ flow with viscous wall scaling. The legend gives measurement positions in  $y^+$ . The lines in the plot are at slopes  $\sim f^{-1}$  and  $\sim f^{-5/3}$ .



**Figure 4.100.** Auto-spectra of the span-wise velocity fluctuations at station 5 in the WBJ flow with viscous wall scaling. The legend gives measurement positions in  $y^+$ . The lines in the plot are at slopes  $\sim f^{-1}$  and  $\sim f^{-5/3}$ .

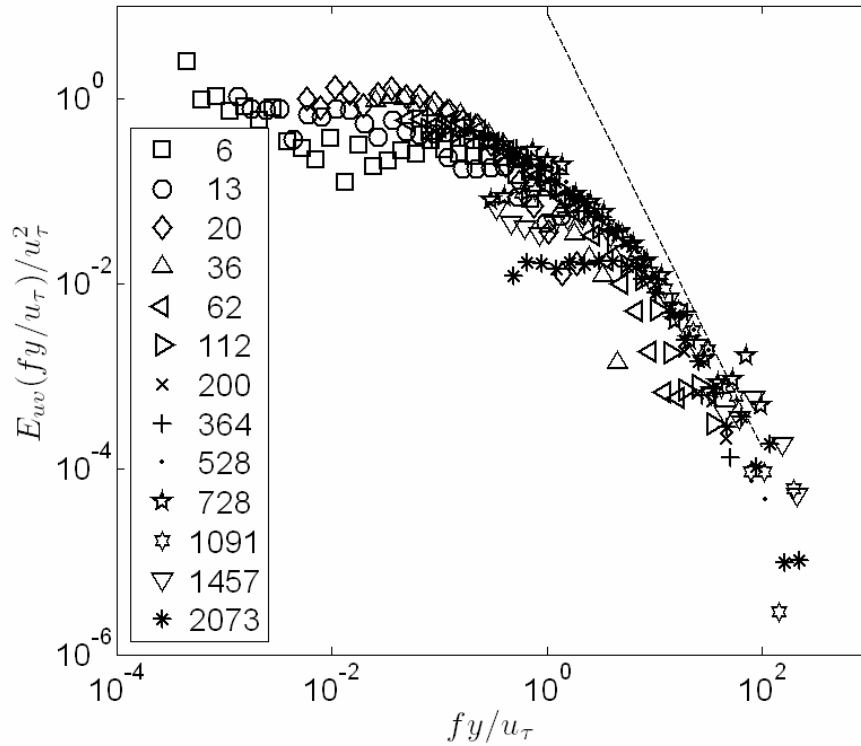


**Figure 4.101.** Cross-spectra of the Reynolds shear stress components,  $u'$  and  $v'$ , at station 5 in the WBJ flow with viscous wall scaling. The legend gives measurement positions in  $y^+$ . The line in the plot is at a slope of  $\sim f^{7/3}$ .

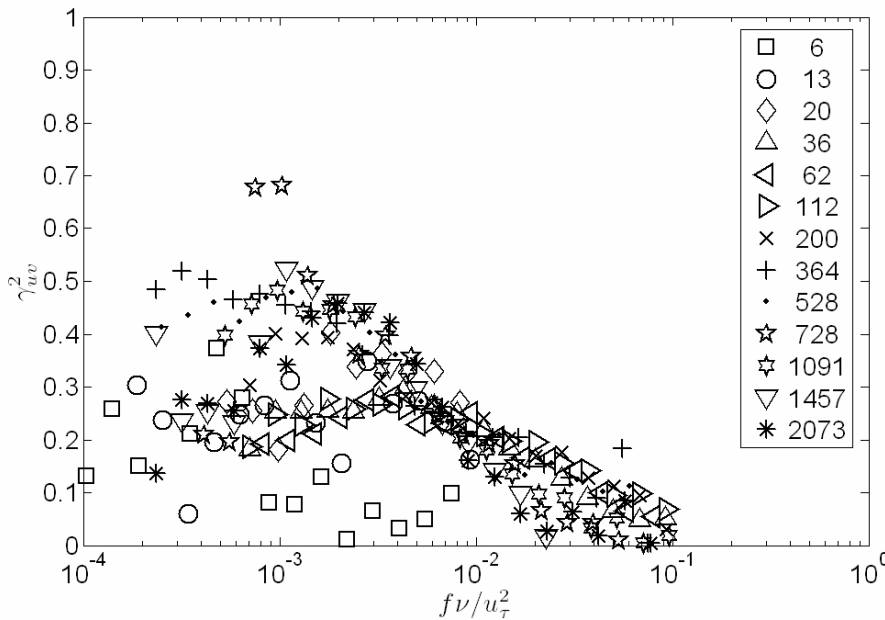


**Figure 4.102.** Coherency measurements for the Reynolds shear stress,  $\overline{uv}$ , at station 5. The legend gives vertical locations in  $y^+$ .

### 4.3.3 Turbulence transport

The velocity gradient dissipation estimation technique has been applied to the data at station 5 of the wing/body junction flow. The same parameters were used to obtain the velocity gradients as discussed in section 4.1.4. Tensor coordinate system rotations were applied to the gradient tensors measured so that the data could be examined in tunnel coordinates. The spectral techniques also discussed for the 2DFPTBL were applied to obtain TKE dissipation rate estimates. The estimates for the TKE dissipation rate are given in Figure 4.103. The spectral dissipation rate estimates closely follow the production values above  $y^+=60$ . The velocity-gradient estimation of the TKE dissipation rate seems to overshoot the value in the outer portion of the boundary layer, but this will benefit from the continuing research discussed concerning point-by-point random noise reduction. The non-isotropic dissipation rates obtained from the velocity gradient tensor estimates are plotted in Figure 4.104. These data are the first such ever obtained in a 3D turbulent boundary layer according to the author's knowledge. These values are seen to be low compared with the 2DFPTBL DNS of Spalart (1988) in the region of  $y^+ < 100$ , indicating the importance of non-equilibrium effects wherein several of the transport terms play significant roles.

The transport rate budgets were computed for station 5 and are presented in Figure 4.105. For these data, the boundary layer form of the Reynolds stress transport equations was again considered such that only vertical gradients of Reynolds-averaged terms were computed. To obtain the velocity/pressure gradient correlation, the balance of equation (4.23) was obtained using the non-isotropic dissipation rates from direct velocity gradient measurements. In the case of the Reynolds shear stress, the statistics of the cross-products of velocity gradients have not yet been computed and the dissipation rate for the shear stress was taken as zero.

Using the novel dissipation rate measurements, these transport budgets are also groundbreaking. Again, the importance of the velocity/pressure gradient term is clear. In the case of the stream-wise Reynolds stress, the velocity/pressure gradient correlation is the major sink of the energy up to at least  $y^+=100$ . For the span-wise normal stress, the sum of the production term and the velocity pressure gradient term result in a function very similar to the production of the stream-wise Reynolds normal stress. The trade-off between these terms sustains the value of the span-wise stress throughout the profile, although through distinctly different mechanisms.

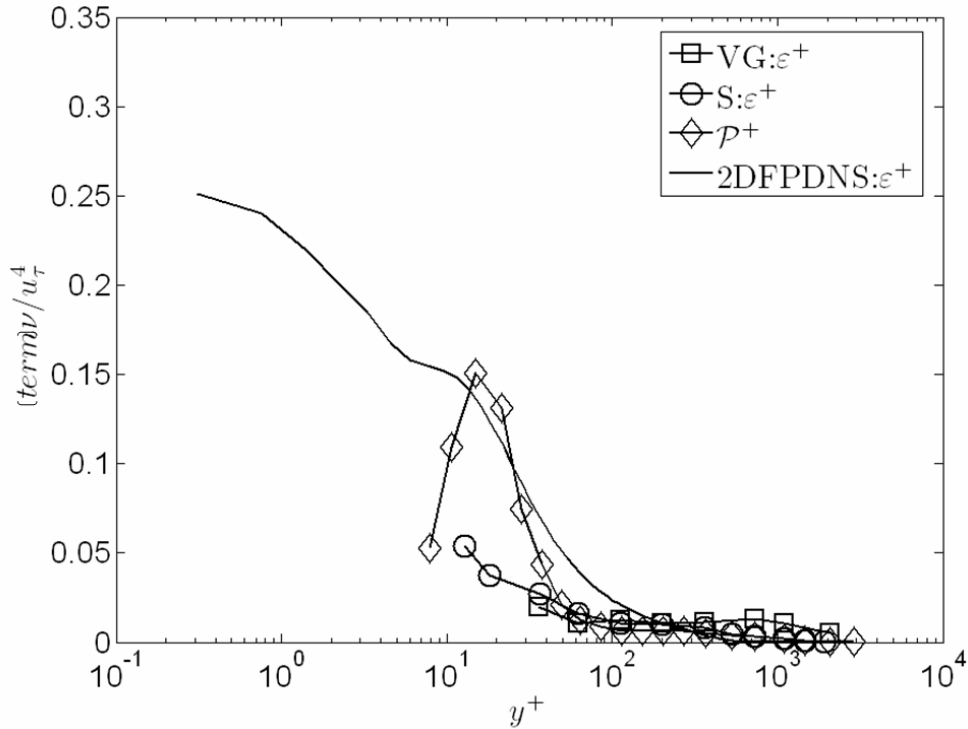


**Figure 4.103. TKE dissipation rate and production for station 5 in the wing/body junction flow. VG, direct estimation of the dissipation rate using the velocity gradient tensor; S, estimation of the dissipation rate using spectral fits; 2DFPDNS, 2D flat plate data of Spalart.**

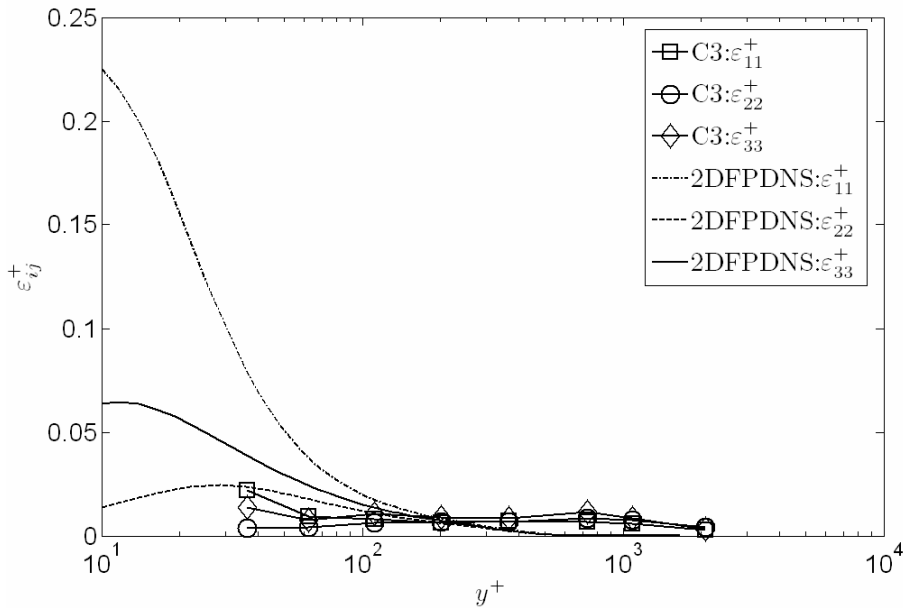
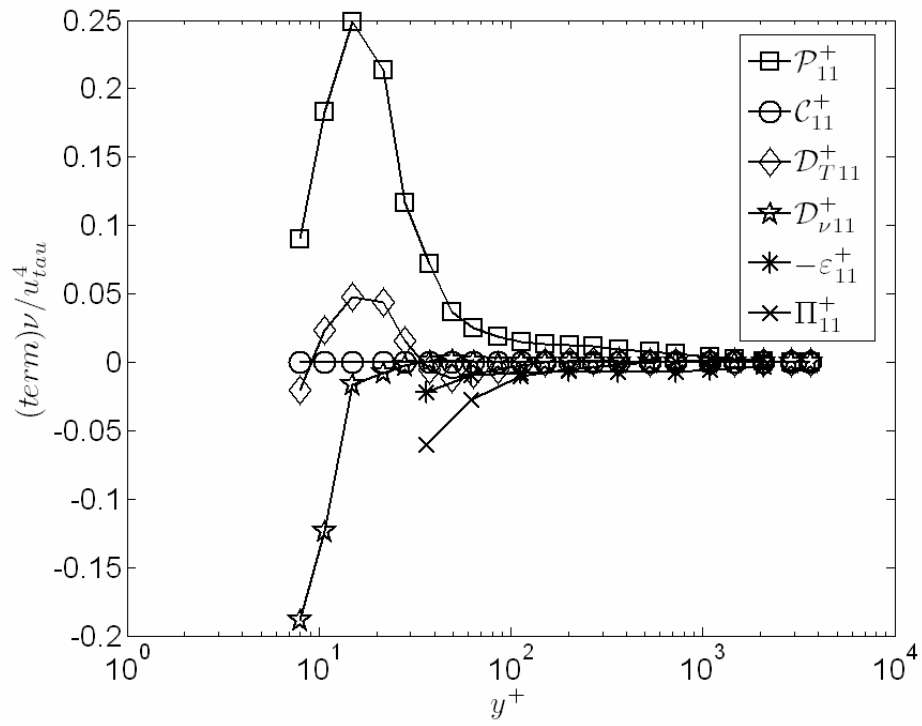
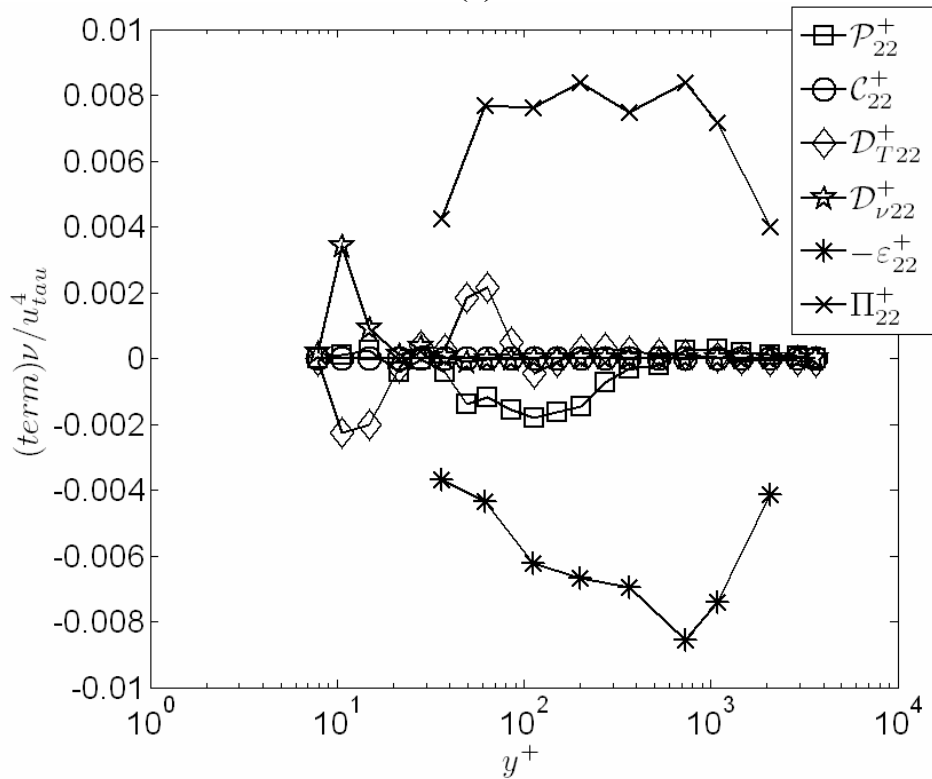


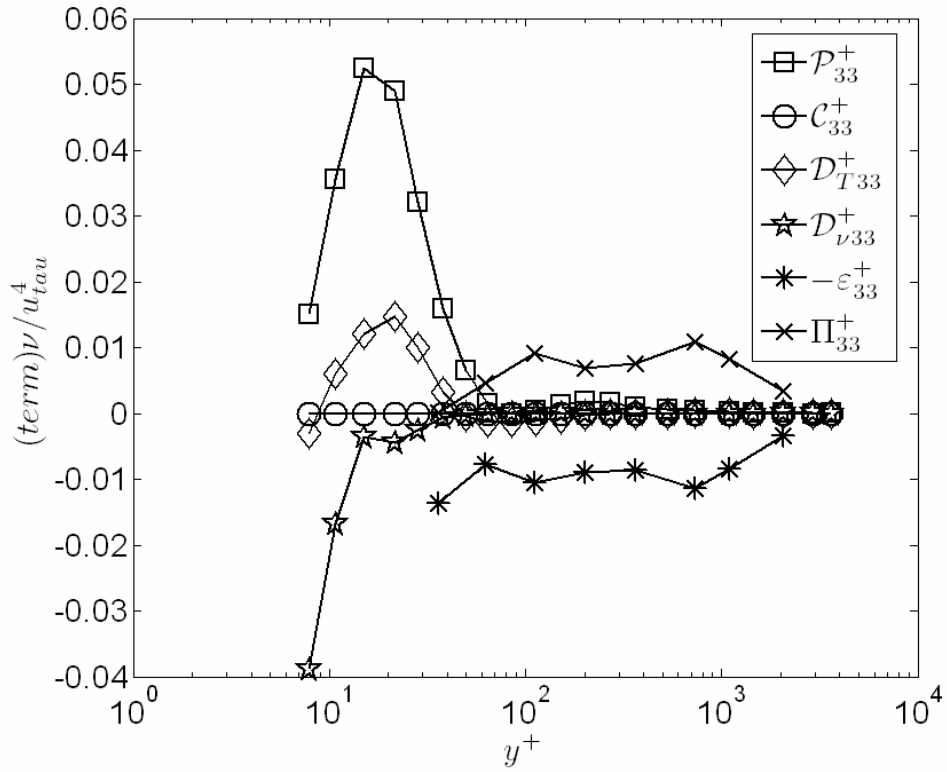
**Figure 4.104. Non-isotropic dissipation rate measurements at station 5 in the wing/body junction flow. C3, CompLDV3 measurement; 2DFPDNS, 2D flat plate data of Spalart.**



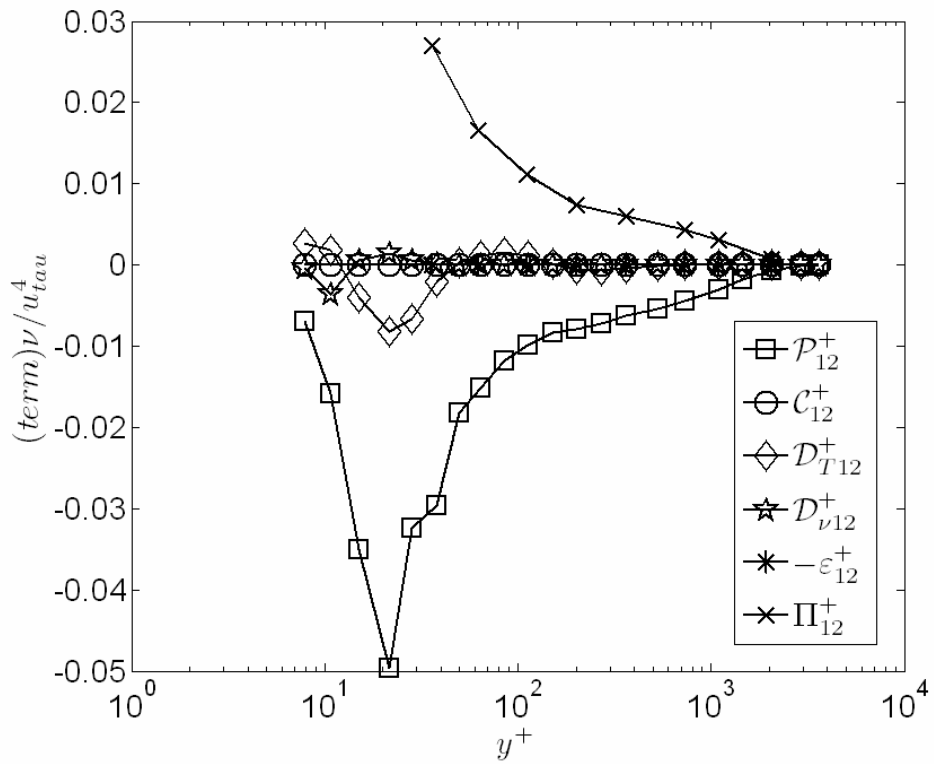
(a)



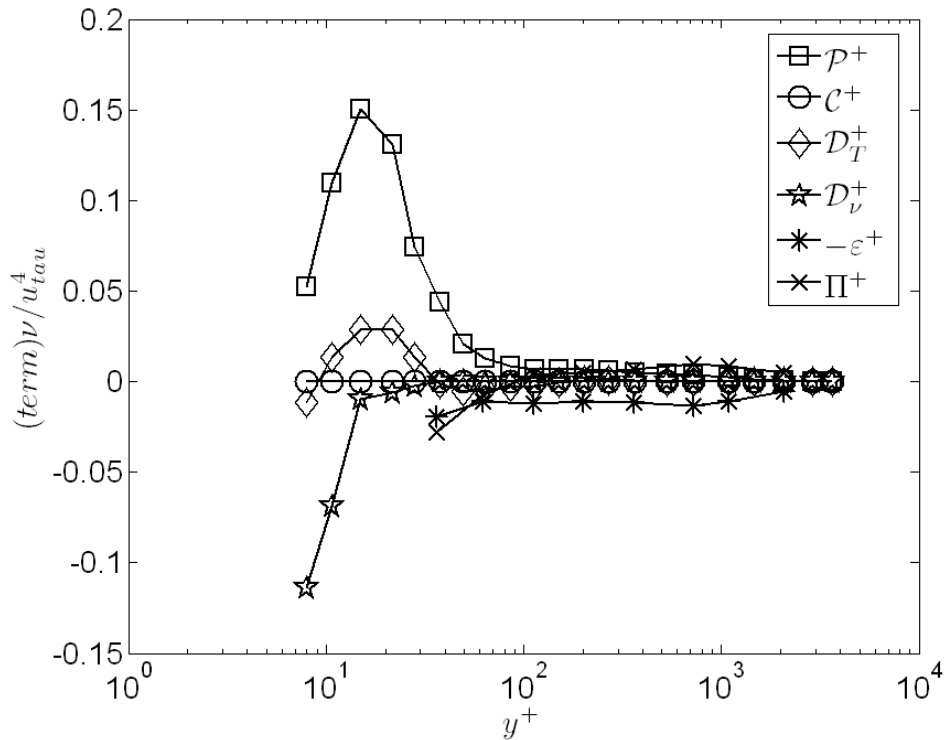
(b)



(c)



(d)



(e)

**Figure 4.105. Reynolds stress transport balances using the non-isotropic dissipation rates for the wing/body junction flow at station 5. (a)  $\overline{u^2}^+$ , (b)  $\overline{v^2}^+$ , (c)  $\overline{w^2}^+$ , (d)  $\overline{uv}^+$ , (e)  $\frac{1}{2}(\overline{u^2}^+ + \overline{v^2}^+ + \overline{w^2}^+)$ .  $\mathcal{P}_{ij}$ =Production;  $\mathcal{C}_{ij}$ =Convection;  $\mathcal{D}_{vij}$ =Viscous diffusion;  $\mathcal{D}_{Tij}$ =Turbulent diffusion;  $\varepsilon_{ij}$ =Dissipation rate;  $\Pi_{ij}$ =Velocity/pressure gradient correlation.**

## 4.4 References

Abe, H., Kawamura, H., and Matsuo, Y. 2001, "Direct numerical simulation of a fully developed turbulent channel flow with respect to the Reynolds number dependence," *J. Fluids Engr.*, Vol. 123, pp. 382-393

Ahn, S. and Simpson, R.L. 1987 "Convective wave speed and spectral features in turbulent boundary layers," *AIAA 25<sup>th</sup> Aerospace Sciences Meeting*, Jan. 12-15, Reno, NV, paper AIAA-87-0198.

Balint, J., Wallace, J.M. & Vukoslavcevic, P. 1991 The velocity and vorticity vector fields of a turbulent boundary layer, Part 2. Statistical properties," *J. Fluid Mech.* Vol. 228, pp. 53-86.

Bennington, J.L. 2004 "The effects of various shaped roughness elements in two-dimensional high Reynolds number turbulent boundary layers," *Ph.D. Dissertation*,

August, Department of Aerospace and Ocean Engineering, Virginia Polytechnic Institute and State University.

Coles, D. 1956 “The law of the wake in the turbulent boundary layer,” *J. Fluid Mech.*, Vol. 1, pp. 191-226.

Davidson, L. and Dahlström, S. 2004 “Hybrid LES-RANS : an approach to make LES applicable at high Reynolds number”, *Proc. of CHT-04*, paper CHT-04-K1.

DeGraaff, D.B. and Eaton, J.K. 2000 “Reynolds-number scaling of the flat-plate turbulent boundary layer,” *J. Fluid Mech.*, Vol. 422, pp. 319-346.

Devenport, W.J. and Simpson, R.L. 1990 “Time-dependent and time-averaged turbulence structure near the nose of a wing-body junction,” *J. Fluid Mech.*, Vol. 210, p.23-55.

Durst, F., Jovanovic', J., and Sender, J. 1995 “LDA measurements in the near wall region of a turbulent pipe flow,” *J. Fluid Mech.* Vol. 295, 305.

George, J. 2005 “Structure of 2-D and 3-D turbulent boundary layers with sparsely distributed roughness elements,” *Ph.D. Dissertation*, February, Department of Aerospace and Ocean Engineering, Virginia Polytechnic Institute and State University.

Honkan, A. and Andreopoulos, Y. 1997 “Vorticity, strain-rate and dissipation characteristics in the near-wall region of turbulent boundary layers,” *J. Fluid Mech.*, Vol. 350, pp. 29-96.

Kolmogorov, A.N., 1991 “The local structure of turbulence in an incompressible viscous fluid for very large Reynolds numbers,” *Proc. R. Soc. London Ser. A* Vol. 434, pp. 9–13.

Labourasse, E. and Sagaut, P. 2002 “Reconstruction of turbulent fluctuations using a hybrid RANS/LES approach,” *J. Comp. Physics*, Vol. 182, No. 1, pp. 301-336.

Lai, Y.G. and So, R.M.C. 1990 “On near-wall turbulent flow modelling,” *J. Fluid Mech.* Vol. 221, pp. 641-673.

Lumley, J.L. 1967 “Similarity of the turbulent energy spectrum,” *Phys. Fluids* Vol. 10, pp. 855-858.

Lumley, J.L. 1978 “Computational modeling of turbulent flows,” *Adv. Appl. Mech.*, Vol. 18, pp. 123-176.

Martinuzzi, R.J., and Tropea, C. 1993 “The flow around surface-mounted, prismatic obstacles placed in a fully developed channel flow,” *Trans. ASME, J. Fluids Eng.*, Vol.115, pp. 85-92.

Millikan, C.B. 1938 “A critical discussion of turbulent flows in channels and circular tubes,” *Proc. 5<sup>th</sup> Int. Congr. Applied Mechanics*, New York, pp. 386-392.

Ölçmen, M.S., and Simpson, R.L., 1995 “An experimental study of a three-dimensional pressure-driven turbulent boundary layer,” *J. Fluid Mech.*, Vol 290, 225-262.

Ölçmen, S., Simpson, R., and George, J. 2001a “Some Reynolds number effects on two and three-dimensional turbulent boundary layers,” *Exp. in Fluids*, Vol. 31, pp 219-228.

Ölçmen, S., Simpson, R., and Goody, M. 2001b “An Experimental Investigation of Two-Point Correlations in Two- and Three-Dimensional Turbulent Boundary Layers,” *Flow, Turbulence and Combustion*, Vol. 66, pp 85-112.

Perry, A.E., Lim, K.L., and Henbest, S.M. 1985, “A spectral analysis of smooth flat-plate boundary layers,” *5<sup>th</sup> Int. Symp. on Turb. Shear Flows*, Cornell University, August 7-9, pp. 9.29-9.34

Pope, S.B. 2000 *Turbulent Flows*, Cambridge University Press, Cambridge, U.K.

Robinson, S.K. 1991 “Coherent motions in the turbulent boundary layer,” *Ann. Rev. Fluid Mech.*, Vol. 23, pp. 601-639.

Rotta, J.C. 1962 “Turbulent boundary layers in incompressible flow,” in *Prog. in Aeronautical Sciences*, Vol. 2,, pp. 1-220.

Saddoughi, S.G. and Veeravalli, S.V., 1994, “Local isotropy in turbulent boundary layers at high Reynolds number,” *J. Fluid. Mech.*, Vol. 268, pp. 333-372.

Sandborn, V.A. and Braun, W.H. 1956 “Turbulent shear spectra and local isotropy in the low-speed boundary layer,” *NACA Tech. Note* No. 3761.

Simpson, R.L. 1996 “Aspects of turbulent boundary layer separation,” *Prog. in Aerospace Sciences*, Vol. 32, pp. 457-521.

Simpson, R.L. 2001 “Junction flows,” *Annual Review of Fluid Mechanics*, Vol. 33, pp. 415-443.

Simpson, R.L. 2003 Class notes from AOE 6154: Turbulent Shear Flows, Virginia Tech, Spring Semester.

Spalart, P. 1988, “Direct simulation of a turbulent boundary layer up to  $Re_\theta = 1410$ ,” *J. Fluid Mech.*, Vol. 187, pp. 61-98.

Tang, G. 2004 “Measurements of the Tip-gap Turbulent Flow Structure in a Low-speed Compressor Cascade,” *Ph.D. Dissertation*, April, Department of Aerospace and Ocean Engineering, Virginia Polytechnic Institute and State University.

Tchen, C.M. 1953 “On the spectrum of energy in turbulent shear flow,” *J. of Research of the Nat. Bur. of Standards*, Research Paper RP2388, pp. 51-62.

Tessicini, F., Li N. and Leschziner M.A. 2005 “Zonal LES/RANS modeling of separated flow around a three-dimensional hill”, *Proc. Direct and Large Eddy Simulation 6*, Poitiers, September.

Tian, Q., Simpson, R.L., and Tang, G. 2004 “Flow visualization on the linear compressor cascade endwall using oil flows and laser-Doppler anemometry,” *Meas. Sci. Tech.*, Vol. 15, pp. 1910-1916.

von Kármán, T. 1930 “Mechanische ähnlichkeit und turbulenz,” *Proc. Third Int. Congr. Applied Mechanics*, Stockholm, pp. 85-105.

## 5 Concluding remarks

A full-cycle research and development study has been conducting with the goal of improving the tools that are available to experimental turbulence researchers. The project undertaken was the development of a novel measurement technique, deemed ‘comprehensive’ laser-Doppler velocimetry (CompLDV), as it is based upon the same fundamentals that govern the laser-Doppler velocimetry (LDV) technique. This new instrument extends the basic LDV to obtain second-order three-dimensional particle trajectory measurements at highly-resolved spatial and time scales very near the boundaries in turbulent flows where limited turbulence structural measurements exist. Several important leaps in measurements capabilities are enabled by the CompLDV technique, including direct-measurement of the complete velocity gradient tensor, sub-measurement-volume velocity statistics profiles, novel velocity-acceleration correlation measurements, and large-dynamic-range velocity spectra measurements very near the wall in turbulent boundary layer flows. These measurements are highly-resolved and allow the application of the technique to nearly any flow scale—there are no fundamental limitations on the technique for a significant range of Reynolds numbers.

The range of this study has spanned the entire spectrum of conceptual design, to prototype realizations, to validation, to application in flows of fundamental interest. Research has been conducted on the fundamental aspects of Gaussian laser beam interference and novel ways to use inhomogeneous interference fields for micron-scale position measurements of sub-micron particle-scatters. A complete hardware development program was accomplished involving all aspects of the instrumentation needs, including custom data acquisition systems; precision, high load traversing; optical design; and signal conditioning electronics. Along the way, new techniques have been developed and validated for extracting Doppler burst signal information, including an algorithm that approaches the theoretically lowest-possible uncertainties in both frequency and rate-of-change-of-frequency estimates for Gaussian-windowed signals in the presence of noise. Complete software suites have been prepared for every aspect of the operation of the CompLDV—from data acquisition, to advanced signal processing, to non-equidistantly-sampled data correlation analysis. Efficient software solutions have been devised for implementing the signal processing and data correlations for the extensive data sets that utilize the SGI-3800—a 512 processor supercomputer that was donated to the Department of Aerospace and Ocean Engineering in part to satisfy the needs of the CompLDV program. The design of prototype probes included high-resolution adjustment mechanisms that allow the user to align the centers of laser beams to within just a few microns of one-another. The operation of the probe has been tested and validated using flows for which previous work has given reasonable predictions for their behavior. No less than 2.5 terabytes of high-quality raw data have been stored during the application phase of the CompLDV.

The CompLDV equipment has been used to give novel results in real flows of fundamental interest to the turbulence research community. Several important ‘firsts’ stem from this study of two- and three-dimensional turbulent boundary layers, listed in

Table 5.1. The first-ever direct measurement of the velocity-acceleration fluctuation correlations in any flow have been measured in this work. These data give a single-point statistical measure of turbulence structural terms in the Reynolds stress transport (RST) equations, with no assumptions. While multi-point measurement schemes are common and give excellent results for some terms in the RST equations such as the production, turbulent and viscous diffusion, and convection, the author knows of no other direct, single-point measurement technique for obtaining such measurements. A novel scheme has been devised for estimating the velocity gradient tensor using the first-order particle trajectories with the CompLDV. This technique has given the first measurements of non-isotropic dissipation rate in turbulent boundary layers at high Reynolds numbers. Also, the first-ever non-isotropic dissipation rate measurements in a three-dimensional turbulent boundary layer have been reported herein. These non-isotropic dissipation rates have been used to obtain RST balances in two-dimensional and three-dimensional turbulent boundary layers. The quality of the measurements results in excellent estimates of the velocity/pressure gradient correlations throughout much of the boundary layer. The information for this difficult-to-model (and measure) term will be used in future studies to evaluate, improve and develop models for its behavior. The most spatially-resolved near-wall measurements of velocity-statistics ever acquired in high Reynolds number turbulent boundary layers have been reported in this study using the position-resolution capabilities of the CompLDV. These measurements show operation of the probe to within 50 microns of the test window. The implications of this to the application of very-high Reynolds number flows are clear—the best estimates of wall-velocity gradients and Reynolds stresses will be possible and fundamental scaling of the high-Reynolds number turbulent boundary layer may truly be assessed. In the current report, extensive spectral measurements through turbulent boundary layers are presented, including near-wall data for these measurements. The non-intrusiveness of the technique makes the instrument extremely capable for these measurements—with no wall-interference phenomena as may be obtained with hot-wire techniques.

Several future applications exist for the CompLDV. First, only a fraction of the data that has already been acquired using the technique is presented in the present report. The richness of the information contained within the measurements is astounding, and each profile acquired yields extensive depths of new data. Additional data have already been acquired in the two-dimensional and three-dimensional turbulent boundary layers presented herein subjected to elevated-freestream turbulence levels. The CompLDV2 and CompLDV3 techniques were synchronized to obtain two-point measurements in those flows, and future work will utilize these data for answering fundamental questions about the role of freestream turbulence in boundary layer flows. Colleagues in the TBLRG are continuing the development of the CompLDV technique to apply it for understanding noise generation due to distributed roughness elements. The velocity gradient measurements available may allow for direct evaluation of the total derivative of the density fluctuations in the vicinity of the roughness elements. The correlations between the turbulence structure and the density-derivative will reveal important information about the mechanisms of roughness noise generation. The possibilities of applications of this novel, one-of-a-kind technique are endless. As the instrument continues to mature and is used by more and more researchers, it is firmly believed that absolutely new

understandings of the fluid dynamics of high Reynolds number turbulent boundary layers will be revealed.

**Table 5.1 List of first-ever-reported measurements obtained in the CompLDV technologies**

- First-ever direct measurements of velocity-acceleration statistics in any turbulent flow
- First-ever non-isotropic dissipation rate measurements in high Reynolds number turbulent boundary layers
- First-ever non-isotropic dissipation rate measurements in a 3D turbulent boundary layer
- Highest-spatial-resolution measurements of velocity statistics in the near wall region of 2D and 3D turbulent boundary layers

## Appendix A.1 The real-time PC-based 3D LDV signal acquisition and processing system: a User's Manual

### Abstract

In this manual, a description of the hardware, software, and user inputs is given for the 3D real-time PC-based LDV DAQ system developed by the authors. At the time of writing, this system has been successfully employed in two- and highly three-dimensional flows for acquisition of turbulence quantities including moments out to triple products. The results have compared favorably with those from the Macrodynes and due to the flexibility in processing options, may lead to lower uncertainties if effective alternative processing schemes are chosen.

### Theory

A personal computer (PC)-based solution to acquisition and processing of 3D laser-Doppler velocimetry (LDV) signals is developed. *This adaptable processor which utilizes commercially available high-speed digitizers installed in a standard PC costs nearly an order of magnitude less than hard-wired LDV processors.* Real-time frequency domain processing and burst validation is achieved for three-measurement-volume coincident data rates as great as 300 events/s with 64 sample record lengths. Direct comparison of the performance of this system with the Macrodyne FDP 3100 (FDP3100) is presented. Actual flow signals in a mean two-dimensional zero-pressure-gradient turbulent boundary layer ( $Re_\theta \approx 6000$ ) were processed by the PC-based system and compared to previous results from the FDP3100. Both datasets were validated using DNS results for this flow at  $Re_\theta \approx 1410$  (Spalart 1988). As expected, both processing systems give very similar results with excellent agreement to the low Reynolds number DNS results near the wall.

### Introduction

Hard-wired frequency domain processors (FDPs) utilizing fast Fourier transform (FFT) processing have been considered the best method for obtaining real-time frequency information from LDV signals for some time (Hepner 1994). FDPs, though useful for obtaining velocity information from signals in many LDV applications, are very specialized in their functions. The highly specialized nature of these devices makes them one of the most significant costs in a LDV system. Furthermore, considerable limitations apply to both the selection of the acquisition parameters (including sampling rates and record lengths) and, more importantly, the processing schemes available.

While the accuracy and speed of the FFT make it a very attractive method for determining Doppler frequencies in relatively noisy LDV data (Shinpaugh et al. 1992; Ibrahim and Bachalo, 1994), extraction of additional burst information may require other processing techniques. Since the FFT chip in FDPs is an enabling technology in these devices, the processing options are confined to the FFT technique. Recent interest in

additional information contained in LDV signals such as flow acceleration (proportional to the time rate of change of Doppler frequency) requires adaptation of the processing techniques (Lehmann, Nobach, and Tropea, 2002). Even in instances where the FFT is the basis for a modified processing scheme, the hard-wired nature of the FDPs makes them virtually impossible to reprogram by the end-user.

In recent studies where a relatively small number of Doppler bursts were processed, PCs have been utilized in acquiring time-series LDV data for offline processing. Lehmann et al. utilized a transient recorder to store time-series bursts for acceleration extraction (2002). Czarske et al. (2002) digitized time-series burst information from two channels for FFT spectral analysis. While these studies recognized the usefulness of PCs in Doppler burst acquisition, there was no mention of real-time processing capabilities.

With the continuing advances in processor and bus speeds available in PCs, it is feasible to replace the function of the FFT chip with software; furthermore, the high digitizing rates needed, formerly only achieved on FDP and oscilloscope platforms, are now available in digitizers which interface to the peripheral component interconnect (PCI) bus in COTS PCs.

In this paper a PC-based three-measurement-volume LDV processor (PCLDV) is described. The specific requirements of such a system are enumerated, followed by the description of the hardware and software used. Flow results in a two-dimensional turbulent boundary layer are presented in which signals were processed by the PCLDV and compared to previous data processed with the FDP3100 in the same flow. Both of these datasets are validated by comparing near wall data to a direct numerical simulation (DNS) of this flow at a lower Reynolds number. The paper concludes by mentioning some future work needed to further enhance the PCLDV performance.

Please note that the use of the FDP3100 as the comparable processor is not necessarily an endorsement of this commercial equipment.

### **Requirements for a PC-based LDV burst acquisition and processing system**

LDV burst acquisition and processing involves four main functions—burst signal recognition, digitization, parameter estimation (e.g. Doppler frequency estimation), and validation. This process establishes several requirements for the PCLDV.

The first requirement is that the system must detect when a burst is present on the analog signal. It is desired that the signal detection system be highly reliable so that nearly all processed signals are validated since signals which fail validation reduce the maximum achievable burst throughput (Qui, Sommerfeld, and Durst 1994). Note also that the signal detection should take into account the need for coincident burst signals from each of the three overlapping measurement volumes.

The second requirement for the PCLDV is that the system must digitize the analog data at more than twice the maximum frequency. This is a statement of the Nyquist criterion, although practically speaking sampling rates should be 2.56 times the greatest frequency expected (Doebelin 1990). The PCLDV is expected to make measurements in low speed flows with very high turbulence intensities where at least 10 MHz of bandwidth is necessary for the fringe spacing being used, requiring 26 MS/s

sampling. The coincidence requirement of the system also means that the digitization from each of the three channels must be synchronized.

To determine the burst frequency, in general, the burst power spectrum must first be constructed. To achieve the same results as the FPDs, this would involve computing the FFT of the digitized signal. Next, a peak detection algorithm is used to determine the spectral line with the greatest spectral power density. To finally estimate the center frequency of the peak, a spectral interpolation algorithm must be run. While the method described here has been shown to be robust for determining Doppler frequency, it is desired that the PCLDV accommodate other processing schemes as well. To do this with the maximum amount of processing freedom, parameter estimation must be done entirely with software.

To complete the acquisition and processing routine, the signal must be validated in the frequency domain. Using the power spectrum already computed, the signal power may be compared to the noise power in the spectrum. Some metric similar to SNR may be formed using this information and compared to a threshold. Information from bursts satisfying the validation should be stored to the PC memory, allowing the acquisition and processing routine to be reset.

## **Hardware**

### **Analog-to-Digital (A/D) Converter Cards**

The A/D converter cards chosen play critical roles in this system. These cards must be chosen based upon sampling rate, synchronization capabilities, and sufficient vertical resolution. A National Instruments model NI 5112 PCI digitizer was chosen to meet the requirements. Each of these boards can simultaneously sample two analog channels at rates up to 100 MS/s. To obtain additional channels, synchronization is achieved by linking the 10 MHz reference clocks in each of the boards using a 32 pin cable between them. The on-board triggering electronics allows specification of either an edge or window trigger for a master channel. The master trigger can then trigger each slave channel to acquire data. Each sample is digitized to 8 bits, which has been shown to be sufficient for frequency domain processing in LDV applications (Hepner 1994). This card also has the feature of time stamping records so that the relative arrival time of each burst may be recorded. This information is useful for estimating low frequency turbulence spectra from LDV signals (Benedict, Nobach, and Tropea 2000).

### **Data Acquisition Host PC**

Without fast processors and high memory transfer rates, real-time processing of LDV signals is impossible. To maximize the data processing capacity of the host PC, the fastest Pentium-4 processor at the time of purchase was chosen, with a 2 GHz clock. The front side bus speed for this computer was 400 MHz. High speed double data rate ram was chosen for the system memory. Essentially, this computer was the top-of-the-line, commercially available PC at the time of purchase, and no specialized components were necessary.

## Acquisition and Processing Software

The software to control the data acquisition was written in National Instruments' graphical programming language, LabView. This program was written so that users already familiar with the operation of the FDP3100 could quickly learn to use the PCLDV.

For velocity measurements, the primary goal of the processing algorithm is to estimate the Doppler frequency of each coincident set of bursts while applying some validation criteria to these events. Figure 1 is a block diagram of the PCLDV implementation of the processes described in the "Requirements..." section. The algorithms to complete these tasks are described in more specific terms to follow.

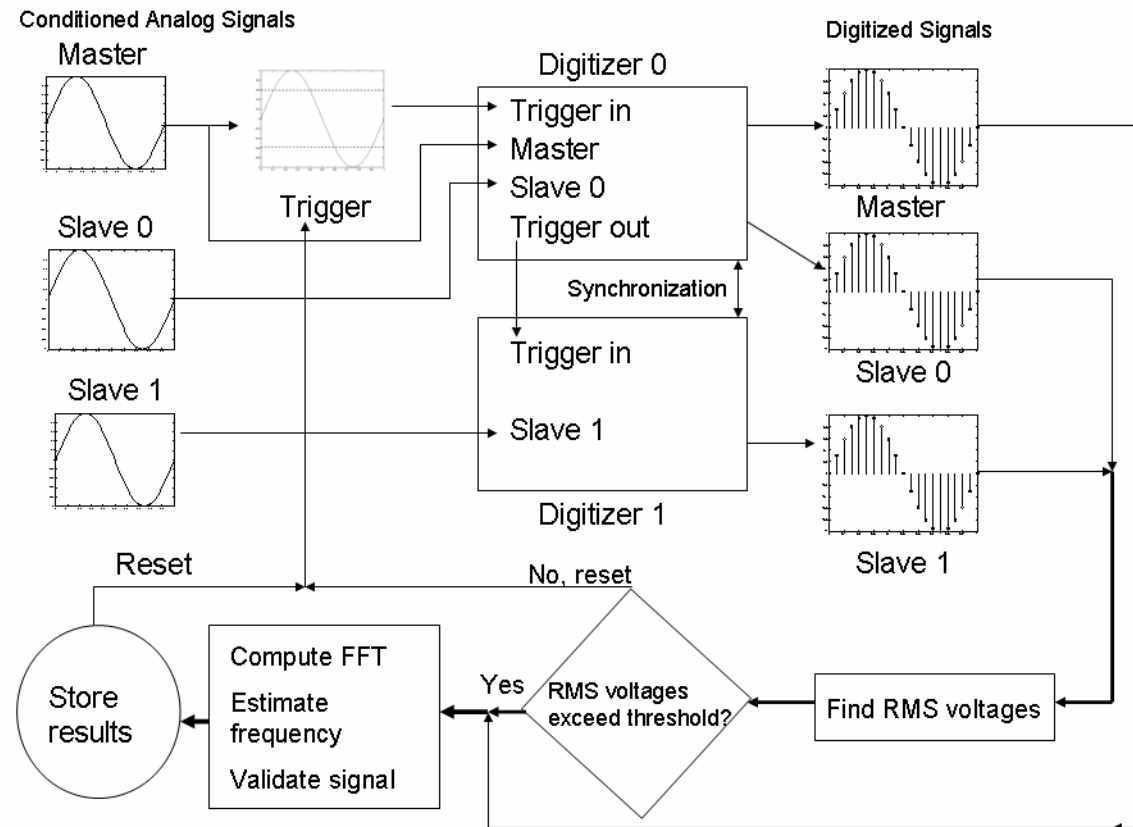


**Figure 1. Block diagram of the signal acquisition and processing system.**

### *Burst recognition and acquisition*

As already mentioned, a suitable burst recognition method is important for ensuring maximum throughput of valid data. In the case of the PCLDV, it was first decided that an electronic voltage threshold trigger on a master channel could be used along with software triggers for the two slave channel for this initial development. The architecture of the digitizers allows for simultaneous acquisition of each channel when triggered by a master signal. A window-type trigger was chosen for the master channel since it will begin a burst acquisition at either a positive or negative user-selectable threshold voltage value. Upon receipt of a trigger on the master channel, each of the three

digitizer channels acquires a record of data simultaneously. Both the record length and sampling rate are user-set as acquisition parameters. Since the slave channels are not considered by the electronic trigger, these channels may or may not contain Doppler bursts. To ensure bursts on the slave channels, the RMS voltage is computed for each of the slave channel records and compared to a threshold. If the RMS voltage is greater than the threshold, processing continues; otherwise, the acquisition is reset. This technique has proven to miss many bursts due to digitization of invalid events while still not being fully effective in limiting noise validation. Two more robust triggering schemes in which an external trigger source is used are discussed to follow.

### *Custom coincident threshold triggering circuitry*

A threshold voltage triggering system that will accommodate up to 6 channels of bursts has been designed, built, and tested for detection of Doppler signals. The system basically consists of twelve setting that adjust the signal amplitude and DC bias so that single-channel triggering occurs at a desired rate. Switches allow the inclusion of 1 to 6 signals for coincidence testing using a NAND-based circuit. The output from the unit is a CMOS pulse signal that triggers the DAQ board to acquire the signal. A more complete discussion of the triggering system is given in Appendix A.2.

### *Macrodyne triggering*

The Macrodyne units are very effective in recognizing bursts of many different amplitudes due to very sophisticated electronics with adaptive gains and electronic SNR monitoring. Such a system was devised by many man-hours of work by electrical engineers and is thus hard to replicate/reverse engineer. Thus, for as long as the Macrodynes are in service, they will be a very effective tool for burst recognition.

### *Doppler frequency estimation*

To estimate the Doppler frequency, first the power spectrum is constructed for each burst. The FFT is computed for each of the three records, and their autospectra are formed. The final estimate for each Doppler frequency is determined using a built-in function in LabView which determines both the power of the dominant spectral peak and the center frequency of that peak for each spectrum. The LabView function contains a peak detection algorithm as well as a spectral interpolation algorithm. The interpolation used is the centroid method, given as

$$\hat{f}_d = \frac{\sum_{i=n_0-\frac{N}{2}}^{n_0+\frac{N}{2}} f_i P_i}{\sum_{j=n_0-\frac{N}{2}}^{n_0+\frac{N}{2}} P_j} \quad (1)$$

where  $\hat{f}_d$  is the Doppler frequency estimate,  $f_i$  is the frequency at spectral line  $i$ ,  $P_i$  is the spectral power density at spectral line  $i$ ,  $n_0$  is the spectral line with the maximum spectral power density, and  $N$  is a 2 or greater. Shinpaugh et al. (1992) showed this interpolation technique to be optimal in computing expense and accuracy.

### *Frequency domain validation and processed data storage*

The ‘energy-ratio’ validation scheme is implemented to further ensure the quality of the data. This method, also used in the FDP3100, compares the power in the primary peak (presumably the Doppler peak) to the power in the entire spectrum. Therefore, it is a loose measure of SNR. The ratio is compared to a user-set maximum validation ratio. If the validation ratio criterion is not met for one or more of the measurement volumes, processing of that burst event ceases, and the hardware is prepared for the acquisition of the next burst. If all signals pass the validation ratio criterion, the program stores the Doppler frequencies and arrival time for that event and the system is reset to acquire the next burst.

Another option which was implemented was the storage of all Doppler frequency data along with the validation ratio. By storing the validation ratio, post-processing can be done to maximize the number of valid events since not all circumstances require the same validation ratio—in some cases the quality of the data is not compromised by accepting a higher validation ratio. This option requires storage of more data, but may prevent unnecessary discarding of otherwise acceptable information.

### **System Performance**

To evaluate its performance, the PCLDV was used to process signals acquired with a three-velocity-component fiber-optic LDV system. The LDV system, developed at Virginia Tech, consists of 5 incident laser beams (2-488 nm and 3-514.5 nm) oriented such that three approximately orthogonal velocity components are measured. The received light from the probe is split into its two primary wavelengths and transformed to voltage signals via two photomultiplier tubes. The voltage signals are amplified and downmixed in frequency so the Doppler peaks from one position in the boundary layer fall within the frequency band 0.5-4.5 MHz. The downmixing was done to match the signal conditioning for the data obtained with the FDP3100. Test points acquired showed that optimal acquisition settings were a sampling rate of 12.5 MSamples/s and a burst window (record length) of 64 samples. For each point in the boundary layer, 15 000-30 000 bursts were processed for statistics.

The test flow was a mean two-dimensional zero-pressure-gradient turbulent boundary layer in the Virginia Tech Aerospace and Ocean Engineering Department Low Speed Boundary Layer Wind Tunnel described by Devenport and Simpson (1990). Data were taken at a streamwise position where the boundary layer thickness was  $\delta = 39\text{mm}$  and the momentum thickness-based Reynolds number was  $\text{Re}_\theta = 5940$ . The probe configuration used in the PCLDV test was not able to traverse the entire height of the boundary layer; thus, for the sake of comparison, only the inner portion of the boundary layer below the wake region was measured.

To validate both the PCLDV and FDP3100, the near wall experimental data are compared to the DNS of Spalart for a 2D, zero-pressure gradient, turbulent boundary layer at  $Re_\theta \approx 1410$  (1988). Despite the Reynolds number discrepancy, it is possible to directly compare the experimental and DNS results for the velocities and Reynolds stresses near the wall when viscous scaling is employed.

The mean velocity in the streamwise direction with viscous scaling is plotted in figure 2. The non-zero Reynolds stresses are plotted in figure 3. Note that the data are plotted for tunnel coordinates with the x-axis aligned with the free stream velocity and the y-axis normal to the wall.

The data from the PCLDV and the FDP3100 exhibit minor differences for each quantity plotted. The two sets of data represent two independent boundary layer profile measurements acquired at different times. It is possible that the small differences exhibited are due to slightly different ambient conditions for the two experiments. The differences may also be due in part to the uncertainty in the calculation of the skin friction velocity used for the viscous scaling.

Agreement with the DNS results is favorable for both processing systems. Figure 2 exhibits an excellent agreement with the DNS results up to the wake region, as expected due to the law of the wall. For each of the Reynolds stresses, there is very good convergence to the DNS results as the measurements approach the wall.

The basic performance features for the PCLDV and the FDP3100 are listed in table 1. ***The two distinguishing features for the PCLDV are relative cost and adaptability.*** A major start-up cost for LDV systems has been the cost of burst acquisition and processing hardware, but the PCLDV stands to make the LDV technique more accessible since ***the per-channel cost of the PCLDV is nearly an order of magnitude less than hard-wired processors.*** The adaptability of the PCLDV makes it a very useful tool for extracting all the useful information from Doppler bursts. While the highly specialized FDP3100 is well-suited for the purpose of obtaining *average* Doppler frequencies from LDV bursts, the PCLDV can be customized to suit the needs of each experimental situation. For example, alternative signal processing techniques, such as quadrature demodulation, can be used to obtain frequency information throughout the burst. Furthermore, the A/D boards allow for permanent storage of time-series burst data for off-line processing, if necessary. Though PC processing capabilities at the time of this study limit the data throughput for the PCLDV to about 300 bursts/sec, the overall potential for the PCLDV as a relatively inexpensive and adaptable research tool is enormous.

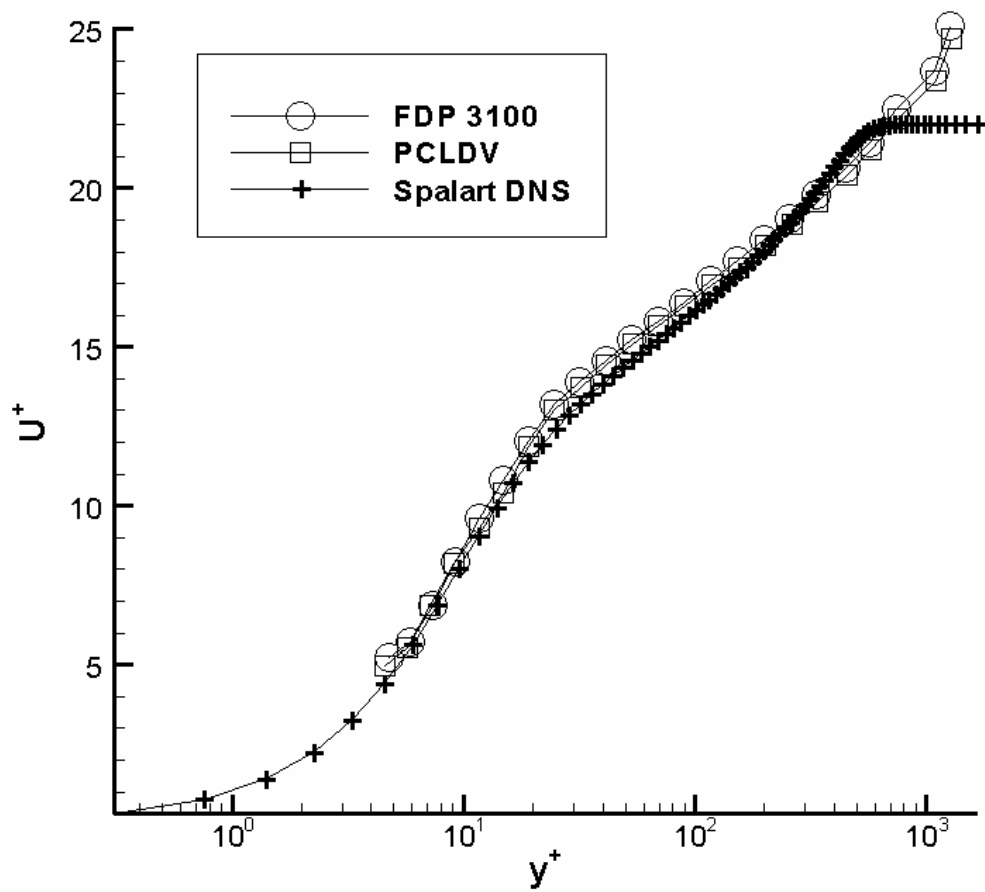
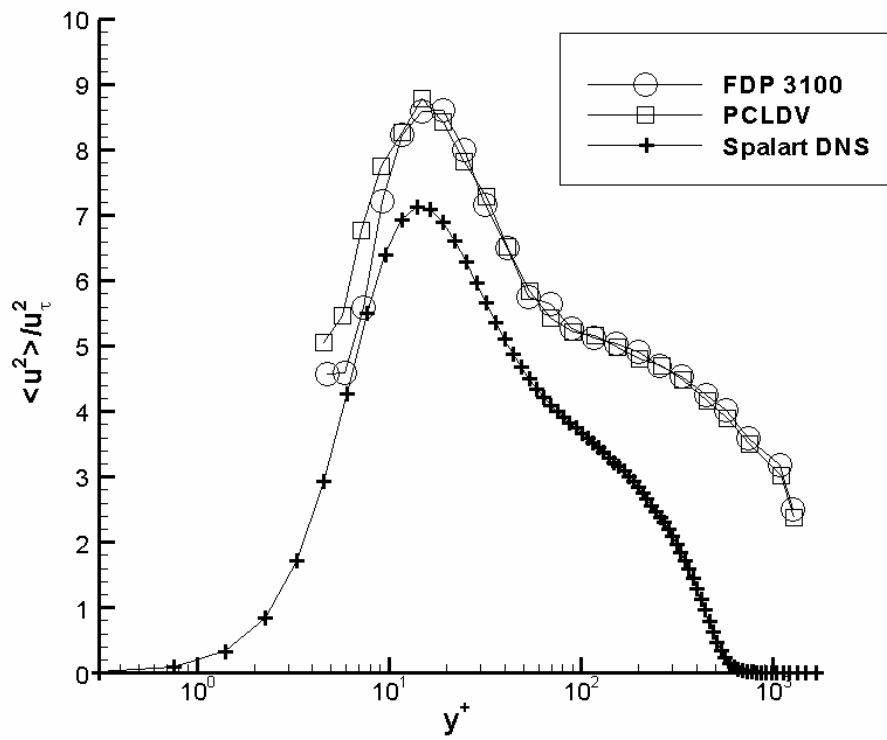
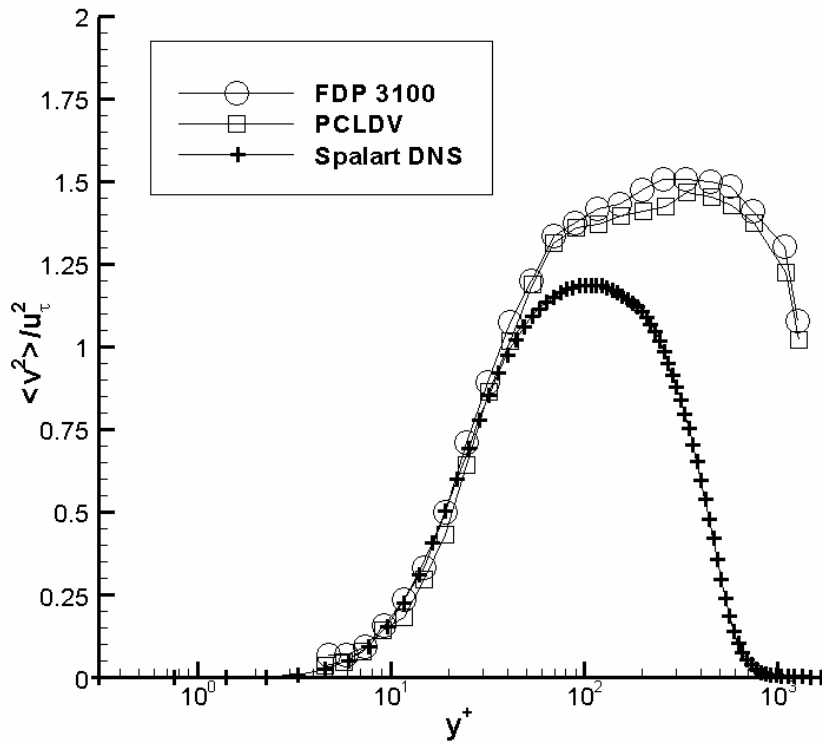


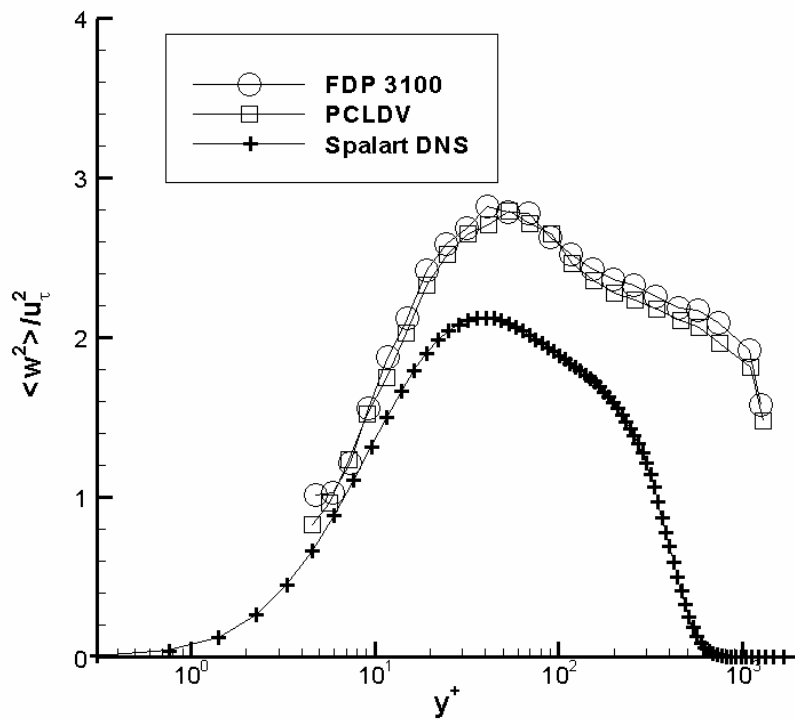
Figure 2. Mean velocity in the free stream direction with viscous scaling for both processing systems and DNS.



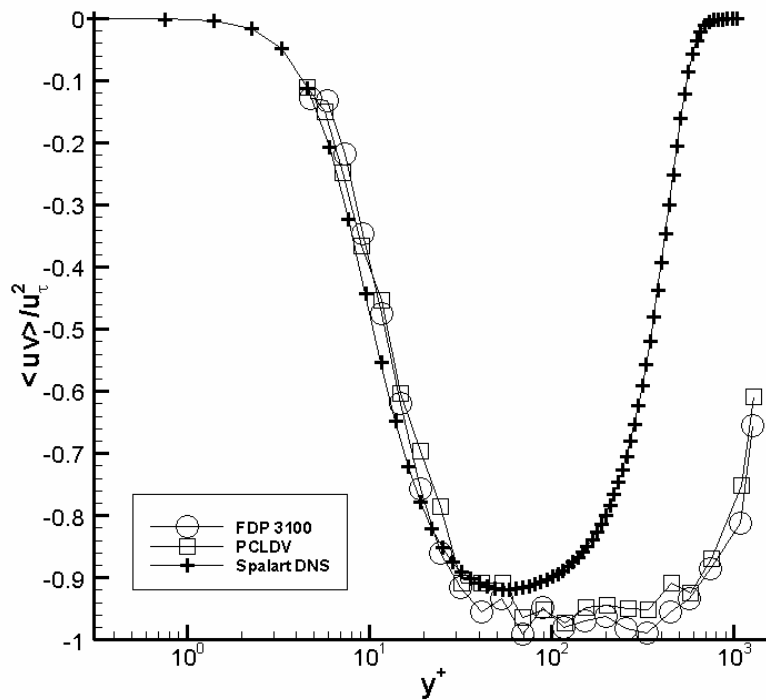
a)



b)



c)



d)

Figure 3. Reynolds stresses with viscous scaling for both processing systems and DNS, a)  $\langle u^2 \rangle / u_\tau^2$ , b)  $\langle v^2 \rangle / u_\tau^2$ , c)  $\langle w^2 \rangle / u_\tau^2$ , d)  $\langle uv \rangle / u_\tau^2$

### Conclusions for the theory section

A *cost-effective and adaptable* PC-based solution for LDV burst acquisition and processing is developed. Flow data are presented which show that velocity measurements made with the PCLDV are comparable to those made with a commercial FDP. Both datasets are validated by comparing them to DNS. At a fraction of the cost of FDPs, the PCLDV considerably reduces the start-up costs for new LDV systems, making the technique more accessible to researchers. And unlike FDPs, the PCLDV allows development and implementation of alternative processing techniques. This flexibility allows for extraction of additional information contained in LDV bursts, thus making the PCLDV a potentially valuable instrument in future turbulence research.

Additional work in refining some parts of the system could further enhance performance. A more sophisticated electronic trigger would increase the throughput of validated bursts dramatically compared to the simple master threshold trigger employed (Qui et al. 1994). Real-time capabilities could also be enhanced through efficient programming using a lower level programming language.

**Acknowledgments** Equipment support for this work was provided by the National Science Foundation under Grant CTS-0079638; K.T. Lowe was supported by VPI &SU.

**Table 1. Comparison of Relative Merits: FDP3100 vs. PCLDV**

<b>Specification</b>	<b>FDP3100</b>	<b>PCLDV</b>
<b>Maximum Sampling rate on each channel</b>	50 MHz	100 MHz
<b>Maximum Bandwidth</b>	20 MHz	40 MHz
<b>Maximum data rate</b>	64 point FFT, 5 MHz bandwidth: 2200 events/s;	3 channel, 64 point FFT: 300 events/s
<b>On-board memory buffer</b>	4 MB	16 MB
<b>Waveform capture</b>	No	Yes
<b>Vertical Resolution</b>	8 bit	8 bit
<b>Programmable for processing other than FFT</b>	<i>No</i>	<i>Yes</i>
<b>Total Cost relative to FDP3100 for 3 channels</b>	<i>1</i>	<i>0.2</i>

## Using the 3D real-time PC-based LDV DAQ

### The graphical user interface

A screenshot of the 3D LDV DAQ graphical user interface (GUI) is given in figure 4. In the sections to follow the fields in the GUI are described.

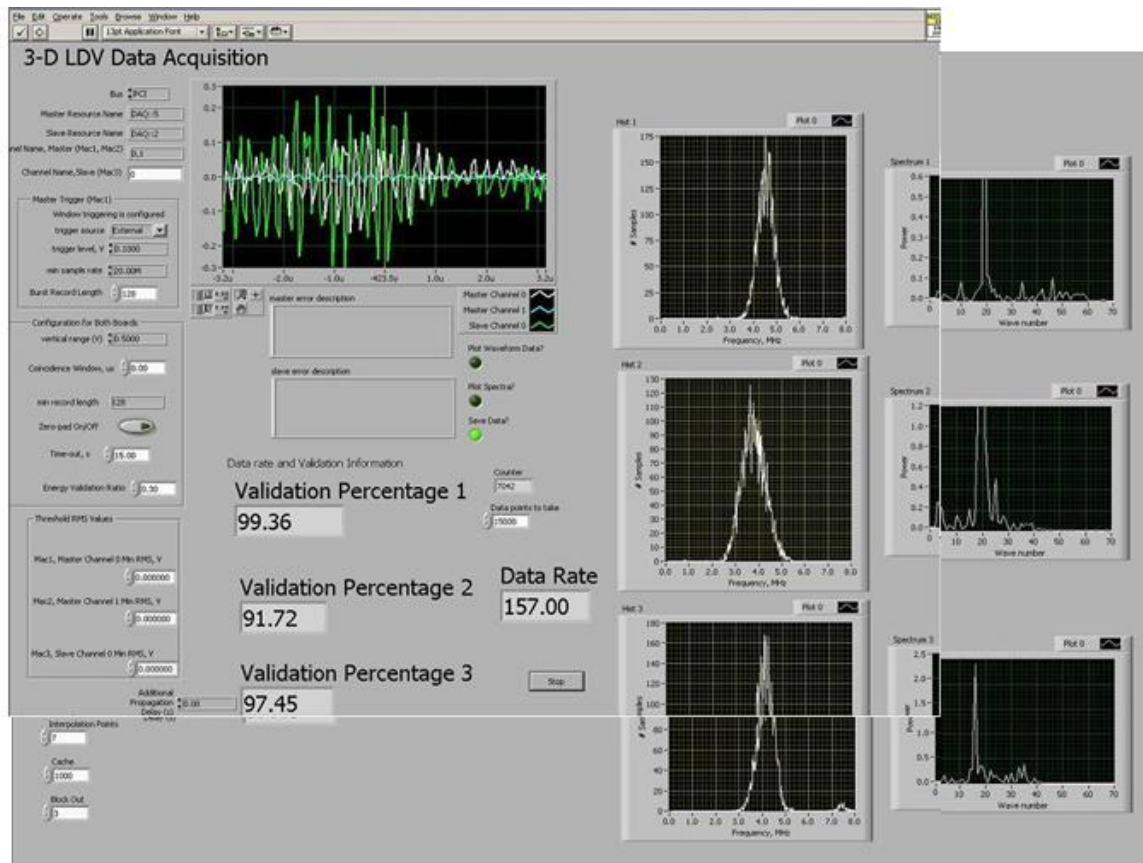


Figure 4. Screenshot of the GUI.

### References

- Benedict, L.H., Nobach, H., and Tropea, C. 2000, "Estimation of turbulent velocity spectra from laser-Doppler data," *Measurement Science and Technology* 11, 1089-1104.
- Czarske, J., Büttner, L., and Razik, T. 2002, "Boundary layer velocity measurements by a laser-Doppler profile sensor with micrometre spatial resolution," *Measurement Science and Technology* 13, 1979-1989.
- Devenport, W.J. and Simpson, R.L. 1990 "Time-dependent and time-averaged turbulence structure near the nose of a wing-body junction," *J. Fluid Mech.* 210, 23-55.

- Doebelin, E. 1990 *Measurement Systems: Application and Design*. 4<sup>th</sup> edition. McGraw-Hill, New York, 836.
- Hepner, T.E. 1994, "State-of-the-Art Laser-Doppler Velocimeter Signal Processors: Calibration and Evaluation," paper AIAA 94-0042, **32<sup>nd</sup> Aerospace Sciences Meeting & Exhibit**, Reno, NV, January.
- Ibrahim, K.M. and Bachalo, W.D. 1994 "Time-Frequency Analysis and Measurement Accuracy in Laser-Doppler and Phase Doppler Signal Processing Applications," paper 8.3, **Inter. Symp. Appl. Laser Techniques to Fluid Mech.**, Lisbon, Portugal, July.
- Lehmann, B., Nobach, H., and Tropea, C. 2002, "Measurement of Acceleration Using the Laser-Doppler Technique," *Measurement Science and Technology* 13, 1367-1381.
- Qui, H-H., Sommerfeld, M., and Durst, F. 1994 "Two novel Doppler signal detection methods for laser-Doppler and phase Doppler anemometry," *Measurement Science and Technology* 5, 769-778.
- Shinpaugh, K.A., Simpson, R.L., Wicks, A.L., Ha, S.M., and Fleming, J.L. 1992, "Signal-processing techniques for low signal-to-noise ratio laser-Doppler velocimetry signals," *Experiments in Fluids*, Vol. 12, pp 319-328.
- Spalart, P.R. 1988, "Direct simulation of a turbulent boundary layer up to  $Re_\theta \approx 1410$ ," *J. Fluid Mech.*, Vol. 187, pp. 61-98.

## Appendix A.2 A multiple channel coincidence-testing trigger for laser-Doppler signal detection

### Motivation

Two PC-based multi-component LDV burst acquisition and processing systems have been developed within the research group. The processing portions of these systems were built to be quite robust, based upon the operation of the Macrodyne FDP3100 and the findings of Shinpaugh et al. (1992). As one would hope, the systems have functioned nominally in processing the data; however an important aspect of burst acquisition is inadequate in these systems—the burst detection process. It is desired that the signal detection system be highly reliable so that nearly all processed signals are validated since signals which fail validation reduce the maximum achievable burst throughput (Qui, Sommerfeld, and Durst 1994). Simple voltage threshold triggering was specified for both systems and resulted in a high percentage of invalid bursts being digitized.

### Initial conceptualization for burst detection circuit

Bursts detection in noisy LDV signals has been studied considerably since before the advent of commercial frequency domain processors (see Qui et al. 1994 and accompanying bibliography). Many methods exist for identifying bursts, but the basic function of an effective burst detector is the identification of the burst envelope amid background noise.

Figure 1 is a schematic of the method proposed for detecting a burst envelope for the current applications. The trends of the intermediate signals within the circuit are given in figure 2. In this method, the Schmitt triggers and filters are applied to the input burst signal to create a trigger signal which is related to the duration of the burst envelope (signal 3 in figure 2). Note that much broadband noise is discriminated from the signal by downmixing the original signal (with frequency,  $f_{burst} = f_{Doppler} + f_{BraggShift}$ ) to a signal in the band from 0-10 MHz. By converting signal 3 to a 1 bit digital signal, an acceptable digital trigger signal is made for a single channel. The primary advantage of this technique over a simple rising or falling edge voltage trigger is that noise spikes are too short in duration to result in a trigger (i.e., the signal from the first Schmitt trigger resulting from a noise spike will be filtered by the subsequent low-pass filter).

The Schmitt trigger is an important enabling part of the circuit. These are available commercially as integrated circuits (ICs) that can trigger as many as six separate signals and cost less than \$1 each. The only limiting part of these devices is that they have a preset threshold voltage. This is somewhat undesirable in this application since the voltage level for valid bursts varies with local flow conditions and laser power fluctuations. To avoid this problem, the voltage level of the input signal must be adjustable. A simple, yet robust solution to the trigger level problem involves adding a DC offset to the signal. By carefully adjusting this offset, one may effectively ‘set’ the trigger level relative to the signal at the desired value.

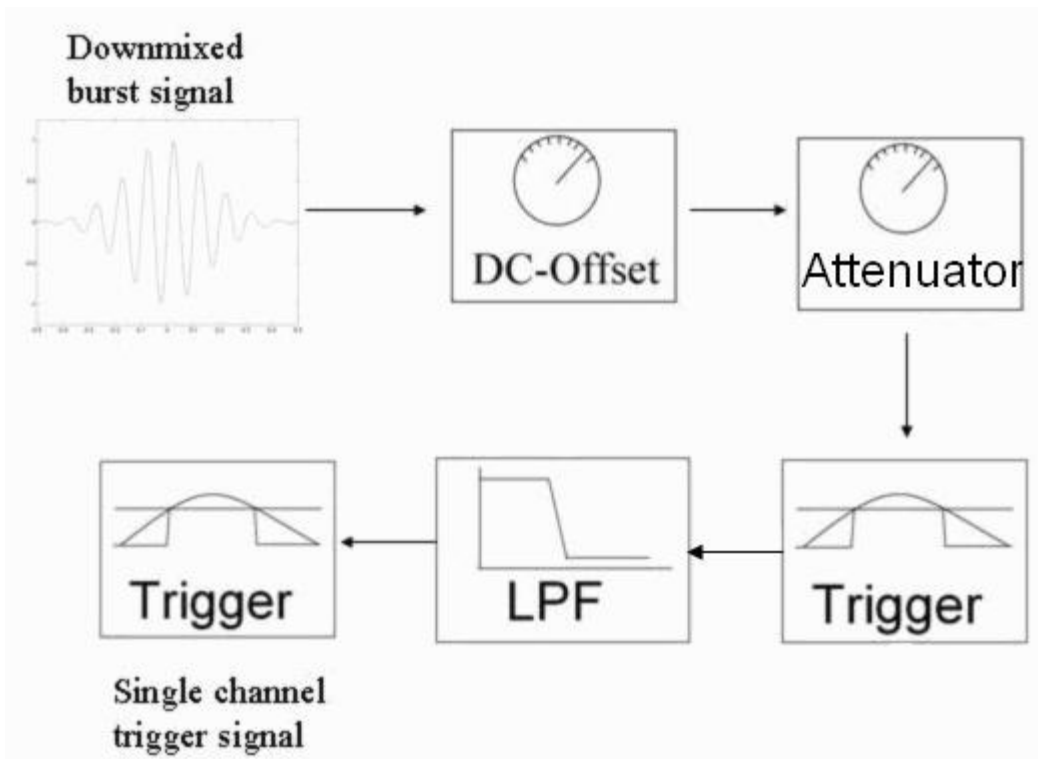
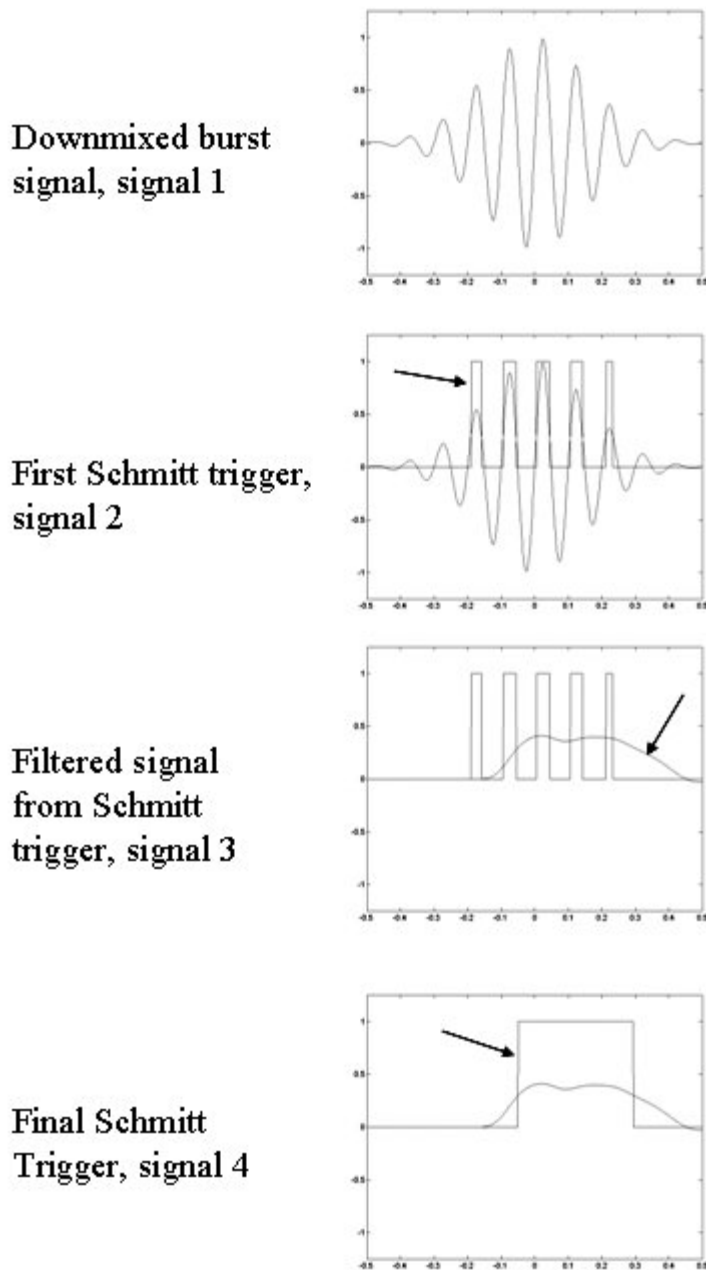


Figure 1. Schematic of the single channel trigger circuit. DC-Offset: biasing circuit; Trigger: Schmitt trigger; LPF: low-pass filter



**Figure 2. Evolution of the signal after each step within the trigger circuit.**

### **Ensuring coincident bursts among channels**

The primary reason for designing a more sophisticated triggering system is the need for coincident bursts among all channels. Since the output from each of the single channel triggers is a logic signal, a digital AND or NAND circuit can be used to test when trigger overlap occurs. This is a very common circuit available inexpensively as ICs. When some portion of each of the triggers overlap the NAND gate changes state and the A/D card gets a trigger pulse. The trigger-in for the A/D cards does not necessarily

consider the duration of the trigger pulse, so any amount of overlap will result in an acquisition. A benefit stemming from the coincidence feature is that it further limits triggers due to noise spikes or flare. This fact allows for the single channel trigger to be based upon threshold voltage values instead of using complicated electronics to estimate quantities such as RMS burst power or instantaneous SNR.

### **Details of the two triggering systems**

#### ***Trigger for the CCLDV***

As mentioned, the CCLDV needs a triggering solution which will ensure coincident bursts on three channels. In this system, the signals from the photomultiplier tubes (PMTs) are split into three lines, one for each channel. As discussed, downmixing is employed to shift the frequency of the burst signals to 10 MHz or less. This maximum frequency is chosen due to the maximum turbulence level in the flow—the Doppler frequencies are distributed in a range as great as 9 MHz at some points in the vortical separating flows being measured for CCLDV fringe spacing. For the triggering step, each of the three signals should be split once again with one line going to the digitizer and one to the triggering circuit. Each line used for triggering goes through the circuit illustrated in figure 1. To finally create the trigger, the three outputs are used as arguments for the NAND circuit described above. The output from this logic circuit is the final trigger signal which is transmitted to the ‘external trigger’ jack on the master A/D board.

#### ***Trigger for the CompLDV***

The trigger system for the CompLDV is very similar to the CCLDV trigger with a few important differences. Figure 3 is a schematic illustration of the CompLDV trigger circuitry. The main difference between the CCLDV and the CompLDV signal is that the CompLDV signals which are digitized are not downmixed. This is done to allow 6 signals to be digitized on only two channels, reducing complexity of the overall system. Since each signal on a single line has a different Bragg shift frequency, it is simple to distinguish each Doppler frequency. This, however, means that the trigger method must involve some way to separate the signals in analog so each can be used in the trigger detection. To do this, downmixing is done, but only for the triggering circuit. The amplified signals from the two PMTs are split with one line from each going directly to the digitizer. The other lines are split again into two sets of three lines for use in the triggering circuit. The trigger lines are downmixed by approximately the Bragg frequencies and low-pass filtered so that each of the six signals is isolated from the others and within a 5-10 MHz bandwidth (see figure 3 for clarification). These low-passed signals are then amplified and used as the input for the triggered circuit shown schematically in figure 1. Each of the single line trigger signals are tested for coincidence using the logical NAND circuit. The output from the NAND gate is again the final trigger used by the A/D board.

Later testing may show the need for additional circuitry to follow the AND gate. It has been estimated (assuming isotropic turbulence) that the Kolmogorov time-scale through the inner portion of the boundary layer for flows to be measured ( $Re_\theta \approx 7000$ ) is

about 35 microseconds. Over this period, it will be found that bursts do not necessarily overlap. Therefore, if it becomes necessary, a circuit for identifying the occurrence of four separate triggers over the course of about 35 microseconds is devised. The final trigger signal from figure 3 is split four ways. The split signals each experience a different delay time by going through a digital delay line. There is one signal not delayed, one delayed 9 microseconds, another 18 microseconds and the last delayed 27 microseconds. Next each signal could be compared to the others using the NAND gate. When each time segment contains a trigger, the NAND gate would send a trigger to the digitizer. Of course there is a delay between the occurrence of the trigger event and the first burst, but this may be accounted for by the number of pre-trigger samples obtained by the digitizer.

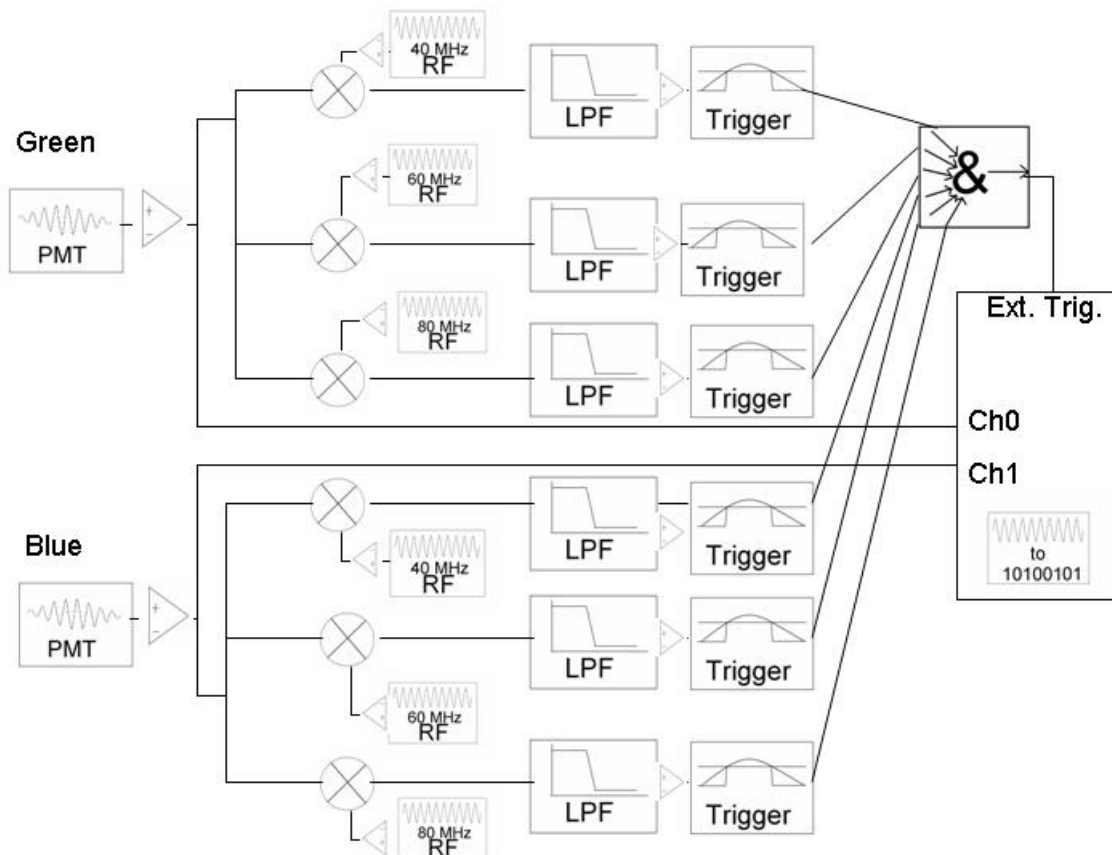


**Figure 3. The ComplDV trigger circuit. PMT: band-passed signal from PMT; x: mixer; RF: RF generator; LPF: low-pass filter; Trigger: single channel trigger in figure 1; &: digital AND gate;**

### Simulation

It is sought to verify the functionality of these systems by simulating their operations with computations. Since the ComplDV is the more demanding application, the simulation is done for that system.

### Description of the simulation

The primary goal of the simulation is to assess the functionality of the proposed trigger system. To do this, it is desired to establish some measure of how well the trigger works for varying signal-to-noise ratios. First, signals are constructed which are about four times longer in duration than the nominal burst duration. The trigger is run for these signals and analyzed. If the trigger algorithm yields trigger signals outside of the nominal burst envelope, the signal is labeled as yielding spurious triggers. If the signal yields no spurious triggers and contains a proper trigger within the burst duration, the trigger procedure is considered successful.

The details of the signal used for simulation follow. For each value of  $SNR_1$  (ranging from about 4 to 24 dB), 100 different signals for each of the six channels were tested, making 600 individual signals. For each signal, a different set of broadband Gaussian noise was added. It was assumed that downmixing and separation of each channel could be done successfully using the same electronics arrangement employed for the CCLDV; therefore, the burst frequencies were in the range from 0 to 5 MHz. Each of the signals had a different burst frequency which was sampled from a random uniform distribution in the range from 0 to 5 MHz. Each of the burst signals also had a different arrival time relative to the reference time which was also sampled from a random uniform distribution in the range from  $-$ 'nominal burst duration'/16 to  $+$ 'nominal burst duration'/16. The 'nominal burst duration' was kept constant at 15 microseconds with  $1/e^2$  duration of 5 microseconds. The sampling rate was set to be the same as the A/D board (250 MS/s), but the signal with noise added was low-pass filtered so that only the noise in the band 0-5 MHz band would contribute. The total length of the signals tested was 40 microseconds. The amplitude of the burst envelope was not varied among signals, so the RMS value of the noise could be easily calculated for each value of  $SNR_1$ . It should be noted that in the general case, it is dangerous to use the same envelope for all the signals, but this is a feasible simplification when monodisperse seeding is used. Note also that the values of  $SNR_1$  were computed with 'N' being the number of samples taken over the nominal burst duration (see Shinpaugh et al. 1992).

The final detail of the simulation is the setting of the threshold value for the first Schmitt trigger. In the electronic version, the threshold values will not be adjusted, but the signal carrier voltage will be adjusted using a bias circuit. However, in this simulation, it is sufficiently rigorous to simply allow adjustment of the threshold voltage. This was varied according to  $SNR_1$ . The threshold voltage was set as the RMS voltage of the noise plus 50% of the peak signal amplitude. Of course, this value is not known *a priori* when acquiring data, but the signal voltage can be empirically adjusted to maximize the valid trigger rates, in effect satisfying the simulation conditions.

## Results

As mentioned, 100 independent six-burst signals were analyzed with the analog trigger process described previously. The trigger signals were tested to determine both if spurious and/or valid triggers were present. If a signal contained any number of spurious triggers outside of the nominal burst envelope, the trigger was considered unsuccessful. Only when trigger signals were present and confined to the nominal burst duration were the signals considered successful.

Figure 4 is a plot of the results. The results are reported as percent of the total number of signal segments analyzed versus  $SNR_1$ . The length of the signal segments relative to the burst contained within makes it possible to infer that the results for the ensemble represent the results to be encountered in real signals. It is seen that the trigger system correctly identifies signals 100% of the time for  $SNR_1$  above 20 dB. This is sufficient since only those signals with  $SNR_1 > 20$  dB yield acceptable Doppler frequency estimate accuracy with the FFT. The high rates of spurious triggers below this value can be avoided by simply increasing the voltage threshold.

The only aspect of signal noise not considered is the appearance of noise spikes. Since these spikes originate independently from the two photomultiplier tubes, the logical NAND gate used will discard the spikes.

## Conclusion

The proposed LDV triggering systems have been validated using computational simulations. It has been shown that even for signals with  $SNR_1$  values too low for accurate frequency domain processing, the presence of a burst envelope is detected a majority of the time. For signals in the acceptable  $SNR_1$  range, burst detection was 100%. These results show that this relatively simple trigger system can be very effective for detecting LDV bursts in multiple channel systems.

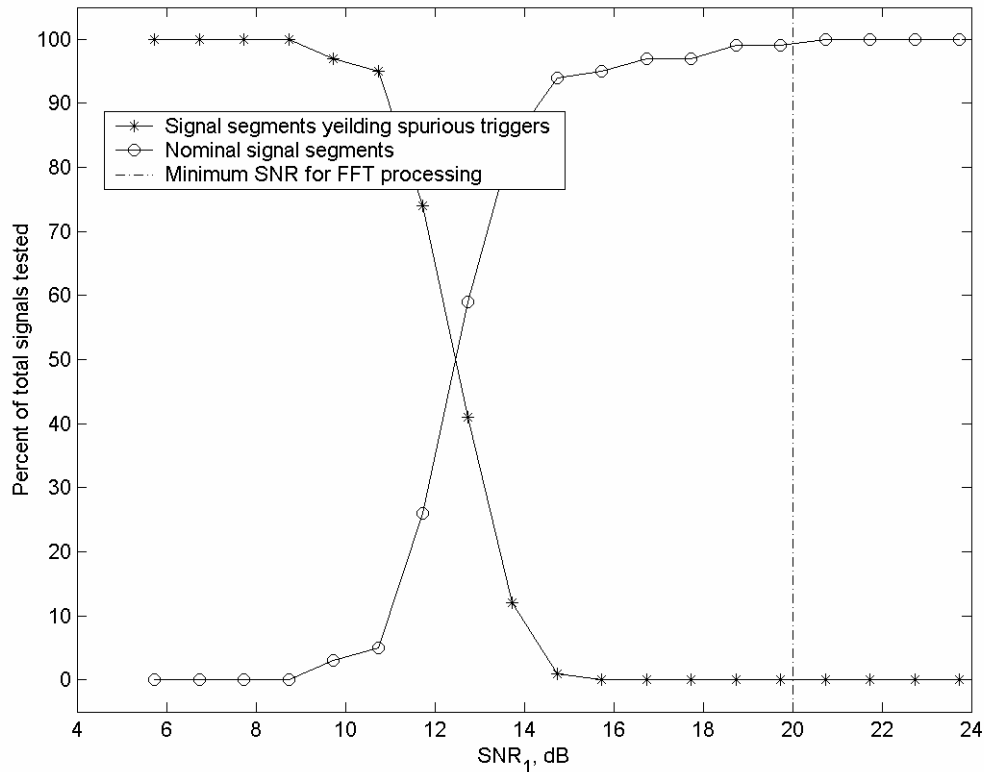


Figure 4. Plot of the simulation results.

### Breadboard Development Process

Benchtop experimentation was used to fine-tune the trigger circuitry. A temporary electronics station was set up with the essential equipment needed to work out the details: 4-VectorVid 0-20V DC regulated power supplies; a multimeter, two function generators up to 2 MHz, one with amplitude modulation; and the Strategic Test PC-based scope. The test signal used was amplitude modulated at 100 kHz to simulate the Gaussian burst window. Using the test signal, each step of the process in figure 1 was tested to ensure the proper behavior.

Three CMOS integrated circuits (IC) packaged as 14-pin DIPs were chosen to perform the essential tasks of the trigger device. A Texas Instruments model CD74HC14E Hex-Inverting Schmitt Trigger (i.e., 6 Schmitt triggers on each IC) was chosen for the first Schmitt trigger illustrated in figure 1. This IC has a high frequency response relative to other CMOS Schmitt triggers available, up to about 8 MHz based upon its low-to-high transition time. Experimentation with the chip revealed overshooting when rapidly changing states, but this behavior was filtered out by the subsequent low-pass filter and thus did not detrimentally affect the circuit. The second Schmitt trigger chosen was a Texas Instruments model CD40106B Hex-Inverting Schmitt trigger. This trigger has a much lower frequency response than the CD74HC14E, but considerably better transient behavior. The NAND function was accomplished with the CD4011BE Quad 2-input NAND gate IC. With two of the CD4011BE's, it is possible to test each of the trigger signals for coincidence.

The digital ICs chosen prefer inputs between ground and the supply voltage (4-6V). This requires a DC offset of the Doppler burst signal. By carefully adjusting the DC offset of the incoming burst, precise control of the effective trigger level of the signal is achieved. The DC offset value is controlled with a voltage divider utilizing a 10-turn 10kOhm potentiometer. The DC offset circuit is based upon the Mini-Circuits bias tee. This circuit, see figure 5, simply consists of a capacitor and an inductor which join the AC and DC signals. Using relatively large values for each of the two components ensures that the DC signal does not affect the AC signal prior to the bias tee, and vice versa. The capacitor used is 0.1 micro-Farads and the inductor is 1000 micro-Henry.

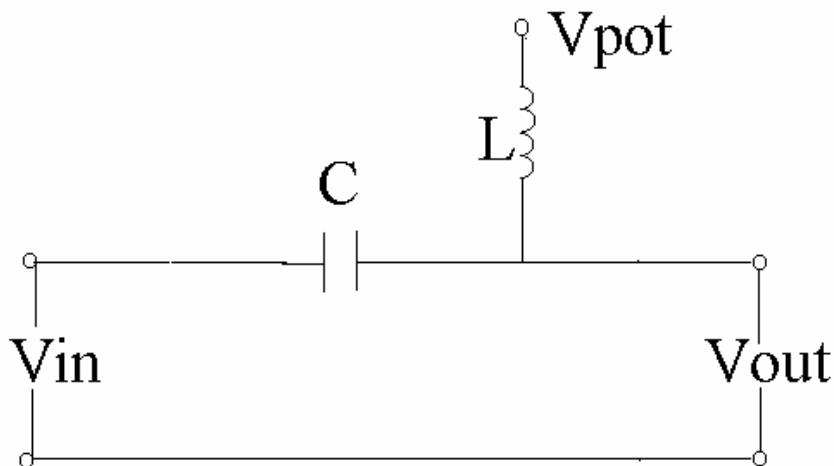


**Figure 5. Bias tee circuit.**

The low-pass filter chosen was a simple RC filter (see figure 6). By considering the expected minimum duration of the bursts, the cutoff frequency for the filter may be determined. The cutoff frequency is determined approximately as

$$f_{co} \approx \frac{1}{RC}$$

Assuming burst durations as short as 3 microseconds,  $f_{co}$  was chosen as 0.667 MHz. Common components were chosen for the resistor, 1 kOhm, and the capacitor, 0.0015 micro-Farads.

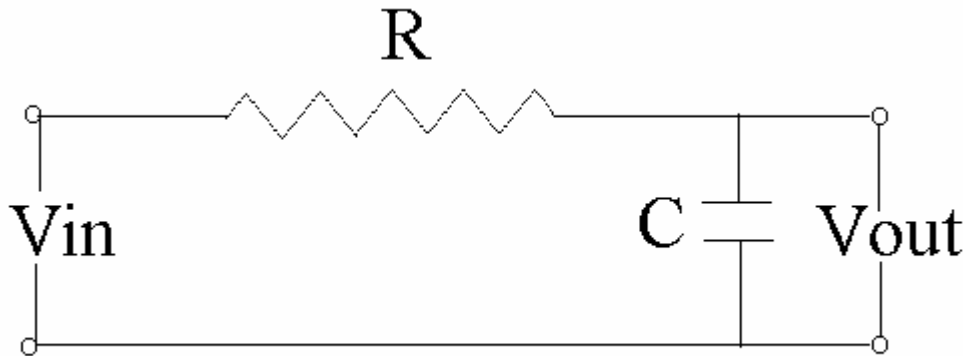


**Figure 6. RC low-pass filter circuit.**

Much time was spent in the development process in attempting to create a monostable trigger pulse. Such a pulse would be the same duration for any triggered signal, thus setting a coincidence window for the LDV signals. The monostable multivibrator pulse was generated using two methods—with the CD40106B, as described in its datasheet and with the famous 555 timer. While either of these circuits would create the desired pulse, generating a proper trigger for these circuits proved difficult. Since the multivibrator will remain ‘high’ as long as the trigger signal is ‘high’, one must control the trigger signal to generate the prescribed pulse. The multivibrator was to be triggered by the output of the second Schmitt trigger which was variable in duration. When this trigger was longer than the desired pulse length, the resulting pulse was too long. A common remedy for this is the RC high-pass filter which is the same as the circuit in figure 6, but with the resistor and capacitor switched. To generate a short enough trigger pulse, the capacitor used was so small that it severely attenuated the peak voltage. If this pulse is amplified, the pulse was broadened and the circuit further complicated. Another solution attempt was to digitally ‘subtract’ the trigger pulse from the multivibrator pulse using the exclusive OR digital gate. This method proved effective for long trigger pulses, but eliminated the multivibrator pulse when the trigger pulse was shorter than the multivibrator pulse. This method also suffered from an increase in complexity. Since this step in the circuit obviously caused an increase in complexity without a huge payoff (i.e., the simulation showed excellent results even with a variable pulse width), in the interest of time the multivibrator pulse circuit was abandoned.

A final feature of the trigger circuitry is the ability to control which signals are desired to be in coincidence. This feature is very important for alignment of the probe. Using a toggle switch on each of the six channels which switches between ground and the

pertinent signals, one can turn on or off the effect of each channel on coincidence. Since the triggered state is ground, the NAND gate will change states when the individual triggers are all grounded. Thus, by setting unused channels at ground state, any transition to ground by the desired channels will result in a trigger edge.

### **Refinement and validation using single channel flow signals**

The single-channel trigger circuit described was tested with actual flow signals in a nominally 2D flat-plate turbulent boundary layer flow at  $y^+=O(300)$ . This test was carried out to refine the downmix circuitry for the PMT signal and to validate the functionality of the trigger circuit with real Doppler burst signals.

Several refinements to the signal conditioning circuitry were made during the flow tests. First, it was discovered that the PMT which measures green light performs much better with a 50 Ohm load attached to its output. By using this load, interference signals were reduced considerably. The PMT signals were amplified by two successive Mini-Circuits ZFL-500LN amplifiers which allowed for lower PMT voltages and thus higher overall SNR. The RF generator used in the tests was amplified by a single ZFL-500LN prior to being mixed with the amplified PMT signal. In the tests, the three-way splitter was not used, though its impedance should not adversely affect the signal. The signal output from the mixer was filtered by the Mini-Circuits BLP-5 low-pass filter with a nominal cutoff frequency of 5MHz. This downmixed and low-passed signal was then amplified by another ZFL-500LN and sent to the trigger circuit.

Using the signal conditioning configuration discussed, consistent triggers were output from the single channel trigger circuit. Figure 7 is a screenshot of the scope during a representative burst/trigger event. In this screenshot, it is actually seen that two bursts are acquired in the time window. Though the on-board trigger for the A/D converter card had to be set too high to acquire the first burst seen in order to avert noise, the narrow-band technique successfully discriminated this bursts from the noise. This screen shot shows the effectiveness of the technique, even in its first trial.

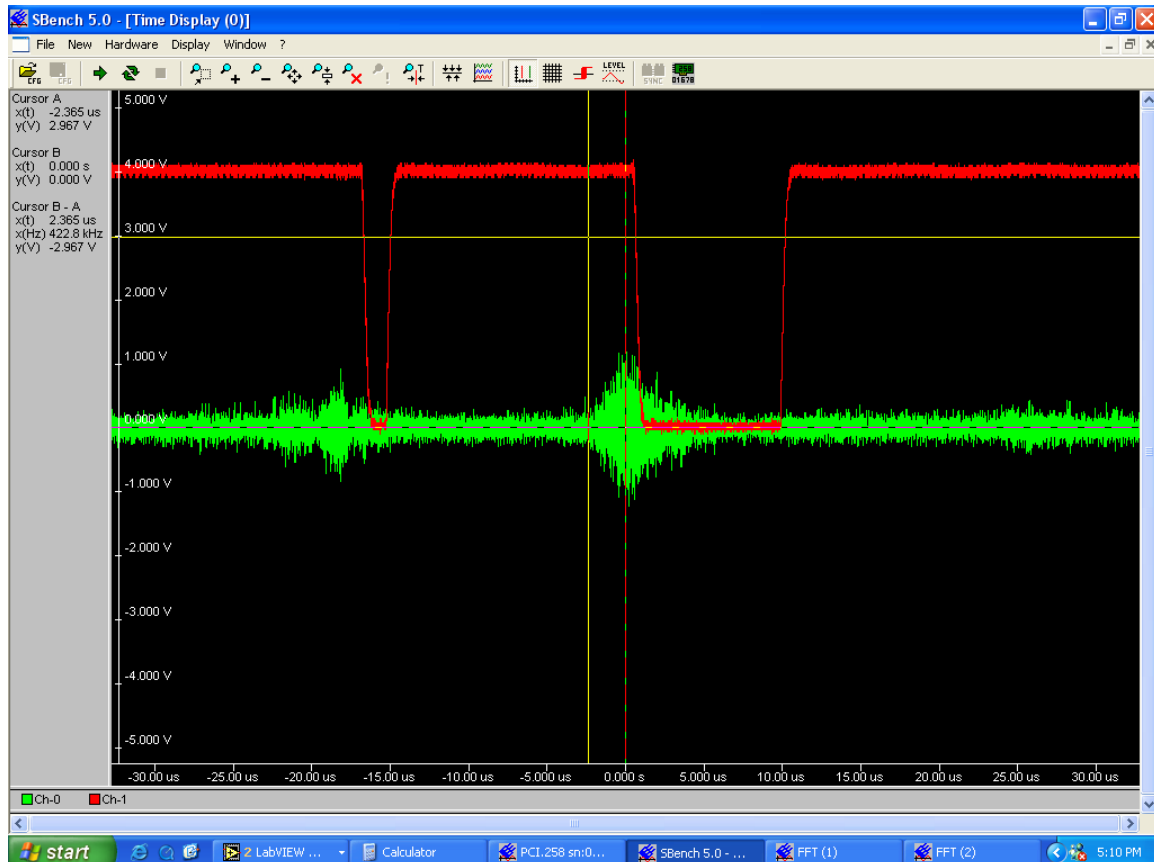


**Figure 7. Screen shot of the scope program displaying the PMT signal (green) with the burst detection signal (red).**

## References

Qui, H-H., Sommerfeld, M., and Durst, F. 1994 “Two novel Doppler signal detection methods for laser-Doppler and phase Doppler anemometry,” *Measurement Science and Technology* **5**, 769-778.

Shinpaugh, K.A., Simpson, R.L., Wicks, A.L., Ha, S.M., and Fleming, J.L. 1992, “Signal-processing techniques for low signal-to-noise ratio laser-Doppler velocimetry signals,” *Experiments in Fluids*, Vol. 12, pp 319-328.

# Vita

Kevin Todd Lowe began attending Virginia Tech in 1997 as a recipient of a Hahn Engineering Scholarship. As a senior in the 2000-2001 academic year, he was part of the International Aircraft Design Team organized by Prof. James Marchman in collaboration with Loughborough University in Loughborough, England. Later that academic year he was honored by his peers as the Virginia Tech Sigma Gamma Tau Student of the Year. He received a B.S. in Aerospace Engineering in May 2001, graduating *summa cum laude*. He continued his education at Virginia Tech as an advisee of Prof. Roger L. Simpson. In more than 5 years of work as a graduate assistant in the Virginia Tech Department of Aerospace and Ocean Engineering, he co-developed advanced laser-Doppler velocimetry instrumentation for the Turbulent Boundary Layer Research Laboratory. During this time, two subsystems for signal detection, acquisition, and processing that he developed were shared through collaborative efforts with researchers at the NASA Langley Research Center to update their capabilities. In this same time, he has served two years as instructor and three as the graduate student administrator of the senior-level Aerospace Engineering laboratory course with duties including experimental setup in subsonic and supersonic flow facilities. He completed a M.S. in Aerospace Engineering in May 2004. He will continue to pursue his research interests in optical flow diagnostics, signal processing, and complex flow research upon graduation.